Liquefaction-Targeted Ground Motion Parameters

Andrew J. Makdisi

A dissertation submitted in partial
fulfillment of the requirements for the degree of

Doctor of Philosophy

University of Washington

2021

Reading Committee:
Steven L. Kramer, Chair
Pedro Arduino
Brett W. Maurer

Program Authorized to Offer Degree:
Civil and Environmental Engineering

University of Washington

Liquefaction-Targeted Ground Motion Parameters

Abstract

Andrew J. Makdisi

Chair of the Supervisory Committee:
Prof. Steven L. Kramer
Civil and Environmental Engineering

Earthquake-induced ground failure, resulting from liquefaction of loose sand and soft clay deposits, has caused tremendous damage to the built and natural environment. Ground failures due to lateral spreading, an effect of soil liquefaction at sites on mildly sloping ground or in close proximity to natural or man-made free faces, has been observed to pose significant risks to bridge pile foundations, underground utilities, and shallow foundation systems. Conventional design guidelines in the United States are typically centered on analysis of the liquefaction triggering limit state, by computing a factor of safety (FS_L) that considers a single, probabilistic level of earthquake ground shaking. When compared with fully probabilistic analyses of liquefaction triggering that consider all levels of ground shaking, conventional analyses may result in inconsistent representations of the actual liquefaction hazard in different regions of the U.S. Furthermore, analyses that focus on the triggering limit state, rather than the effects of liquefaction (i.e. ground deformations), are generally insufficient in predicting physical damage and losses, particularly in probabilistic frameworks.

In this study, a computational platform for fully probabilistic liquefaction hazard analysis (PLHA) is developed and utilized to evaluate the degree to which conventional liquefaction hazard analyses deviate from the actual liquefaction hazard for the triggering limit state. A comparison study between PLHA-based and conventional estimates of FS_L indicates a large degree of inconsistency both at the regional and national scale, with some parts of the U.S. designing for nearly three times the implied hazard as others when using conventional analyses. To address this inconsistency, a framework is presented for mapping a liquefaction-targeted ground motion intensity measure for a reference soil and site condition, that, in conjunction with site-adjustment factors can be used in conventional analyses to obtain hazard-consistent estimates of FS_L. The framework is validated for a range of geographic locations, seismotectonic environments, soil parameters, and site conditions.

Finally, recognizing the need to focus on the effects of liquefaction, a large-scale, simulation-based parametric study, consisting of nonlinear finite-element dynamic analyses performed via a high-performance computing platform, is presented for investigating the physical mechanisms that contribute to lateral spreading-type ground failures. The results of this study are used to develop and present a probabilistic framework for predicting post-triggering ground deformations that accounts for the time of liquefaction during during earthquake motions, as well as system-level effects such as the reduction in seismic demands due to liquefaction in deeper soil strata.

Contents

List of Figures

List of Tables

Acknowledgments

First and foremost, I would like to extend my gratitude towards Dr. Steven L. Kramer for his mentorship, guidance, support, and friendship over the past few years. Without his vision, technical expertise, and years of experience as a leader in the field of earthquake geotechnics, none of the work presented in this dissertation would have been remotely possible. Without his sense of humor, approachability, and his collaborative spirit, my experience as a doctoral student would not have been nearly as enjoyable and rewarding as it was. I have learned so much from working with him over the years, both in academics and in life, and am beyond grateful for the opportunity to have done so. I also would like to thank Dr. Pedro Arduino, Dr. Brett W. Maurer, and Dr. Kenneth C. Creager for their roles on my dissertation reading committee. Their feedback and advice was essential, and I highly enjoyed my conversations with them over the course of the final year of my research work. I would additionally like to thank Dr. Arduino, Dr. Long Chen, and the rest of the Computational Geotechnics group at the University of Washington for their collaboration and technical advice in a large portion of my dissertation research. This research was made possible through funding from the National Institute of Standards and Technology, the Washington State Department of Transportation, and the EERI FEMA/NEHRP Graduate Fellowship; the support from these groups is gratefully acknowledged.

I am very fortunate to be a part of the University of Washington community, and would like to extend my gratitude to my student cohort and faculty in the Geotechnical and Structures graduate groups at the U.W., for their friendship and support over the years. This was truly an amazing group, and one that I hope to stay connected beyond my graduate school days. I would also like to thank my friends and family; my mother Rima, my father Faiz, and my sister Joy. I cannot thank them enough for their guidance, support, and love, and I could not have gotten this far without them. Finally, I have to thank my partner Sarah, who has been there for me every step of the way, who picked me up every time I was down, and whose belief in me never seemed to waver for a second even if I was doubting myself. Thanks again to all those mentioned here, and many countless others.

Chapter 1

Introduction

Among the many types of natural disasters throughout the world, none seem to mystify and confound society - from scientists, engineers, lawmakers, and the general public - more than earthquakes. While other events such as hurricanes and wildfires are certainly as destructive, damaging, and terrifying, earthquakes occur essentially without warning, forcing policymakers to grapple with preparing for an event that can happen at any moment, with no way to warn or evacuate citizens beforehand.

Earthquakes pose a diverse array of threats to all facets of society, with some of the most immediately observable and tangible effects on the built environment. Strong ground shaking can severely damage buildings and their contents, roadways, or bridges. Even when shaking isn't necessarily strong enough to cause direct structural damage, significant damage to buildings, bridges, dams, and critical underground infrastructure can occur due to failure of the ground supporting these systems.

The phenomenon of *soil liquefaction* is a process by which loosely deposited sands or soft clays lose their strength and stiffness during relatively strong, sustained ground shaking. First observed in the field in 1964, soil liquefaction has been the subject of intense research, scrutiny, and debate over the past half-century or so, and its effects remain among the most difficult seismic hazards to characterize and predict in practice. In particular, one of its most damaging effects, known as *lateral spreading*, which occurs in gently sloping ground and leads to permanent horizontal ground deformations ranging from several centimeters to a few meters, has long been notoriously difficult to predict in practice.

Much of the uncertainty inherent to liquefaction-related problems is due to a combination of the uncertainty in predicting earthquakes and ground motions, the variability in soil conditions

at a particular site, and the limitations of our ability to model and capture all of the factors that contribute to surface manifestations of liquefaction at a given site. This uncertainty naturally lends itself to approaching these problems within a framework known as *performance-based earthquake engineering*, which seeks to combine the uncertainties inherent to predicting various types of seismic response and damage in structural or geotechnical systems in a manner that allows for probabilistic estimation of losses.

Critical to the effective use of PBEE is the identification of ground shaking intensity measures that are closely related to the types of response engineers wish to predict. Historically, ground shaking intensity characterization has been focused on peak amplitude parameters, such as peak or spectral accelerations, due to their intuitive connection to estimating peak structural loads or stresses. However, more and more evidence over the past couple of decades has indicated that peak intensity measures are typically not the most efficient way to predict a wide range of response variables, particularly because they fail to capture the effects of shaking duration on the degradation in strength and stiffness of structural materials and soils alike.

Recognizing such inefficiencies, this dissertation explores the concept of characterizing ground shaking intensity specifically through the lens of liquefaction-related hazards. Chapter 2 presents the mechanics behind liquefaction and lateral spreading, as well as various methods for analyzing and predicting these problems, and the performance-based earthquake engineering framework. Chapter 3 combines many of these aspects to present the concept of probabilistic liquefaction hazard analysis (PLHA), and a Python-based code platform that was developed as part of this research for performing such analyses. In Chapter 4, current methods for liquefaction hazard evaluation are shown to result in inconsistent representations of the actual liquefaction hazard across the United States, and a framework for mapping liquefaction-targeted ground motion intensity measures is presented to correct this non-uniformity, and result in more consistent applications of conventional liquefaction hazard analyses around the United States.

Motivated by the need to focus more on the effects of liquefaction - rather than on the liquefaction triggering limit state, as is the case in current liquefaction hazard evaluations - Chapter 5 presents the development of a large-scale numerical parametric study for investigating the physical mechanisms that contribute to lateral spreading displacements, and highlights the need to consider the timing of liquefaction and its impacts liquefaction-related effects. A generalized timing-based framework is presented, based on partitioning the analysis into pre- and post-triggering components, and evaluating the ground motion intensity measures that are most efficient at predicting each of the two limit states (triggering and deformations). Chapter 6 presents the results of this large-scale parametric study by developing functional forms for the prediction of post-triggering permanent shear strains, as well as a first-order method for accounting for seismic demand reduc-

tion in liquefiable systems. Chapter 7 validates these predictive components against a larger set of randomized profiles, and synthesizes them to presents a semi-empirical, timing-based framework for predicting post-triggering lateral spreading displacements. A method for incorporating this predictive framework into a fully-probabilistic analysis of lateral spreading displacements is also presented, with a novel application of conditional intensity measures to estimate the joint ground motion hazard curve of pre- and post-triggering IMs, and the eventual computation of hazard curves for lateral spreading displacements.

Chapter 2

Background and Motivation

2.1 Introduction

One of the most prominent and important aspects to geotechnical earthquake engineering is soil liquefaction and its related hazards. Over the past six decades, numerous instances of tremendous damage in earthquakes, attributed to the loss in shear strength and stiffness of loosely-deposited sands and silts, have been observed, documented, studied, debated, and re-hashed by researchers and practitioners alike. Soil liquefaction has caused the collapse of apartment buildings and bridges, triggered spectacular failures in embankment dams and port facilities, and destroyed critical underground infrastructure, causing severe environmental damage and disruption to basic human services.

Liquefaction has also proven to be a notoriously difficult problem to constrain over the decades. It seems that whenever the state of the art and practice has reached anything resembling a consensus on the matter, an earthquake occurs with the potential to cause (or not cause) soil liquefaction in conditions that haven't been seen before, that previous models either over-predict or under-predict, and that highlights certain aspects of the problem that may not have been considered in the past. Such difficulties are simply a part of earthquake geotechnics - geotechnical systems are highly uncertain in the way they are characterized. Soil deposits can be highly heterogeneous in three dimensions, and the mechanical properties even within a geologic unit can be highly variable and difficult to directly measure. Combine this spatial variability in soils with the difficulty we face in predicting earthquakes and ground shaking intensities, and the uncertainty in the problem can seem almost intractable. However, if the problem is approached from a probabilistic standpoint, where time, money, and energy is spent understanding, quantifying, and ultimately reducing uncertainty in such problems, engineers can provide a rational framework for placing earthquake-induced

liquefaction (and any other natural hazard) within a larger context of *risk-based analysis*.

In this chapter, a history of soil liquefaction in earthquakes is presented, along with the physical mechanisms that contribute to its occurrence, and the various approaches currently employed by practitioners for predicting its occurrence and effects. Subsequently, a discussion on one of the most damaging effects of liquefaction, known as *lateral spreading* is also presented, with further discussion on current methods for predicting lateral spreading displacements and the challenges inherent to doing so. Throughout this chapter, emphasis will be placed on the various forms of uncertainty and potential bias in many of the current methods in use, in order to motivate an overview and discussion on the framework in use by many researchers and practitioners for incorporating uncertainty into earthquake engineering problems, known as *performance-based earthquake engineering*.

2.2 Soil Liquefaction

As it relates to soil mechanics, the first use of the term "liquefaction" can be traced to Mogami & Kubo (1953), in a discussion on the response of soils to vibratory loading. The phenomenon gained widespread recognition 11 years later, as the 1964 Great Alaskan and Niigata, Japan earthquakes caused tremendous damage to their respective surrounding areas, primarily due to extensive ground failure attributed to soil liquefaction.

In March of 1964, on Good Friday, the most powerful earthquake recorded in the history of North America (magnitude-9.2) struck about 125 km east of Anchorage. Tremendous damage to many buildings and underground utilities was caused by liquefaction-induced landslides in a particularly sensitive clay referred to as Bootlegger Cove Clay (Figure 2.1).

About three months later, a magnitude-7.6 event occurred in Japan, about 50 km south of the city of Niigata. Throughout the city, widespread liquefaction of young deltaic deposits produced stunning images of high-rise residential buildings, otherwise largely unaffected by the actual ground shaking (a PGA of approximately 0.20 g was estimated within the city), partially or completely toppled over due to bearing failure of the shallow foundations (Figure 2.2). Elsewhere in the city, multiple deck sections of the over 300 m-long Showa Bridge collapsed reportedly some 70 seconds after the end of ground shaking (Figure 2.3). It was found that the collapse of the simply supported spans was due to a combination of inertial forces due to ground shaking, and a reduction in subgrade reaction and flow failure due to liquefaction within alluvial soils along the banks of the river (Yoshida et al. 2007).

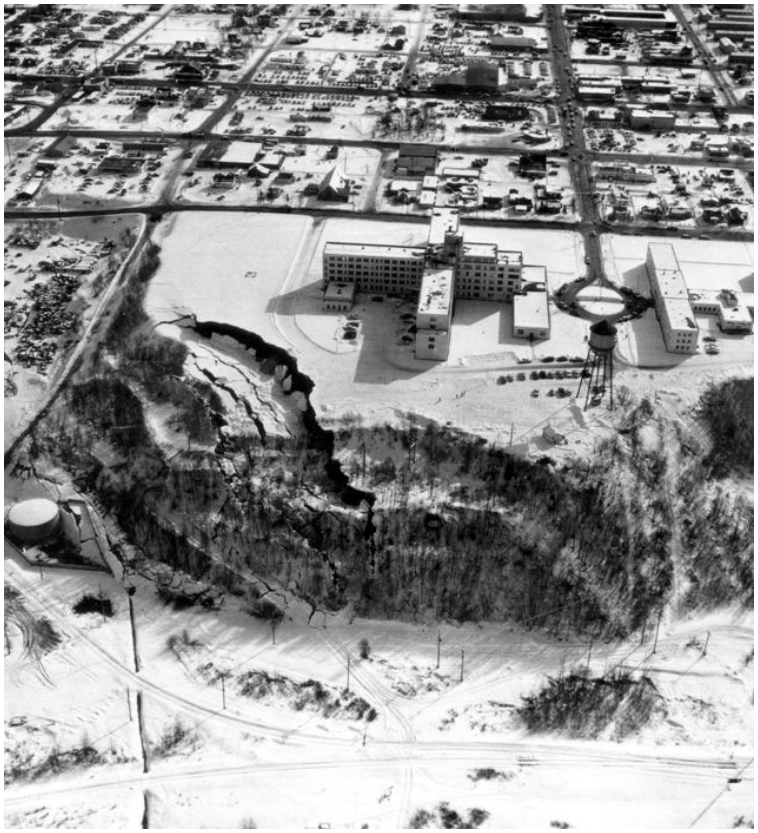

Figure 2.1: Aerial view of the Native Hospital Slide in Anchorage, Alaska, after the 1964 Great Alaskan Earthquake (U.S. Geologic Survey)

Figure 2.2: Collapse of a series of apartment buildings in Niigata city due to liquefaction-induced bearing failure from the 1964 Niigata Earthquake (U.S. Geologic Survey)

Figure 2.3: Collapse of simply supported deck sections of the Showa Bridge in Niigata city, due to ground shaking and liquefaction from the 1964 Niigata Earthquake (U.S. Geologic Survey)

The severity of these events and the time span in which they occurred established soil liquefaction as a significant seismic hazard and key engineering consideration in areas of high seismicity. In the more than 60 years since these earthquakes, the database of liquefaction case histories has expanded tremendously. Some events have served to confirm many of the hazards and mechanisms that were observed in 1964, such as steep landslides (e.g. 1970 Peru), building settlement and bearing failure (e.g. 1999 Kocaeli, Turkey), bridge foundation failure (e.g. 1987 Edgecumbe, New Zealand and 1990 Luzon, Philippines), and underground utility failure (e.g. 1989 Loma Prieta and 2010 Canterbury).

Other events have shed new light on the types of conditions in which liquefaction can occur, and the components of the natural and built environment that can be at risk. The 1971 San Fernando earthquake (magnitude-6.6), which featured the nearly catastrophic failure of the Lower San Ferndando Dam due to liquefaction in hydraulic fill (Figure 2.4), resulted in a decades-long ongoing effort to evaluate and retrofit the seismic stability of many hydraulic fill dams in the western United States. The 1989 Loma Prieta earthquake, undoubtedly the most high-profile seismic event in American history, was notable for, among many other hazards, being one of the earlier events in which lateral spreading deformations were observed to cause extensive damage to shallow foundations (Figure 2.5). The 2010 Canterbury earthquake sequence in New Zealand stands out as one of the most data-rich case histories of liquefaction and lateral spreading, and is particularly notable in highlighting the importance of vertical and horizontal continuity of liquefiable material

(now known as “system response”) on surface manifestation of liquefaction effects (Cubrinovski et al 2018).

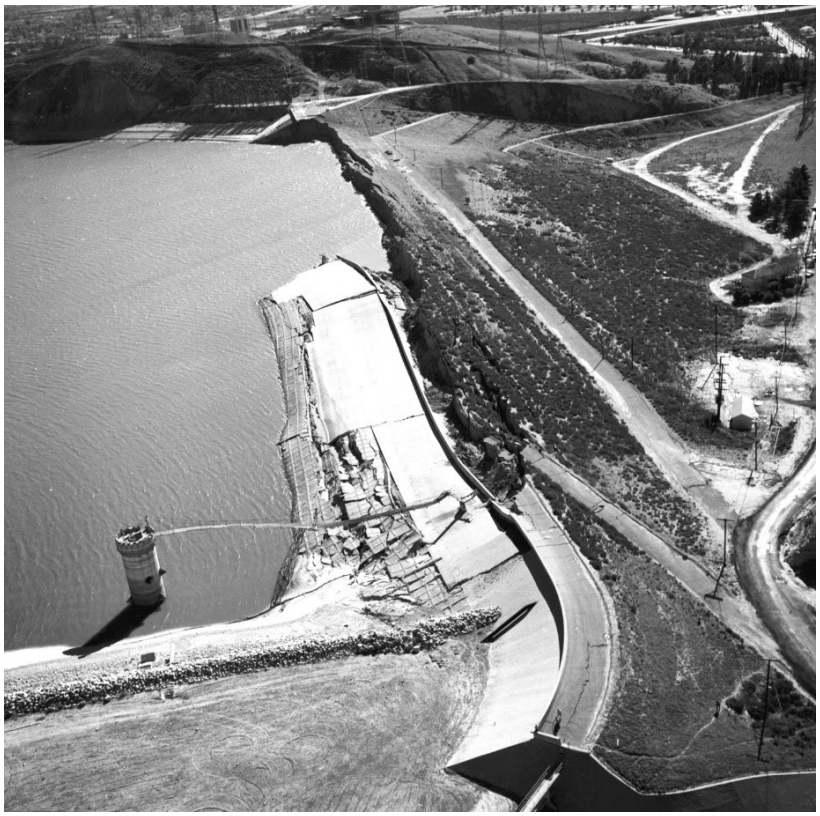

Figure 2.4: Partial failure of the Lower San Fernando Dam due to liquefaction in the the base of the upstream shell. (U.S. Geologic Survey)

Figure 2.5: Damage to Marine Laboratory building in Moss Landing, CA, due to lateral spreading deformations of over 1 meter. (U.S. Geologic Survey)

These events, along with numerous others, have illustrated the variety of ways in which liquefaction can be triggered, and the wide range of site and soil characteristics that contribute to its hazards. At the smallest scales, the triggering of liquefaction in an element of soil results from a relatively straightforward relationship between the characteristics of earthquake loading and the density, plasticity, and stress state of the soil. However, characterizing the effects of liquefaction at the system level requires knowledge of a complex set of factors, including the vertical and horizontal layering of liquefiable deposits, the regime of hydraulic conductivity, surface topography, and presence of structural components such as pipelines, piles, retaining walls, and foundation footings. In this section, the fundamental mechanics of liquefaction are explored at the elemental level, while in Section 2.3 the aforementioned system-wide factors are examined through the lens of lateral spreading.

2.2.1 Mechanics of Liquefaction

The occurrence of liquefaction is fundamentally linked to the stress-strain behavior of cohesionless material when it is subjected to shear and the resulting interaction between the soil skeleton and pore water (Kramer 2009). The response of sand to shear stress is dependent on a wide range of factors, including the grain-size characteristics of the sand, its depositional environment, and the characteristics of the induced stresses such as amplitude of loading, and drainage conditions. This section explores how each of these factors affect the stress-strain response of sand, and in turn how

stress-strain behavior provides a framework for understanding the mechanics of liquefaction as a whole.

Response of Cohesionless Soils to Drained Loading

The basis of our understanding of the behavior of sands when subjected to shear loads can be traced to a series of drained, strain-controlled triaxial tests performed by Casagrande (1936). In this seminal work, Casagrande described the mechanics governing the volume change characteristics of sands using a simple schematic of an assemblage of sand particles (Figure 2.6). For a densely-packed arrangement of particles to accommodate shearing deformations, the sand particles must roll and slide up and over each other, resulting in an ultimately looser arrangement, and therefore a positive volume change. Conversely, a looser arrangement of particles will collapse into a denser arrangement when subjected to shear loading, resulting in a decrease in volume.

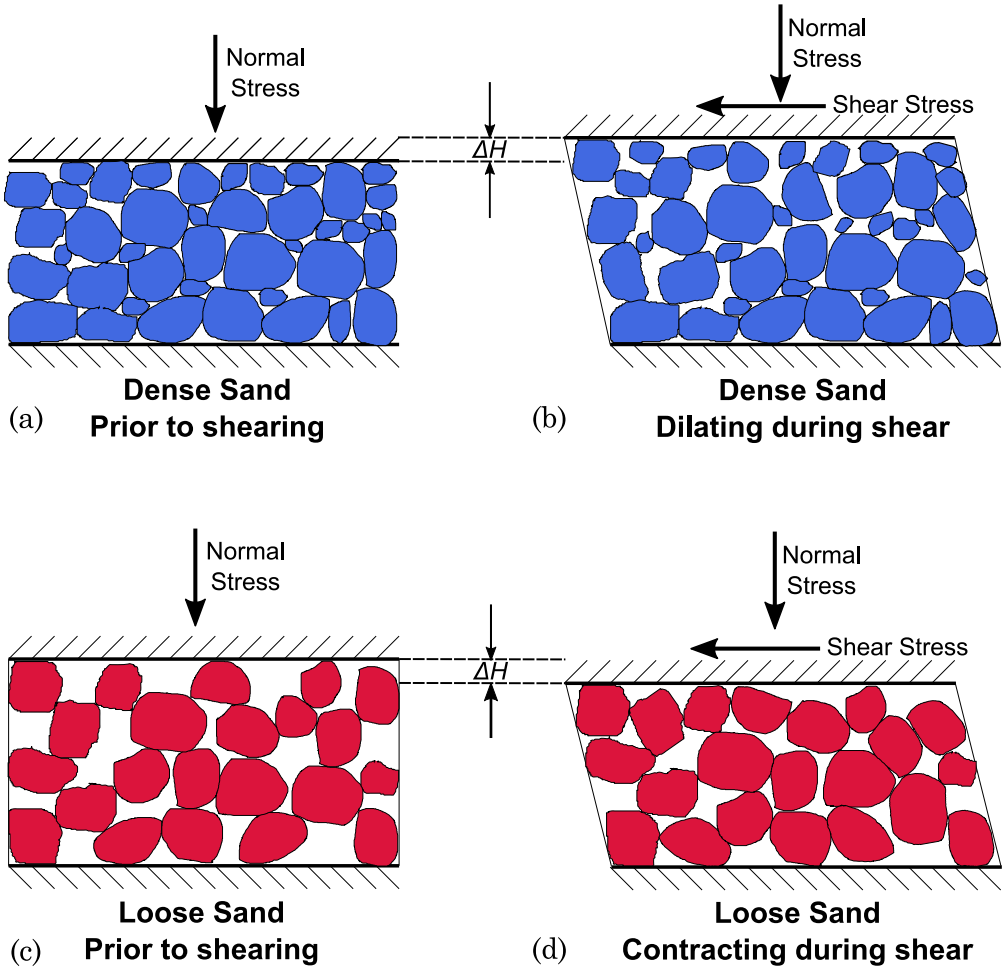

Figure 2.6: Particle assembly schematic illustrating the volume change tendencies of loose and dense sands when subjected to drained shear (after Casagrande, 1936).

Casagrande further observed, based on test results of samples prepared at different densities but consolidated to the same confining pressures, that samples of the same material reached the same ultimate shearing resistance and density at failure (Figure 2.7). Casagrande referred to the sample void ratios at this state as the "critical void ratio", which formed the basis of the critical state description of soil mechanics. The state at which a soil is being sheared continuously with no changes to shearing resistance, density, effective stress, or strain rate is referred to as the *steady state of deformation*.

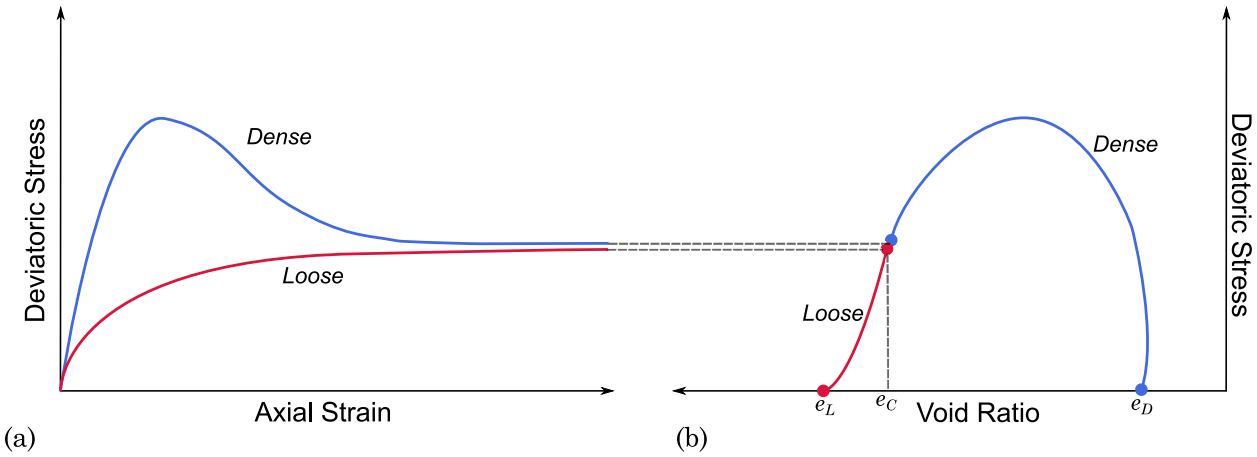

Figure 2.7: (a) Stress-strain and (b) Stress-void ratio curves illustrating the behavior of loose and dense sands in response to drained shear, under the same initial confining pressure. Note the tendency for both densities to reach the same shearing resistance and void ratio at critical state (after Kramer, 1996).

Response of Cohesionless Soils to Undrained Loading

When a saturated specimen of sand is instead subjected to undrained loading, the interparticle interactions outlined above do not result in increases or decreases in volume, since the specimen is a closed system. A series of undrained triaxial tests performed by Lee and Seed (1969) showed that the tendency for dense sands to dilate during shear is accommodated by a decrease in porewater pressure (and a corresponding increase in the effective stress), while the tendency for loose sands to contract during shear is accommodated by an increase in porewater pressure (and a decrease in effective stress). In contrast to the case of drained loading, specimens prepared at different void ratios, but the same initial effective stresses, tend to reach different shearing resistances and effective stresses at failure (Figure 2.8).

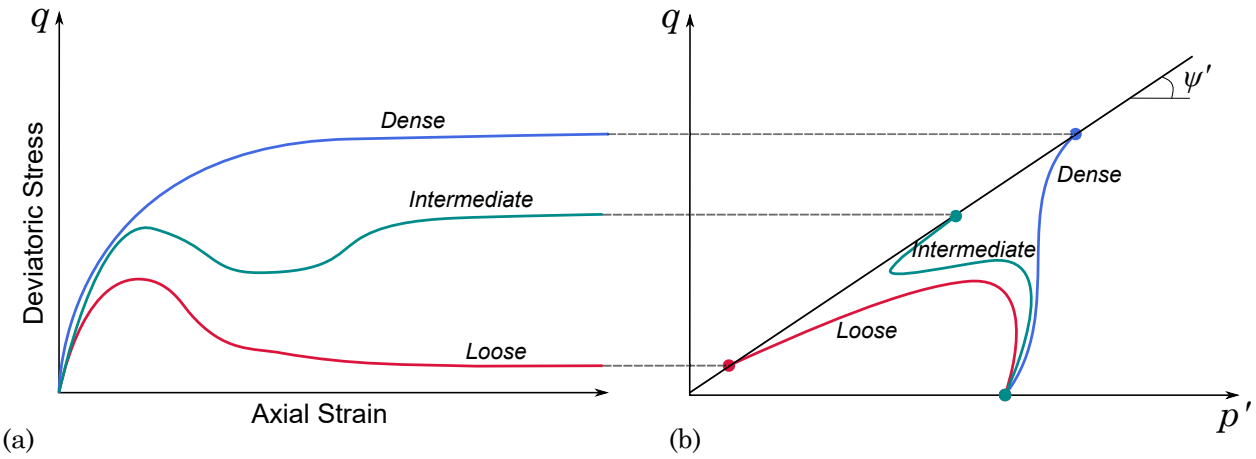

Figure 2.8: (a) Stress-strain curves and (b) Stress paths, illustrating the behavior sand at different densities in response to undrained shear, under the same initial confining pressure. (after Kramer, 1996)

However, Seed and Lee observed that specimens prepared at different densities, but consolidated to the same initial effective stress tended towards the same effective stress and shearing resistance at failure (Figure 2.9).

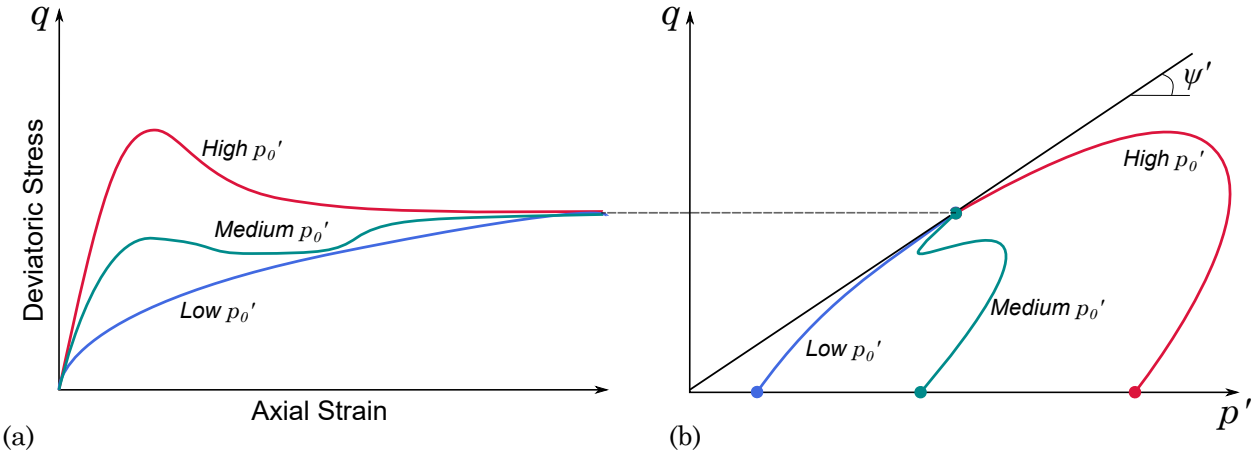

Figure 2.9: (a) Stress-strain curves and (b) Stress paths, illustrating the behavior sand at a constant density in response to undrained shear, under varying confining pressures. Note the tendency for each sample to reach the same shearing resistance at critical state (after Kramer, 1996).

The behavior of the intermediate density specimen in Figure 2.8 and the medium confining pressure specimen in Figure 2.9 reveal some important complexities in the behavior of soils in undrained loading. In both cases, the soil reaches an initial peak shearing resistance, followed by an increment of strain-softening response before ultimately dilating to its critical state conditions. Yoshimine and Ishihara (1998) formalized this type of behavior by proposing several distinct states of undrained shear.

The general set of behaviors outlined by Yoshimine & Ishihara are shown in Figure 2.10. Yoshimine & Ishihara used the term *ultimate steady state* to describe the condition at the final stage of undrained shearing (USS). Materials that have undergone post-peak strain softening and no subsequent hardening were described to have reached a *critical steady state* (CSS), which coincides with the portion of the USSL at extremely low void ratios and extremely high confining stresses. The term *phase transformation* (PT) was used to described the point at which the minimum effective stress is reached and the shearing behavior transitions from contractive to dilative. Material with higher initial void ratios or confining stresses that experience post-peak strain softening, thereby reaching a local minimum state before ultimately dilating to reach USS, are said to reach a *quasi-steady state* (QSS) at this local minimum of shearing resistance.

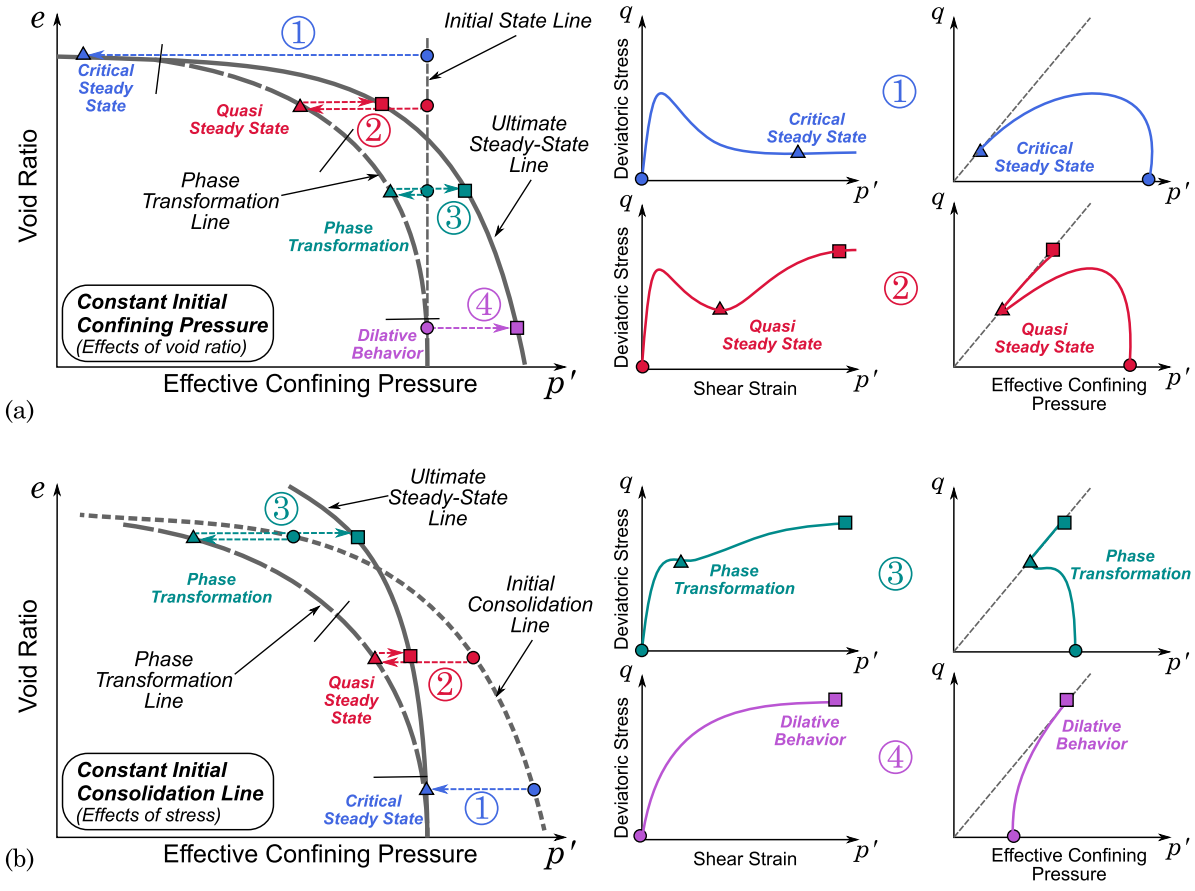

Figure 2.10: General undrained shear behavior of sand under large deformations (after Yoshimine & Ishihara 1998)

How a soil reaches the ultimate steady state, whether via complete contraction (CSS) or some intermediate minimum effective stress (PT or QSS) depends on the soil's initial state relative to the ultimate steady state and phase transformation lines of that soil. The shapes and point of convergence of the USSL and PTL are generally a function of the soil composition and fabric -

cleaner sands tend to have relatively narrow CSS ranges in terms of density (Figure 2.11a), while siltier materials may exhibit the critical steady state more readily (2.11b).

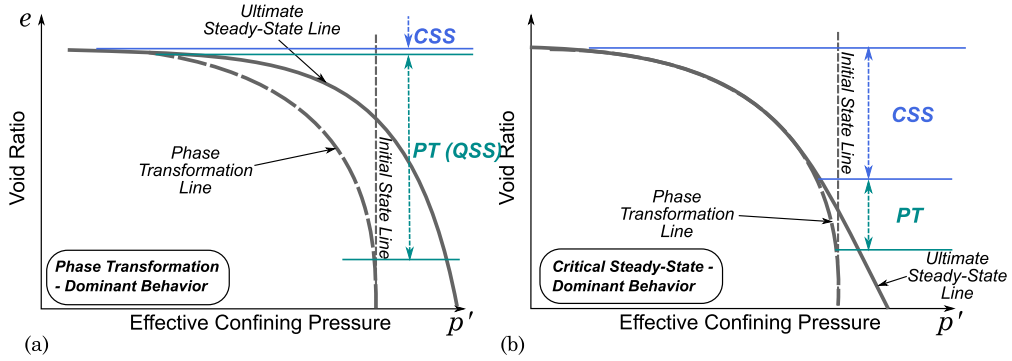

Figure 2.11: Characteristics of undrained shear behavior in material types controlled by (a) phase transformation and (b) critical steady-state behavior (Yoshimine & Ishihara 1998)

The Critical State Concept

The concept that soils in a given depositional environment will tend towards a particular density for a given initial confining stress in drained loading, and a particular effective stress for a given initial density in undrained loading lends itself naturally to describing the shearing behavior of soils using a unique relationship between the void ratio and effective stress once it has reached the point of constant shearing resistance, density, effective stress, and strain rate. This relationship is known as the *critical state line* (CSL); knowing the position of the critical state line for a particular type of soil gives us an idea of how that soil will behave under certain combinations of initial density and effective stress for drained or undrained loading conditions.

Whether or not a soil is will contract or dilate upon shearing is highly dependent on its initial void ratio (or density) and effective stress. Thus, it is useful to examine the combined effects of e_0 and σ'_{v0} by using both parameters to define the soil's initial *state*. By plotting e vs. σ'_{v0} or p' in Figure 2.12, the general response of the soil to shearing can be inferred by its position relative to the CSL. Soil states that plot below the CSL exhibit dilative behavior, and are considered *dense of critical*, while soil states that plot above the CSL will tend to contract, and are described as *loose of critical*.

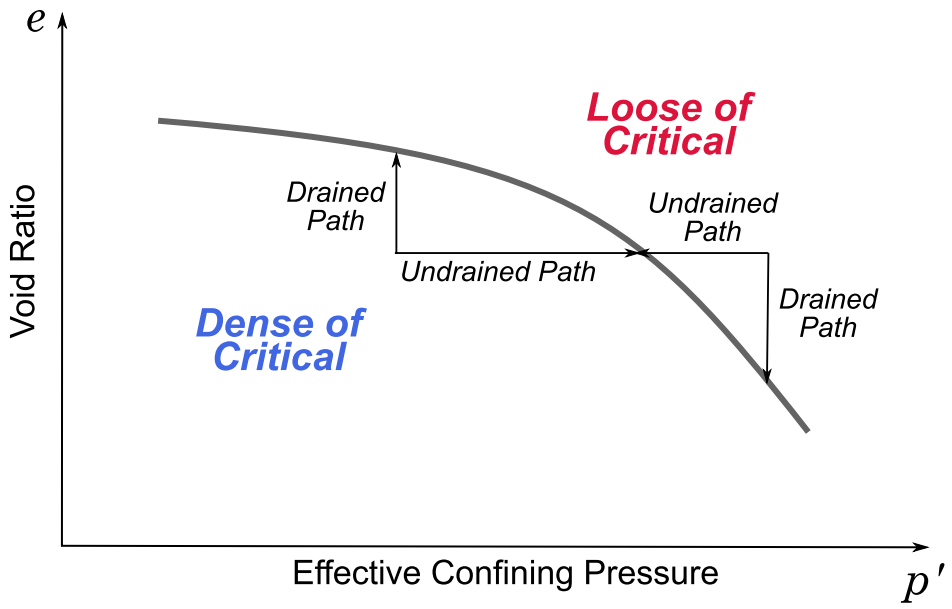

Figure 2.12: Illustration of the Critical State Line (CSL) in void ratio-mean effective stress space, including undrained and drained paths for loose- and dense-of-critical initial states (after Idriss & Boulanger 2008)

It is important to make the distinction between a material's relative density and its density relative to the solid state line. Been and Jeffries (1985) extended the concept of critical state to show that the behavior of sands is related to the proximity of the initial state to the critical state line, and proposed the *state parameter*, ψ, to represent this proximity, defined at a given p' as:

$$\psi = e - e_{cs} \tag{2.1}$$

where e and e_{cs} are the initial and critical state void ratios, respectively (Figure 2.13). A positive state parameter indicates a material that is initially looser than critical state, and would be expected to exhibit contractive behavior in undrained shear, while a negative state parameter indicates dilative behavior of a dense-of-critical material. It is expected that soil states that are similar distances from the CSL will exhibit comparable responses to shear.

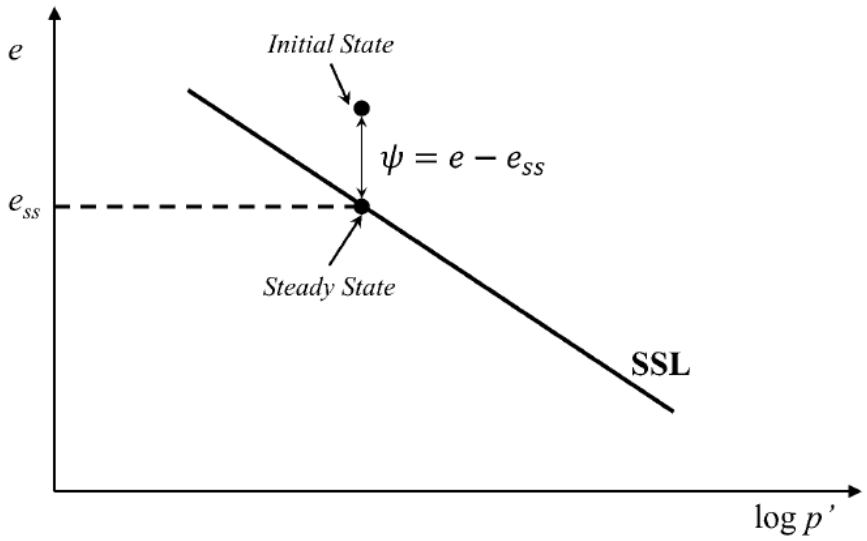

Figure 2.13: Illustration of the state parameter in relation to the steady-state line for an initially loose-of-critical state (after Kramer 1996)

Konrad (1988), found that normalizing the state parameter by (e_{max}–e_{min}) correlated better with dilatant shearing behavior. However, such a normalization requires the determination of its maximum and minimum void ratios, as well as the determination of its critical state line. Idriss and Boulanger (2008) argued that while these characteristics can be determined via careful laboratory testing, the inherent complexities of *in situ* deposits of sand render these types of tests both impractical and not particularly reliable. Alternatively, Boulanger (2003a) introduced the *relative state parameter*, ξ_R, which is defined as:

$$\xi_R = D_{R,CS} - D_R \tag{2.2}$$

where D_R is the current relative density, which can be estimated from penetration resistance test data, and $D_{R,CS}$ represents the relative density at critical state for a given sand. $D_{R,CS}$ is defined empirically, based on the work of Bolton (1986), as:

$$D_{R,CS} = \frac{1}{Q - \ln \frac{100(1+2K_0)\sigma'_{vc}}{3P_a}} \tag{2.3}$$

where σ'_{vc} is the effective overburden stress, K_0 is the coefficient of lateral earth pressure, P_a is atmospheric pressure, and Q is a constant relating to the stress at which particle crushing becomes significant. Intuitively, Q depends on grain type; Bolton (1986) indicated that is approximately 10

for quartz and feldspar, 8 for limestone, 7 for anthracite, and 5.5 for chalk. Boulanger's relative state parameter can be related to the response of sand to shear without using complex and inefficient laboratory test procedures on a case-by-case basis. All that is required is the relative density and *in situ* confining pressure of the soil in question, as well as its granular composition. Boulanger (2003a) used cyclic triaxial and simple shear tests on Fraser Delta sand to show that there is an inverse relation between ξ_R and the ability of saturated sand to resist liquefaction when subjected to cyclic loading when $\xi_R < 0$. In other words, the closer D_R is to $D_{R,CS}$ the less dilative the soil is, and the less resistant it will be to generating excess pore pressures when subjected to undrained shear. Note that $D_{R,CS}$ contains a term that accounts for the in situ effective stress of the soil, thus $D_{R,CS}$ effectively characterizes the interaction between relative density and stress in relation to the critical state.

Cyclic Loading of Sands

Generally, granular soils rarely exhibit undrained response under monotonic loading. The permeability of sandy soils is so high that any momentary excess pore pressures caused by an applied shear load are almost instantaneously dissipated through the relatively large pores of the soil mass. Unless there are significant impedances to drainage of water (such as clay layers or seams), the response of sand to a monotonic load (such as a structural footing or embankment) is modeled in terms of drained strength. However when dealing with rapid cyclic loading, such as those associated with earthquake-induced ground motions, excess pore pressure that is momentarily generated from a single loading cycle often does not have time to dissipate before the next loading cycle (generally a reversal of stress) occurs. It is for this reason that characterizing the undrained response of sand is critical in geotechnical earthquake engineering.

Drained Cyclic Loading

It is instructive to first examine the nature of drained cyclic behavior, since many of its features can be directly related to undrained cyclic loading (Idriss and Boulanger 2008). Figure 2.14 shows the results of a drained, strain-controlled cyclic simple shear test on Ottawa sand (Youd 1972). The general trend throughout the test is an incremental, ratcheting-type net contraction of the specimen. It can be seen that within a particular cycle, the specimen will initially contract after the reversal of the direction of stress. Once the horizontal strain reaches approximately zero, the behavior transitions from contractive to dilative (point D in Figure 2.14). In general, the contractive increments are of a larger magnitude than the dilative increments, resulting in accumulated net contraction.

The magnitude of the net contraction depends on a number of factors. Similar to monotonic

loading, the degree to which the specimen will contract overall is dependent on both its initial density and effective stress. It also depends on the characteristics of the cyclic load being applied to it. Specifically, the larger the magnitude of the applied cyclic shear stress (and thus the greater shear strain the specimen undergoes), the greater the magnitude of contraction the sand will undergo. Of equal importance is the number of applied loading cycles; with each progressive cycle, the sand will accumulate more vertical strain, with the change in void ratio becoming smaller with each cycle.

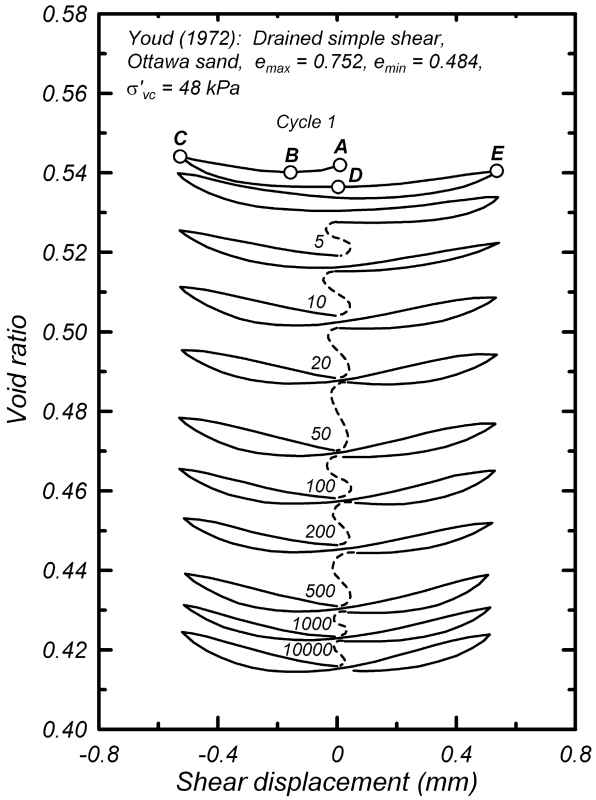

Figure 2.14: (a) Results of a drained cyclic shear test on dry Ottawa Sand (Idriss and Boulanger 2008, after Youd 1972)

Undrained Cyclic Loading

The characteristics of drained cyclic loading introduced in the previous section can be applied in a similar fashion to characterize the response of sand to undrained cyclic loading. In the undrained case, the net contraction, as well as the alternating contractive and dilative behavior seen throughout a single drained loading cycle, is manifested through changes in pore pressure, rather than volumetric strain. These concepts are classically illustrated by the results of an undrained cyclic triaxial test on Sacramento River sand in Figure 2.15 (Boulanger and Truman 1996). The specimen used for this test was a medium-dense clean sand that was anisotropically consolidated to an initial static shear stress ratio ($q/2p'_c$) of about 0.1. We see that with each progressive harmonic

loading cycle, the specimen experiences an increase in pore pressure due to incremental contraction similar to that seen in the drained cyclic loading. As the pore pressure increases, the effective stress decreases, and the specimen moves towards the left in stress path space. In stress-strain space, the sand initially deforms along the same curve throughout the first several cycles, exhibiting relatively small decreases in stiffness.

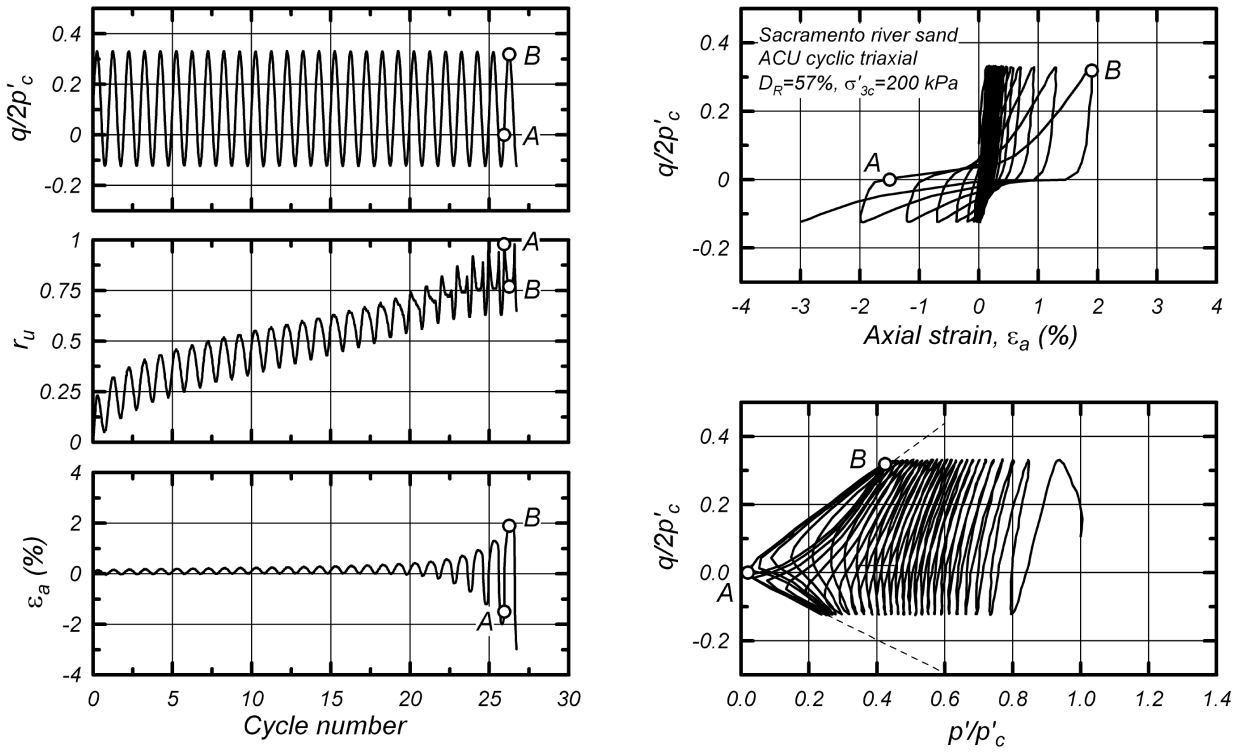

Figure 2.15: (a) Results of an undrained cyclic triaxial test on Sacramento River sand (Idriss and Boulanger 2008, after Boulanger and Truman 1996)

However, as the specimen approaches the failure envelope in stress path space, we see larger decreases in effective stress within each cycle, and increasingly flatter stress-strain hysteresis loops, indicating significant softening of the soil mass. Finally, at about the 27th loading cycle, the effective stress has been reduced to zero (Point A), resulting in the onset of liquefaction. At this point, the total stress in the sample is completely accounted for by the pore water pressure, and thus a large reduction in stiffness occurs, as evidenced by the very flat curve as the specimen is loaded from point A to point B. The accompanying plots of excess pore pressure ratio ($r_u = \delta u/\sigma'_{3c}$) and shear strain show that while the pore pressure increase is relatively consistent throughout the loading sequence, the shear strains are relatively small up until just a couple of cycles before the onset of liquefaction. It is also important to note that when the specimen reaches the failure envelope during a particular loading cycle, it will suddenly dilate within that same cycle before the stress reversal occurs. In stress path space, the sequence of dilation occurs along the same slope as the

failure envelope, and the subsequent cycles after the onset of liquefaction seem to indicate that the system has stabilized somewhat. However, the accompanying stress-strain curve shows that even though the stress path appears to be stable, the shear strain amplitudes continue to increase with subsequent cycles. These seemingly contradictory results can be resolved by noting that this softening is unrelated to the reduction in effective stresses, and is more a result of the softening of the fabric of the soil (Kramer 2009).

Factors Affecting Generation of Excess Pore Pressures

There are numerous factors that can affect the rate at which excess pore pressures are generated during cyclic loading. These factors are generally related to the soil grain characteristics, the soil's initial state, and the characteristics of the applied cyclic load. The effects of these factors can be summarized as follows:

- *Soil Plasticity*: Purely frictional soils such as sands and gravels derive all of their strength from their effective stress. Thus, frictional soils will exhibit increasingly large strains as their effective stress moves towards zero during cyclic loading. More cohesive soils, such as silts and clays, tend to still exhibit some strength even at low effective stresses, and thus are less contractive and less sensitive to reductions in effective stress during cyclic loading, resulting in stress paths that tend to stabilize at a higher effective stress than in purely frictional soils.
- *Amplitude of Cyclic Loading*: In general, the rate of pore pressure generation is directly related to the amplitude of cyclic shear stress imposed on the soil. Larger amplitudes of cyclic loading will cause a larger reduction in effective stress on a per-cycle basis, resulting in a higher rate of excess pore pressure generation, and a few number of cycles required to trigger liquefaction.
- *Initial State*: As discussed previously, the degree to which a soil will exhibit contractive or dilative behavior depends on its position relative to the critical state line. On a per-cycle basis, materials in a looser state or higher confining pressure will see larger reductions in effective stress, requiring fewer cycles to trigger liquefaction.
- *Initial Static Shear Stress*: Soil in sloping ground is subjected to an initial static shear stress prior to any earthquake shaking. In very loose soils, the existence of a static shear stress usually results in lower liquefaction resistance, i.e. fewer loading cycles required to reach initial liquefaction. In medium dense to dense soils, however, the existence of static shear stress can actually increase liquefaction resistance. Increases in pore water pressure generally occurs at points of zero shear stress in the material, when the soil particles begin to reorient

themselves. During cyclic loading, these zero shear stress instances occur during reversals in stress, at the moment in which the sign of the shear stress is changing. For soils subjected to high enough static shear stresses, such a reversal in shear stress may not occur during cyclic loading, and thus pore pressure generation may be somewhat inhibited. In many cases, liquefaction may not occur because the zero effective stress condition is not reached.

2.2.2 Analysis of Liquefaction Triggering

Two conditions typically must be satisfied for liquefaction to occur. First, the soil deposit in question must be sufficiently *susceptible* to liquefaction. Secondly, the seismic loading conditions must be significant enough (i.e. have a large enough amplitude and long enough duration) to trigger liquefaction in the soil deposit in question. Susceptibility is typically characterized by considering several contextual, largely qualitative factors related to the soil's geographic location and geologic characteristics. Analysis of liquefaction triggering involves estimating quantitative representations of both the seismic loading characteristics, as well as the soil's ability to resist such seismic loading.

Liquefaction Susceptibility

Characterizing the liquefaction susceptibility of a soil deposit requires the consideration of multiple criteria. One of the most straightforward criteria for whether or not a material is susceptible to liquefaction is historical - if a particular area has experienced liquefaction in past earthquakes, then it is susceptible to do so again in future seismic events. An obvious method of historical characterization of liquefaction is a review of literature concerning liquefaction case histories at or near the site in question. However, detailed documentation of liquefaction has only been in practice for about the last half century or so, which makes up a very small portion of the geologic time scale that a practicing engineer is interested in. Furthermore, post-earthquake liquefaction reconnaissance is generally limited to examining the evidence of surface liquefaction, such as sand boils, other sediment ejecta, lateral spreading, ground cracks, and ground subsidence. The absence of all of these phenomenon does not completely rule out the occurrence of liquefaction.

Engineers can also consider geologic criteria by considering areas where soils have been deposited under low-energy processes, resulting in loose, uniformly-graded geologic units. This points us primarily towards water-borne modes of deposition, such as alluvial, fluvial, and colluvial deposits. Geologic age should also be considered; Holocene-age deposits are more likely to be susceptible to liquefaction than Pleistocene deposits, due to their tendency to be looser and less cemented, particularly at sites with high groundwater levels.

Special consideration should be given to sites underlain by hydraulic fill material - it has often

been remarked that there is hardly a more effective way to manufacture liquefiable soil than via hydraulic filling. This method was favored in the construction of embankment dams and artificial reclamation projects for decades before liquefaction became a well-known seismic hazard, due to its speed and ease of material transport from quarry to site. However, the process of hydraulic filling fulfills nearly every criterion outlined in this section. It involves the deposition of coarse-grained, purely frictional material in water; it usually occurs in sites where high groundwater conditions are present; and it is obviously very young geologic material with very low density. Indeed, many observed cases of liquefaction have occurred at sites where artificial fill has been placed in order to reclaim land, such as in Dagupan city in the 1990 Luzon, Philippines earthquake; or to build large embankment dams, as was the case in the Lower San Fernando Dam discussed in Section. In particular, the failure of the San Fernando Dam in 1971 forced state government agencies throughout the western United States to re-evaluate the seismic stability of their many embankment dams, resulting in large-scale retrofitting initiatives that are still continuing to this day.

Finally, it is important to at least qualitatively consider the composition and potential volume-change behavior of soils. Doing so, by analyzing the grain size characteristics and *in situ* test data may provide a valuable screening tool for engineering prior to delving into more sophisticated analyses of liquefaction triggering.

Cyclic Stress-Based Method for Liquefaction Triggering

The most common empirical methods, which were initially developed in the 1960s and 1970s and have been continuously refined to the present day, describe the earthquake loading in terms of cyclic shear stresses, and the resistance in terms of the amplitude and number of cycles of shear stresses required to initiate liquefaction. This approach is now commonly known as the *cyclic stress method*.

The deterministic form of the cyclic stress method involves comparing the *cyclic resistance ratio*, or *CRR* with the *cyclic stress ratio*, or *CSR*. The primary index for evaluating the liquefaction potential of a particular element of soil is simply the ratio of these two parameters, known as the *factor of safety against liquefaction* (FS_L):

$$FS_L = \frac{CRR}{CSR} \tag{2.4}$$

Among the most ubiquitous forms of this method in use today comes from Idriss and Boulanger (2008) for SPT and CPT data. Building on the work of Seed and Idriss (1971), this approach

involves representing the earthquake loading as an equivalent ratio of the induced cyclic stress at a given depth in a soil profile to the vertical effective stress at that same depth:

$$CSR = \frac{\tau_{cyc}}{\sigma'_{v0}} \tag{2.5}$$

The approach developed by Seed and Idriss for representing the amplitude of cyclic stress is based on estimating the peak ground acceleration (PGA) at the surface of the site. The use of PGA is convenient in that it can be directly converted into an actual estimate of shear stress by multiplying it by the the total stress at a given depth:

$$(\tau_{max})_r = (\gamma z)a_{max} = \sigma_v a_{max} \tag{2.6}$$

However, the equation above is valid at all depths only if we are considering a rigid mass. Soil columns, particular those susceptible to liquefaction, tend to behave quite flexibly under dynamic loading, thus necessitating a correction factor r_d that reduces the peak amplitude with depth. Furthermore,earthquake time histories generally consist of many cycles, with a wide range of acceleration amplitudes. The demand energy induced by seismic shaking can be approximated as a series of uniform loading cycles; thus, the peak ground acceleration, which can often be the result of a single large pulse, is not the best representation of the earthquake demand energy. Seed and Idriss chose to represent the applied cyclic shear stresses as 65% of the peak value, which is known as the *equivalent uniform value*. By applying the reduction factors due to depth and the equivalent uniform cycles, the applied cyclic shear stress at a given depth can be represented by:

$$\tau_{cyc} = 0.65 r_d \sigma_{vc}(a_{max}) \tag{2.7}$$

Finally, the CSR is modified to a value associated with a consistent earthquake magnitude ($M_w = 7.5$), using a magnitude scaling factor (MSF). The need for a magnitude scaling factor arises from the fact that cyclic resistance of soil is dependent on the number of *equivalent* loading cycles. An equivalent loading cycle is considered to be any exceedance of 65% of the PGA in a given time history; the number of loading cycles has been found to be most closely related to earthquake magnitude. The final CSR in this approach can be expressed as:

$$CSR = 0.65 a_{max} \frac{\sigma_{vc}}{\sigma'_{vc}} \frac{r_d}{MSF} \tag{2.8}$$

The cyclic resistance ratio can be estimated using liquefaction triggering correlations that relate the *in situ* penetration resistance (SPT or CPT), corrected for overburden and fines content, with the CSR defined in Equation 2.8 required to trigger liquefaction. The development of these correlations was based on case histories in which potentially liquefiable materials were subjected to strong ground motions. For each case, the penetration resistance in the susceptible soils was obtained from *in situ* tests, and a corresponding CSR was estimated using the earthquake magnitude and the estimated PGA at the site. Very few case histories have the benefit of having coincided with ground motion recording stations; as a result, the estimates of the PGA at each site are highly uncertain (along with several other components of this procedure). Each case was classified as "Liquefaction", "No Liquefaction", or "Marginal Liquefaction", and the estimated cyclic stress ratio was plotted against the estimated penetration resistance. Various boundary curves separating the "Liquefaction" and "Non-Liquefaction" cases have been proposed by researchers, with the most prominent shown in Figure 2.16 for CPT resistance.

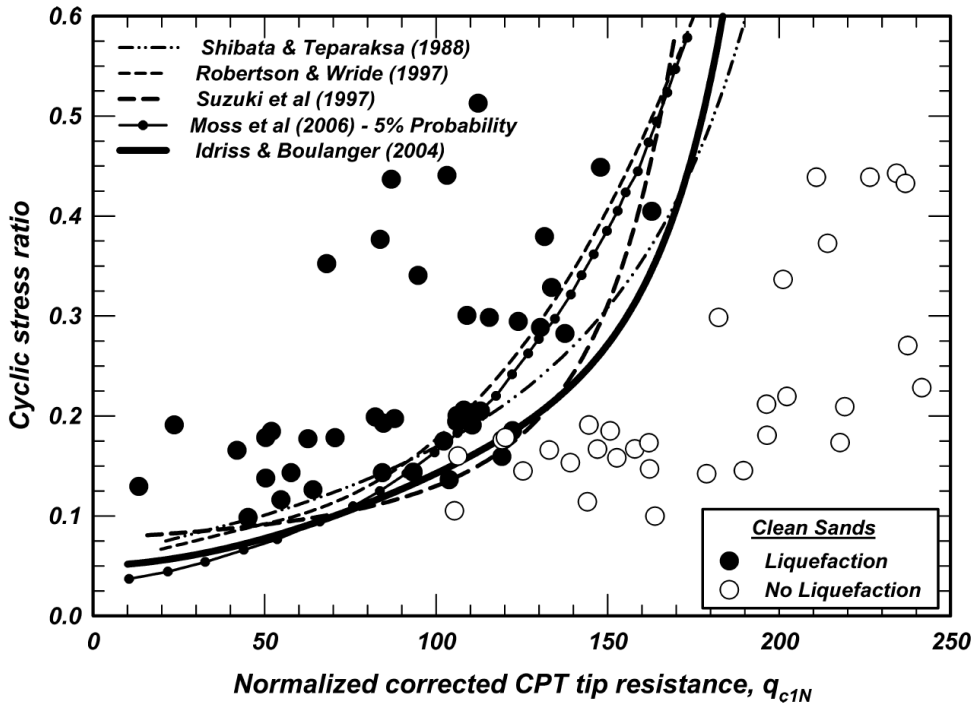

Figure 2.16: Curves relating cyclic resistance ratio to q_{c1N} for clean sands with $M_w = 7.5$ and $\sigma'_v = 1$ atm (Idriss & Boulanger 2008

In this approach, a factor of safety provides an indication of the conditions under which liquefaction is expected to occur. A value of FS less than unity indicates that the cyclic demands imposed by earthquake loading will exceed the capacity of the soil to resist such cyclic stresses. Conversely, a value of FS greater than one suggests that ground shaking is too weak, or that the

soil is too dense to cause the type of sustained contractive behavior needed to trigger liquefaction.

Factor of Safety-Based Liquefaction Hazard Characterization

While the cyclic stress-based simplified procedure forms the cornerstone of liquefaction hazard evaluation to date, it should be recognized that the factor of safety against liquefaction (FS_L) has limited utility in and of itself in terms of characterizing the extent, severity, or type of ground damage due to liquefaction. Nevertheless, significant efforts have been made over the past four decades to develop indices for characterizing the severity of ground damage from FS_L estimates. Ishihara (1985) considered a set of case histories from the 1983 Nihonkai-Chubu Earthquake, and drew attention to the influence of the thickness of non-liquefied surface layers on the occurrence of liquefaction-induced ground damage (Figure 2.17).

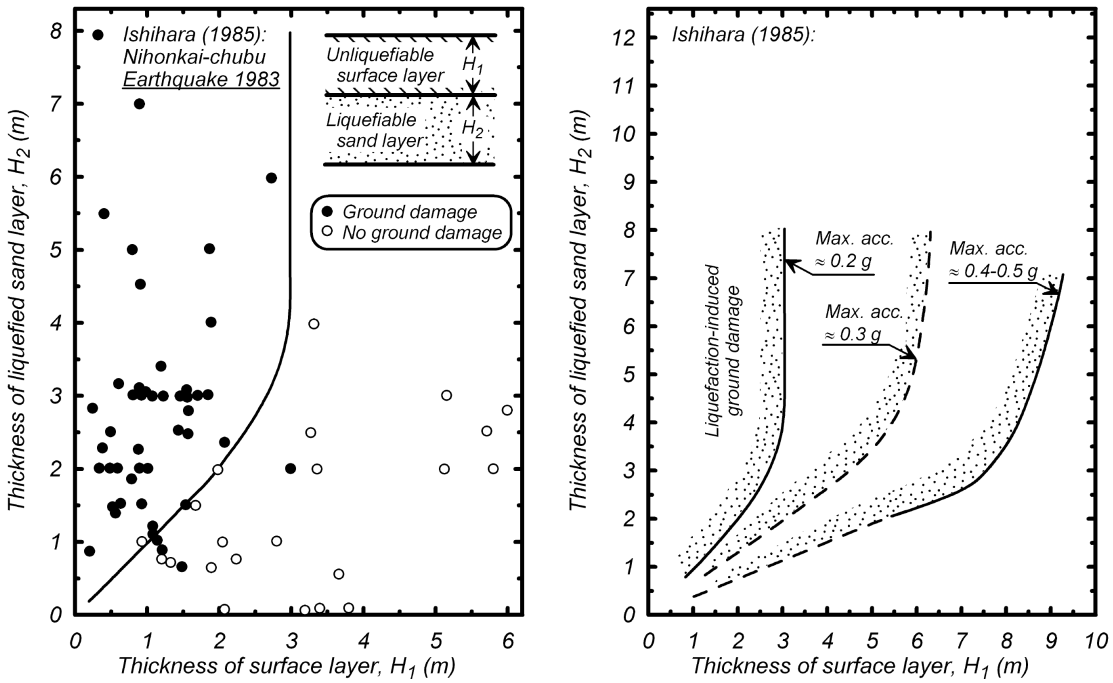

Figure 2.17: Combinations of non-liquefied surface layer thickness, liquefied layer thickness, and peak ground acceleration that distinguish between ground surface damage and the absence of such damage (Ishihara 1985, reprinted from Boulanger & Idriss 2008

The first quantitative parameter for considering liquefaction severity was proposed by Iwasaki et al. (1982). They defined a Liquefaction Potential Index LPI as the summation of liquefaction severity in each soil layer (defined by its computed FS_L) weighted by a factor that decreases with depth:

$$LPI = \int_0^{20\text{m}} F \cdot w(z)dz \tag{2.9}$$

where $F = 1 - FS_L$ for $FS_L \leq 1$ and $F = 0$ for $FS_L > 1$, and $w(z) = 10 - 0.5z$. Typical estimates of LPI range from 0 (no liquefaction vulnerability) to 100 (extreme liquefaction vulnerability), with $LPI > 15$ indicating very high risk of severe liquefaction. Maurer et al. (2014) evaluated the efficacy of LPI in some 1,200 CPT soundings from the Christchurch, New Zealand area, and found that while LPI was reasonably effective in predicting moderate-to-severe liquefaction manifestations, it performed poorly in terms of predicting more marginal liquefaction cases. Maurer et al. (2015) proposed an improved, "Ishihara-inspired" liquefaction potential index, accounting more explicitly for the thickness of the non-liquefied crust:

$$LPI_{ISH} = \int_{H_1}^{H_1+H_2} F \cdot w'(z)dz \tag{2.10}$$

where H_1 and H_2 are the thickness of the liquefiable soils and non-liquefiable surface crust, respectively, and $w'(z)$ is a revised depth-weighting function. Van Ballegooy et al. (2014) also found inconsistencies in traditional LPI-based predictions in the Christchurch area, and proposed a *Liquefaction Severity Number*, LSN, based on estimating the volumetric strain in each sublayer:

$$LSN = 1000 \int \frac{\varepsilon_v}{z} dz \tag{2.11}$$

Van Ballegooy et al. posited that basing LSN on volumetric strains, which are estimated as a continuous function of FS_L (Zhang et al. 2004 and Ishihara & Yoshimine 1992) allows for a surface manifestation index that is sensitive to the effects of relative density on liquefaction surface manifestation, and allows for the potential contribution to liquefaction manifestation of layers with FS_L greater than, but still close to one.

Practical Considerations in FS_L-Based Simplified Procedures

As stated previously, the cyclic stress-based procedure has been nearly ubiquitous in qeotechnical earthquake engineering over the past few decades. It has a relatively clear mechanistic basis, a low barrier to application in practice, and it can be deployed at scale with relatively low computational investment. However, certain elements of the simplified method are highly uncertain, such as the characterization of a "representative" penetration resistance and estimation of PGA in case histories, and accounting for the effects of earthquake duration and depth reduction in cyclic

stresses in the estimation of CSR. When such uncertainties are accounted for in fully probabilistic analyses of liquefaction triggering (see Chapter 3), they can result in highly uncertain estimates of the factor of safety. Recognizing that FS_L is not directly that useful in predicting ground damage, and that it is typically used as an intermediate parameter in predicting shear or volumetric strains, or ground damage indices (which also involve uncertainties), such a multi-step framework for characterizing the effects of liquefaction can result in extremely high uncertainties in ground damage estimates.

Furthermore, certain simplifications inherent to the simplified procedure often result in inaccurate predictions of ground damage. Cubrinosvki et al. (2018) found a systematic over-prediction of ground damage in certain types of sites using FS_L-based methods. Specifically, such methods failed to capture some of the system-wide mechanisms that cause surface manifestation and ground failure, such as the tendency for liquefaction in deep layers to reduce seismic demands in shallower susceptible layers, and a lack of hydraulic connectivity between distinct liquefiable layers inhibiting upward migration of excess pore pressures (Figure 2.18).

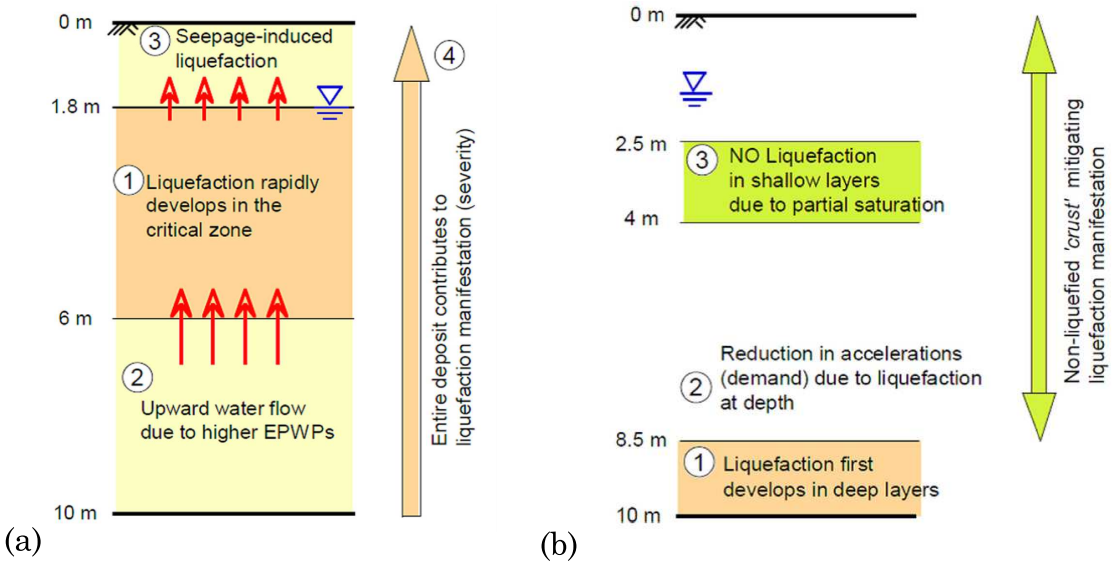

Figure 2.18: Schematic illustrations of system response mechanisms in soil profiles in which simplified FS_L-based procedures (a)Mildly under-predict liquefaction surface manifestation, and (b) Significantly over-predict surface manifestation. (Cubrinosvki et al. 2018)

Alternative Ground Motion Intensity Measures for Liquefaction Triggering

While peak ground acceleration is a commonly-used ground motion *intensity measure* (IM) for representing cyclic stresses in the prediction of liquefaction triggering, it is just one of a literally infinite number of ways to characterize ground shaking intensity. Peak acceleration and other spectral amplitudes have a long history of use in structural and geotechnical earthquake engineering,

due primarily to their relatively direct relation to peak loads in structural elements or peak stresses in soils. However, it has been established for decades that dynamic performance of structural and geotechnical systems are as much a function of the duration of loading as the amplitude of the peak load - most structural materials and nearly all soils exhibit some degree of cyclic fatigue and degradation, and it is thus critical to account for the effects of loading duration when analyzing seismic performance.

As discussed previously, use of PGA in the analysis liquefaction triggering requires the additional use of a magnitude scaling factor (MSF) to account for the effects of duration. Because of this fact, PGA has often been described as an *insufficient* intensity measure for liquefaction evaluation (Kramer and Mitchell 2006), since the parameter it is purported to predict is not conditionally independent of other earthquake quantities such as magnitude or distance (Shome and Cornell 1999). In order to employ the simplified procedure in a fully probabilistic prediction of FS_L, the engineer must characterize not only the uncertainty in the range of PGA levels expected at the site, but also the range of event magnitudes that might contribute to ground shaking (see Chapter 3).

Kramer and Mitchell (2006) identified a set of *evolutionary intensity measures* that could potentially characterize the loading and resistance for liquefaction hazard analyses in a more efficient and sufficient manner. Evolutionary intensity measures, such as Arias Intensity, are integrated over the duration of shaking, and thus are typically larger for motions with longer significant durations. This property allows for such IMs to encapsulate characteristics of both the shaking amplitude and duration such that additional source information is not required in order to represent the seismic demand. In their study, Kramer and Mitchell performed a series of numerical analyses on a set of generic liquefiable profiles, using a wide range of input ground motion recordings. By plotting various IMs against the depth-averaged pore pressure ratio $\hat{r_u}$, and fitting a statistical model to the $IM - \hat{r_u}$ relationship, the efficiency of each IM considered could be compared using the model variances (Figure 2.19). The study showed that CAV_5 (which uses a threshold of 5 cm/s) was the most efficient predictor of excess pore pressures, suggesting its use in liquefaction triggering analysis could reduce uncertainty in many geotechnical earthquake engineering problems.

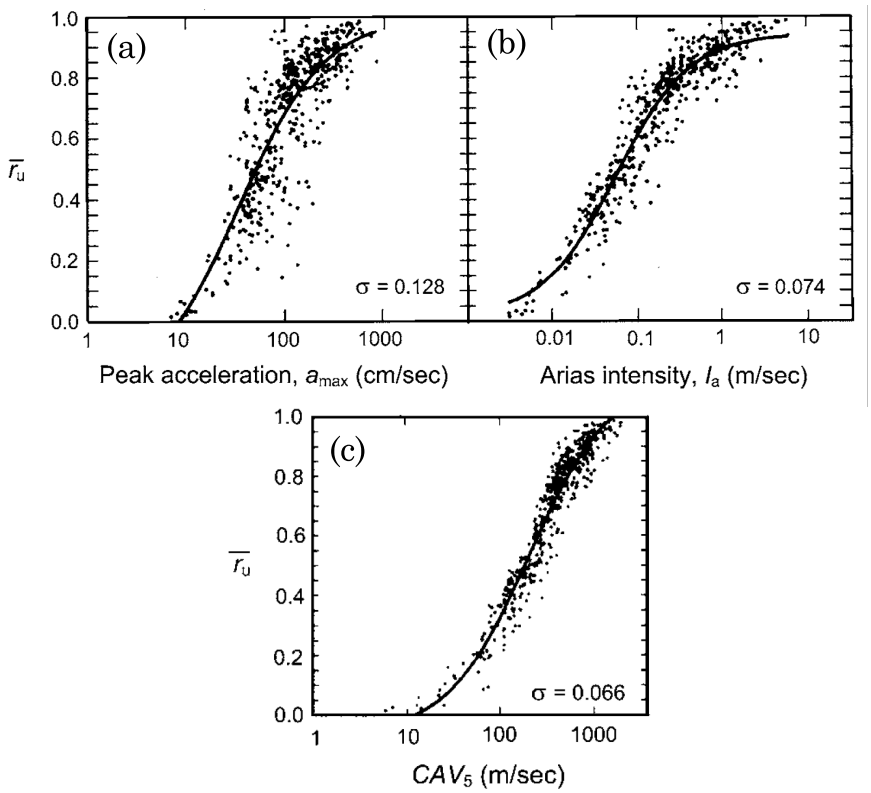

Figure 2.19: Average pore pressure ratio efficiency plots, from a series of numerical analyses for (a) PGA, (b) Arias intensity, and (c) cumulative absolute velocity-5 (CAV_5)

The Timing of Liquefaction

Much of the previous research presented in this chapter has focused on estimation of various intensity measures for characterizing liquefaction triggering. All of the methods presented so far are based on characterizing a particular intensity measure from the full duration of ground shaking. However, recognizing that the seismic response of a geotechnical system is closely related to the stiffness of the soil, and that liquefiable systems tend to undergo drastic changes in their stiffness, and therefore significantly affect the characteristics of the eventual surface motion, Kramer et al. (2016) proposed a method for analysis of liquefaction triggering by accounting for the time at which liquefaction occurs, and using evolutionary intensity measures to divide the analysis into pre- and post-triggering portions. The timing of liquefaction can be ascertained by examining the shift in frequency content of the surface motion, using a normalized Stockwell spectrogram, which essentially shows the evolution in the dominant frequencies of a given recording over time. The Stockwell spectrogram shown in Figure 2.20 is from the Kawagishi-cho recording from the 1964 Niigata earthquake. Red colors in the spectrogram indicate high Stockwell amplitudes, while blue colors indicate low amplitudes. In this record, a clear shift in Stockwell amplitudes towards lower frequencies can be seen at around 16 seconds, indicating that this point in time was likely the time

at which liquefaction was triggered.

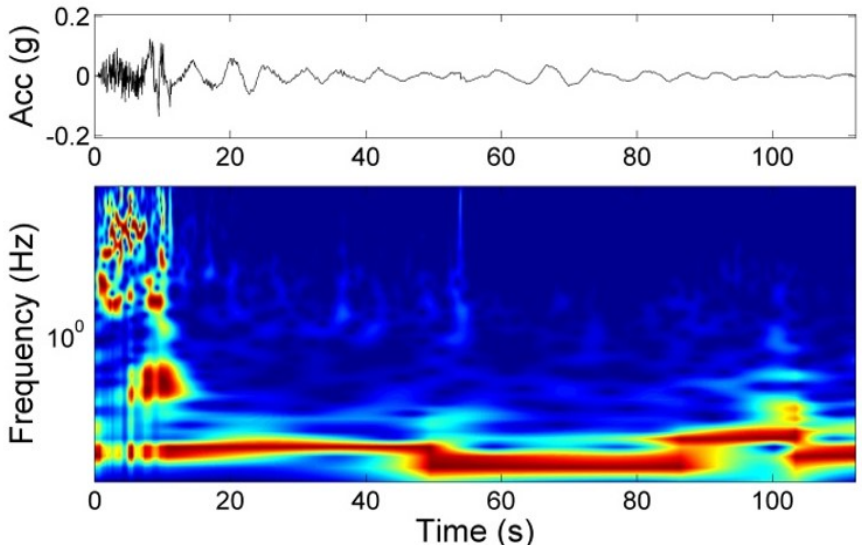

Figure 2.20: Normalized Stockwell spectrogram for the Kawagishi-cho recording in the 1964 Niigata earthquake (Kramer et al. 2016.)

Such a framework allows for more refined estimates of the effects of liquefaction; if liquefaction is triggered relatively early during ground shaking, due to some combination of very loose soil and very strong shaking, its effects are expected to be significant, since a large portion of ground motion energy still remains to enter the system in its liquefied state. If liquefaction is triggered relatively late in shaking, surficial effects are likely to be less significant, since very little input energy remains to cause volumetric or shear strains in the now-liquefied soil (Figure 2.21).

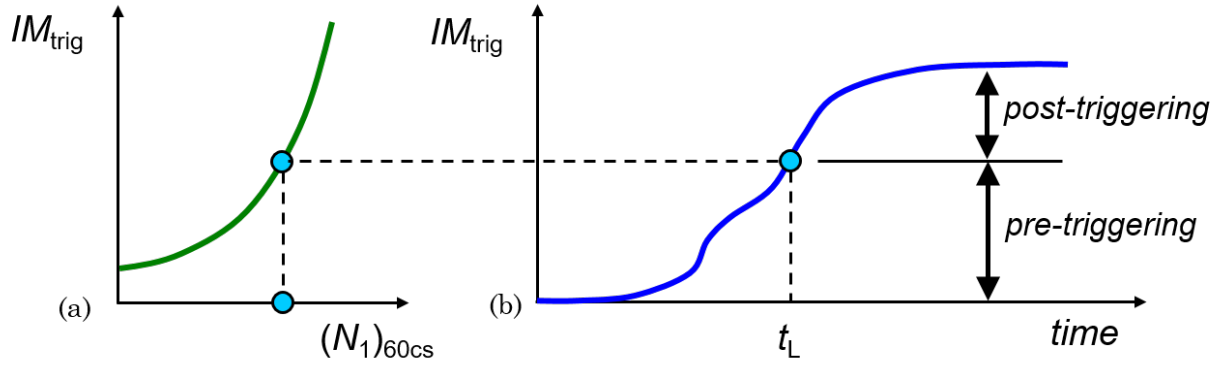

Figure 2.21: Illustration of the characterization of the relative timing of liquefaction, using (a) a hypothetical generalized IM_{trig}-SPT resistance triggering correlation and (b) the evolution time history of IM_{trig} (after Kramer et al. 2016.)

2.3 Lateral Spreading

One of the most significant and damaging effects of soil liquefaction is the horizontal displacement of soil on mildly sloping ground or in the vicinity of a free face, a phenomenon known as *lateral spreading* (Figure 2.22). Lateral spreading has caused severe damage to roadways, embankments, bridge pile foundations, and critical underground infrastructure such as water and gas mains and sewage pipelines. Among geotechnical hazards, lateral spreading is among the most notoriously difficult to predict and characterize in the field. The various mechanisms that contribute to lateral spreading can be exceedingly complex and challenging to observe directly. There exists a wide range of approaches for dealing with lateral spreading problems, with varying methodologies and technical sophistication. This section presents the underlying mechanisms that drive lateral spreading, the system-level factors that influences its extent and severity, the current state of methodology for its characterization, and the numerous challenges involved in its prediction.

Figure 2.22: Ground cracks in pavement on a residential street, due to liquefaction-induced lateral spreading in the 2011 Christchurch Earthquake (Wikipedia Commons)

2.3.1 Mechanics of Lateral Spreading

When liquefaction occurs in soils subjected to an initial static shear stress, such as those in sloping ground or in the vicinity of a steep free face, the ensuing ground deformations will depend strongly on the magnitude of that initial shear stress relative to the residual strength of the liquefied

material. *Flow liquefaction*, which occurs when static shear stresses are greater than the available shearing resistance, results in the most dramatic manifestations of liquefaction-induced failures. Once liquefaction has been triggered in such cases, extremely large deformations can occur, driven almost entirely by static shear stresses. One of the most dramatic cases of such failures occurred in the 2018 Palu Earthquake in Indonesia, which was notable for the stunning Jono Oge flowslide, which extended over a footprint of 1.35 square kilometers, and featured over one kilometer of lateral displacement in some areas (Figure 2.23).

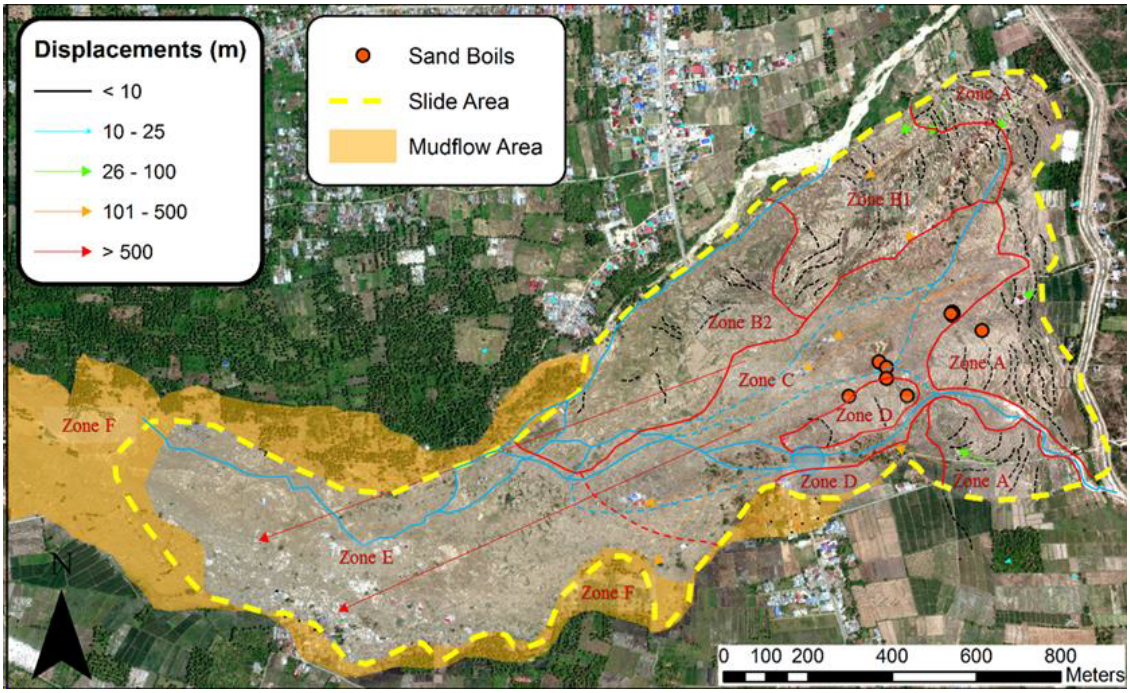

Figure 2.23: Orthomosaic map indicating limites of Jono Oge landslide from 2018 Palu, Indonesia Earthquake. Included are locations of sand boils, vector displacements, and zones delimited by morphological features and key observations (Geotechnical Extreme Events Reconnaissance, 2019)

At the element level, flow liquefaction is the result of the type of behavior illustrated previously in Figure 2.10, when very loose specimens or specimens under extremely high confining pressures reach large deformations at the critical steady state. Rather than dilating at large strains, the specimen becomes unstable, and collapse to a state of extremely low effective stress and shearing resistance.

Lateral spreading, which typically features less dramatic displacements, is the result of a type of phenomenon known as *cyclic liquefaction*. Cyclic liquefaction occurs in conditions where liquefied specimens dilate at large strains, rather than experience complete collapse of soil fabric. While the initial static shear stress in such cases does not exceed the strength of the liquefied soil, momentary cyclic strain increments occur when the combination of the initial static stress and cyclic stress

amplitude combine to exceed the liquefied strength.

It is important to recognize that lateral spreading sites are extremely complex systems. While researchers and practitioners often describe lateral spreading cases using a single displacement magnitude, a single description of topographic conditions, and a single critical layer of liquefied material, the reality is that lateral spreads are highly variable in space, and such variability results in complex deformation patterns (Figure 2.24).

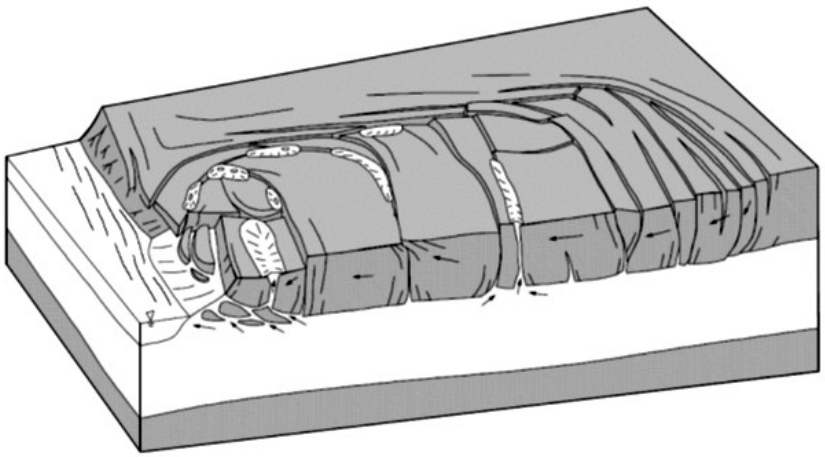

Figure 2.24: Schematic of deformation patterns in a lateral spread (Rauch 1997)

Since lateral spreading deformations are driven by both static and dynamic stresses, the magnitude of those stresses plays a critical role in how displacements manifest. The static stress field is natural a function of the surface topography. Soils that are below sloping ground will experience an ambient static stress that increases with increasing ground slope inclination. Soils in the vicinity of a steep free face will also experience static stresses that increase with proximity to the free face. The dynamic stresses needed to initiate momentary increments of shear strain in liquefied material are related to the amount of seismic energy going into the liquefied system after the onset of liquefaction - the more cycles of stress a liquefied soil undergoes, the larger the accumulation of permanent strains. As a result, the time at which liquefaction occurs relative to ground shaking strongly influences the magnitude of deformation patterns.

Permanent ground surface deformations can be thought of as an accumulation of deformations within individual sublayers of the underlying liquefied soil. As a result, the vertical extent and properties of the liquefied soil plays a key role in the magnitude of surface deformations. Thicker, continuous layers of liquefied soil tend to result in larger surface displacements - both due to the accumulation of shear stains over the depth of the layer, as well as the high likelihood of horizontal continuity. Conversely, when liquefiable soils are present in more interbedded, highly stratified

layers, surface displacements tend to be inhibited by (a) the reduced likelihood of liquefaction in shallower layers (see Figure 2.18), and (b) the relative lack of horizontal continuity needed to manifest pervasive shear strains.

Another phenomenon that has been subject of much debate in earthquake geotechnics is the effects of *void redistribution*, due to the potential presence of a highly impermeable capping later, which inhibits complete dissipation of excess pore pressures to the ground surface, and can theoretically result in zones of extremely weak liquefied soil or water films just below the capping layer. Void redistribution has been demonstrated in centrifuge experiments by Malvick et al. (2008), by designing a model of an embankment composed of loosely pluviated Nevada sand, capped by a continuous, curved surface of low-permeability silt (Figure 2.25). The results of the centrifuge test show a clear concentration of strains along this surface due to the development of a water film. While theoretically possible, the possibility of void redistribution occurring in the field is highly uncertain and difficult to quantify due in large part to geologic heterogeneity and the formation of sand boils or ground cracks.

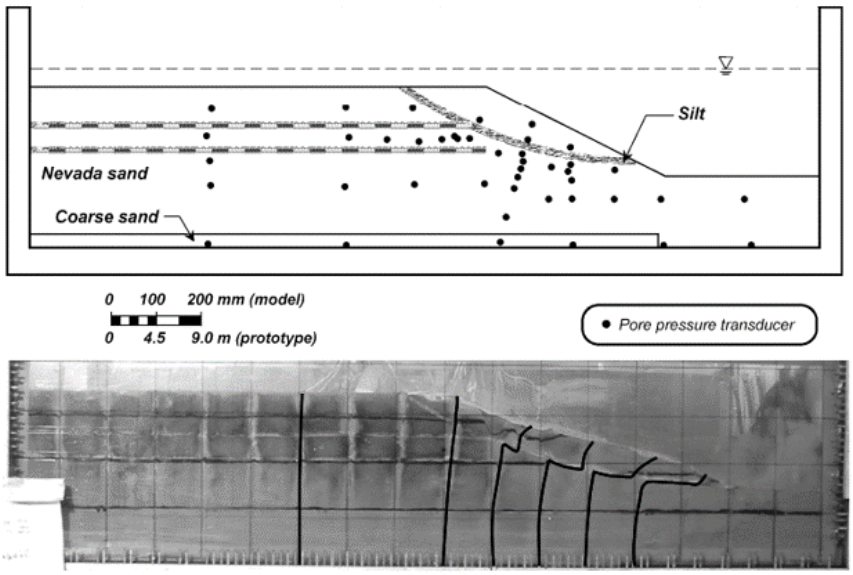

Figure 2.25: Centrifuge test on a saturated and slope, demonstrating the localization of shear deformations along a low-permeability silt layer (Malvick et al., 2008).

2.3.2 Methods for Analyzing Lateral Spreading

The complexities inherent to characterizing lateral spreading present numerous challenges to its prediction in engineering practice. Several different types of methods have been proposed and developed in the past few decades, including simple empirical methods based purely on statistical regression of case histories, methods based on integration of estimated shear strains throughout

the depth of the liquefied material, simplified time-history analyses of sliding blocks, and more sophisticated numerical methods that incorporate advanced constitutive models capable capturing liquefiable behavior on an element level.

One of the most common empirical approaches in use was initially developed by Bartlett and Youd (1992), and updated by Youd et al. (2002). The Youd model was based on a database of lateral spreading displacement measurements taken from sites in Japan and the western U.S. The multilinear regression equation uses event magnitude and source-site distance to represent ground shaking intensity, the cumulative thickness, average fines content, and average median grain size of liquefiable material with SPT $(N_1)_{60} < 15$ to represent the effects of the liquefiable layer, and accounts for topographic effects using either a free-face ratio or ground slope inclination. The Youd et al. model is significant in that it is widely considered to be one of the first instances of purely statistical regression in geotechnical earthquake engineering, and ushered in an era of statistical analysis in geotechnics that is now ubiquitous. Nevertheless, it is important to highlight several practical considerations concerning its use. The database used to develop the model is weighted heavily towards two Japanese earthquakes of relatively similar magnitudes and distances, with no effort made to account for this sampling disparity. Additionally, all displacement vectors were treated as statistically independent, including those measurements taken at the same site. The use of the T_{15} parameter to represent the effects of the liquefiable layer also warrants further consideration. By establishing a binary cutoff of $(N_1)_{60} < 15$, the model implicitly assumes that sites with extremely low N-values will experience the same deformations as sites with N-values of 15, and furthermore implies that soils with N-values greater than 15 do not mobilize significant shear strains at all. Another source of uncertainty for practitioners is the forced classification of sites as either "ground slope" or "free-face" sites; most lateral spreading sites usually involve some combination of both topographic conditions.

By and large, the Youd et al. model and other methods based purely on statistical regression (e.g. Rauch and Martin 2000) have their applicability limited by the available lateral spreading case history data. Such methods generally cannot be extrapolated outside the bounds of their datasets, and have often been shown to be ill-equipped to predict lateral spreading deformations in future case histories (e.g. Youd et al. 2004, Cubrinovski et al. 2018). An alternative class of methods has been to approach the problem from an elemental level, by using simplified cyclic stress-based procedures (which incorporate both case histories and laboratory data) to estimate maximum shear strains from FS_L throughout the depth of the profile, and integrate those strains to calculate the surface displacement (e.g. Zhang 2004). As discussed previously, such methods requiring a two-step characterization of FS_L, followed by surface displacements can be highly uncertain, and also fail to capture many of the aforementioned system-wide mechanisms that are now known to influence

surface manifestation.

Newmark sliding block analyses, with yield accelerations based on back-calculated liquefied shear strengths, have also been proposed for prediction of lateral spreading displacements (Olson and Johnson 2008). The fundamental assumptions of the sliding block approach – that a rigid mass of soil slides on a thin failure surface upon which shearing resistance remains constant – are approximately satisfied for many important, practical cases. Lateral spreads, however, typically involve distributed straining of materials whose shearing resistance fluctuates over the course of ground shaking, which is inconsistent with the assumptions of sliding block analyses. Further examination of Olson and Johnson's sliding block-based method suggested significant uncertainties in the methods used to back-calculate liquefied shear strengths (e.g. Moss and Hollenbeck 2011, Park and Kutter 2011), as well as its use in forward predictions of lateral spreading displacements (Kramre and Makdisi 2017). Additional studies (Makdisi and Kramer 2019) also showed that many of the mechanistic inconsistencies in the sliding block assumption had the potential to significantly under-predict moderate lateral spreading displacements magnitudes.

The most reliable approach for predicting lateral spreading displacements is to use numerical methods to directly model the site in a dynamic analysis. There are numerous finite element (e.g. OpenSees, PLAXIS, FLIP) and finite-difference (e.g. FLAC) software platforms available, as well as a variety of constitutive models capable of capturing the mechanics and effects of pore pressure generation in liquefiable soil (e.g. PM4Sand, PDMY, stress-density, cocktail glass). Despite their clear relative advantages over the aforementioned simplified procedures, the effective use of such methods requires large investments of time, money, and expertise that is not widely available in industry. As such, the use of numerical models is typically limited to higher-budget projects that are not burdened by extremely short timelines.

The Timing of Liquefaction and its Use in Lateral Spreading Prediction

Kramer et al. (2016) proposed a generalized framework for predicting lateral spreading displacements by characterizing the timing of liquefaction, which is illustrated in Figure 2.26. The procedure first involves relating the liquefaction resistance of the soil profile (in this case represented by SPT resistance $(N_1)_{60,cs}$) to an evolutionary intensity measure specifically selected for its efficiency in predicting liquefaction triggering, denoted as IM_{trig}. For a given SPT resistance, the value of IM_{trig} at the time of liquefaction can be obtained from the triggering curve. A plot of the time history of IM_{trig} can be used to determine the time of liquefaction triggering, t_L. Knowing t_L, as well as the time history of the remaining evolutionary IM that is targeted to most efficiently predict permanent deformations (denoted as IM_{eff}) allows for the determination of the post-triggering quantity of the effects IM, IM_{eff}^{post}. Finally, the level of post-triggering loading can

be used to estimate lateral displacements via an effects prediction model.

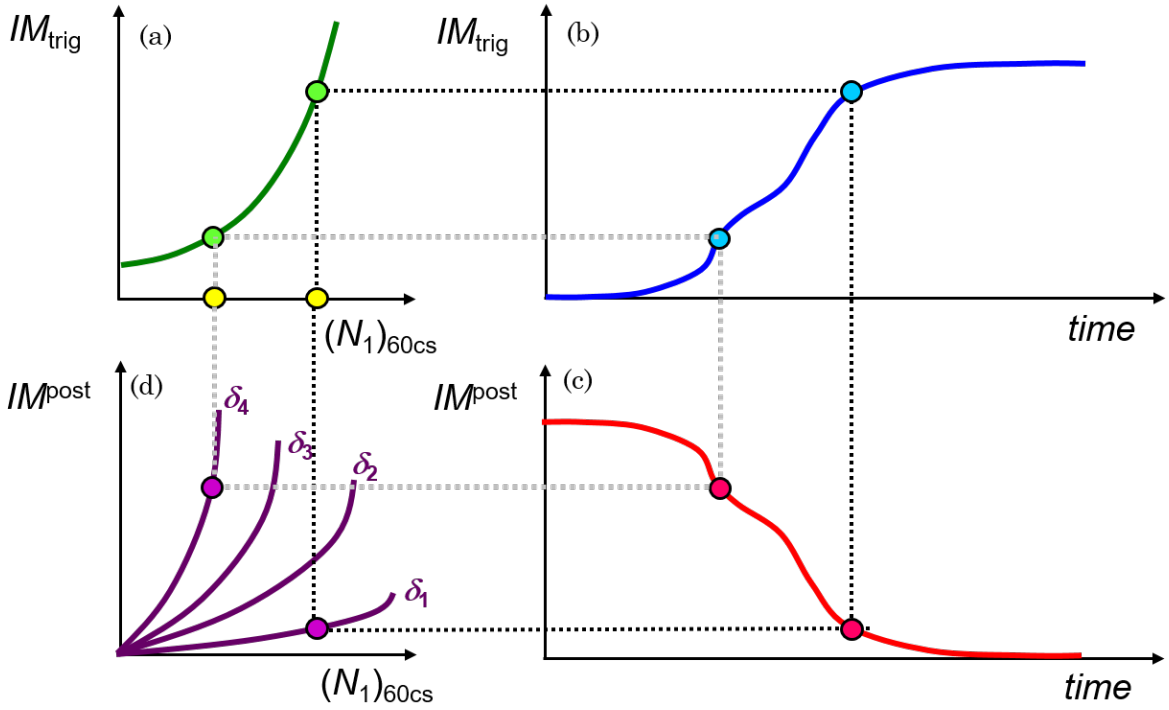

Figure 2.26: Schematic illustration of a timing-based approach to predicting lateral spreading displacements, using (a) a hypothetical generalized relationship between IM_{trig} and SPT resistance, (b) the evolution time history of IM_{trig}, (c) the evolution time history of the remaining quantity of IM^{post}, and (d) a hypothetical generalized relationship between SPT resistance, IM^{post}, and permanent lateral displacement (Kramer et al. 2016).

The dashed lines in Figure 2.26 illustrate this prediction for two different soil densities. The looser soil is expected to liquefy at a lower value of IM_{trig}, and thus will liquefy early in ground shaking, leaving a larger quantity of the remaining IM_{eff}^{post}, thus leading to larger estimates of permanent deformation. The denser soil is expected to liquefy at a higher IM_{trig} value later in ground shaking, leading to a lower value of remaining IM_{eff}^{post} and a smaller magnitude of estimated displacement. In this framework, the effect of the differences in density between the two soil elements is twofold. Not only does the looser material undergo larger deformations for the same value of IM_{eff}^{post}, but that material will also experience a *higher* value of IM_{eff}^{post} due to the earlier time at which it liquefies.

The procedure was demonstrated by Kramer et al. in a series of numerical analyses for a range of simplified subsurface profiles and a suite of ground motions. The timing-based approach was compared to a total intensity measure approach by comparing the standard deviations of the predicted displacements, using three different evolutionary intensity measures (PGA_M, I_a, and

CAV). For each intensity measure, the timing-based framework significantly improved the precision of displacement prediction, with the results suggesting that for these simplified profiles that Arias intensity was the most efficient predictor of displacements.

2.4 Performance-Based Earthquake Engineering

The importance of characterizing the uncertainty in liquefaction hazard analyses can be contextualized by considering its role in the broader concept of performance-based earthquake engineering (PBEE). PBEE is a framework for seismically designing or retrofitting various types of structures with the goal of achieving a desired performance criterion. Performance criteria are typically defined by the stakeholders of a particular facility or structure (e.g. property owners or local, state, or federal authorities) in such a way as to provide relevant data for making informed decisions on seismic risk mitigation (Moehle and Deierlein, 2004). This concept represents a significant departure from prescriptive, code-based design criteria, which (as the name implies) provide minimum guidelines on how a structure should be designed and constructed. Typically, such guidelines are developed in order to satisfy a criterion of "failure prevention" for the structure in question. However, a stakeholder may desire a higher level of performance than that implied by code-based guidelines (Mayfield, 2007). Using a performance-based design framework generally allows for a more flexible definition of acceptable performance, particularly when dealing with structures that are far more complex than those covered by minimum design standards, and when a variety of stakeholders are involved.

In PBEE, the risk associated with earthquake ground motions is evaluated in a fully probabilistic framework, with the end goal being to express the seismic risk in terms of the annual rate of exceedance of some *decision variable (DV)*. Depending on the stakeholders involved, decision variables can take a variety of forms, such as economic loss (due to cost of repair, lost property value, or downtime), injuries, or fatalities. DVs generally require the characterization of several intermediate variables to in order to relate ground shaking to the performance outcome of interest. In doing so, it is critical to evaluate and include the uncertainties in the characterization of ground shaking intensities, as well as those in the intermediate variables to produce a reasonable assessment of the seismic risk.

2.4.1 The PEER Performance-Based Earthquake Engineering Integral

The overall seismic risk assessment for a given site and structure can be broken down into four main components, each consisting of the probabilistic characterization of a key variable in the PBEE equation. The first component consists of the seismic hazard characterization for one or

more ground motion *intensity measures* (IM) of interest. Then, a relationship between the IM and a particular measure of system response, known as an *engineering demand parameter* (EDP) must be established. The damage resulting from the system demand must then be quantified, and is referred to as the *damage measure* (DM). Finally, the decision variable (DV), typically evaluated in terms of economic or human cost, is quantified in relation to the estimated damage measure. These variables are related to each other via response, damage, and loss models, which can have varying levels of complexity, accuracy and uncertainty.

Intensity Measures and Probabilistic Seismic Hazard Analysis

The PBEE calculation begins with analyzing the seismic hazard at a site with respect to a certain ground motion IM of interest. This generally involves calculating the mean annual rates of exceedance of a range of IM values, producing what is commonly referred to as a ground motion hazard curve. The choice of IM for a particular application may be based on a number of factors, including the structure or geotechnical system, the EDP of interest and the methods available for estimating it, the available ground motion models (GMMs) that can be utilized to estimate IM at a given site, and the uncertainty in either estimating the IM or relating it to a particular EDP (or both).

An IM hazard curve is calculated using a framework known as Probabilistic Seismic Hazard Analysis (PSHA). A PSHA considers all potential earthquake sources that may produce significant ground motions at a particular site, as well as the uncertainties in magnitude (M_w), source-site distribution (R), and the estimated IM for each combination of M_w and R for each source. For a particular value of an IM, the annual rate of exceedance (λ_{IM}) is approximated in discrete form as follows:

$$\lambda_{IM}(im) = \sum_{i=1}^{N_s} \nu_i \sum_{j=1}^{N_M} \sum_{k=1}^{N_R} \mathrm{P}[IM > im | M_w = m_j, R = r_k] \mathrm{P}[M = m_j] \mathrm{P}[R = r_k] \tag{2.12}$$

where ν_i (known as the *activity rate*) refers to rate of occurrence at the i^{th} source of any event exceeding some minimum magnitude. All of the probability terms in Equation (C.1) are implicitly presented as conditional on the exceedance of the minimum magnitude. The first probability term is the probability of exceeding a particular value of the intensity measure, im, for a given magnitude and distance scenario, which is a function of the lognormal mean ($\mu_{\ln IM}$) and standard deviation ($\sigma_{\ln IM}$) of the GMM prediction. For that scenario, the conditional probability of exceedance is then multiplied by the probability of the earthquake magnitude ($\mathrm{P}[M_w = m_j]$), which is character-

ized using source-specific magnitude-frequency relationships, and the probability of the source-site distance ($\mathrm{P}[R = r_k]$), based on the geometry of the source and its position relative to the site of interest. For a given source, the exceedance probabilities are summed up for all combinations of magnitude and distance, and multiplied by the activity rate to obtain the mean annual rate of exceedance of *im* for that particular source. This process is repeated for all sources, and the individual source exceedance rates are summed up to obtain the overall exceedance rate. The calculation in Equation (C.1) can be repeated for a range of *IM* values to produce a complete ground motion hazard curve.

One of the most common *IM*s used in PBEE is the spectral acceleration at a particular oscillator period, $S_a(T)$. The period, T, is typically selected to coincide with (or to be slightly longer than) the first mode of vibration of the system under consideration. Traditionally, the spectral acceleration has been used because it is closely related to the peak loads that a structure may experience during ground shaking. Similarly, the simplified method of the cyclic stress approach for evaluating liquefaction triggering uses the peak ground surface acceleration, *PGA*, to estimate the cyclic stress in an element of soil. As a result, much of the development in GMMs and seismic hazard mapping over the last few decades has emphasized spectral amplitudes. An example of a series of hazard curves for various spectral amplitudes is shown in Figure 2.27.

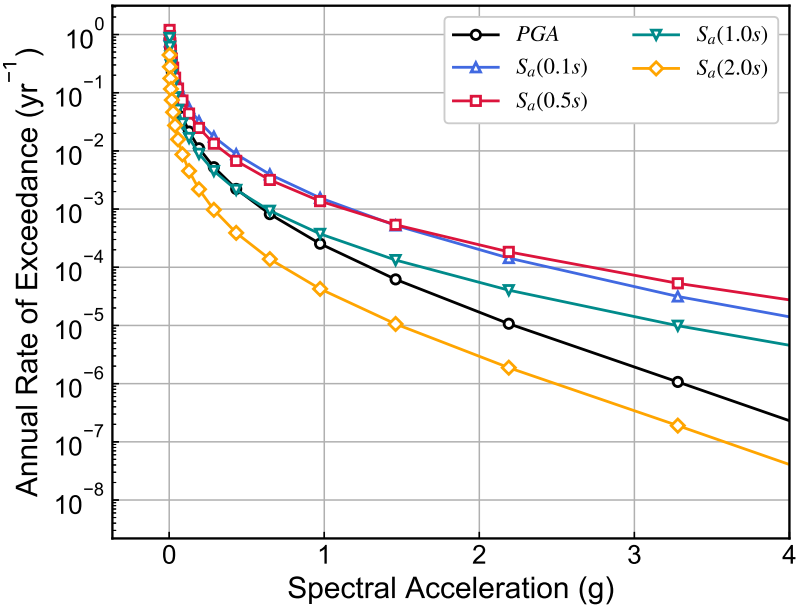

Figure 2.27: Hazard curves for various spectral amplitudes, obtained from a series of PSHAs for a site in Los Angeles, CA

However, more recent developments in both structural and geotechnical earthquake engineering have necessitated the development of GMMs for other intensity measures. Kramer and Mitchell (2006), Dashti and Karimi (2017), and Karimi and Dashti (2017) have shown that *IM*s that accumulate in magnitude over the course of ground shaking, rather than those that simply measure transient peaks, tend to be more efficient predictors of liquefaction triggering. These metrics, such as Arias intensity, I_a, and cumulative absolute velocity, *CAV*, (which has several variants), are known as *evolutionary intensity measures*, and have an advantage of capturing, in addition to amplitude, the effects of duration and frequency content on liquefaction triggering in ways that *PGA* alone cannot.

While the current suite of GMMs is still overwhelmingly skewed towards predicting spectral amplitudes, numerous developments have been made in the last two decades in predicting evolutionary *IM*s such as Arias intensity and *CAV* (e.g. Campbell & Bozorgnia [2012], Bullock et al. [2017]). These models have largely been developed with similar source and site parameters as those used to predict spectral amplitudes. Thus, hazard curves for evolutionary *IM*s can be estimated using largely the same source models implemented in most current PSHA computation platforms (e.g. nshmp-haz, EZ-FRISK, HAZ), requiring only a justifiable GMM weighting tree. Alternatively, it has been proposed (Macedo et al. 2019) that hazard curves for evolutionary *IM*s can be estimated from spectral amplitude-based hazard curves, using the fact that different types of ground motion *IM*s are strongly correlated to one another within a given ground motion. By developing *conditional ground motion models* that relate, for instance, $S_a(2s)$ to *CAV*, researchers and practitioners can take advantage of the decades of development and consensus that underpin modern, S_a-based GMMs, an advantage that does not exist in the current suite of evolutionary GMMs.

Engineering Demand Parameters and Fragility Curves

With the seismic hazard associated with the ground motion intensity measure fully characterized, the next step in the PEER PBEE framework is to relate the *IM* hazard to some desired measure of system response, referred to as the *engineering demand parameter* (*EDP*). The *EDP* is generally selected with the goal of being able to characterize the physical damage of the structure - some examples include interstory drift, base shear, excess pore pressure, factor of safety against liquefaction, and vertical settlement or lateral extension of a foundation element or embankment crest.

The relationship between the *IM* and *EDP*, often expressed by a *response model*, must be characterized probabilistically with the following general form (assuming here a lognormally distributed *EDP*):

$$\ln EDP = \overline{\ln EDP}(IM) + \sigma_{\ln EDP}(IM) \cdot \varepsilon \tag{2.13}$$

where $EDP(IM)$ is the mean response as a function of IM, $\sigma_{EDP}(IM)$ is the model standard deviation, and ε is the model error term. Note that the uncertainty is generally expressed here as a function of IM, but may also simply be a constant value. Once a response model is established , it can be then numerically integrated with the IM hazard curve defined in Equation (C.1) as follows:

$$\lambda_{EDP}(edp) = \nu \sum_{k=1}^{N_{IM}} \mathrm{P}[EDP > edp | IM = im_k] \Delta \mathrm{P}[IM > im_k] \tag{2.14a}$$

$$= \sum_{k=1}^{N_{IM}} \mathrm{P}[EDP > edp | IM = im_k] \Delta \lambda_{IM}(im_k) \tag{2.14b}$$

The term $\mathrm{P}[EDP > edp|IM = im]$ is the probability of exceedance of a particular value of the EDP (denoted as lower case edp), conditional on a particular IM value (denoted as lower case im). For a given IM, the probability of exceeding a particular edp can be calculated from the standard normal distribution function Φ as:

$$\mathrm{P}[EDP > edp|IM = im] = 1 - \Phi\left(\frac{\ln edp - \overline{\ln EDP}(im)}{\sigma_{\ln EDP}(im)}\right) \tag{2.15}$$

For a given edp value, the variation in $\mathrm{P}[EDP > edp|IM = im]$ with respect to IM can be expressed graphically as a *fragility curve*. In order to generate a full EDP hazard curves, a set of EDP-IM fragility curves can be obtained for multiple EDP values from the probabilistic response model.

There are a number of ways to estimate the EDP. In many cases, simplified procedures can be used to relate a ground motion IM to the EDP of interest. A common case is the one explored in this chapter, in which the cyclic stress method is used to relate peak ground acceleration and earthquake magnitude to the factor of safety against liquefaction (FS_L). More sophisticated methods involving numerical dynamic analysis are often used, with the advantage that they often reduce the uncertainty in predicting the EDP given the IM. In such cases, ground motion time histories can be selected as input to the dynamic analysis in a number of ways. The most direct method is to select a large number of ground motions with a broad range of values of the IM of interest. For instance, if the EDP and IM of interest are excess pore pressure generation (r_u) and CAV_5, respectively, one might run a series of dynamic, effective stress analyses for a large number of ground motions. The

resulting relationship may resemble that shown in Figure 2.28 from Kramer and Mitchell (2006); a statistical model can then be developed from the analysis results and used to generate the fragility curves required for integration with the IM hazard curve.

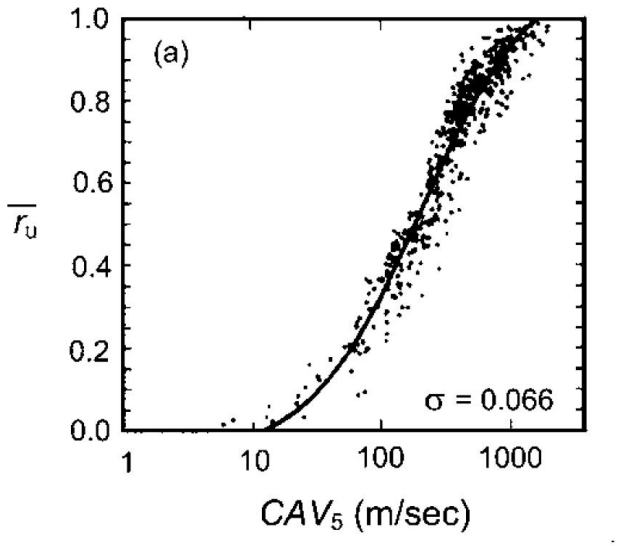

Figure 2.28: Variation of maximum excess pore pressure ratio r_u with respect to CAV_5 (Kramer & Mitchell, 2006)

Damage Measures

The penultimate component of the PBEE framework involves identifying a relevant, quantifiable description of the physical damage to a system, known as *damage measure* (DM). DMs should be defined with an eye towards the overall performance criteria,and should be good predictors of loss (i.e. the DV). Damage measures can range considerably in severity; some examples include damage to non-structural components, crack dimensions in columns or footings, failure in structural elements, or even partial or total collapse of a structure. Such damage measures can be related to their corresponding EDPs in a variety of ways, either by relying on data specific to the project itself, or through relationships established in literature. For example, when determining the probability of structural collapse via dynamic analysis, the relationship of Hueste et al. (2009) for the drift capacity of slab-column connections can be used to estimate the probability of collapse damage measure from inter-story drift EDP (Marafi et al., 2019) (Figure 2.29). Integrating the EDP-DM fragility curves with the EDP hazard curve (see Equation (2.14a)) yields the hazard curve for the

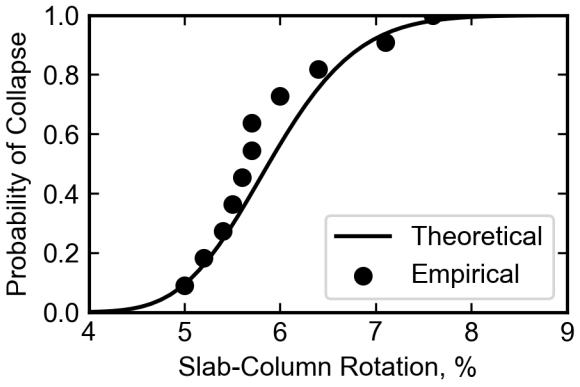

Figure 2.29: Probability of collapse due to slab-column punching shear failure with respect to the maximum story drift, based on experimental data from Hueste et al. (2009) (Marafi et al., 2019)

damage measure:

$$\lambda_{DM}(dm) = \sum_{i=1}^{N_{EDP}} \mathrm{P}[DM > dm | EDP = edp_i] \Delta\lambda_{EDP}(edp_i) \tag{2.16a}$$

$$= \sum_{j=1}^{N_{EDP}} \sum_{k=1}^{N_{IM}} \mathrm{P}[DM > dm | EDP = edp_j] \mathrm{P}[EDP > edp_j | IM = im_k] \Delta\lambda_{IM}(im_k) \tag{2.16b}$$

Decision Variables

Finally, the hazard curve of the damage measure is used to predict the annualized rate of exceedance of some indicator of system performance, referred to as the *decision variable* (DV). The DV is typically geared towards one of two general performance criteria: economic losses (typically in dollars or some other currency), or human cost (mental or physical injuries, fatalities). For less severe damage measures, establishing the DM-DV relationship may consist of adding up the costs of replacing various non-structural components in a building, as well as the economic effects of downtime that their damage may incur. In many cases, the the damage to the contents of a structure may be more valuable than the structure itself, and thus the potential economic impacts of damage to those assets must be accounted for as well. For damage to more critical structural components, the cost of downtime may also need to be factored into the DV characterization - for critical infrastructure such as bridges, underground utilities, or levees, indirect economic losses due to downtime may far exceed the material repair costs, and may involve much higher uncertainty in their characterization. When the partial or total structural collapse is being considered as a DM, it

inevitably leads towards the consideration of human cost as a *DV*. Estimating injuries or fatalities conditional on partial or total structural collapse is also a highly uncertain undertaking, requiring the consideration of occupancy (which fluctuates with time), various modes of structural failure, and other factors.

The resulting *DM-DV* relationship, also known as a *loss model* describes the probability distribution, is defined by the mean and uncertainty of the decision variable as a function of the damage measure. This can then be numerically integrated with the *DM* hazard curve from Equation (2.16a) to produce the final product of the PBEE analysis framework - a curve describing the annualized losses:

$$\lambda_{DV}(dv) = \sum_{i=1}^{N_{DM}} \mathrm{P}[DV > dv | DM = dm_i] \Delta\lambda_{DM}(dm_i) \tag{2.17}$$

The annualized loss curve can be expressed in terms of all of the intermediate variables as:

$$\begin{aligned}\lambda_{DV}(dv) = \sum_{i=1}^{N_{DM}} \sum_{j=1}^{N_{EDP}} \sum_{k=1}^{N_{IM}} & \mathrm{P}[DV > dv | DM = dm_i] \mathrm{P}[DM > dm_i | EDP = edp_j] \\ & \times \mathrm{P}[EDP > edp_j | IM = im_k] \Delta\lambda_{IM}(im_k)\end{aligned} \tag{2.18}$$

Summary of PBEE Calculation Framework

The overall PBEE framework can be summarized as follows:

- A ground motion hazard curve describing the annualized rate of exceeding a particular *IM* is generated, using a PSHA that involves characterization of all the seismic sources that contribute to ground shaking at the site, as well as a suite of GMMs for predicting the ground motion *IM* of interest.
- A probabilistic response model, relating the *IM* and *EDP* (representing the system response) is established, using either simplified methods or more advanced numerical techniques. The *IM-EDP* response model is then integrated with the *IM* hazard curve to generate an *EDP* hazard curve.
- The *EDP* is then used to predict the damage to the system (*DM*), again through either simplified or more advanced methods. The *EDP-DM* fragility curves are integrated with the *EDP* hazard curve to get the *DM* annualized exceedance rate curve.

- The damage measure is finally used to estimate the resulting economic or human losses (decision variable DV). The DM-DV loss model is in turn integrated with the DM annualized exceedance curve, resulting in the final annualized loss curve.

2.5 Summary and Concluding Remarks

The discussion presented in this chapter has sought to highlight and emphasize the importance of soil liquefaction, specifically lateral spreading, in natural hazards engineering. Its historical context has been presented, along with several examples of the tremendous damage it has caused in past earthquakes. Its mechanics have been studies in detail at the elemental level, while its complexities at the site-specific scale have been explored. Various approaches for its prediction have been outlined, each with its advantages and disadvantages, and all carrying a level of uncertainty that must be understood and quantified in order to to be used in a rational, probabilistic, risk-based analysis framework.

Within the realm of earthquake engineering, this risk-based framework is often referred to as performance-based earthquake engineering (PBEE). The various elements of PBEE have been presented, methodically progressing from the characterization of uncertainty in earthquake loading using PSHA, to relating those ground motions to measures of engineering demand, to using those demand parameters to predict damage and, ultimately, economic or human losses. As we will see in the rest of this document, PBEE is a powerful and flexible tool, with a wide variety of applications in both research and practice. The research presented herein will focus mainly on the first two aspects of PBEE: the probabilistic prediction of intensity measures, specifically those that are found to be the most predictable, as well as efficient and sufficient in predicting liquefaction-related phenomena, and the probabilistic relationship between those intensity measures and the liquefaction demand parameter of interest.

Chapter 3

Improved Methodologies and a Python-Based Computational Platform for Probabilistic Liquefaction Hazard Analysis

3.1 Introduction

In order to effectively evaluate liquefaction-related hazards on a risk-consistent basis, it is necessary to perform fully probabilistic analyses that consider all levels of earthquake shaking from all plausible scenarios to determine the probability of liquefaction-related hazards occurring within a particular period of time. To address this type of problem, as well as other earthquake-related hazards, the Pacific Earthquake Engineering Research center (PEER) developed the Performance-Based Earthquake Engineering (PBEE) framework (Section 2.4) in the latter portion of the 20th century (Cornell & Krawinkler 2000, Krawinkler 2002). The PBEE framework is based on integrating the uncertainties in the prediction of ground motions, structural or geotechnical response, system damage, and economic and human losses in a manner that allows stakeholders to understand how potential system vulnerabilities ultimately translate to risk, in terms of annualized losses.

In this chapter, the concept of probabilistic liquefaction hazard analysis (PLHA) (Kramer & Mayfield 2007) is presented as a specific example of PBEE, and a computational method for performing PLHA, using a Python-based code (in conjunction with a java-based platform for computing ground motion hazard curves, developed and maintained by USGS) is presented. The Python

code, `PyLHA`, incorporates several established probabilistic models for liquefaction triggering. The implementation of these models is validated, as is the numerical integration scheme for calculating the annualized rate of non-exceedance of factor of safety against liquefaction FS_L. The code's ability to compute FS_L hazard curves is demonstrated using an example CPT profile for a site in Seattle, Washington, and further validated using a set of nine geographic locations throughout the United States. Additional methods for determining risk-consistent FS_L profiles that correspond to a particular return period, as well as computing the deaggregated liquefaction hazard are also presented. Finally recommended calculation parameters are presented that minimize calculation runtime, while maintain sufficient accuracy of results.

The code can be used to obtain FS_L hazard curves and profiles for user-defined return periods for any site in the contiguous United States, at any value of $V_{s,30}$, using either CPT or SPT data, can support the addition of future liquefaction triggering models, and can additionally be extended to incorporate other liquefaction-related demand parameters (e.g. vertical settlement or lateral displacements) where relevant probabilistic models exist for such values.

3.2 Probabilistic Liquefaction Hazard Analysis

Kramer and Mayfield (2007) showed that analysis of liquefaction triggering could be performed in a fully probabilistic manner using the PBEE framework, with a few minor modifications to the generic PEER framing equations. Traditionally, a soil element's potential for liquefaction triggering has been expressed in terms of a factor of safety against liquefaction (FS_L), in which an estimate of the soil's cyclic resistance is compared with an estimate of the cyclic stress it is expected to experience during ground shaking. Simplified methods for estimating both the cyclic loading and resistance have been developed and refined since the early 1970s. Since the early 2000s, more emphasis has been placed on developing such models in a probabilistic framework, a development that has paved the way for incorporating the uncertainty in estimating FS_L into a fully performance-based framework. More details regarding such models are presented in Section 3.4.

In the fully probabilistic representation of liquefaction hazard proposed by Kramer and Mayfield, the factor of safety (estimated from the simplified cyclic stress-based methods) is treated as the *EDP* of the system, while the *IM* is represented by a combination of the maximum acceleration a_{max}, which is used to estimate the peak cyclic stress that the soil element experiences, and the moment magnitude M_w, which is used to account for the effects of loading duration on the incremental pore pressure rise observed in contractive soils. The basic *IM-EDP* relationship in Equation (2.14a) is thus modified to incorporate the *joint* probability distribution of a_{max} and M_w, and their combined

influence on the FS_L hazard. Note here the use of *non*-exceedance rates, as opposed to exceedance rates, since the limit state of interest is the factor of safety dropping *below* (rather than exceeding) some threshold value. If the *EDP* of interest was, for example, the excess pore pressure ratio r_u, then the probabilistic calculation would be performed in terms of the rate of exceedance. To obtain the annual rate of non-exceedance of a given factor of safety, $\Lambda_{FS_L}(fs_L)$, the probability of non-exeedance of fs_L is calculated for each combination of a_{max} and M_w, and multiplied by the incremental annual rate of exceedance of that a_{max}-M_w combination. The product is then summed over all a_{max}-M_w pairs to obtain the overall rate of non-exceedance.

$$\begin{aligned}\Lambda_{FS_L}(fs_L) &= \sum_{j=1}^{N_m}\sum_{i=1}^{N_{pga}} \mathrm{P}\left[FS_L < fs_L | a_{max,i}, M_{w,j}\right] \mathrm{P}\left[M_w = m_{w,j} | a_{max,i}\right] \Delta\lambda_{a_{max,i}} \\ &= \sum_{j=1}^{N_m}\sum_{i=1}^{N_{pga}} \mathrm{P}\left[FS_L < fs_L | a_{max,i}, M_{w,j}\right] \Delta\lambda_{a_{max,i},m_{w,j}}\end{aligned} \tag{3.1}$$

This calculation is repeated for a range of fs_L values to generate a hazard curve for the factor of safety against liquefaction. The non-exceedance rate calculation requires only two pieces of information: the overall a_{max} ground motion hazard curve plus the conditional distribution of M_w given a_{max} at the site of interest, and a model that allows for estimation of the mean and standard deviation FS_L values, conditional on a particular a_{max} and M_w for an element of soil. In the following sections, procedures used for obtaining and calculating each of the components in Equation (3.1) in the implementation of `PyLHA` are presented in detail.

3.3 Probabilistic Data for Peak Acceleration

The ground motion hazard curve data used in `PyLHA` are obtained from `nshmp-haz`, the Java-based platform created and maintained by the USGS National Seismic Hazard Mapping Project (https://github.com/usgs/nshmp-haz). The `nshmp-haz` platform is capable of running multi-site PSHA calculations to generate hazard curves for spectral amplitude *IM*s, as well as perform deaggregation calculations to characterize the distribution of magnitudes, source-site distances, and epsilons that contribute to the hazard at a particular rate of exceedance (Baker 2013). It includes the full catalog of seismic source models and ground motion model (GMM) logic trees used by USGS in the development of their National Seismic Hazard Maps, and is used as the source code for the deaggregation calculations that can be performed on the USGS seismic hazard website.

3.3.1 Generating Hazard Curves for a_{max}

The primary functionality of the `nshmp-haz` platform is its `HazardCalc` module, which performs PSHA calculations to produce hazard curves for a variety of spectral amplitude-based intensity measures. A hazard curve is generated by calculating the mean annual rate of exceedance of a discrete set of values of a given ground motion *IM* using Equation (C.1). Generally, the set of values is exponentially spaced, and selected to encompass the range of physically reasonable values of the *IM* of interest. A typical ground motion hazard curve, showing the variation in the annual rate of exceedance with respect to peak acceleration a_{max}, for a site in Seattle, Washington, is shown in Figure 3.1. In order to perform the PLHA calculation at regularly-spaced intervals of a_{max}, interpolation in a_{max}-$\log \lambda$ space using cubic splines is required

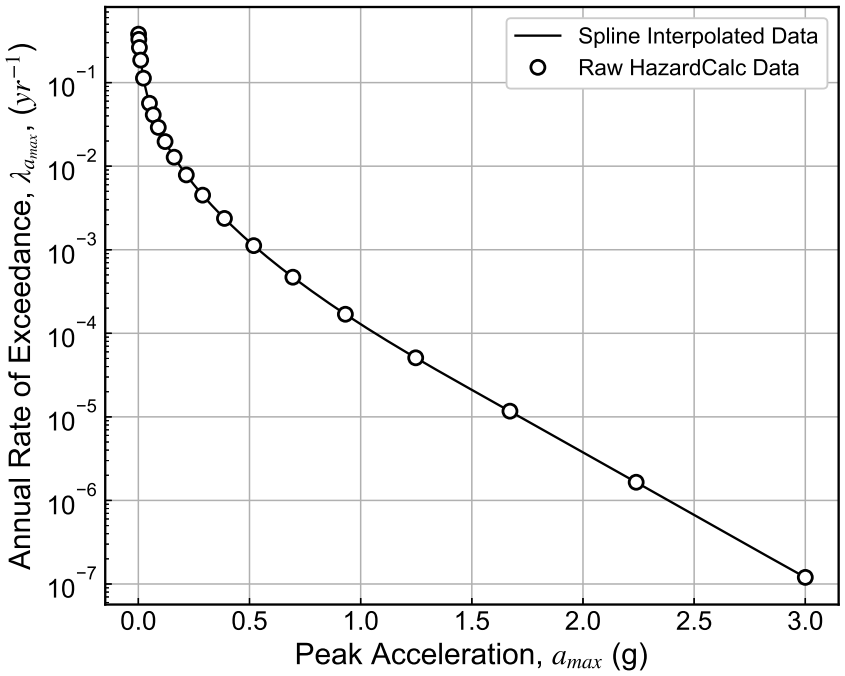

Figure 3.1: Hazard curve for peak acceleration a_{max}, obtained using the 2014 National Seismic Hazard Map (NSHM14) for a site in Seattle, Washington ($V_{s30} = 215$ m/s)

3.3.2 Deaggregating a_{max} Hazard by Magnitude

Since the cyclic stress-based PLHA framework for estimating FS_L requires probabilistic information about magnitude in addition to a_{max}, the overall hazard curve shown in Figure 3.1 is insufficient for use in Equation (3.1). Thus, for the range of a_{max} values considered, the conditional distribution of M_w must be characterized through a process known as *deaggregation*. Deaggregating the hazard at a particular period consists of determining, given that a particular level of intensity measure has been exceeded, what the probability was that the contributing earthquake

featured a particular magnitude, distance, or combination of both (Baker, 2015). The `DeaggCalc` module in `nshmp-haz` calculates this probability for all combinations of magnitude and distance at a particular return period via:

$$P\left[M_w = m_i, R = r_j | IM > im\right] = \frac{\lambda_{IM}(im|m_i, r_j)}{\lambda_{IM}(im)} \tag{3.2}$$

The resulting output can be plotted as a three-dimensional histogram as shown in Figure 3.2, where $P\left[M_w = m_i, R = r_j | IM > im\right]$, often referred to as the *percent contribution to overall hazard*, is plotted for each combination of magnitude and distance. Given some additional knowledge about the positions of major seismic sources relative to the site of interest, one can infer which types of characteristic events are most likely to contribute to the ground shaking intensity at this hazard level. The areas of highest percent contribution in Figure 3.2 are consistent with the three major sources of seismicity in greater Seattle area: (1) Near-fault crustal events, in the magnitude 6.5-7.5 range, attributed primarily to the Seattle Fault Zone (accounting for roughly 25% of the overall hazard at this return period); (2) Events that originate deep in the boundary between the Juan de Fuca and North American plates, known as *intraslab* events (about 50% contribution); and (3) Large magnitude-9 subduction earthquakes, originating offshore in the Cascadia Subduction Zone (about 25% contribution).

For a particular a_{max} value with a given total rate of exceedance, the exceedance rates corresponding to specific magnitude bins can be obtained by multiplying the overall $\lambda_{a_{max}}$ by the probability density of each magnitude bin, which can be calculated by summing $P\left[M_w = m_i, R = r_j | IM > im\right]$ over all values of R:

$$\mathrm{P}\left[M_w = m_i | IM > im\right] = \sum_{j=1}^{N_R} \mathrm{P}\left[M_w = m_i, R = r_j | IM > im\right] \tag{3.3}$$

The resulting marginal magnitude distribution for a particular return period is shown in Figure 3.3. It is important to note, however, that the contributions of different sources, magnitudes, and distances to ground shaking at a particular site will vary with respect to the intensity of shaking. At the lower a_{max} values associated with shorter return periods, the hazard might see higher contributions from more frequent events with relatively smaller magnitudes than those at longer return periods. As a result, the marginal magnitude distribution given a_{max} is not constant with return period, and therefore requires multiple deaggregation calculations to be performed over a broad range of shaking intensities. This is achieved by first calling the `DeaggCalc` module multiple times for a predetermined range of return periods, ranging from extremely short (roughly 5

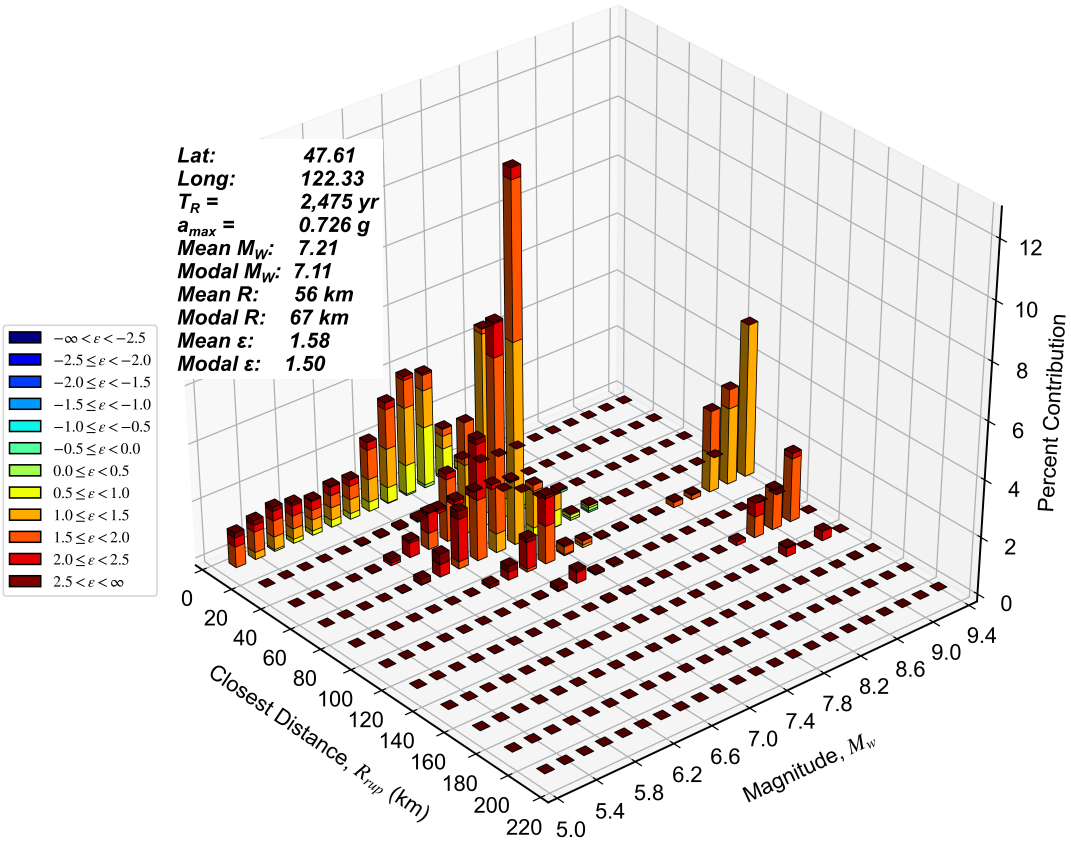

Figure 3.2: Deaggregated hazard plot for a site in Seattle with $V_{s30} = 215$ m/s, for the peak acceleration a_{max} corresponding to a 1 in 2,475-year rate of exceedance.

years or so) to the maximum return period possible in the `DeaggCalc` module, which is currently 20,000 years. The resulting magnitude distribution for a given return period is then calculated via Equation (3.3). An annual rate of exceedance corresponding to a given a_{max}, for a particular magnitude bin, centered at $M_w = m_i$, can be determined by multiplying the marginal magnitude probability by the overall rate of exceedance:

$$\lambda_{a_i | M_w = m_i} = \lambda_{a_i} \mathrm{P}\left[M_w = m_i | a_{max} > a_i\right] \tag{3.4}$$

If this is performed for a series of return periods, a set *magnitude-specific* a_{max} *hazard curves* can be constructed. The hazard curve values for several magnitudes are shown, along with the overall hazard curve, in Figure 3.4.

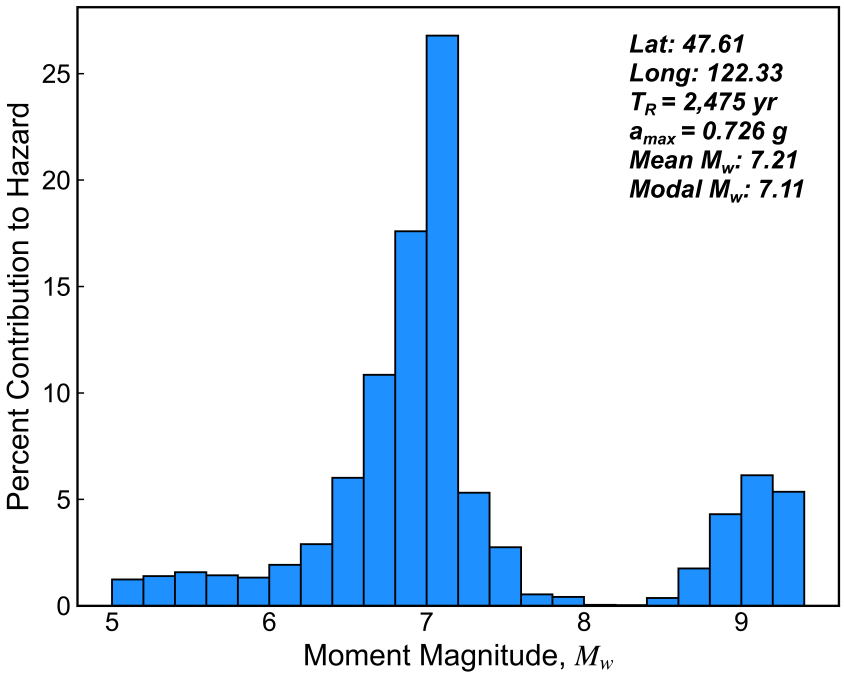

Figure 3.3: Deaggregated moment magnitude distribution for a site in Seattle, Washington with $V_{s30} = 215$ m/s, for peak acceleration a_{max} corresponding to a 2,475-year return period.

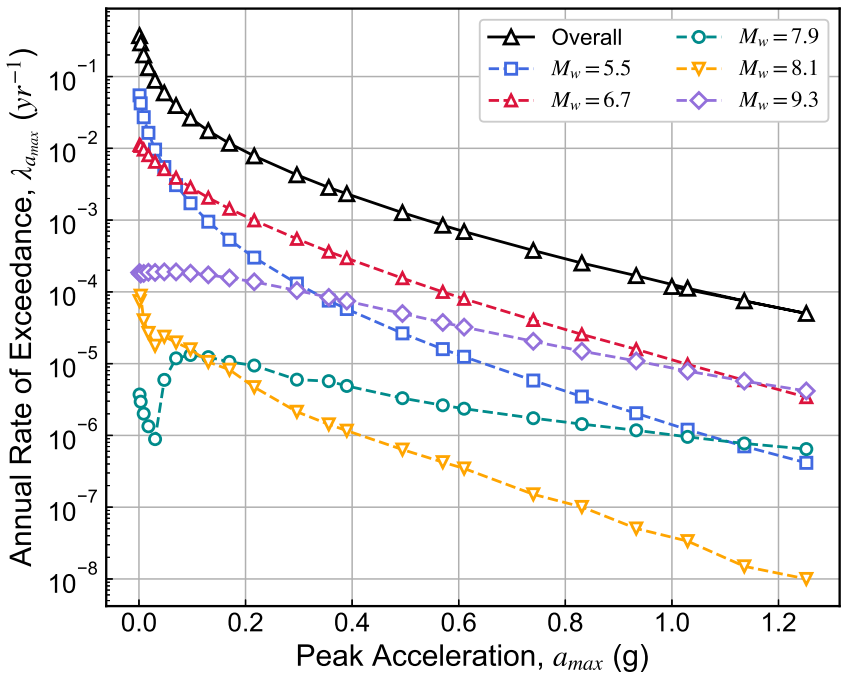

Figure 3.4: Overall hazard curve and selected magnitude-specific hazard curves, obtained from deaggregated hazard data at various return periods for a site in Seattle, Washington with with $V_{s30} = 215$ m/s,

Interpolation of Magnitude-Specific a_{max} Hazard Curves

In order to perform the PLHA calculations at regularly-spaced intervals of a_{max}, the marginal magnitude distributions must be interpolated from the raw deaggregation data. The most direct and robust way to do this is to interpolate the M_w-hazard curve values ($\lambda_{a_{max}|M_w}$) calculated using Equation (3.4). This can be done using a similar cubic spline interpolation in a_{max}-log λ space as that employed to interpolate the overall hazard curve shown in Figure 3.1. However, it is important to recognize that the M_w-specific hazard curves calculated here are reconstructed from the product of the overall hazard curve and magnitude distribution data as obtained from `nshmp-haz`, rather than via a direct PSHA for a given magnitude bin. The deaggregation output from `DeaggCalc` module truncates all M_w bin percentages below 0.01% and presents them as zero-valued (as shown for $8.0 < M_w < 8.4$ in Figure 3.3). In processing the data for a given deaggregation calculation, a correction scheme was adopted where the difference between the sum of all the magnitude percentages and 100% was re-distributed evenly among all magnitude bins, thereby eliminating zero-valued magnitude probabilities. Because the differences in percent contribution were generally very small (less than about 0.3%), the probabilities assigned to those magnitude intervals were very low, and the changes in marginal probabilities across all bins from the re-distributed difference were practically insignificant.

As a result, certain M_w hazard curves do not exhibit the same smooth behavior as the overall a_{max} hazard curves usually do, often displaying sharp irregularities that render basic spline fitting inapplicable. Referring back to Figure 3.4, such irregular behavior can be seen in the M_w7.9 and M_w8.1 curves, particularly at very low values of a_{max} where the percent contribution for that particular magnitude bin was exceedingly small. Based on a review of raw deaggregated M_w curves from 10 sites representing varying seismo-tectonic environments distributed throughout the U.S. (Table 3.1), a slightly modified interpolation scheme was developed to account for such irregularities at low hazard levels and low percent-contribution portions of the M_w hazard curves. The scheme is based on identifying a "linear subset", where potentially irregular behavior is accounted for by reverting to a simple linear interpolation scheme in a_{max}-log λ space, and splicing that subset to the "spline subset", which consists of the smoothly varying datapoints that can be interpolated accurately using a cubic spline. The scheme is implemented in the following series of steps for given M_w-specific hazard curve:

1. Beginning with the lowest a_{max} value and working upwards, track the number of consecutive λ_{a_i,M_w} values for which the percent contribution of the M_w bin is less than 2% to the overall hazard. These value comprise the linear subset.

   (a) However, if *any* value of $a_{max} < 0.02$ g has a percent contribution less than 2%, all data

points less than 0.02 g are considered to be in the linear subset.

2. Once a value greater than 2% contribution is reached, this value is also appended to the linear subset, in order to ensure that at least two points are used to linearly interpolate.

3. The remaining data points comprise the spline subset, which shares a common endpoint with the linear subset.

4. If there are no points in the linear subset, the entire hazard curve is interpolated using a cubic spline.

5. If there are fewer than four points in the spline subset, the entire set is interpolated linearly in a_{max}-log λ space.

6. Otherwise, the data from the two subsets are interpolated using their respective methods, and combined to form the full M_w-specific interpolated hazard curve.

Table 3.1: Summary of test sites used in development and validation of PLHA code

Site	Latitude	Longitude
Charleston, SC	32.78	-79.93
Eureka, CA	40.8	-124.16
Los Angeles, CA	34.05	-118.24
Memphis, TN	35.15	-90.05
Minneapolis, MN	44.98	-93.27
New York, NY	40.71	-74.01
Salt Lake City, UT	40.76	-111.89
San Francisco, CA	37.77	-122.42
Seattle, WA	47.61	-122.33

Extrapolating Magnitude-Specific a_{max} Hazard Curves Beyond 20,000-year Return Period

When any sort of analysis involving integration of fragility curves with *IM* hazard data is undertaken, it is important to ensure that a sufficiently broad range of intensity measure values is used, so that the resulting fragility curves reach stable probabilities of exceedance of a particular *EDP*. In the case of PLHA, this means that the M_w-specific a_{max} hazard curves must extend out to large enough values of a_{max} such that the non-exceedance term in Equation (3.1) can reach a

value of 1.0. However, as noted previously, the `DeaggCalc` module requires a target return period as input, rather than a desired a_{max} value, and is limited to performing deaggregation calculations up to a return period of 20,000 years. Depending on the seismic environment and site conditions, this return period may coincide with a_{max} values that are lower than those that would produce stable estimates of Λ_{FS_L} from fully-developed fragility curves. Thus, it is preferable to develop a_{max} hazard curves to a uniform maximum a_{max} value, taken here to be 3.0 g. This can necessitate extrapolation of some of the M_w hazard curves, and an assumption that the M_w distribution at 20,000 years is constant for longer return periods. Such an assumption is reasonable because at longer return periods corresponding to high a_{max} values, the source contribution is typically at or very near the maximum magnitude (M_{max}) and minimum distance (R_{min}) bins. Beyond that point, any increase hazard is largely controlled by an increase in ε, which is the number of standard deviations above the mean a_{max} for the M_{max}-R_{min} bin. The marginal magnitude distributions shown in Figure 3.5 for four of the sites from Table 3.1 generally confirm that the magnitude distributions stabilize at long return periods, and the use of the 20,000-year marginal magnitude distribution in extrapolating the magnitude hazard curves is reasonable.

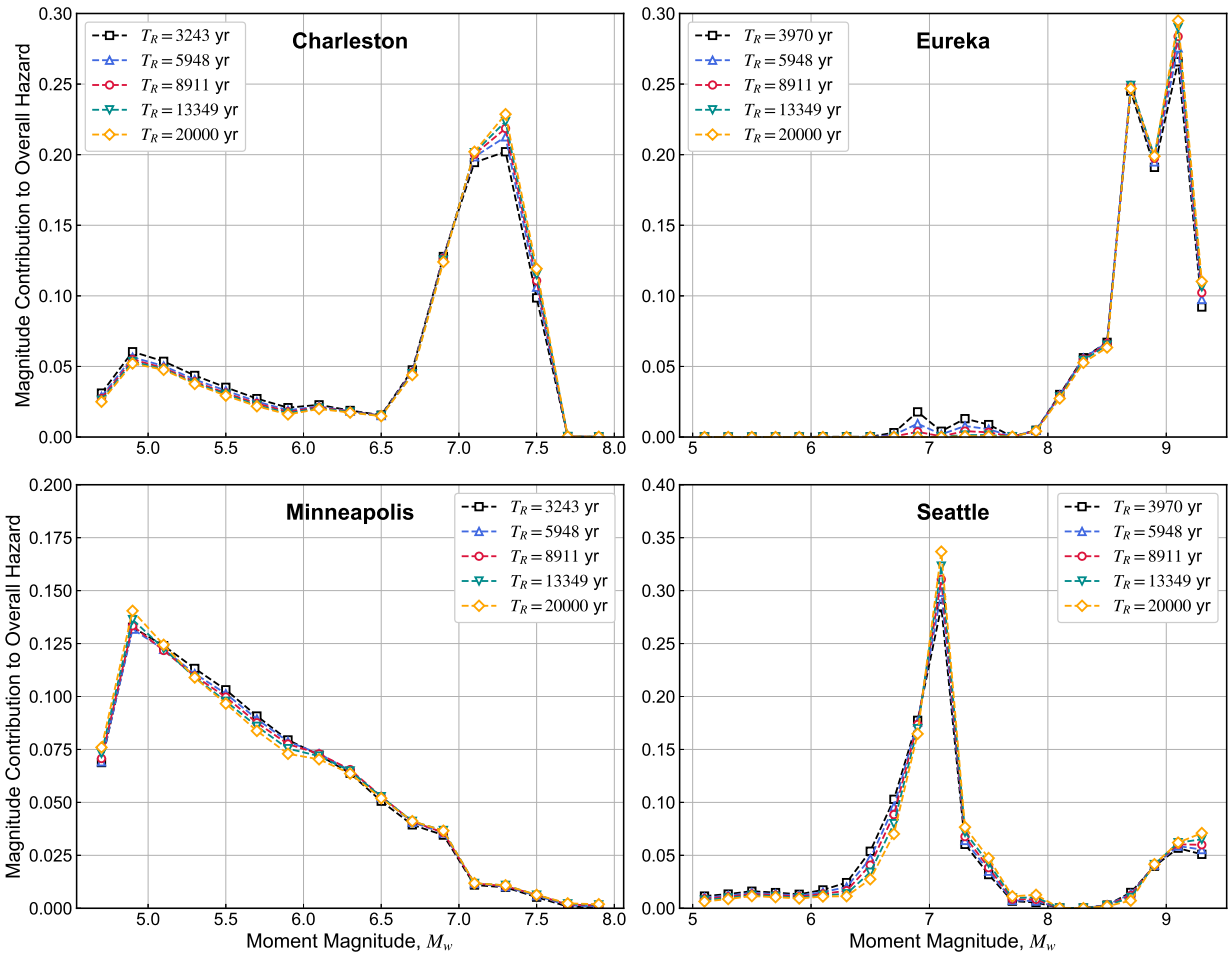

Figure 3.5: Marginal magnitude distributions for increasing a_{max} return periods, for four geographic locations with $V_{s30} = 215$ m/s

For return periods greater than 20,000 years, the cubic spline-interpolated values for the overall hazard curve (obtained from the `HazCalc`) are multiplied by the percent contribution from the 20,000-year deaggregation (Figure 3.6).

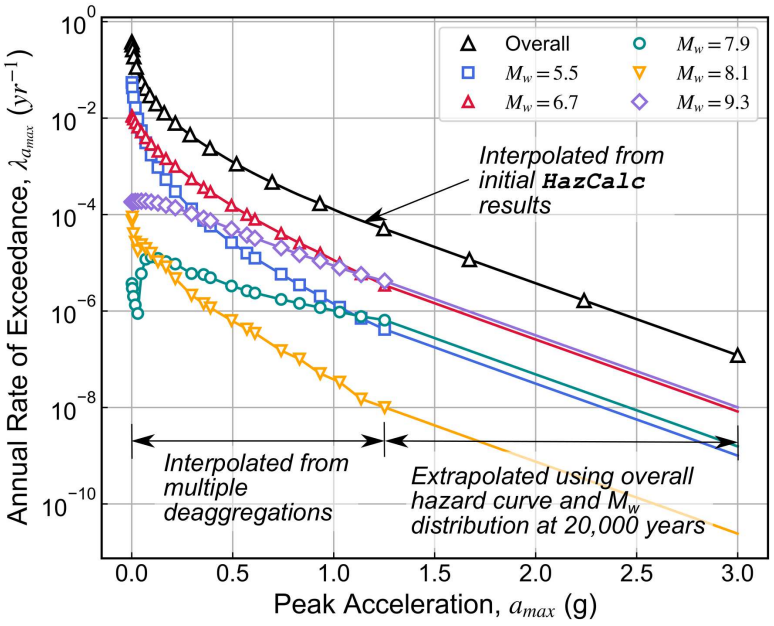

Figure 3.6: Selected interpolated/extrapolated magnitude hazard curves for a site in Seattle, Washington

To fully characterize the λ_{a_{max},M_w} term in Equation (3.1), the procedure for interpolating and extrapolating the raw deaggregation data is repeated for all M_w bins. The resulting full set of M_w hazard curves is shown for a site in Seattle in Figure 3.7. Note that the specific M_w values denote the *midpoints* of the magnitude bins, and are therefore influenced by the parameters of the deaggregation calculations, namely the minimum and maximum magnitudes, as well as the magnitude bin size.

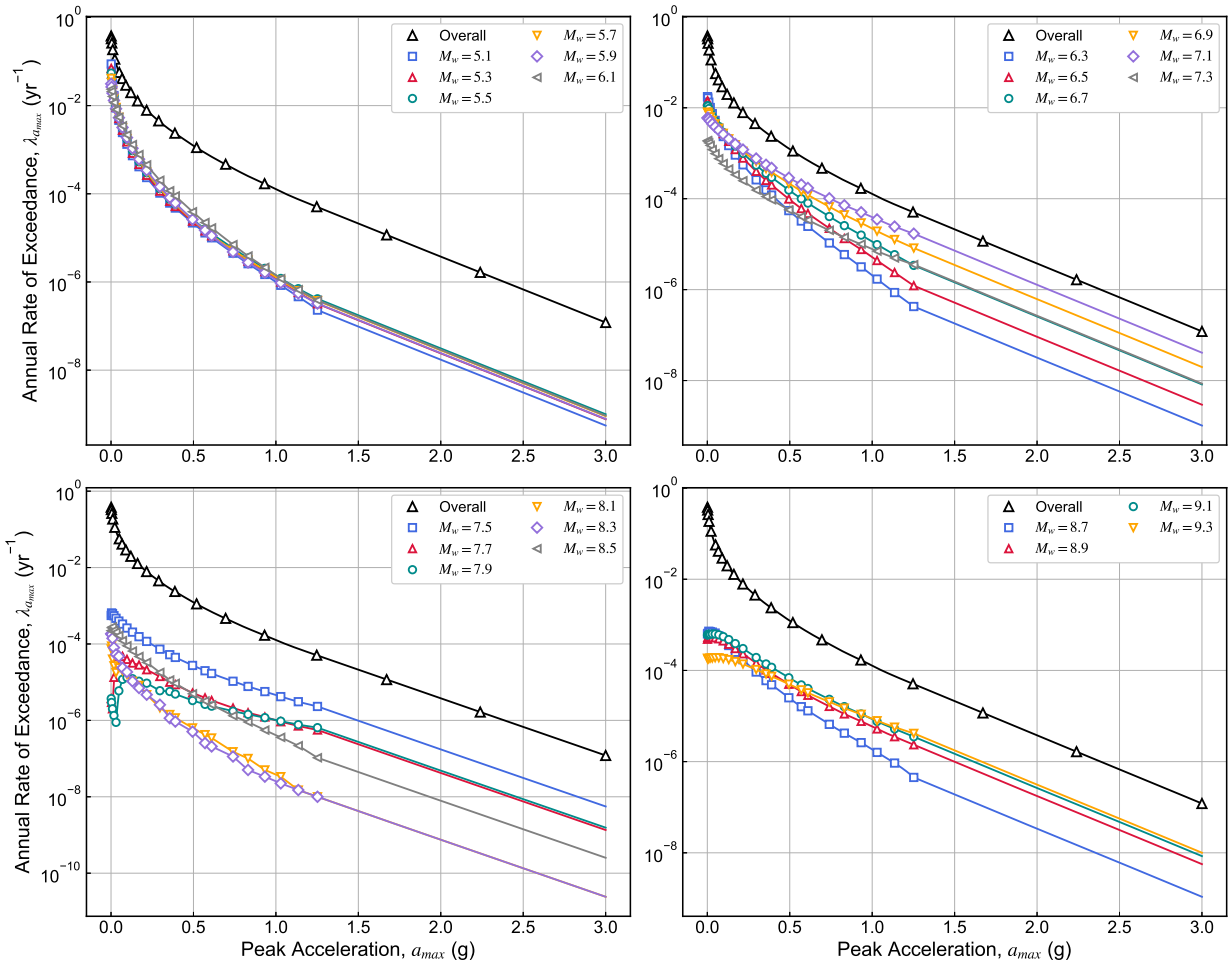

Figure 3.7: Full set of interpolated/extrapolated magnitude hazard curves for a site with $V_{s30} = 215$ m/s in Seattle, Washington. Curves have been divided into four magnitude ranges for visual clarity.

Maximum Acceleration for use in PLHA Calculations

As stated previously, the M_w-specific hazard curves are extrapolated in a consistent manner out to $a_{max} = 3.0$ g for all sites, in all seismo-tectonic regions. The selection of 3.0 g is based on the maximum PGA used by USGS in their PSHA framework to develop the national seismic hazard maps. Due to the fact that the USGS hazard maps are developed for soft rock sites, an argument could be made that the maximum a_{max} considered in probabilistic liquefaction calculations, which naturally occur at softer soil sites, should be lower due to non-linear considerations. However, the general consensus in engineering seismology appears to be that there is little justification in truncating ground motion distributions, either at a maximum "physically possible" PGA or at some number of standard deviations above the median predicted PGA (Hanks et al. 2005, Strasser et al. 2008). Furthermore, in terms of calculating Λ_{FS_L}, a scenario where the fragility curves are truncated at an unreasonably low a_{max} has the potential to result in lower exceedance rates

than what would be calculated from the full distribution, thus producing a slightly unconservative estimate of the liquefaction hazard. The inclusion of the full range of a_{max} thus might produce, at worst, a slightly conservative representation of the liquefaction hazard, but currently there is no strong justification to do otherwise.

3.4 Probabilistic Liquefaction Triggering Models

Most current empirical methods for analyzing liquefaction triggering involve characterization of the earthquake loading on an element of soil and the soil's resistance to liquefaction. The two measures are typically compared to one another, and then compared to an existing database of field observations from potentially susceptible sites where liquefaction either occurred or did not occur during seismic events.

The most common empirical methods, which were initially developed in the 1960s and 1970s and have been continuously refined to the present day, describe the earthquake loading in terms of cyclic shear stresses, and the resistance in terms of the amplitude and number of cycles of shear stresses required to initiate liquefaction. This approach is now commonly known as the *cyclic stress method*.

The deterministic form of the cyclic stress method involves comparing the *cyclic resistance ratio*, or *CRR* with the *cyclic stress ratio*, or *CSR*. The primary index for evaluating the liquefaction potential of a particular element of soil is simply the ratio of these two parameters, known as the *factor of safety against liquefaction* (FS_L):

$$FS_L = \frac{CRR}{CSR} \tag{3.5}$$

In this approach, a factor of safety of 1.0 represents the condition under which liquefaction is expected to occur. While FS_L provides a useful index for liquefaction susceptibility in a deterministic sense, its incorporation into the PBEE framework as an engineering demand parameter (EDP) requires a probabilistic representation of liquefaction potential that accounts for the relevant sources of aleatory and epistemic uncertainty in the observations used to develop the empirical model.

The probabilistic triggering models incorporated herein (Cetin et al. [2004], Boulanger and Idriss [2012], and Boulanger and Idriss [2015]) are based on a limit-state function g, which is a function of both loading and resistance parameters, e.g. $g = CRR - CSR$. For cases where $g \leq 0$, liquefaction is assumed to have occurred. For $g > 0$, liquefaction is assumed to have not occurred. This class of cyclic stress models was developed using a likelihood function based on the probability

of liquefaction, which can be expressed in terms of the limit-state function as follows:

$$P_L(\mathcal{L}, \mathcal{R}, \theta, \varepsilon) = P[g(\mathcal{L}, \mathcal{R}, \theta, \varepsilon) \leq 0] \tag{3.6}$$

where $\mathcal{L}$ and $\mathcal{R}$ represent the loading (e.g. a_{max}, M_w) and resistance (e.g. $(N_1)_{60}$, q_{c1N}, FC, σ'_v) parameters, respectively; θ represents the set of unknown model parameters (e.g. model coefficients); and ε is the model standard error. The various models were developed using maximum likelihood solutions to the limit-state function to produce estimates of the unknown parameters and standard deviation. The methods used to characterize the loading and resistance, as well as the parameter estimation methods, differ slightly across the empirical models employed here, and are discussed in detail in the following sections.

3.4.1 Cetin et al. (2004)

The probabilistic SPT-based triggering model proposed by Cetin et al. (2004), which will herein be referred to as CEA04, presents the overall correlation for the probability of liquefaction as follows:

$$P_L(N_{1,60}, CSR_{eq}, M_w, \sigma'_v, FC) = \Phi\left\{-\frac{N_{1,60}\cdot(1+C_0\cdot FC) - C_1\cdot\ln CSR_{eq} - C_2\cdot\ln M_w - C_3\cdot\ln\frac{\sigma'_v}{P_a} + C_4\cdot FC + C_5}{\sigma_\varepsilon}\right\} \tag{3.7}$$

where Φ is the standard normal cumulative probability function, σ_ε is the model standard deviation, and $C_0, C_1, ...C_5$ are the model coefficients.

Equivalent Cyclic Stress Ratio

In this formulation, CSR_{eq} is the *equivalent uniform cyclic stress ratio*, which is defined as:

$$CSR_{eq} = 0.65 a_{max}\frac{\sigma_v}{\sigma'_v}r_d \tag{3.8}$$

Note that, in contrast to many other cyclic stress methods, the CSR here is not corrected to a reference magnitude to account for duration effects. Rather, the effects of duration (via moment magnitude) are considered explicitly in the third term of limit-state function. Additionally, a re-

vised formulation for the depth reduction factor, r_d (also referred to as the "nonlinear shear mass participation factor"), was presented in CEA04. Previous researchers (Seed and Idriss [1971], Golesorkhi [1989], and Idriss [1999]) proposed that the variation in shear stress with respect to depth could be adequately expressed as a function of moment magnitude (M_w). CEA04, using a broader range of input ground motions, and soil profiles based on actual liquefiable sites, proposed two additional descriptive variables: the representative shear wave velocity at the site in the upper 12 m, $V^*_{s,12m}$; and the peak horizontal ground acceleration, a_{max}. The CEA04 depth reduction factor can be calculated as follows:

For $z < 20$m:

$$r_d(z, M_w, a_{max}, V^*_{s,12m}) = \frac{\left[1 + \frac{A(a_{max}, M_w, V^*_{s,12m})}{B(z, V^*_{s,12m})}\right]}{\left[1 + \frac{A(a_{max}, M_w, V^*_{s,12m})}{B(V^*_{s,12m})}\right]} \pm \sigma_{\varepsilon_{r_d}} \tag{3.9}$$

where:

$$A(a_{max}, M_w, V^*_{s,12m}) = -23.013 - 2.949a_{max} + 0.999M_w + 0.0525V^*_{s,12m}$$

$$B(z, V^*_{s,12m}) = 16.258 + 0.201e^{0.341(-z+0.0785V^*_{s,12m}+7.586)}$$

$$B(V^*_{s,12m}) = 16.258 + 0.201e^{0.341(0.0785V^*_{s,12m}+7.586)}$$

For $z \geq 20$m:

$$r_d(z, M_w, a_{max}, V^*_{s,12m}) = \frac{\left[1 + \frac{A(a_{max}, M_w, V^*_{s,12m})}{B(z, V^*_{s,12m})}\right]}{\left[1 + \frac{A(a_{max}, M_w, V^*_{s,12m})}{B(V^*_{s,12m})}\right]} - 0.0046(z - 20) \pm \sigma_{\varepsilon_{r_d}} \tag{3.10}$$

where:

$$B(z, V^*_{s,12m}) = 16.258 + 0.201e^{0.341(-20+0.0785V^*_{s,12m}+7.586)}$$

and $A(a_{max}, M_w, V^*_{s,12m})$ and $B(V^*_{s,12m})$ are the same as those in Equation (3.9) for $z < 20$m. The standard deviation, $\sigma_{\varepsilon_{r_d}}$, is expressed as:

$$\sigma_{\varepsilon_{r_d}} = 0.0198z^{0.8500} \quad \leq 0.1637 \tag{3.11}$$

and reaches its limiting value at a depth of 12 m.

These relationships were developed using a set of ground motions ranging in magnitude from 5.7 to 8.1, and with scaled PGAs ranging from 0.05 to 0.55 g. The nature of PLHA obviously necessitates the evaluation of r_d outside of these ranges of M_w and a_{max}, and thus the reader should recognize the practical implications of using the CEA04 method in performance-based calculations. Cetin et al. also recommended that $V^*_{s,12m}$ be limited to 120 to 250 m/s. Figure 3.8 illustrates how the variation in r_d with respect to depth is sensitive to M_w, V_{s12m}, and a_{max}.

Bayesian Regression and Probabilistic Relationships

Cetin et al. used a Bayesian updating scheme assuming a diffuse prior distribution to estimate the model parameters C_0 through C_5, and assumed a uniform distribution (also known as a non-informative prior) to estimate σ_ε. The recommended values for these parameters are presented in Table 3.2.

Table 3.2: Summary of recommended parameter values in CEA04 model

Parameter	Recommended Value
C_0	0.004
C_1	13.32
C_2	29.53
C_3	3.7
C_4	0.05
C_5	16.85
σ_ε	2.7

The probabilistic correlation presented in Equation (3.7) can be rearranged to compute the cyclic resistance ratio for a given value of P_L and soil parameters ($(N_1)_{60}$, FC, etc.):

$$CRR(N_{1,60}, M_w, \sigma'_v, FC, P_L) = \exp\left[-\frac{N_{1,60}\cdot(1+C_0\cdot FC) - C_2\cdot\ln M_w - C_3\cdot\ln\frac{\sigma'_v}{P_a} + C_4\cdot FC + C_5 + \sigma_\varepsilon\cdot\Phi^{-1}(P_L)}{C_1}\right] \tag{3.12}$$

For use in deterministic analyses to calculate the factor of safety FS_L, the CRR can be computed using Equation (3.12) for a given probability of liquefaction, and then divided by $CSReq$ using the methods described in Equations (3.8) and (3.9). The original recommendation in Cetin et al. was

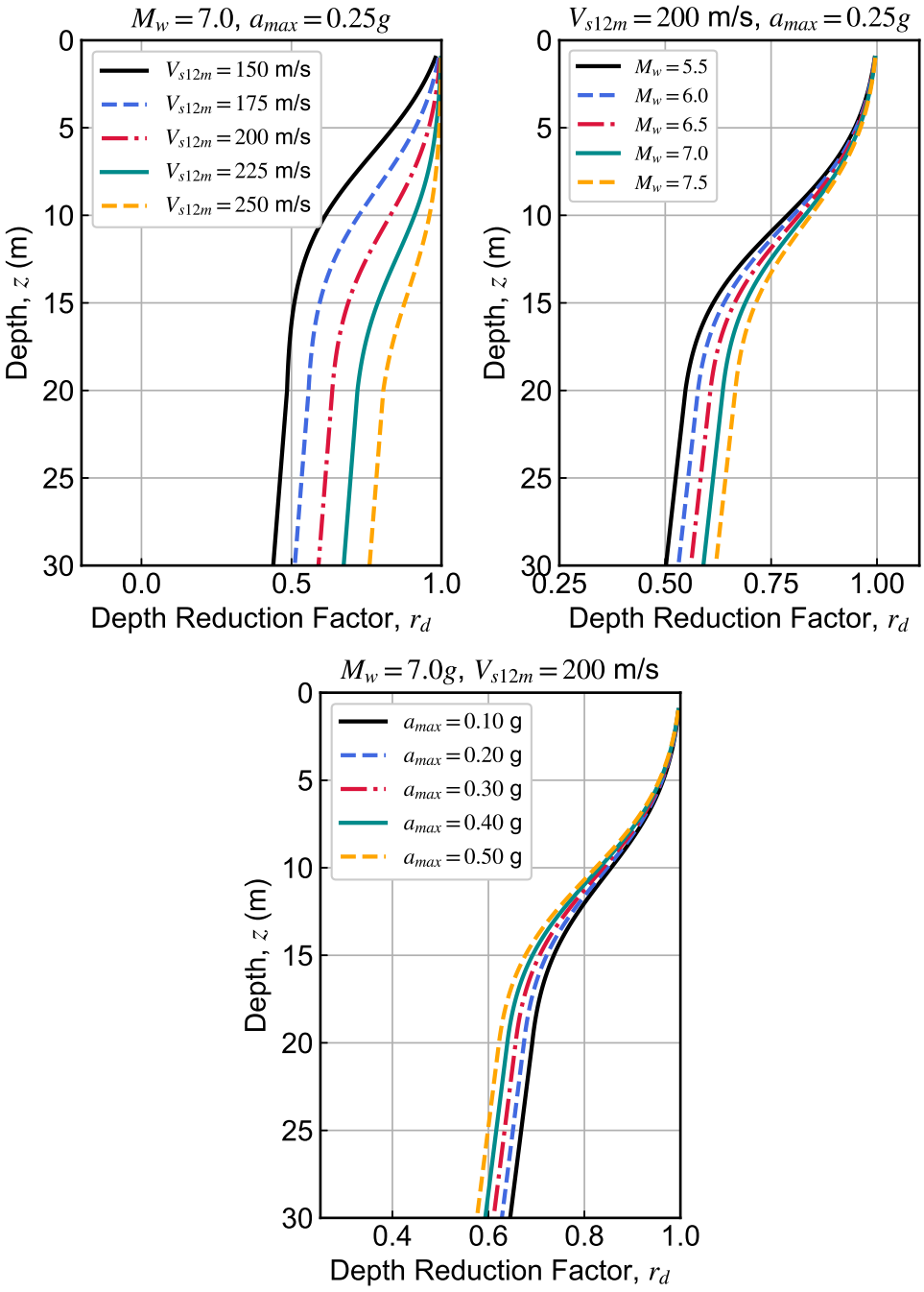

Figure 3.8: Variation of CEA04 stress reduction factor with depth and (a) Shear wave velocity (V_{s12m}), (b) moment magnitude (M_w), and (c) peak ground acceleration (a_{max})

to use a P_L of 15%; similarly, the deterministic triggering curves of Idriss and Boulanger (2008) and Boulanger and Idriss (2012) appear to coincide with a P_L of about 16%. Probabilistic correlations for the CRR of clean sands for $P_L = 5\%, 20\%, 50\%, 80\%, 95\%$ are shown in Figure 3.9.

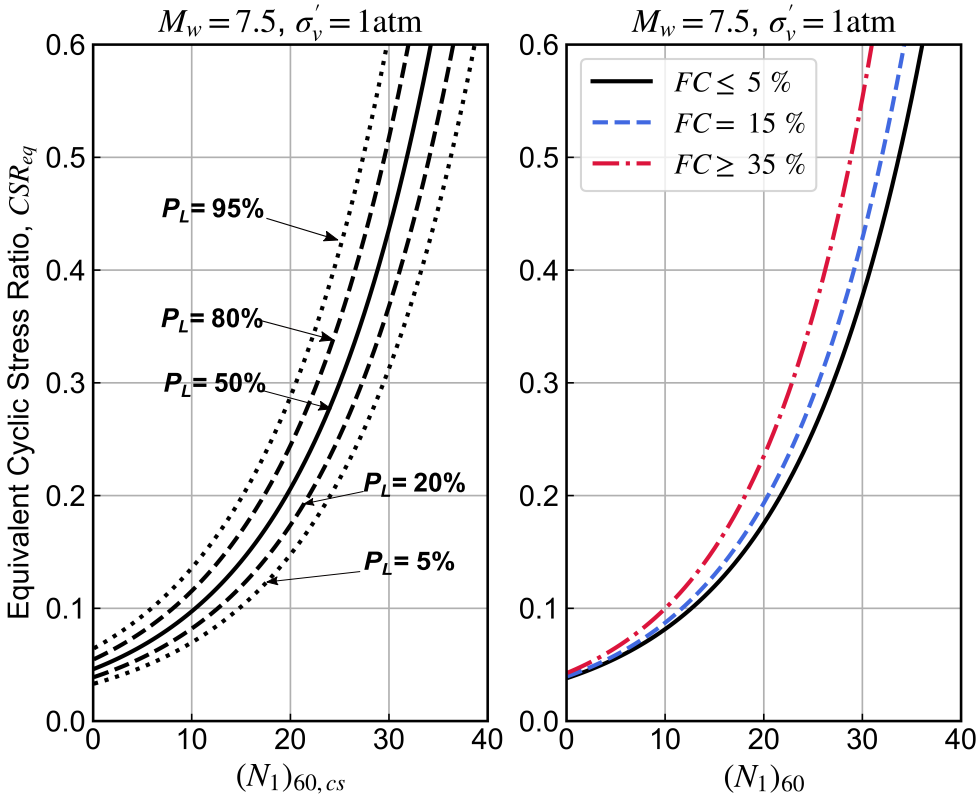

Figure 3.9: Liquefaction triggering curves, based on Cetin et al. (2004) model: (a) SPT-based probabilistic correlations for clean sands for various probabilities of liquefaction, using model uncertainty. (b) Deterministic triggering curves for a probability of liquefaction of 15%, for various fines contents

In order to fully utilize the probabilistic liquefaction relationship into a performance-based framework, the relationship for P_L in Equation (3.7) can be adapted to formulate an expression for the probability of non-exceedance for FS_L. Such an expression can be easily achieved by multiplying CSR_{eq} in Equation (3.7) by the desired factor of safety, fs_L. The resulting expression is thus:

$$P[FS_L < fs_L] = \Phi\left\{-\frac{N_{1,60}(1+C_0FC) - C_1\ln(fs_L CSR_{eq}) - C_2\ln M_w - C_3\ln\frac{\sigma'_v}{P_a} + C_4FC + C_5}{\sigma_\varepsilon}\right\} \tag{3.13}$$

3.4.2 Boulanger and Idriss - SPT (2012) and CPT (2015)

Boulanger and Idriss (2012, 2015) developed probabilistic forms of the CPT- and SPT-based triggering curves presented in Idriss and Boulanger (2008). The probability of liquefaction is expressed in terms of the cyclic stress and cyclic resistance ratios that were traditionally developed for the deterministic form of the simplified method, which are corrected to a reference magnitude ($M_w = 7.5$) and effective stress ($\sigma'_v = 1\text{atm}$):

$$P_L = \Phi\left\{-\frac{\ln(CRR_{M=7.5,\sigma'_v=1\text{atm}}) - \ln(CSR_{M=7.5,\sigma'_v=1\text{atm}})}{\sigma_{\ln(CRR)}}\right\} \tag{3.14}$$

Magnitude- and Overburden-Corrected Cyclic Stress Ratio

The reference CSR takes the same basic form as Equation (3.8), with additional corrections for earthquake duration and the effect of overburden stress on cyclic resistance:

$$CSR_{M=7.5,\sigma'_v=1\text{atm}} = 0.65 \cdot a_{max}\frac{\sigma_v}{\sigma'_v} \cdot r_d \frac{1}{MSF}\frac{1}{K_\sigma} \tag{3.15}$$

where MSF refers to the magnitude scaling factor, a measurement of the dependence of a soil's liquefaction on the duration of shaking, and K_σ is the overburden correction factor. The stress reduction factor, r_d is calculated differently in the Boulanger and Idriss models than in Equation (3.9), and depends only on depth and magnitude:

$$r_d = \exp[\alpha(z) + \beta(z) \cdot M_w] \tag{3.16}$$

where

$$\alpha(z) = -1.1012 - 1.126\sin\left(\frac{z}{11.73} + 5.133\right)$$

$$\beta(z) = 0.106 + 0.118\sin\left(\frac{z}{11.28} + 5.142\right)$$

The variation of stress reduction factor with depth and magnitude is shown in Figure 3.10. While r_d relationship in Equation (3.16) is mathematically applicable for depths as large as 34 m, Boulanger and Idriss (2008) recommend that their use be limited to depths no greater than 20 m, due to the large increase in uncertainty in r_d with increasing depth.

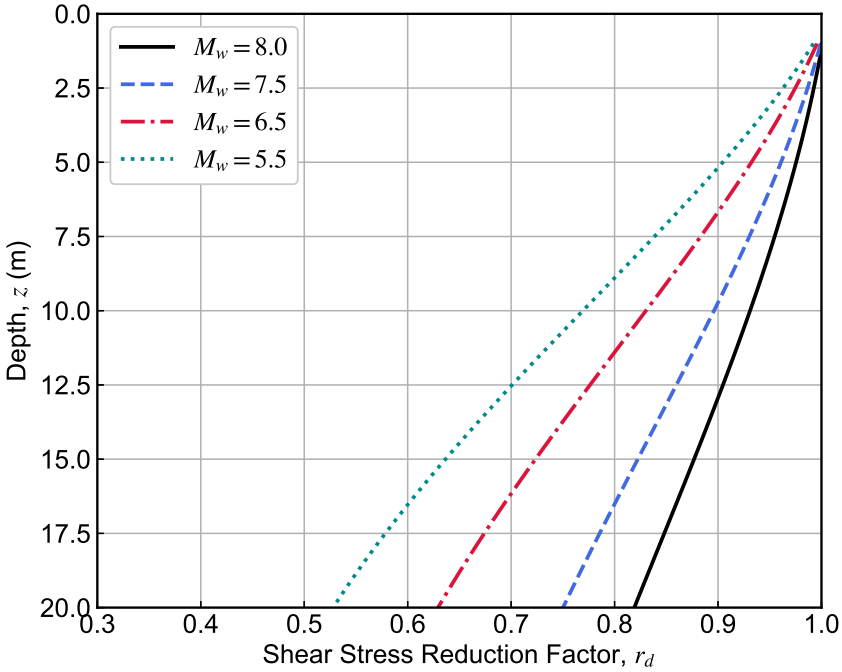

Figure 3.10: Variation of Boulanger and Idriss (2008) stress reduction factor with depth for various earthquake magnitudes.

The updated MSF relationships (Boulanger and Idriss [2015a]) are based on the results of cyclic testing of sands, as well as the analysis of ground motion recordings. Where the original MSF relationship proposed by Idriss and Boulanger (2008) depended only on earthquake magnitude, the updated relationship incorporates an additional dependence on soil density:

$$MSF = 1 + (MSF_{max} - 1)\left[8.64 \exp\left(\frac{-M_w}{4}\right) - 1.325\right] \tag{3.17}$$

where

$$MSF_{max} = 1.09 + \left(\frac{q_{c1Ncs}}{180}\right)^3 \leq 2.2$$

or

$$MSF_{max} = 1.09 + \left[\frac{(N_1)_{60,cs}}{31.5}\right]^2 \leq 2.2$$

Magnitude scaling relationships for selected penetration resistance values are shown in Figure 3.11. The overburden correction factor K_σ (Boulanger [2003]) was derived by relating the relative state parameter ξ_R to cyclic resistance initially for laboratory tests on reconstituted sands, then for *in situ* conditions (by mapping representative penetration resistances to ξ_R). The resulting relationship is applicable for both CPT- and SPT-based analyses:

$$K_\sigma = 1 - C_\sigma \ln\left(\frac{\sigma'_v}{P_{atm}}\right) \qquad \leq 1.1 \tag{3.18}$$

where

$$C_\sigma = \frac{1}{37.3 - 8.27(q_{c1Ncs})^{0.264}} \qquad \leq 0.3$$

or

$$C_\sigma = \frac{1}{18.9 - 2.55\sqrt{(N_1)_{60,cs}}} \qquad \leq 0.3$$

The overburden correction relationship is presented for selected penetration resistance values in Figure 3.12.

It is important to note that the calculation of MSF and K_σ involve maximum values, or "caps". In the case of MSF, the cap is applied in the intermediate MSF_{max} parameter; with K_σ, caps are introduced in both the intermediate C_σ parameter and the final K_σ value. These caps were originally introduced as judgment-based limits on these parameters, with the intention of producing suitably conservative results in deterministic analyses. As a result, the direct use of the deterministic caps in probabilistic triggering analyses may not be entirely appropriate - probabilistic analyses, by their very nature, are used in order to avoid the necessity of conservative and somewhat subjective limits. The caps are expected to produce some degree of bias toward low FS_L values under the conditions that engage them.

Characterization of Cyclic Resistance

The CPT- and SPT-based relationships between clean sand-corrected penetration resistance and cyclic resistance ratio are of the same form as those presented in Idriss and Boulanger (2008):

$$CRR_{M=7.5,\sigma'_v=1\text{atm}} = \exp\left[\frac{q_{c1Ncs}}{113} + \left(\frac{q_{c1Ncs}}{1000}\right)^2 - \left(\frac{q_{c1Ncs}}{140}\right)^3 + \left(\frac{q_{c1Ncs}}{137}\right)^4 - C_0\right] \tag{3.19}$$

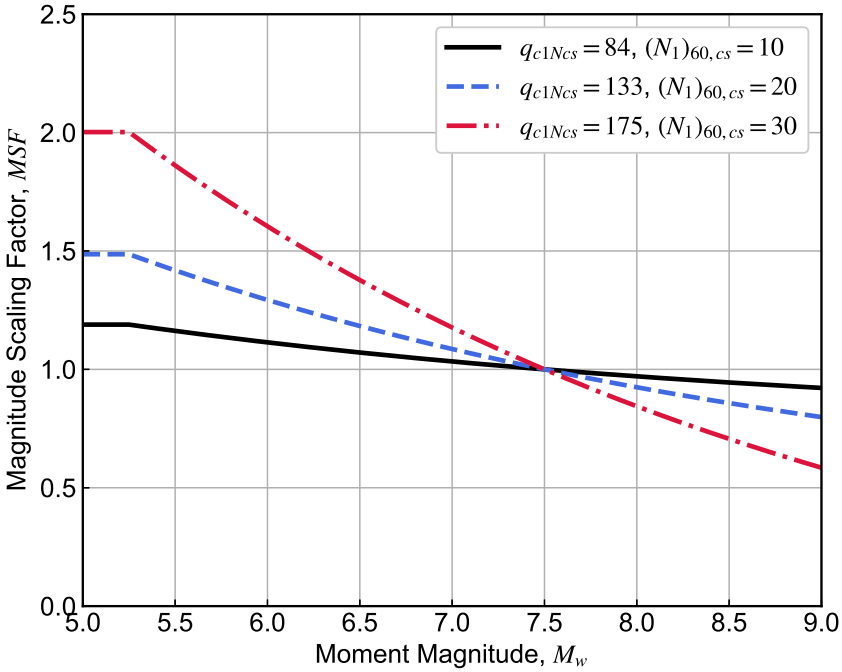

Figure 3.11: Variation in Boulanger and Idriss (2012,2015) magnitude scaling factor for various values of q_{c1Ncs} and corresponding $(N_1)_{60,cs}$.

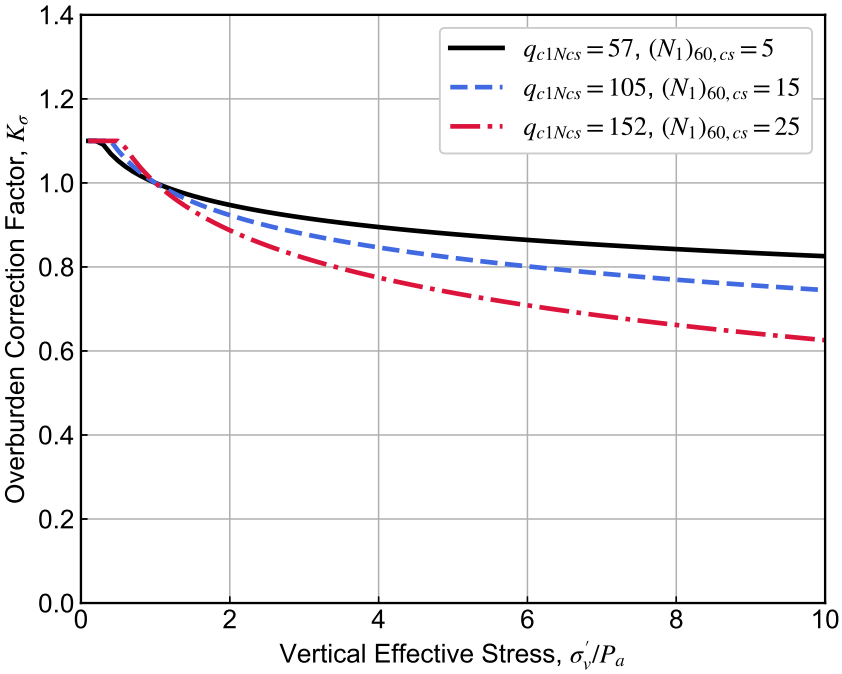

Figure 3.12: Variation in overburden correction factor for various values of q_{c1Ncs} and $(N_1)_{60,cs}$ (after Boulanger and Idriss [2014])

$$CRR_{M=7.5,\sigma'_v=1\text{atm}} = \exp\left[\frac{(N_1)_{60,cs}}{14.1} + \left(\frac{(N_1)_{60,cs}}{126}\right)^2 - \left(\frac{(N_1)_{60,cs}}{23.6}\right)^3 + \right. \\ \left. + \left(\frac{(N_1)_{60,cs}}{25.4}\right)^4 - C_0\right] \tag{3.20}$$

For the development of a probabilistic triggering procedure, C_0 was treated as the only unknown parameter to be estimated in the maximum likelihood solution. Otherwise, the SPT-based CRR formula is identical to that presented in Idriss and Boulanger (2008), while the CPT-based formula is based on a revised correlation presented in Boulanger and Idriss (2014). This has the effect of simply translating the position of the CRR curve up or down at different liquefaction probability levels, but the shape of the curve itself remains constant. In contrast, the CEA04 procedure allows for the actual shape of the curve to change at different probability levels (along with its vertical position).

The clean sand-corrected penetration resistances are estimated by applying fines content adjustments to the normalized penetration resistances. The fines content adjustments for both CPT- and SPT-based analyses are given in Equation (3.21) and shown in Figure 3.13.

$$q_{c1Ncs} = q_{c1N} + \Delta q_{c1N} \tag{3.21a}$$

$$(N_1)_{60,cs} = (N_1)_{60} + \Delta(N_1)_{60} \tag{3.21b}$$

where

$$\Delta q_{c1N} = \left(11.9 + \frac{q_{c1N}}{14.6}\right) \exp\left[1.63 - \frac{9.7}{FC+2} - \left(\frac{15.7}{FC+2}\right)^2\right]$$

$$\Delta(N_1)_{60} = \exp\left[1.63 - \frac{9.7}{FC+0.01} - \left(\frac{15.7}{FC+0.01}\right)^2\right]$$

Maximum Likelihood Estimation and Probabilistic Relationships

Recall that Cetin et al. (2004) used a Bayesian updating scheme to estimate all of the coefficients in Equation (3.7), as well as the total standard deviation σ_ε. CEA04 additionally incorporated an unknown weighting factor to correct for sampling disparity between liquefied and non-liquefied cases, which was also included in the parameter estimation. A key difference, therefore, in the form adopted by Boulanger and Idriss is that the various components of the model are constrained *a priori* by experimental and theoretical considerations. In other words, the dependence of liquefaction

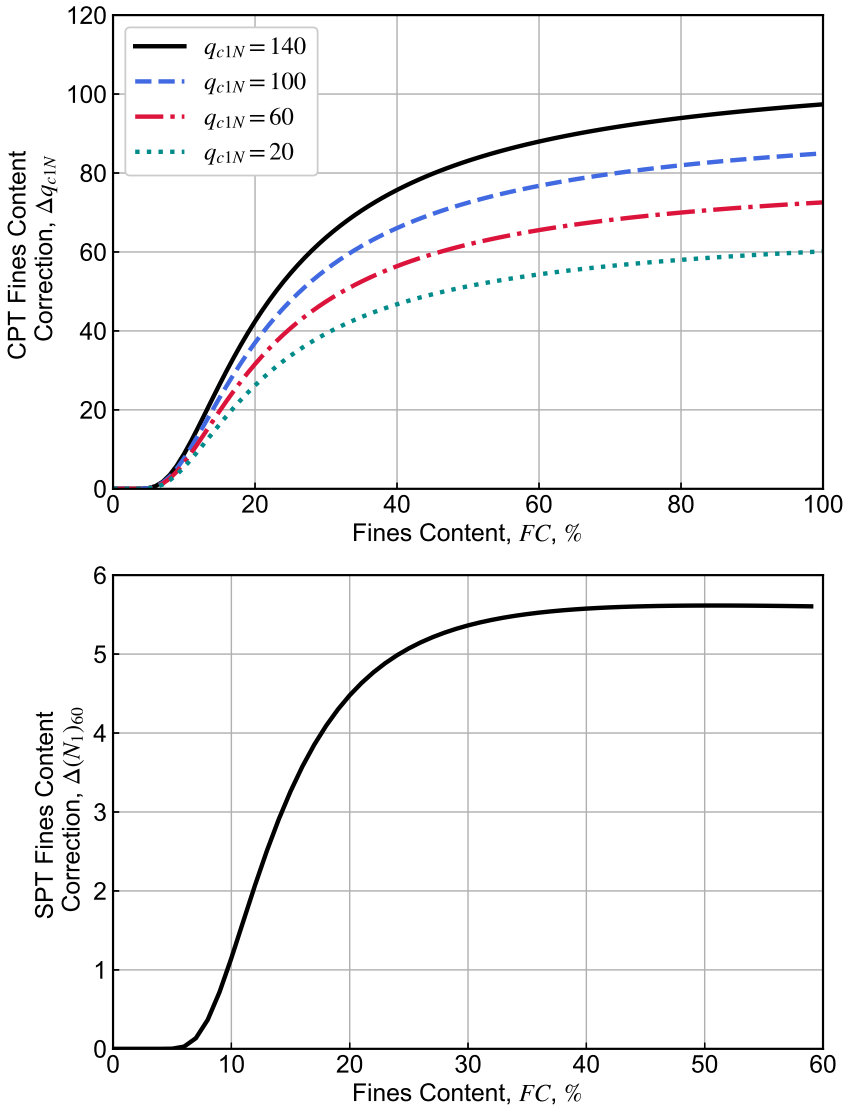

Figure 3.13: Clean-sand fines content corrections from Boulanger and Idriss models, for (a) CPT-based and (b) SPT-based triggering procedures.

potential on factors such as earthquake duration, overburden, relative density, and fines content are accounted for in the Boulanger-Idriss models by factors that were characterized *outside* of the model regression, via the MSF, K_σ, CRR, and clean-sand correction factors, respectively. Thus, the only unknown parameters estimated were the fitting parameter, C_0, and the standard deviation in cyclic resistance ratio, represented here by $\sigma_{\ln CRR}$ for either SPT- or CPT-based methods.

The parameter estimates of C_0 and $\sigma_{\ln CRR}$ were shown to depend on the assumed uncertainties in the database of case histories, as well as the assumed relative weights between liquefied and non-liquefied case histories. For CPT-based triggering analyses, Boulanger and Idriss (2015) recommend $C_0 = 2.60$ and $\sigma_{\ln CRR} = 0.20$ as reasonable values for use in forward predictions. For SPT-based analyses, Boulanger and Idriss (2012) recommend $C_0 = 2.67$ and $\sigma_{\ln CRR} = 0.13$. Thus, the CPT- and SPT-based probabilities of liquefaction can be calculated by substituting the expressions for $CRR_{M=7.5,\sigma'_v=1\text{atm}}$ from Equation (3.19) into Equation (3.14), using the recommended values of C_0 and $\sigma_{\ln CRR}$. The recommended probabilistic correlations are shown for CPT-based and SPT-based triggering analyses in Figure 3.14 and Figure 3.15, respectively, for constant P_L values of 15, 50, and 85 %. Also included in each figure are the deterministic triggering relationships, which coincide with a probability of liquefaction of about 16%.

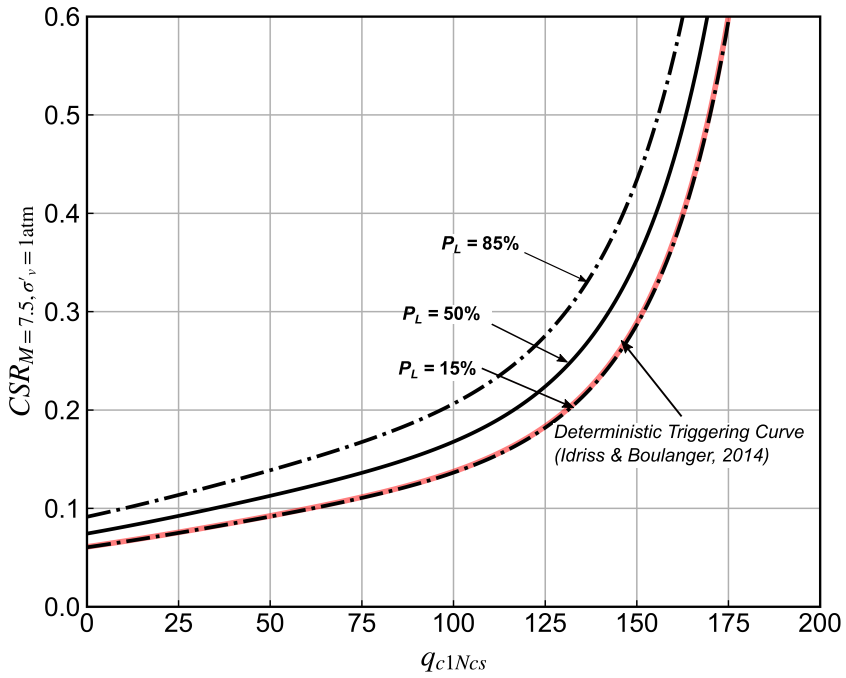

Figure 3.14: Recommended Boulanger and Idriss (2014) CPT-based probabilistic liquefaction triggering curves for $P_L = 15, 50$, and 85%

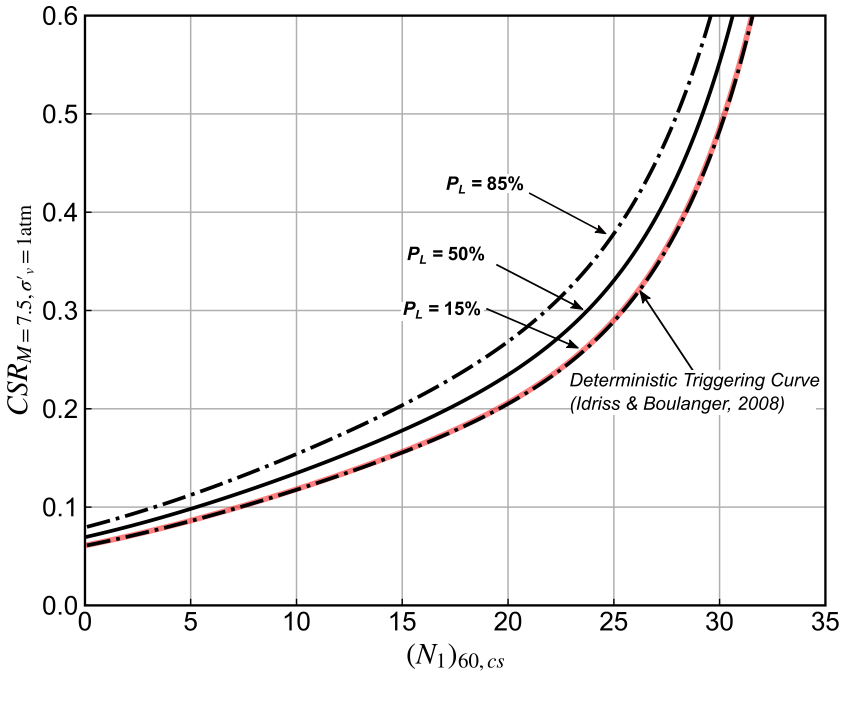

Figure 3.15: Recommended Boulanger and Idriss (2012) SPT-based probabilistic liquefaction triggering curves for $P_L = 15, 50$, and 85%

Note that recommended values for the model standard deviation for forward prediction of liquefaction triggering assume that there is no uncertainty in $CSR_{M=7.5,\sigma'_v=1\text{atm}}$ and q_{c1Ncs} or $(N_1)_{60,cs}$. The uncertainty in $CSR_{M=7.5,\sigma'_v=1\text{atm}}$ is readily accounted for in the PBEE framework by calculating P_L over the joint probability distribution of M_w and a_{max}. In order to account for parametric uncertainty in the representative penetration resistance, which includes both sampling error and spatial heterogeneity and variability, the Boulanger and Idriss recommend branching the probabilistic liquefaction analysis over not only the range of seismic hazards, but additionally the "range of site characterizations". Such a framework could range in sophistication from performing several "scenario" PBEE calculations, for instance for upper-bound, lower-bound, and best-estimates of q_{c1Ncs}, to fully-integrated PBEE calculations that include mean and uncertainty estimates for q_{c1Ncs}, depth, and σ'_v. Such uncertainties stem from measurement error, spatial variability of soil properties, and uncertainty in groundwater depth, and must be accounted for in any truly probabilistic framework - failure to do so will lead to unconservative evaluations of the liquefaction hazard at a particular site.

3.4.3 Validation of Python Code for Triggering Models

The curves shown in Figures 3.9, 3.14, and 3.15 for the CEA04 and the Boulanger-Idriss CPT- and SPT-based triggering models, respectively, validate the the code's ability to calculate CRR for a given P_L. More important to the PBEE calculation framework, however, is the calculation of a previously unknown P_L given a set of known cyclic stress and cyclic resistance parameters. In order to validate the code's forward prediction functionality of P_L, a broad range of hypothetical sublayers was analyzed with randomized penetration resistance values and fines contents, varying in depth from 0 to 30 meters. For each sublayer, the probability of liquefaction was calculated for a range of a_{max} values from 0.01 g to 1.0 g. For validation of the CEA04 model, the effective stress was kept constant at 1 atm, and M_w was taken as 7.5, in order to maintain consistency with the P_L contours Figure 3.9. For validation of the Boulanger-Idriss models, σ'_v was taken as $9.81z$ and σ_v was taken as $19.62z$ (approximately corresponding to a surface groundwater table condition), and M_w varied from 5.0 to 9.0.

From the set of calculated P_L values, a subset of values corresponding to $P_L = 15\%, 50\%, 85\%$ were extracted (within a tolerance of $\pm 1.5\%$). For CEA04 data points with these P_L values, CSR_{eq} was plotted against $(N_1)_{60}$ (assuming zero fines content) for cases with $M_w = 7.5$ and $\sigma'_v = 1$ atm. For the BI SPT and CPT data points with the aformentioned P_L values, the magnitude- and overburden adjusted $CSR_{M_w=7.5,\sigma'_v=1}$ values were plotted against their corresponding q_{c1Ncs}. These data points are overlain on the existing P_L curves in Figures 3.16, 3.17, and 3.18, and indicate that the code's P_L calculation is compatible with the inverse calculation of CRR, and is validated for a broad range of soil and ground motion conditions.

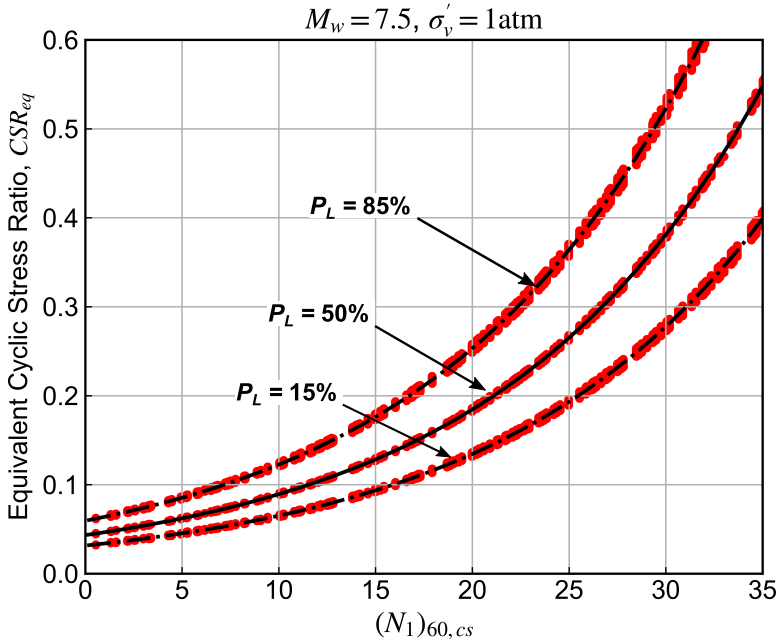

Figure 3.16: Probability of liquefaction curves and corresponding forward-predicted P_L values for a range of hypothetical sublayers, calculated using Cetin et al. (2004) model with $M_w = 7.5$ and $\sigma_v' = 1$atm.

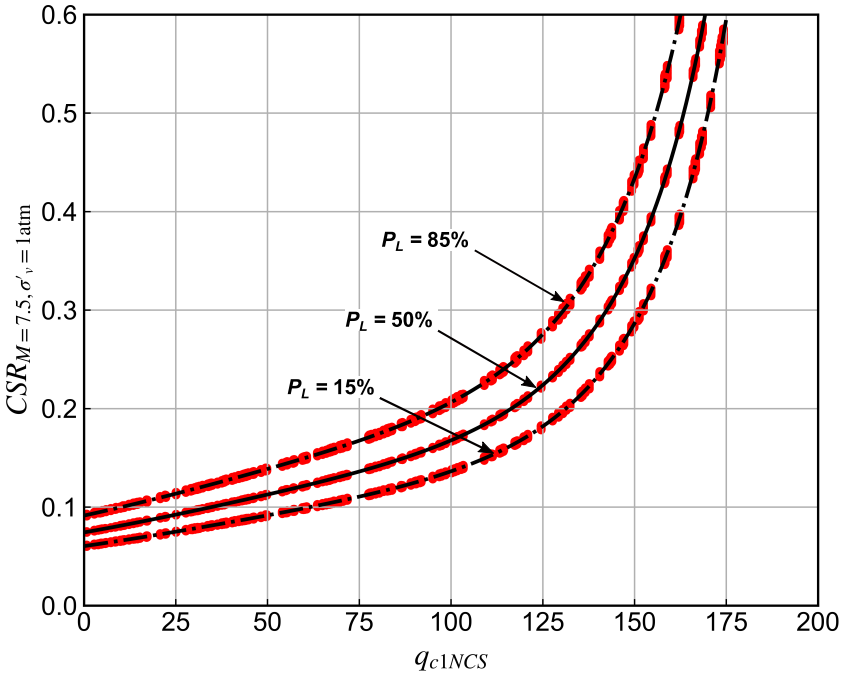

Figure 3.17: Probability of liquefaction curves and corresponding forward-predicted P_L values for a range of hypothetical sublayers, calculated using Boulanger and Idriss (2015) CPT-based model.

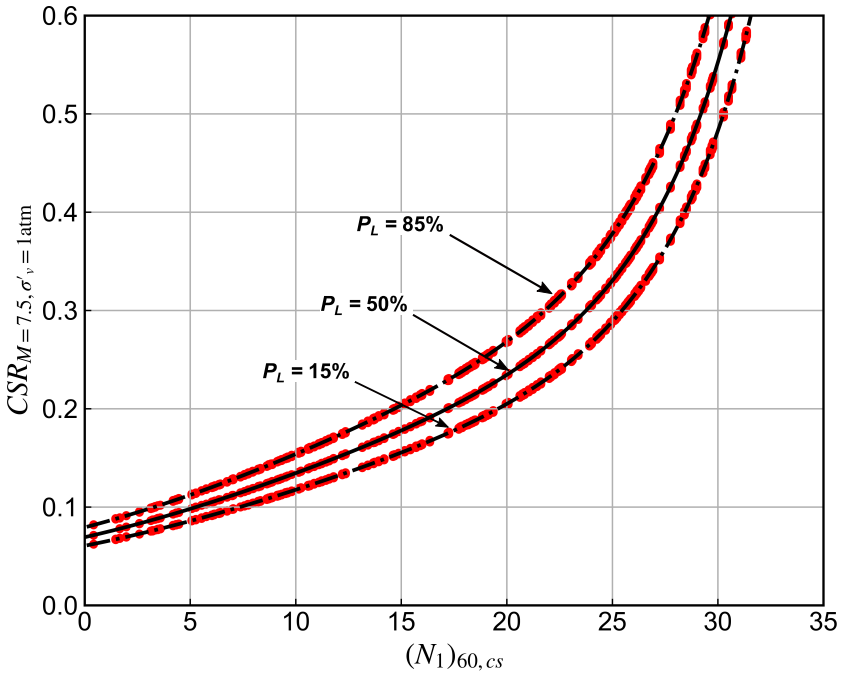

Figure 3.18: Probability of liquefaction curves and corresponding forward-predicted P_L values for a range of hypothetical sublayers, calculated using Boulanger and Idriss (2012) SPT-based model.

3.5 Numerical Evaluation of PLHA Integral

It is important to recognize that the expression presented in Equation (3.1), and indeed all of the PBEE equations presented in Section 2.4, are numerical approximations of integral expressions. In an ideal world, it would be possible to express all of the various relationships that comprise the PBEE formulation (*IM* hazard curves, *IM-EDP* fragility curves, etc.) as analytical formulas, with the various integrals and double-integrals required to derive the *EDP*, *DM*, and *DM* hazard curves having closed-form solutions. However, this is rarely the case in practice; while demand parameter response models can often be approximated with mathematical functions, real ground motion hazard curves rarely follow a consistent mathematical form over a wide range of ground shaking intensities and seismo-tectonic regimes. This is due to the fact that ground motion hazard is usually comprised of an aggregation of hazards from multiple seismic sources. Each source may be characterized by magnitude and distance distributions that are truncated due to physical constraints - such truncations, as well as their combinations with lognormally-distributed ground motion models, do not lend themselves particularly well to hazard curves that can be expressed analytically. Nevertheless, closed-form solutions of hypothetical *EDP* hazard integrals can be useful in validating numerical integration schemes. In this section, the numerical method used to integrate the PLHA expression in Equation (3.1) is validated against a hypothetical analytical solution.

3.5.1 Validation of Numerical Integration Scheme

Taking advantage of the fact that various closed-form solutions exist for both seismic hazard curves and response models, the numerical integration scheme used herein to calculate the hazard curve for FS_L was compared with a theoretical FS_L hazard curve, calculated assuming power law relationships for both the a_{max} hazard curve and $FS_L|a_{max}, M_w$ response model. For the sake of this exercise, if the hazard curves for a_{max} are assumed to be linear in log-log space over a reasonable range of ground motion intensities, then the relationship between λ and a_{max} can be expressed by a power law:

$$\lambda_{a_{max}} = k_0(a_{max})^{-k} \tag{3.22}$$

A hypothetical power law-based a_{max} hazard curve is shown in Figure 3.19, with fitting parameters k_0 = 1.16e-4 and k = 1.62. The relationship between a_{max} and the response variable FS_L, given fixed values of the magnitude, penetration resistance, and total and effective stress, can also be represented using a power law:

$$FS_L = m(a_{max})^n \tag{3.23}$$

with a lognormal standard deviation of $\sigma_{\ln FS_L|a_{max}}$. The power law mean response model is shown in Figure 3.19, for a = 0.12, b = 1, and $\sigma_{\ln FS_L|a_{max}}$ = 0.15. Note that both the hazard curve and response curves are plotted out to a_{max} = 10 g. While this may seem like an excessively high upper-limit, it is necessary to validate the numerical integration scheme limits for both functions that come close to simulating infinite bounds (i.e. the conditions under which the integration of the closed-form solution is carried out). Based on Jalayer (2003), a closed-form solution for the resulting non-exceedance rate of FS_L can be expressed as:

$$\Lambda_{FS_L}(fs_L) = k_0 \left(\frac{fs_L}{m}\right)^{-k/n} \exp\left[\frac{k^2}{2n^2}\sigma^2_{\ln FS_L|a_{max}}\right] \tag{3.24}$$

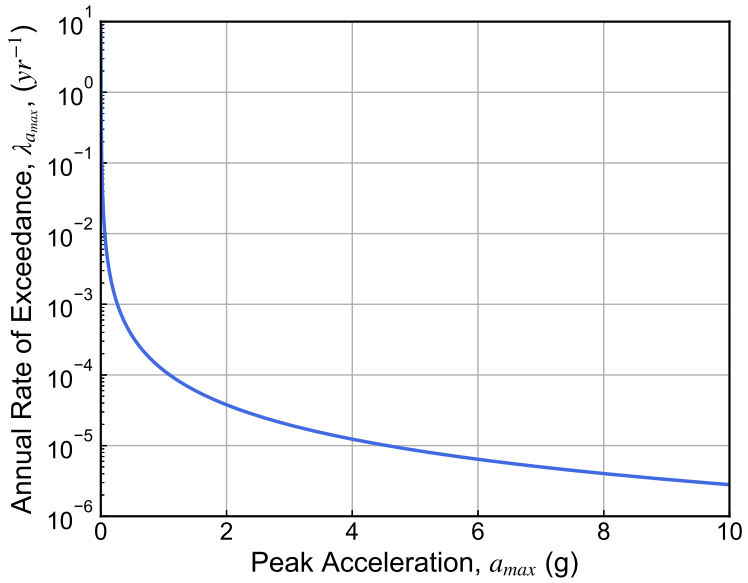

Figure 3.19: Hypothetical power-law representation of the annual rate of exceedance of a_{max}, with fitting parameters $k_0 = 1.16\text{e-}4$ and $k = 1.62$.

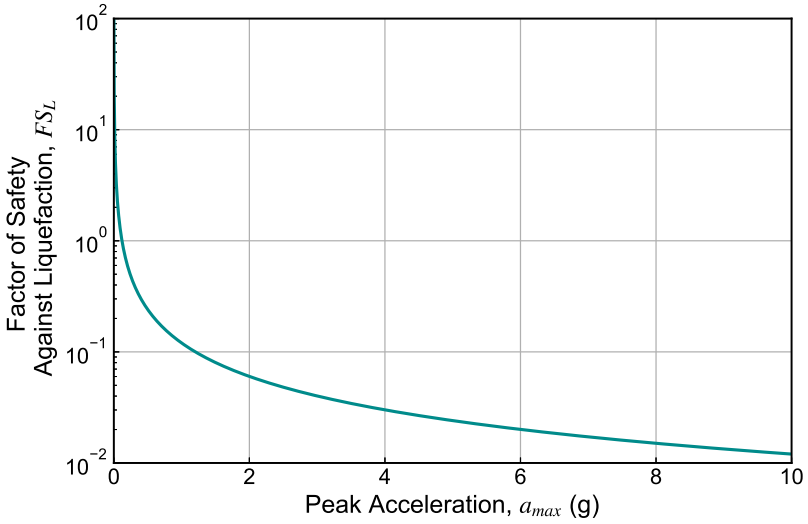

Figure 3.20: Power-law representation of the a_{max}-FS_L response model for $q_{c1Ncs} = 100$, and reference values of M_w, depth, and total and effective stress.

The corresponding numerical solution for Λ_{FS_L} is calculated as follows:

$$\Lambda_{FS_L}(fs_L) = \sum_{i=1}^{N_{pga}} \mathrm{P}\left[FS_L < fs_L | a_{max,i}\right] \Delta\lambda_{a_{max,i}} \tag{3.25}$$

where $\mathrm{P}[FS_L < fs_L|a_{max,i}]$ is calculated from the mean FS_L and $\sigma_{\ln FS_L|a_{max}} = 0.15$. The $\Delta\lambda_{a_{max}}$ term is computed using the gradient function in `numpy`, a commonly used Python package. The gradient is computed using second order central differences in the interior points, and a first-order difference at the boundaries (forward difference at the lower boundary, backward difference at the upper boundary), with an a_{max} increment of 0.01 g. The numerical methodology used in this validation is the same as that used in the full `PyLHA` code.

Figure 3.21 shows a comparison of the two FS_L hazard curves, indicating that the numerical approximation is consistent with the hypothetical close-form solution for a broad range of factors of safety. The numerical approximation does slightly over-predict the non-exceedance rate at FS_L values less than about 0.2. However, these values imply an extremely high probability of liquefaction (greater than 99%, based on the Juang et al. [2013] proposed relationship between probability of liquefaction and factor of safety), and are of little practical significance.

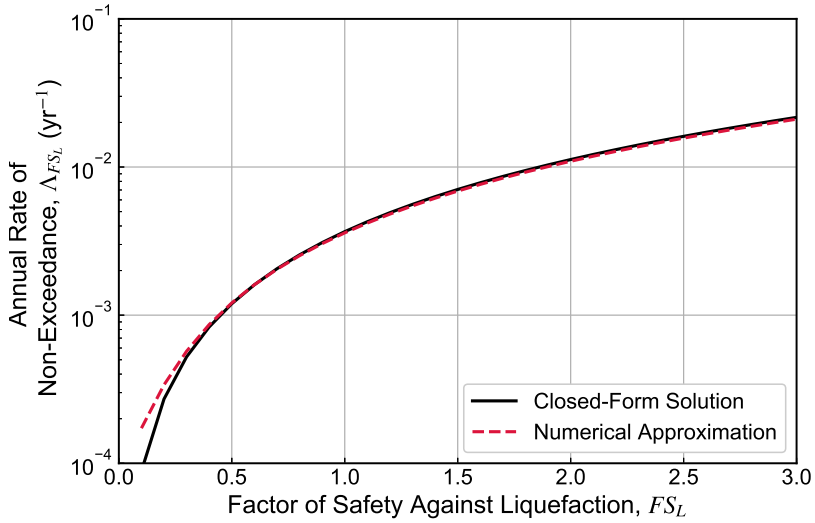

Figure 3.21: Power-law representation of the a_{max}-FS_L response model for $q_{c1Ncs} = 100$, and reference values of M_w, depth, and total and effective stress.

3.6 Example PLHA Calculation Procedure

In the following section, the full PLHA calculation procedure is demonstrated for a sample CPT profile, at a site in Seattle, Washington. The probabilistic ground motion data obtained for this site is the same as that presented in Section 3.3, using the 2014 National Seismic Hazard Map source characterization, for a site condition with $v_{s30} = 215$ m/s. The interpolated magnitude-specific hazard curves for a_{max} can be seen in Figure 3.7.

3.6.1 Example CPT Profile

A synthetic, 20 m-deep CPT profile was generated by assuming an initial, smoothly varying mean profile of q_{c1Ncs}. The profile consists of 2 meters of non-liquefiable crust with a mean $q_{c1Ncs} = 180$, underlain by a layer of liquefiable silty sand, with q_{c1Ncs} increasing linearly from 60 to 200. Local variation in q_{c1Ncs} was added to the profile using a sinusoidal function with a wavelength of 8m and amplitude of $q_{c1Ncs} = 8$, along with a random noise function with amplitude $q_{c1Ncs} = 15$. The resulting profile is shown in Figure 3.22.

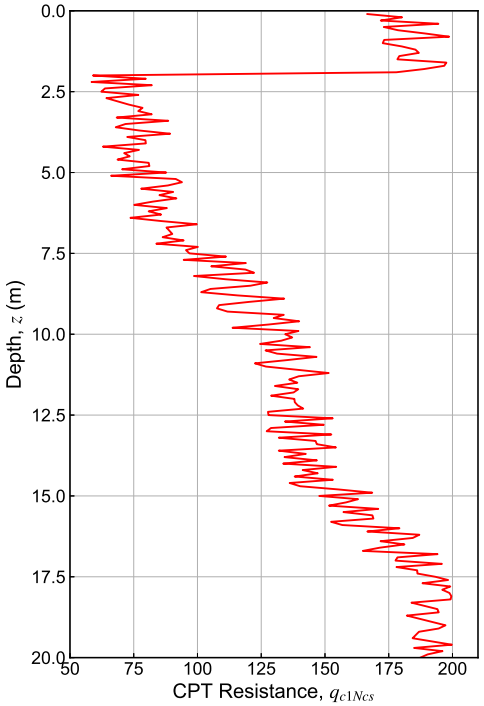

Figure 3.22: Synthetic, 20 m-deep CPT profile.

3.6.2 Fragility Curves for FS_L

For each depth increment in the CPT profile, the probability of non-exceedance of FS_L is calculated for all combinations of a_{max} and M_w using the Boulanger and Idriss (2015) probabilistic triggering model (Equations [3.14] through [3.19]). The fragility curves obtained for $FS_L = 1.0$ are shown in Figure 3.23 for several magnitude bins. For a given magnitude, the probability of liquefaction (i.e. the probability of FS_L *not* exceeding a unity) increases as the peak acceleration increases (due to an increase in the cyclic stress ratio, and thus a decrease in the limit-state function for liquefaction). Similarly the fragility curves associated with higher magnitude bins result in higher probabilities of non-exceedance at a given value of a_{max}, since larger magnitudes result in a higher number of equivalent loading cycles, and thus a higher CSR. In comparing the fragility curves for the 3.0 m-deep soil element, which has a q_{c1Ncs} of 80, and the 8 m-deep soil element with a q_{c1Ncs} of 120, it is clear that the increase in cyclic resistance of the deeper soil element has the effect of pushing the fragility curves to higher levels of peak acceleration. In other words, the denser the soil, the higher the cyclic stress required to predict the same probability of liquefaction as a much looser soil. It is also important in this case to recognize that the deeper soil element will experience a lower CSR for a given combination of a_{max} and M_w as a result of the increase in the stress reduction factor due to depth, thus further pushing the fragility curves to higher a_{max} values.

To calculate the overall non-exceedance rate of a certain value of FS_L, the expression within the double-summation in Equation 3.1 is obtained via the product of the non-exceedance probability for a given $a_{max} - M_w$ combination by the incremental rate of exceedance of the corresponding $a_{max} - M_w$ hazard curve. For a given M_w, the incremental exceedance rate is obtained numerically using the same central-difference scheme described in Section 3.5.1. This product is illustrated graphically for several combinations of a_{max} and M_w for the 3 m-deep and 8 m-deep soil elements in Figure 3.23.

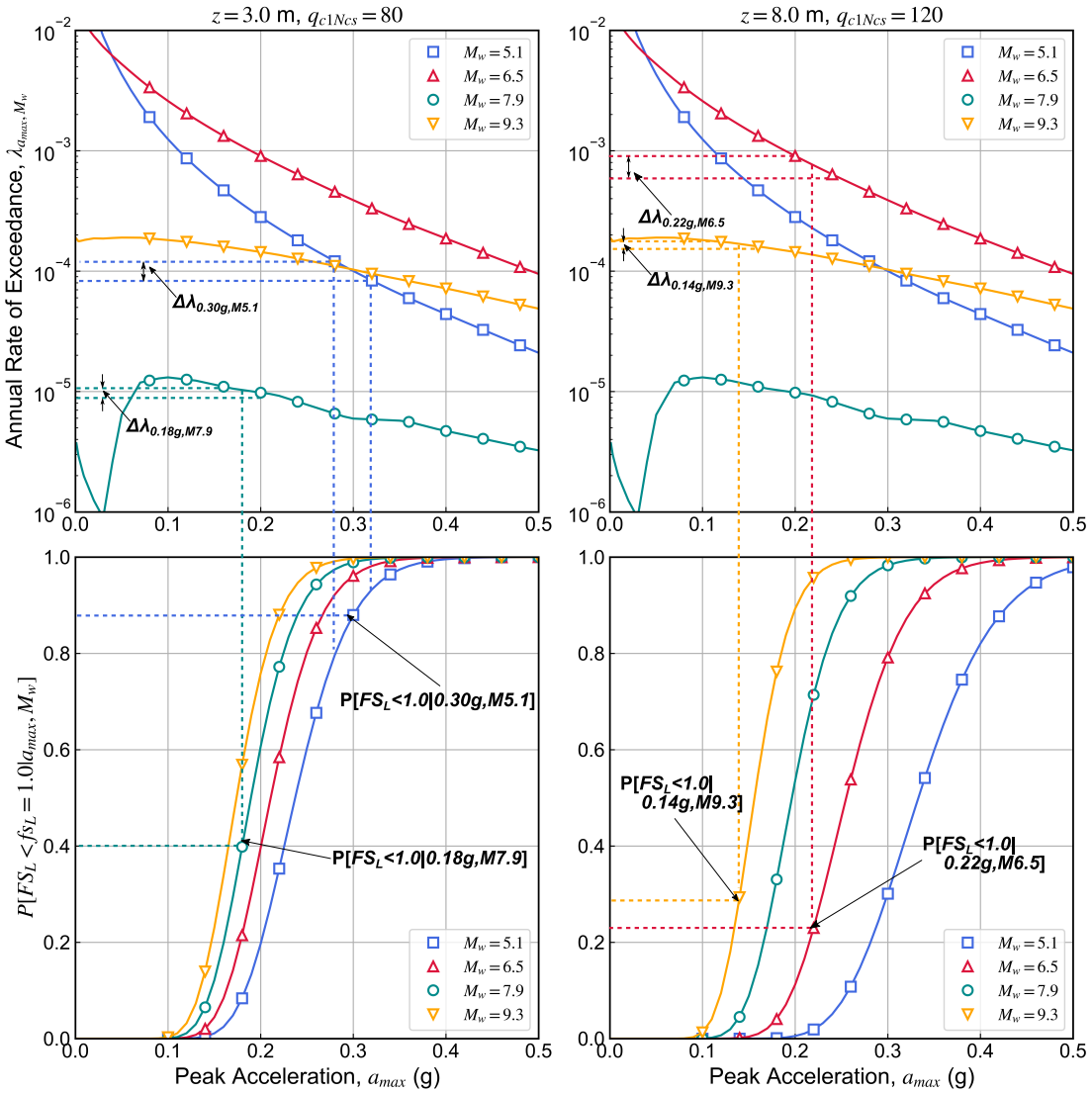

Figure 3.23: Graphical schematic of numerical integration used to calculate non-exceedance rates of $FS_L = 1.0$, for a subset of magnitudes, for a 3 m-deep soil element with $q_{c1Ncs} = 80$ and an 8 m-deep soil element with $q_{c1Ncs} = 120$.

3.6.3 Generating FS_L Hazard Curves

This calculation procedure is repeated for a wide range of FS_L values, producing the FS_L hazard curves shown at several increments of depth in Figure 3.24. As expected, the overall annual rate of non-exceedance at a given FS_L decreases as the CPT resistance and depth increases. Note that the hazard curves between 3 m and 15 m are relatively evenly spaced, as their corresponding CPT resistances (78 to 147) generally lie on a generally linear portion of the probabilistic triggering curve (see Figure 3.14) - even at the value of 147, which fall well above the point where the triggering curve begins to steepen, this effect is counteracted somewhat by the large shear stress reduction

factor. It is generally above this value, however, that the cyclic resistance ratio becomes extremely high, and the overall non-exceedance rates quickly become quite low (in this case, at a depth of 20 m).

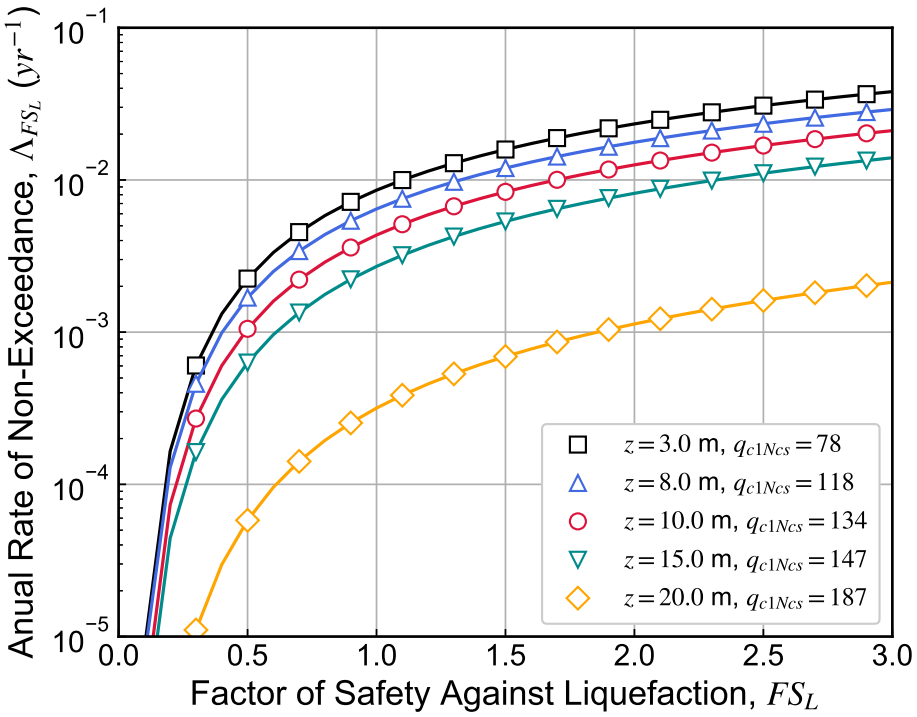

Figure 3.24: Hazard curves for factor of safety against liquefaction, for a range of depths and CPT resistances from a sample CPT profile at a site in Seattle.

3.6.4 Return Period of FS_L

In many current engineering guidelines and standards (e.g. International Building Code [IBC], ASCE 7, ACE 41), the seismic basis of design is typically specified using ground motions that correspond to a particular return period. In the past decade, efforts have been made to extend design criteria to instead target a specified risk of structural collapse. For example, prior to 2009, ASCE 7 and IBC defined the Maximum Considered Earthquake (MCE) as the seismic basis of design, which is used for design of new buildings, as the event causing ground motions with a 1 in 2,475 exceedance rate. In ASCE 7-10, the basis of design was changed to the Risk-Targeted Maximum Considered Earthquake (MCE_R), which corresponds to ground motions causing a 1% probability of structural collapse in 50 years. The MCE_R ground motion maps were developed for the United States by initially developing ground motion hazard curves for the entire country (via the National Seismic Hazard Map Project), and integrating those curves with a generic fragility

curve describing the relationship between ground motion amplitude and probability of collapse (Luco et al. 2007).

This concept of extending probabilistic ground motions to defining probabilistic EDPs or DMs can be similarly applied to liquefaction problems. In this case, one might be interested in determining the factor of safety (or factor of safety depth profile) that corresponds to a specific return period. This can be determined by first performing a full PLHA, and from the resulting FS_L hazard curves (see Figure 3.24) interpolating at the specified reciprocal of the return period to obtain the liquefaction risk-consistent factor of safety. Figure 3.25 shows the variation in FS_L values with depth corresponding to 475-, 975-, and 2,475-year return periods. These FS_L values were estimated using cubic spline interpolation in $FS_L - \log \Lambda$ space. For all three return periods, the FS_L values tend to increase very gradually until a depth of about 15 m - in fact, due to the counteracting effects of the increasing cyclic resistance and increasing stress reduction factor, the FS_L values are practically constant (even decreasing slightly) between 2 and 8 m. Below about 15 m, the mean trend of FS_L increases significantly as the q_{c1Ncs} values increase into the very steep portion of the liquefaction triggering curve; because the probability of liquefaction is highly sensitive to small changes in CPT resistance in this portion of the curve, the variation in FS_L is much higher at these large depths, despite relatively minor variations in CPT resistance.

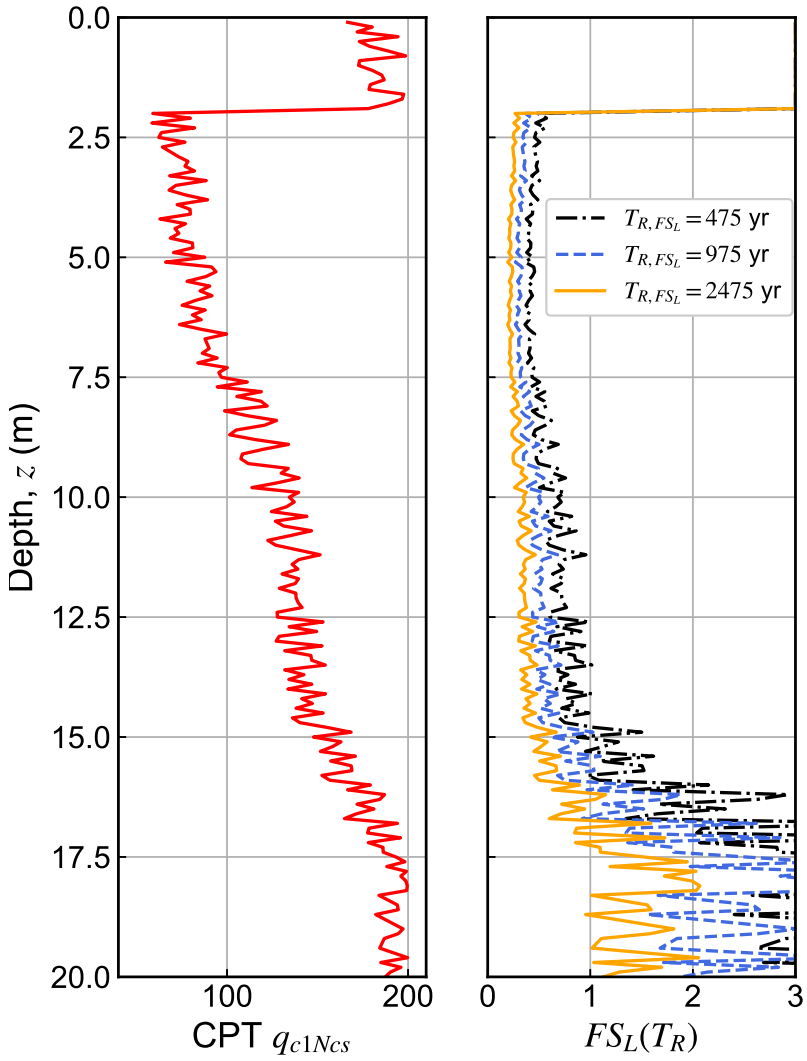

Figure 3.25: Variation with depth of factors of safety corresponding to return periods of 475, 975, and 2,475 years for a sample CPT profile at a site in Seattle.

3.6.5 Deaggregating Liquefaction Hazard by a_{max} and M_w

Similar to the manner in which ground motion hazard can be deaggregated with respect to the various components that go into the PSHA calculation (e.g. magnitude, distance, epsilon, source type), it is also possible to deaggregate the FS_L hazard with respect to many of the same components. In this case, since the key seismic components of the PLHA calculation are magnitude and peak acceleration, the liquefaction hazard corresponding to a particular FS_L value (or FS_L

return period) can be deaggregated by calculated the joint marginal distribution of a_{max} and M_w as follows:

$$P\left[a_{max} = a_i, M_w = m_j | FS_L < fs_L\right] = \frac{\Lambda_{FS_L}(fs_L | a_i, m_j)}{\Lambda_{FS_L}(fs_L)} \tag{3.26}$$

The joint marginal $a_{max} - M_w$ distributions given the factors of safety close to a 975-year return period are shown for several different soil elements in Figure 3.26. Across all four soil elements, the most prominent contributions to the FS_L hazard seem to be located at two distinct clusters of magnitude. Similar to the interpretation of the a_{max} deaggregation shown in Figure 3.2, the cluster centered at around **M**7 can be attributed to the combination of the Seattle Fault Zone and deeper intraslab seismicity, while the higher **M**9 cluster clearly is due to the Cascadia Subduction Zone contribution. The relative dominance of each cluster is clearly a function of the 975-year FS_L value; at shallow depths (and lower relative densities), the **M**7 is clearly the largest contributor, as reflected in the mean magnitude of 7.2. As the depth, relative density, and FS_L value increases, the increased cyclic stress ratio required to produce the same FS_L exceedance rate is driven primarily by larger magnitude events - thus, the CSZ contribution plays a larger role, and the mean magnitude increases.

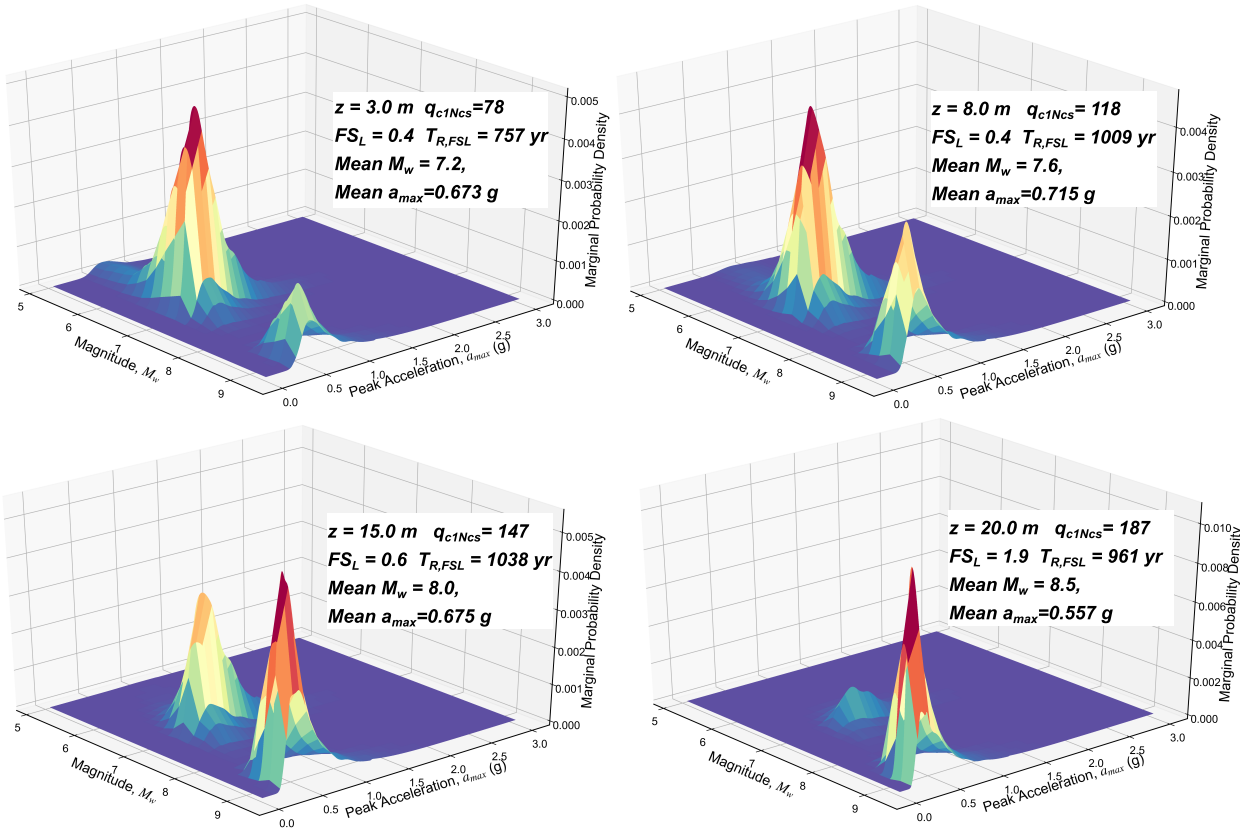

Figure 3.26: Deaggregation surface plots of FS_L hazard for joint M_w-a_{max} contribution for various depths increments of a sample CPT profile, using ground motion data from Seattle, WA.

3.7 Practical Considerations for PLHA Calculation Procedure

Relative to a conventional liquefaction hazard analysis, i.e. one that considers just a single combination of a_{max} and M_w in determining FS_L, the calculations required for the probabilistic analysis framework outlined in the preceding sections are considerably voluminous. While both frameworks require calculating a hazard curve for a_{max}, the conventional analysis requires a single deaggregation at the return period of interest to determine the appropriate M_w value, and a single factor of safety calculation per depth increment. On the other hand, the PLHA procedure requires multiple deaggregation calculations (it will be shown later in this section that a set of about eight calculations generally yields stable results), and, more critically, calculating the probability of exceedance of a range of FS_L values for every plausible combination of a_{max} and M_w. For the example case outlined in Section 3.6, this resulted in almost 400,000 FS_L non-exceedance calculations per element of soil. A typical 30 meter-deep CPT profile, which can have a sampling resolution as fine as 0.02 m, could thus require more than half a *billion* calculations to obtain the risk-consistent FS_L profiles shown in Figure 3.25.

To execute such a large volume of calculations within a practical time frame, the FS_L exceedance calculations and subsequent numerical integration were implemented as four-dimensional matrix calculations, using the Python library `xArray`, rather than via sequential calculations in four nested loops (Figure 3.27). The time required to generate a full FS_L hazard curve for a single depth increment using the matrix calculation is about 0.07 seconds on a typical desktop PC. To perform the same calculation using a nested looping procedure requires about 4.5 seconds, over 60 times slower, and would require about 45 minutes to generate hazard curves for a typical CPT profile, compared to about 42 seconds using matrix calculations.

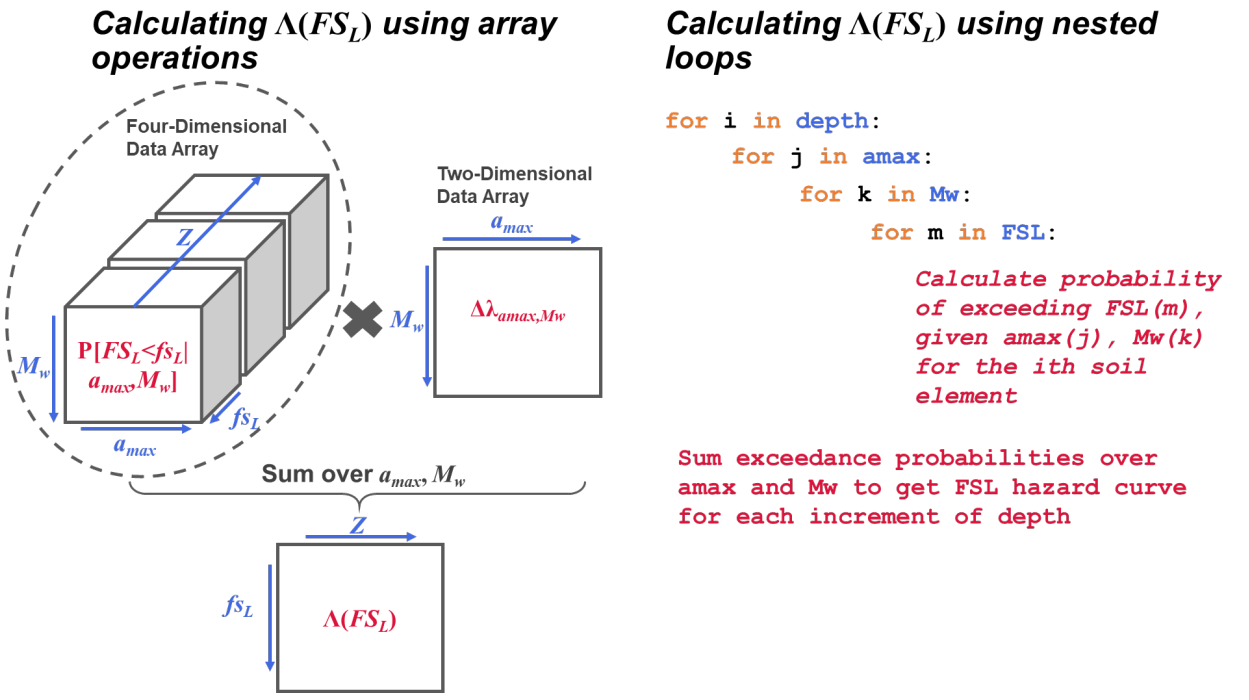

Figure 3.27: Schematic illustration comparing FS_L non-exceedance calculation using array operations versus sequential looping.

3.7.1 Sensitivity of PLHA Results to Deaggregation Calculation Parameters

With the substantial reduction in the time required to calculate FS_L hazard curves using matrix calculations, the computational bottleneck in `PyLHA` exists at the multiple deaggregation calculations using `nshmp-haz`, which are required to establish the M_w-a_{max} joint distribution. On a typical PC, running the `DeaggCalc` module in `nshmp-haz` for a single return period requires about 10-15 seconds to complete for a CEUS site, and about 20-30 seconds for a WUS site. The difference in runtimes between source catalogs is attributed to the significantly greater number of earthquake sources contained in the WUS catalog. The example PLHA calculation in Section 3.6, which used results from 25 deaggregation calculations to establish the M_w-a_{max} joint distribution,

thus required about 8 minutes to complete.

In order to make the calculation procedure more efficient, the PLHA calculations were repeated for the test sites in Table 3.1 by varying the deaggregation parameters that most significantly influence calculation speed. The most important parameter is the number of return periods at which deaggregation calculations were performed (N_{T_R}). Of secondary important were the bin sizes for magnitude (ΔM_w) and source-to-site distance (ΔR); halving or doubling either of the bin sizes in the deaggregation calculation would halve or double the number of hazard curve and deaggregation calculations. The values of the number of return periods and bin sizes that were evaluated are summarized in Table 3.3. For each combination of parameters, the PLHA results were compared to the baseline combination ($N_C = 50$, $\Delta M_w = 0.10$, $\Delta R = 10$km), representing a very highly (and likely impractical) discretized level of resolution.

Table 3.3: Summary of deaggregation calculation parameters evaluated in sensitivity analysis

Parameter Name	Values
Number of Deag Calcs, N_C	8, 13, 25, 50
Magnitude Bin Size, ΔM_w	0.10, 0.20
Distance Bin Size, ΔR	10 km, 20 km

Sensitivity to Number of Deaggregation Return Periods

The optimal number of deaggregation calculations was evaluated by determining the lowest number of return periods needed to obtain stable PLHA results, i.e. results that are consistent with those obtained using the baseline parameter combination. The consistency of results was initially evaluated by visual inspection of the FS_L hazard curves from the sample CPT data at various depths. Figure 3.28 shows hazard curves for four depth increments, each of which had different cyclic resistances, for the Seattle test site. The results indicate that the FS_L hazard curves are largely consistent for N_{T_R} values as low as 8 across the full range of FS_L values of engineering interest.

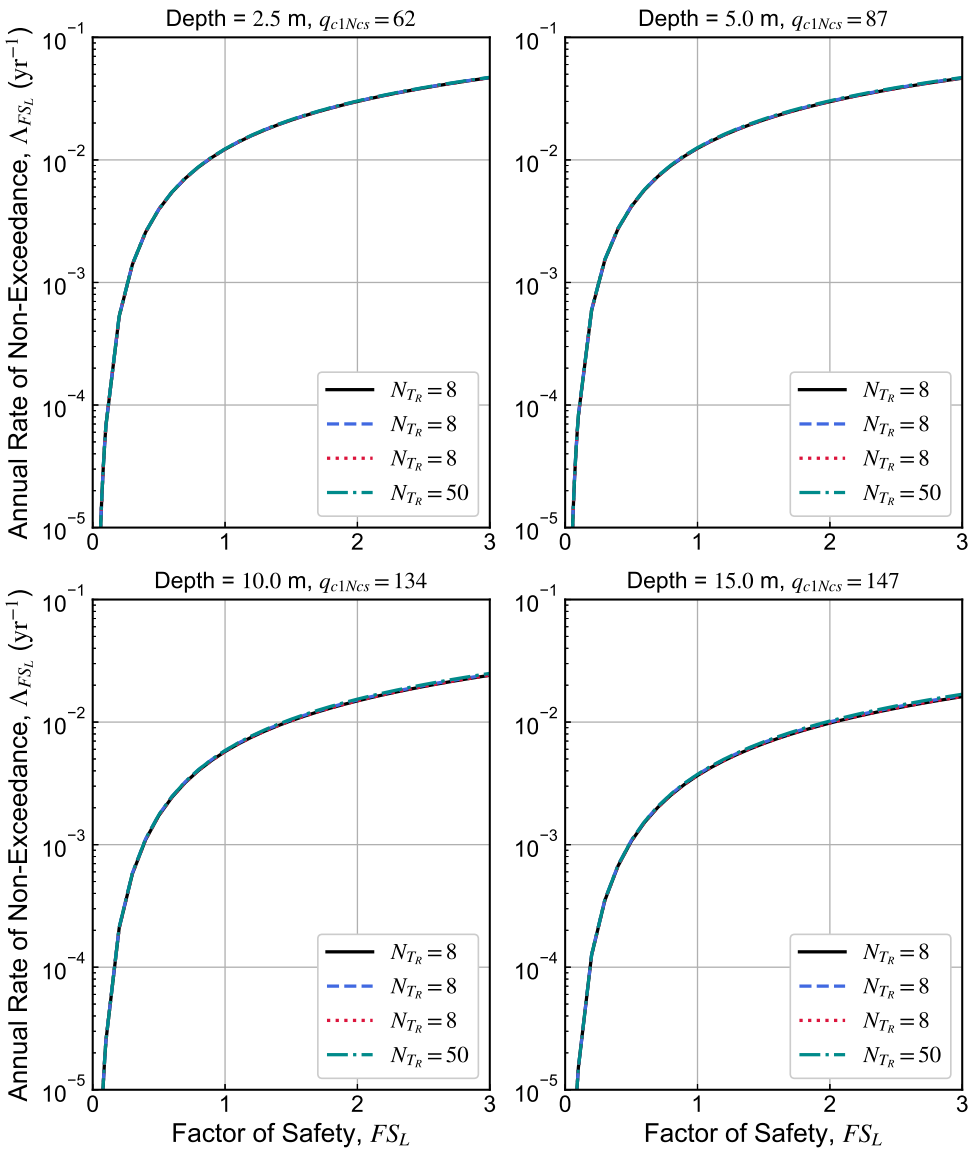

Figure 3.28: Sensitivity of FS_L hazard curves to the number of deaggregation calculations ($\Delta M_w = 0.10$, $\Delta R = 10$km) for various depths increments of a sample CPT profile, using ground motion data from Seattle, WA.

For all nine test locations, the results are summarized in terms of the percent error relative to the baseline results for the FS_L values corresponding to 475, 975, and 2,475-year return periods. For a given site, N_{T_R}, and return period, the percent error ranges summarized in Table 3.4) correspond to the 5th and 95th percentile values from the entire sample CPT profile. In order to focus on results within a range of FS_L values with practical significance, FS_L values below 0.10 and above 3.0 were filtered out in a given FS_L profile before obtaining the 5-95th percentile error values. The results confirm that eight return periods for deaggregation calculations generally yield stable PLHA

Table 3.4: Summary of error in calculated factor of safety (relative to 50 calculations) for cases with 25, 13, and 8 deaggregation calculations for test sites

Site	FS_L Error Range (5th to 95th Percentile), Relative to $N_C = 50$								
	$T_R = 475$ yrs			$T_R = 975$ yrs			$T_R = 2475$ yrs		
	$N_{T_R} = 25$	$N_{T_R} = 13$	$N_{T_R} = 8$	$N_{T_R} = 25$	$N_{T_R} = 13$	$N_{T_R} = 8$	$N_{T_R} = 25$	$N_{T_R} = 13$	$N_{T_R} = 8$
Eureka	0 to 0.01%	-0.03 to 0%	-0.64 to -0.04%	0 to 0%	0 to 0.01%	0.02 to 0.1%	0 to 0%	0.01 to 0.01%	0.05 to 0.07%
Los Angeles	0 to 0%	0 to 0%	0 to 0.18%	-0.01 to 0%	-0.01 to 0%	-0.04 to -0.01%	-0.01 to 0%	-0.02 to 0%	-0.07 to -0.01%
Salt Lake City	0 to 0%	-0.02 to 0%	0.07 to 0.35%	-0.01 to 0%	-0.02 to 0%	0.14 to 0.53%	-0.01 to 0%	-0.02 to 0%	0.04 to 0.13%
San Francisco	0 to 0.01%	-0.03 to 0%	0 to 0.15%	0 to 0.02%	-0.03 to 0%	-0.02 to 0.03%	0 to 0.02%	-0.01 to 0%	-0.01 to 0.01%
Seattle	0.01 to 0.12%	0.01 to 0.09%	-0.02 to 0.85%	0.01 to 0.09%	0 to 0.04%	-0.02 to 0.24%	0 to 0.04%	0 to 0.01%	-0.02 to 0.01%
Charleston	0 to 0.02%	-0.34 to -0.02%	-0.86 to -0.19%	0 to 0%	0.05 to 0.22%	-0.63 to -0.13%	0 to 0%	0.01 to 0.07%	-0.04 to -0.02%
Memphis	0.01 to 0.07%	0 to 0.02%	-0.54 to -0.11%	0.01 to 0.05%	0.01 to 0.08%	-0.14 to -0.03%	0 to 0.02%	0.01 to 0.04%	0.01 to 0.28%
Minneapolis	–	–	–	–	–	–	–	–	–
New York City	–	–	–	-0.02 to 0%	-0.07 to -0.02%	-0.26 to -0.07%	-0.01 to 0%	-0.13 to -0.03%	-0.14 to -0.05%

results, with FS_L values within about 1 % for all of the test sites.

The benefit of using eight deaggregation calculations as the default number going forward is clear, as it requires about one-fifth of the calculation time as the full set of 50 calculations (Table 3.5), and generally produces the same results.

Table 3.5: Calculation speeds for deaggregation calculation sets of 8, 13, 25, 50 for nine test sites.

Return Periods	Calculation Speeds (minutes) $\Delta M_w = 0.10$, $\Delta R = 10$km								
	Charleston	Eureka	Los Angeles	Memphis	Minneapolis	New York	Salt Lake City	San Francisco	Seattle
8	1.5	2.9	3.3	1.5	1.5	1.5	3.0	3.0	2.9
13	2.4	4.6	5.3	2.4	2.4	2.3	4.8	4.5	4.7
25	4.1	8.1	9.5	4.1	4.1	4.0	8.4	8.4	8.9
50	7.7	15.4	17.9	7.7	7.6	7.5	16.1	16.0	16.0

Sensitivity to Deaggregation Bin Sizes

While using smaller bin sizes has a much smaller effect on PLHA calculation speeds than reducing the number of deaggregation return periods, there is still value in their optimization. In partic-

ular, reducing the number of magnitude values in the array calculation of $P[FS_L < fs_L|a_{max}, M_w]$ can significantly minimize potential issues with memory limits, particularly with densely sampled CPT data. The sensitivity of the PLHA results to the four combinations of bin sizes was evaluated in a similar manner to the sensitivity to the number of deaggregation return periods. Since it was established in the previous section that eight return periods are sufficient to obtain stable results, the FS_L hazard curves for the combination cases (Table 3.6) where one or more coarser bin sizes are used (i.e. [$\Delta M_w = 0.20$ or $\Delta R = 20$km]) are obtained using eight return periods, and compared to the 50-return period baseline case ($\Delta M_w = 0.10$, $\Delta R = 10$km).

Table 3.6: Combinations of magnitude and source-site distance bin sizes evaluated in sensitivity study.

Combination ID	ΔM_w	ΔR (km)
A	0.20	20
B	0.10	20
C	0.20	10
D	0.10	10

A comparison of the FS_L hazard curves using the four bin size configurations is shown in Figure 3.29 for four increments of depth, with increasing cyclic resistance, for the Seattle test site. For this case, the FS_L hazard curves are practically identical for the range of FS_L values below 3.0. The 5th to 95th percentile FS_L error values, for cases where $0.1 \leq FS_L \geq 3.0$, are tabulated for each test site in Table 3.7. The sensitivity of the PLHA results to the various bin sizes is relative minor, with errors generally less than 2% for the FS_L return periods evaluated. The cases where the error was greater than 1% generally corresponded to FS_L values that were near or greater than about 2.0, which are higher than the range of applicability for predicting maximum cyclic shear strains (roughly 2.0, using Ishihara & Yoshimine [1992]) or post-liquefaction volumetric strains (1.6, using Ishihara & Yoshimine [1992]).

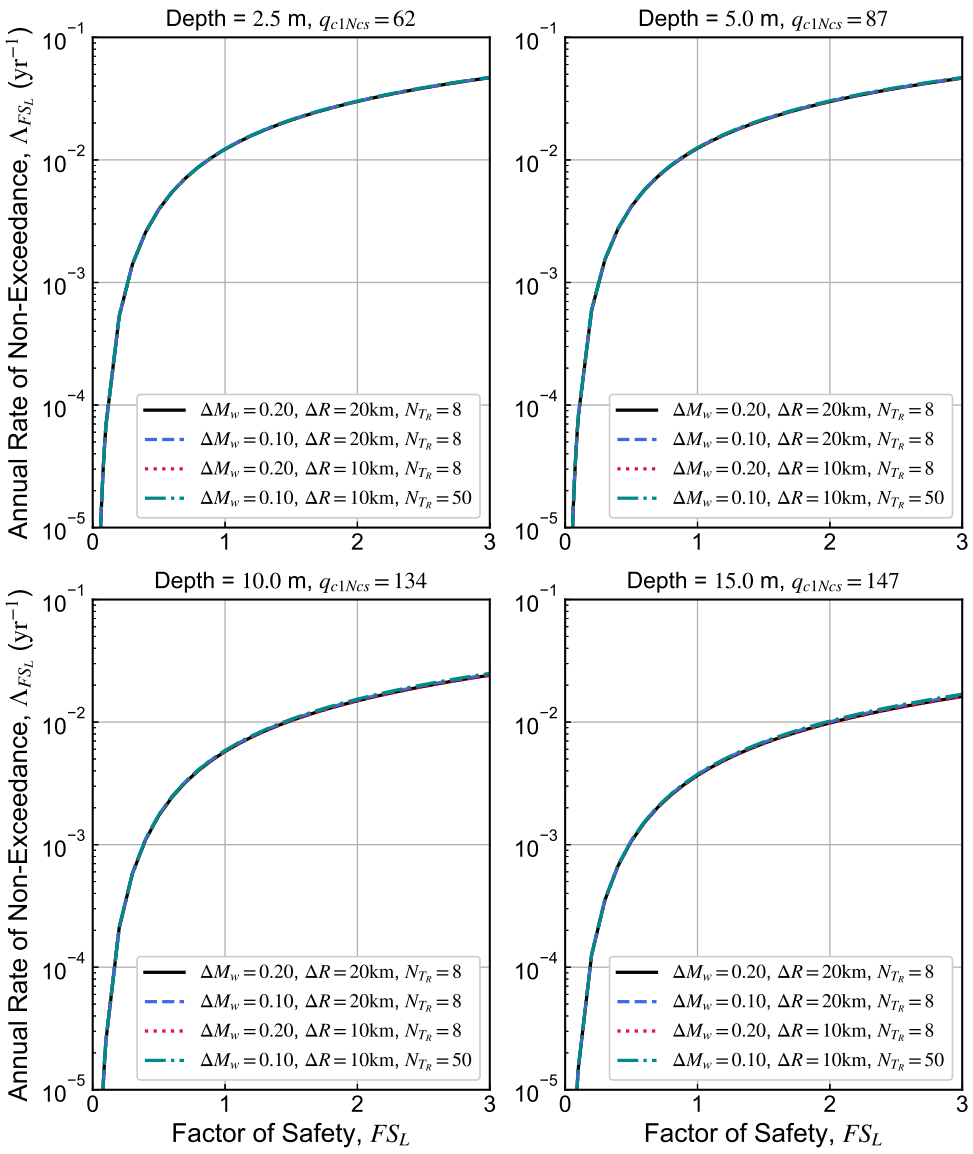

Figure 3.29: Sensitivity of FS_L hazard curves to the deaggregation bin size configuration for various depths increments of a sample CPT profile, using ground motion data from Seattle, WA.

Table 3.7: Summary of error in calculated factor of safety (relative to $\Delta M_w = 0.10$, $\Delta R = 10$km with 50 deaggregation return periods) for cases with varying bin size combinations (with 13 deaggregation return periods) for test sites

Site	FS_L Error Range (5th to 95th Percentile), Relative to Combination D								
	$T_R = 475$ yrs			$T_R = 975$ yrs			$T_R = 2475$ yrs		
	A	B	C	A	B	C	A	B	C
Eureka	-1.08 to 0.1%	-0.67 to -0.04%	-1.04 to 0.1%	-1.44 to 0.08%	0.02 to 0.21%	-1.51 to 0.08%	-1.9 to -0.32%	0.09 to 0.17%	-1.96 to -0.35%
Los Angeles	0.15 to 0.42%	-0.02 to 0.09%	0.15 to 0.47%	0.12 to 0.26%	-0.11 to -0.02%	0.13 to 0.27%	0.01 to 0.22%	-0.13 to -0.01%	0.04 to 0.23%
Salt Lake City	0.15 to 0.62%	0.06 to 0.32%	0.16 to 0.66%	0.15 to 0.41%	0.13 to 0.5%	0.15 to 0.44%	-0.22 to 0.01%	0.04 to 0.11%	-0.21 to 0.02%
San Francisco	-0.37 to 0.05%	-0.02 to 0.09%	-0.33 to 0.05%	-0.59 to 0.03%	-0.02 to 0.02%	-0.58 to 0.03%	-0.77 to 0.01%	-0.01 to 0.01%	-0.76 to 0.01%
Seattle	0.27 to 1.72%	-0.03 to 0.77%	0.28 to 1.85%	0.26 to 0.71%	-0.04 to 0.23%	0.27 to 0.75%	-0.64 to 0.55%	-0.03 to 0.04%	-0.63 to 0.58%
Charleston	0.09 to 0.37%	-0.84 to -0.17%	0.08 to 0.33%	0.08 to 0.31%	-0.58 to -0.12%	0.06 to 0.22%	0.1 to 0.38%	-0.03 to -0.02%	0.09 to 0.36%
Memphis	-0.11 to -0.02%	-0.67 to -0.14%	-0.08 to -0.01%	0.05 to 0.76%	-0.17 to -0.08%	0.05 to 0.77%	0.2 to 1.98%	0 to 0.29%	0.2 to 1.97%
Minneapolis	–	–	–	–	–	–	–	–	–
New York City	–	–	–	-0.01 to 0.11%	-0.77 to -0.15%	0.17 to 0.24%	0.07 to 0.16%	-0.92 to -0.15%	0.14 to 0.36%

3.7.2 Summary of Recommended Deaggregation Calculation Parameters

The series of PLHA calculations for the various test sites have shown that the most critical factor affecting the efficiency of `PyLHA` is the number of PGA deaggregation return periods used to define the seismicity of the site in the initial step. The sensitivity of the final FS_L hazard curves to the initial number of return periods indicates that stable results can be achieved with as little as eight return periods, which reduces the run time for a given site from about 8 and 16 minutes for CEUS and WUS sites, respectively, to about 1.5 and 3 minutes. For use in engineering practice, such reductions in calculation speeds are particularly significant. It is also important to note that `nshmp-haz` can perform PSHA and deaggregation calculations on multiple sites simultaneously, a capability that has been integrated into `PyLHA`. Multi-site analyses, as one would expect, have longer calculation times than single-site analyses, but the calculation times do not scale linearly with

the number of sites (e.g. a 1.5 minute calculation time for a single CEUS site requires significantly fewer than 15 minutes for ten comparable CEUS sites). Nevertheless, for potentially large sets of multi-site analyses, it is even more critical to optimize the number of deaggregation calculations, and thus eight return periods appears to be close to the minimum needed to achieve stable results.

While the size of the magnitude and distance bins has little effect on the overall calculation times, processing data and performing 4-dimensional matrix calculations, particularly for CPT profiles of up to 600 data points, can impose significant demands on virtual memory - this is especially true when performing multi-site analyses. Thus, the ability to use magnitude bin sizes of 0.20, rather than 0.10, results in a halving of the virtual memory required to carry out the calculations, thus increasing the number of sites that can be analyzed for a given CPT profile. It was shown that the final FS_L hazard curves are largely insensitive to the magnitude or distance bin sizes used in the initial deaggregations, with FS_L errors less than 2% for all sites and return periods. The PLHA calculations can therefore be carried out with a recommended magnitude bin size of 0.20 and source-site distance bin size of 20 km.

3.8 Summary and Conclusions

The development and validation of `PyLHA`, a Python-based platform for performing Probabilistic Liquefaction Hazard Analysis (PLHA) was presented, along with the principles of Performance-Based Earthquake Engineering (PBEE) that underpin it. The framework of PBEE was presented in terms of the components that comprise it (ground motion intensity measures, engineering demand parameters, damage measures, and decision variables) as well as the total probability concepts that are used to integrate all of these components. PLHA can be thought of as a specific application of PBEE, where the magnitude-adjusted a_{max} is used as the ground motion intensity measure to estimate the factor of safety against liquefaction FS_L, which serves as the engineering demand parameter of interest; the two parameters are linked probabilistically using simplified cyclic stress-based liquefaction triggering models (e.g. Boulanger and Idriss 2015, Cetin et al. 2004).

`PyLHA` consists of a set of modules. The first module is responsible for obtaining and processing probabilistic ground motion data for the a_{max}, and does so by interfacing with the USGS open-source java tool `nshmp-haz`. A series of deaggregation calculations are performed, and the results are processed and interpolated, thereby generating an overall hazard curve for a_{max} and a marginal distribution of moment magnitude M_w for each value of a_{max}. The next module interprets the site-specific CPT or SPT data, and for each element of soil calculates the cumulative distribution of FS_L for each combination of a_{max} and M_w via one of the three triggering models presented in this documentation (Cetin et al. 2004, Boulanger & Idriss 2012, and Boulanger & Idriss 2015).

The implementation of each triggering model was validated against the original documentation. Finally, the FS_L CDFs are integrated numerically with the a_{max} hazard curve and joint a_{max}-M_w distributions to produce a hazard curve of non-exceedance for FS_L; the numerical integration scheme was validated against a hypothetical case where the a_{max} hazard curve and FS_L response models could be described by closed-form power law solutions.

The code was then demonstrated for a sample CPT profile, using ground motion data for a site in Seattle, Washington. In addition to producing FS_L hazard curves at each increment of depth, it was shown that the hazard curves could be interpolated at a desired annualized rate of non-exceedance in order to produce risk-consistent FS_L profiles corresponding to a particular return period (e.g. 475, 975, or 2475 years). Furthermore, similar to the manner in which IM hazard curves can be deaggregated by magnitude and distance, it was shown that FS_L hazard data can be deaggregated at a particular return period to reveal the joint marginal distribution of a_{max} and M_w.

Finally, a procedure for optimizing the code to generate stable results with minimum calculation time was used to determine the recommended deaggregation calculation parameters in `nshmp-haz`. It was shown that a minimum of eight deaggregation calculations are needed to establish stable results, with calculation run times on the order of 1.5 to 3 minutes for a single site. Furthermore, it was shown that magnitude and distance bin size of 0.20 and 20 km, respectively, can be used to obtain sufficiently accurate results, and that the benefit of the larger magnitude bin size can reduce virtual memory loads, particularly in analyses involving multiple sites.

3.8.1 Future Developments

This platform, while initially implemented for the purposes of performing probabilistic analyses within the framework of cyclic stress-based simplified methods, has been developed to be modular enough to support a wider array of simplified methods. As suggested in Section 2.4.1, future methods for predicting liquefaction and its related hazards may utilize more efficient ground motion IMs than PGA - as long as such methods are fully probabilistic in nature, their implementation in this platform is relatively straightforward. A broader challenge, however, lies in the ability to obtain hazard curves for such "non-traditional" IMs via the USGS `nshmp-haz` code. The increased use of evolutionary IMs in engineering response models points to the development of a more flexible and expansive ground motion hazard mapping infrastructure, where a wider array of ground motion models are needed, and can be readily folded into existing PSHA codes. A shorter-term alternative is to utilize within-motion correlations between different ground motion intensity measures, and use a total probability calculation to generate the needed IM hazard curve. While such an approach is useful in terms of generating hazard curves quickly, it may involve higher uncertainty than a

fully-developed suite of GMMs in a PSHA, and thus produce conservative hazard curve results for the demand parameter of interest (e.g. pore pressure generation, ground displacement).

Chapter 4

A Framework for Mapping Liquefaction-Targeted Intensity Measures

4.1 Introduction

The preceding chapter presented the development of a Python-based code for performing fully-probabilistic liquefaction hazard analyses. While the code is open-source and widely available for use by practitioners and researchers alike, it should be recognized that the capability of running voluminous analyses in Python is not universal for geotechnical practitioners. It should also be recognized that there are certain geographic regions where seismicity is low enough to render fully probabilistic analyses largely unnecessary. However, it has been shown that the current basis for which to evaluate liquefaction, which consists of performing a deterministic analysis using the a_{max} and mean M_w corresponding to the return period of interest results in a non-uniform assessment of liquefaction risk with respect to geographic location (Kramer and Mayfield 2007). This framework, which will be referred to as *Conventional Liquefaction Analysis* (CLHA), is generally inconsistent with the principle of uniformly applied design guidelines and standards.

Presented here is a framework for developing liquefaction-targeted ground motion maps corresponding to a uniform risk of the liquefaction triggering limit state. The magnitude-adjusted Peak Ground Acceleration intensity measure, PGA_M is used as the intensity measure of interest, and is mapped for a particular return period such that it can be used in a deterministic analysis of triggering to obtain the same value of FS_L as would be obtained from a full PLHA. The mapped PGA_M is shown to be somewhat sensitive to site-specific properties such as soil density, depth of

liquefiable layer, and site V_{s30}; as a result, the sensitivity of PGA_M is systematically evaluated in a parametric study for a series of 100 geographic locations throughout the United States, and site adjustment equations are developed and presented. The performance of this framework is assessed by comparing the fitted FS_L values at several return periods of interest to those obtained from a full PLHA; to assess the relative improvement of this framework over current conventional analyses, the fitted FS_L values are also compared to those obtained from corresponding CLHA, with PLHA-based FS_L values as the benchmark. The framework is further validated in a similar fashion for a second set of geographic locations and a set of realistic CPT profiles. Finally, the framework is applied at scale for four geographic locations throughout the U.S., resulting in high-resolution maps of $PGA_{M,ref}$.

4.2 Characterizing the Mapped PGA_M Value

The procedure for mapping PGA_M is illustrated in Figure 4.1. On the left side of the figure, the factor of safety (FS_L) corresponding to the target annualized non-exceedance rate Λ_{FS_L} is shown. The mapped PGA_M value is determined by finding the value on the deterministic PGA_M-FS_L curve on the right side of the figure corresponding to the same hazard curve-based value of FS_L.

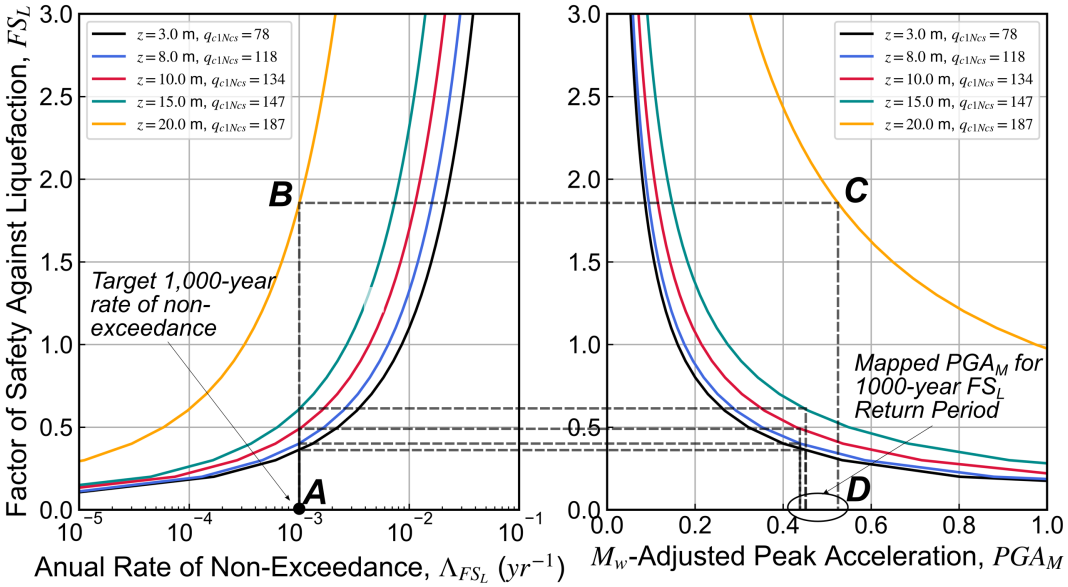

Figure 4.1: Schematic for determining mapped PGA_M for a 1000-year return period of FS_L, for a range of depths and densities

In an ideal framework for mapping PGA_M, any change in site conditions (i.e. cyclic resistance,

depth, vertical stress) that would shift the FS_L hazard curve vertically would cause an identical shift in the deterministic PGA_M-FS_L relationship. In other words, at a particular geographic location, the mapped PGA_M for a given return period would be insensitive to site conditions, and would generate a liquefaction hazard-consistent FS_L for all depths, densities, and stresses. It is clear, however, from Figure 4.1, that while the mapped PGA_M values are relatively consistent for the soil elements below about 15m depth, they still do not quite line up perfectly for the return period of interest. It thus stands to reason that one or more components of the full PLHA calculation, when varied, affect the probabilistic and deterministic LHA procedures differently, and that a single mapped PGA_M value for a given geographic location may not result in perfectly consistent estimates of FS_L.

4.2.1 Sensitivity of PGA_M With No Uncertainty in Ground Shaking

To understand how and why the mapped PGA_M exhibits some sensitivity to various site conditions, it is useful to begin with the simplest possible case: a highly idealized scenario where there is no uncertainty in a_{max} and M_w. In such a case it is possible to analytically calculate the mapped PGA_M and determine what it is sensitive (or insensitive) to.

For the sake of simplicity in this demonstration, the PGA_M is mapped relative to a probability of FS_L non-exceedance, P_{FS_L} , rather than an annualized rate. This value can be expressed as a function of the cyclic resistance ratio CRR, cyclic stress ratio CSR, and the standard deviation in cyclic resistance $\sigma_{\ln R}$ as follows:

$$P_{FS_L} = \Phi\left\{-\frac{\ln CRR - \ln(CSR \cdot FS_L)}{\sigma_{\ln R}}\right\} \tag{4.1}$$

where Φ is the standard normal cumulative probability distribution function, and it is assumed that CRR and CSR are already corrected for overburden, depth, and duration. For a target value of P_{FS_L}, the corresponding factor of safety is thus:

$$\ln FS_L = \ln CRR - \ln CSR + \sigma_{\ln R}\Phi^{-1}(P_{FS_L}) \tag{4.2}$$

On the deterministic side of things, PGA_M can be calculated using the traditional, deterministic definition of factor of safety:

$$FS_L = \frac{CRR}{CSR} = \frac{CRR}{\frac{0.65 a_{max}\sigma_v r_d}{\sigma'_v \cdot MSF \cdot K_\sigma}} \tag{4.3}$$

$$PGA_M = \frac{a_{max}}{MSF} = \frac{CRR}{FS_L \cdot 0.65\frac{\sigma_v r_d}{\sigma'_v K_\sigma}} \tag{4.4}$$

Taking the logarithm of Equation 4.4 and substituting Equation 4.2 in for FS_L, we obtain:

$$\ln PGA_M = \ln CRR - \ln\left(0.65\frac{\sigma_v r_d}{\sigma'_v K_\sigma}\right) - \ln FS_L \tag{4.5a}$$

$$= \ln CRR - \ln\left(0.65\frac{\sigma_v r_d}{\sigma'_v K_\sigma}\right) - \ln CRR + \ln CSR - \sigma_{\ln R}\Phi^{-1}(P_{FS_L}) \tag{4.5b}$$

$$= -\ln\left(0.65\frac{\sigma_v r_d}{\sigma'_v K_\sigma}\right) + \ln\left(\frac{a_{max}}{MSF}\right) + \ln\left(0.65\frac{\sigma_v r_d}{\sigma'_v K_\sigma}\right) - \sigma_{\ln R}\Phi^{-1}(P_{FS_L}) \tag{4.5c}$$

$$= \ln\left(\frac{a_{max}}{MSF}\right) - \sigma_{\ln R}\Phi^{-1}(P_{FS_L}) \tag{4.5d}$$

Finally, taking the exponential of both sides yields:

$$PGA_M = \frac{a_{max}/MSF}{\exp[\sigma_{\ln R}\Phi^{-1}(P_{FS_L})]} \tag{4.6}$$

In this case, a_{max}/MSF refers to the (hypothetically) deterministic peak acceleration and magnitude values. In more realistic cases where the earthquake characteristics are uncertain, a_{max} and MSF would be random variables, resulting in far more complex expressions for P_{FS_L} and PGA_M. This equation for the mapped PGA_M, while unrealistic, is instructive in demonstrating the effects of both the targeted P_{FS_L} and, more importantly, the model uncertainty $\sigma_{\ln R}$. As we might expect, if the target probability of non-exceedance is quite low, corresponding to a more restrictive performance criteria and lower FS_L value, then we would expect the denominator to decrease, resulting in a higher mapped PGA_M. Similarly, the increase in model uncertainty acts as an uncertainty amplifier, decreasing the denominator and thus increasing the mapped PGA_M.

More importantly, it is clear that for a given target P_{FS_L} the mapped PGA_M value in this case depends only on the earthquake loading parameters, and not any change in site conditions. Any change in density, depth, or stress would result in changes to CRR or CSR, which cancel out in Equation 4.5a. Although we will soon see that this condition does not hold when variability in earthquake loading is introduced, the result is significant in that it confirms that any sensitivity in PGA_M is due entirely to uncertainty in the ground motion parameters.

4.2.2 Sensitivity of PGA_M for Different Types of Uncertainties in Ground Shaking

For a situation where the loading parameters are characterized deterministically, it was shown in Equations 4.2-4.6 that, for a target probability of non-exceedance of FS_L, any change in either the CRR (via CPT resistance q_{c1Ncs}) or CSR (via depth or stress) will shift the probabilistic $FS_L - P_{FS_L}$ and deterministic PGA_M–FS_L curves by the same amount. This is confirmed for a series of PLHA calculations on hypothetical soil elements in Table 4.1, where varying the CPT q_{c1Ncs} value (i.e. the cyclic resistance) produces no changes in the mapped PGA_M parameter (while obviously producing significant changes to the FS_L). This is shown for three different probabilities of non-exceedance, assuming deterministic values of $a_{max} = 0.25$ g, and $M_w = 7.5$.

Table 4.1: Sensitivity to CPT resistance q_{c1Ncs} for case with no uncertainty a_{max} (0.25 g) or M_w(7.5)

CPT q_{c1Ncs}	$P[FS < fs] = 0.25$		$P[FS < fs] = 0.50$		$P[FS < fs] = 0.75$	
	FS_L	PGA_M (g)	FS_L	PGA_M (g)	FS_L	PGA_M (g)
70	0.61	0.298	0.86	0.209	1.24	0.147
100	0.78	0.298	1.11	0.209	1.58	0.147
130	1.12	0.298	1.6	0.209	2.27	0.147

Similarly, the sensitivity of PGA_M with respect to depth (and consequently total and effective stress) was evaluated for the same case of deterministic loading parameters. The results in Table 4.2 indicate that PGA_M was insensitive to changes in the CSR when no uncertainty in a_{max} or M_w is assumed.

Table 4.2: Sensitivity to depth and stress for case with no uncertainty a_{max} (0.25 g) or M_w(7.5)

z (m), σ_v (kPa), σ'_v (kPa)	$P[FS < fs] = 0.25$		$P[FS < fs] = 0.50$		$P[FS < fs] = 0.75$	
	FS_L	PGA_M (g)	FS_L	PGA_M (g)	FS_L	PGA_M (g)
1 m, 20 kPa, 20 kPa	0.78	0.356	1.11	0.25	1.58	0.176
5 m, 100 kPa, 70.6 kPa	0.54	0.356	0.77	0.25	1.09	0.176
10 m, 200 kPa, 121.6 kPa	0.47	0.356	0.67	0.25	0.96	0.176

Sensitivity of PGA_M for Case with a_{max} Hazard Curve, no Uncertainty in M_w

A similar set of PLHA calculations was performed for a case where uncertainty in earthquake loading was limited to just a_{max}, represented by a real hazard curve from Charleston, South Carolina. Once again, no uncertainty in M_w was assumed – this would be akin to deaggregating the hazard curve for this site, and finding that the hazard was controlled by a single magnitude scenario. PGA_M values were mapped corresponding to 475-year, 975-year, and 2,475-year return periods. The resulting mapped PGA_M values indicate that when there is no uncertainty in M_w, the mapped PGA_M is insensitive to changes in relative density (Table 4.3), depth, or stress (Table 4.4). Separately, the deterministic M_w was varied from its base value of 7.5, and again no sensitivity in PGA_M was observed.

Table 4.3: Sensitivity to CPT resistance q_{c1Ncs} for case with a_{max} hazard curve, no uncertainty in $M_w(7.5)$

CPT q_{c1Ncs}	$\Lambda_{FS_L} = 1/475$ yr^{-1}		$\Lambda_{FS_L} = 1/975$ yr^{-1}		$\Lambda_{FS_L} = 1/2475$ yr^{-1}	
	FS_L	PGA_M (g)	FS_L	PGA_M (g)	FS_L	PGA_M (g)
70	1.06	0.204	0.64	0.341	0.38	0.571
100	1.36	0.204	0.81	0.341	0.49	0.571
130	1.96	0.204	1.17	0.341	0.7	0.571

Table 4.4: Sensitivity to depth and stress for case with a_{max} hazard curve, no uncertainty in $M_w(7.5)$

z (m), σ_v (kPa), σ'_v (kPa)	$\Lambda_{FS_L} = 1/475$ yr^{-1}		$\Lambda_{FS_L} = 1/975$ yr^{-1}		$\Lambda_{FS_L} = 1/2475$ yr^{-1}	
	FS_L	PGA_M (g)	FS_L	PGA_M (g)	FS_L	PGA_M (g)
1 m, 20 kPa, 20 kPa	1.36	0.204	0.81	0.341	0.49	0.571
5 m, 100 kPa, 70.6 kPa	0.94	0.204	0.56	0.341	0.34	0.571
10 m, 200 kPa, 121.6 kPa	0.82	0.204	0.49	0.341	0.29	0.571

Sensitivity of PGA_M for Case with a_{max} Hazard Curve, Normal Distribution of M_w

The next set of PLHA calculations were performed with uncertainty in M_w incorporated into the hazard curve calculations, by assuming that M_w conditional on a_{max} follows a normal distribution that is constant across all levels of a_{max}, for simplicity. Table 4.5 summarizes the sensitivity of the mapped PGA_M to CPT resistance for the three target return periods, and for different levels of variance in the M_w distribution. For cases of low variance, PGA_M remains almost entirely

insensitive to changes in CRR when the mean magnitude is at the reference 7.5 level. However, it can be seen that increases in the standard deviation of the magnitude distribution begins to introduce some minor sensitivity into the mapped PGA_M values (about 2% variation in PGA_M at most). Similar results can be seen for the sensitivity of PGA_M to depth and stress in Table 4.6.

Table 4.5: Sensitivity to CPT resistance q_{c1Ncs} for case with a_{max} hazard curve, M_w normally distributed with mean of 7.5 (constant over all a_{max} levels)

CPT q_{c1Ncs}	$\Lambda_{FS_L} = 1/475$ yr^{-1}			$\Lambda_{FS_L} = 1/975$ yr^{-1}			$\Lambda_{FS_L} = 1/2475$ yr^{-1}		
	PGA_M (g)			PGA_M (g)			PGA_M (g)		
	$\sigma = 0.5$	$\sigma = 1.0$	$\sigma = 1.5$	$\sigma = 0.5$	$\sigma = 1.0$	$\sigma = 1.5$	$\sigma = 0.5$	$\sigma = 1.0$	$\sigma = 1.5$
70	0.203	0.202	0.199	0.341	0.338	0.333	0.571	0.566	0.559
100	0.203	0.2	0.196	0.341	0.337	0.33	0.571	0.565	0.553
130	0.203	0.2	0.193	0.341	0.336	0.326	0.571	0.565	0.549

Table 4.6: Sensitivity to depth and stress for case with a_{max} hazard curve, M_w normally distributed with mean of 7.5 (constant over all a_{max} levels)

z (m), σ_v (kPa), σ'_v (kPa)	$\Lambda_{FS_L} = 1/475$ yr^{-1}			$\Lambda_{FS_L} = 1/975$ yr^{-1}			$\Lambda_{FS_L} = 1/2475$ yr^{-1}		
	PGA_M (g)			PGA_M (g)			PGA_M (g)		
	$\sigma = 0.5$	$\sigma = 1.0$	$\sigma = 1.5$	$\sigma = 0.5$	$\sigma = 1.0$	$\sigma = 1.5$	$\sigma = 0.5$	$\sigma = 1.0$	$\sigma = 1.5$
1 m, 20 kPa, 20 kPa	0.203	0.201	0.196	0.341	0.337	0.33	0.571	0.565	0.553
5 m, 100 kPa, 70.6 kPa	0.204	0.2	0.195	0.341	0.336	0.328	0.571	0.565	0.551
10 m, 200 kPa, 121.6 kPa	0.204	0.2	0.193	0.342	0.336	0.325	0.573	0.566	0.548

When the mean magnitude is varied, however, the PGA_M sensitivity becomes far more significant. Table 4.7, which summarizes the sensitivity for cases where the M_w is 6.0, 7.0, and 8.0, indicates that the further the mean magnitude is from 7.5, the more sensitive PGA_M is with respect to CPT resistance. Furthermore, we see that when the mean M_w is greater than 7.5, PGA_M increases with CPT resistance. When the mean M_w is less than 7.5, PGA_M *decreases*. Similar trends can be seen with increases in depth and stress in Table 4.8. It is also interesting to note

that the degree sensitivity in PGA_M relatively consistent across different return periods.

Table 4.7: Sensitivity to CPT resistance q_{c1Ncs} for case with a_{max} hazard curve, M_w normally distributed with varying mean and constant $\sigma_{M_w} = 1.0$ (constant over all a_{max} levels)

CPT q_{c1Ncs}	$\Lambda_{FS_L} = 1/475$ yr^{-1}			$\Lambda_{FS_L} = 1/975$ yr^{-1}			$\Lambda_{FS_L} = 1/2475$ yr^{-1}		
	PGA_M (g)			PGA_M (g)			PGA_M (g)		
	$\mu = 6.0$	$\mu = 7.0$	$\mu = 8.0$	$\mu = 6.0$	$\mu = 7.0$	$\mu = 8.0$	$\mu = 6.0$	$\mu = 7.0$	$\mu = 8.0$
70	0.187	0.197	0.206	0.314	0.33	0.344	0.546	0.553	0.577
100	0.177	0.193	0.207	0.298	0.324	0.348	0.499	0.543	0.583
130	0.163	0.187	0.211	0.273	0.315	0.355	0.46	0.53	0.596

Table 4.8: Sensitivity to depth and stress for case with a_{max} hazard curve, M_w normally distributed with varying mean and constant $\sigma_{M_w} = 1.0$ (constant over all a_{max} levels)

z (m), σ_v (kPa), σ'_v (kPa)	$\Lambda_{FS_L} = 1/475$ yr^{-1}			$\Lambda_{FS_L} = 1/975$ yr^{-1}			$\Lambda_{FS_L} = 1/2475$ yr^{-1}		
	PGA_M (g)			PGA_M (g)			PGA_M (g)		
	$\mu = 6.0$	$\mu = 7.0$	$\mu = 8.0$	$\mu = 6.0$	$\mu = 7.0$	$\mu = 8.0$	$\mu = 6.0$	$\mu = 7.0$	$\mu = 8.0$
1 m, 20 kPa, 20 kPa	0.177	0.193	0.207	0.298	0.324	0.348	0.499	0.543	0.583
5 m, 100 kPa, 70.6 kPa	0.171	0.191	0.209	0.287	0.32	0.35	0.482	0.538	0.588
10 m, 200 kPa, 121.6 kPa	0.161	0.187	0.212	0.27	0.314	0.356	0.454	0.529	0.598

4.2.3 Characteristics of PGA_M Sensitivity

The series of PLHA calculations shown above, while purely hypothetical, reveal some important characteristics in the mapped PGA_M, and how and why it varies with changes in site conditions. These characteristics are summarized as follows:

- For any return period, the mapped PGA_M is completely insensitive to site conditions if there is no uncertainty in the underlying magnitude distribution.
- The degree to which PGA_M is sensitive to site conditions depends on the degree to which

the magnitude distribution departs from the deterministic case of $M_w = 7.5$

- If the majority of the magnitude distribution lies above the 7.5 reference value, then PGA_M *increases* with both CPT resistance and depth.
- If the majority of the magnitude distribution lies below the 7.5 reference value, then PGA_M *decreases* with both CPT resistance and depth.
- The degree of PGA_M sensitivity appears to be generally consistent across different return periods of FS_L.

The results of these hypothetical PLHA calculations indicate that, for actual sites with far more complex seismicity, the variation in PGA_M may be relatively significant - more importantly though, it appears to be systematic and predictable. It thus stands to reason that if the underlying magnitude distribution for an actual geographic site can be adequately represented, then the mapped PGA_M for some reference soil condition at that site can be adjusted for its sensitivity to density and depth, thereby producing fully hazard-consistent FS_L estimates across a wide range of soil conditions.

4.3 Characterizing the Sensitivity and Predictability of Mapped PGA_M

In order to be able to map PGA_M across the U.S. that result in truly hazard consistent liquefaction analyses, a rational framework must be developed for accounting for the sensitivity of PGA_M to different soil and site conditions. A large-scale parametric study was performed, for a broad range of geographic locations in the U.S. and a wide range of soil conditions, in order to assess the viability of such a predictive framework.

4.3.1 Selection of Geographic Study Sites

A series of about 100 test sites were selected from across the United States. An initial set of 50 sites was selected from the most populous city in each state, while an additional 50 sites were selected on the basis of capturing the full range of seismo-tectonic environments, as well as important sites of infrastructure, cultural significance, or large populations. The 100 locations are shown in Figure 4.2. To provide a visual representation of the seismo-tectonic environments represented, the 2,475-year PGA contour map from the 2014 USGS National Seismic Hazard Map is included.

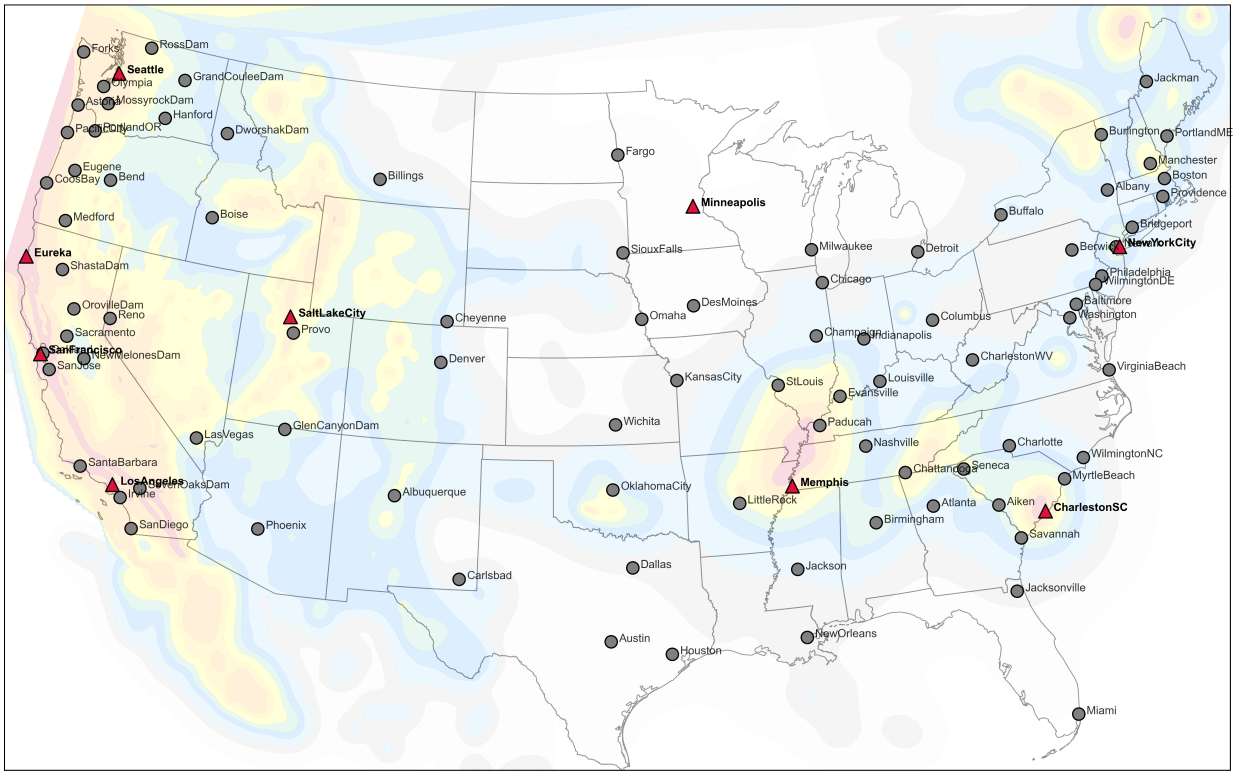

Figure 4.2: Locations of 100 geographic sites evaluated in parametric study. Sites in bold marked by red triangle were part of initial detailed study to determine the functional form of PGA_M adjustment factor. Site locations are overlaid on 2,475-year PGA contour map from 2014 USGS National Seismic Hazard Map.

An initial set of nine sites were selected from this pool to be examined in a detailed study of the sensitivity of PGA_M to soil conditions, in order to establish a functional form for the predictive relationship of PGA_M to various site parameters.

4.3.2 Selection of Soil Parameters for Full Parametric Study

An initial assessment of the sensitivity of PGA_M to various site parameters for the nine test sites indicated that PGA_M would need to be adjusted for three parameters: density (represented here by CPT resistance), depth, and site V_{s30}. It was found that PGA_M was completely insensitive to levels of vertical total and total stress (σ_v and σ'_v, respectively), as well as the ratio of total to effective stress. Therefore, the sensitivity to depth and stress that was observed in the hypothetical cases in Section 4.2 can be attributed entirely to depth (due to the magnitude-dependence of the depth reduction factor in the Boulanger & Idriss 2016 triggering model). A series of profiles with

uniform CPT resistance were developed for each of the combinations of q_{c1Ncs} and V_{s30} shown in Table 4.9. For a given site, PLHA calculations were performed on 70 profiles for a total of 1470 soil elements. For all geographic locations, this resulted in over 150,000 PLHA calculations.

Table 4.9: Summary of reference values and ranges of soil parameters used in parametric sensitivity study

Parameter	Reference Value	Range
CPT q_{c1Ncs}	120	20 to 200
Depth, z (m)	4	0.5 to 20
V_{s30} (m/s)	200	150 to 300

4.3.3 Calculation of PGA_M at Reference Soil Condition for a Target Return Period

As discussed previously, the mapped PGA_M is defined as the magnitude-adjusted value of PGA that, for some target return period of FS_L, yields the same factor of safety in a deterministic analysis of liquefaction triggering as would be obtained from the full PLHA. For use in liquefaction hazard-consistent ground motion maps, PGA_M must be calculated from probabilistic liquefaction hazard curves for a reference soil condition, and some means must be provided for correcting that PGA_M to the specific soil conditions at a given site. At the reference condition, PGA_M can be calculated for a target return period as follows:

$$PGA_{M,ref}(T_{R,FS_L}) = \frac{CRR(q_{ref})}{FS_{L,ref}(T_{R,FS_L}) \cdot 0.65 \frac{\sigma_v}{\sigma'_v K_\sigma}} \cdot \frac{1}{r_d[z_{ref}, \overline{M_{wr,ef}}(T_{R,FS_L})]} \tag{4.7}$$

where $FS_{L,ref}$ is the factor of safety obtained from the FS_L hazard curve, corresponding to the target return period, T_{R,FS_L}. It is important to note that while PGA_M is already magnitude-adjusted, a magnitude is still required to calculate the depth reduction factor, r_d. The selection of which magnitude to use is largely immaterial, so long as the same magnitude used to calculate PGA_M is used by the practitioner in the deterministic calculation of FS_L. Here, the magnitude is taken as the mean value of the conditional magnitude distribution, as obtained from the deaggregated FS_L hazard at T_{R,FS_L} (see Section 3.6.5). Figure 4.3 shows the reference 2475-year PGA_M values calculated for each of the 100 test locations. In a similar manner to the USGS seismic hazard mapped values for PGA, the liquefaction-consistent PGA_M values are relatively high in areas of high seismicity, and relatively low in areas of low seismicity.

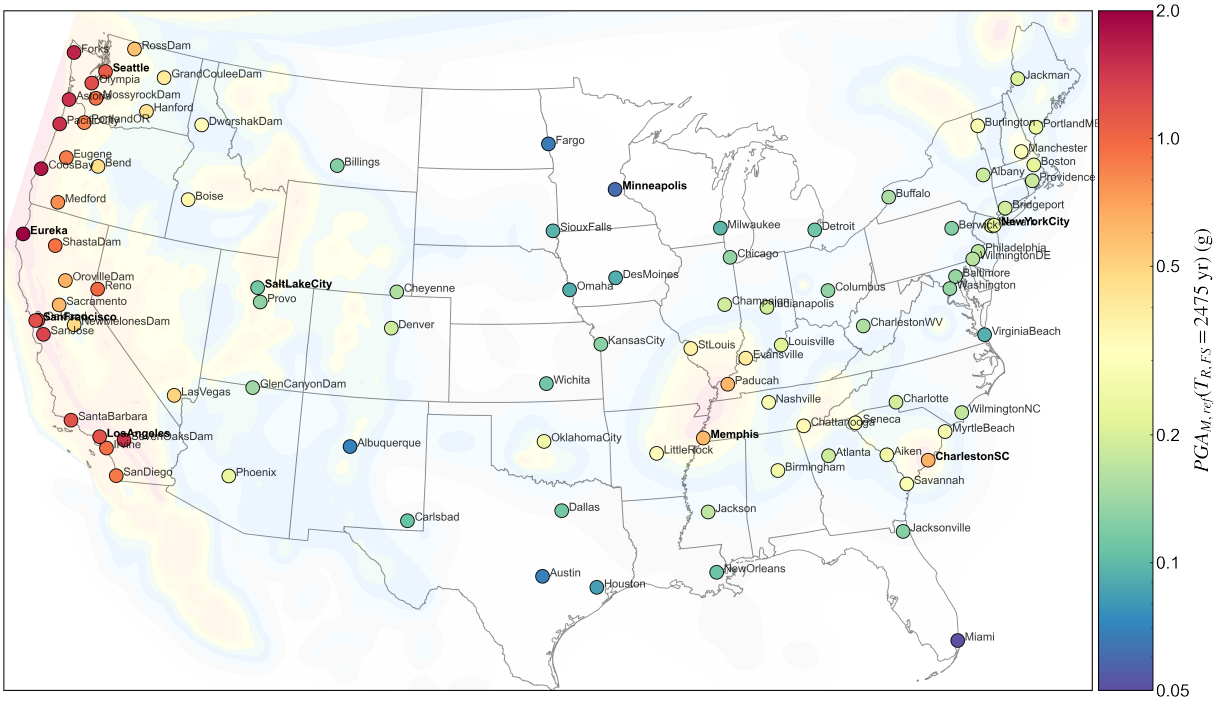

Figure 4.3: Colormap scatterplot of mapped 2475-year liquefaction-consistent PGA_M at reference site conditions (z = 4 m, q_{c1Ncs} = 120, V_{s30} = 200 m/s) for 100 test locations. Site locations are overlaid on 2,475-year PGA contour map from 2014 USGS National Seismic Hazard Map.

4.3.4 Regression Model for PGA_M Adjustment Factor for Site Conditions

It has been shown that the degree of sensitivity of PGA_M to changes in site conditions depends almost entirely on the distribution of event magnitudes likely to be experienced at a given site. Thus, the method for correcting PGA_M to a specific site V_{s30}, soil density, and soil depth, will require factors that depend on geographic location. Therefore, a two-step regression procedure was employed, wherein site-specific regression models of the same functional form were fitted for each of the 100 test sites. Then, each coefficient was regressed against a set of metadata obtained from the PLHA calculations performed at the reference site condition. The metadata consists of the PGA_M and FS_L at the reference condition, as well as the mean, standard deviation, and skew of the deaggregated conditional magnitude distribution at the reference condition.

Step-One Regression: Predicting PGA_M Sensitivity for Individual Sites

The functional form for the adjustment factor regression equation was based on the results from a series of sensitivity analyses on the nine initial test sites highlighted in Figure 4.2. Figures 4.4, 4.5, and 4.6 show the sensitivity of PGA_M normalized to its reference value as a function of CPT resistance, depth, and V_{s30}, respectively. The curves indicate relatively smooth sensitivity behavior across a wide range of soil parameters, geographic sites, and targeted return periods.

A functional form was selected such that the density dependence follows a third-order polynomial, the depth and V_{s30} dependence follows a quadratic function, and that there is some interaction between density and depth. The equation for the natural logarithm of the normalized PGA_M at a given site is thus:

$$\ln P = c_0 + c_1 Q + c_2 Q^2 + c_3 Q^3 + c_4 Z + c_5 Z^2 + c_6 V + c_7 V^2 + c_8 QZ \tag{4.8}$$

where $P = PGA_M / PGA_{M,ref}$, and Q, Z, and V are the CPT q_{c1Ncs}, depth, and V_{s30} normalized to their reference values, respectively.

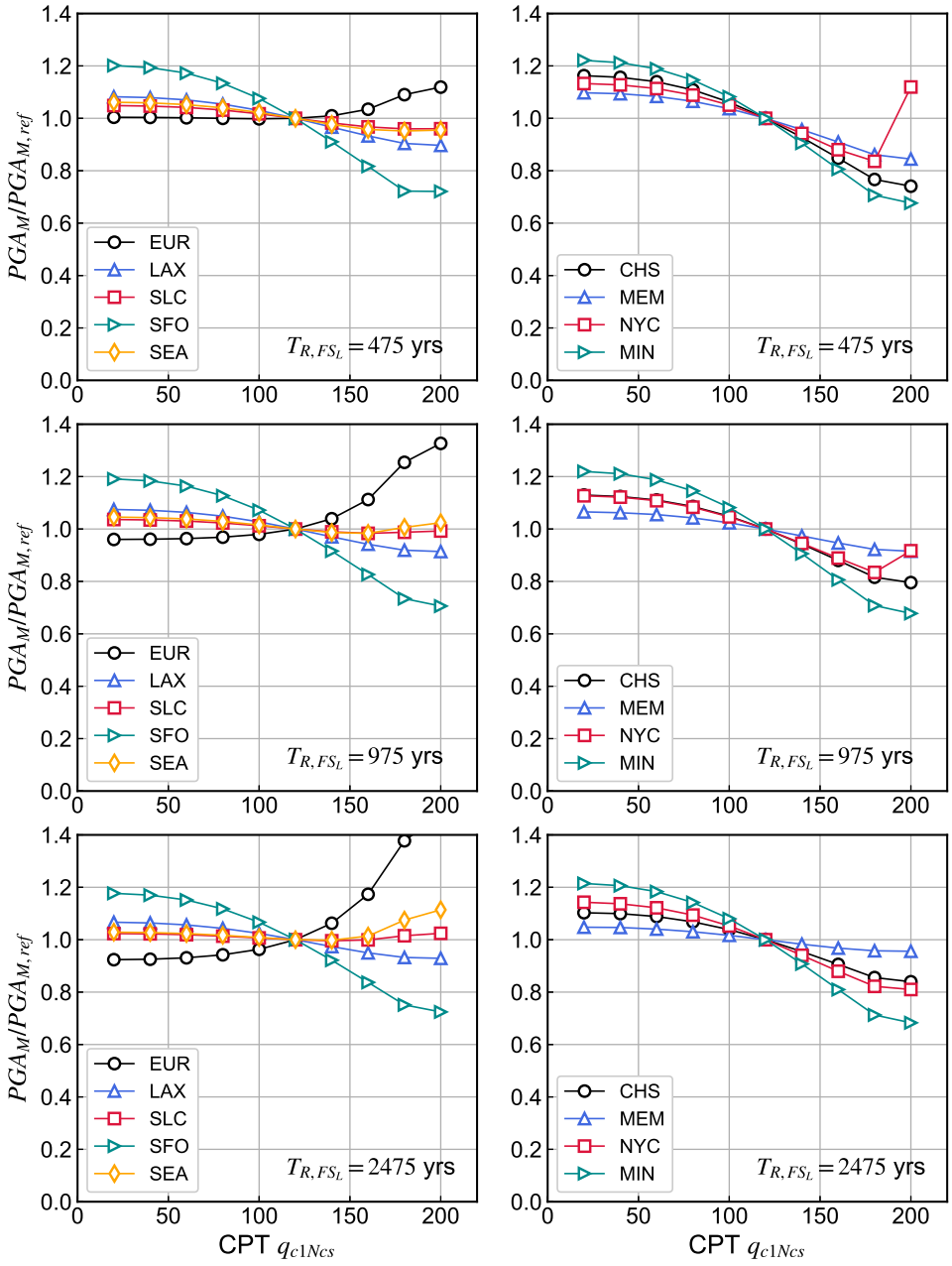

Figure 4.4: Sensitivity of mapped PGA_M for three FS_L return periods to CPT resistance at nine initial geographic locations.

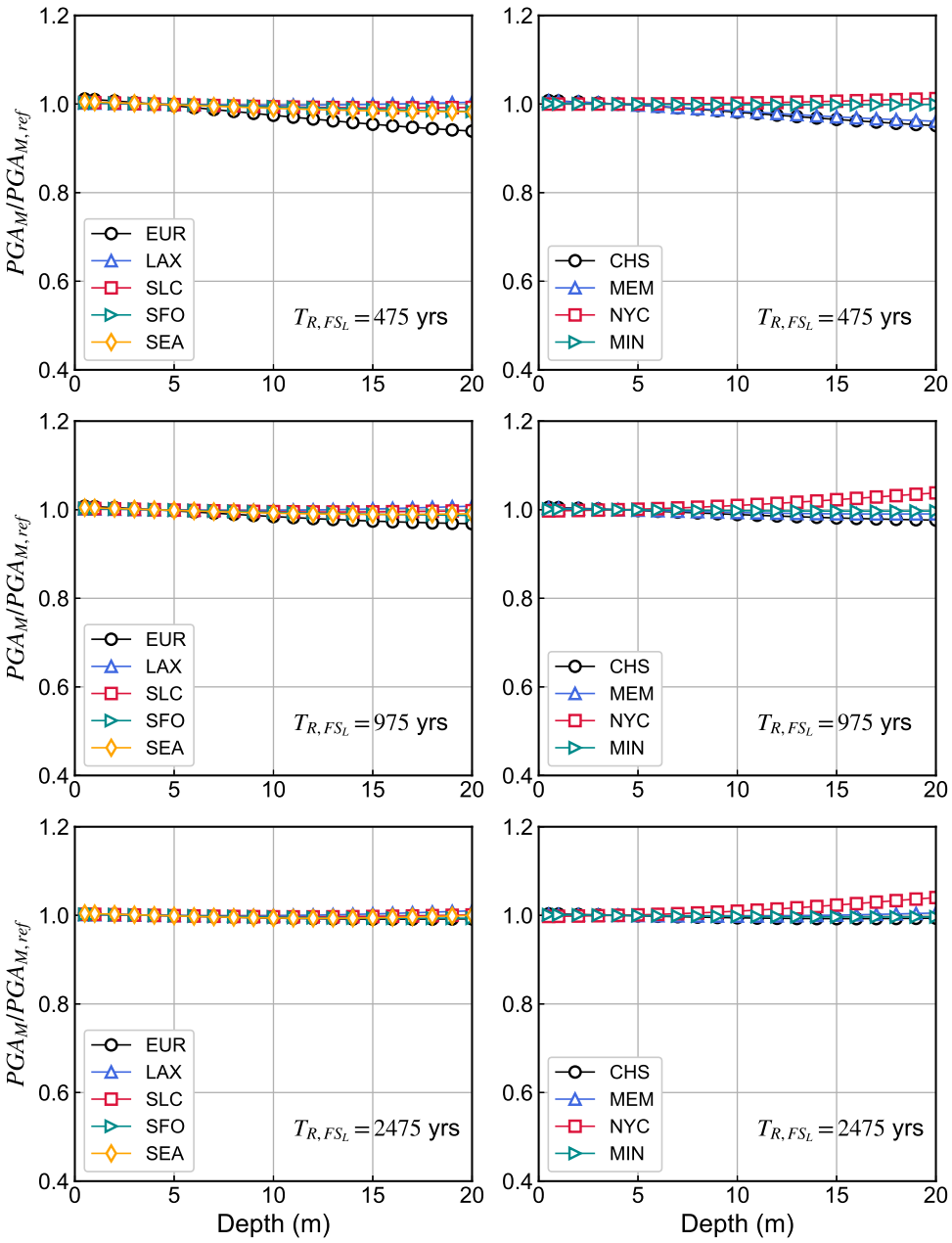

Figure 4.5: Sensitivity of mapped PGA_M for three FS_L return periods to depth at nine initial geographic locations.

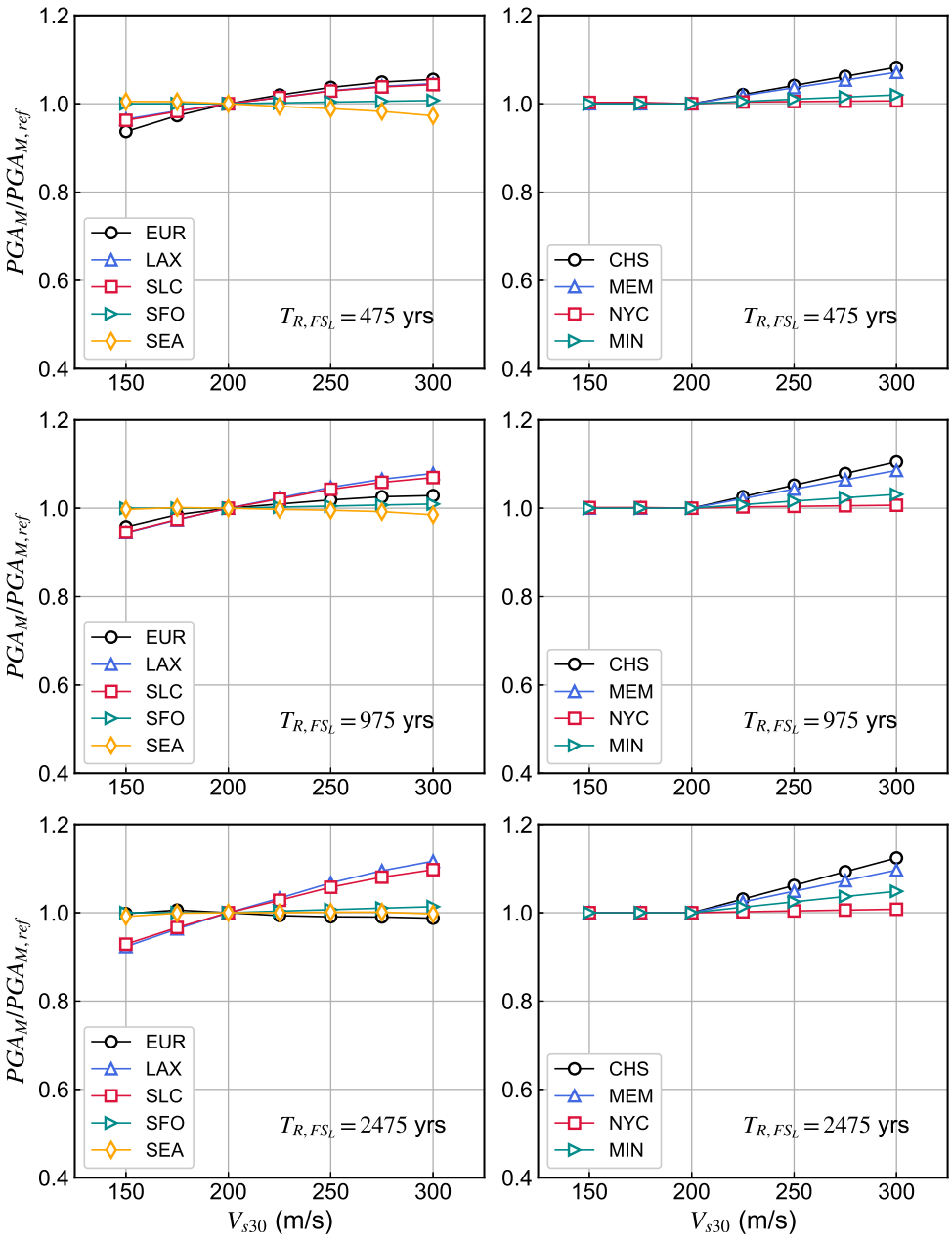

Figure 4.6: Sensitivity of mapped PGA_M for three FS_L return periods to site V_{S30} at nine initial geographic locations.

The coefficients of Equation 4.11 were estimated for each of the 100 test sites. The fitted models were relatively precise across all sites, largely due to the fact that a wide range of predictor variables was used to develop the dataset, allowing for a well-constrained functional form.

Step-Two Regression: Predicting Site-Specific Coefficients from PLHA Metadata at Reference Condition

For use in a forward prediction framework, practitioners should be able to obtain the adjusted PGA_M at their site of interest using only the information available from the PLHA calculation used to map the reference PGA_M at that site. It was found that the set of coefficients in Equation 4.11 could be predicted using the following information from the FS_L hazard curve at the reference soil condition at a given return period:

- The factor of safety corresponding to the target return period, $FS_{L,ref}$
- The corresponding mapped $PGA_{M,ref}$ value
- The mean magnitude of the conditional M_w distribution at the target return period, $E[M_w]$
- The standard deviation of the conditional M_w distribution at the target return period, σ_{M_w}
- The skewness of the conditional M_w distribution at the target return period, γ_{M_w}

A regression model was fitted separately for Western U.S. (WUS) and Central & Eastern U.S. (CEUS) sites for each coefficient in Equation 4.11 using the following form:

$$c_i = b_0 + b_1 PGA_{M,ref} + b_2 FS_{L,ref} + b_3 E[M_w]_{ref} + b_4 \sigma_{M_w,ref} + b_5 \gamma_{M_w,ref} \tag{4.9}$$

Recognizing that the coefficients at a given site are highly correlated with one another, a multivariate multiple regression procedure was used in the `R` software package to account for the correlation between the coefficients. The final coefficients for WUS and CEUS sites are summarized below in Tables 4.10 and 4.11

Table 4.10: Estimated coefficients for use in prediction of 2475-year PGA_M adjustment factor for sites in the Western United States (WUS)

PLHA Metadata	WUS Coefficients for Site-Specific Model								
	Intercept	Q	Q^2	Q^3	Z	Z^2	V	V^2	QZ
	c_0	c_1	c_2	c_3	c_4	c_5	c_6	c_7	c_8
Intercept	-2.9364	1.0826	-1.4826	-0.1267	0.0188	0.0006	4.1916	-0.7897	-0.0103
$PGA_{M,ref}$	-0.6100	-0.0054	0.0106	-0.0183	-0.0054	0.0000	0.8112	-0.1849	0.0016
$FS_{L,ref}$	0.1228	0.0297	-0.0500	0.0216	0.0006	-0.0003	-0.1582	0.0368	-0.0024
$E[M_w]_{ref}$	0.5185	-0.1397	0.1902	0.0254	-0.0001	-0.0001	-0.7275	0.1396	0.0005
$\sigma_{M_w,ref}$	-0.4048	0.0082	-0.1933	0.0909	-0.0396	0.0018	0.6430	-0.1349	0.0283
$\gamma_{M_w,ref}$	0.3031	0.0222	-0.0514	0.0325	0.0009	0.0001	-0.3998	0.0892	0.0013

Table 4.11: Estimated coefficients for use in prediction of 2475-year PGA_M adjustment factor for sites in the Central & United States (CEUS)

PLHA Metadata	CEUS Coefficients for Site-Specific Model								
	Intercept	Q	Q^2	Q^3	Z	Z^2	V	V^2	QZ
	c_0	c_1	c_2	c_3	c_4	c_5	c_6	c_7	c_8
Intercept	0.7331	1.3667	-2.1062	0.2607	0.0415	-0.0012	-0.7689	0.4921	-0.0282
$PGA_{M,ref}$	0.2604	-0.0490	0.0255	-0.0176	-0.0139	0.0001	-0.6066	0.4189	0.0061
$FS_{L,ref}$	-0.0020	-0.0084	0.0132	-0.0053	0.0001	0.0000	0.0058	-0.0033	0.0001
$E[M_w]_{ref}$	-0.1033	-0.1361	0.2018	-0.0052	-0.0074	-0.0001	0.1268	-0.0811	0.0031
$\sigma_{M_w,ref}$	0.0281	-0.2931	0.3767	-0.0956	-0.0039	0.0031	-0.0651	0.0412	0.0207
$\gamma_{M_w,ref}$	-0.0176	0.0439	-0.1036	0.0505	-0.0047	0.0000	0.0672	-0.0428	0.0024

Prediction of PGA_M Adjustment Factor Model for Example Case in Seattle

The procedure for estimating the PGA_M from the mapped $PGA_{M,ref}$ value and corresponding metadata is demonstrated here for a site in Seattle. The PLHA metadata for the reference condition, summarized in Table 4.12, can be used to estimate each of the coefficients (c_0 through c_8).

Table 4.12: Metadata from PLHA calculation at reference condition for a site in Seattle.

Parameter	Value
$PGA_{M,ref}$ (g)	0.814
$FS_{L,ref}$	0.177
$E[M_w]_{ref}$	7.54
$\sigma_{M_w,ref}$	1.05
$\gamma_{M_w,ref}$	0.42

The estimated intercept coefficient $\hat{c_0}$, for example, is calculated using the first column of coefficients in Table 4.10:

$$\begin{aligned}\hat{c_0} = &-2.9364 - 0.0475 PGA_{M,ref} + 0.1228 FS_{L,ref} + 0.5185 E[M_w]_{ref} \\ &- 0.4048 \sigma_{M_w,ref} + 0.3031 \gamma_{M_w,ref} \\ &= 0.2032\end{aligned} \tag{4.10}$$

The calculation can be repeated for the remaining c-coefficients, yielding an equation for the estimate of the adjusted PGA_M value:

$$\ln\left(\frac{PGA_M}{PGA_{M,ref}}\right) = 0.2032 + 0.0475Q - 0.273Q^2 + 0.163Q^3 - 0.0276Z + 0.0017Z^2 - 0.159V + 0.0162V^2 + 0.0242QZ \quad (4.11)$$

which can be used, along with the reference PGA_M value of 0.814 g to calculate the mapped, liquefaction-hazard consistent value of PGA_M for any combination of density, depth, and site V_{s30}. For this particular location, the estimated values of PGA_M, denoted as $\widehat{PGA}_M$ can be compared to the actual values of PGA_M that were obtained from the full parametric study. After filtering out cases where FS_L was less than 0.10 or greater than 3.0, it was found that the mean error for the estimated PGA_M was about 0.3%, with a standard deviation of about 3%. This indicates that the model results in an unbiased estimate of PGA_M, with 90% of estimated values falling within 5% of the actual value.

4.4 Performance of PGA_M Mapping Framework, and Comparison with Existing Procedures

In order to assess the value of this method for mapping PGA_M and adjusting it for various soil parameters in a broader context, it must be evaluated against the current standard of practice for performing liquefaction hazard assessments. As referenced in Section 4.1, the conventional method for analyzing liquefaction hazards (CLHA) is applied using a single set of values for a_{max} and M_w that correspond to a particular return period of ground shaking. The consistency of both the conventional and mapped PGA_M frameworks can be evaluated for the large set of parametric analysis data generated in this study. For each geographic location, the liquefaction-hazard consistent FS_L values corresponding to three return periods (475, 975, and 2475 years), and for all combinations of soil parameters were used as the benchmark FS_L values for evaluating the accuracy and precision of both the conventional and mapped PGA_M analyses.

4.4.1 Inconsistencies Between Conventional and Probabilistic Liquefaction Hazard Analyses

Figure 4.7 shows the mean percent error in the predicted 2475-year FS_L using conventional analyses, across all soil conditions for each of the 100 test sites. It is clear from these results that at the 2475-year hazard level, the CLHA procedure significantly over-predicts the true, hazard-consistent FS_L - it should be noted that this is results in un-conservative estimates of the true liquefaction hazard, as the CLHA is predicting a higher FS_L, and thus a safer condition, than that

implied by the corresponding FS_L hazard curves. On average, FS_L was over-predicted by about 18% in Western U.S. sites, and about 11% in Central & Eastern U.S. sites. Over-prediction errors on the West Coast were the highest in the country - in most of California, prediction errors were in the range of +30 to +45%, and in non-coastal areas of Oregon and Washington errors were in the range of +15 to +25%. The exception to this systematic over-prediction appears to along the Northwest coast, where prediction errors in areas dominated by Cascadia Subduction Zone seismicity were about -5% or so. Overall, only 20% of the sites had mean FS_L errors of less than 5%.

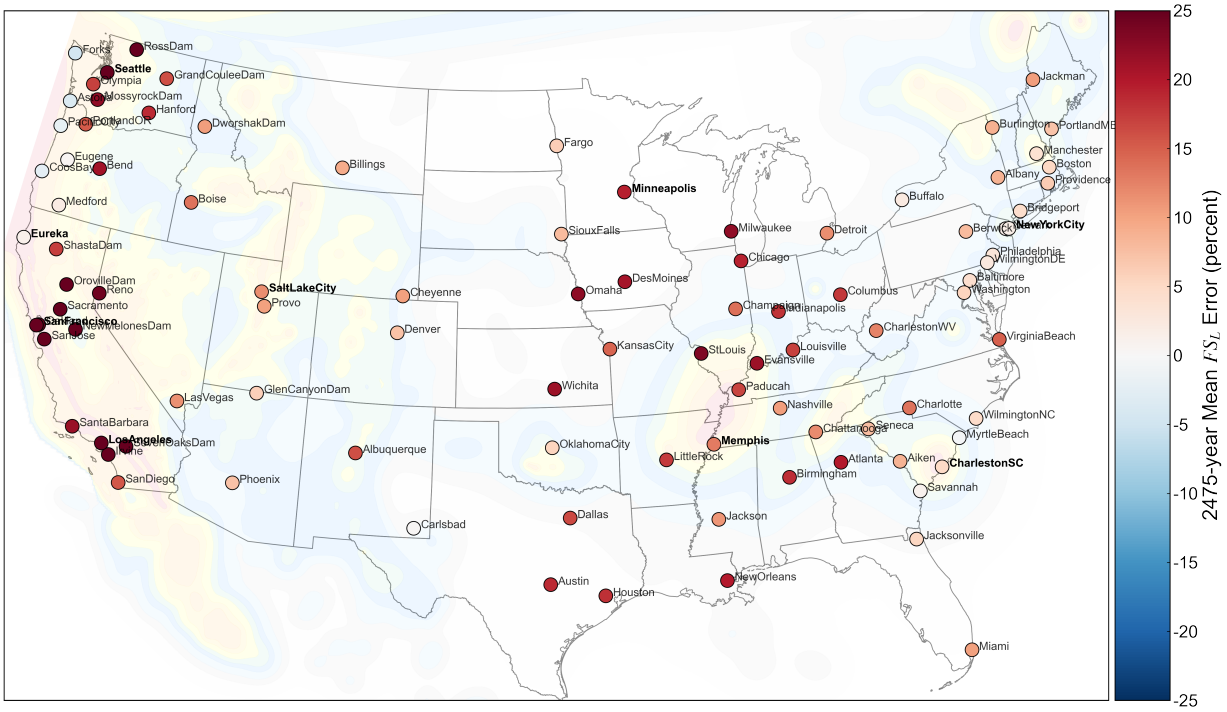

Figure 4.7: Mean percent error in predicted 2475-year factor of safety using conventional liquefaction hazard analysis procedures.

Another way of contextualizing the accuracy of certain liquefaction hazard analyses is to determine the "effective" return period of the estimated FS_L, by calculating where on the corresponding FS_L hazard curve the estimated value lies. The difference between the effective return period and the actual target return period can be a useful indicator of how consistent or inconsistent the liquefaction hazard is represented by a given method. Figure 4.8 shows the mean effective return period

of the CLHA-based estimates for all sites, and indicates that the effective return period in much of the Western U.S. is less than half of the target 2475-year return period - in fact the effective return period in Northern California is closer to the 975-year return period. In terms of 50-year non-exceedance rates, this means that such sites are designing to about half of the liquefaction hazard (10% non-exceedance in 50 years) than the target (2% in 50). The largest difference in effective return periods between test locations is between Forks, WA (2692 years, or 1.84% in 50 years) and San Jose, CA (900 years, or 5.52% in 50 years).

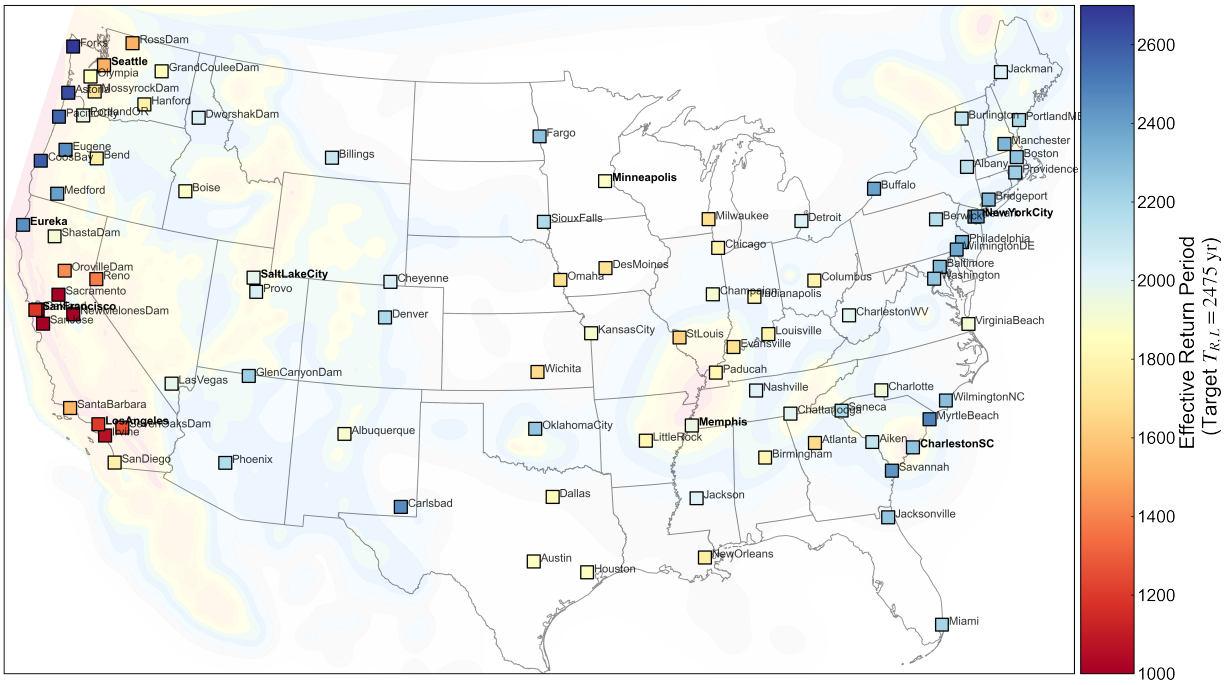

Figure 4.8: Mean effective return period of predicted FS_L values using conventional liquefaction hazard analyses (target 2475-year return period).

4.4.2 Comparison of Mapped, Liquefaction-Targeted PGA_M Results with Probabilistic Liquefaction Hazard Analyses

A similar comparison can be made to evaluate the effectiveness of the proposed mapped PGA_M procedure. Figure 4.9 shows the mean percent error in FS_L values, this time predicted using the reference mapped PGA_M value and estimated site adjustment factors for each site. A significant

improvement in both the accuracy and consistency of the mapped PGA_M framework can be seen, with the mean errors effectively zero across all sites. Additionally, the total model standard deviation across all sites was about 0.82% and 0.15% for WUS and CEUS sites, respectively, compared to about 5% and 2% for the CLHA-based estimates.

Figure 4.9: Mean percent error in predicted 2475-year factor of safety using the mapped PGA_M procedure with estimated site adjustment factors.

The accuracy and consistency of the mapped PGA_M and CLHA frameworks are formally summarized in Table 4.13, with additional results for the 475-year and 975-year return periods. The mapped PGA_M procedure is shown to produce unbiased estimates of the true, hazard-consistent FS_L value at all three return periods, with standard deviations within about 1% of the actual value. This is also reflected in the mean effective return periods and 50-year non-exceedance rates that are almost identical with the target hazard level.

In contrast, current procedures appear to be significantly biased, in an un-conservative fashion, across all three return periods. Estimated FS_L values are significantly higher than the fully-

probabilistic values, resulting in much shorter effective return periods, and higher rates of non-exceedance. It is important to note that these tabulated results also mask the geographical non-uniformity of these errors to a certain degree. For instance, at the 975-year hazard level (5% in 50 years), the effective non-exceedance rate of conventional FS_L estimates at the New Melones Dam site in Northern California is about 10.1%, while the same estimates at Myrtle Beach, South Carolina result in a rate of about 4.4% - a difference of more than a factor of two. A detailed summary of the mapped $PGA_{M,ref}$ values, FS_L errors, and effective return periods for each of the 475, 975, and 2475-year liquefaction return periods can be found in Appendix A.

Table 4.13: Comparison of errors in estimated factors of safety, effective return periods, and 50-year non-exceedance rates using mapped PGA_M (designated as "MAP") and conventional analyses ("CON"). Errors are with respect to fully-probabilistic liquefaction hazard analyses (PLHA)

$T_{R,FS}$	Catalog	FS_L Error (%)				Effective Return Period				50-year Non-Exceedance Rate (%)			
		Mean		Std		Mean		Std		Mean		Std	
		MAP	CON	MAP	CON	MAP	CON	MAP	CON	MAP	CON	MAP	CON
2475 yr	WUS	0.03	18.2	0.82	4.9	2485	1777	79	78	2.0	3.1	0.06	0.35
(2% in 50)	CEUS	0.08	11.1	0.15	2.2	2472	2053	10	55	2.0	2.4	0.01	0.10
975 yr	WUS	0.05	9.5	0.65	2.7	976	818	19	25	5.0	6.3	0.10	0.41
(5% in 50)	CEUS	0.05	5.4	0.13	1.1	974	901	4	12	5.0	5.4	0.02	0.09
475 yr	WUS	0.06	3.7	0.54	1.6	475	436	7	9	10.0	11.2	0.13	0.40
(10% in 50)	CEUS	0.22	1.3	0.27	0.7	474	467	2	4	10.0	10.2	0.04	0.08

4.4.3 Validation of Mapping Procedure with Real CPT Data and Test Sites

The preceding two sections clearly demonstrated that the framework for mapping $PGA_{M,ref}$ has the ability to estimate liquefaction hazard-consistent FS_L values; however, the scope of the performance evaluation is limited to the sites and soil conditions that were originally analyzed to develop the model coefficients, akin to an analysis of residuals and estimate of model variance that is undertaken in a typical statistical regression. A more critical measure of this framework's applicability is achieved by using it in a forward-predictive sense, i.e., to assess its ability to approximate fully-probabilistic FS_L values for geographic locations and site and soil conditions not originally represented in the parametric study dataset.

In order to evaluate the framework's forward-predictive ability, an additional 39 geographic locations were identified across the United States, representing a similar distribution of geography and seismotectonic environments to the original 100 sites (Figure 4.10). At each of these locations, the values of $PGA_{M,ref}$ were mapped using a PLHA calculation at the reference soil and V_{s30} condition (see Table 4.9). The metadata from the reference PLHA calculations ($FS_{L,ref}$,$E[M_w]_{ref}$,

$\sigma_{M_w,ref}$, and $\gamma_{M_w,ref}$) were obtained and used to calculate the site and soil adjustment coefficients in the same manner demonstrated in Equations 4.9 through 4.11 for the 475, 975, and 2475-year target FS_L return periods.

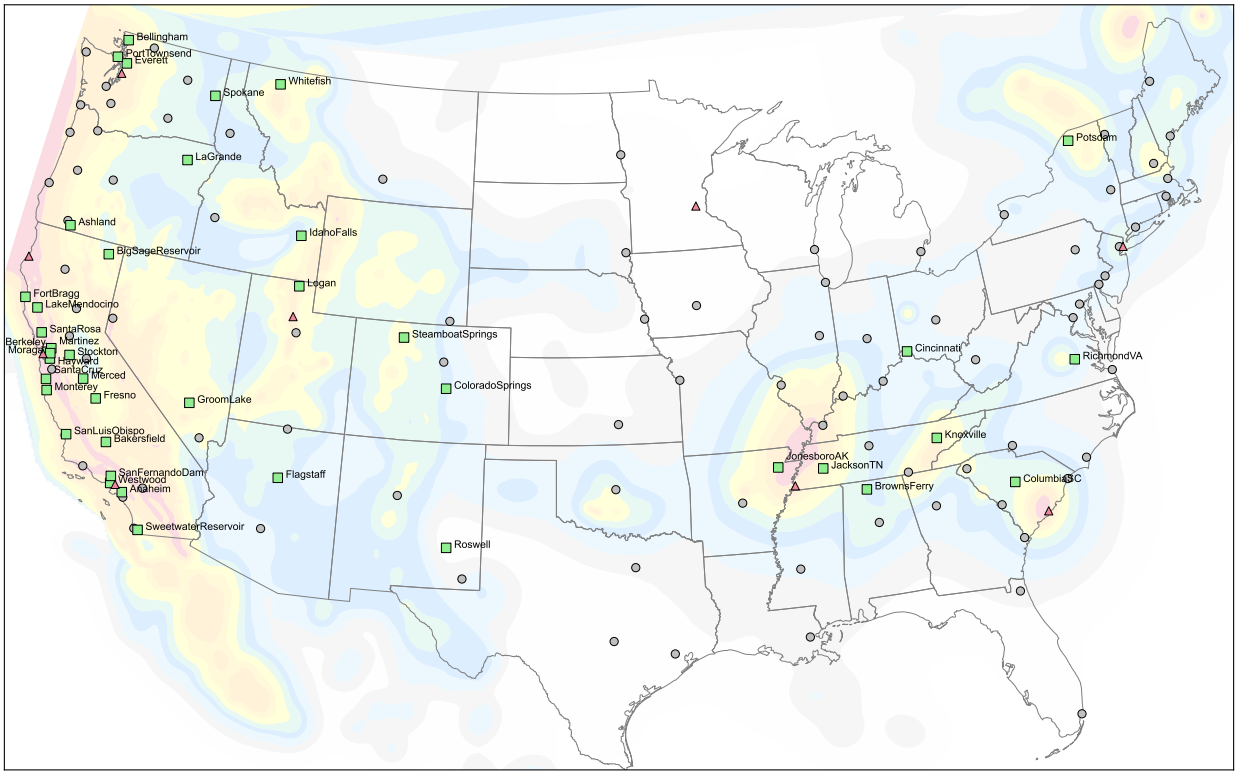

Figure 4.10: Locations of 39 geographic sites evaluated in forward-prediction validation of mapped $PGA_{M,ref}$ with site adjustment factors, shown as light green squares. Gray circles and red triangles correspond to locations evaluated in initial parametric study. Site locations are overlaid on 2,475-year PGA contour map from 2014 USGS National Seismic Hazard Map.

For each site and return period, the mapped $PGA_{M,ref}$ values and adjustment factors were applied to four real CPT profiles (Figure 4.11), which provided different combinations of depth, CPT resistance, stress conditions, and V_{s30} values not represented in the original profiles used to develop the model. Additionally, full PLHA calculations were performed at each susceptible CPT depth increment (shaded in red in Figure 4.11), and FS_L values were extracted from the resulting hazard curves for the 475, 975, and 2475-year return periods as a basis of comparison for the mapped PGA_M-based FS_L estimates.

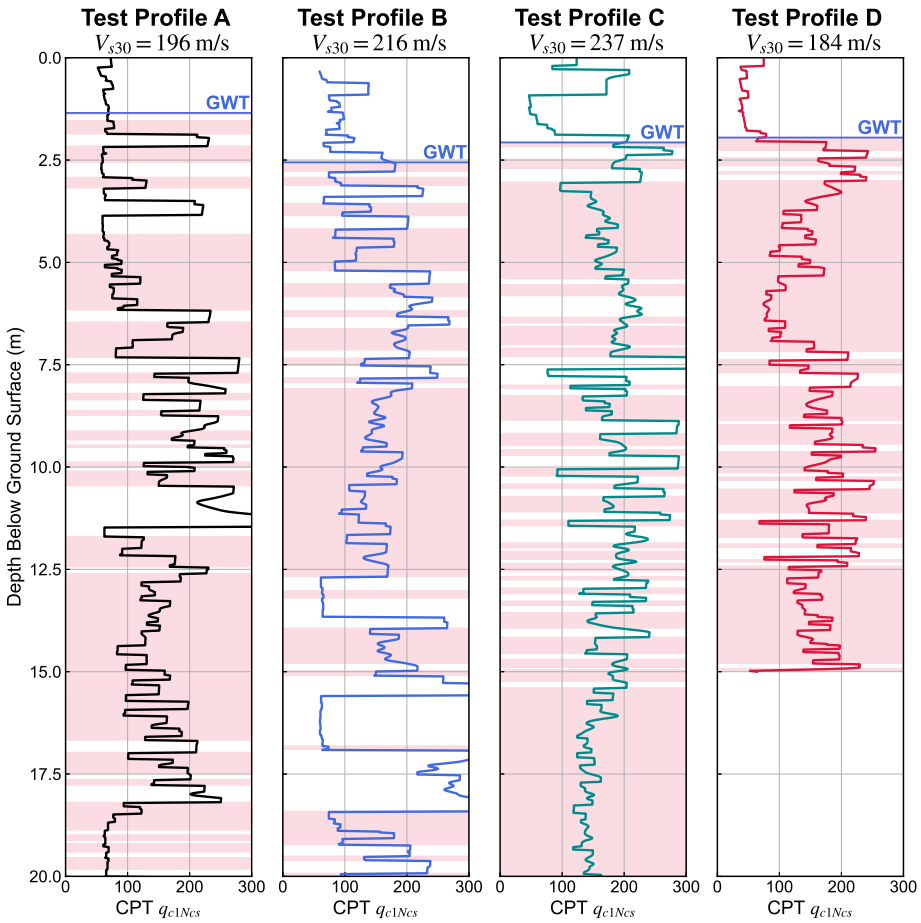

Figure 4.11: Depth profiles of clean sand- and overburden-corrected CPT resistance (q_{c1Ncs}) for four CPT profiles used in forward-prediction validation. Susceptible depths, corresponding to I_c values less than 2.6 and q_{c1Ncs} less than 200 are shaded in red.

The errors in estimated FS_L and effective return periods are summarized in Tables 4.14 and 4.15, respectively. Recall that negative FS_L errors correspond to overly conservative cases relative to full PLHA FS_L values, while positive FS_L errors correspond to un-conservative estimates, implying a safer condition than a fully-probabilistic analysis might. Similar to the data shown in Table 4.13, the forward-predictive application of the framework produces generally unbiased estimates of FS_L within about 1% of the fully-probabilistic values on average, with comparable standard deviations, resulting in effective return periods that are generally consistent with fully-probabilistic FS_L return periods that these estimates are targeted to correspond to.

These results indicate that the synthetic CPT profiles used to initially constrain the sensitivity of PGA_M with respect to site- and soil-specific conditions were sufficiently comprehensive, and that the original geographic locations represented the full range of conditions needed to establish the relationship between the underlying magnitude distribution and the sensitivity coefficients. Overall,

the framework developed and presented in this chapter for mapping $PGA_{M,ref}$ and adjusting it for non-reference site conditions appears to be quite robust, generating relatively accurate and precise estimates of the fully-probabilistic, liquefaction hazard-consistent factors of safety for a wide range of geographic and seismotectonic conditions, as well as a broad spectrum of complex soil conditions.

Table 4.14: Average percent error in estimated FS_L, using mapped PGA_M with predicted adjustment factors, for validation sites and CPT profiles for 2475, 975, and 475-year FS_L return periods. Errors are with respect to PLHA-based FS_L baselines.

T_{R,FS_L}	Catalog	FS_L Error (%)							
		Profile A		Profile B		Profile C		Profile D	
		Mean	Std	Mean	Std	Mean	Std	Mean	Std
2475 yr	WUS	-0.08	0.87	-0.24	0.80	-0.22	0.75	0.28	0.82
	CEUS	-0.31	0.65	0.01	0.60	-0.02	0.40	1.01	0.53
975 yr	WUS	-0.09	0.74	-0.14	0.66	-0.07	0.58	0.14	0.70
	CEUS	-0.33	0.58	0.19	0.46	0.65	0.21	0.52	0.43
475 yr	WUS	0.00	0.85	-0.03	0.76	0.05	0.61	0.20	0.74
	CEUS	0.11	0.18	0.12	0.16	0.17	0.09	1.47	0.13

Table 4.15: Average effective return periods, using mapped PGA_M with predicted adjustment factors, for validation sites and CPT profiles for 2475, 975, and 475-year target FS_L return periods.

T_{R,FS_L}	Catalog	Effective Return Period, $T_{R,eff}$ (yr)							
		Profile A		Profile B		Profile C		Profile D	
		Mean	Std	Mean	Std	Mean	Std	Mean	Std
2475 yr	WUS	2480	52	2491	48	2495	43	2469	49
	CEUS	2491	31	2477	28	2482	18	2427	24
975 yr	WUS	977	16	979	14	978	12	972	15
	CEUS	980	9	972	7	965	3	967	7
475 yr	WUS	475	8	476	7	475	5	473	7
	CEUS	474	1	474	1	474	0	466	1

4.5 Liquefaction-Targeted Ground Motion Maps

The framework presented in this study can be applied in much the same way that seismic hazard ground motion maps are currently developed, by mapping the liquefaction-targeted PGA_M value at the reference soil condition; recall that the reference condition has been selected to correspond to a CPT resistance q_{c1Ncs} of 120, a depth of 4 m, and a site V_{s30} of 200 m/s:

Table 4.16: Summary of reference values for CPT resistance, depth, and site V_{s30} for mapping of liquefaction-targeted PGA_M

Parameter	Reference Value
CPT q_{c1Ncs}	120
Depth, z (m)	4
V_{s30} (m/s)	200

$PGA_{M,ref}$ can be mapped at regularly-spaced and sufficiently dense gridpoints over a regional or national scale. To demonstrate the framework's applicability, liquefaction-targeted maps were developed for four seismically active regions across the United States: the San Francisco Bay Area in northern California, the Puget Sound Region in western Washington state, the Los Angeles Metropolitan Area in southern California, and parts of several states surrounding the New Madrid Fault Zone (Missouri, Illinois, Indiana, Kentucky, Tennessee, and Arkansas).

The procedure for generating these regional maps consisted of:

1. Identifying the range and desired sampling interval and generating the list of coordinates for each region. For the San Francisco Bay Area, the base sampling interval was approximately 1.8 km (0.02°), with some areas in the proximity of major faults selected at a higher resolution of 0.8 km (0.01°), for a total of about 6500 gridpoints. The Puget Sound and Los Angeles regions were sampled at 0.02°, for a total of 2700 and 950 gridpoints, respectively, and the New Madrid Zone was sampled at 3.5 km (0.04°), for a total of just under 10,000 gridpoints.

2. Performing large-scale, multi-site PSHA deaggregation calculations at the reference site V_{s30} of 200 m/s, using `nshmp-haz` to obtain the joint a_{max}-M_w hazard curves needed for the fully probabilistic liquefaction triggering calculation. The initial PSHA deaggregation data was obtained using for eight PGA return periods (see Section 3.7.2). For each gridpoint, the $a_{max} - M_w$ hazard curve data for all eight deaggregation return periods was compiled into a single `xArray` dataset and saved, thus ensuring that the gridded `nshmp-haz` runs only needed to be performed once.

3. Using the a_{max}-M_w hazard curve data at each gridpoint as input to a multi-site PLHA calculation using `PyLHA` to generate FS_L hazard curves for the reference soil condition (CPT resistance of 120, depth of 4m). The FS_L hazard curve data, along with the deagregated a_{max}-M_w percent contribution data (which are used for calculating the moments of the magnitude distribution at a given return period to obtain the soil adjustment coefficients), are once again saved for each grid point as `xArray` datasets for later use.

4. For a desired target return period of liquefaction, the corresponding FS_L values and magnitude distribution moments ($E[M_w]$, σ_{M_w}, and γ_{Mw}) are interpolated from PLHA hazard curve and deaggregation results for each gridpoint. $PGA_{M,ref}$ is then calculated at each grid point using Equation 4.7.

The resulting liquefaction-targeted maps for $PGA_{M,ref}$ are shown for the 2,475-year FS_L return period in Figures 4.12, 4.14, 4.16, and 4.18. The high-resolution data obtained from this study was also useful in examining more closely the manner in which the effective return periods produced by conventional FS_L analyses (see Figure 4.8) seem to vary within certain regions, the maps for which are shown for the target 2,475-year hazard level in Figures 4.13, 4.15, 4.17, and 4.19. The corresponding $PGA_{M,ref}$ and T_{R,FS_L} values are included for the 475- 975-year return periods in Appendix A.

San Francisco Bay Area

The 2,475-year $PGA_{M,ref}$ map for the San Francisco area shows a relatively broad range of ground motions, from values of about 0.75 to well over 1.25 g. This variation (as is the case with any type of targeted ground motion map) largely reflects the region's highly varying seismic environment. $PGA_{M,ref}$ is generally highest in the areas between the Hayward and Calaveras faults, as well as along the San Andreas fault, and generally decreases to the east.

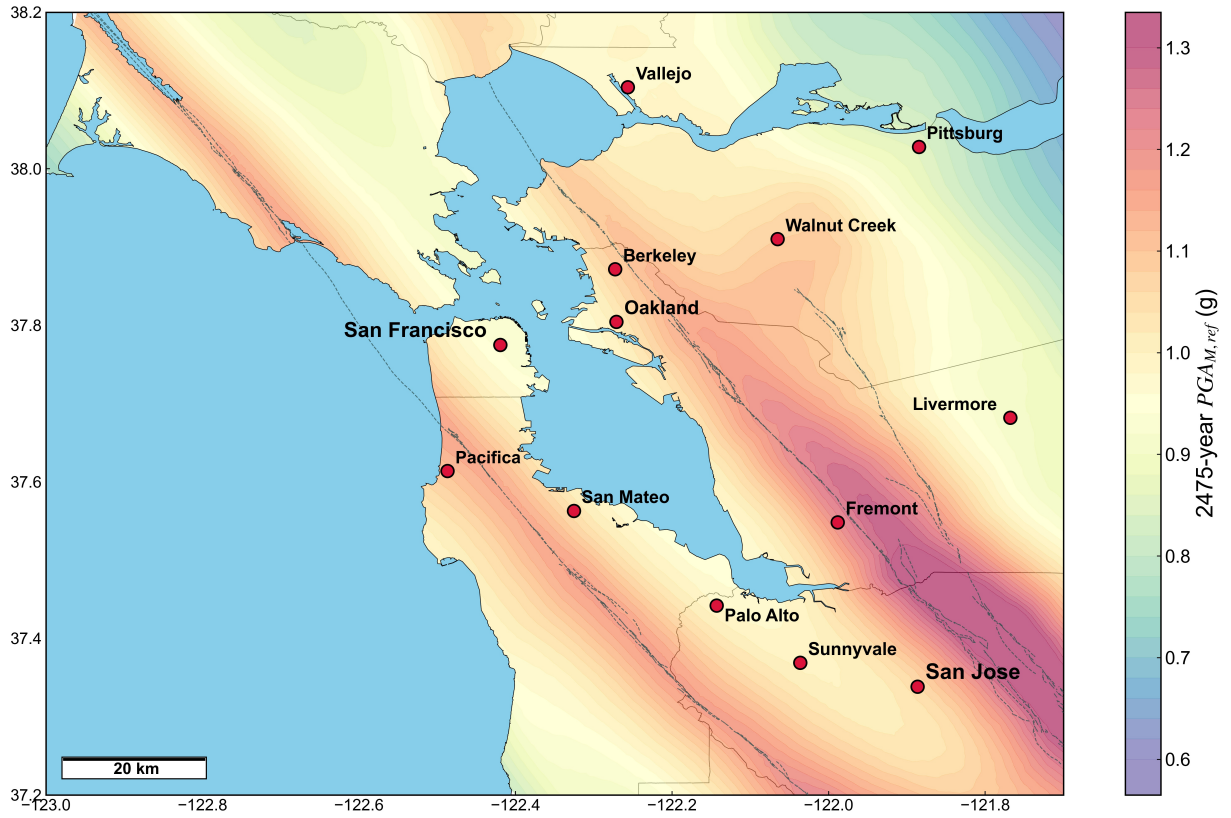

Figure 4.12: Liquefaction-targeted $PGA_{M,ref}$ map of the San Francisco Bay Area, corresponding the 2,475-year FS_L return period. The San Andreas, Hayward, and Calaveras fault traces are shown from west to east.

Perhaps more interesting is the variation in the effective return periods implied by current, conventional analyses in the Bay Area, which are considerably lower than the 2,475-year (2% in 50 year non-exceedance rate) target over the entire region. The CLHA-based effective return periods vary between about 900 years (nearly 5.5% in 50) and 1900 years (about 2.5% in 50), with no areas reaching the actual 2,475-year target. Recall that a lower effective return period is considered a relatively un-conservative design condition, resulting in higher factors of safety than those obtained from full PLHAs, or from conventional LHAs in areas with higher effective return periods. Similar patterns of inconsistency are found in the 475- and 975-year return periods; the $PGA_{M,ref}$ and effective return periods maps for these can be found in Appendix A.

The under-predictions seem to be most extreme in areas that tend to lie between two major faults. San Jose is roughly equidistant from the Sand Andreas and Hayward Faults, while Livermore lies between the Calaveras and Greenville Faults; both locations have seismic hazards controlled by highly variable event magnitudes, and therefore less suitably represented by the single mean or modal magnitude that is used in conventional FS_L calculations. Additionally noteworthy in the Bay

Area map is the extremely high degree of variation in effective return period over relatively short distances - the distance between the maximum and minimum values of T_{R,FS_L} in the mapped area is less than about 20 km, indicating that conventional procedures are providing highly inconsistent safety and performance over very small distance within particular regions. Such a high degree of inconsistency over these short distances could have wide-ranging implications on infrastructure in the area, particularly distributed systems such as highways, public transit, and critical pipelines.

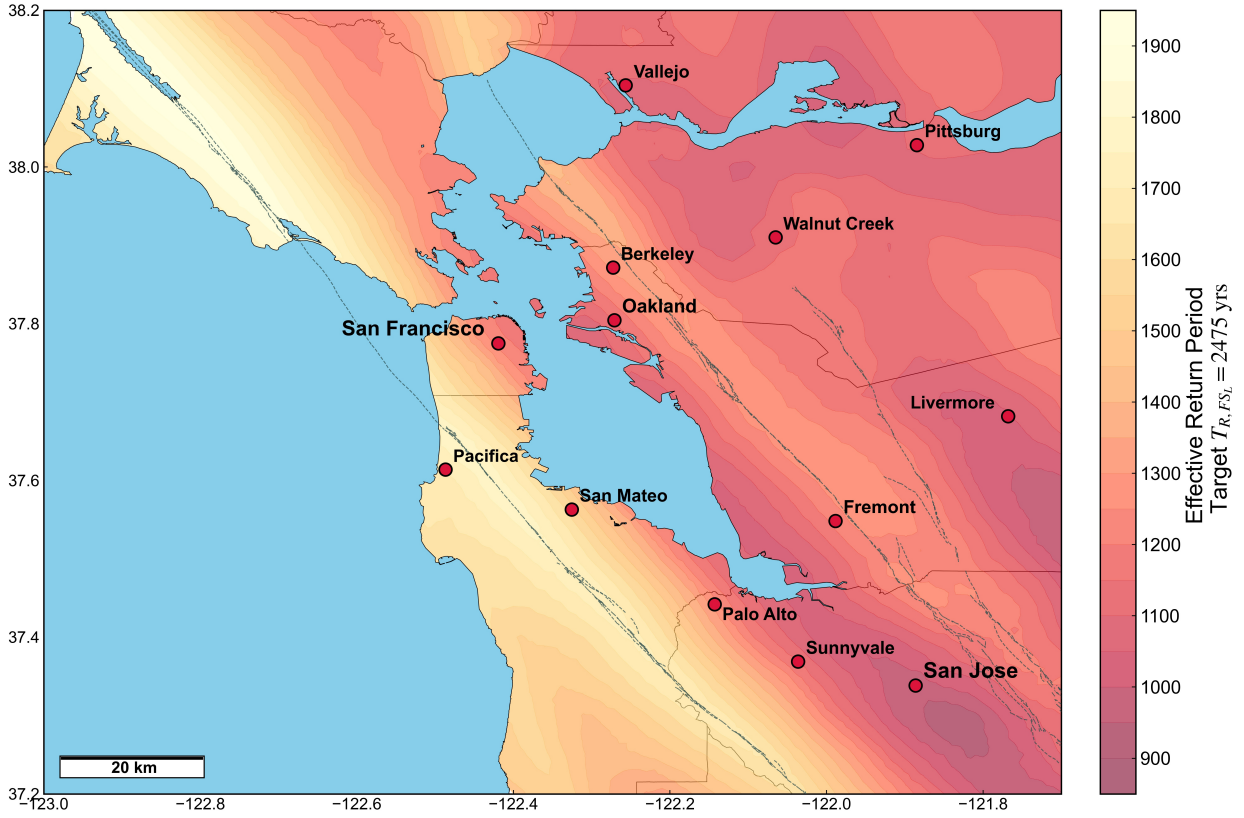

Figure 4.13: Effective return period of predicted FS_L (target 2,475-year return period) for the San Francisco Bay Area at the reference soil condition.

Puget Sound Region

In contrast to the Bay Area, where several major crustal faults (and numerous smaller faults) combine to create a highly complex and varied PGA_M map, the geographic variation in 2475-year $PGA_{M,ref}$ in the Puget Sound region, which ranges from about 0.7 g to just over 1.0 g, is largely controlled by a single seismic source: the Cascadia Subduction Zone (CSZ). This is clearly evident in Figure 4.14, where a general increase in PGA_M from east to west clearly coincides with the proximity to the offshore CSZ. This does not mean that regional crustal faults do not play a role: sites near the Seattle, Tacoma, and South Whidbey Island fault systems all seem to coincide with a characteristic "elbow" in the PGA_M contours (although the shape of the subducting slab, which

curves with a similar shape in this region, also plays a strong role). It is the presence of these fault systems that helps explain why, for example, the mapped PGA_M at a site in Seattle is about 10-15% higher than a site about 20 km directly north in Lynnwood, despite both cities being roughly the same distance from the CSZ.

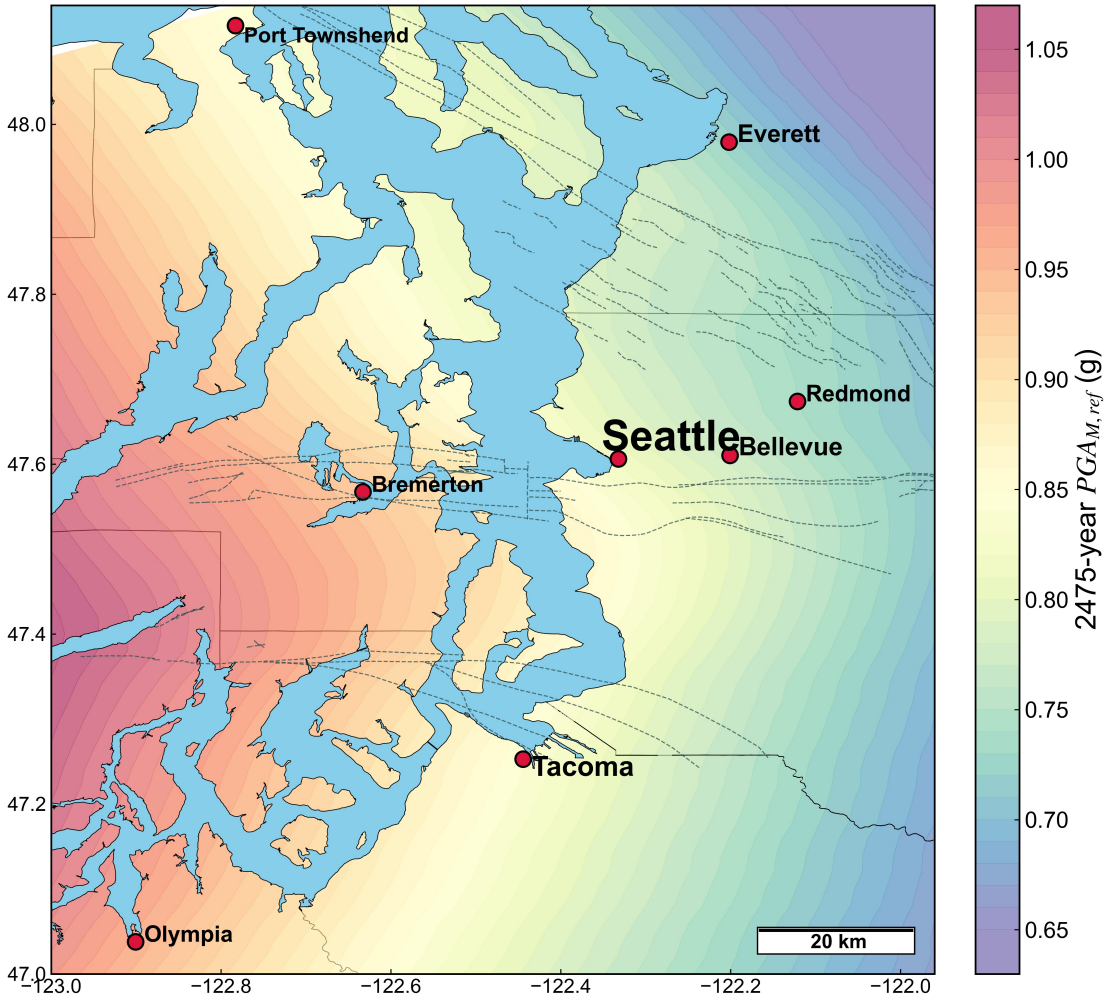

Figure 4.14: Liquefaction-targeted $PGA_{M,ref}$ map of the Puget Sound Region, corresponding the 2,475-year FS_L return period. The South Whidbey Island, Seattle, and Tacoma fault zone traces are shown from north to south, respectively.

A similar east-west pattern is observed in the effective return period, which varies between 1600 and 2200 years (about a 2 to 3% 50-year non-exceedance), indicating that sites near the coast are currently designing for marginally safer liquefaction conditions than those further inland. Also observed, albeit to a lesser degree, are more examples of the effects seen in the Bay Area, that the sites with the most unconservative applications of conventional FS_L calculations are those situated between multiple sources of significant seismic hazards, as evidenced by the localized hotspots in effective return period around Redmond and Bellevue.

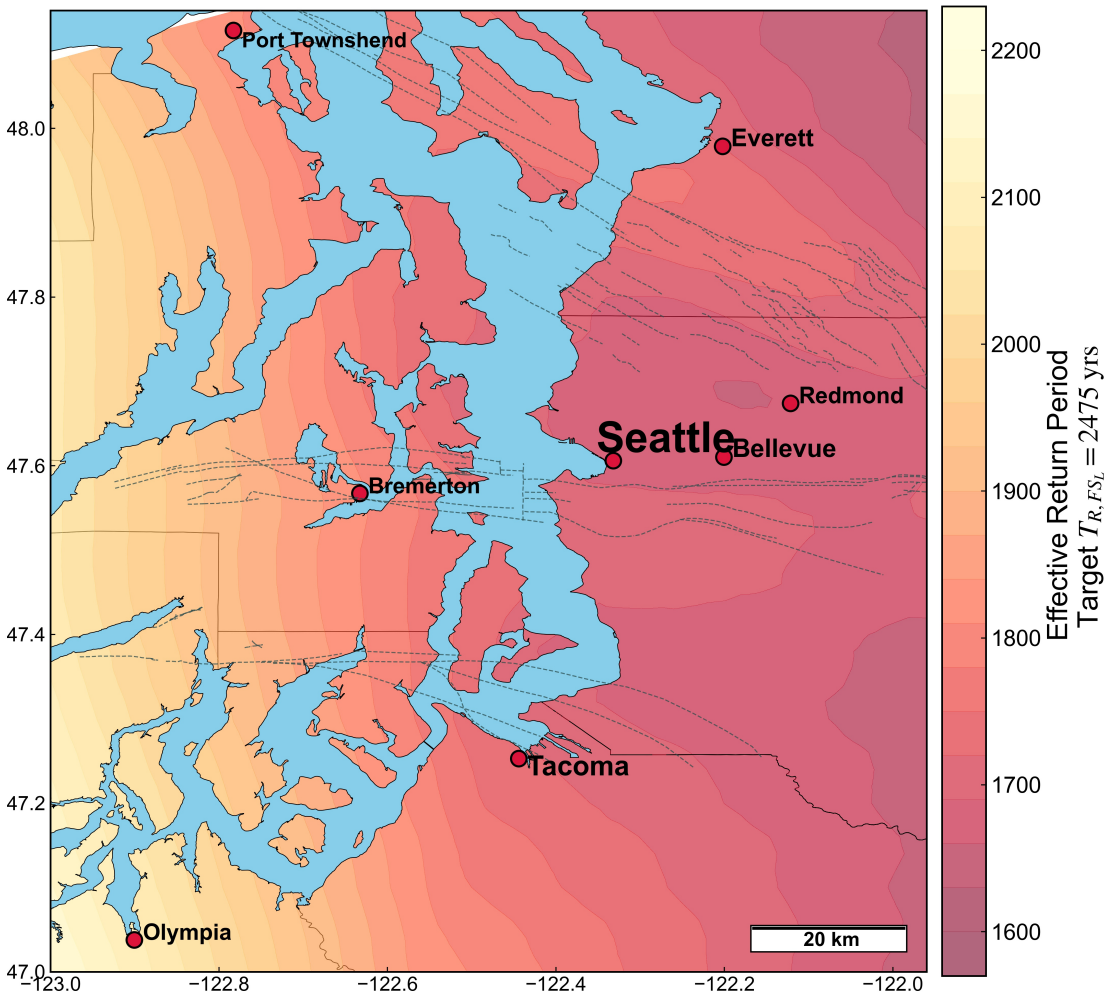

Figure 4.15: Effective return period of predicted FS_L (target 2,475-year return period) for the Puget Sound Region at the reference soil condition.

Los Angeles Metropolitan Area

Liquefaction-targeted PGA_M values in the area surrounding Los Angeles are generally on the order of 0.7 to 1.0 g for the 2,475-year return period, with values generally increasing from south to north, coinciding with the proximity to the San Gabriel, Sierra Madre, and San Andreas fault zones.

Effective return periods in this region are generally on the order of 1,000 to 1,500 years, corresponding to 50-year non-exceedance rates of about 3.5 to 5% (where 2% is the target). Areas where the effective return periods are lowest include north of Santa Monica near the coast, parts of the Inland Empire, and the areas surrounding Santa Ana - all locations that generally lie between multiple major faults.

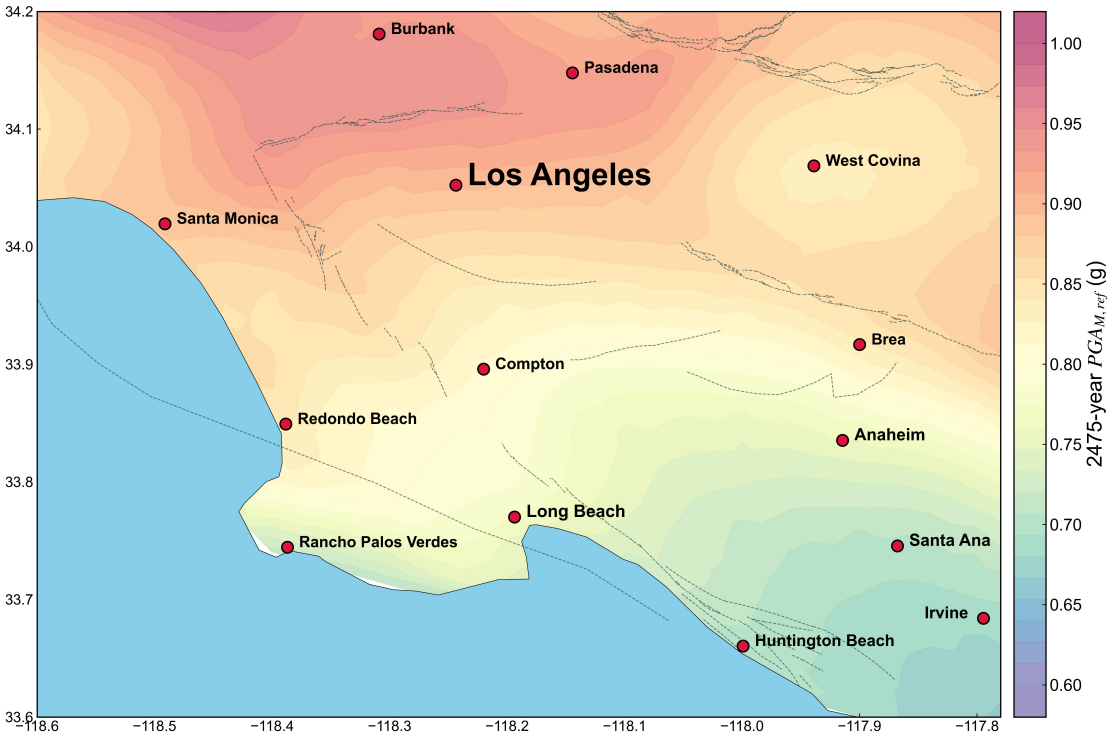

Figure 4.16: Liquefaction-targeted $PGA_{M,ref}$ map of the Los Angeles Metropolitan Area, corresponding the 2,475-year FS_L return period.

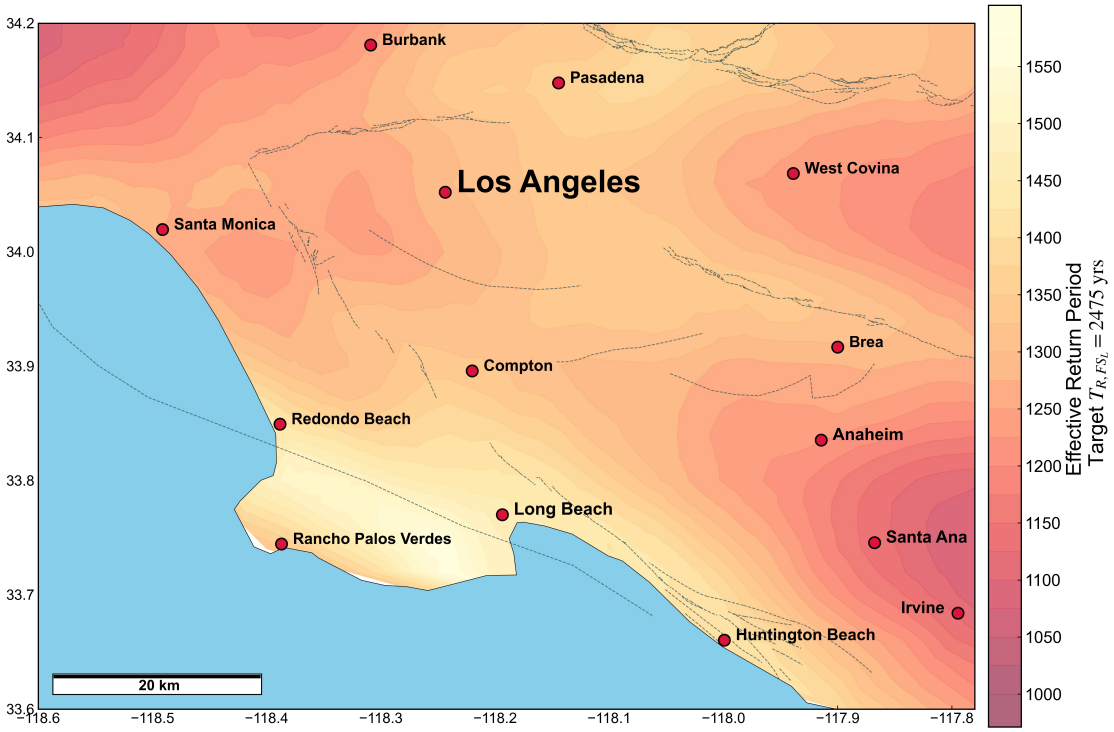

Figure 4.17: Effective return period of predicted FS_L (target 2,475-year return period) for the Los Angeles Metropolitan area at the reference soil condition.

New Madrid Fault Zone Region

As the name implies, the liquefaction-targeted PGA_M levels in the region around the New Madrid Fault Zone (NMFZ) are highly dependent on proximity to the NMFZ. The highest hazard areas near the Mississippi River where Missouri, Kentucky and Tennessee meet have mapped PGA_M values comparable with those in the highest seismicity areas in other parts of the U.S - here the hazard is dominated almost entirely by various NMFZ representations (cluster and fault) in the USGS National Seismic Hazard Model. At greater distances from the NMFZ, the hazard contribution transitions to CEUS gridded background seismicity models, with a large decrease in mapped PGA_M to around 0.20 g.

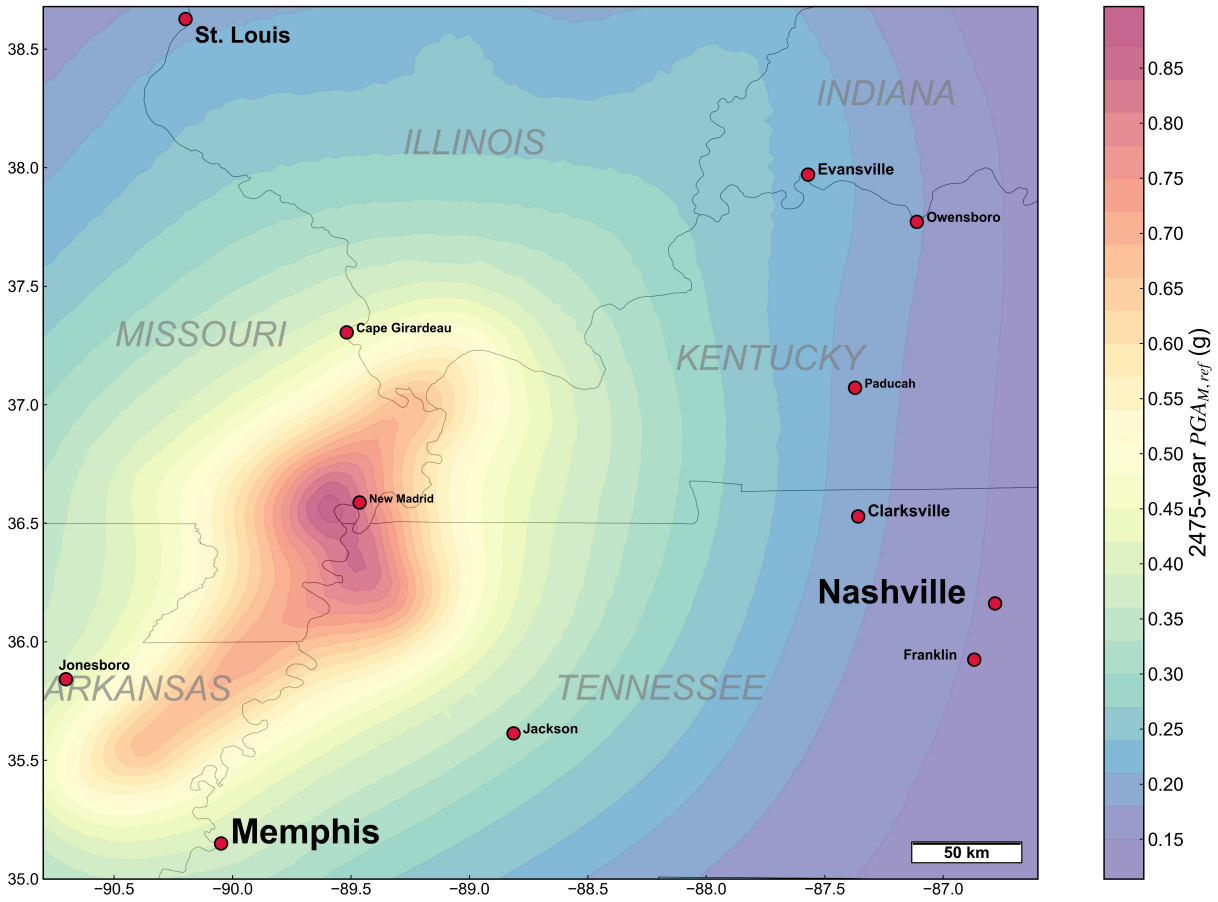

Figure 4.18: Liquefaction-targeted $PGA_{M,ref}$ map of the region surrounding the New Madrid Fault Zone, corresponding the 2,475-year FS_L return period.

Effective return periods are generally closer to the 2475-year target in this region, exceeding 2300 years in the areas closest to the NMFZ, where a very narrow range of event magnitudes controls the hazard, to around 1800 years in areas with more diffuse magnitude distributions associated with background seismicity.

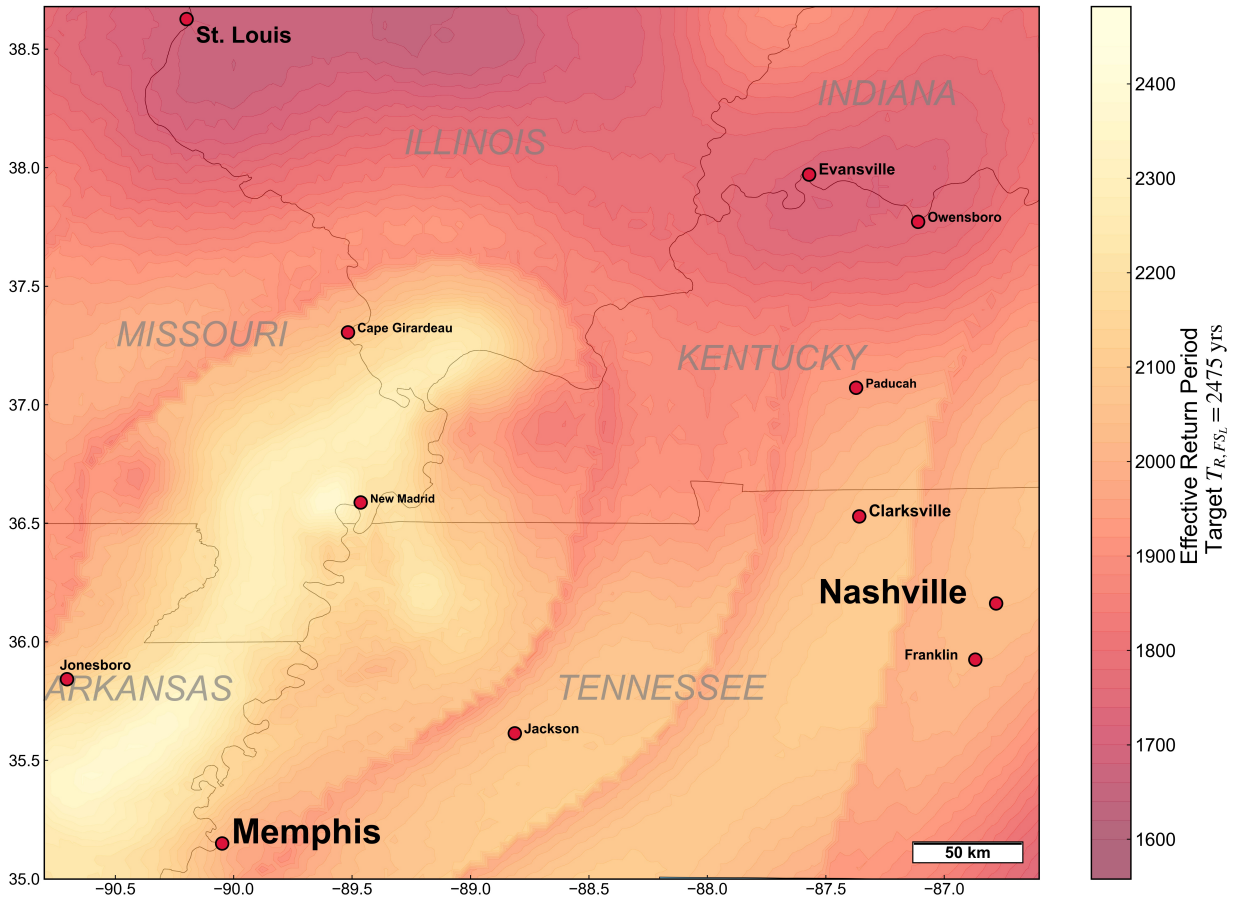

Figure 4.19: Effective return period of predicted FS_L (target 2,475-year return period) for region surrounding the New Madrid Fault Zone at the reference soil condition.

For each of the detailed mapped areas presented in this section, the minimum and maximum effective return periods for the 475-, 975-, and 2475-year FS_L return periods are summarized in Table 4.17. These effective return periods generally coincide with the nationwide results shown in Figure 4.8, further confirming not only the significant inconsistencies in liquefaction risk produced by current design standards from region to region, but within particular regions as well.

Table 4.17: Ranges of CLHA-based effective return periods at reference condition for four regions mapped in detail.

Map Region	$T_{R,eff}$ (475-yr Target)		$T_{R,eff}$ (975-yr Target)		$T_{R,eff}$ (2475-yr Target)	
	min	max	min	max	min	max
S.F. Bay Area	305	493	504	900	915	1942
Puget Sound	418	496	761	957	1617	2204
Los Angeles Area	325	384	556	707	1075	1564
New Madrid	469	587	829	1146	1650	2387

4.6 Summary and Concluding Remarks

While a fully-probabilistic framework for analyzing liquefaction hazards is clearly the most rigorous method to account for uncertainties in both earthquake ground shaking and the estimation of liquefaction triggering, its use requires voluminous, repeated calculations that may be currently impractical for many engineering professionals. In this study, a framework for developing a mapped ground motion intensity measure PGA_M that can be used in deterministic liquefaction triggering analyses to obtain hazard-consistent estimates of the factor of safety was developed and presented.

The framework is based on calculating a PGA_M value at a particular geographic site for a reference soil condition (q_{c1Ncs} = 120, z = 4 m, V_{s30} = 200 m/s), and providing practitioners with a set of coefficients for adjusting the mapped $PGA_{M,ref}$ to their specific soil conditions. The coefficients were estimated via a two-step regression procedure; in the first step the sensitivity of PGA_M to soil density, depth, and site V_{s30} was characterized for broad range of soil conditions at each of 100 geographic locations, and a predictive equation was estimated to adjust PGA_M from its reference condition to site-specific conditions for each location. In the second step, the site-adjustment coefficients were compiled for all sites, and regressed against parameters related to the PLHA results at the reference condition: $PGA_{M,ref}$, $FS_{L,ref}$, and the three moments of the conditional magnitude distribution. This procedure was developed for three FS_L return periods: 475, 975, and 2475 years.

The accuracy and precision of this framework was initially assessed by using the mapped $PGA_{M,ref}$ and estimated coefficients at each site in a deterministic triggering analysis to calculate FS_L values and compare them to the fully-probabilistic values obtained from the corresponding FS_L hazard curves. The method was shown to produce unbiased predictions of the hazard-consistent FS_L values across a wide range of sites and target return periods, with estimates generally within

about 1% of the target values. The model was further validated in a forward-prediction framework, by applying the site coefficients to 39 new geographic locations and four real CPT profiles; similarly unbiased FS_L predictions were found in the validation dataset.

Furthermore, it was shown that the mapped PGA_M method represents a significant improvement over current conventional liquefaction hazard analysis procedures. A similar comparison between CLHA-predicted FS_L values and their corresponding fully probabilistic values suggests that current methods tend to result in extremely inconsistent representations of the liquefaction hazard across the U.S. This leads to non-uniform levels of liquefaction risk produced by current design standards, where engineers in certain parts of the country are designing to a significantly higher standard for liquefaction than others, and confirms many of the findings discussed in Kramer and Mayfield (2007).

The framework presented here provides a basis for correcting such non-uniformities. Its implementation is relatively uncomplicated; a large-scale set of PLHA calculations can be performed for a single reference soil element over a range of gridpoints in the United States, similar to the manner in which the USGS seismic hazard maps are produced. From those calculations, reference PGA_M values can be obtained for any number of return periods (e.g. 475, 975, or 2475 years). The FS_L hazard curves can be deaggregated for each return period to generate the magnitude distribution required (along with the reference FS_L value) to determine the coefficients for the PGA_M adjustment equation at a particular site. The $PGA_{M,ref}$ and coefficients can be provided at a given location by an online lookup tool similar to what is currently maintained by USGS for retrieving seismic hazard map ground motions, and can be used by practitioners to obtain final estimates of the PGA_M values needed to accurately and consistently characterize the liquefaction hazard at their site of interest.

Chapter 5

Development of a Numerical Parametric Study to Investigate Liquefaction- and Lateral Spreading-Related Mechanisms

5.1 Introduction

The two preceding chapters focused on the probabilistic analysis of liquefaction triggering, primarily through the lens of the liquefaction Factor of Safety, FS_L. This parameter has seen widespread use in geotechnical earthquake engineering for many years as an index for analyzing liquefaction potential using empirical models that don't require detailed laboratory tests or complicated numerical analyses. While FS_L does provide an indication of the likelihood and an indirect sense of the severity of liquefaction, it does not inherently provide the engineer with any information about the *effects* of liquefaction, such as ground settlement, lateral deformations, or direct impacts on structural systems such as deep foundations or critical pipelines.

It is also important to note that the simplified method addresses liquefaction potential by considering each susceptible liquefiable layer separately, an approach that has been shown to have some deficiencies in describing broader system-level effects. The suite of simplified methods currently used in practice for estimating liquefaction-induced ground deformation tend to be anchored to FS_L, and as a result suffer from these same deficiencies. This presents a significant challenge for the current state of practice in earthquake geotechnics; it is clearly impossible to character-

ize system-level effects from laboratory testing data on small soil elements, and while the current database of liquefaction case histories can yield some insights on a case-by-case basis, it is simply not broad enough to be useful in characterizing such effects systematically.

Numerical models allow for a more detailed understanding of liquefaction and its associated impacts on geotechnical systems, and have been used for years by pracitioners as an improvement on simplified empirical methods, and by researchers to gain more insight from case histories and to investigate liquefaction-related problems more rigorously and methodically. This chapter presents some of the basic concepts of geotechnical numerical modeling, specifically as it relates to soil liquefaction, as a basis for the development of a parametric study to investigate the sensitivity of lateral spreading displacements to soil, site, and ground motion factors. Two established constitutive models, used to capture the behavior of sands and silts under cyclic loading, are presented, and utilized within a finite-element modeling framework for analyzing liquefaction in one-dimensional soil columns under infinite slopes. A large suite of ground motion recordings is developed and assembled in order to investigate the effects of earthquake motions from a wide range of tectonic environments, event magnitudes, source mechanisms, and source-to-site paths. Finally, an example analysis is presented, wherein several important features of liquefiable systems are identified and explored, including the timing of liquefaction and its utility in evaluating lateral spreading displacements.

5.2 Numerical Modeling of Liquefiable Systems

Geotechnical analyses are involved to varying degrees in nearly all civil engineering problems. Typical design requirements in such problems consider both local and global stability of the soil structure system, and involve characterization of how a proposed structure may cause ground movements, and how those movements may further impact those structural forces. A complete theoretical solution to such problems must satisfy four conditions: force equilibrium, strain compatibility, constitutive behavior, and boundary conditions (Potts and Zdravkovic, 1999). Many conventional methods of geotechnical analysis (e.g. limit equilibrium solutions) fail to satisfy at least one of these fundamental requirements. As a result such methods commonly resort to highly simplified constitutive models in order to obtain close-form analytical solutions, fail to provide information on either global or local stability conditions, or are difficult to apply in complex, heterogeneous soil environments.

These limitations are further compounded when liquefaction-susceptible soils are involved. From a boundary condition standpoint, with the exception of static liquefaction cases, engineers are faced with a dynamic loading problem in which the seismic loading imposed by the system must be

adequately characterized. From a constitutive behavior standpoint, the effects of the seismic loading on the behavior of liquefiable soils must be adequately captured in ways that account for highly complex behavior such as pore pressure generation, phase transformation, critical/steady state, initial static shear stress effects, and post-triggering behavior (see Section 2.2.1). Liquefaction-related problems also create additional complications in terms of assessing global system effects, where interactions between different soil deposits can affect both the characterization of seismic loading and pore pressure generation (see Figure 2.18) in ways that make it difficult to simply evaluate liquefaction potential on a layer-by-layer (or an element-by-element) basis.

In many ways, it can be argued that these limitations, specifically as they pertain to earthquake engineering problems, have been a primary driver of the advances made over the past few decades in the development and proliferation of more advanced geotechnical modeling methods. The following section provides an overview of how such methods are formulated and deployed, as well as their advantages and potential pitfalls.

5.2.1 Geotechnical Finite Element Analysis

Full numerical analyses such as finite difference or finite element methods, are based on discretizing the geotechnical and/or structural domain into smaller, simpler parts, employing more sophisticated constitutive models to more realistically represent soil behavior, and approximating the solution of the domain's boundary value problem. The finite element method can be relatively succinctly summarized as follows (after Potts and Zdravkovic, 1999):

- **Discretization of model domain into elements**: The process of representing the model geometry as an assemblage of smaller, *finite elements*, such as the embankment shown in Figure 5.1. The selection of element size is based on numerous considerations (e.g., proximity to areas of interest or areas of potential instability, accuracy in wave propagation representation, or direction of stress/strain gradients), and can vary within the model domain. The location of an individual element is defined by its nodal locations.
- **Element formulation and equations**: Because an element is defined primarily by its nodal coordinates. Depending on the type used, a two-dimensional element may consist of three (triangular), four (quadrilateral), or even six or nine nodes in more complex quadrilateral elements. A relationship must be established defining how the element strain or stress can be approximated from the primary variable (e.g. displacements or stresses) of each of its nodes. This typically involves some type of interpolation between nodal variables, using a shape function that describes the variation of displacement for given nodal point displacements. Element strains are computed as gradients of the displacements, and stresses are computed

from strains based on the assumed constitutive behavior of the element, to relate the incremental displacements (the vector $\Delta \boldsymbol{u_E}$) and forces ($\Delta \boldsymbol{F_E}$) via the element stiffness matrix ($[\boldsymbol{K_E}]$):

$$[\boldsymbol{K_E}]\Delta \boldsymbol{u_E} = \Delta \boldsymbol{F_E} \tag{5.1}$$

- **Global equations**: The equations for each element are assembled to for the global equation for the model:

$$[\boldsymbol{K_G}]\Delta \boldsymbol{u_G} = \Delta \boldsymbol{F_G} \tag{5.2}$$

  This is hardly a trivial component of the finite element method, as combining the stiffness matrices of hundreds or thousands of elements requires significant amounts of memory storage and organization - essentially we are tasked with taking numerous two-dimensional data structures and combining them into one data structure that remains two-dimensional. Solving the global equations requires considerably large matrix computations, and as such there are numerous methods for constructing these matrices in the most efficient method possible, the details of which are outside the scope of this dissertation.

- **Boundary conditions**: Boundary conditions come in many different forms. Element nodes along certain model boundaries may be specified to be fixed with respect to displacement in one or more directions, affecting the $\Delta \boldsymbol{u_G}$ term in Equation 5.2 (occasionally referred to, quite esoterically, as a Dirichlet-type boundary condition). Other boundary conditions occur when static or dynamic loads are imposed at the surface or base of the model, or when the modeler wishes to simulate a specific groundwater regime; these types of boundary conditions typically generate a specified nodal force at point of application, affecting the $\Delta \boldsymbol{F_G}$ term in Equation 5.2 (also known, just as esoterically, as a Neumann-type condition).

- **Solution of global equations**: The global equations are solved as a large set of simultaneous equations, to obtain the individual incremental nodal displacements. Those displacements are then used to obtain the element stresses and strains from the constitutive behavior for each element. Again, the solution of these equations can be highly complex and computationally quite intensive; numerous numerical approximations for obtaining those solutions are typically used in most finite element platforms.

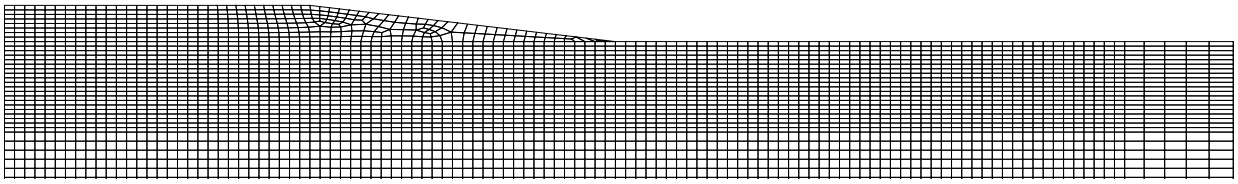

Figure 5.1: A finite element mesh constructed in OpenSees for an embankment, using quadrilateral elements.

Finite element methods approximately satisfy all four of the aforementioned conditions and generally can provide information on a range of geotechnical and structural design requirements. Advances in computing power and increases in availability of both proprietary and open-source software platforms have made numerical analyses far more accessible to researchers and practitioners alike. However, with great power comes great responsibility: finite-element analyses are highly complex, and as such require an analyst who possesses, among other things, considerable experience with the software platform (and an understanding of its underpinnings and limitations), a strong grasp of soil mechanics and the constitutive models used by the software (again, as well as the limitations of said constitutive models), an understanding of how model domains should be discretized and boundary conditions applied, and above all a healthy amount of curiosity and skepticism.

5.2.2 Constitutive Modeling of Liquefiable Soils

Relative to other types of engineering materials, the mechanical behavior of soils is highly complex, and as such any constitutive model that purports to capture the stress-strain behavior of soils must account for, in varying degrees, its nonlinearity, inelasticity, anistropy, coupled deviatoric-volumetric behavior, and stress-dependent characteristics (Chen 2020). Classical, rate-independent plasticity concepts provide fertile ground for describing at least the basics of some of the aforementioned characteristics of soil behavior, such as:

- Transition from elastic to plastic deformations through the definition of a yield surface
- The evolution of plastic strains after yielding occurs (known as a flow rule)
- Strain-hardening or strain-softening behavior and the evolution of the yield surface and other internal variables, using linear or non-linear hardening laws (e.g. isotropic, kinematic, or a combination of the two).

However, classical plasticity reaches somewhat of a natural ceiling in its utility in capturing the full range of behaviors that soils exhibit in response to cyclic loading, such as the transition

between contractive and dilative response (phase transformation), the generation of excess pore pressure and associated liquefaction- and cyclic mobility-type behaviors, and the effects of changes to soil fabric. From a practical standpoint, any constitutive model for liquefiable soils should be able to capture the general trends in liquefaction behavior reflected in established empirical and laboratory data. These aspects may include, but are not limited to (after Boulanger and Ziotopoulo 2013):

- Shear modulus reduction and damping behavior over a large range of shear strains
- A soil's cyclic resistance ratio (CRR), and its dependence on relative density, confining pressure, and static shear bias
- The response of soils under irregular cyclic loading regimes of varying duration
- Post-triggering behavior, including the accumulation of shear strains, losses in stiffness and strength, and volumetric strains
- Degradation of soil fabric, and its effects on stiffness and compressibility after triggering

In response to such limitations, various classes of constitutive models has seen widespread development and use in recent decades, which utilize the concepts of critical state soil mechanics within a traditional elastoplasticity framework to better simulate cyclic response of soils. The bounding surface plasticity framework (Dafalias 1986) is one such class of models, and forms the basis of the PM4Sand and PM4Silt constitutive models used in this numerical parametric study.

PM4Sand Model

Following earlier bounding surface developments of Manzari and Dafalias (1997) and Dafalias and Manzari (2004), Boulanger and Ziotopoulou (2013) proposed an effective stress, critical state-based, bounding surface plasticity model for sand, known as PM4Sand. The key concept behind these models is a limiting (i.e. "bounding") state of stress that any stress-strain curve eventually converges to. Bounding surface models base their flow rules and hardening laws on the distance in stress space between the current stress state and this bounding surface, and allow for the tracking of loading history through reversals in stress.

The model incorporates bounding, dilatancy, and critical surfaces, the slopes (in p-q space) of which depend on the state of the sand relative to the critical state line (see Figures 2.12 and 2.13). Whereas Dafalias and Manzari used the state parameter ($\psi = e - e_{cs}$) to describe the state, the PM4Sand formulation instead adopts the relative state parameter index ξ_R. The effects of fabric

were initially introduced by Dafalias and Manzari (2004) via a fabric tensor to account for the effects of prior straining by tracking the plastic volumetric strain. The fabric tensor was modified in PM4Sand to evolve in response to deviatoric strains instead; additionally, the rate of evolution of the fabric tensor decreases as plastic strains increase, allowing for the accumulation of progressive strains (whereas earlier bounding surface models tended to lock up into a single, repeating stress-strain loop). An additional fabric term, accounting for the "memory of fabric formation history", was incorporated in PM4Sand in order to improve the model's dependency on static shear bias (see Section 2.2.1), by tracking the initial fabric tensor at the start of a given load path.

The key advantages in using PM4Sand stem from an implementation standpoint; in contrast to many existing models, its calibration requires relatively few parameters, most of which are related soil properties correlated to commonly-available *in situ* data. All that is needed the apparent relative density D_R (which can be estimated from SPT or CPT resistance, a dimensionless shear modulus coefficient G_o (either from shear wave velocity measurements or estimated from D_R, and a contraction rate parameter h_{po}. For a given combination of D_R and G_o, the calibration typically consists of simulating the stress-strain response under drain-controlled cyclic direct simple shear (DSS) with varying values of h_po, adjusting this value to obtain the desired CRR for the apparent D_R of interest (based on liquefaction triggering correlations by Idriss and Boulanger [2008]). Typical stress-strain and stress-path behaviors simulated in an undrained, cyclic DSS loading regime are shown for three model calibrations in Figure 5.2. The variation in cyclic stress ratio and the number of cycles to liquefaction (defined as reaching 3% single-amplitude strain), is shown for the three calibrations in Figure 5.3.

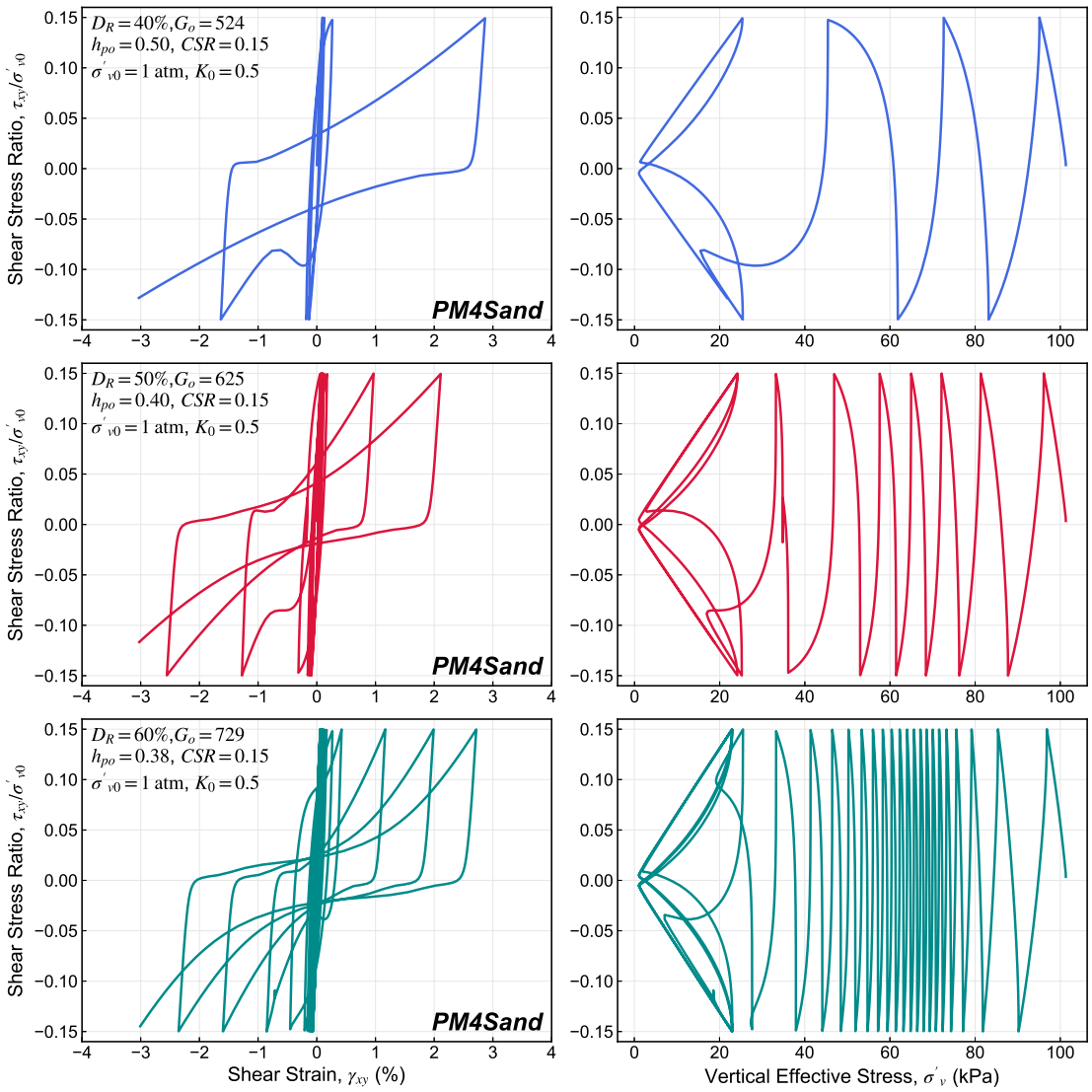

Figure 5.2: Stress-strain and stress path behavior of three PM4Sand model calibrations simulated at the element level under undrained, cyclic, direct simple shear conditions in OpenSees.

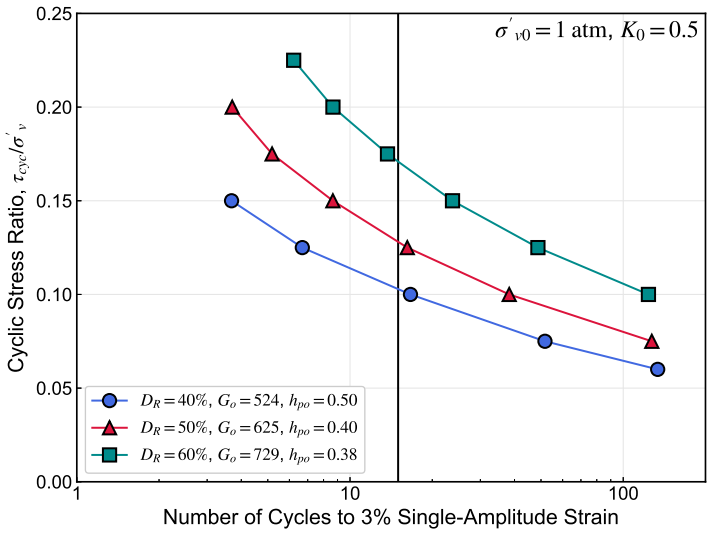

Figure 5.3: Number of cycles to liquefaction for varying cyclic stress ratios and three calibrations of PM4Sand, based on element-level simulations in OpenSees of undrained, cyclic, direct simple shear tests.

An equally important aspect of sand behavior, particularly in lateral spreading problems, is its behavior under a constant static shear stress, both in terms of the differences in liquefaction resistance relative to level-ground conditions, as well as the accumulation of shear strains after triggering. Figure 5.4 shows the stress-strain response and stress paths for the same series of PM4Sand calibrations presented in this section, for varying relative densities, CSRs, and static shear stress ratios ($\alpha = \tau_{st}/\sigma'_v$). Of particular interest is the set of curves where α is varied between 0.05 and 0.15, with constant relative density and CSR. For $\alpha = 0.05$ and 0.10 the behavior varies as one would expect, with larger shear strains occurring with increasing α. However, at $\alpha = 0.15$, the static shear stresses are high enough to prevent any stress reversals from occurring, and thus the element does not liquefy, accumulating shear strains of only 1.5%.

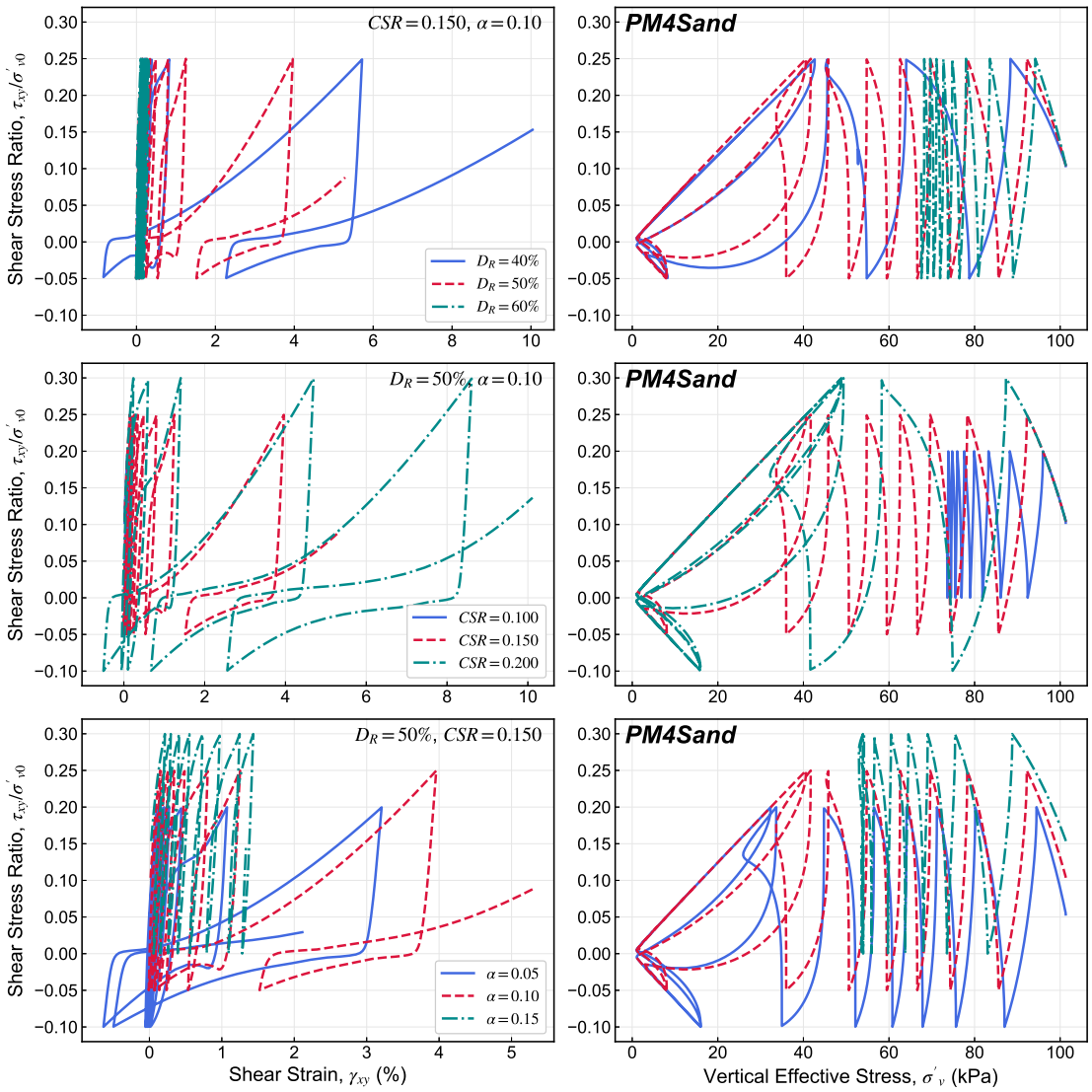

Figure 5.4: Stress-strain and stress path behavior of three PM4Sand model calibrations simulated at the element level under undrained, cyclic, direct simple shear conditions, subjected to varying levels of static shear bias α.

PM4Sand does include a sizable set of secondary parameters, controlling various aspects of the model including, but not limited to, the phase transformation stress-ratio, the positions of the bounding and critical surfaces, rate of strain accumulation, and the relationship between relative density and cyclic strength. All of these parameters are given default values meant to approximate the behaviors seen in typical design correlations. In this way, PM4Sand is default-calibrated to represent something like an "average sand", making it quite useful in the type of parametric study undertaken here, where the aim is primarily to decipher the trends in soil, site, and ground motion conditions that contribute to lateral spreading. For specific sands at specific sites, the secondary parameters can calibrated to better represent the behavior of the soil.

PM4Silt Model

The PM4Silt model was developed by Boulanger & Ziotopoulou (2019) to represent the cyclic response of plastic clays and silts. It is formulated in a directly analogous manner to PM4Sand as a stress ratio-controlled, critical state-based, bounding surface plasticity model. There are some key differences between the two models, which are summarized as follows:

- A critical state line that is linear in $e - \log p'$ space; the CSL in PM4Sand was characterized using a power-law relationship
- The use of the state parameter (Been & Jeffries 1985), rather than the relative state parameter index ξ_R
- A different characterization of shear modulus stress dependencies
- A bounding surface relationship that depends on whether the soil is loose or dense of critical
- A dilatancy relationship that has different forms for contractive and dilative behavior

The remaining model formulation is very similar to PM4Sand, with identical characterization of the yield criterion, plastic modulus, fabric tensor, and hardening coefficient, among other aspects.

The primary input parameters to PM4Silt are the soil's undrained strength at critical state under earthquake loading (either S_u or the ratio S_u/σ'_v), the dimensionless shear modulus coefficient G_o, and the contraction rate parameter h_{po}. The undrained shear strength specification is used by the model to position the critical state line (conditional on additional input parameters such as the void ratio, critical state friction angle, and compressibility). G_o is used in a similar (although not identical) manner as for PM4Sand to calculate the shear modulus in the soil element, from the mean stress p:

$$G = G_o p_A \left(\frac{p}{p_A} \right)^{n_G} \tag{5.3}$$

Note that the shear modulus exponent n_G is not strictly 0.5 here, as it is in the PM4Sand formulation. The default value is set to 0.75 but may vary depending on the model calibration; Boulanger and Ziotopoulou (2019) present several calibrations indicating that n_G may be as high as 1.0 in more plastic silty clays, and as low as 0.6 in lower-plasticity silts. The contraction rate parameter serves a similar purpose as it does in the PM4Sand model, namely to adjust the contraction rate to achieve a desired cyclic strength. Typical stress-strain and stress path behaviors for three calibrations are shown in Figure 5.5, while the variation in number of cycles to 3% strain is shown

for varying cyclic strength ratios in Figure 5.6 for the same three calibrations. The response of the PM4Silt calibrations under initial static shear conditions is shown, for a series of undrained strengths, CSRs, and α values, in Figure 5.7.

In general, the stress-strain behavior of the PM4Silt calibrations presented here differ from the PM4Sand calibrations in several important aspects, namely their significantly lower rates of pore pressure generation (in none of the DSS element tests does the vertical effective stress reach zero), fatter hysteric loops that dissipate more energy, and generally less of an accumulation of strains. These behaviors are consistent with the relative behaviors of sands and silts under cyclic loading, and indicate that the PM4Silt and PM4Sand model calibrations presented herein can reasonably approximate a realistic response for both types of materials.

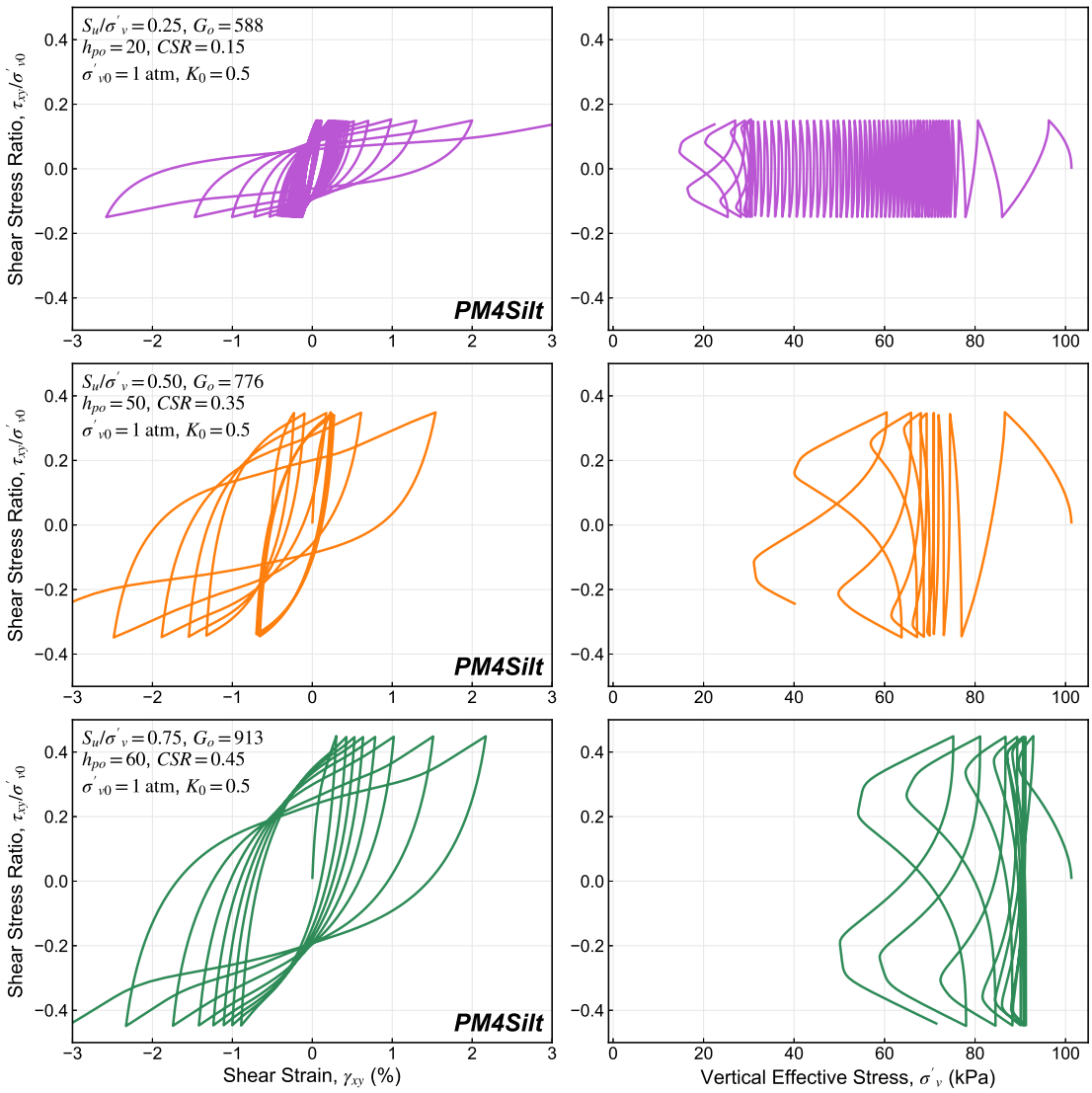

Figure 5.5: Stress-strain and stress path behavior of three PM4Silt model calibrations simulated at the element level under undrained, cyclic, direct simple shear conditions in OpenSees.

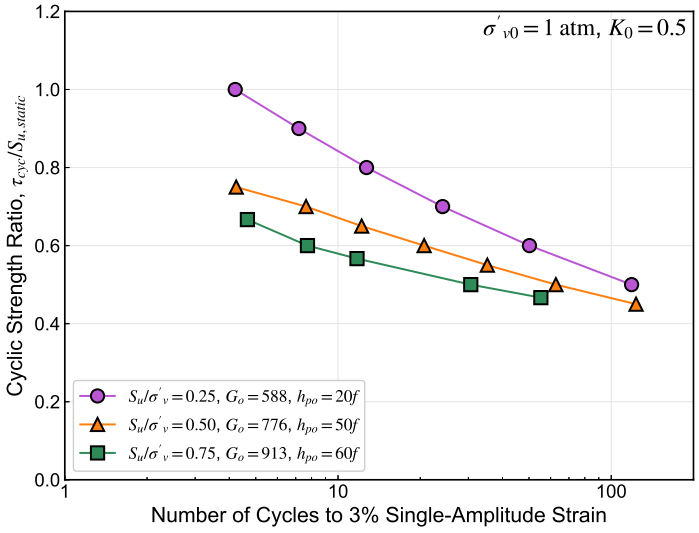

Figure 5.6: Number of cycles to 3% single-amplitude strain for varying cyclic strength ratios and three calibrations of PM4Silt, based on element-level simulations in OpenSees of undrained, cyclic, direct simple shear tests.

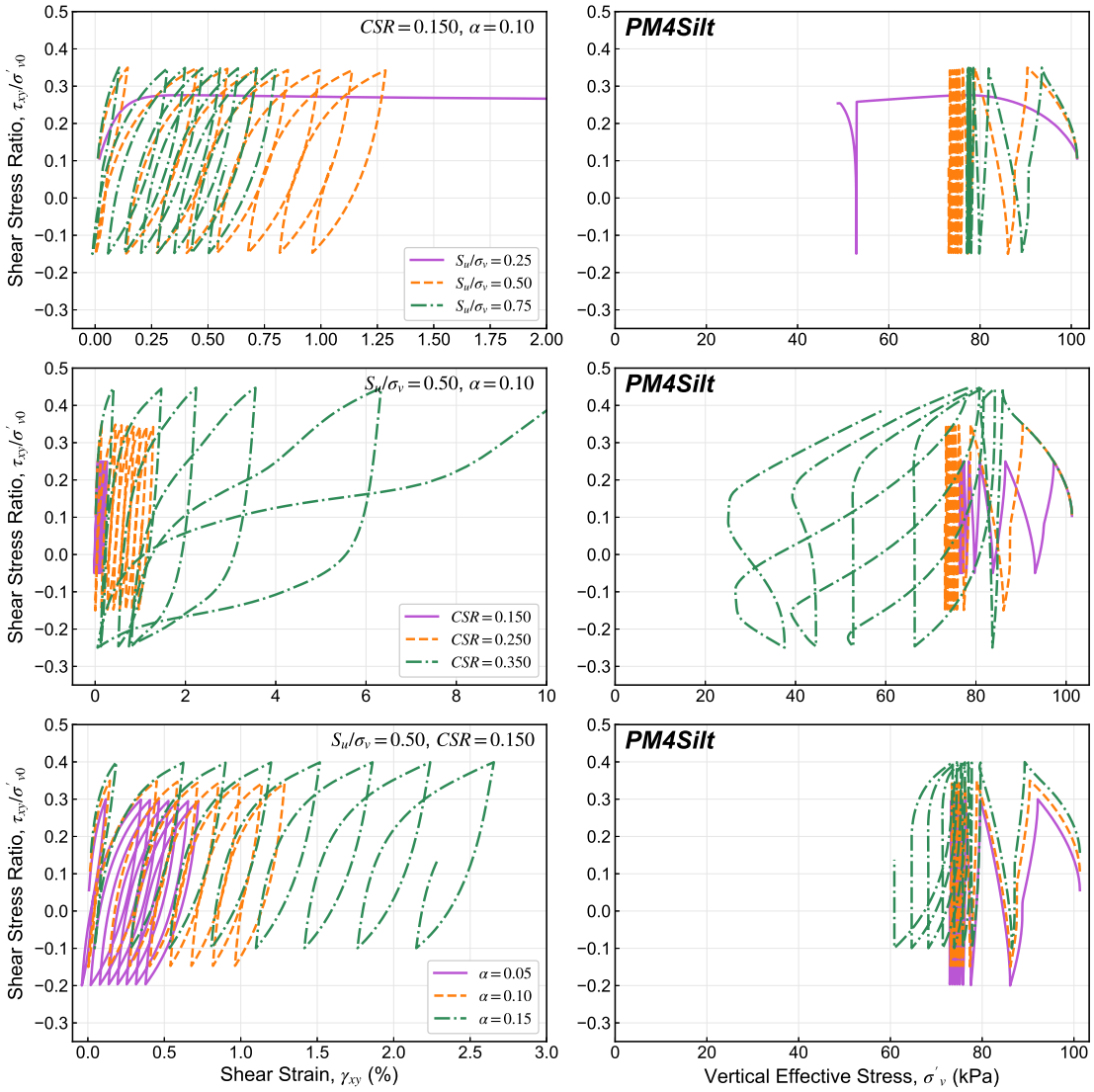

Figure 5.7: Stress-strain and stress path behavior of three PM4Silt model calibrations simulated at the element level under undrained, cyclic, direct simple shear conditions, subjected to varying levels of static shear bias α.

5.3 Development of Representative Ground Motion Set

In order to investigate the effects of ground shaking intensity on both the timing of liquefaction and subsequent lateral spreading deformations numerically, a suite of 188 ground motion records from a wide range of geographic locations, with varying seismotectonic environments, earthquake magnitudes, source mechanisms, and path characteristics, was developed. 80 ground motion time histories from soft-rock sites for shallow crustal events were obtained from the NGA-West2 (Bozorgnia et al. 2014) database, and an additional 20 near-field records classified as featuring velocity pulses were selected from the database of Shahi & Baker (2014). An additional 88 time histories

from subduction events were obtained from the preliminary NGA-Subduction database (Bozorgnia & Stewart 2020). The source, path, and site characteristics for all of the selected motions are summarized in Table 5.1.

The non-pulse crustal and subduction records were selected separately for compatibility with GMM-based target response spectra corresponding to 16 magnitude-distance combinations for each tectonic regime. Rather than relying on one of the as-recorded components of the selected records, the time histories in each bin were rotated to the orientation that provided the closest match to that bin's corresponding target spectrum. The motions were scaled by varying factors in order to represent higher-epsilon motions and produce a wider range of liquefaction triggering and lateral displacement conditions in the non-linear effective stress models. The acceleration time histories were converted into velocity histories for input to the compliant-base OpenSees models.

Table 5.1: Summary of magnitudes, distances, and site V_{s30}s for selected ground motion records.

Record Type	No. of Records	M_w Range	Dist. Range (km)	V_{s30} Range (m/s)
Crustal	80	6.0 - 7.85	0.9 - 90.1	600 - 1043
Pulse-Like	20	5.74 - 7.62	1.5 - 72.6	607 - 1070
Subduction	88	6.55 - 9.12	34.0 - 289.8	600 - 1200

5.3.1 Screening of Candidate Motions and Selection of Magnitude-Distance Bins

The full NGA-West2 and NGA-Subduction databases contain over 21,000 and 71,000 records, respectively. Initial sets of candidate motions were developed by applying several screening criteria. In order to ensure that the majority of input motions in OpenSees would trigger liquefaction in most model archetypes without resorting to exceedingly high scaling factors, only records with peak ground accelerations greater than 0.04 g were selected. Additionally, due to the desire for the soil columns to extend down to soils with high stiffnesses, records with V_{s30} values between 600 and 1200 m/s were considered. The resulting magnitude and source-site distance distributions of crustal and subduction records are shown in Figures 5.8 and 5.9.

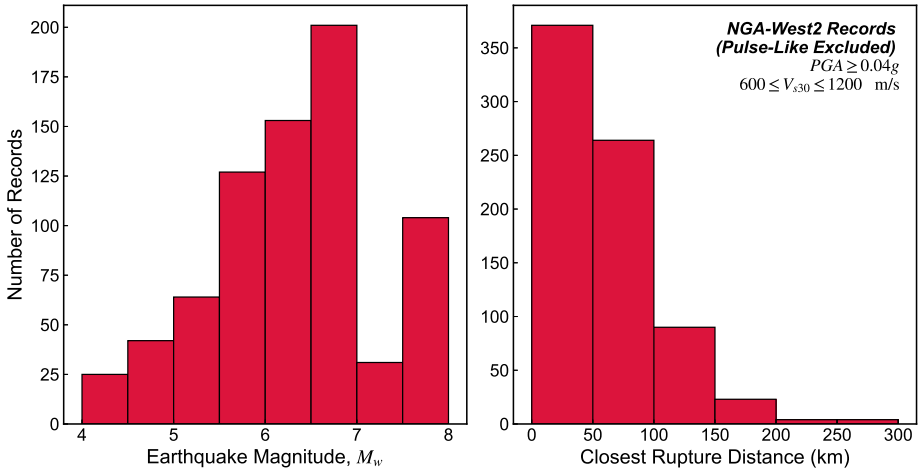

Figure 5.8: Magnitude and source-site distance histograms for records from crustal events meeting initial PGA and V_{s30} screening criteria.

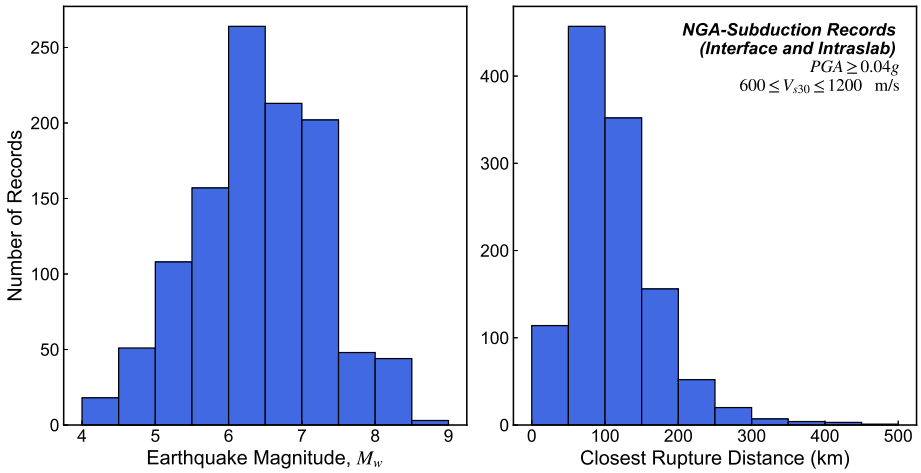

Figure 5.9: Magnitude and source-site distance histograms for records from subduction events meeting initial screening criteria.

The ground motion records were eventually selected based on their compatibility with a range of GMM-estimated response spectra. These target spectra were based on 16 magnitude-distance bins for each of the crustal and subduction regimes. The magnitude and distance bins were broadly selected based on the quartiles of the available candidate records, after minimum magnitudes of 6.0 and 6.5 were established for the crustal and subduction suites, respectively. Adjustments were made to certain bins subject to the availability of records in each magnitude-distance combination, as well as preventing the pool of records from being over-saturated with low-amplitude records. The final magnitude and distance bins are summarized in Tables 5.2 and 5.3 for the crustal and subduction records, respectively.

Table 5.2: Summary of magnitude and distance bins and bin designations used for estimating mean target spectra for crustal motions

Magnitude Bin	Source-Site Distance Bin (km)			
	0-15	15-30	30-60	60-90
6.0-6.5	M1R1crust	M1R2crust	M1R3crust	M1R4crust
6.5-7.0	M2R1crust	M2R2crust	M2R3crust	M2R4crust
7.0-7.5	M3R1crust	M3R2crust	M3R3crust	M3R4crust
7.5-8.0	M4R1crust	M4R2crust	M4R3crust	M4R4crust

Table 5.3: Summary of magnitude and distance bins and bin designations used for estimating mean target spectra for subduction motions

Magnitude Bin	Source-Site Distance Bin (km)			
	0-80	80-120	120-160	160-300
6.5-7.0	M1R1sub	M1R2sub	M1R3sub	M1R4sub
7.0-7.5	M2R1sub	M2R2sub	M2R3sub	M2R4sub
7.5-8.0	M3R1sub	M3R2sub	M3R3sub	M3R4sub
8.0-9.2	M4R1sub	M4R2sub	M4R3sub	M4R4sub

5.3.2 Ground Motion Selection Methodology

For each magnitude-distance bin, five unscaled records were selected for their compatibility with the corresponding target spectrum of that bin. The exception to this was for the M_w $8.0 - 9.2$ subduction bins, where seven records were selected for each corresponding distance bin in order to obtain a suitable number of long-duration records from some of the larger subduction interface events in recorded history (e.g., Tohoku, Japan; and Maule, Chile). Target ground motion spectra were calculated from a suite of GMMs, using the midpoint of each magnitude-distance bin and assuming a V_{s30} value of 760 m/s.

The crustal target spectra were calculated as equally weighted averages of the four NGA-West2 GMMs (Abrahamson et al. 2013, Campbell & Bozorgnia 2014, Boore et al. 2014, Chiou & Youngs 2014), and are shown for each bin in Figure 5.10.

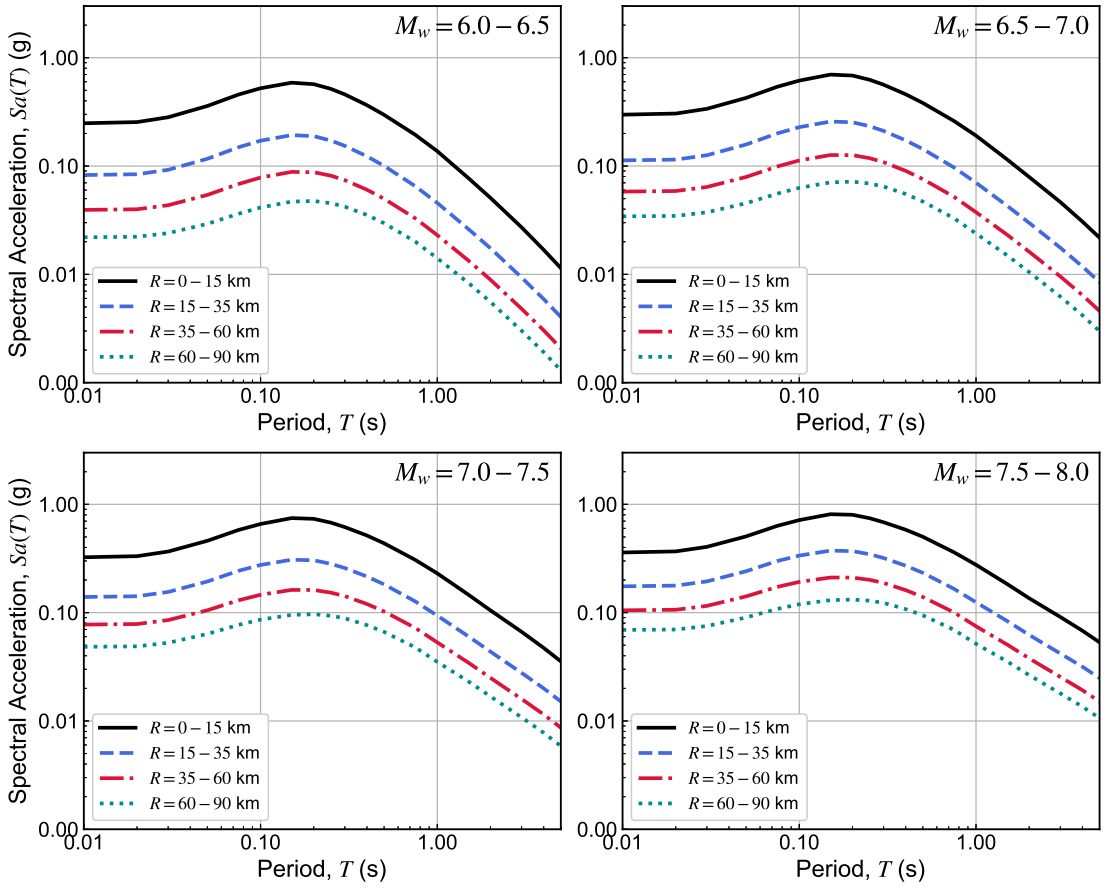

Figure 5.10: Target spectra for crustal ground motion magnitude-distance bins, based on the weighted average of four NGA-West2 ground motion models.

The target spectra for the subduction bins were based on an equally-weighted average of two NGA-Subduction GMMs (Kuehn et al. 2020, and Parker et al. 2020). An additional complication in the prediction of spectral amplitudes from subduction events is the significant dependence on focal mechanisms, specifically between interface and deeper intraslab events. Therefore, the estimated spectra from each GMM was calculated as the weighted average between the interface and intraslab spectra, with the weighting factor based on the relative number of records from each mechanism in that particular magnitude-distance bin (Figure 5.11). The resulting overall subduction target spectra are shown for each of the bins in Figure 5.12.

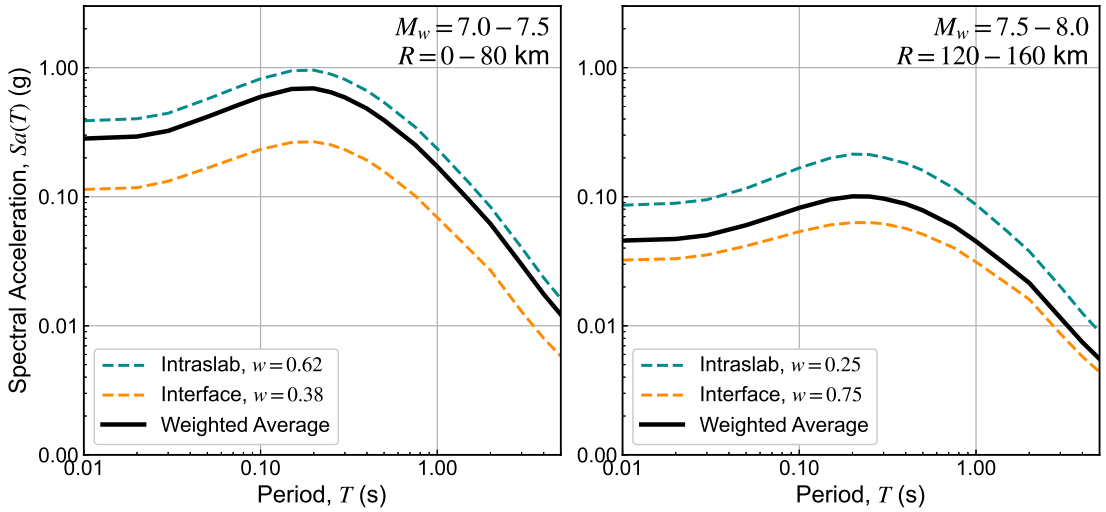

Figure 5.11: Illustration of weighted average target spectrum for subduction events, accounting for differences between spectral amplitudes resulting from interface and intraslab mechanisms.

Records were selected for each magnitude-distance bin with multiple objectives and criteria in mind. While it was important to select a set of records that was generally within the 16th and 84th percentiles of the target spectrum, it was also necessary to select motions from a broad set of geographic regions and events, and much of the record selection reflected a balance between these criteria. For the interface motions, the relative proportion of interface and intraslab records in a given bin was based on the same weighting factor used to calculate the overall target spectrum; to the extent possible, interface and intraslab records were selected for compatibility with their corresponding mechanism-specific target spectrum (see Figure 5.11), and the overall mean spectum of the selected records was checked against the weighted-average mean.

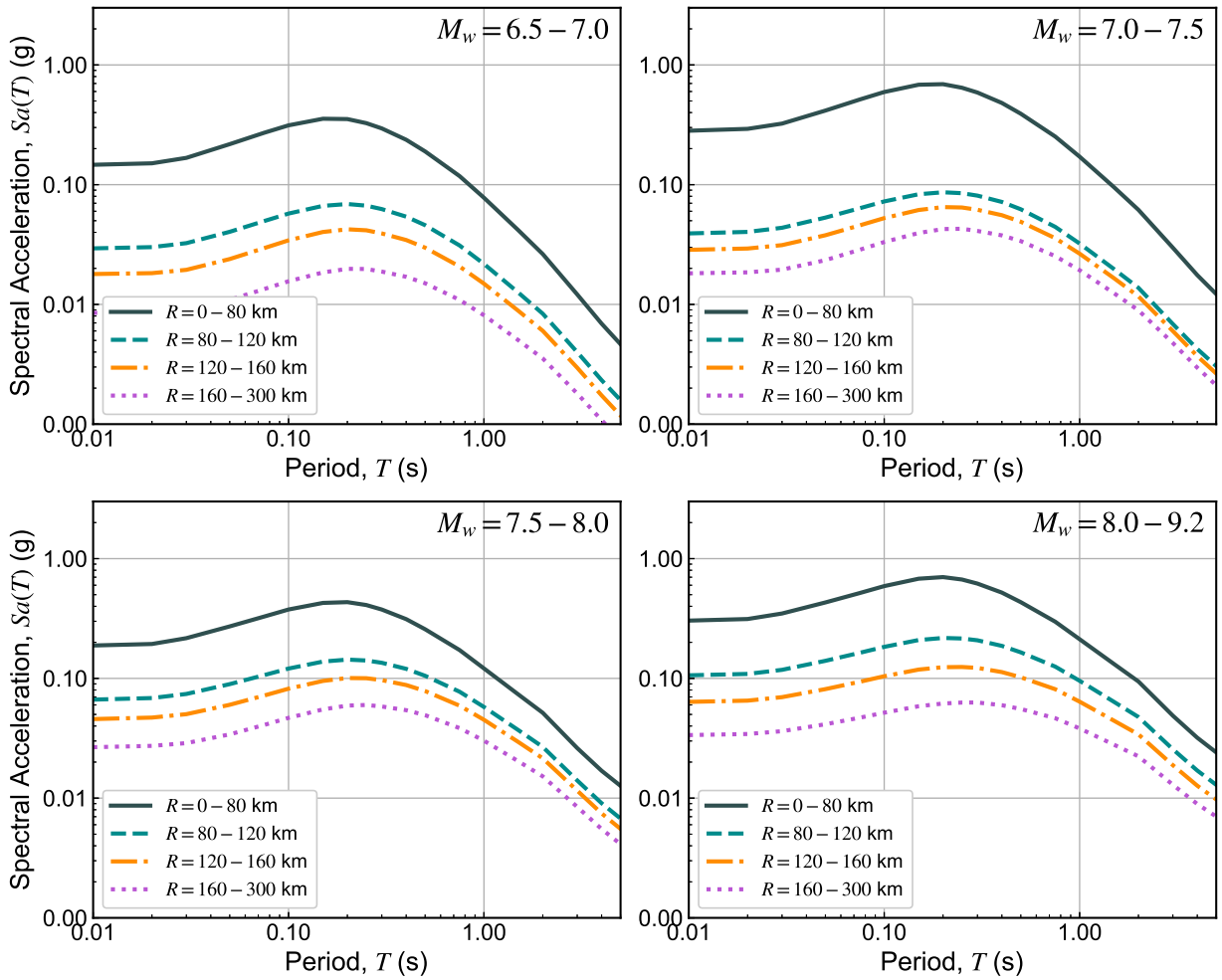

Figure 5.12: Target spectra for subduction ground motion magnitude-distance bins, based on the weighted average of two NGA-Subduction ground motion models (weighted for intraslab and interface events).

The individual, mean, and standard deviation response spectra of the selected crustal records for the four $M_w 6.5-7.0$ bins are shown in Figure 5.13 in comparison with the mean and plus/minus one standard deviation target spectra. Similarly, Figure 5.14 shows the same information for the subduction records in the four $M_w 8.0-9.2$ bins. The selected spectra for all magnitude-distance bins are shown in the Appendix B.

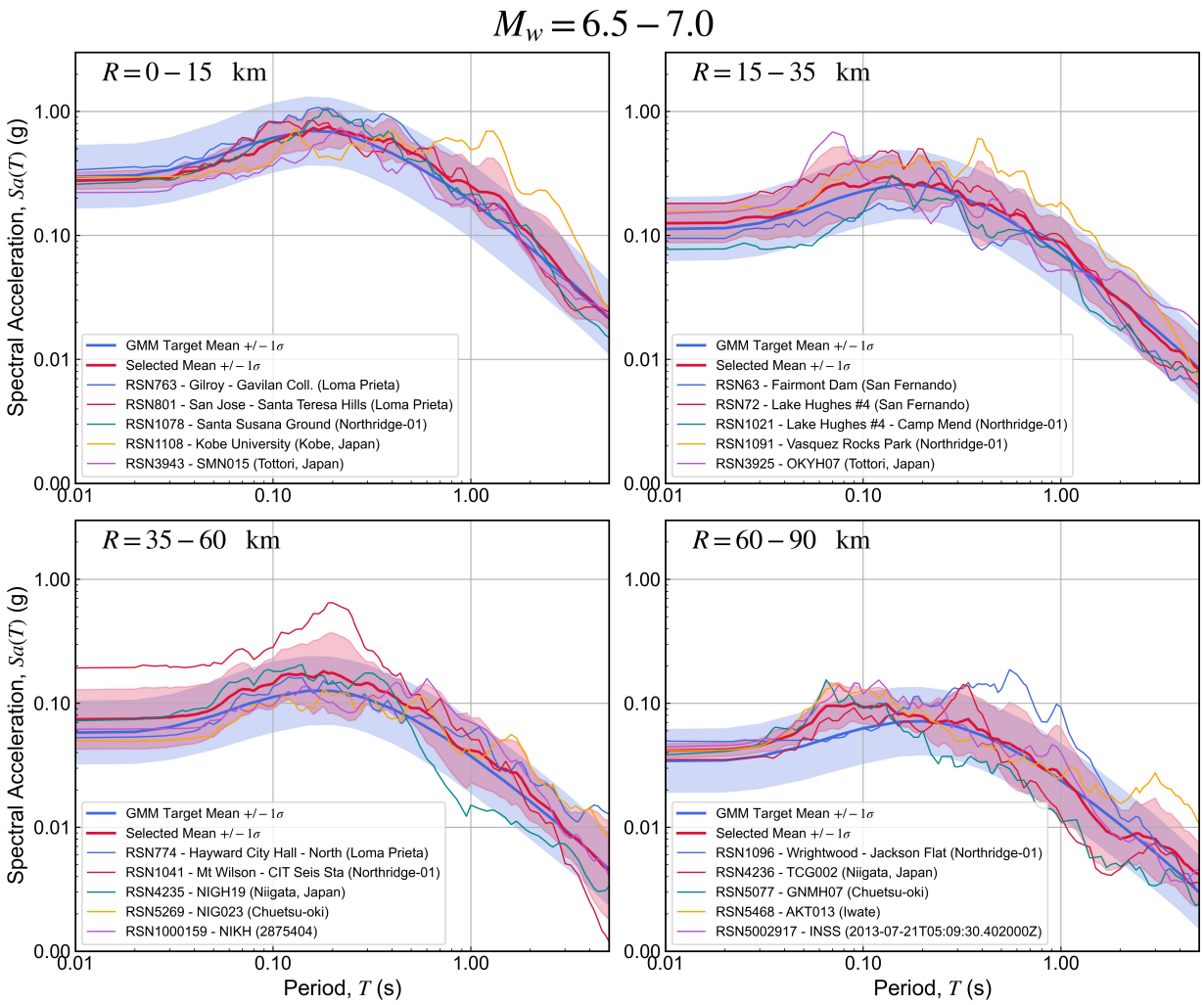

Figure 5.13: Response spectra of selected crustal records for four distance bins corresponding to $M_w 6.5 - 7.0$.

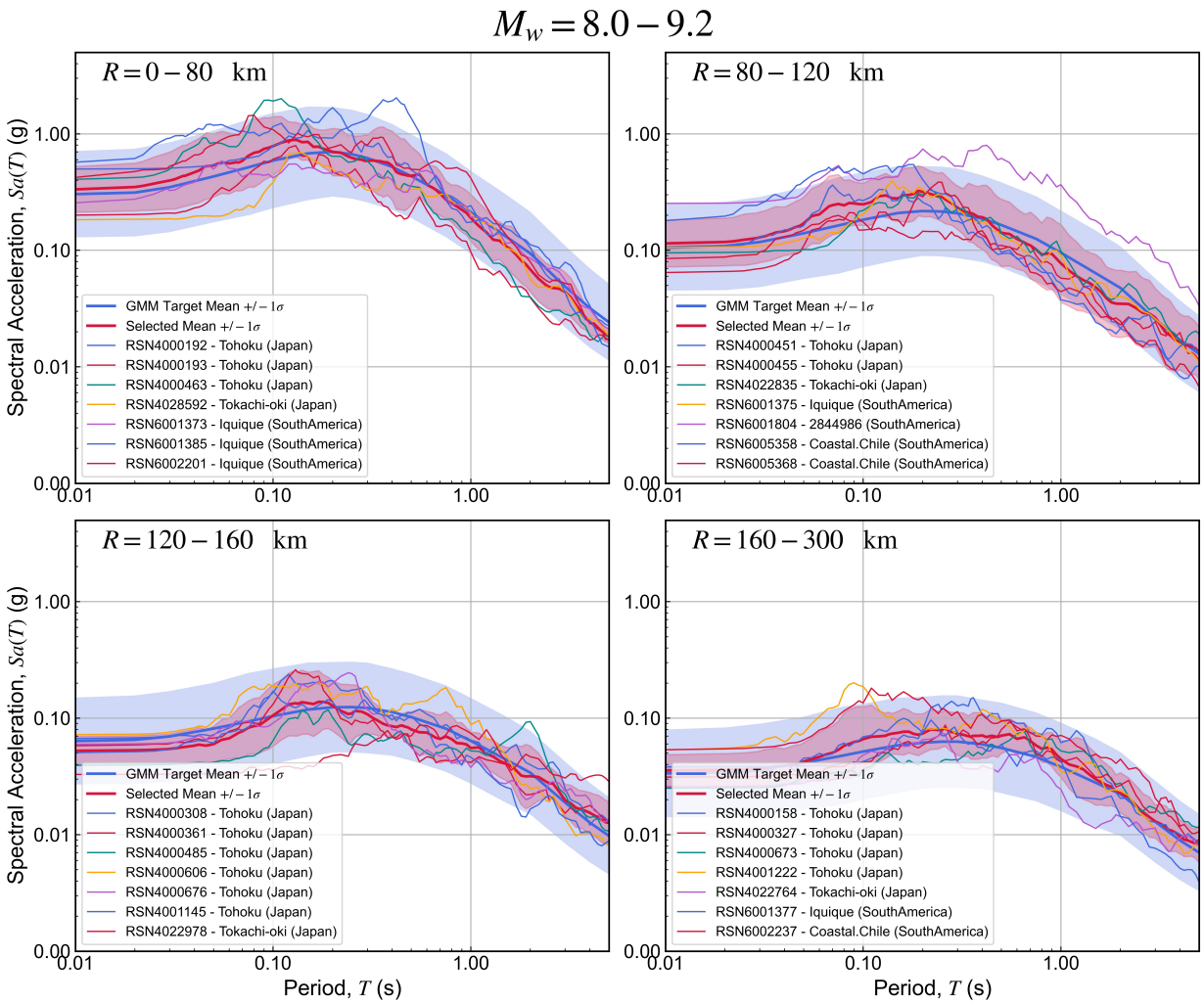

Figure 5.14: Response spectra of selected subduction records for four distance bins corresponding to $M_w 8.0 - 9.2$.

The response spectra for the pulse-like motions, which were not selected according to any sort of spectral compatibility, are shown in Figure 5.15. The pulse periods of these motions, as provided by Shahi and Baker (2014), are shown in Figure 5.16.

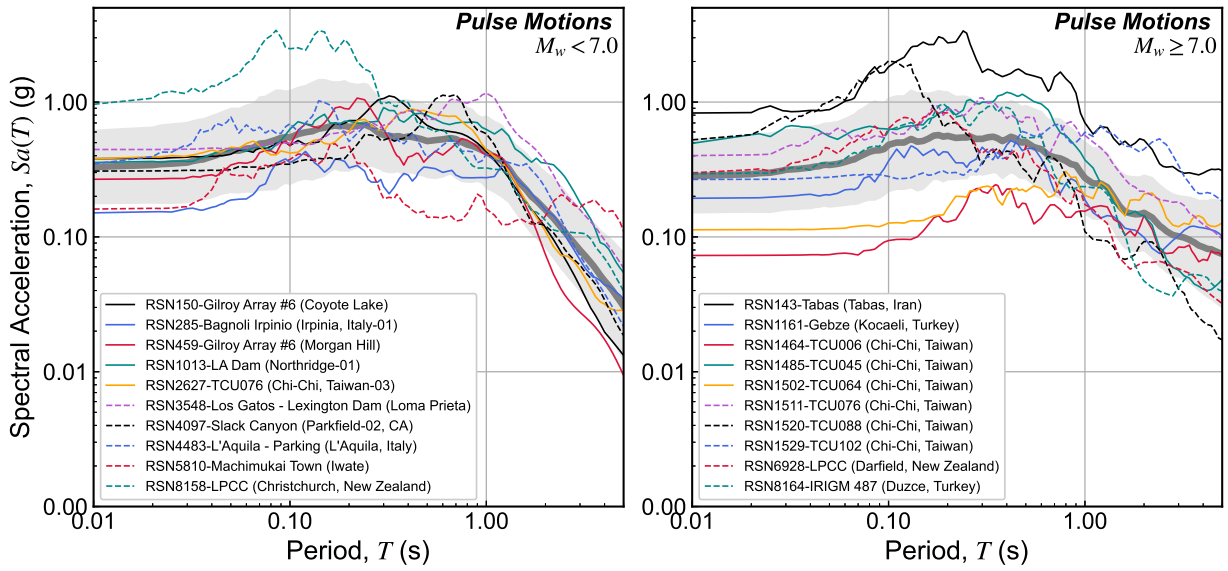

Figure 5.15: Response spectra for selected crustal motions classified as pulse-like, according to criteria of Shahi & Baker (2014). Mean and plus/minus one standard deviation of each subset are shown in the background in gray.

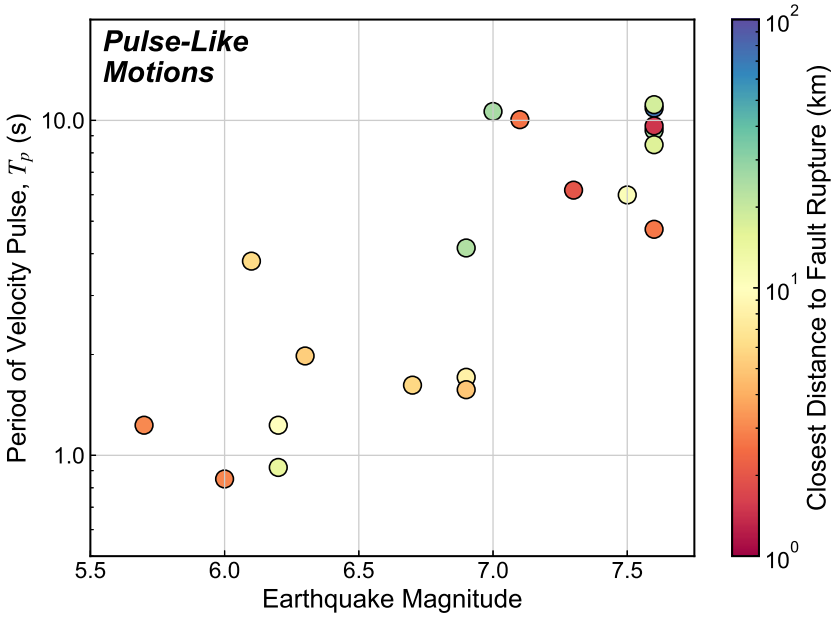

Figure 5.16: Distribution of pulse periods of selected pulse-like motions, plotted against magnitude. Markers are color-shaded according to rupture distance.

5.3.3 Processing of Selected Records for Input to OpenSees

It is important to note that the spectral amplitudes provided for each record in the NGA databases are the median of the geometric means of all potential orthogonal orientation angles,

commonly known as the RotD50 spectra (Boore et al. 2006). Given that the numerical analyses performed in this study are of the one- and two-dimensional variety, it was thus necessary to select a single component orientation for each record to use as input to the OpenSees models, with a response spectrum that will not be the same as the RotD50 spectrum provided in the NGA databases.

For each non-pulse record, the single-component orientation was selected by first calculating the acceleration time history at a range of non-redundant rotation angles θ from the as-recorded horizontal time histories (acc_1 and acc_2):

$$acc(t,\theta) = acc_1(t,0)\cos\theta + acc_2(t,0)\sin\theta \tag{5.4}$$

The response spectra for each orientation were then calculated and compared to the corresponding target spectrum, via an error function, as follows:

$$\mathrm{err}(\theta) = \frac{1}{N_T}\sum_{i=1}^{N_T}(\ln S_a(\theta,T_i) - \ln S_a^*(T_i))^2 \tag{5.5}$$

where $Sa(\theta,T_i)$ and $S_a^*(T_i)$ are the rotated component and target spectral amplitudes, respectively. The optimal rotation angle is the one that minimizes the error function. Figure 5.17 illustrates this process for a crustal record from the Loma Prieta earthquake, where the rotated component at 100° relative to the first horizontal as-recorded component produces the best match to the target spectrum.

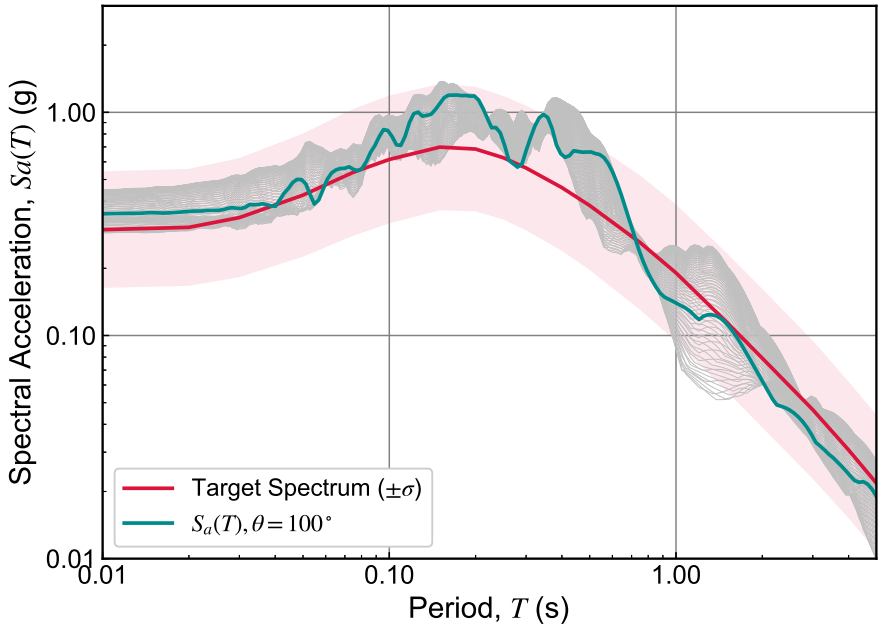

Figure 5.17: Illustration of optimal single-component orientation selection for a Loma Prieta record (RSN763: Gilroy-Gavilan College), for a target spectrum from the $M_w = 6.5 - 7.0$ and $R = 0 - 15$ km bin. The red shaded region represents one-standard deviation range of the target spectrum.

Since the pulse-like records were not selected for compatibility with a GMM-based target spectrum, they were rotated to the orientation of the velocity pulse, as provided by Shahi & Baker (2014).

The final step before generating the input velocity histories for the OpenSees models involved checking the oriented time histories for any irregularities in the waveforms, and adding zero-padding at the end of the records. The motivation for zero-padding the time histories was due to certain records having been been truncated before intermediate- and longer-frequency content had been fully damped out in their original processing. This effect is often difficult to detect by visual examination the acceleration or velocity waveforms, but can be better quantified by considering the evolution of the Cumulative Absolute Velocity (CAV)over time. For example, the record of ground shaking from the 1999 Kocaeli, Turkey earthquake, at the Gebze station, appears to have been cut off before the ground shaking had entirely damped out (left side of Figure 5.18). In the last five seconds of the record, the change in CAV was about 0.15 m/s, or just over 3% of the overall CAV. Preliminary dynamic analyses of liquefiable soil columns in sloping ground using this raw velocity history resulted in ongoing increases in shear strains in liquefied elements, and continuing ground surface displacements, even at the end of the recording. As the Gebze record was one of

the more extreme cases, the addition of 20 seconds of zero values to the end of the velocity history resulted in models that had reached constant deformations by the end of the dynamic analysis phase, with relatively minor impacts on run-times. The remaining velocity histories were padded with between 5 and 20 seconds of near-zero values, depending on the increase in CAV in the final 5 seconds of the original recording.

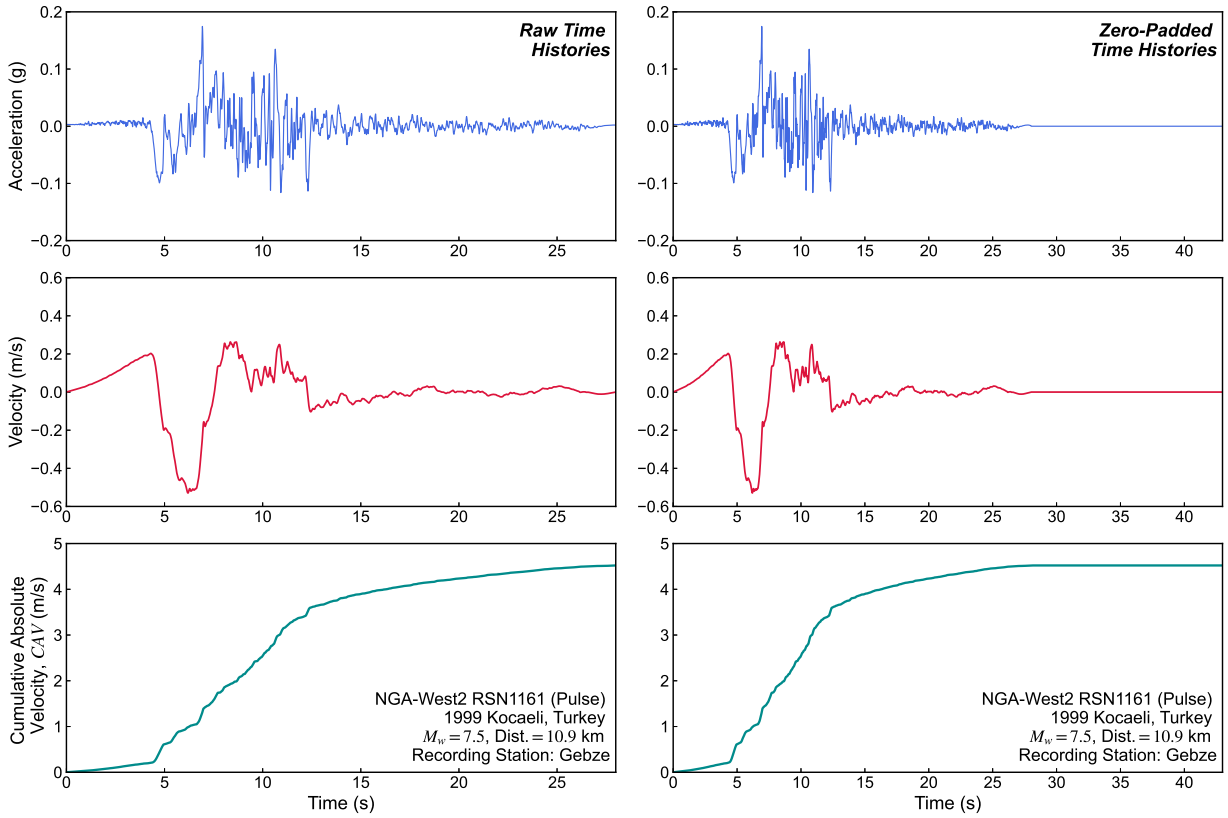

Figure 5.18: Comparison of raw and zero-padded acceleration, velocity, and CAV time histories for the Gebze recording station from the 1999 Kocaeli, Turkey earthquake.

5.3.4 Application of Scaling Factors and Characteristics of Final Ground Motion Set

Initial examination of the selected and processed records indicated a range of ground motion amplitudes that was somewhat lower, on average, than desired for this study. The median magnitude-adjusted peak acceleration of the time histories PGA_M, which is generally found to be the intensity measure best correlated with liquefaction triggering, was about 0.10 g (0.12 g for crustal, and 0.08 g for subduction), and ranged overall from about 0.03 to 0.90 g. This range of intensities would have resulted in significant numbers of cases where liquefaction likely would not have been triggered in the numerical models. A simple procedure was developed for scaling up these motions by a factor that was based a series of PSHA deaggregations for PGA at several high-

seismicity sites in throughout the United States, indicating that the PGAs corresponding to the higher end of the hazard curve (around 2,475 years) typically had epsilon values (i.e. the number of standard deviations by which the hazard curve PGA differs from the mean predicted PGA for a given source and site condition) in the range of 0.8 to 1.8. Given that ground motion IMs are normally distributed, this range of ε values would correspond to a scaling factor range of about 3.50, on average. A simple inverse linear relationship to the unscaled PGA_M was used to select the eventual applied scaling factor:

$$SF = 4.0 - 3.5 \cdot PGA_M \tag{5.6}$$

The distributions of three evolutionary intensity measures, PGA_M, I_a, and CAV, and the significant duration, d_{595} are shown in Figure 5.19, along with the lognormal mean, standard deviation, and one-standard deviation range for each parameter.

The variation of the three evolutionary IMs considered with rupture distance is shown separately for the selected crustal and subduction motions in Figure 5.20. Generally speaking, the attenuation in IMs for subduction records seems to feature a significantly higher variance than the crustal attenuation, likely due to the inclusion of records from both intraslab and interface events, which can have significantly different attenuation characteristics.

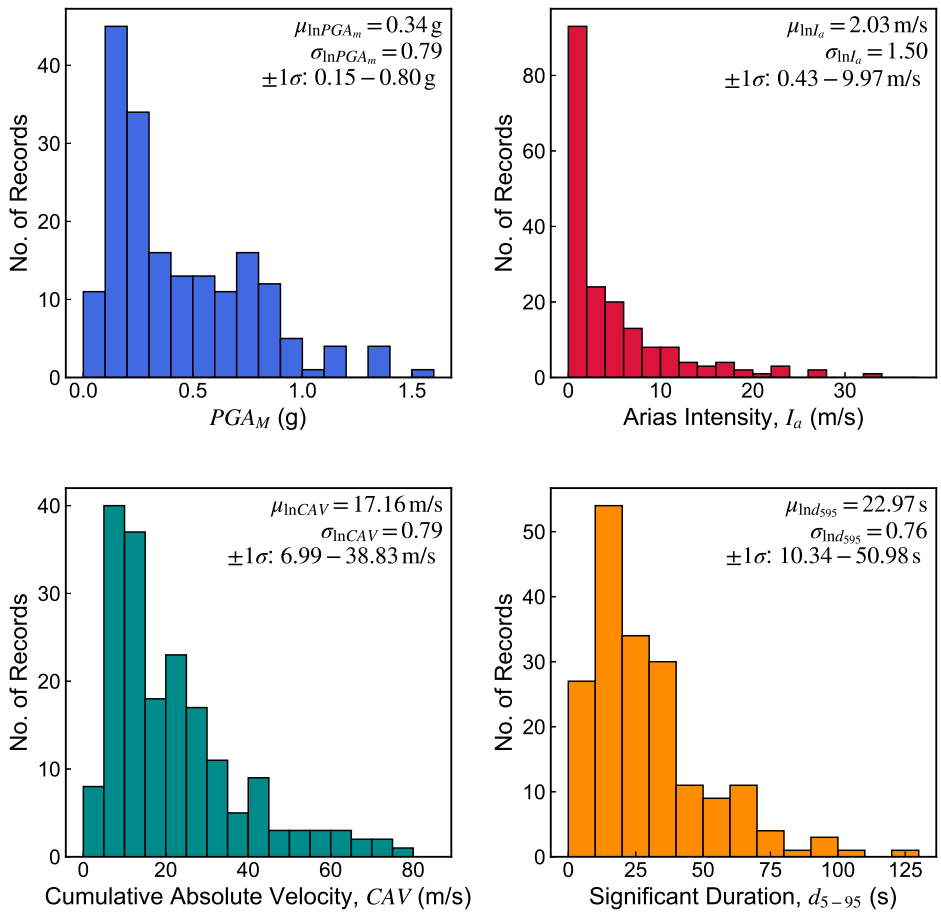

Figure 5.19: Distributions of magnitude-adjusted peak acceleration PGA_M, Arias Intensity I_a, cumulative absolute velocity CAV, and significant duration d_{595} of selected ground motions.

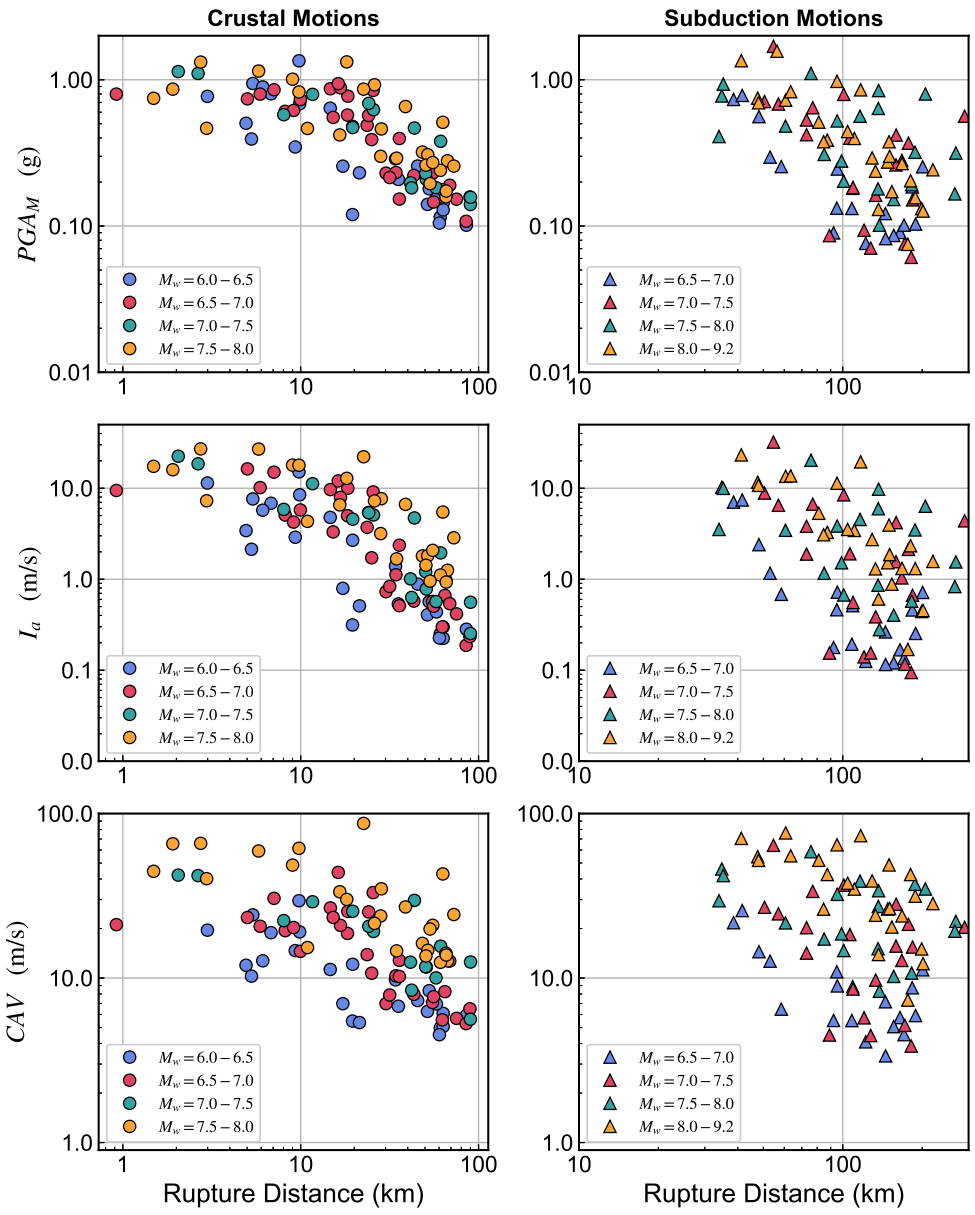

Figure 5.20: Attenuation of PGA_M, I_a, and CAV with source-site distance for selected crustal and subduction records.

The locations of event hypocenters and recording stations for the final suite of 188 motions are shown in Figure 5.21. The suite includes records from events in California, the Pacific Northwest, Alaska, South America, Southern Europe and the Middle East, Taiwan, Japan, and New Zealand. Detailed maps of hypocenters and recording stations in each region can be found in Appendix B.

Figure 5.21: Global distribution of event hypocenters and ground motion recording station for 188 selected time histories.

The suite of motions presented in this section was selected to represent as broad a range as possible of earthquake scenarios and source mechanisms, with a broad range of motions with different amplitudes, frequency contents, and durations. As demonstrated in this section, there are nearly an infinite number of ways to visualize and present the range of characteristics of the selected ground motion set - perhaps the most concise can be found in Figures 5.22 and 5.23. The compiled response spectra illustrate the range of amplitudes and frequency contents of the motions, essentially as a band of relatively constant thickness across all oscillator periods of interest, while the Husid plots demonstrate the broad range of significant durations represented by the motions, as well as the rates at which the cumulative intensity increases over time. The reason for using multiple criteria in a broadly holistic selection framework, rather than simply selecting motions purely based on their compatibility with a target spectrum, or how they fit within a target IM distribution, is that there is no single, completely sufficient way to characterize earthquake ground motions. The best way to understand how a particular structural or geotechnical system (in our case lateral spreading sites) responds to earthquakes is to consider many cross-sections and combinations of seismotectonic environments, event magnitudes and mechanisms, source-to-site paths and motion characteristics.

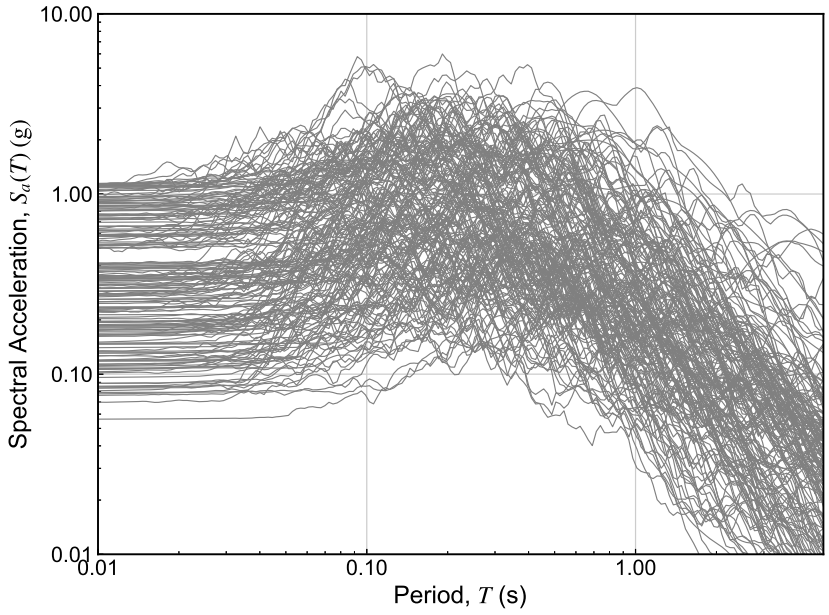

Figure 5.22: Distribution of response spectra of all 188 motions selected for lateral spreading parametric study.

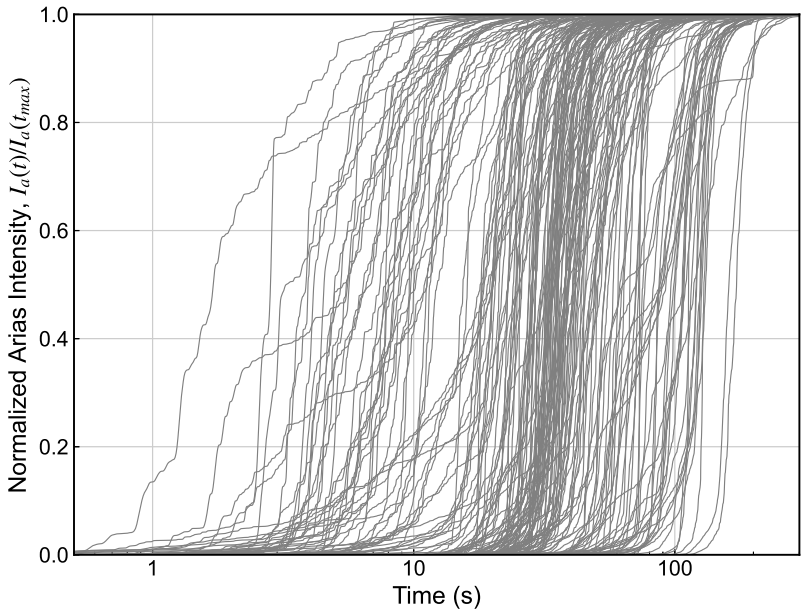

Figure 5.23: Husid plots for all 188 motions selected for lateral spreading parametric study.

5.4 Development of Nonlinear Effective Stress Model for Infinite Slope Conditions in OpenSees

A parametric was undertaken to explore the influence of a wide range of factors on the triggering of liquefaction and subsequent lateral spreading displacement under sloping ground conditions. Lateral spreading is frequently observed at sites with relatively constant gentle slopes; case histories of such failures are described as ground slope case histories (Bartlett & Youd (1992), Youd et al. 2002). The parametric study investigated the effects of ground motion characteristics such as amplitude, frequency content and duration; static stress conditions, and subsurface conditions such as density, thickness, and continuity of liquefaction-susceptible soils on lateral spreading displacements. The computational demands of this study necessitated the development of a workflow for efficiently generating and large sets of numerical analyses, whereby specific aspects of the soil column could be systematically varied, and in later cases randomized, from a baseline, template model. This section presents the development of the baseline soil column model using the open-source, finite-element platform OpenSees (McKenna et al. 2010) and facilitated by the Python library `OpenSeesPy` (Zhu et al. 2018), the methods used to analyze the results of a single analysis.

The Open System of Earthquake Engineering Simulation, or OpenSees, is an object-oriented, open source software framework, primarily developed for simulating the response of geotechnical, structural, or coupled soil-structure systems to earthquake loading. Its object-oriented underpinnings has resulted in a highly flexible, modular, and extensible platform, with a rich and wide-ranging development community, and larger-scale deployment on parallel computing platforms.

The construction of the soil one-dimesnional column model generally follows the implementation outlined by McGann and Arduino, as presented as a Geotechnical example in the OpenSees documentation, as well as more recent versions utilized by Chen, Ghofrani, and Arduino (personal communication). The general schematic of the model is shown in Figure 5.24, for an arbitrary soil layering sequence.

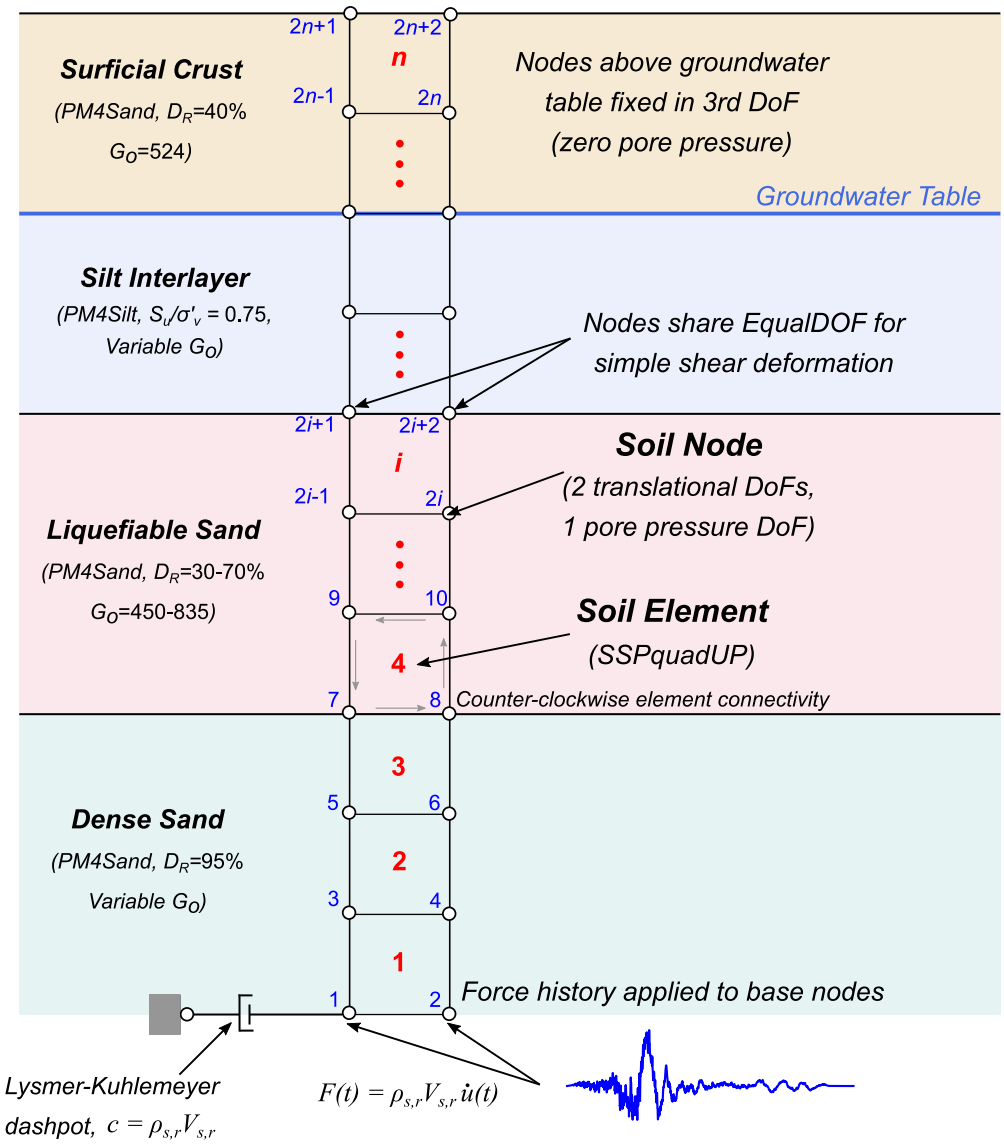

Figure 5.24: Schematic of one-dimensional soil column model in OpenSees, adapted from McGann and Arduino.

5.4.1 Mesh Geometry and Soil Nodes

The mesh is initially constructed by defining the sequence of nodal coordinates from the base of the bottom towards the surface in a left-to-right, bottom-to-top convention. The soil layers were modeled using four-node quadrilateral SSPquadUP elements (McGann et al. 2012), which use physically stabilized single-point integration (SSP) and a mixed displacement-pressure formulation ($\boldsymbol{u} - p$) to model the dynamic response of fluid saturated porous media. The nodes assigned to the SSPquadUP have two translation degrees of freedom (horizontal and vertical) and one pore pressure degree of freedom.

The element thicknesses are specified such that the minimum wavelength λ (corresponding to a specified maximum frequency of interest f_{max}) can be represented with adequate resolution. The minimum wavelength is determined using the minimum shear wave velocity expected to be encountered in the model via $\lambda_{min} = V_{s,min}/f_{max}$ The element size is then determined based on a specified number of elements to be represented per wavelength, specified here to be 10. For these analyses, a maximum cutoff frequency of 20 Hz, and a minimum shear wave velocity of 100 m/s were assumed, resulting in uniform element thicknesses of 0.5 m. The minimum shear wave velocity of 100 m/s is based on the fact that V_s is not directly specified by the user when generating the PM4Sand material; rather, the dimensionless reference shear modulus parameter G_o is used to calculate shear moduli from the mean effective stress, which can lead to extremely low velocities near the ground surface. Deeper, stiffer elements could in theory be considerably thicker, but models with uniformly thick elements provided advantages in post-processing that significantly offset the computational cost due to the additional elements.

5.4.2 Boundary Conditions and Dashpot Nodes

The base nodes of soil column (nodes 1 and 2) are fixed against vertical translation, and are "tied" together for horizontal translation using an equal-degrees-of-freedom condition. The left-hand nodes throughout the rest of the soil column are similarly tied to the right-hand nodes, in order to simulate a simple-shear deformation mode throughout the model. Soil nodes at or above the groundwater elevation (specified externally by the user) are fixed in the third degree of freedom (no fluid pressure) to simulate dry conditions.

To simulate a compliant base that absorbs downward-traveling waves, a Lysmer-Kuhlemeyer (1969) dashpot is utilized at the base of the model. The dashpot is comprised of two additional nodes - one is completely fixed (the left-hand node in see Figure 5.24, the other is fixed against vertical translation and tied to the coincident soil node for horizontal translation - and is modeled using a zero-length element and assigned a viscous uniaxial material. Specification of the viscous uniaxial material type requires only the viscosity (i.e. the dashpot coefficient), which is equal to the product of the desired mass density and shear wave velocity of the material underlying the soil column in the model domain. In order to generally preserve the characteristics of the input time history, the dashpot coefficient should represent a soft rock condition; to achieve that condition, the dense sand layer underlying the liquefiable zone was extended downwards until a shear wave velocity of 760 m/s was reached, with the shear wave velocity of the dashpot coefficient corresponding to a 1.10 impedance ratio to avoid large impedance contrasts.

5.4.3 Soil Material Specifications

The surficial crust, liquefiable sand layers, and dense underlying sands were all modeled using the PM4Sand `nDMaterial` implementation in OpenSees (Chen and Arduino, in review). The calibrations used for each of these layers are summarized in Table 5.4, with secondary parameters maintained as default values as specified by Ziotopoulou & Boulanger (2013).

Table 5.4: Summary of primary soil parameter inputs to PM4Sand for non-linear dynamic effective stress analyses. Secondary parameters are maintained as default values, as summarized in Ziotopoulou & Boulanger (2013)

Soil Layer	D_R (%)	q_{c1Ncs}	$N_{1,60cs}$	G_o	h_{po}	ρ (Mg/m^3)
Surficial Crust	40	69	7.5	524	1.5	1.59
Liquefiable Sand	30	53	4.1	430	0.50	1.98
	40	69	7.5	524	0.50	1.99
	50	89	12	625	0.40	2.01
	60	112	17	729	0.38	2.03
	70	140	23	836	0.44	2.05
Dense Sand	95	230	42	Variable	2.5	2.1

The material specifications for the surficial crust and liquefiable layers are based primarily on apparent relative density. The shear modulus coefficient can be related to D_R via (Boulanger and Ziotopoulou 2013):

$$G_o = 167\sqrt{46 \cdot D_R + 2.5} \tag{5.7}$$

The mass density depends on whether or not the material is saturated or unsaturated. For the surficial crust, the dry density is used:

$$\rho_d = G_s/(1 + e_0) \tag{5.8}$$

where G_s is the specific gravity of solids, assumed to be 2.67, and the void ratio e_0 is calculated from the apparent relative density, assuming $e_{min} = 0.50$ and $e_{max} = 0.80$:

$$e_0 = e_{max} - D_r(e_{max} - e_{min}) \tag{5.9}$$

For any material below the water table, the saturated density is instead used, and calculated as:

$$\rho_s = \rho_d \cdot (1 + e_0/G_s) \tag{5.10}$$

The contraction rate parameters for relative density are calibrated to produce cyclic resistance ratios consistent with those from established empirical correlations (Idriss and Boulanger 2008. To achieve this, a series of strain-controlled DSS simulations are performed at each relative density and G_o, with a CSR corresponding to the Idriss and Boulanger-based CRR for the given relative density; h_{po} was varied until liquefaction is triggering (using a 3% single-amplitude strain criterion) in 15 loading cycles (see Figure 5.2).

The underlying dense sand was modeled using a D_R of 95% with the saturated density estimated using Equations 5.9 and 5.10. Rather than estimating the shear modulus coefficient using Equation 5.7, G_o was specified such that the impedance ratio between the shallowest dense sand element and the deepest liquefiable sand element was no greater than 1.10. To do this, an initial effective stress profile can be computed from the densities of each sublayer. The shear wave velocity of the deepest liquefiable element can then be determined from the mean effective stress ($p' = 2/3\sigma'_v$ for $K_o = 0.5$ conditions) and G_o via:

$$V_s = \left[\frac{G_o p_A}{\rho}\sqrt{\frac{p'}{p_A}}\right]^{0.5} \tag{5.11}$$

The impedance ratio of a shear wave traveling upwards from Layer i to Layer j is calculated as:

$$\alpha_j = \frac{2}{1 + \frac{\rho_i V_{si}}{\rho_j V_{sj}}} \tag{5.12}$$

from which the shear wave velocity (and subsequently G_o, by inverting Equation 5.11) in the dense sand layer can be specified as:

$$V_{sj} = \frac{\rho_j V_{sj}}{\rho_i (2/\alpha_i - 1)} \tag{5.13}$$

Rather than assigning a single material (with a single G_o) to the dense sand layer, thus resulting in a relatively slow rate of shear wave velocity increase with depth (and therefore requiring a significantly more elements to reach the soft-rock condition at the dashpot interface), subsequent elements in the dense sand layer are specified in a similar fashion using Equations 5.11 through 5.13 with an impedance ratio of 1.10. The result is a reasonably large reduction in the number of elements required in each model, while preventing the effects of large impedance contrasts in the soil column response.

PM4Silt calibrations were initially considered for modeling the silty interlayers at three undrained strength ratios, as summarized in Table 5.5. Ultimately it was determined that the silt layers should generally not contribute significant shear strains in the numerical models, since the eventual goal was to assess liquefaction-induced lateral spreading in granular soils. As a result, the highest-strength and stiffest calibration (S_u/σ'_v) is used to model the non-liquefiable interlayers. Rather than using a constant shear modulus coefficient irrespective of the stiffnesses of adjacent soil layers, G_o was computed based on the shear wave velocities of the overlying and underlying layers to ensure that impedance ratios were less than 1.10, again using Equations 5.11 through 5.13.

Table 5.5: Summary of primary soil parameter inputs to PM4Silt model for non-linear dynamic effective stress analyses. Secondary parameters were maintained as default values, as summarized in Boulanger & Ziotopoulou (2019)

Soil Layer	S_u/σ'_v	G_o	h_{po}	ρ Mg/m^3
Silt Interlayer	0.25	variable	20	1.88
	0.50	variable	50	1.88
	0.75	variable	60	1.88

5.4.4 Soil Element Specifications

In the finite element method, an element is defined first and foremost by its nodal points. In the case of the SSPquadUP element, the nodes are defined in counterclockwise order starting from the lower left-hand side. For instance, the fourth element in Figure 5.24 would be defined by nodes `7 8, 10` and `9`, in that order. The element must also be assigned a material, in the case of the soil column, any of the materials corresponding to Tables 5.4 or 5.5. The physical characteristics of the element that must be specified are the out-of-plane thickness (taken here as 1.0 meter), fluid bulk modulus (2.2×10^6 kPa), mass density of the pore fluid (1.0 Mg/m^3), the permeability coefficients, and the void ratio. The SSPquadUP element in OpenSees uses a *dynamic permeability coefficient*, which is the conventional hydraulic conductivity (with units of $[L/T]$) divided by the unit weight

of water ($[F/V]$). The permeability coefficients are initially set to 1.0 in both directions prior to gravity loading to allow full drainage to occur, and are subsequently updated to material-specific values used by Chen (2020) for similar material types prior to the dynamic analysis phase. The permeability coefficients k_x and k_y are summarized, along with the void ratios in Table 5.6.

Table 5.6: Summary of material-dependent parameters for SSPquadUP element specification.

Soil Layer	D_R (%)	S_u/σ'_v	k_x	k_y	Void Ratio, e_0
Surficial Crust	40	-	1×10^{-9}	1×10^{-9}	0.68
Liquefiable Sand	30	-	3×10^{-6}	3×10^{-6}	0.71
	40	-	3×10^{-6}	3×10^{-6}	0.68
	50	-	3×10^{-6}	3×10^{-6}	0.65
	60	-	3×10^{-6}	3×10^{-6}	0.62
	70	-	3×10^{-6}	3×10^{-6}	0.59
Dense Sand	95	-	3×10^{-6}	3×10^{-6}	0.52
Silt Interlayer (non-liquefiable)	-	0.25	3×10^{-8}	3×10^{-8}	0.90
	-	0.50	3×10^{-8}	3×10^{-8}	0.90
	-	0.75	3×10^{-8}	3×10^{-8}	0.90

Finally, the element body forces must be specified to incorporate gravity into the analysis; for the SSPquadUP element these are specified as the components of the gravitational vector (other element types, such as the standard 4-node, employ the soil unit weights). In other words, for level ground conditions at a site on the planet Earth, the horizontal body force would be specified as zero, and the vertical as -9.81 m/s^2 (using SI units). It is in this manner that sloping ground conditions can be simulated, e.g. for a 2% sloping ground condition, the horizontal gravitation acceleration coefficient is instead specified as 0.196 m/s^2 (0.02×9.81).

5.4.5 Gravity Loading Phase

The gravity loading phase is used to initialize the stresses in the model via the self weight of the soil; in OpenSees, static and dynamic loading problems are solved via an `analysis` object, which is defined by several component objects. The components and specified values were selected

based on Chen and Arduino (personal communication), and are summarized as follows:

- A **Constraint Handler** is specified to determine how the model boundary conditions (e.g. node fixities or applied stresses)are applied; the transformation method is used in this model.
- A **Numberer** system is used to map nodal degrees-of-freedom to the equation numbers; a Reverse Cuthill-McKee (RCM) numbering scheme is used here.
- An **Integrator Method** must be specified to define each of the terms in the system of equations. The Newmark Method is used here with $\gamma = 5/6$ and $\beta = 4/9$ for the gravity phase; these values are higher than those typically used for the dynamic phase in order to ensure rapid convergence of the static solution.
- A **Solution Algorithm** is used to solve the non-linear equation at the current time step; the Newton-Raphson method is used here.
- A **System** object is specified to construct the global system of equations for the entire model; the `SparseGeneral` command is used here.
- A **Convergence Test** to check convergence of the system of equations; a Norm Displacement Increment test is used here, where the norm of the left-hand-side solution vector of the matrix equation is checked, with a tolerance criteria of 1×10^{-4} m, and a maximum of 15 iterations. Note that while this tolerance criterion is more than adequate for the gravity phase, a dynamic sub-stepping algorithm was employed during the dynamic phase whenever this criteria failed after the maximum number of iterations, which is briefly described in the "Dynamic Analysis" section.

The gravity loading is conducted in two transient analysis phases, each consisting of ten 1-second time steps to allow for the response to settle down prior to dynamic excitation: an initial elastic phase, where the PM4Sand and PM4Silt `nDMaterial` material stage specifications are set to "Elastic", and a subsequent phase where the material stages are updated to allow elasto-plastic response. In early phases of model development, element responses were recorded in order to validate that desired initial effective stress regime was correctly captured by the model specifications and gravity analysis phases.

5.4.6 Dynamic Analysis Phase

Prior to the application of dynamic loading at the base of the model, the element permeability coefficients are updated from 1.0 to the values listed in Table 5.6. Additionally, Rayleigh damping

must be included in the model in order to generate small-strain damping in addition to the hysteric damping inherent to the elasto-plastic material used here. Rayleigh damping is specified in OpenSees through stiffness and mass factors α and β for the damping matrix. These factors are calculated from the specified small-strain damping ratio ($\xi = 2\%$, commonly used for small-strain damping in OpenSees) and the minimum and maximum circular frequencies ω_1 and ω_2, which are based on the specified minimum and maximum frequencies of 0.20 and 20 Hz, respectively (selected to bracket the natural frequency of the soil column and the highest frequency of interest of the ground motion):

$$\omega_1 = 2\pi f_{min} \tag{5.14a}$$

$$\omega_2 = 2\pi f_{max} \tag{5.14b}$$

$$\alpha = \frac{2\xi\omega_1\omega_2}{\omega_1 + \omega_2} \tag{5.14c}$$

$$\beta = \frac{2\xi}{\omega_1 + \omega_2} \tag{5.14d}$$

The input motion is applied as a force load pattern in OpenSees, which is based on the velocity time history multiplied by the dashpot coefficient, m_C:

$$m_C = H_{E,X} \cdot \rho_{rock} \cdot V_{s,rock} \tag{5.15}$$

where $H_{E,X}$ is the width of the base element (0.5 m here), and ρ_{rock} and $V_{s,rock}$ are the density and shear wave velocity of the underlying bedrock. The dynamic analysis phase is conducted with the same `analysis` specifications in OpenSees as the gravity loading phase, with the Newmark integrator parameters modified to $\gamma = 1/2$ and $\beta = 1/4$ to ensure no numerical damping. Finally, as introduced briefly in the Convergence Test discussion, a dynamic sub-stepping scheme is used as part of the TCL model script to handle analysis time-steps in which the model does not converge in the specified 15 iterations, in which the offending time-step is initially split into two smaller, equally-sized sub-steps. The first sub-step is analyzed; if the model converges, then the process is repeated with the subsequent half sub-step. If the model does not converge in the first sub-step, it is divided further into two quarter-sized sub-steps (relative to the original timestep), and the process is repeated. Once the second half-sized sub-step is reached, the same logic is employed before moving on to the subsequent analysis timestep.

5.5 Non-Linear, Effective Stress Deformation Analysis of a Liquefiable Soil Column

An an example simulation, generated using the modeling framework described in this chapter, is presented here for a single soil column and ground motion. The soil profile (Figure 5.25) consists of a 2 m-thick surficial crust, the bottom of which coincides with the groundwater table. The underlying liquefiable zone extends from 2 to 8 m below ground surface, consisting of two 2 m-thick liquefiable sublayers of 40% and 60% relative density, separated by a 2 m-thick layer of silt. The liquefiable zone is underlain by a continuous layer of dense sand down to the bottom of the model at 21 m depth; the deepest element in the model has a shear wave velocity of 806 m/s.

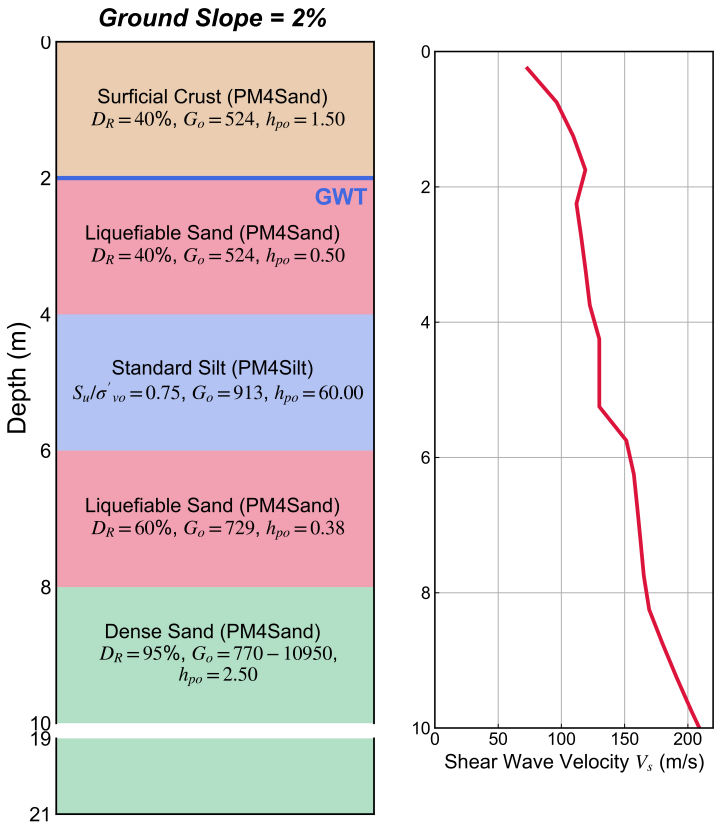

Figure 5.25: Soil layers and shear wave velocity profile for example soil column analysis.

The model was subjected to a crustal motion selected from the suite of 188 records developed in Section 5.3. The record is from the M_w-7.1, 1999 Hector Mine, California earthquake, from the Heart Bar State Park, about 60 km southwest of the earthquake rupture (Figure 5.26). The seed record was scaled by a factor of 3.64, and has a peak ground acceleration of 0.30 g. Time histories for two evolutionary intensity measures, PGA_M and CAV are also shown in Figure 5.26. Note

that while the PGA of the ground motion is reached at about 17 seconds, a significant amount of shaking intensity clearly remains after that point in the recording. These additional cycles produce the higher PGA_M value, the peak of which is reached at about 25 seconds into the shaking. It is clear, however, in examination of the CAV time history, that more energy remains even *still* after the maximum PGA_M is reached, with the CAV trace reaching only about 75% of its overall value. Clearly a significant amount of lower-frequency content remains after 25 seconds, even though the maximum acceleration after this point is only about 0.07 g.

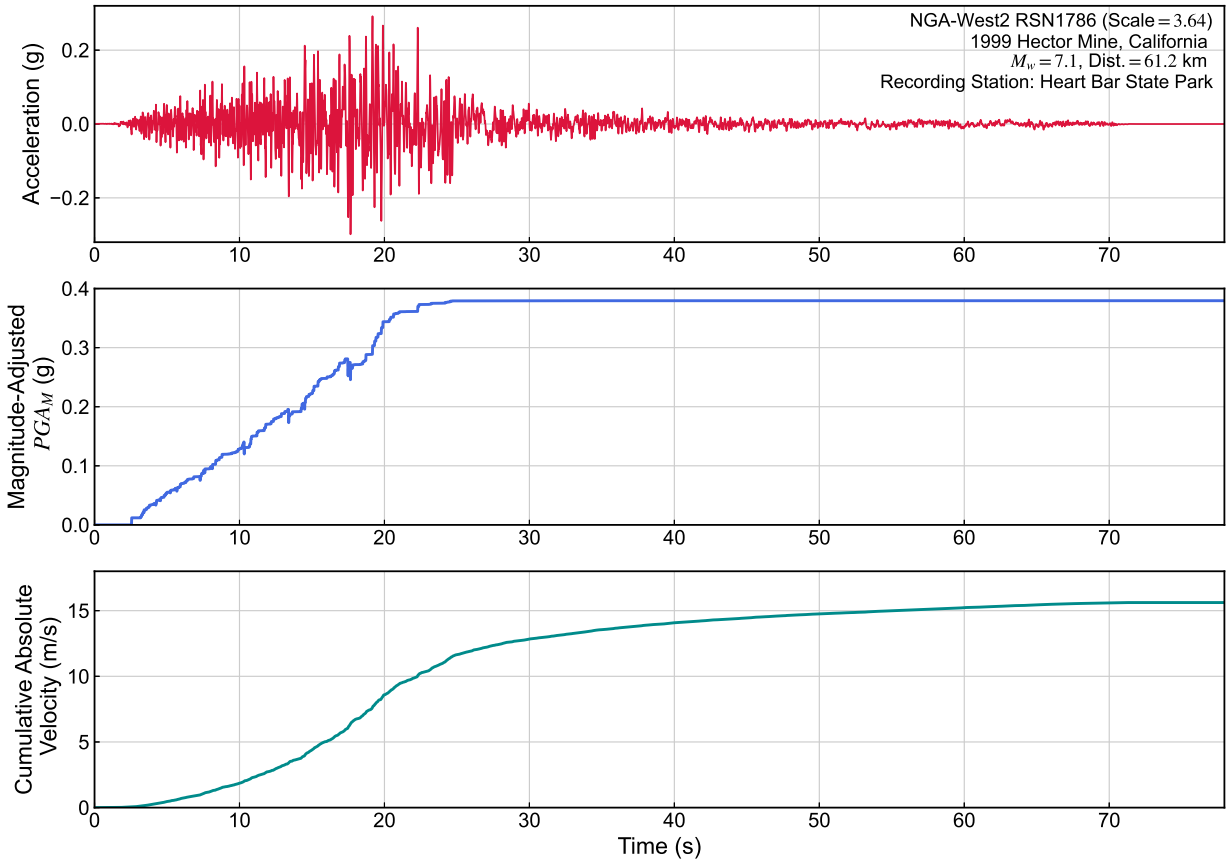

Figure 5.26: Time histories for acceleration, magnitude-adjusted PGA_M, and cumulative absolute velocity (CAV) for input motion for example soil column analysis

The results of the effective stress analysis are shown in Figure 5.27. The final surface displacement was 56 cm, driven primarily by over 40 cm of displacement in the shallower, looser, 40% relative density layer, and to a lesser extent by 10 cm of displacement in the deeper 60% relative density layer. Portions of both the D_R = 40% and D_R = 60% layers liquefied, reaching peak strains in excess of 40% and 15%, respectively. The silt interlayer contributed almost no strain or displacement, generating less than 50% excess pore pressure in the center of the layer, with somewhat higher pore pressures near the top and bottom of the layer due to flow from the overlying

and underyling liquefied layers.

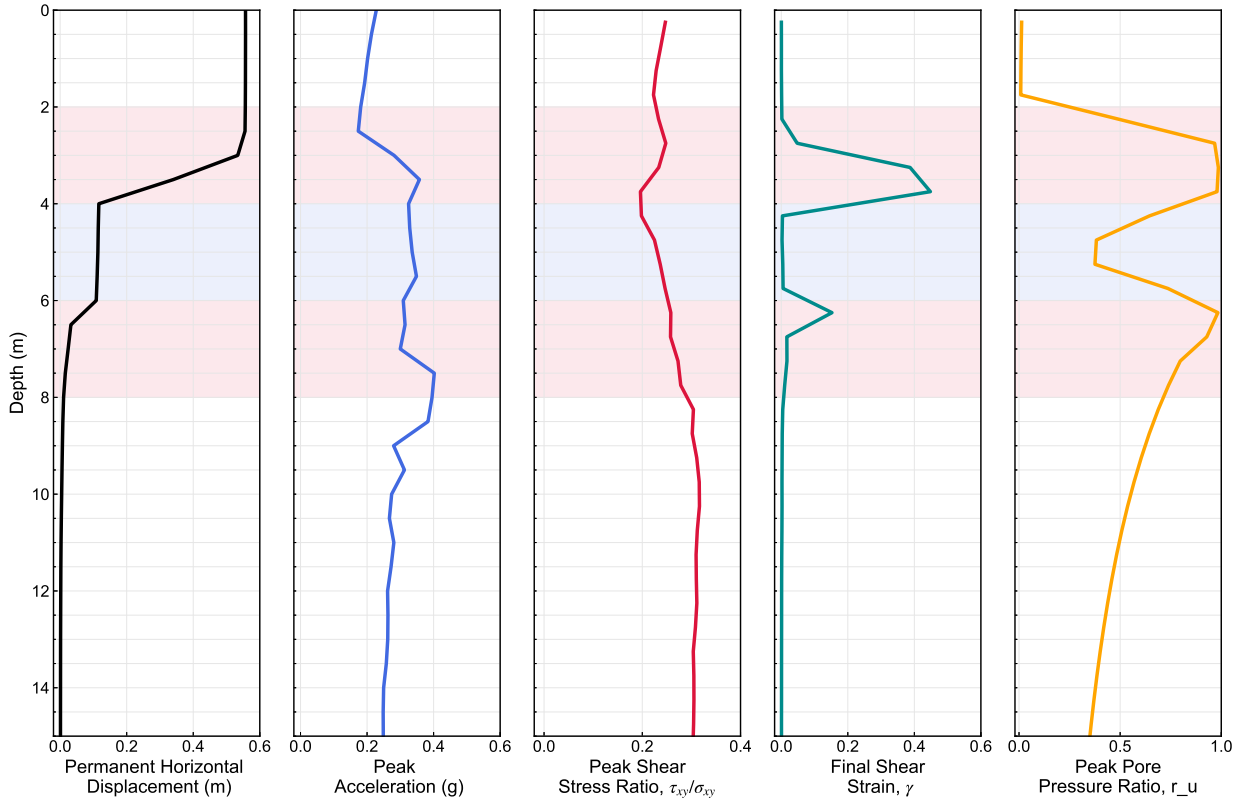

Figure 5.27: Depth profiles of final horizontal displacement, and peak acceleration, shear stress ratio, shear strain, and pore pressure ratio for example soil column analysis. Liquefiable layers are shaded in red, while the silt interlayer is shaded in blue.

Stress and strain histories were recorded for all model elements, and extracted for three of the elements in the soil column: a $D_R = 40\%$ element at 3.25 m depth, a PM4Silt interlayer element at 4.25 m depth, and a $D_R = 60\%$ element at 6.25 m depth. The stress-strain curves and stress paths for these elements are shown in Figure 5.28, with the curves color-shaded with respect to time. As expected, shear strains were much larger in the $D_R = 40\%$ layer (note the different shear strain axis scales). The behavior in both elements from around 22 seconds through the end of the motion is somewhat notable as well. It is clear that several stress pulses, occurring between about 22 and 25 seconds cause large strain increments in both liquefiable elements, pushing them to about 28% and 5% total strain, respectively - recall this is the point at which the PGA_M of the input motion has reached its maximum value, but a significant portion of the CAV remains. This remaining portion of shaking intensity, mainly low-frequency waves, couples with the constant static shear stress due to the sloping ground to cause an additional 10% strain in both soil layers in their softened states.

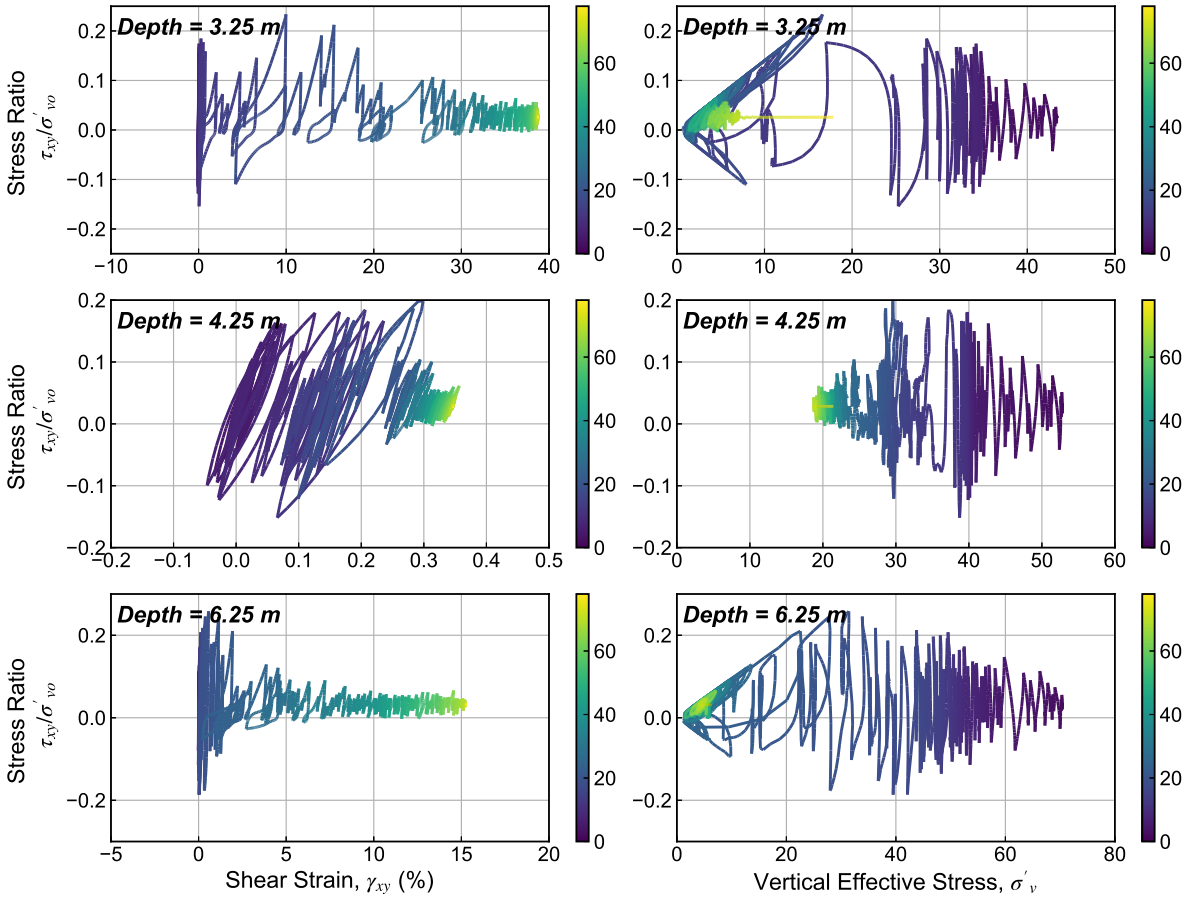

Figure 5.28: Stress-strain and stress path plots for three elements, extracted from example soil column analysis. Curves are color-shaded with respect to time

5.5.1 Timing of Liquefaction

In Section 2.2.2, the idea of utilizing different types of intensity measures, depending on their suitability for the type of engineering demand parameter in consideration was presented and discussed. The suitability of an IM can be evaluated in terms of its *efficiency* (i.e. whether it can predict the EDP with minimal variability), *sufficiency* (i.e. whether IM-EDP relationship is conditionally independent of earthquake source characteristics), and *predictability* (i.e. whether the IM can be predicted with enough precision to be useful in fully-probabilistic analyses). Various studies over the past 15 years (e.g. Kramer and Mitchell 2006, Kramer et al. 2016, Dashti and Karimi 2017) have suggested that for many geotechnical earthquake engineering applications, evolutionary intensity measures, which capture the effects of both amplitude and duration, are better suited in predicting EDPs than traditional peak amplitude parameters using these criteria.

Kramer et al. (2016) and Greenfield (2017) (see Section 2.3) utilized evolutionary IMs to better

understand how they might be used in a timing-based framework for evaluating the liquefaction triggering limit state and the subsequent prediction of lateral spreading ground deformations, generally PGA_M to be the most efficient predictor of triggering and CAV to provide the best combination of predictability and efficiency in predicting post-triggering deformations. In theory, predicting the time at which liquefaction occurs in a geotechnical system allows for the problem to be split into pre- and post-triggering portions in order to utilize the most efficient IM for each portion.

For the example analysis presented here, the time of liquefaction can be characterized using a number of methods, including examination of pore pressure or shear strain time histories, analysis of surface-to-downhole frequency content, and evolution of profile travel time as calculated from element tangent stiffnesses. The most direct method is based on examining the evolution of pore pressures throughout the model over time, as shown in Figure 5.29. As expected, the shallower and looser $D_R = 40\%$ layer is the first to liquefy, triggering about 13 seconds into ground shaking, and essentially coinciding with the onset of significant horizontal surface displacements, as shown in the accompanying time history in Figure 5.29. The deeper $D_R = 60\%$ layer liquefies about 8 seconds later, its higher density requiring a greater amount of energy to trigger liquefaction.

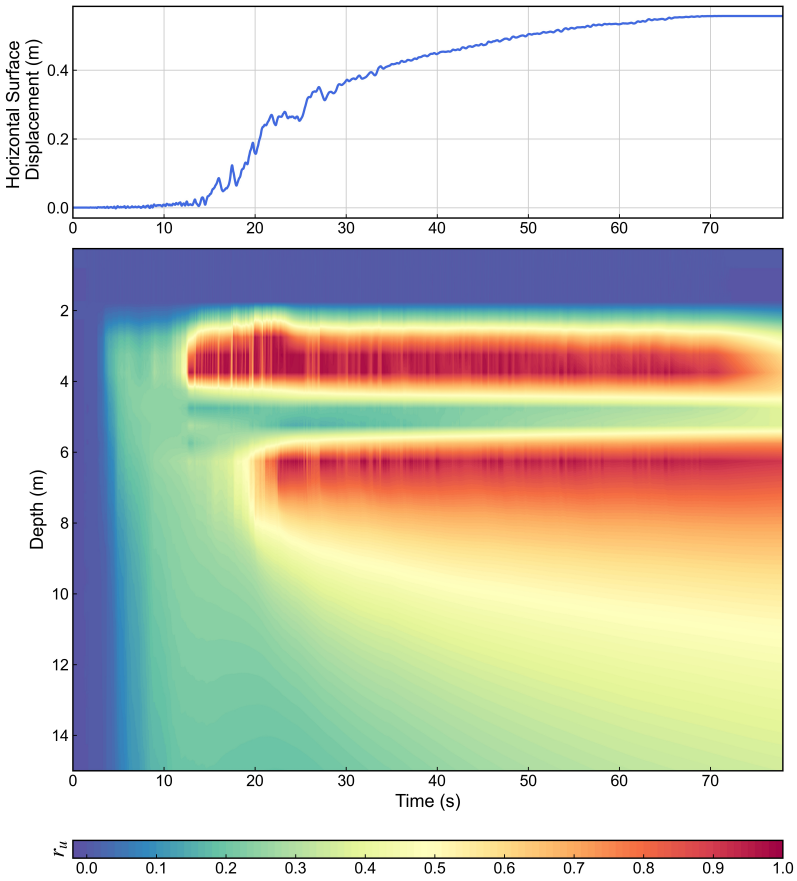

Figure 5.29: Depth-time colormap plot of excess pore pressure ratio generation, with horizontal surface displacement time history, for example soil column analysis.

Studies on the timing of liquefaction have generally focused to date on what can be referred to as a "system-level" triggering time, based on investigations of recorded ground motions at sites known to have liquefied in past earthquakes (Kramer et al. 2016). Using a Stockwell spectrogram to track the evolution of the predominant frequencies , the time at which liquefaction occurs can be estimated as the point at which the largest decrease in frequency content of the surface motion (or the ratio of the surface-to-downhole motion, if downhole recordings are available) occurs, as characterized by the error function of the modal frequency. The Stockwell spectrogram for the example analysis is shown, along with the error function of a step function fit to the modal frequency, in Figure 5.30. Through visual examination of the Stockwell spectrogram, there is a clear drop in modal frequencies that coincides with the time at which the shallower $D_R = 40\%$ layers liquefy, a time that is clearly captured by the minimized error function. However, it is also clear from Figure 5.29 that there are multiple, distinct soil layers that liquefied in this ground motion, and while the

Stockwell spectrogram adequately characterizes the liquefaction time of one layer, it cannot readily detect the liquefaction of multiple layers.

Another "system-level" characterization of the liquefaction time, albeit one that can be applied only to numerical studies, and not field case histories, is the evolution in "travel time" of the profile. This consists of calculating a profile of tangent element shear moduli at each time-step, $G(z,t)$ from the recorded stress-strain data. The shear moduli can be converted to shear wave velocities via:

$$V_s(z,t) = \sqrt{\frac{G(z,t)}{\rho(z)}} \tag{5.16}$$

The travel time through an individual element i is calculated from the element thickness H_i via:

$$T(z_i,t) = H_i/V_s(z_i,t) \tag{5.17}$$

And the travel time of the full profile is calculated by summing up element travel times:

$$T_{prof}(t) = \sum_{i=0}^{N_{ele}} T(z_i,t) \tag{5.18}$$

The profile travel time provides a useful manner in which to evaluate the changes in stiffness at a system level. When excess pore pressures are generated in soils, their stiffnesses decrease, thus reducing wave velocities and increasing the overall time required for a shear wave to propagate through a soil column. However, examination of the travel time plot in Figure 5.30 illustrates its potential utility in characterizing the time of liquefaction on a system level, corresponding to the point at which the soil profile is generally at its softest, and indicating something of an average liquefaction time over the various liquefiable sublayers.

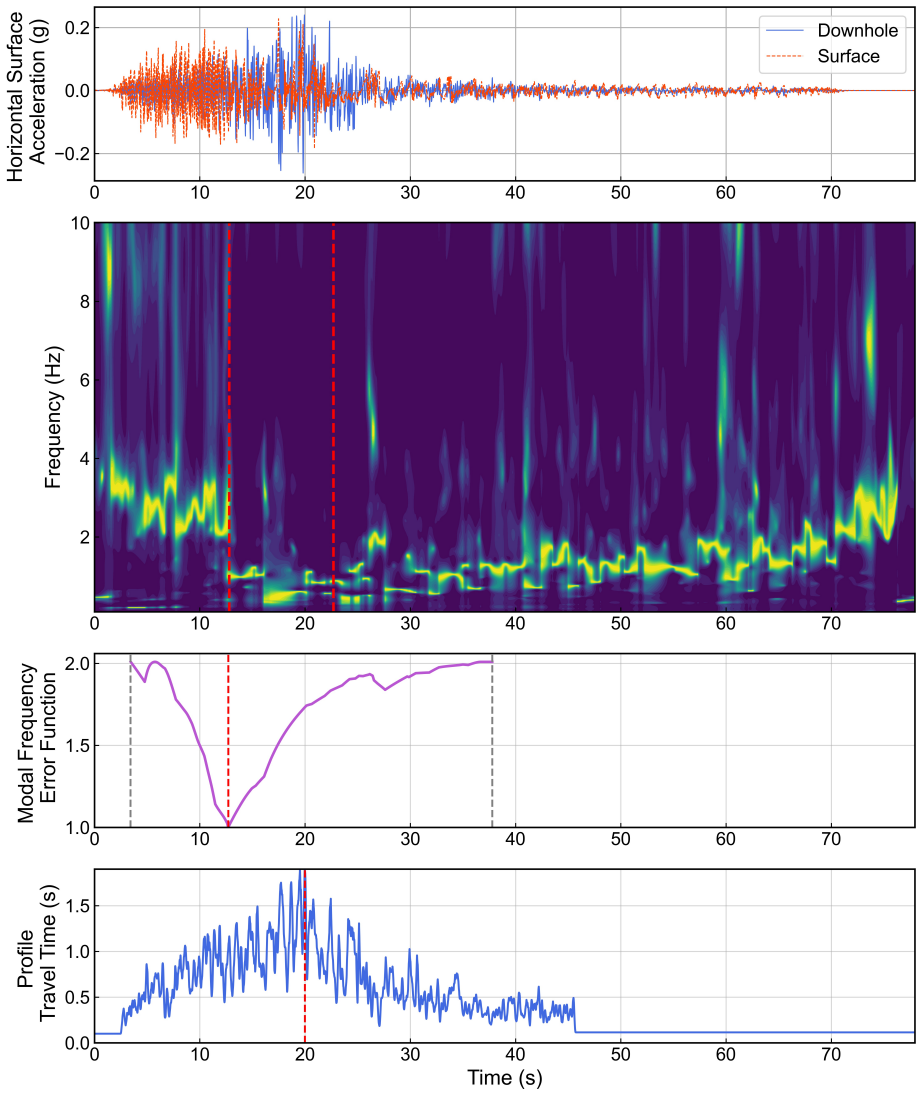

Figure 5.30: Time history plots of surface and downhole accelerations, normalized Stockwell spectrogram, and modal frequency error function for example soil column analysis. Liquefaction times for individual soil elements are shown as vertical dashes lines in red. The modal frequency error function is extracted for the time between the first and last exceedances of 0.04 g in order to avoid consideration of low-amplitude changes in frequency content.

The limitations of characterizing the system-level liquefaction time, rather than element-level times, can be understood by considering how evolutionary intensity measures can potentially be used to predict liquefaction triggering and its associated effects. Kramer et al. (2016) present a hypothetical time-based framework for characterizing lateral spreading displacements as follows, and summarized in Figure 5.31:

1. For a given relative density D_R, there exists a liquefaction triggering relationship by which a

magnitude-adjusted PGA_M that causes the triggering limit state can be estimated, termed $PGA_{M,trig}$

2. If the ground motion time history for the site in question is known, $PGA_{M,trig}$ can be compared with the final PGA_M from the time history $PGA_{M,f}$ to determine the time at which liquefaction has occurred, T_L.

3. The post-triggering intensity measure is taken to be cumulative absolute velocity, CAV, the time history of which is subtracted from its final value to obtain a time history for the *remaining* CAV during the ground motion, or CAV_{post}. The time of liquefaction is used to determine the amount of post-triggering CAV_{post}.

4. For the same relative density, there exists some relationship between CAV_{post} and lateral spreading deformations, such that permanent displacement can be estimated.

Kramer et al. (2016) and Greenfield (2017) showed that using this framework yielded more efficient displacement predictions than estimating displacements directly from the relative density and a final intensity measure (PGA_M, CAV, or I_A) without accounting for the timing of liquefaction. These results were based on a series of numerical analyses of simple profiles consisting of thick layers of uniform relative densities, with the $PGA_{M,trig}$ and CAV_{post} based on the input time history, and the time of liquefaction estimated using the surface-to-downhole Stockwell spectrogram extracted from the numerical models.

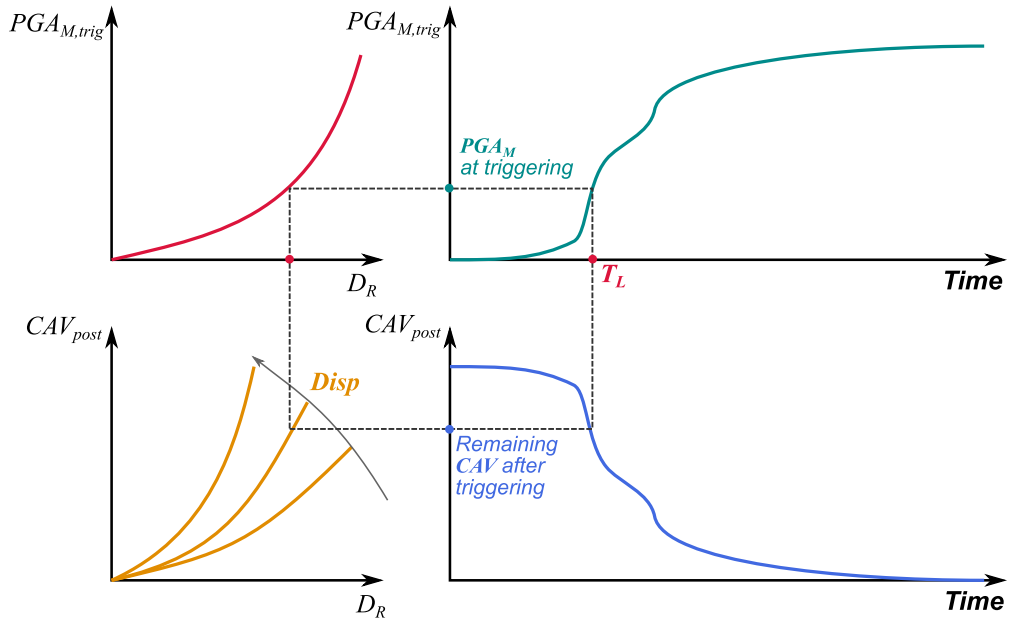

Figure 5.31: Illustration of a timing-base framework for predicting and characterizing liquefaction-induced lateral spreading displacements for a site underlain by a single liquefiable layer with uniform relative density (after Kramer et al. 2016)

These findings provide an extremely useful basis for any sort of timing-based predictive framework. The efficiency of PGA_M in predicting liquefaction triggering allows for a framework that is related to traditional, simplified triggering procedures that practitioners are likely to be using in liquefaction triggering analyses. However, in considering more complicated profiles such as the one demonstrated in this section, it is clear that modifications must be made to account for the fact that elements with different relative densities will liquefy at different times and experience different levels of post-shaking intensity, as demonstrated in Figure 5.32. Using a single, system-based liquefaction time such as the Stockwell spectrogram may over- or under-predict the liquefaction times in different layers, thus necessitating a framework wherein the timing-based framework is applied at the element level; in this case, post-triggering intensities are related to shear strains, rather than directly to surface displacements, and those predicted shear strains are integrated over the thickness of each liquefiable zone to obtain final relative displacements.

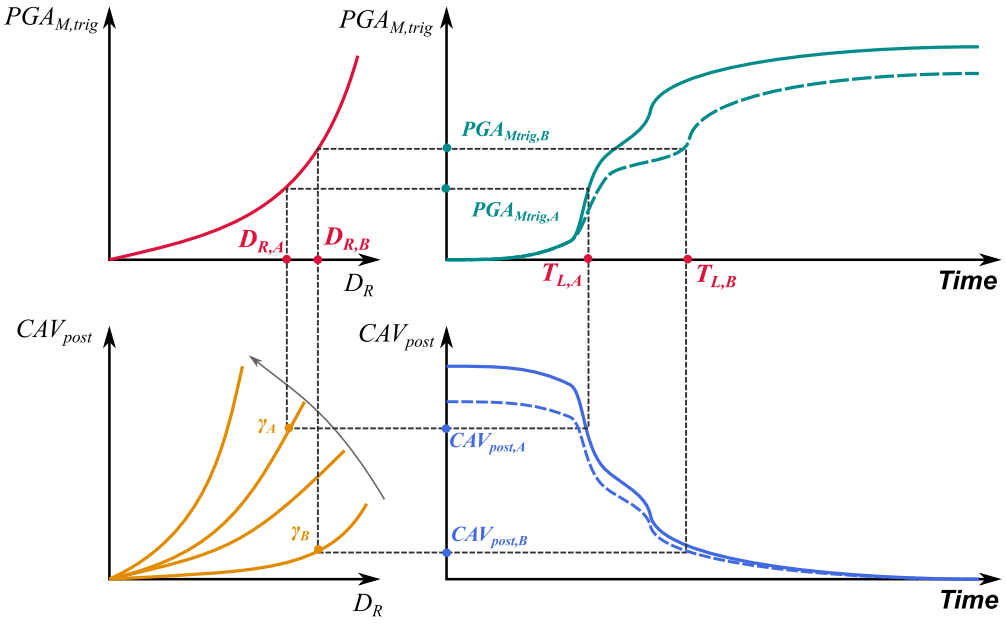

Figure 5.32: Illustration of a modified form of the timing-based framework for lateral spreading displacement predictions for a hypothetical site, with multiple liquefiable layers of differing relative densities.

Another potential modification arises when considering more complex profiles, specifically in the characterization of the intensity measures needed to predict the timing of liquefaction and post-triggering strains. The time histories of $PGA_{M,trig}$ and CAV_{post}, shown in Figure 5.33 for four of the liquefied elements from this example analysis indicate significant amplification and deamplification effects - such differences are expected in any sort of site response analysis, and are accounted for in traditional liquefaction hazard analyses via the depth reduction factor (see Section 3.4.2). An important aspect to note here is that, while typical depth reduction factors, which are based on total stress analyses and don't account for the effects of excess pore pressures, assume a higher

PGA at shallow depths, the $PGA_{M,trig}$ time histories appear to have largely the opposite trend, particular after the first onset of liquefaction in the 3.75 m-deep element. This "shielding effect", as described by Cubrinovski et al. (2018) (see Section 2.2.2) represents a key shortcoming of conventional liquefaction triggering analyses; within the proposed timing-based framework shielding may cause delayed triggering (or no triggering at all) in some elements and subsequent reductions in post-triggering intensities. Neglecting to consider this type of system response effect can lead to significant overestimation of the post-triggering demand experienced by shallower layers of potentially liquefiable soils. Overestimation of demand can lead to overestimation of permanent strains in these layers, and ultimately to overestimation of lateral spreading displacements.

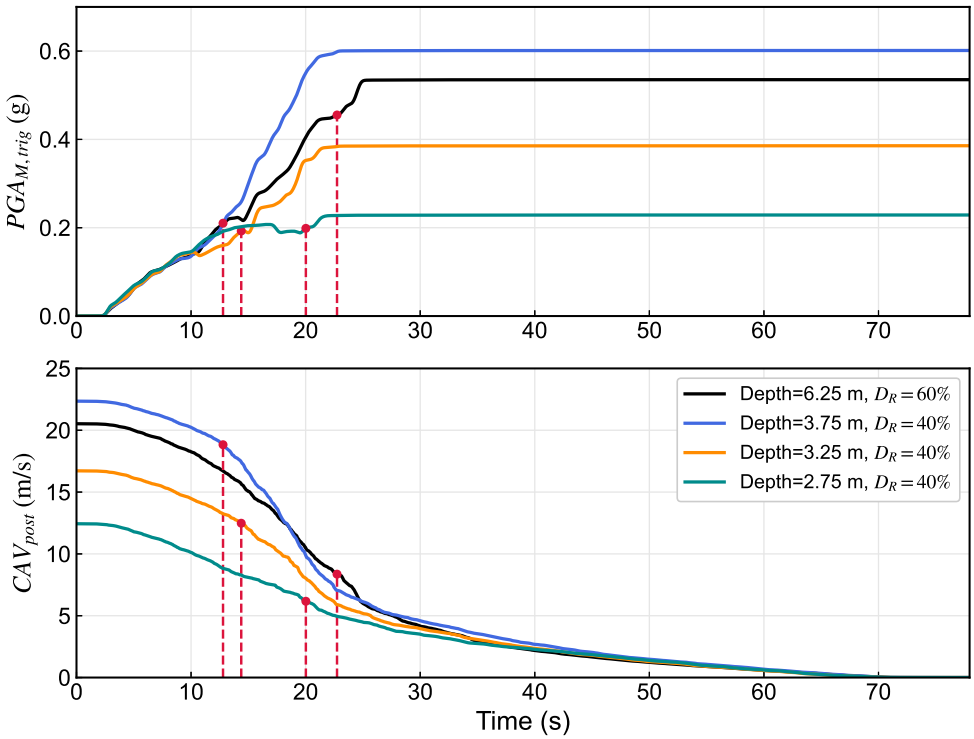

Figure 5.33: Time histories of pre-triggering PGA_M and post-triggering CAV for four liquefied elements in example soil column analysis. Liquefaction times for each are indicated with red dashed lines.

The hypothetical timing-based framework outlined initially in this section has been presented in terms of the actual time at which liquefaction occurs, assuming that the IM time histories of PGA_M and CAV are known. In reality, as has been discussed by Kramer et al. (2016), a forward-predictive framework cannot predict the exact ground motion time histories, and is limited to predicting only the final IMs, with some uncertainty. Kramer et al. (2016) showed that pre- and post-triggering evolutionary intensity measures were systematically correlated to one another. This concept becomes somewhat clearer when the same IM time histories in Figure 5.33 are instead plotted against each other, as in Figure 5.34. If $PGA_{M,trig}$ at any given time is low relative to its

final value, then it is likely that the remaining CAV_{post} will be relatively high, and vice-versa. This is a feature of characterizing ground motions using evolutionary intensity measures - in fact, if the same two pre- and post-triggering IMs were considered, the curves in Figure 5.34 would plot as straight lines.

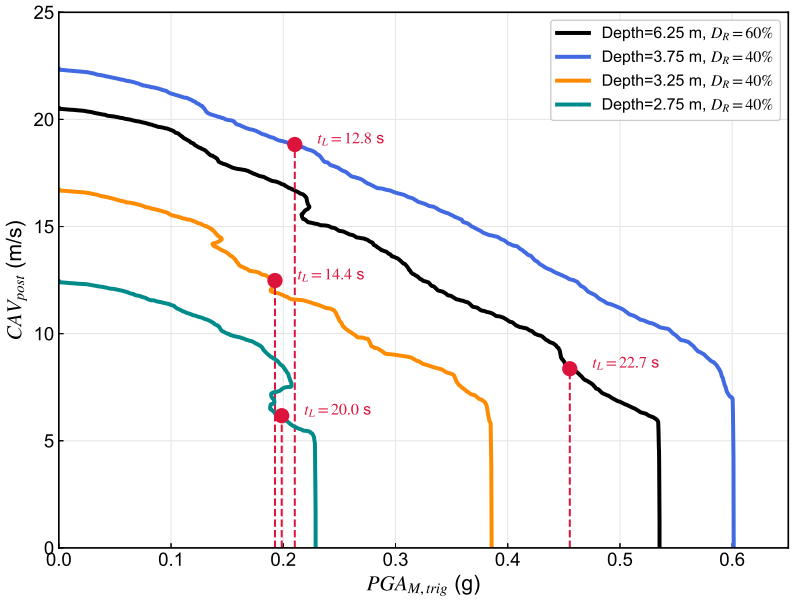

Figure 5.34: Pre-triggering PGA_M versus post-triggering CAV plots for four liquefied elements in example soil column analysis. Liquefaction times for each are indicated with red dashed lines.

Greenfield (2017) normalized the relative evolution of these IMs by their final values as follows:

$$\alpha_1 = \frac{PGA_{M,trig}}{PGA_{M,F}} \tag{5.19}$$

$$\alpha_2 = 1 - \frac{CAV_{post}}{CAV_F} \tag{5.20}$$

and found a relatively stable and systematic relationship between α_1 and α_2 based on a large set of crustal and subduction motions recorded at stiff sites, modeling the distribution of α_2 conditional on α_1 using a beta distribution:

$$p(a,b) = \frac{\Gamma(a)\Gamma(b)}{\Gamma(a+b)} x^{(a-1)}(1-x)^{(b-1)} \tag{5.21}$$

where Γ is the gamma function, and a and b are the beta distribution coefficients, which vary with

α_1 as follows:

$$\ln a = 2.75 - 0.31 \ln \alpha_1 + 0.14 \ln(1 - \alpha_1) \tag{5.22a}$$

$$\ln b = 1.91 + 0.93 \ln \alpha_1 - 0.10 \ln(1 - \alpha_1) \tag{5.22b}$$

The Greenfield (2017) $\alpha_1 - \alpha_2$ relationship is shown in Figure 5.35, along with the corresponding plots for the liquefied elements and the input motion for this example analysis. It is important to note once again that Greenfield's model is based on soft rock motions from crustal and subduction events, and are not affected by pore pressure generation like the motions in this particular example case. It is difficult to extract broader conclusions about the suitability of a total stress-based $\alpha_1 - \alpha_2$ relationship for effective stress motions from a single case, but the effective stress motions do plot well below the Greenfield mean function for α_2, although the input motion trace (which is also from a soft-rock condition) also plots quite low. A more comprehensive look at the suitability of this relationship is explored in Chapter 7.

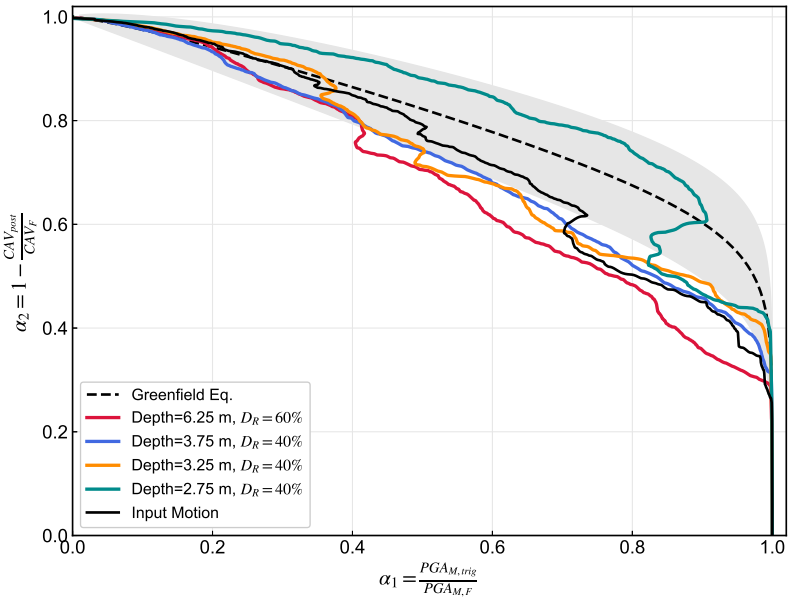

Figure 5.35: Normalized evolutionary intensity measure relationships for pre-triggering PGA_M and post-triggering CAV plots of four liquefied elements in example soil column analysis and input motion. The Greenfield (2017) mean $\alpha_1 - \alpha_2$ function is shown with the shaded region plus/minus one standard deviation.

5.6 Summary and Conclusions

This chapter developed and presented the basic components of a large-scale, numerical parametric study for the investigation of liquefaction-induced lateral spreading. Numerical analyses can allow researchers to systematically investigate the various factors that contribute to natural hazards such as liquefaction-induced ground failure in ways that are not possible through laboratory testing or evaluation of field case histories (although both of these are critical components nonetheless). For large-scale parametric studies that are computational in nature, it is critical to be able to utilize software that is flexible and scaleable - the open-source finite element platform OpenSees is particularly useful in this regard, as it allows for highly efficient and automated model generation, and the ability to run a large number of analyses on parallel computing platforms.

OpenSees also benefits from the its open-source nature in that it contains numerous material models developed and implemented by various researchers. Two such soil constitutive models were utilized in this study to simulate the cyclic response of granular sands (PM4Sand) and silts (PM4Silt). These computational components - a finite element platform and constitutive models - were used to construct a one-dimensional model of a soil column, which served as the base model for the larger set of analyses performed in the next two chapters. A test analysis of a profile with multiple liquefiable layers was presented, the results of which illustrate the complexities inherent to characterizing liquefaction at both the element and system level. This complexity can be reduced somewhat by considering the time at which liquefaction occurs, and splitting the problem into pre- and post-triggering portions for analysis, and characterizing and predicting shaking intensities in both phases of the time history at the element level. These concepts are utilized in the next two chapters to develop a framework for predicting lateral spreading displacements in a manner that accounts for the timing of liquefaction and system response effects.

Chapter 6

Development of a Semi-Empirical Model for Predicting Post-Liquefaction Shear Strains and Reductions in Ground Shaking Demands

6.1 Introduction

In the preceding chapter, the basis for conducting a large-scale numerical parametric study was presented to enable the investigation of the factors that contribute to liquefaction-induced lateral spreading. The basic components of the timing-based framework for lateral spreading prediction were presented, wherein the lateral spreading problem is split into pre- and post-triggering components, enabling the use of optimal intensity measures to characterize each portion. The examination of a demonstration analysis of a liquefiable soil column, subjected to strong ground shaking under infinite slope conditions, motivated several potential refinements of the original predictive framework outlined by Kramer et al. (2016). In particular, the analysis demonstrated the importance of predicting the timing of liquefaction at the sublayer level, rather than the system level, and characterization of the reduction of demands at shallower depths due to excess pore pressure generation and liquefaction at larger depths.

This chapter presents the development of a more specific functional form of this framework. An

initial set of nearly 80 soil profiles was analyzed with systematic variations in the relative density, thickness, depths, and continuity of the liquefiable soil layer, as well as slope inclination of the profile. Each one-dimensional OpenSees profile was subjected to the set of 188 motions presented in Section 5.3, for a total of about 15,000 non-linear effective analyses using OpenSees. Performing such a large number of analyses necessitated a method for efficiently generating these profiles and deploying them in parallel using the Stampede2 supercomputer at the Texas Advanced Computing Center (TACC) (http://www.tacc.utexas.edu), the workflow of which is presented here. Based on the results of these analyses a predictive form for the permanent shear strains as a function of post-triggering CAV, relative density, and slope inclination is presented. A predictive form is also presented for the reduction of the motion from the base of the liquefiable zone up to shallower depths by accounting for the thickness and density of the underlying soil layers, in order to estimate final PGA_M and CAV profiles.

6.2 Workflow for Performing Large-Scale Non-Linear Effective Stress Analyses

The non-linear analyses for the parametric study presented herein (as well as the randomized profiles discussed in the next chapter) were generated and performed in relatively small sets of profiles, or "series". For a given analyses series, a single parameter would be varied for each profile (e.g., relative density, slope inclination, depth). The OpenSees models were specified and generated for a given series using a Python script, wherein the soil layering for each individual model were specified using dataframes via the `pandas` Python library, with each soil layer referring to a specified, predefined OpenSees model calibration (Tables 5.4 and 5.5).

Each profile layering scheme was then used as input, along with a specified groundwater table and slope inclination, to a Python script for generating the OpenSees model files, which use the TCL scripting language. These files contain all of the node, element, material, boundary condition, recording, and loading analysis information described in Section 5.4 - on a local machine, it is this TCL file that is called to actually run the OpenSees model. In addition to the TCL files generated for each profile, a single "control" TCL file is used to call and run each profile via the multi-processing version of OpenSees, OpenSeesMP. The control file also reads in a text file specifying all of the input motion filenames that are being analyzed, along with the number of motion steps and the timestep.

The control file, profile TCL files, and input motion files were then moved to the Stampede2 supercomputer, a TACC resource for running natural hazard-related simulations, and submitted to one or more compute nodes a single job. Once through the queue, a series of five profiles subjected

to 188 motions each (for a total of nearly 1,000 analyses) ran in less than 2 hours using four compute nodes (totaling 196 processors). For this set of analyses, three variables were recorded at each time step in OpenSees: the nodal accelerations, the element stresses (horizontal, vertical, and shear), and element strains (horizontal, vertical, and shear). For the nearly 1,000 analyses, these recording files typically require about 35-40 GB of storage.

Post-processing the raw output data also occured in parallel on Stampede2, via a post-processing Python script that was submitted as part of the run job. For a given profile and input motion, acceleration, stress, and strain time histories at each node and element were read from the raw output files and compiled into an `xArray` dataset in Python, which allows for multidimensional, labeled depth-time data to be accessed and processed easily in Python. Included in each dataset are metadata on each soil layer (its model type and specific calibration ID, relative density, depth, and initial stress), as well as information on the ground motion (event name, recording stateion, source type, magnitude, distance, scaling factor, and input motion traces). Additional data of interest, such as nodal velocities and displacements, evolutionary IM time histories, and element pore pressure ratios r_u, were computed from the raw nodal and element data, . Liquefaction times are computed as the times at which the pore pressure ratio first exceeds 0.97.

Finally, the data from all motions for a given profile were compiled as a single `xArray` dataset. The time dimension of each ground motion dataset was eliminated for storage purposes, with the pertinent time series data extracted for each element (i.e., the final values of PGA_M and CAV, the times of liquefaction and PGA_M and CAV values the liquefaction times, maximum r_u values, and final shear strains). The final dataset for a given profile is two dimensional with respect to depth and input motion, containing the aforementioned data in each soil element, for each input motion. The final horizontal surface displacement, maximum r_u throughout the entire model, first liquefaction time in the model, IMs for the input trace, and the aforementioned ground motion metadata, were also included for each motion.

6.3 Initial Parametric Analysis for Investigating Sensitivity of Shear Strain to Soil and Site Conditions

In order to develop a functional form for the prediction of post-triggering shear strains, a series of simple soil profile models with systematically varying relative densities, liquefiable layer depths, and ground slope inclinations, were generated and analyzed in OpenSees. These profile schematics are shown in Figure 6.1. The "relative density series" was developed as a set of five simple profiles with a 2% ground slope inclination, consisting of a 2 m-thick surficial crust (coinciding with a 2 m-deep groundwater table), underlain by a 5 m-thick continuous zone of liquefiable sand with uniform

relative density, ranging from 30% to 70%, in steps of 10%. The liquefiable zone was underlain in turn by a continuous layer of dense sand, increasing in stiffness until a shear wave velocity of 800 m/s was reached, typically between 20 and 25 m below ground surface, depending on the density of the liquefiable zone. The "depth series" consisted of a set of profiles with a 2 m-thick layer of liquefiable sand with $D_r = 50\%$, with the depth to the top of the layer varying from 2 to 8 meters. Soils between the liquefiable layer and surficial crust were modeled using the high-strength PM4Silt interlayer material calibration (see Figure 6.1). The "ground slope series" consisted of a set of profiles with a 2 m-thick surficial crust of non-liquefiable material, underlain by a uniform 5 m-thick layer of liquefiable sand with $D_r = 50\%$; the ground slope inclination varied from 0.5 to 8 percent.

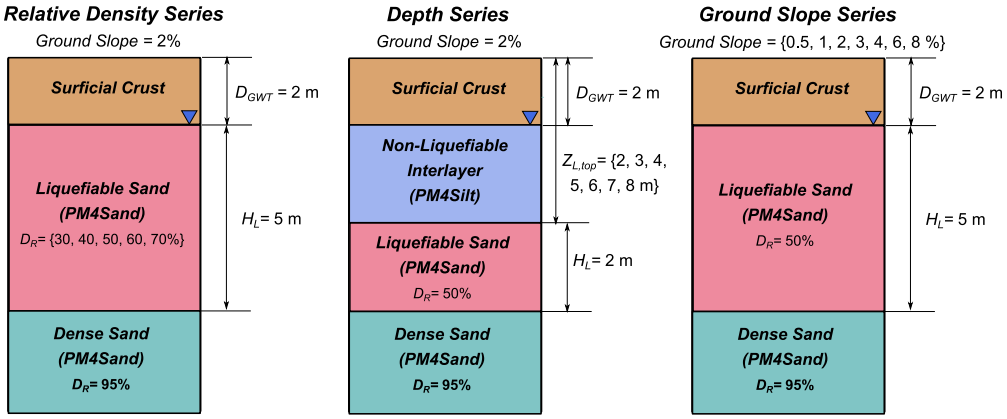

Figure 6.1: Soil layering sequence for relative density, depth, and slope inclination sensitivity series.

6.3.1 Sensitivity of Shear Strain to Relative Density

The effect of relative density on the accumulation of permanent shear strains can be initially illustrated by considering the maximum strain profiles of two of the D_R series profiles for the same crustal motion from the Parkfield (2004) earthquake, as shown in Figure 6.2. An unsurprising feature is that the looser profile ($D_R = 40\%$) experiences significantly larger strains than the denser profile ($D_R = 60\%$), but what is more interesting is how the strains are distributed throughout the liquefiable zone in each case. In the $D_R = 40\%$ profile, there is a larger concentration of strains at the base of the profile, with an average of about 45% strain in the bottom one meter decreasing to less than half that in the upper portion of the liquefied zone. In contrast, the $D_R = 60\%$ profile sees a much more even distribution in strains, with a consistent average of about 15% from approximately 4 to 7 m depth. Figure 6.3 shows the normalized strains for the same two analyses, illustrating more clearly the relative reduction in strains at shallow depths.

These results, as well as the example analysis in Section 5.5 indicate that this reduction in strains is due primarily to a reduction in shaking demands, caused by the triggering of liquefaction

in deeper layers and corresponding dissipation of energy. Figures 6.2 and 6.3 illustrate two key factors that contribute to this effect. One factor is the relative density (and by extension, shear strains), in the sense that looser soils tend to increase the reduction in demands due to their earlier liquefaction triggering times and larger post-triggering shear strains. The other is the cumulative thickness over which the shear strains occur; despite the relatively even distribution of strains in the $D_R = 60\%$ profile in the lower 3 m of the liquefiable zone, there is still a severe drop off in strains at depths of less than 4 m.

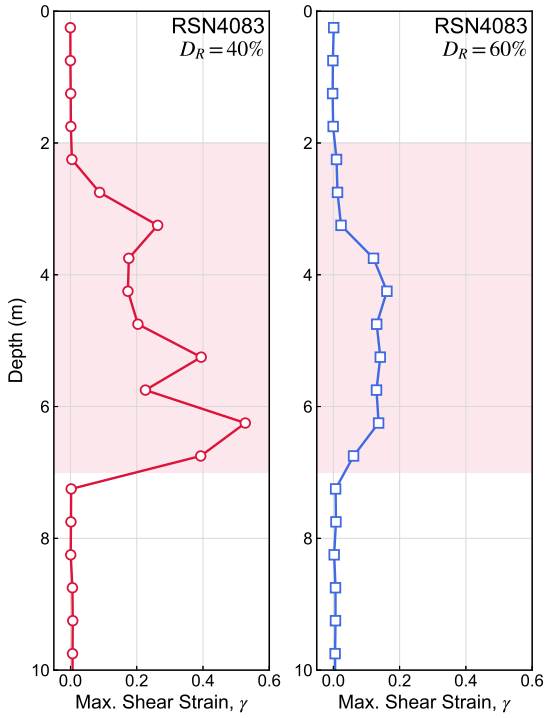

Figure 6.2: Variation in maximum shear strain with depth for $D_R = 40\%$ and $D_R = 60\%$ relative density series profiles, for crustal motion from the Parkfield, CA (2004) Earthquake (M_w6.0)

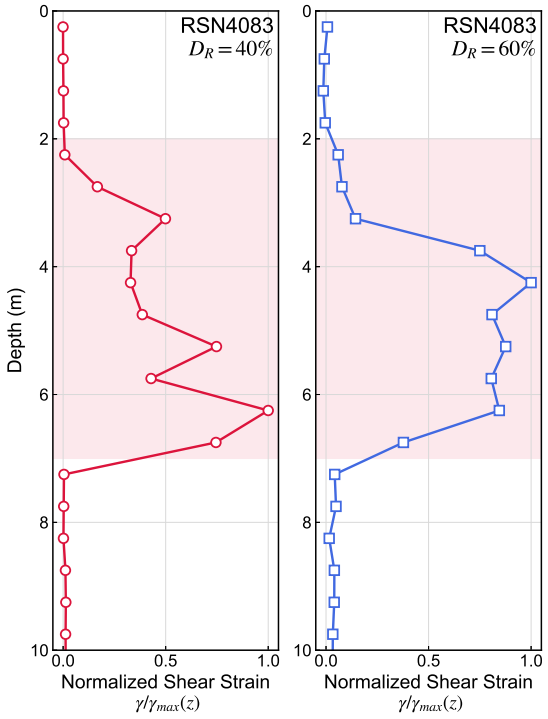

Figure 6.3: Variation in normalized maximum shear strain with depth for D_R = 40% and D_R = 60% relative density series profiles, for crustal motion from the Parkfield, CA (2004) Earthquake (M_w6.0)

A critical step in developing the timing-based framework is establishing an element-level relationship between post-triggering shaking intensity at a given depth $CAV_{post}(z)$ and the corresponding shear strain $\gamma(z)$ (Figure 5.32). This relationship is visualized for the D_R = 30, 50 and 70% profiles, at four element depths, in Figure 6.4; the best fit lines are constrained to pass through the origin, corresponding to a condition where zero post-shaking intensity (resulting from a condition of no liquefaction), would correspond to no post-triggering strains. The data suggests that γ can be estimated from CAV_{post} using a simple linear relationship, with a stronger correlation between the two at larger depths, where a wider range of strains and CAV_{post} values produce a more stable relationship:

$$\gamma(z) = \beta(z) CAV_{post}(z) \tag{6.1}$$

where the parameter $\beta(z)$ represents the slope of the CAV_{post}-γ data. It is clear from Figure 6.4 that β increases as the relative density decreases, pointing to a D_R-dependency of shear strains, even after the timing of liquefaction has been accounted for. Also noteworthy is a significant reduction in the ranges of CAV_{post} and shear strain at shallower depths. Such reductions are not seen in the types of total stress response inherently assumed in existing procedures for estimation of lateral

spreading displacements, and can be interpreted as resulting from "shielding" of the shallower layers by the triggering of liquefaction in deeper layers.

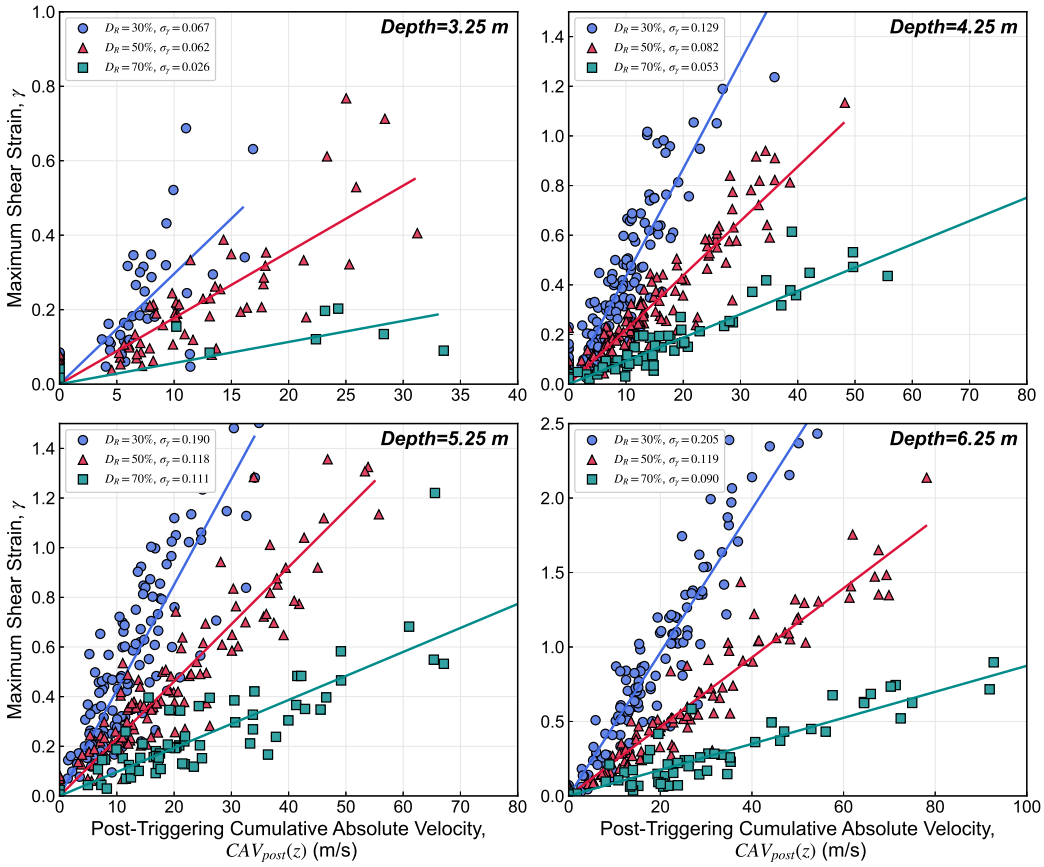

Figure 6.4: Variation of shear strain with respect to post-triggering CAV for D_R = 30, 50, and 70% relative density series profiles, at element depths of 3.25, 4.25, 5.25, and 6.25 m.

This behavior is illustrated more clearly for the Parkfield (2004) ground motion data in Figure 6.5. The final CAV values decrease above the base of the liquefiable layer, and the CAV_{post} values drop in a significant and complex manner, providing further evidence of the effects of shielding on both the final and post-triggering CAV values. The CAV depth profiles for the D_R = 70% case are particularly interesting, as it appears that the reduction in overall CAV from about 6.5 to 5.5 m depth, while relatively small, were enough to prevent liquefaction from being triggered in any of the shallower layers, and thereby drop the CAV_{post} values to essentially zero.

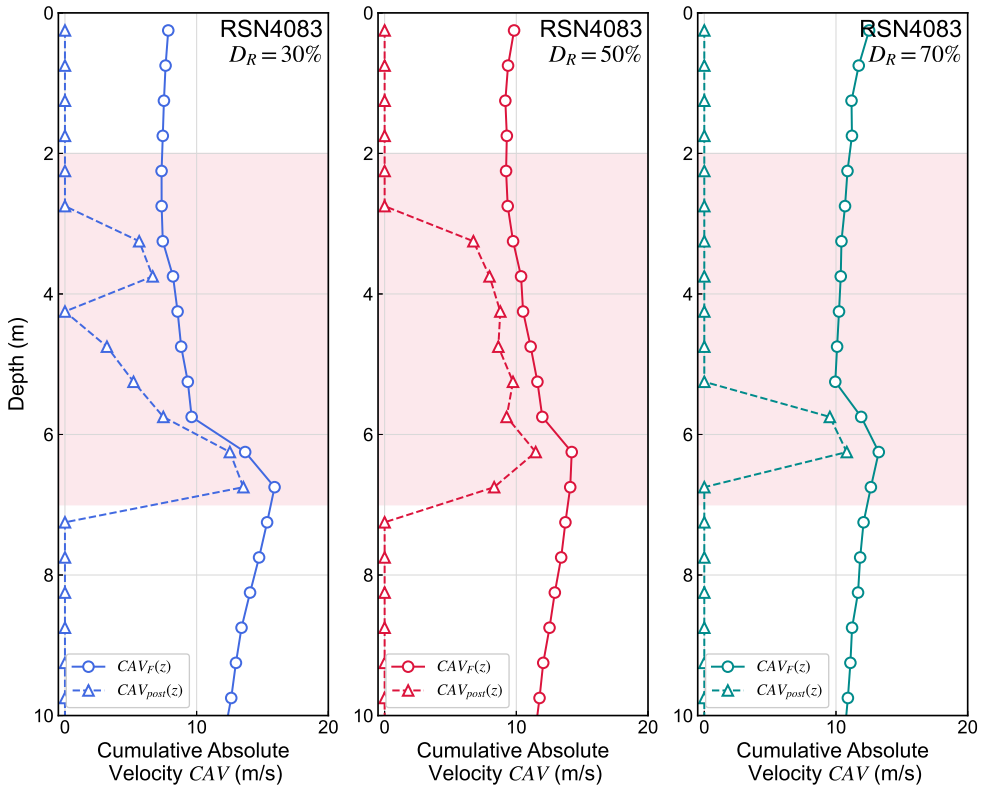

Figure 6.5: Variation in post-triggering and final CAV with respect to depth for $D_R = 30$, 40, and 60% relative density series profiles, for crustal motion from the Parkfield, CA (2004) Earthquake (M_w6.0)

For each profile, the β values were computed at each element depth, and smoothed using a 1.0 m-thick window within the liquefiable zone to simplify the data presentation. These values and their coefficients of determination are plotted with respect to depth in Figure 6.6. These depth profiles indicate strong within-profile consistency in β for a given density between about 3.5 and 7 m depths, as well as clear trend of increasing β with relative density. The reduction in both β and the correlation between CAV_{post} and γ at shallower depths indicates very low strains in elements that did not liquefy, either due to their proximity to the zero-pore pressure boundary condition at the water table, or due to large demand reductions due to liquefaction of underlying layers, i.e., the aforementioned shielding effect.

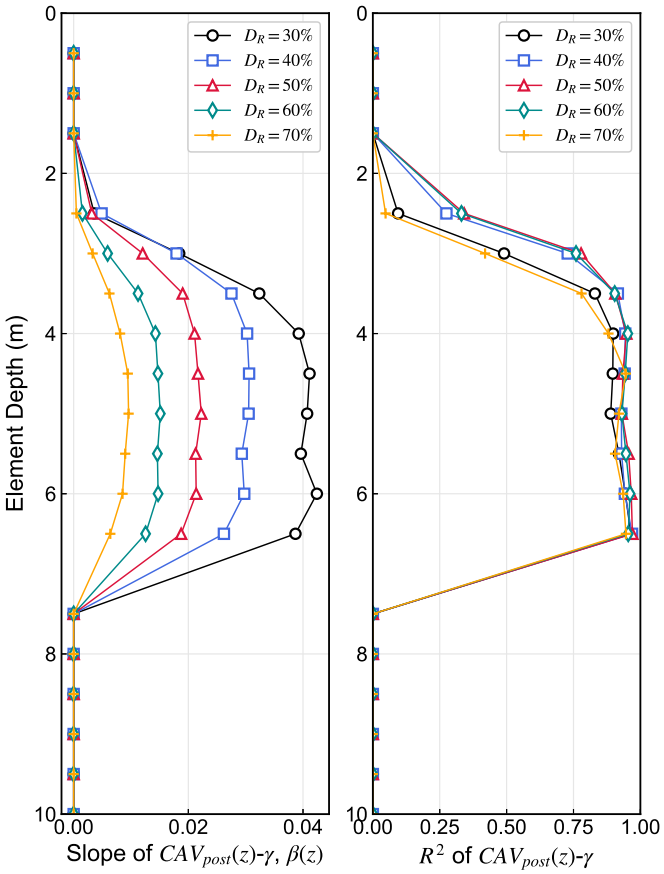

Figure 6.6: Variation in $CAV_{post} - \gamma$ coefficient β and the correlation coefficient, with respect to depth for the five relative density series profiles.

Figure 6.7 shows the variation in β with respect to relative density, considering only the liquefied elements from all the relative density series profile data. The data suggest an exponentially-decaying relationship between D_R and β; this relationship has a strong mechanistic basis; it is well established that shear strains to tend towards zero as soils become dense (see Section 2.2.2), and for the 2% slope inclination case, the exponential decay model a high degree of precision. With the D_R-dependency established, β in Equation 6.1 can be expanded such that the shear strains are now a function of both the post-triggering CAV and the relative density:

$$\gamma(z) = b_0 \exp[b_1 D_r(z)] CAV_{post}(z) \tag{6.2}$$

where b_0 and b_1 are regression coefficients.

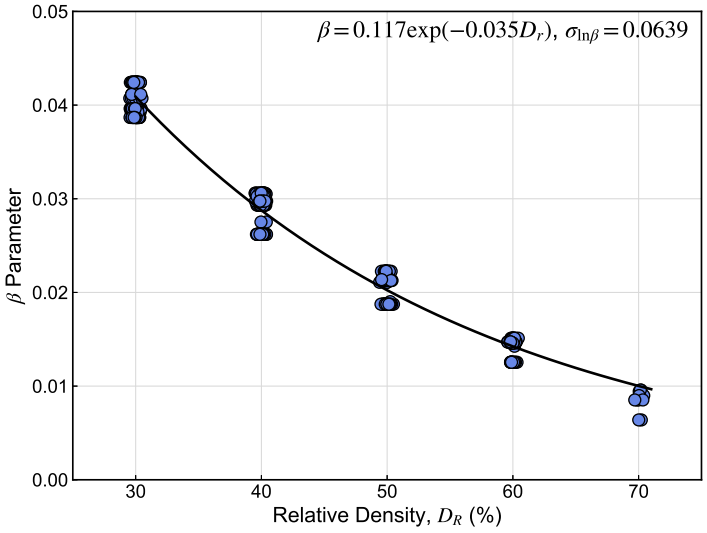

Figure 6.7: Variation in β parameter with relative density at all liquefied depths, from five relative density series profiles, with best-fit exponential function. D_R values are jittered slightly to illustrate point density.

6.3.2 Sensitivity of Shear Strain to Depth

The $\beta(z)$ values obtained from the results of the previously described Depth Series analyses were extracted in a similar fashion to the relative density series data, and are shown in Figure 6.9. Some within-layer variation in the β values for each depth profile was observed, with the shallowest sublayers consistently producing larger post-triggering strains than the deeper sublayers - this effect is due to differences in the hydraulic regime between the top and bottom of the liquefiable layer, with the silt layer acting essentially as a "capping" layer, preventing excess pore pressures from dissipating upwards and creating a persistent condition of very soft and weak liquefied soil, as shown in the comparison of the depth series profile and corresponding density series profiles with the bottom of liquefiable layers at the same depth of 7 m in Figure 6.8. In both cases, the dense underlying sand allows for some dissipation, and thus the lower half of the liquefied zone experiences some recovery in effective stress after triggering. This effect can also be seen to a certain extent in the example soil column analysis in Figure 5.27.

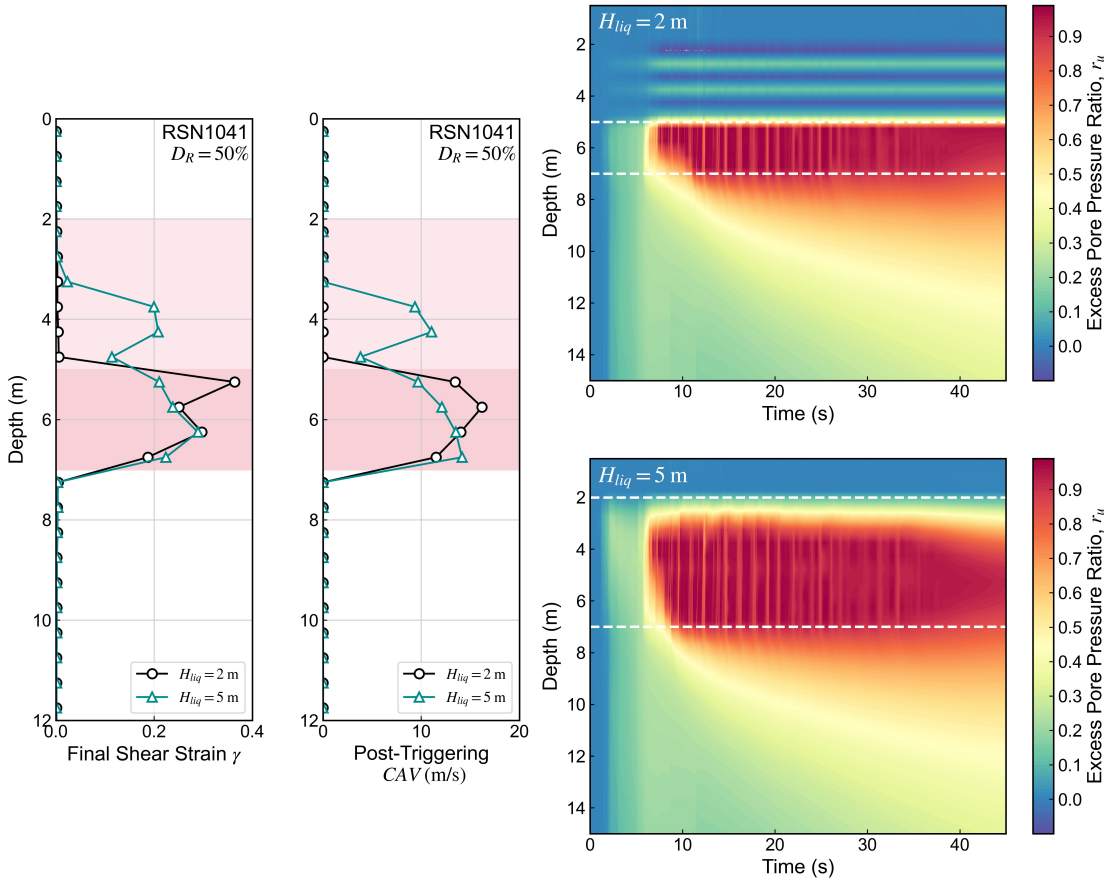

Figure 6.8: Comparison in permanent shear strains, post-triggering CAV, and pore pressure time histories between depth series profile with a 2 m-thick liquefiable layer and corresponding relative density series profile with a 5 m-thick liquefiable layer.

Comparing the different profiles shows a slight sensitivity in the shear strains to the depth of the liquefied soil, with the average strains in the profile decreasing at shallower depths. This is likely an effect of confining pressure, and can be potentially be captured by considering the influence of the relative state parameter index ξ_R in addition to relative density, which combines the effects of density (see Equation 2.3)

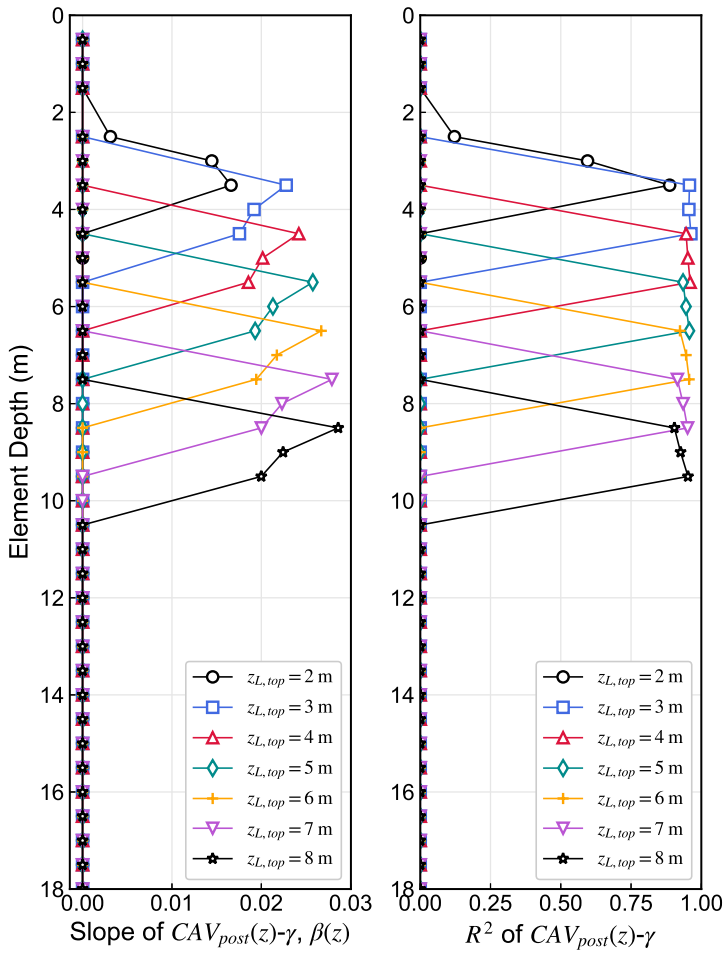

Figure 6.9: Variation in $CAV_{post} - \gamma$ coefficient β and correlation coefficient, with respect to depth for the seven depth series profiles.

However, if the β coefficient relationship from Figure 6.6 is recast in terms of ξ_R, and plotted with the $\xi_R - \beta$ values from the depth series (Figure 6.10), little predictive power appears to be added, with most of the depth series values (apart from capping-layer affected sublayers) coinciding with the original density series data. This may not be a surprising result after all, given that the variation in β with depth in from the relative density series data (see Figure 6.6) exhibited very little systematic trend with depth, with the exception of elements just below the groundwater table.

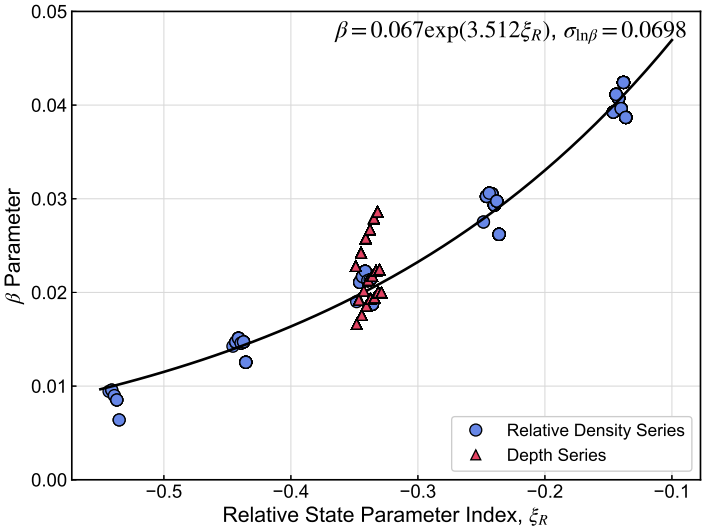

Figure 6.10: Variation in β parameter with relative state parameter index ξ_R at all liquefied depths, from five relative density series profiles and seven depth series profiles, with best-fit exponential function.

6.3.3 Sensitivity of Shear Strains to Slope Inclination

Profiles of β for each slope inclination S (Figure 6.11) indicate that there is initially a clear increase in β with respect to S at a given depth, but that it appears to reach a plateau as S exceeds about 4%. Such a variation should make sense mechanistically - profiles with steeper slopes, and therefore, larger static shear stresses, are likely to be less sensitive to post-triggering shaking intensity as a higher proportion of strains are driven by constant static stresses, rather than dynamic stress pulses associated with shear waves. There is also the effect of static shear stresses on liquefaction resistance, i.e., the K_α effect; for denser soils, steeper slopes may delay triggering (or inhibit it entirely) due to fewer stress reversals. This effect, however, would be expected to be reflected in the reduction of post-triggering shaking intensity, rather than in the $CAV_{post} - \gamma$ dependence.

The correlation between CAV_{post} and shear strain is once again quite strong, and was found to be consistently so throughout the thickness of the liquefiable layers (except at shallower depths, for the same reasons discussed in Section 6.3.1) for nearly all slope cases. The correlation at the shallowest slope inclination, $S = 0.5\%$, however, is somewhat lower than that of the rest of the slope inclinations. This effect is mainly due to a significantly larger proportion of shear stress reversals, and corresponding shear strain increments in the upslope directions. Such cases are likely to produce more variability in shear strains with respect to CAV_{post}; in a forward-prediction framework, it is expected that there may be higher variability in estimates displacements at sites

with flatter slopes.

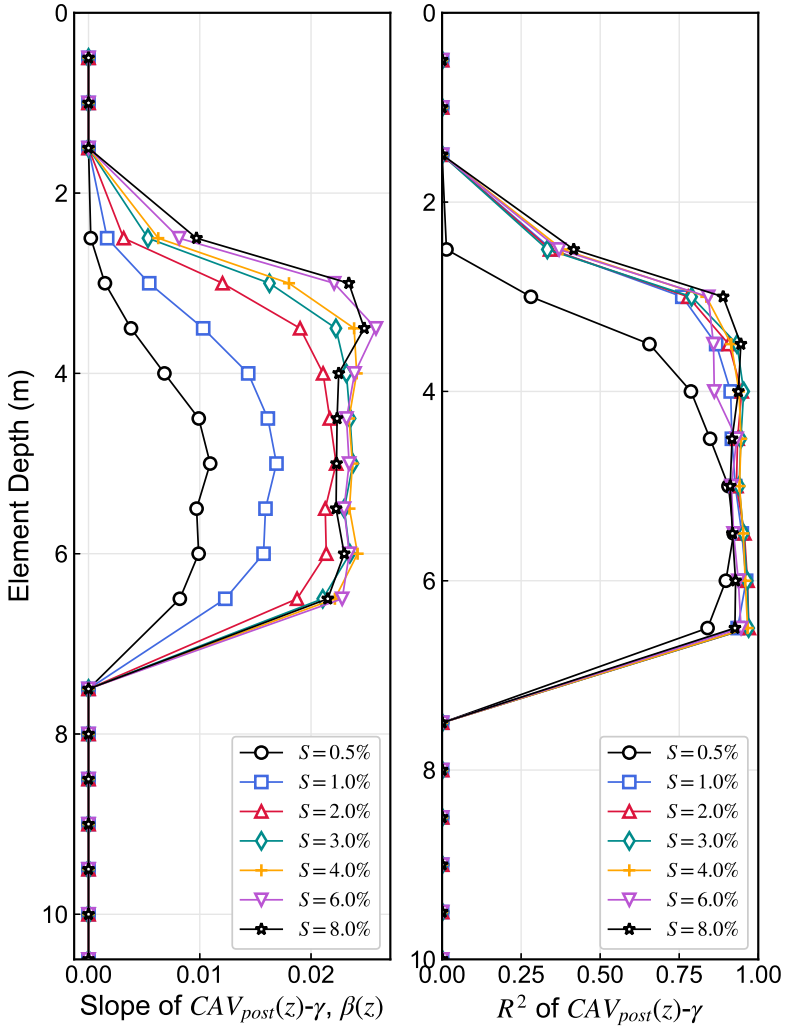

Figure 6.11: Variation in $CAV_{post} - \gamma$ coefficient β and the correlation coefficient, with respect to depth for the seven ground slope series profiles.

The variation of β with slope inclination is shown for all liquefiable depths in Figure 6.12, confirming the plateau-like behavior initially seen in Figure 6.11. A functional form relating β and S, a functional form was established as follows:

$$\beta = \exp\left[\frac{b_2}{S} + b_3\right] \tag{6.3}$$

where b_2 and b_3 are regression coefficients. The fitted relationship, with coefficients estimated from the slope series data, are shown in Figure 6.12, indicating good agreement of the functional form

for this particular relative density.

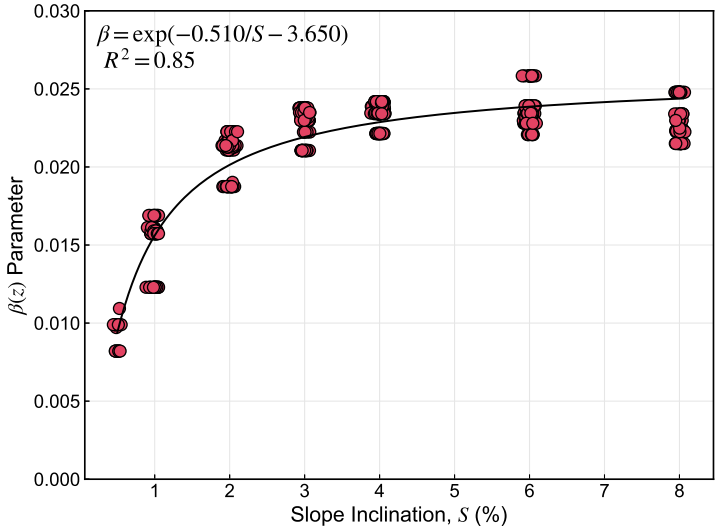

Figure 6.12: Variation in β parameter with slope inclination S (in percent) at all liquefied depths for a relative density of 50%, from seven ground slope series profiles, with best-fit exponential function.

6.3.4 Combined Sensitivity of Relative Density and Ground Slope

As discussed in Section 2.2.1, the effects of initial static shear stress on liquefaction triggering depend on how contractive or dilative a soil is. At low relative densities, initial static stresses tend to reduce liquefaction resistance, while generally increasing resistance at intermediate and higher relative densities due to a reduction in stress reversals. The combined effects of relative density and slope inclination on post-triggering strains were assessed via another series of analyses, essentially by combining the relative density and ground slope series profiles to analyze each combination of relative density and ground slope inclination. The same exponential functions shown in Figure 6.12 were fit for each relative density, as shown in Figure 6.13. The data indicate that the slope coefficients b_2 and b_3 both become more negative as D_R increases; the change in b_2 indicates that strains are less sensitive to slope inclination at larger densities, suggesting that an interaction term may be required in the characterization of the β parameter, while the variation in b_3 represents a simple vertical shift in the slope-β curves, related to the pure D_R-dependency characterized in Section 6.3.1.

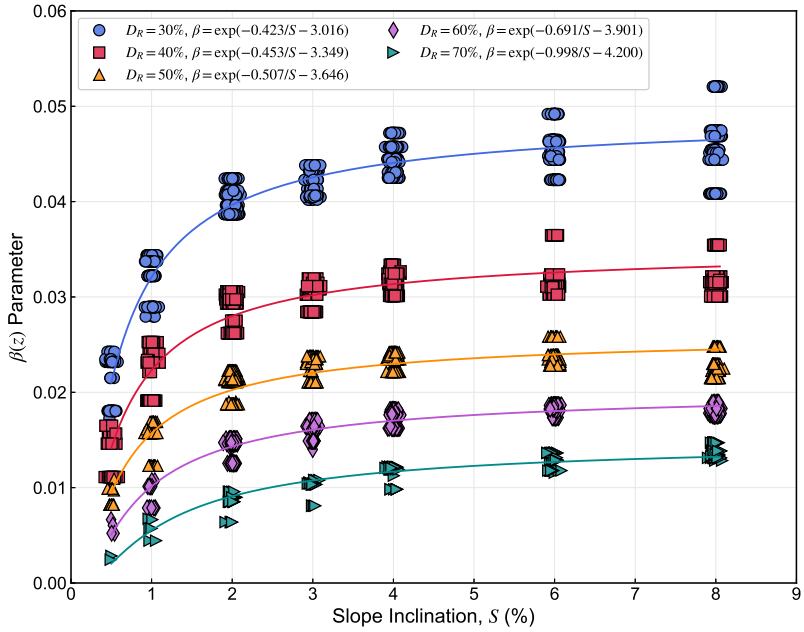

Figure 6.13: Variation in β parameter with slope inclination S at all liquefied depths for a relative density of 50%, from seven ground slope series profiles, with best-fit exponential function.

The final functional form for the predictive model relating CAV_{post} to shear strain, can be expressed as follows:

$$\gamma(z) = \beta(z) \cdot CAV_{post}(z) \tag{6.4}$$

where:

$$\ln \beta(z) = b_0 + b_1 D_R(z) + b_2/S + b_3 D_R(z)/S \tag{6.5}$$

6.4 Characterization of Demand Reduction Due to Excess Pore Pressure Generation

It is important to recognize that the shielding effects described in Section 6.3.1 are not accounted for in current empirical models for liquefaction triggering or lateral spreading displacements. Liquefaction-induced reductions in ground motion intensities have been shown to not only

reduce strains at shallower depths by limiting post-shaking demands, but in some cases to prevent triggering from occurring entirely in layers that would otherwise be expected to liquefy based on current empirical procedures. In this section, a framework is presented for the characterization of demand reductions in terms of the final intensity measures of interest $PGA_{M,F}$ and CAV_F, based on factors that have been shown to affect permanent shear strains (i.e., relative density, slope inclination, and cumulative thickness) in ways that cause reduced transmission of ground motions to shallower layers.

Figures 6.14 and 6.15 illustrate the variation in PGA_M and CAV, respectively, with depth through the liquefiable zone for the base case of $D_R = 50\%$ and $S = 2\%$. The curves are divided into 6 bins according to the IM value at the base of the liquefiable zone, termed $IM(z_{max})$.

For low-intensity motion bins, the analyses show a characteristic amplification of both IMs below a limiting depth, and slight deamplification at shallower depths. This limiting depth varies with the ground motion amplitude, becoming progressively deeper and eventually disappearing for the higher-intensity bins. Overall, the larger the ground motions, the larger the reduction in total IM at shallower depths. It is also worth noting the general similarities between the shapes of the $PGA_{M,F}(z)$ and $CAV_F(z)$ curves, indicating that their reduction behaviors may exhibit some degree of correlation to one another. There is a considerable within-bin variance - particularly in the case of PGA_M reduction at high shaking amplitudes. The higher variance in PGA_M has a dynamical basis, related mainly to its higher-frequency nature compared with CAV; the shorter wavelengths associated with PGA_M would result in higher variability within a soil profile. As will be demonstrated in Section 6.4.2, some of this variation can be explained using an estimate of the level of shaking at the base of the deepest liquefiable zone, defined here as z_{max}. In a practical sense, it may not always be clear what depth coincides with the "deepest liquefiable zone", particularly in profiles where the relative density varies smoothly with depth from a value that may not trigger to a value that does trigger. In such cases, it is important to recognize what the shaking intensity at z_{max} represents, which is a measure of the shaking intensity going into the liquefiable zone, and should be selected at a depth where the motion is unlikely to be altered by excess pore pressure generation, and could be estimated using ground motion prediction equations (i.e., total stress-based motions).

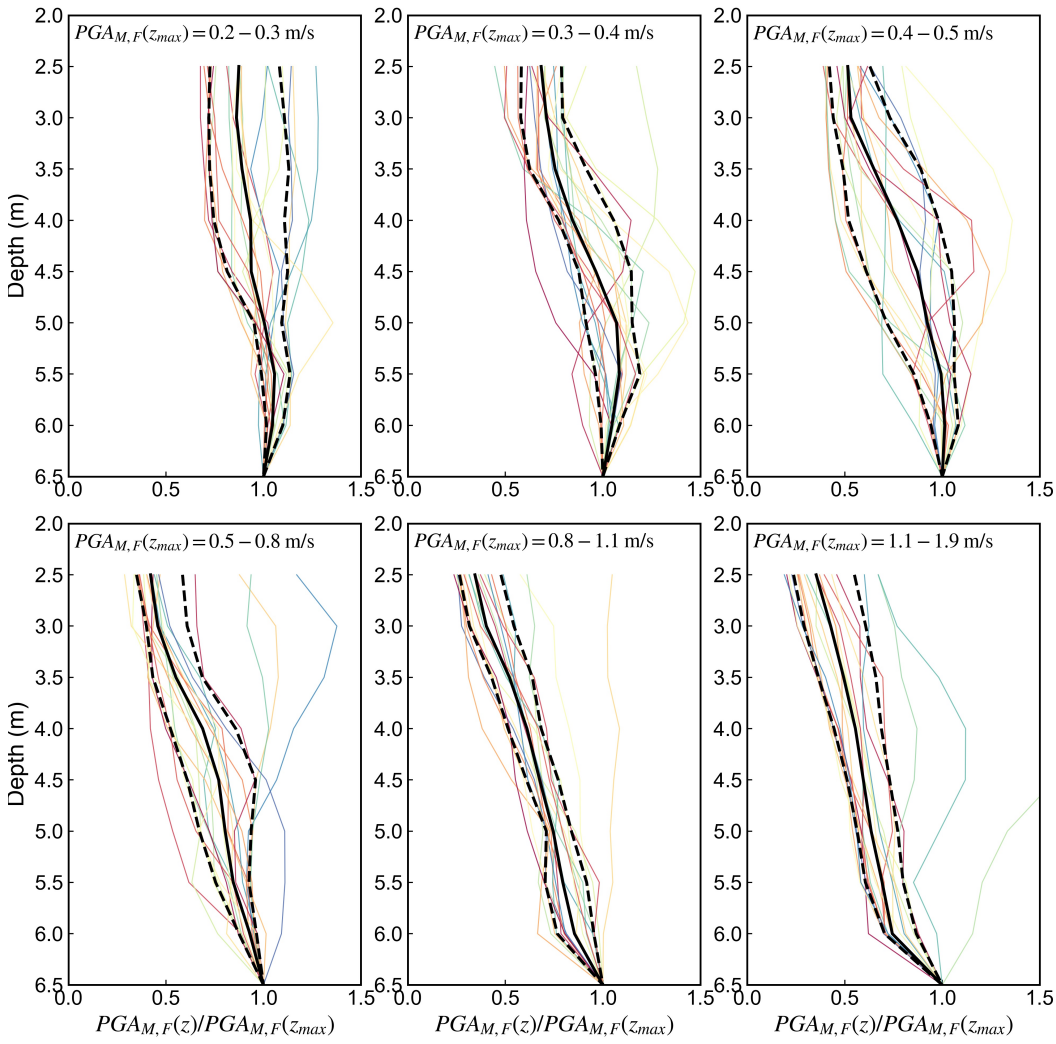

Figure 6.14: Median, 16th, and 84th percentile curves showing variation in $PGA_{M,F}$ through liquefiable zone for the base case profile with $D_R = 50\%$ and $S = 2\%$. Curves are binned by $PGA_{M,F}$ value at the base of the liquefiable zone. Individual ground motion curves are color-shaded from blue (minimum bin value) to red (maximum bin value), according to $PGA_{M,F}(z_{max})$

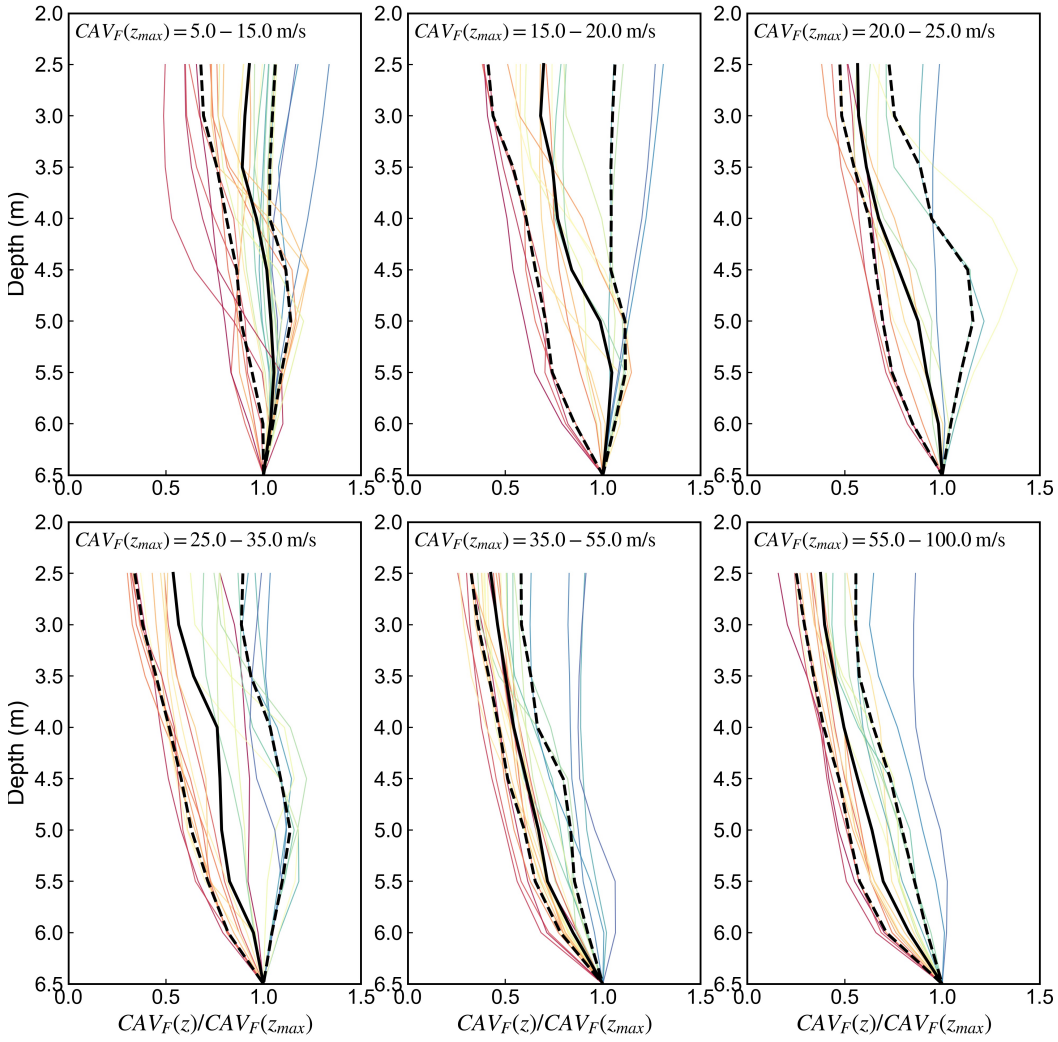

Figure 6.15: Median, 16th, and 84th percentile curves showing variation in CAV_F through liquefiable zone for the base case profile with $D_R = 50\%$ and $S = 2\%$. Curves are binned by CAV_F value at the base of the liquefiable zone. Individual ground motion curves are color-shaded from blue to red according to $CAV_F(z_{max})$

The *demand reduction ratios* for PGA_M and CAV, are defined for the final shaking intensities as the ratio of the IM at a depth z to the IM value at the base of the liquefied zone at depth z_{max}:

$$r_P(z) = PGA_M(z)/PGA_M(z_{max}) \tag{6.6}$$

$$r_C(z) = CAV(z)/CAV(z_{max}) \tag{6.7}$$

6.4.1 Variation in Demand Reduction with Cumulative Thickness

From a physical standpoint, it is not the depth, but rather the cumulative thickness of liquefiable soils, that contributes to a reduction in ground motion intensities, due not only to the dissipation of energy due to inelastic behavior in liquefied soils, but wave scattering effects due to impedances between the non-liquefied and liquefied zones. This wave scattering effect is discussed in Kramer (1996) in terms of heterogeneities in density and/or stiffness in geologic materials that causes increases in reflection and refraction in seismic waves at material boundaries. Kramer (1996) showed mathematically for a simple case of an elastic rod that stress amplitudes are reduced when waves travel from a stiff material into a material with lower stiffness (e.g., a liquefied soil) become larger with both the impedance ratio and length of the softer material. In terms of wave propagation through a liquefied zone, the impedance ratio is a function of the degree of softening that occurs, which depends on the initial density of the soil and the intensity of the input motion, and the length of the "inclusion" in the elastic rod can be thought of as the thickness of the liquefied zone.

As a result, any predictive form for r_P and r_C should thus be expressed in terms of the cumulative thickness of liquefiable soils underlying a particular depth, which is described by the term $H_{j,Liq}$. The motivation for using the cumulative thickness $H_{j,liq}$ instead of just depth is that it will later be modified to be applicable to more complex profiles with differing layer depths, relative densities, and layer sequences.

For the same base case profile ($D_r = 50\%$), OpenSees analyses using a small pool of about 25 motions from relatively narrow range of $IM(z_{max})$ values produced the the variation in r_P and r_C with $H_{j,Liq}$ shown in Figure 6.16. Despite a degree of variability, there is a clear decrease in the demand relative to the base of the liquefiable layer as $H_{j,liq}$ increases (i.e. at shallower layers), with a small number of motions exhibiting amplification behavior at some or all depths. The fitted curves in Figure 6.16 were obtained using regression based on an exponential function on this particular pool of data, with an intercept of $r_{IM} = 1.0$ at the base of the liquefied zone ($H_{liq} = 0$ m), suggesting an initial form for a first-order approximation of the relationship between the IM reduction factor (generically referred to as r_{IM} here) and accumulated thickness:

$$r_{IM} = \exp(C_{1,IM} H_{j,Liq}) \tag{6.8}$$

where $C_{1,IM}$ is a regression coefficient for either r_P ($C_{1,P}$) or r_C ($C_{1,C}$). Note that while both fitted curves reasonably seem to capture the reduction behavior in an average sense, the presence of a significant data in which the reduction ratios are greater than one (corresponding to amplification, rather than deamplification) contributes to the uncertainty in the fitted data, and provide strong

justification for relating the log of r_{IM} to $H_{j,Liq}$.

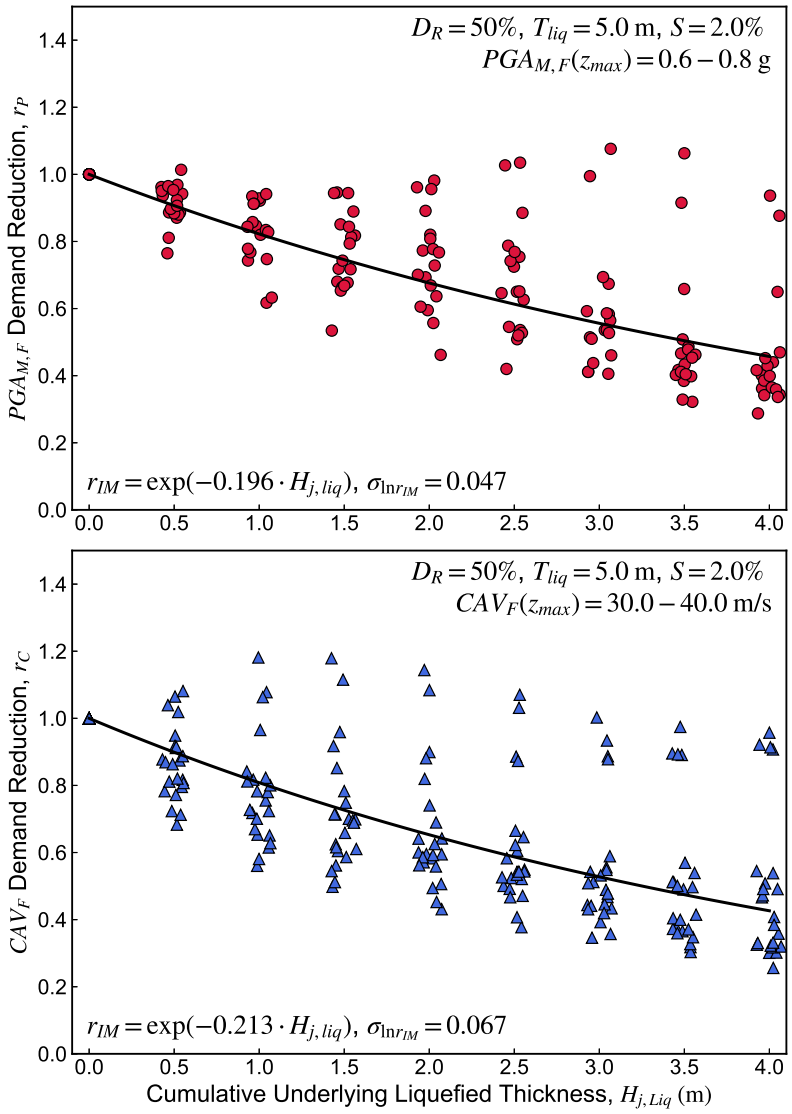

Figure 6.16: Variation in demand reduction ratios for PGA_M (r_P) and CAV (r_C) with respect to accumulated thickness $H_{j,liq}$, for $D_R = 50\%$ profile and median ground motion bin

6.4.2 Variation in Demand Reduction with Shaking Intensity

To investigate the effects of shaking intensity on the demand reduction behavior, the r_{IM}-$H_{j,Liq}$ data were fit with the exponential model for the full set of motions for the $D_R = 50\%$ profile. The variation in $C_{1,IM}$ with PGA_M and CAV at the base of the liquefied zone are shown in Figure 6.17, indicating that both the coefficients $C_{1,p}$ and $C_{1,C}$ are correlated to the base ground motion. Based on the standard deviations for C_1, the more efficient predictor of the demand reduction is $PGA_M(z_{max})$ for both $C_{1,P}$ and $C_{1,C}$; although it appears that the coefficient for r_P is somewhat

less predictable than that of r_C. That PGA_M is the more efficient predictor of the demand reduction should not come as a surprise; many ground motion models for PGA and spectral amplitude use the estimate soft rock PGA value (at $V_{s30} = 760$ m/s) to account for nonlinearity in amplification factors for soft sites.

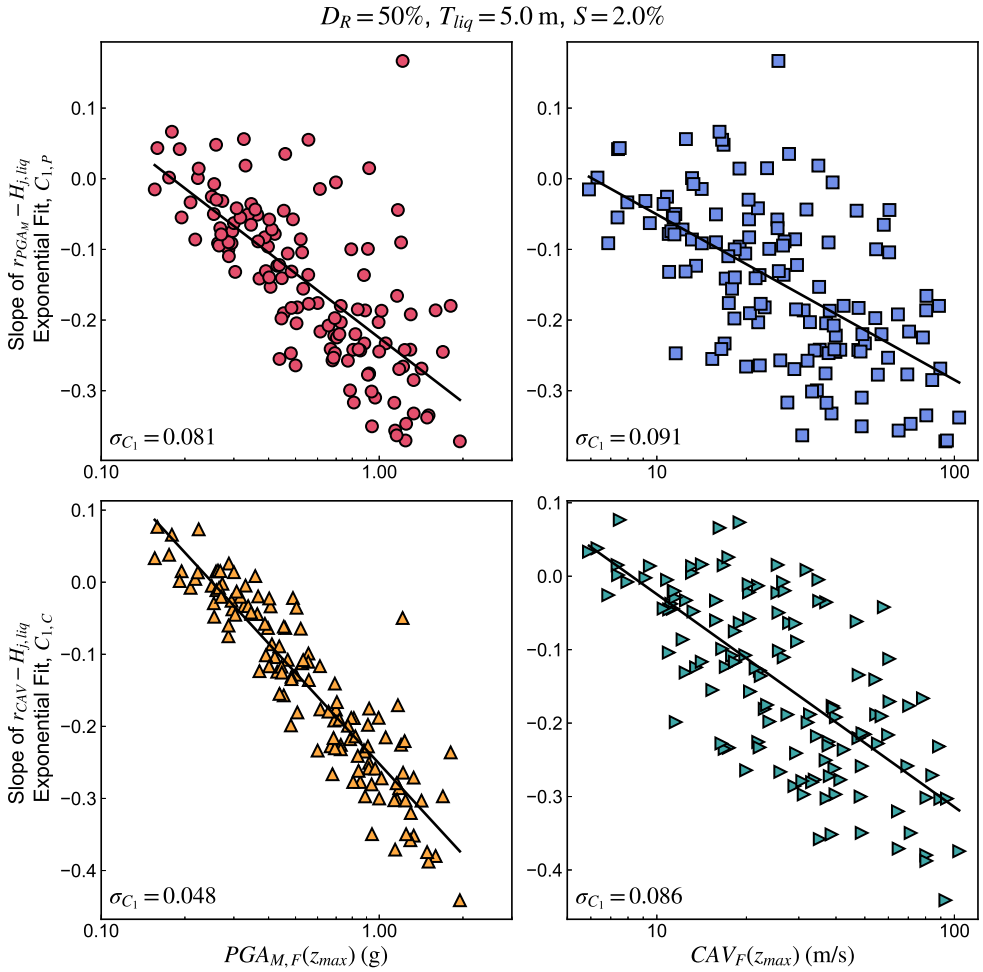

Figure 6.17: Variation in $r_{IM} - H_{j,Liq}$ exponential coefficient, $C_{1,IM}$ with respect to PGA_M and CAV values at the base of the liquefiable zone, for $D_R = 50\%$ relative density series profile.

Based on the data in Figure 6.17, the dependence of the $C_{1,IM}$ parameter on $PGA_M(z_{max})$ can be be modeled as follows:

$$C_{1,IM} = d_1 \ln[PGA_M(z_{max})] + d_0 \tag{6.9}$$

where d_1 and d_0 are coefficients for either r_P (d_{1p}, d_{0p}) or r_C (d_{1c}, d_{0c}).

6.4.3 Variation in Demand Reduction with Relative Density

The effects of relative density on the demand reduction behavior were investigated by fitting the r_{IM}-$H_{j,Liq}$ data with the exponential model (see Equation 6.8) for the full set of relative density series profiles. Figure 6.18 shows the variation in the $C_{1,P}$ and $C_{1,C}$ coefficients with respect to the base $PGA_{M,F}$ for all relative density cases. For the PGA_M reduction factor coefficient $C_{1,P}$, both the slope d_1 and intercept d_0 increase (i.e., become less negative) as D_R increases, although the correlation between $C_{1,P}$ and PGA_M becomes quite weak for the denser profiles. This effect makes sense from a mechanics standpoint, as soil layers with higher relative densities, and thus more resistance to liquefaction, will inhibit the reduction of demands at shallower depths (see Figure 6.5); in the exponential decay representation of demand reduction, this would lead to a coefficient that is less negative. Initially, this behavior suggests some interaction in the PGA_M reduction behavior between the base PGA_M and relative density, and the expression for $C_{1,P}$ in Equation 6.9 can be expanded to account for the effects of density via:

$$C_{1,P} = d_{0p} + d_{1p} \ln PGA_M + d_{2p} D_R + d_{3p}(D_r \cdot \ln PGA_M) \tag{6.10}$$

In the case of the CAV reduction coefficient $C_{1,C}$, the slope d_{1c} is largely insensitive to relative density (and thus there is no interaction between PGA_M and D_R), while the intercept d_0 appears to increase with increasing relative density, and can be estimated as a linear function of D_R. Accounting now for relative density, $C_{1,C}$ can be estimated via:

$$C_{1,C} = d_{0c} + d_{1c} \ln PGA_M + d_{2c} D_R \tag{6.11}$$

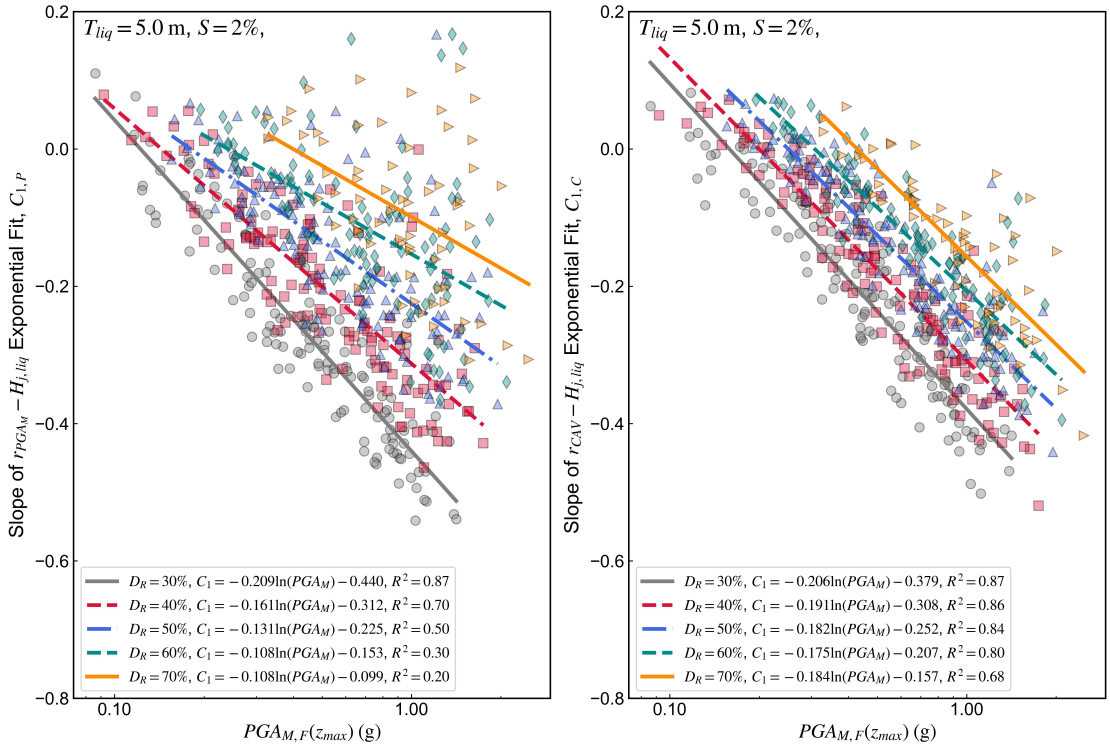

Figure 6.18: Variation in $C_{1,P}$ and $C_{1,C}$ coefficients with respect to $PGA_{M,F}(z_{max})$ for all relative density series profiles.

6.4.4 Variation in Demand Reduction with Ground Slope Inclination

Revisiting the ground slope analysis series profiles from Section 6.3.3, the r_{IM}-$H_{j,Liq}$ data were fit once again with the exponential model in Equation 6.8. Figures 6.19 and 6.20 show the variation in the $C_{1,P}$ and $C_{1,C}$ coefficients, respectively, with respect to the base $PGA_{M,F}$ for all ground slope cases. The coefficient of the exponential function C_1 is negative over nearly all slope conditions, and increases as the slope inclination increases. This variation is to be expected, since steeper slopes (and thus larger static stresses) result in fewer reversals of stress during ground shaking, thereby delaying the triggering of liquefaction, reducing fabric-related softening in the profile, and inhibiting the dissipation of energy in deeper liquefiable layers.

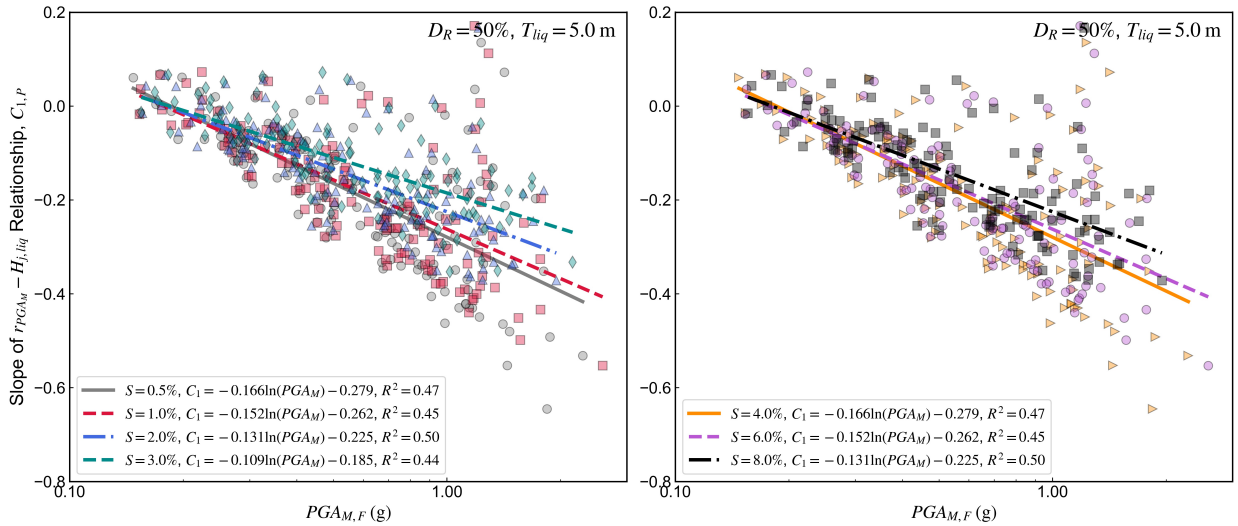

Figure 6.19: Variation in PGA_M reduction coefficient $C_{1,P}$ with base $PGA_{M,F}$ for all ground slope series profiles

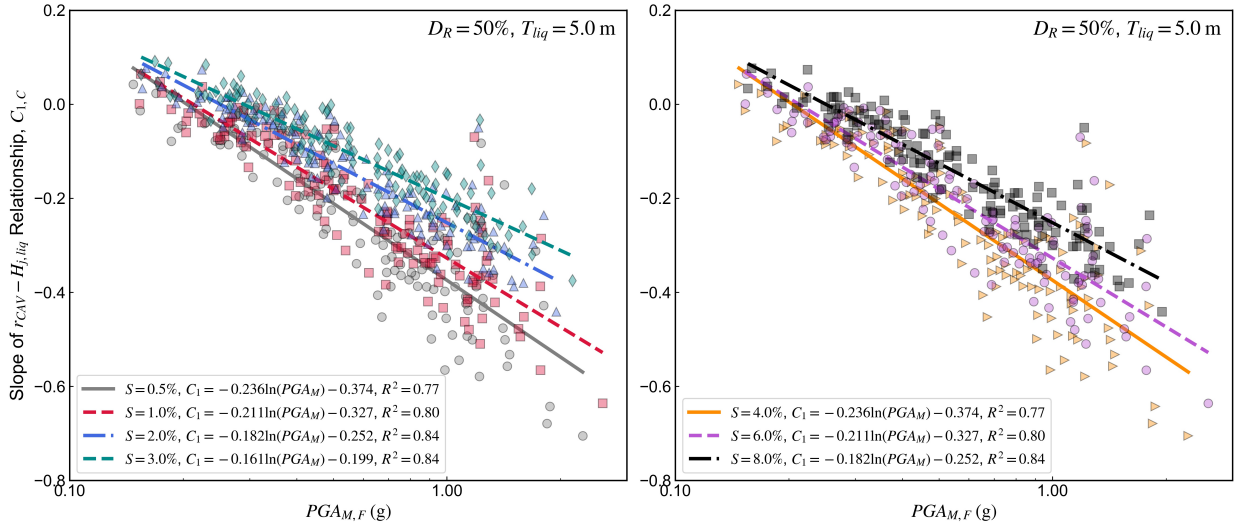

Figure 6.20: Variation in CAV reduction coefficient $C_{1,C}$ with base $PGA_{M,F}$ for all ground slope series profiles.

The results shown in Figures 6.19 and 6.20 indicate some sensitivity in the slope d_1 and intercept d_1 of the $C_{1,IM}$-ln PGA_M relationships coefficients to ground slope inclination. Figure 6.21 shows the $C_{1,IM}$ values from two $PGA_M(z_{max}$ bins plotted against ground slope. In addition to a clear trend of increasing C_1 with increasing S, the slope of the $C_{1,IM}$-ln S best fit lines are also sensitive to the ground motion bin, suggesting that an interaction term between $PGA_M(z_{max})$ and S may be needed in the equations for both the PGA_M and CAV reduction coefficients.

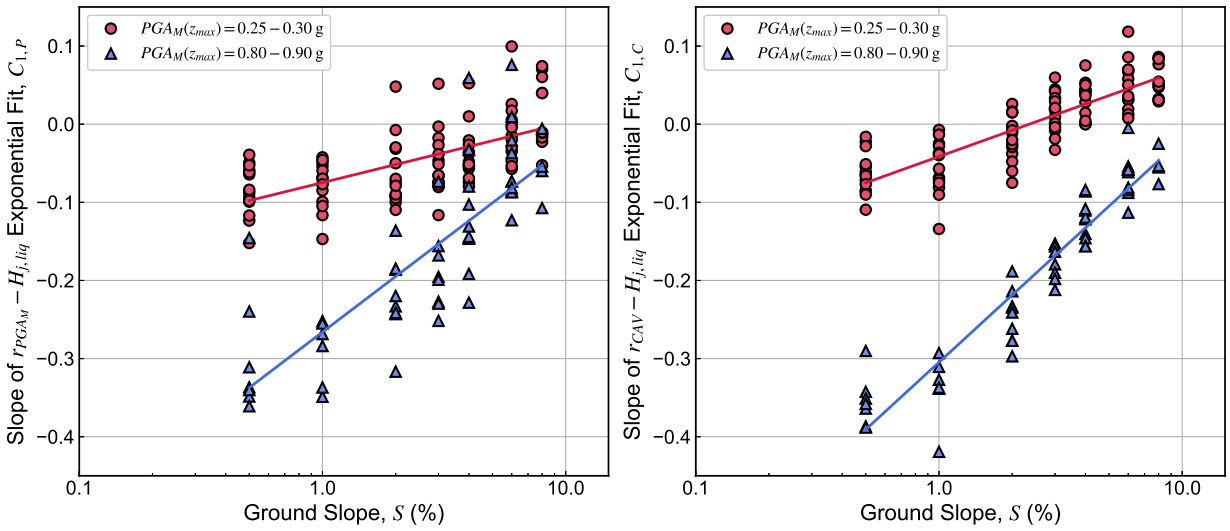

Figure 6.21: Variation of PGA_M and CAV reduction coefficients $C_{1,IM}$ with ground slope inclination for two $PGA_{M,F}$ bins.

Combined Effects of Relative Density and Slope on Demand Reduction

Because the effects of static shear stress on liquefaction triggering and its related effects can vary significantly depending on the relative density of the soil in question, it stands to reason that there will be a combined effect of the two on the demand reduction behavior. The significance of this interaction was investigated by considering a "combined D_R-S series" where models of each combination of relative density and slope inclination were analyzed. The $C_{1,IM}$-$\ln S$ data from these analyses are shown in Figure 6.22 for the median $PGA_M(z_{max})$ bin. The sensitivities of the slopes of the best fit lines to D_R for both the PGA_M and CAV reduction factors indicate at least some contribution of the combined effects of S and D_R, potentially more so for $C_{1,C}$.

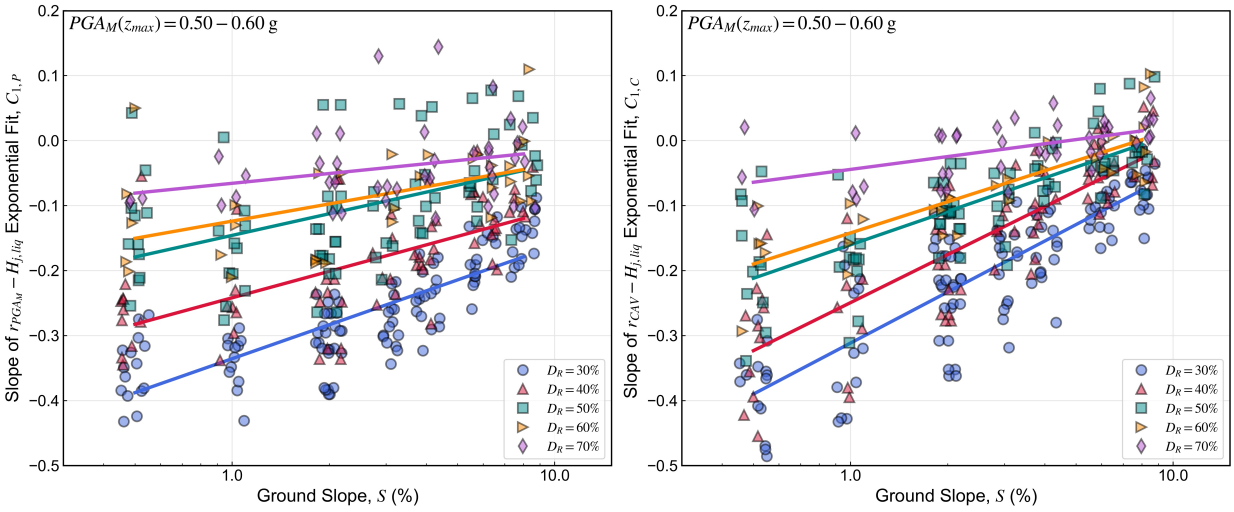

Figure 6.22: Variation of PGA_M and CAV reduction coefficients $C_{1,IM}$ with ground slope inclination and relative density, for a single $PGA_{M,F}$ bins. Ground slope values are randomly jittered to illustrate point density.

The functional form for $C_{1,P}$ from Equation 6.10 is thus modified to include the slope dependency and D_R-slope interaction terms as follows:

$$C_{1,P} = d_{0p} + d_{1p} \ln PGA_M + d_{2p} D_R + d_{3p}(D_r \cdot \ln PGA_M) + d_{4p} \ln S + d_{5p}(\ln PGA_M \cdot \ln S) + d_{6p}(D_R \cdot \ln S) \tag{6.12}$$

while the expression for $C_{1,C}$ from Equation 6.11 is similarly modified:

$$C_{1,C} = d_{0c} + d_{1c} \ln PGA_M + d_{2c} D_R + d_{3c} \ln S + d_{4c}(\ln PGA_M \cdot \ln S) + d_{5c}(D_R \cdot \ln S) \tag{6.13}$$

where all d variables are regression coefficients.

6.4.5 Statistical Model for Predicting Demand Reduction Behavior for Uniform Relative Density Profiles

The proposed equations for predicting the final $PGA_{M,F}(z)$ at depths where soils are underlain by continuous layers of liquefiable deposits are presented as follows:

$$PGA_{M,F}(z) = r_P \cdot PGA_{M,F}(z_{max}) \tag{6.14}$$

where $PGA_{M,F}(z_{max})$ corresponds to the motion at the base of the liquefiable zone, and r_P is a reduction factor that relates to the cumulative thickness of underlying liquefiable soils, $H_{j,Liq}$ via:

$$r_P = \exp(C_{1,P} H_{j,Liq}) \tag{6.15}$$

where the coefficient $C_{1,P}$ can be predicted from $PGA_{M,F}(z_{max})$, the relative density of the underlying liquefiable soils D_R, and the ground slope inclination S via:

$$\begin{aligned} C_{1,P} = d_{0p} + d_{1p} \ln PGA_M + d_{2p} D_R + d_{3p}(D_r \cdot \ln PGA_M) \\ + d_{4p} \ln S + d_{5p}(\ln PGA_M \cdot \ln S) + d_{6p}(D_R \cdot \ln S) \end{aligned} \tag{6.16}$$

Similarly, the proposed equations for predicting the final value of $CAV_F(z)$ are as follows:

$$CAV_F(z) = r_C \cdot CAV_F(z_{max}) \tag{6.17}$$

where $CAV_F(z_{max})$ is computed from the motion at the base of the liquefiable zone, and:

$$r_C = \exp(C_{1,C} H_{j,Liq}) \tag{6.18}$$

The coefficient $C_{1,C}$ can be predicted via:

$$C_{1,C} = d_{0c} + d_{1c} \ln PGA_M + d_{2c} D_R + d_{3c} \ln S + d_{4c}(\ln PGA_M \cdot \ln S) + d_{5c}(D_R \cdot \ln S) \tag{6.19}$$

All d variables are regression coefficients, which were estimated using the combined data from the relative density, ground slope, and combined D_R-S parametric analysis series. The results of the linear regression indicate that the interaction between slope and relative density is significant for both IM reduction factors; the estimated coefficients are summarized in Table 6.1. The lognormal standard deviation of the forward-predicted $PGA_M(z)$ and $CAV(z)$ values was 0.171 and 0.122,

respectively.

Table 6.1: Linear regression of coefficients for PGA_M and CAV reduction factors

Predictor	Coefficient	Value	
		r_{PGA_M}	r_{CAV}
Intercept	d_0	-0.715	-0.643
$\ln PGA_M(z_{max})$	d_1	-0.225	-0.217
Relative Density, D_R	d_2	0.889	0.65
$\ln PGA_M(z_{max}) \cdot D_R$	d_3	0.19	-
Slope inclination, $\ln S$	d_4	0.149	0.189
$\ln PGA_M(z_{max}) \cdot \ln S$	d_5	0.0276	0.0448
$D_R \cdot \ln S$	d_6	-0.1733	-0.17
	$\sigma_{\ln IM}$	0.171	0.122

The demand reduction behavior for the fitted PGA_M and CAV reduction models is shown in Figures 6.23 and 6.24, respectively, showing the model sensitivity to relative density, slope inclination and PGA_M at the base of the liquefied soil for the simplified profiles analyzed in the parametric study.

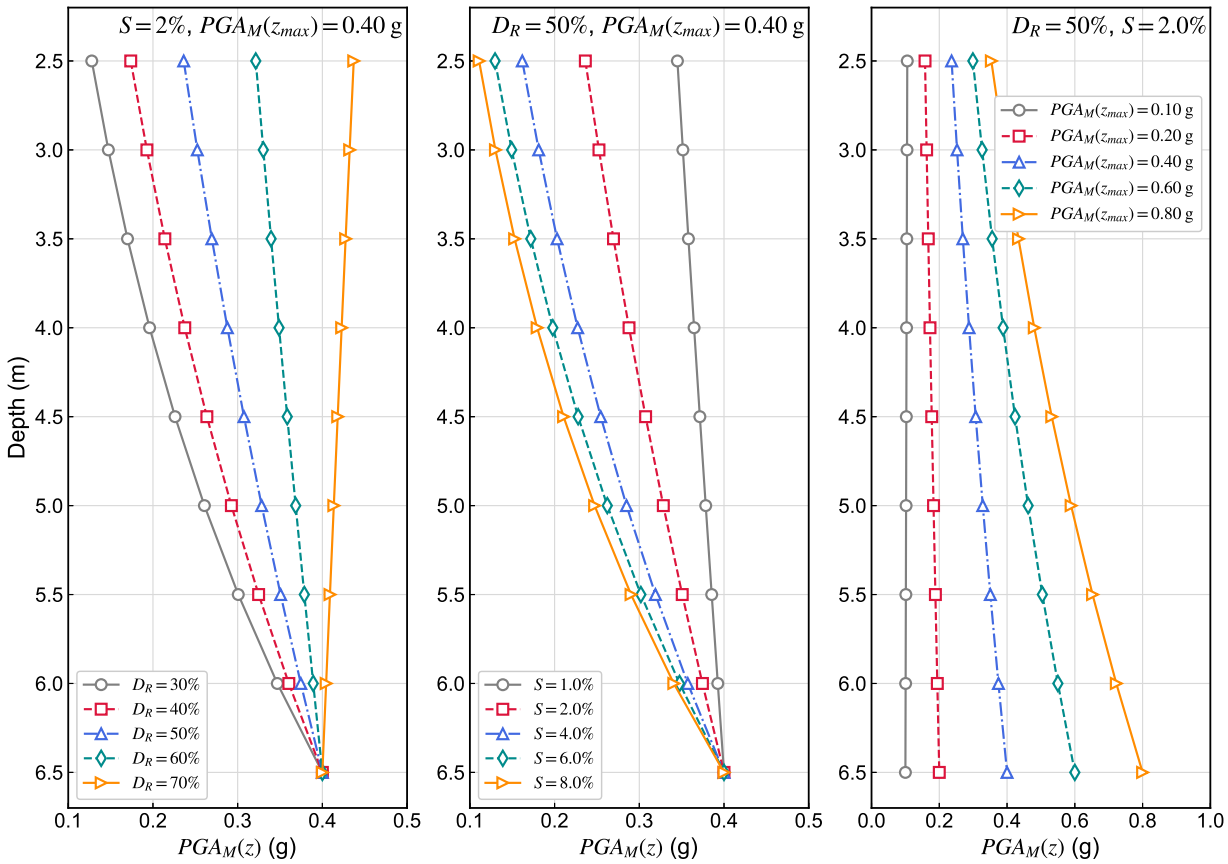

Figure 6.23: Sensitivity of proposed PGA_M demand reduction model to relative density, ground slope inclination, and ground shaking intensity.

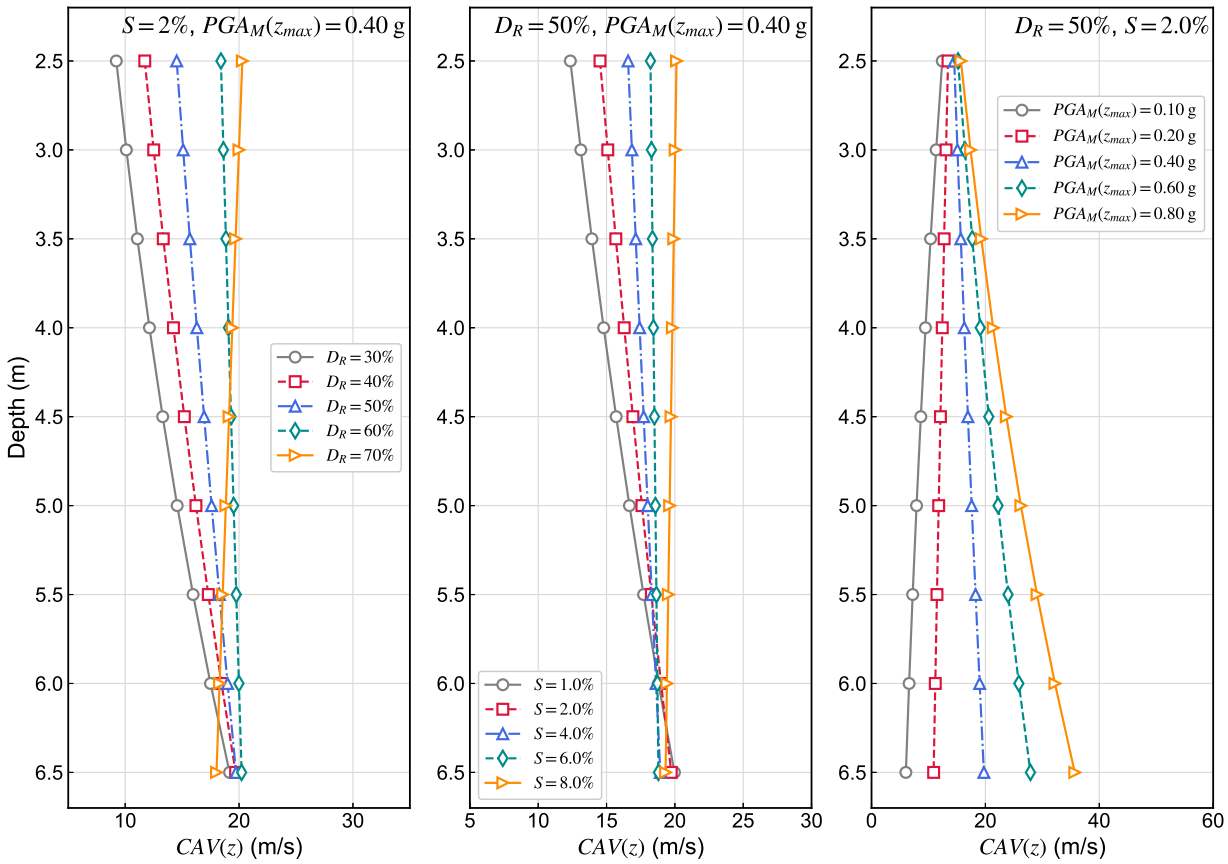

Figure 6.24: Sensitivity of proposed CAV demand reduction model to relative density, ground slope inclination, and ground shaking intensity.

6.5 Summary and Concluding Remarks

This chapter presented a large-scale parametric study, aimed at systematically investigating the factors that influence lateral spreading deformation within a timing-based framework. The data used in this study was developed from a series of nonlinear effective stress analyses of one-dimensional soil columns, using the finite-element platform OpenSees. The generation and execution of these models was facilitated by a workflow that was developed to efficiently create large batches of models, systematically vary certain parameters, run a large set of ground motions through each model, and post-process and compile the data on the Stampede2 supercomputer, a resource of the Texas Advanced Computing Center (TACC).

The sensitivity of post-triggering permanent shear strains to various factors such as ground shaking intensity, the relative density, depth, and thickness of the liquefiable layers; and inclination of the ground surface, was systematically investigated using a series of relatively simple models, and a functional form for predicting permanent strains as a function of these factors was developed

and presented in Equations 6.4 and 6.5.

Also of interest in this study was an effect consistently observed in a wide range of analysis cases, namely significant non-uniformity of shear strains within specific liquefiable layers, attributed to a reduction in shaking demand in shallow layers due to the occurrence of liquefaction in deeper layers (also referred to as the "shielding effect"). The reduction of two intensity measures, PGA_M and CAV, by this shielding, from the entire ground motion was also investigated in this chapter, leading to the development of a predictive model for estimating reduction factors for these two IMs at particular depth. The analyses showed that the demand reduction could be represented as a function of the cumulative thickness and relative density of the underlying liquefiable soils, the shaking intensity at the base of the liquefied zone, and the ground slope inclination. This iteration of the model is applicable to the simple, uniform profiles that were used in its development and coefficient estimation, but will serve as a useful basis for extension to the more realistic and complex soil profiles that will be presented in the next chapter.

Chapter 7

A Probabilistic, Timing-Based Framework for Predicting Lateral Spreading Deformations

7.1 Introduction

The previous chapter presented a sensitivity study, based on a large set of numerical analyses of simple soil profiles in OpenSees, in which two critical components of the lateral spreading problem were characterized within a timin-based framework. A relative simple relationship was developed for relating post-liquefaction permanent shear strains in soils to their static stress conditions (represented by the ground slope inclination), relative density, and post-triggering ground motion intensity. Additionally, recognizing that current procedures for estimating liquefaction triggering and shear strains tend to neglect system effects, a simple method for characterizing the reduction in seismic demands due to liquefaction in deeper soil layers was developed based on the input shaking intensity into, and the relative density and thickness of the liquefiable zone.

The following chapter extends these two concepts to more complicated profiles and shows how they might be utilized in a broader, timing-based framework for predicting lateral spreading displacements probabilistic. The shear strain and demand reduction formulations are modified and regressed against a larger set of numerical analyses of more complex and randomized soil profiles to obtain a more complete understanding of the variability in predicting system effects and shear strains. Finally, these components are incorporated into a hypothetical strain-integration procedure, which is applied to a fully-probabilistic, timing-based framework for predicting hazard curves for lateral spreading displacements.

7.2 Development and Analysis of Randomized Soil Profiles

The soil profiles that were analyzed in Chapter 6 isolated the effects of shaking intensity, relative density, layer thickness, and ground slope inclination in order to establish the basic functional forms for characterizing the shielding effect and relating the permanent shear strains to the post-triggering shaking intensity. However, to assess the applicability of the model framework and to gain a more complete understanding of the uncertainties in each prediction component, these equations must be regressed against more realistic soil profiles. In particular, the initial sets of profiles consisted mainly of single layers of liquefiable soils with a uniform relative density, and may not have exhibited the full range of complex system behaviors that may be expected from typical liquefiable sites. This motivated the need to consider more complex profiles containing multiple liquefiable layers with different relative densities that may or may not be separated by non-liquefiable layers.

To generate such data, a randomization scheme was developed for four types of profiles, corresponding to soil profiles consisting of one, two, three, or four layers of liquefiable soils. The basic layering sequences and randomized parameters are shown in Figure 7.1. The procedure for generating the profile is described as follows, with all layer thicknesses sampled at 1 m-thick resolution.

1. The depth to groundwater (D_{GWT}) was randomly chosen from 0 to 4 m, with equal weighting, and a corresponding layer of surficial crust (PM4Sand with zero-pore pressure boundary condition) was modeled from the surface to D_{GWT}.

2. The depth to the top of the liquefiable zone $D_{L,top}$ was randomly sampled from D_{GWT} to 8 m, with uniform weighting from 0 to 6 m, and 10% relative weight for depths greater than 6 m. The material between D_{GWT} and $D_{L,top}$ was modeled as a stiff PM4Silt material.

3. The thickness of the liquefiable *zone* H_L (including potentially non-liquefiable interlayers) was randomly selected from 2 to 6 times the number of liquefiable layers N_L; in the case of the four-layer profiles, the maximum critical zone thickness was capped at 20 m. H_L was selected according to a triangular distribution, with weights varying from 0.15 at the upper- and lower-bounds to 0.35 at the middle of the range, in order to obtain a slightly more representative sample of liquefiable zone thicknesses that one might encounter in field conditions.

4. The number of non-liquefiable interlayers, N_{NL} was randomly selected from zero to one fewer than N_L, with a uniformly weighted distribution. Including zero layers in the sampling range allows for profiles with continuous zones of liquefiable soil, but with potentially different relative densities.

5. The thickness T_s of the each sublayer within the critical zone were selected sequentially, with the minimum and maximum thicknesses of each layer controlled by the minimum layer

thickness in the model (1.0 m in this study), and the maximum "available" thickness remaining in the liquefiable zone. For instance, the thickness of the first layer to be sampled would have a range of:

$$T_{min,1} = 1.0 \tag{7.1}$$

$$T_{max,1} = H_L - 1.0[(N_L - 1) + N_{NL}] \tag{7.2}$$

where the second term in the expression for $T_{max,1}$ allows for the remaining sublayers to have non-zero thickness, should the maximum value be randomly chosen. For subsequent layers, T_{max} was calculated via:

$$T_{max,j} = H_L - \left(\sum_{n=0}^{n=j-1} H_{L,n} \right) - 1.0[(N_L - j) + N_{NL}] \tag{7.3}$$

where the summation term represents the cumulative thickness of sublayers that have been sampled so far, which must be subtracted from the overall thickness to get overall remaining available thickness. The thicknesses were sampled from a uniform distribution; the same process was repeated for the non-liquefiable sublayers.

6. Relative densities in the liquefiable layer were also randomly selected at the same time that the sublayer thickness was assigned. D_R was selected from [30, 40, 50, 60, 70%], with slightly more weight given to the middle of the range ([0.18, 0.21, 0.22, 0.21, 0.18]). Relative densities in different sublayers were assumed to be independent of one another.

7. The locations of each sublayer were assigned by randomly sequencing them, with the constraint that the shallowest and deepest layers in the zone be liquefiable sublayers.

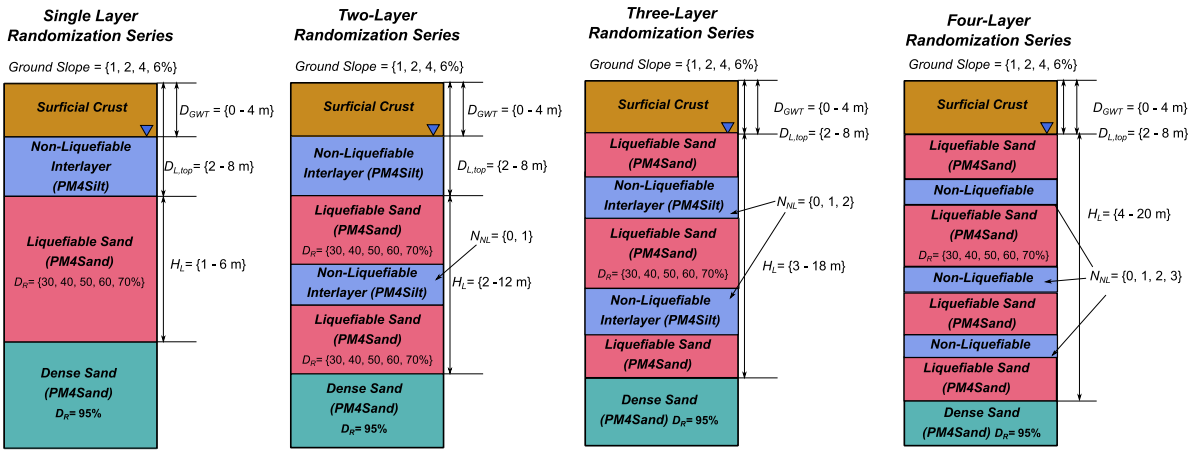

Figure 7.1: Soil layering sequence and parameter summary for randomized profiles.

For each layer series, 24 profiles were randomly generated for each slope inclination in the range of 1, 2, and 3 %; 18 profiles were generated with a slope angle of 4%, and 10 profiles were generated with a slope angle of 6%. Each profile was subjected to all 188 time histories developed for this study (Section 5.3) for a total of 57,000 analyses. The results were post-processed using the same methods outlined in Section 6.2; results where large strains due to liquefaction in PM4Silt interlayers were screened out in order to focus on the characterization of lateral spreading due to liquefaction in granular soils. The range of relative density depth profiles are shown for each randomly-generated series in Figure 7.2

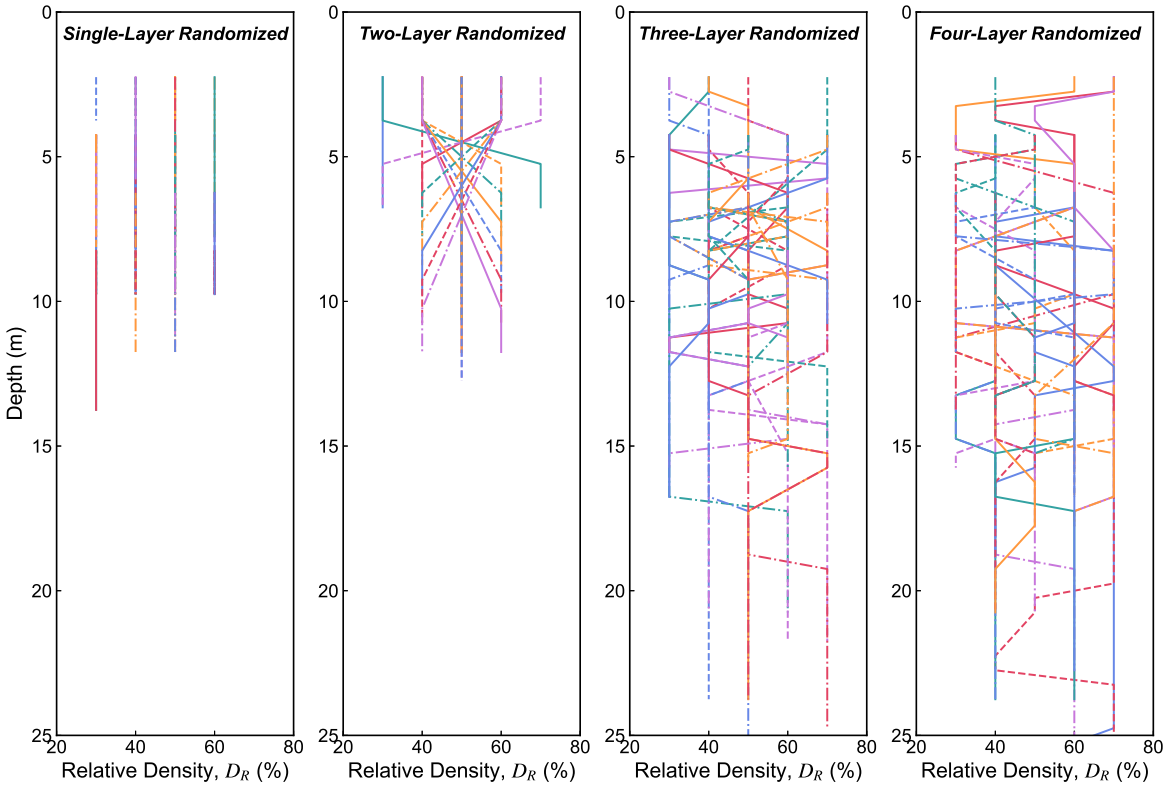

Figure 7.2: Randomly-generated relative density depth profiles for randomized soil profile series.

7.3 Regression of Probabilistic Model for Lateral Spreading Displacements Against Simulated Data

As discussed in Chapter 6, the proposed framework for predicting lateral spreading is based on characterizing two key mechanisms: the reduction of shaking demands in shallower layers due to liquefaction in deeper layers, and the relationship between post-triggering shaking intensity and permanent shear strains at the element level. These two components can be utilized in a broader framework to predict lateral spreading displacements in infinite sloping ground, conditional

on PGA_M and CAV at the base of the liquefiable zone and a given $PGA_{M,trig}$ at the time of liquefaction, as follows:

1. For a given combination of the final (end-of-motion) IMs at the base of the liquefied zone ($PGA_{M,F}(z_{max})$ and $CAVF(z_{max})$), profiles of the final IMs ($PGA_{M,F}(z)$ and $CAV_F(z)$ at other depths in the soil column are calculated using demand reduction factors that account for the system response by considering the density and thickness of the liquefiable soils, the slope inclination, and the base shaking intensity.

2. In each liquefiable sublayer, $PGA_{M,trig}(z)$ is estimated using an appropriate liquefaction triggering procedure (e.g., Boulanger and Idriss 2015), and divided by the final, estimated $PGA_M(z)$ to obtain the $\alpha_1(z)$ parameter (Equation 5.19).

3. At each depth, $\alpha_2(z)$ is estimated from $\alpha_1(z)$ using the model developed by Greenfield (2017) (Equation 5.22a). The value of α_2 is then used to estimate the post-triggering CAV, $CAV_{post}(z)$ using $CAV_F(z)$ (from Step 1) and Equation 5.20.

4. At each depth, the permanent shear strain $\gamma(z)$ is estimated from $CAV_{post}(z)$ and the $\beta(z)$ parameter presented in Section 6.3.

5. The final surface displacement D_H is estimated by integrating the shear strain profile with the individual sublayer thicknesses as follows:

$$D_H = \sum_{j=1}^{N_{liq}} [\gamma(z_j) \cdot \Delta H_j(z)] \tag{7.4}$$

In this section, each of the components listed above are regressed against the full dataset of randomized profiles. The suitability and uncertainty in each component is presented and discussed, and the overall displacement model is presented and evaluated. It is once again important to note that the coefficients presented herein are based only on simulated data from infinite slope models. The use of these models in practice requires calibration to field case histories, which is outside of the scope of this current study.

7.3.1 Regression of PGA_M and CAV Demand Reduction Model and Modification of Functional Form for Complex-Layered Soil Profiles

Recall from Chapter 6 that the $PGA_{M,F}(z)$ and $CAV_F(z)$ profiles could be estimated initially the $PGA_{M,F}(z_{max})$ and $CAV_F(z_{max})$ values at the base of the liquefied zone. In a forward-prediction framework, these values can be estimated from one or more empirical ground motions

models (GMMs) at the V_{s30} of the soil below the liquefiable soil. The values are then modified at various depths in the liquefiable zone using factors to account for the reduction in demand of PGA_M and CAV due to the presence of liquefiable layers:

$$PGA_{M,F}(z) = r_P(z) \cdot PGA_{M,F}(z_{max}) \tag{7.5}$$

$$CAV_F(z) = r_C(z) \cdot CAV_F(z_{max}) \tag{7.6}$$

As discussed previously, the initial formulation from Chapter 6 was based on profiles consisting of a single continuous zone of liquefiable soil with uniform relative density. In these cases, the ratio of IM in a given layer j to the IM at the base of the liquefied zone was characterized as an exponentially decaying function of the thickness liquefiable layers underlying layer j, $H_{j,Liq}$. For the purposes of applying this factor to the more complicated profiles generated for this study, the cumulative thickness is now presented as a summation of the underlying sublayers as $\sum_{i=1}^{j-1} H_{i,L}$, and the reduction factors are expressed as:

$$r_P(z_i) = \exp(C_{1P} \cdot \sum_{i=1}^{j-1} H_{i,L}) \tag{7.7}$$

$$r_C(z_i) = \exp(C_{1C} \cdot \sum_{i=1}^{j-1} H_{i,L}) \tag{7.8}$$

where the exponential coefficients $C_{1,P}$ and $C_{1,C}$ were shown to depend on the $PGA_{M,F}$ value at the base of the liquefiable zone, the ground slope inclination, and the relative density of the underlying layers as presented in Equations 6.16 and 6.19. The original formulation assumes that the relative density of the soil underlying the layer of interest is uniform. For more complicated profiles, however, the soil underlying a particular depth may consist of multiple sublayers, with different thicknesses and different relative densities. As such, D_R may vary within the liquefied zone in a manner that cannot be accommodated by Equations 7.7 and 7.8.

This variation in D_R can be accounted for by including the density-dependent terms in C_1 as part of the summation in Equations 6.16 and 6.19. The PGA_M reduction factor r_P, for example, can be split into two components, one that depends only on slope and PGA_M (C_{1PS}, which does not vary with depth), and a second component C_{1PL} that includes all terms involving D_R:

$$\ln r_{P,i} = C_{1PS} \sum_{i=1}^{j-1} H_L(z_i) + \sum_{i=1}^{j-1} [C_{1PL}(z_i) \cdot H_L(z_i)] \tag{7.9}$$

where the site term is:

$$C_{1PS} = d_{p0} + d_{p1} \ln PGA_M + d_{p3} \ln S + d_{p4} (\ln PGA_M \cdot \ln S) \tag{7.10}$$

and the density-dependent term is:

$$C_{1PL}(z) = d_{p2} D_R(z) + d_{p5} (D_r(z) \cdot \ln PGA_M) + d_{p6} (D_r(z) \cdot \ln S) \tag{7.11}$$

and d_{p0} through d_{p6} are regression coefficients. For the CAV reduction factor the equations look quite similar:

$$\ln r_{C,i} = C_{1CS} \sum_{i=1}^{j-1} H_L(z_i) + \sum_{i=1}^{j-1} [C_{1CL}(z_i) \cdot H_L(z_i)] \tag{7.12}$$

where:

$$C_{1CS} = d_{c0} + d_{c1} \ln PGA_M + d_{c3} \ln S + d_{c4} (\ln PGA_M \cdot \ln S) \tag{7.13}$$

and:

$$C_{1CL}(z) = d_{c2} D_R(z) + d_{c6} (D_r(z) \cdot \ln S) \tag{7.14}$$

and d_{c0} through d_{c6} are regression coefficients. This modified formulation produced the same result of Equations 7.7 and 7.7 in profiles with uniform relative densities, but allow for the different contributions in layers with different thicknesses and relative densities in more complex profiles to be accounted for.

The estimated coefficients for the regression of the reduction factors in Equations 7.9 and 7.12 are summarized in Table 7.1; the lognormal standard deviations reported are for the fitted values of $PGA_{M,F}(z)$ and $CAV_F(z)$, calculated by multiplying the fitted reduction factors from the regression by the known $PGA_{M,F}(z_{max})$ from each individual profile and ground motion combination. The standard deviations are higher for each IM using the full dataset of randomized profiles than those obtained for the simple profiles (Table 6.1), which were 0.17 and 0.12 for PGA_M and CAV, respectively. This is not a surprising result, considering the increase in complexity of profiles, as well as the range of types of profiles considered for the full model.

Table 7.1: Linear regression of coefficients for PGA_M and CAV reduction factors. D_R is in decimal, not percent.

Prediction Term	Coefficient	Value	
		r_P	r_C
Intercept	d_0	-0.281	-0.264
$\ln PGA_{M,F}(z_{max})$	d_1	-0.141	-0.131
Relative Density, D_R	d_2	0.873	0.105
$\ln PGA_{M,F}(z_{max}) \cdot D_R$	d_3	0.267	0.238
Slope inclination, $\ln S$	d_4	0.118	0.0906
$\ln PGA_{M,F}(z_{max}) \cdot \ln S$	d_5	0.0127	0.023
$D_R \cdot \ln S$	d_6	-0.0847	-0.0882
	$\sigma_{\ln IM}$	0.29	0.249

The average within-profile log-residuals for $PGA_{M,F}(z)$ and $CAV_F(z)$ are plotted against the cumulative thickness, ground slope, and base $PGA_{M,F}(z_{max})$ in Figures 7.3 and 7.4. The residuals are generally stable with respect to each predictor variable across the a wide range of applicable values; the residuals do become slightly negative on average at PGA_M values greater than about 0.80 g, indicating a slight over-prediction in $IM(z)$ profiles in extremely high-intensity motions. The behavior of the fitted model for various combinations of relative density, slope inclination, and $PGA_M(z_{max})$ is similar to the corresponding plots shown in Figures 6.23 and 6.24 for the uniform-layer model in the preceding chapter.

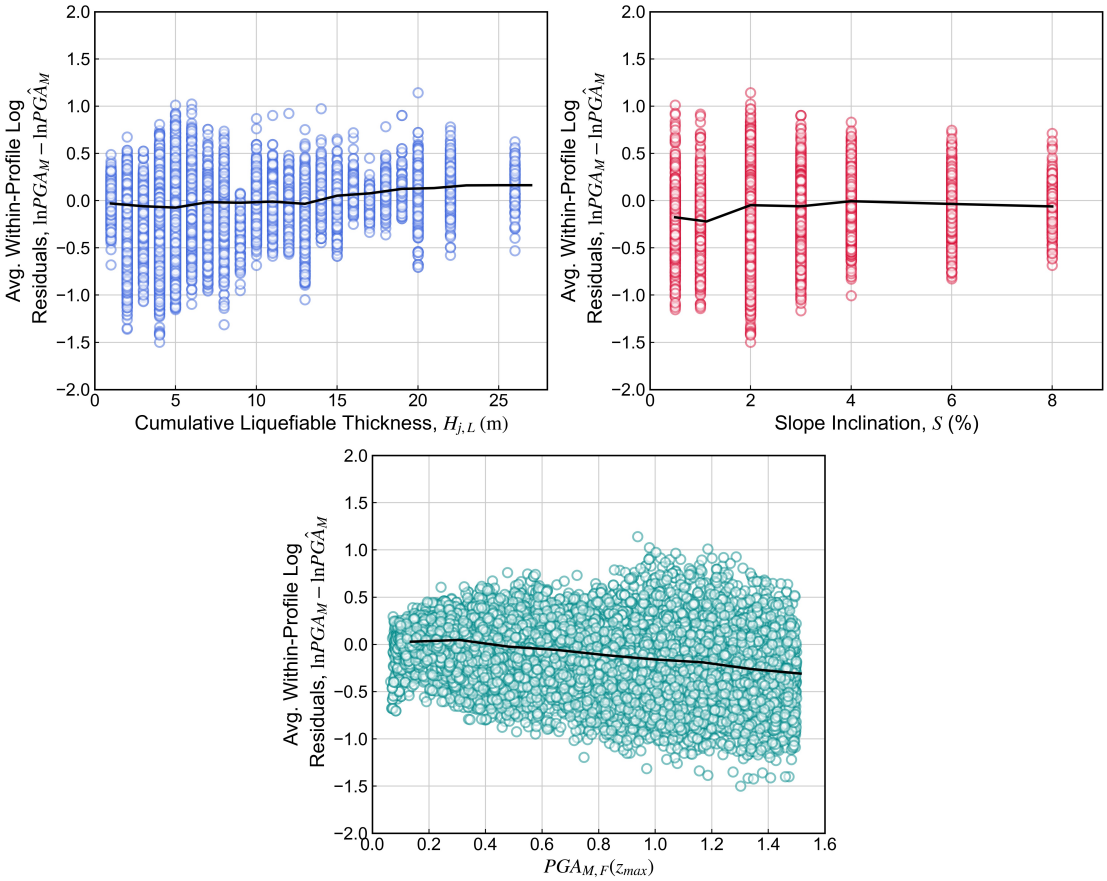

Figure 7.3: Within-profile average log-residuals of $PGA_{M,F}$, with moving averages, plotted against cumulative liquefiable thickness, slope inclination, and base $PGA_{M,F}(z_{max})$.

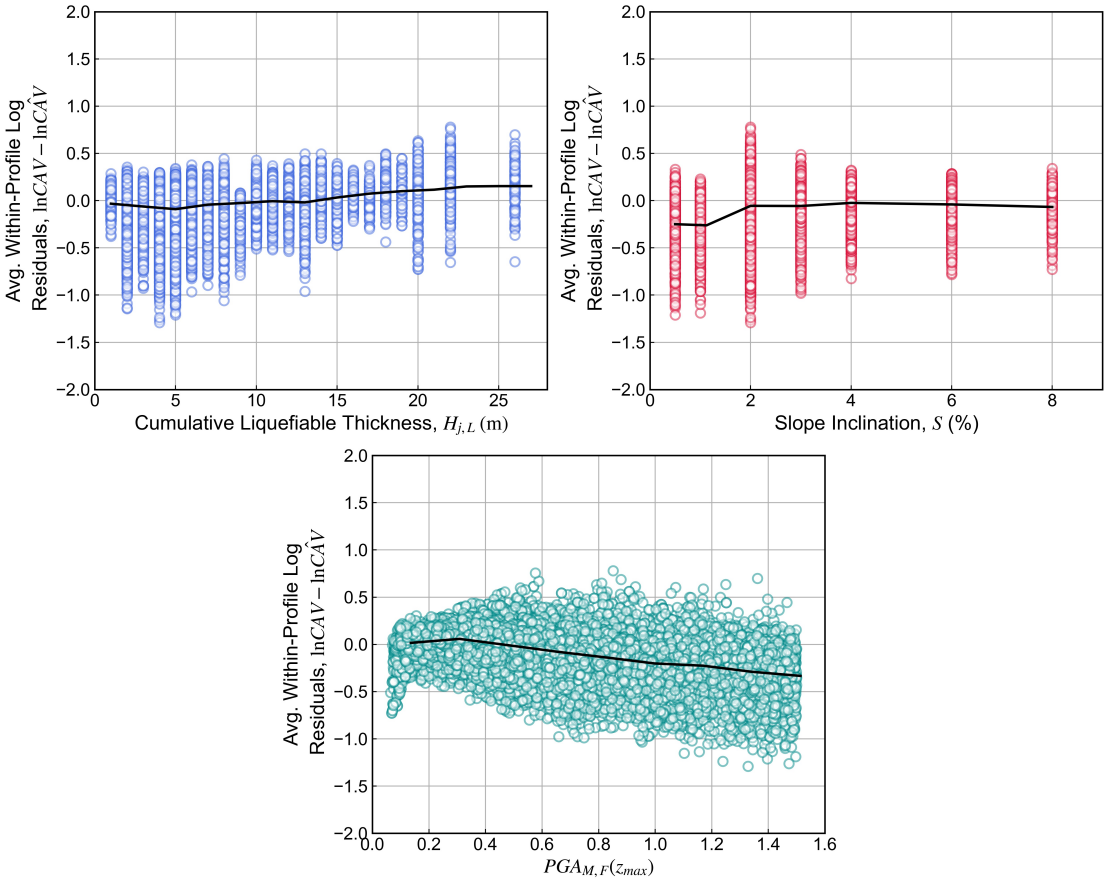

Figure 7.4: Within-profile average log-residuals of $CAVF$, with moving averages, plotted against cumulative liquefiable thickness, slope inclination, and base $PGA_{M,F}(z_{max})$.

7.3.2 Prediction of Post-Triggering CAV Using Normalized Evolutionary IM Correlations

As discussed in Section 5.5.1, Greenfield (2017) showed that, for soft-rock ground motions, the ratio of $PGA_M/PGA_{M,F}$ at the time of triggering could be related to the corresponding ratio of post-triggering CAV/CAV_F via:

$$\alpha_2 = \frac{a(\alpha_1)}{a(\alpha_1) + b(\alpha_1)} \tag{7.15}$$

where:

$$\ln a = 2.75 - 0.31 \ln \alpha_1 + 0.14 \ln (1 - \alpha_1) \tag{7.16}$$

$$\ln b = 1.91 + 0.93 \ln \alpha_1 - 0.10 \ln (1 - \alpha_1) \tag{7.17}$$

The suitability of this relationship for motions affected by pore pressure generation was evaluated in this study by extracting the $PGA_{M,trig}$ and CAV_{post} values at the time of liquefaction in all potentially liquefiable soil elements in the large-scale OpenSees analyses, dividing them by their respective final PGA_M and CAV values, and comparing the resulting effective stress $\alpha_1\alpha_2$ values with the Greenfield model. The results, shown in Figure 7.5, indicate that α_1-α_2 evolution behavior of effective stress motions is quite similar those from stiffer site; there is a relatively consistent downward shift of about 0.02 in the median, 16th, and 84th percentile curves, but the curve shapes and uncertainties are comparable.

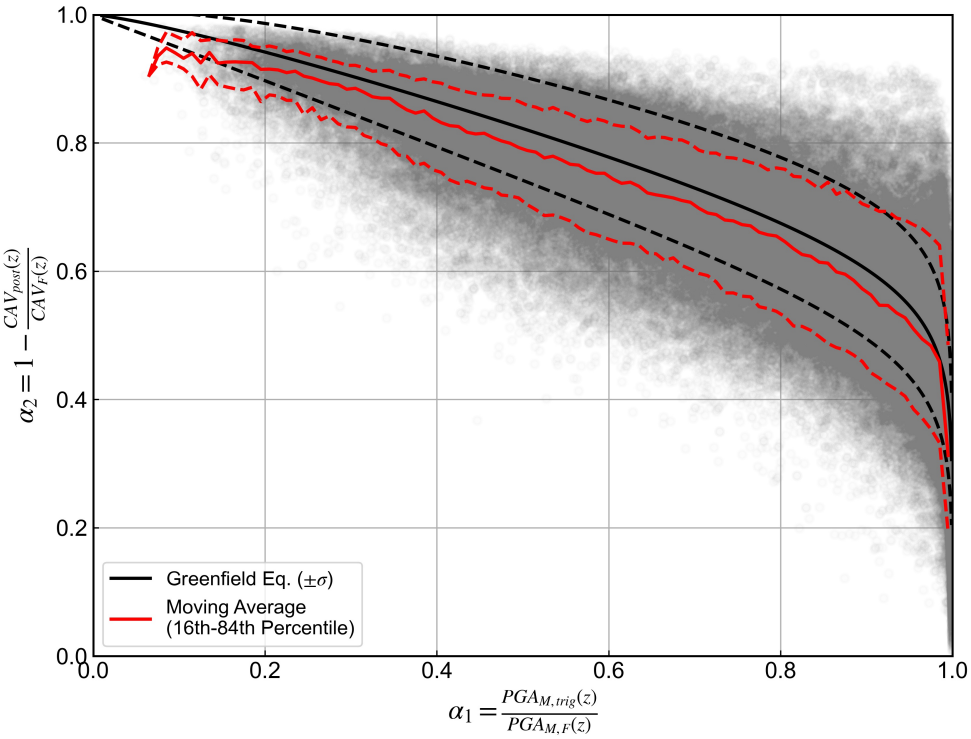

Figure 7.5: Comparison of α_1-α_2 relationships for total stress-type motions from stiff sites (represented by the Greenfield model) and pore pressure-affected motions extracted from OpenSees effective stress analyses. Raw data from OpenSees are shown in grey, with mean, 16th, and 84th percentile moving averages shown in red.

The residuals of the predicted α_2 values are plotted against α_1 in Figure 7.6. Overall the predicted values are slightly greater than the observed, reflecting the vertical offset between the

two curves in Figure 7.5. The trend of increasing variance in α_2 as α_1 increases is consistent with the standard deviations obtained from the fitted Beta-distributions from the Greenfield model, and is reasonable from a physical standpoint. Because PGA_M increases less gradually than CAV, in a manner that is driven in many case by a few large acceleration peaks, its evolution with respect to its final value is less correlated in time with CAV's relative evolution. Recall the input time histories for the example analyses in Section 5.5, where the PGA_M trace had reached its peak value at about 23 seconds; at the same point in time, the corresponding CAV trace had only reached about 75% of its final value. For the overall displacement model evaluation in this study, the Greenfield model was considered to be suitable for predicting α_2 (and subsequently CAV_{post}) in liquefiable soil layers. The coefficients a and b could be estimated and revised separately for pore pressure-affected motions; future studies should consider the entire time histories of these motions in a similar manner to how the α_1-α_2 relationships were developed by Greenfield.

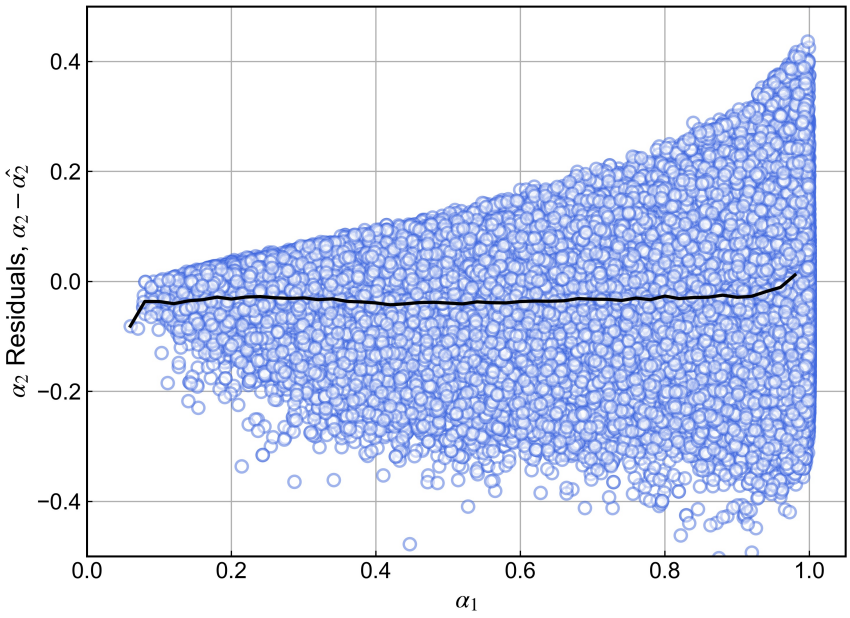

Figure 7.6: Residual plots of α_2 estimated using Greenfield (2017) model; observed values based on CAV_{post} values extracted from liquefiable elements in OpenSees effective stress analyses.

Once α_2 is estimated at all depths, it is multiplied by the estimated $CAV_F(z)$ profile to obtain the post-triggering $CAV(z)$ to be used in the prediction of strains.

7.3.3 Regression of Post-Triggering Strain Model

The functional form for the prediction of permanent strains from the post-triggering CAV at a given depth, as developed in Section 6.3 is:

$$\gamma(z) = \beta(z) \cdot CAV_{post}(z) \tag{7.18}$$

where $\beta(z)$ is a material and site parameter that depends on the relative density and slope inclination via:

$$\ln \beta(z) = b_0 + b_1 D_R(z) + \frac{b_2 + b_3 D_R(z)}{S} \tag{7.19}$$

and b_0 through b_3 are regression coefficients, which were estimated using linear regression against the full dataset of randomized soil profiles, and are summarized in Table 7.2. The standard deviation of the shear strain (conditional on $CAV_{post}(z)$) from the full set of effective stress analyses was 0.19 (or 19%). The residuals of the fitted shear strain values are plotted against relative density, slope inclinations, and $CAV_{post}(z)$ in Figure 7.7. While the model is essentially unbiased over the full range of relative density and slope inclination, the behavior of the residuals with respect to CAV_{post} is noteworthy, particularly the large cluster of positive residuals at $CAV_{post} = 0$ m/s. These data points correspond to elements in which liquefaction did not trigger under the $r_u \geq 0.97$ criterion adopted in this study (and thus would have no post-triggering shaking intensity), but underwent large permanent strains.

The original r_u criterion assumed in this study was selected based on an initial evaluation of the relative density series profile results presented in Chapter 6, specifically at a system-wide level, in which the maximum global r_u of all elements in a particular analyses was compared to the model's nodal surface displacements. This simple comparison indicated that an r_u of 0.97 most closely corresponded with a large increase displacements, generally exceeding 5 cm, and was adopted as the threshold value for calculating the system-level liquefaction times.

At an element-level, it is possible that this threshold is too high, given the number of elements with large shear strains at $CAV_{post} = 0$ in Figure 7.7. There is also a possibility that the PM4Sand model is potentially over-predicting the accumulation of shear strains prior to triggering; numerous laboratory studies have shown that permanent strains remain quite limited up until liquefaction is triggered, after which the stiffness of the sand decreases suddenly and the rate of shear strain accumulation increases significantly. Nevertheless, the functional form presented here for the post-triggering strains appears to be valid and unbiased in elements that did in fact liquefy; at non-zero values of CAV_{post}, the residuals are relatively stable out to very large values of CAV_{post}, beyond which the model tends to over-predict strains. Future studies should focus on the sensitivity of the element-level liquefaction criterion, specifically examining different values of r_u or using shear strain criterion to potentially re-calibrate the model for $\beta(z)$.

Table 7.2: Regression coefficients for post-triggering shear strain model. γ and D_R are in decimal units.

Predictor	Coefficient	Value
Intercept	b_0	-1.987
Relative Density, D_R	b_1	-0.316
Slope inclination, S^{-1}	b_2	-0.38
$D_R \cdot S^{-1}$	b_3	-0.77
	σ_γ	0.193

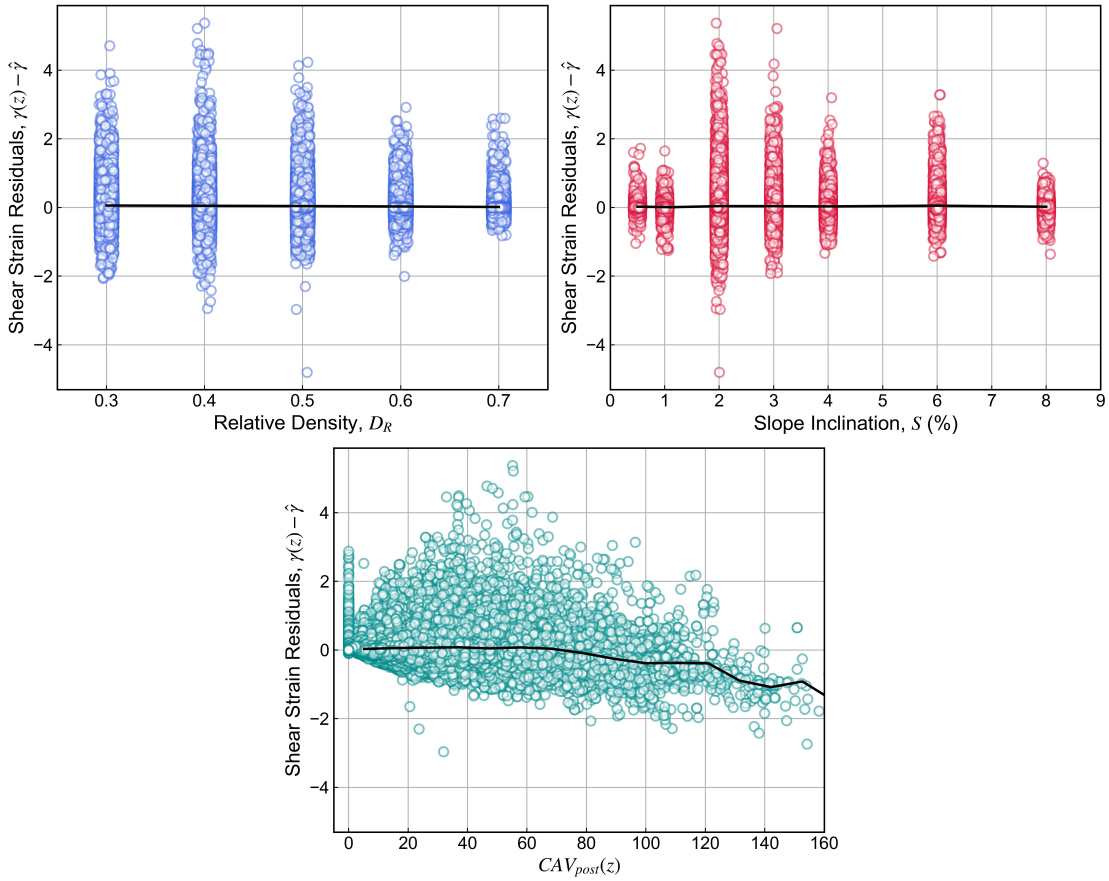

Figure 7.7: Residuals of fitted shear strain values, plotted against relative density, slope inclination, and post-triggering CAV.

The sensitivity of the fitted strain model to relative density, slope inclination, and post-triggering CAV is shown in Figure 7.8 through 7.10. In each case, the model reflects the behaviors observed in the sensitivity study in Chapter 6 and used to develop the functional form. For a fixed value of CAV_{post}, the shear strains decrease exponentially with increasing relative density (Figure 7.8), reflecting the density-dependence of shear strains that is not tied to differences in triggering times.

This behavior is generally consistent with laboratory data; Ishihara and Yoshimine (1992) showed that post-triggering maximum shear strains depended not only on the FS_L, which can be considered in this context to be an indicator of the timing of liquefaction, but the initial relative density. For a given FS_L, the D_R-dependency the maximum shear strains implied by their laboratory data have a similar behavior to the numerical-based strain model presented here.

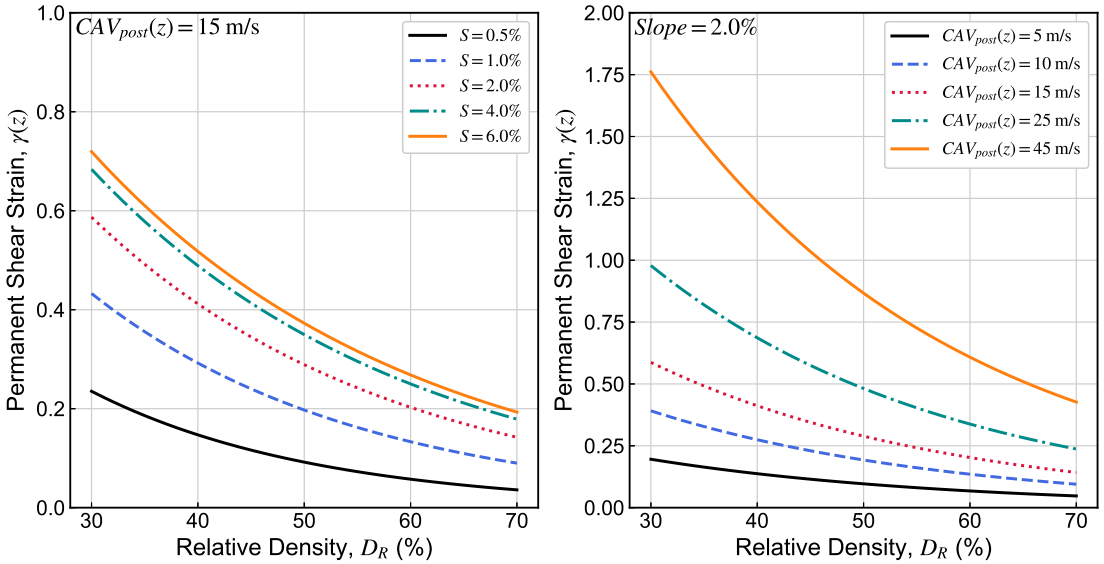

Figure 7.8: Sensitivity of fitted shear strain model to relative density for varying slope inclinations and levels of post-triggering CAV.

With respect to slope inclination (Figure 7.9), the shear strains increase with steeper slopes before reaching a plateau. The behavior implied by the fitted model reflects the combined effects of the static shear strain contribution (in that the shear strains naturally increase with increasing slope inclination, all other factors being equal), as well as the K_α effect that reduces stress reversals at large static stresses, and produces the plateaus in permanent shear strain at large slope inclinations.

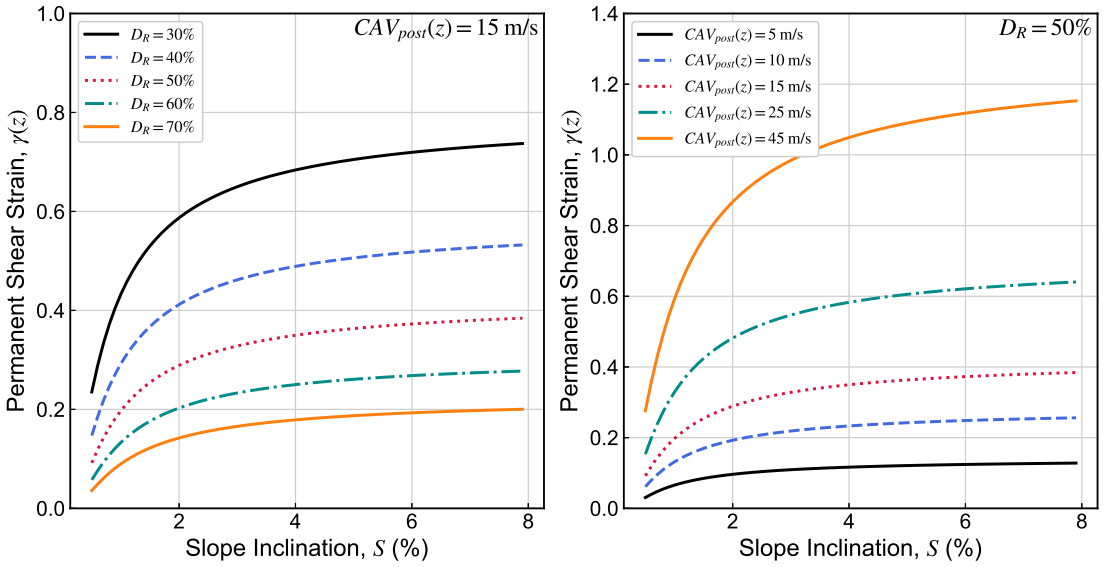

Figure 7.9: Sensitivity of fitted shear strain model to slope inclination for varying relative densities and levels of post-triggering CAV.

The variation in permanent shear strains with post-triggering CAV shown in Figure 7.10 reflects the efficiency CAV_{post} as a predictor of shear strains (Kramer et al. 2016). There are two aspects to this efficiency: one is the advantage of using the post-triggering intensity measure, which better represents the ground motion characteristics that drive the vast majority of deformations in soils in their liquefied states, and the other is the use of CAV_{post} itself (rather than $PGA_{M,post}$ or $I_{a,post}$, which is generally correlated more to lower-frequency content, and thus captures the frequencies that are closer to the natural period of the liquefied soil.

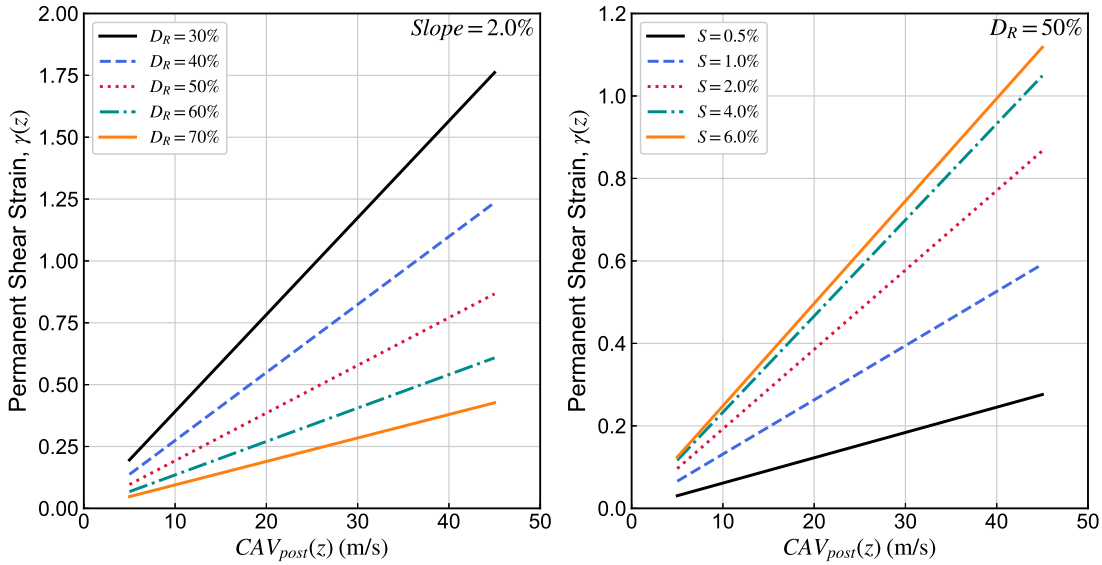

Figure 7.10: Sensitivity of fitted shear strain model to post-triggering CAV for varying relative densities and slope inclinations.

7.3.4 Fitted Surface Displacements Conditional on CAV_{post}

The lateral spreading framework proposed herein is based on computing ground surface displacements by integrating the post-triggering strain profile. In order to initially assess the efficacy of the post-triggering strain model in predicting displacements, median surface displacements were calculated from the fitted strain values estimated using Equations 7.18 and 7.19, and the CAV_{post} values extracted directly from the OpenSees analysis data:

$$\hat{D}_H = \sum_{j=1}^{N_{liq}} [\hat{\beta}(z_j) \cdot CAV_{post}(z) \cdot \Delta H_j(z)] \tag{7.20}$$

The log-residuals of $\hat{D}_H$ are shown in Figure 7.11; the average log-residual across all cases is 0.42, corresponding to estimated displacements that are lower than the observed values by about 35% on average, and varying significantly with the displacement levels. This is illustrates the impacts of basing the strain prediction entirely on the assumption that all strains occur after triggering; the cases in which the displacement residuals are largest correspond to OpenSees profiles where significant strains occurred in layers that were considered not to have liquefied by the $r_u \geq 0.97$ criteria discussed earlier. This discrepancy prevents a direct comparison between integrated strain displacements and the displacements computed by OpenSees in this particular study, and motivates future work to consider the prediction of strains for soils in which liquefaction has not been triggered in a particular scenario, or to adjust the liquefaction criteria for determining the time of liquefaction

in these analyses to capture a larger portion of the elements that contribute to deformations.

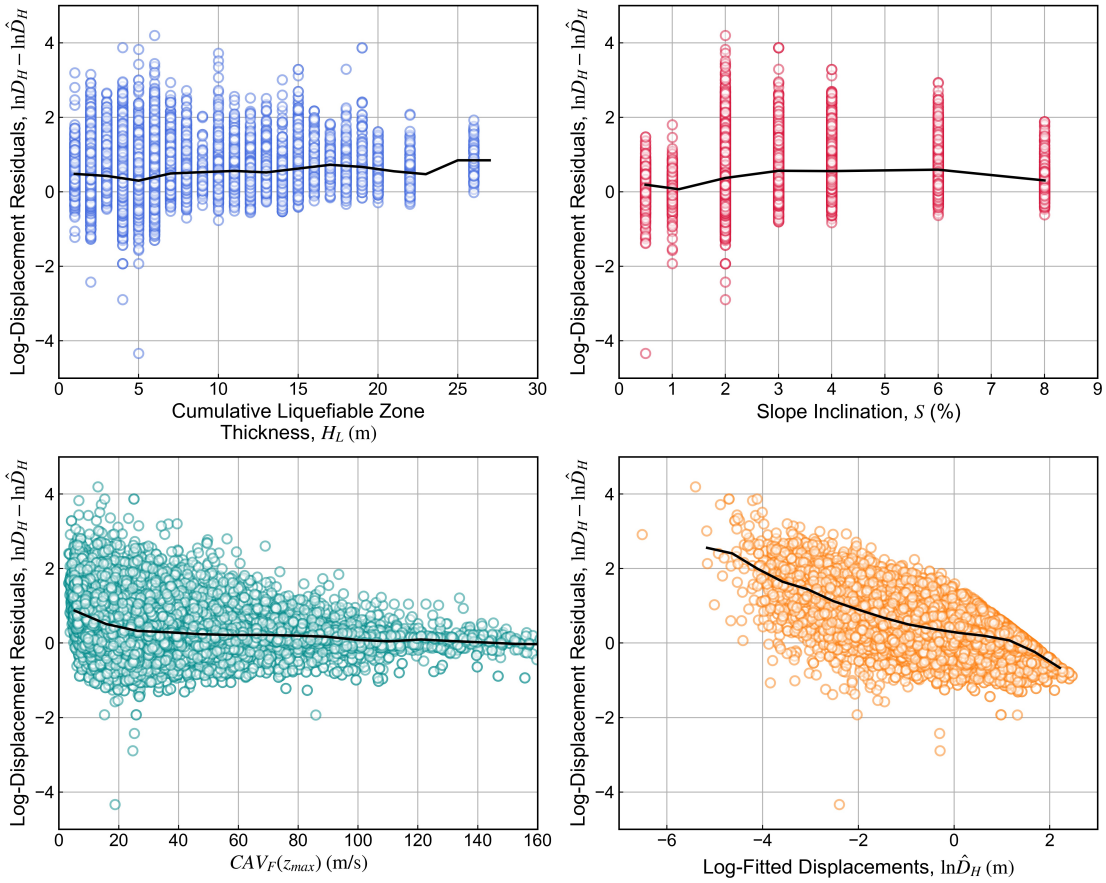

Figure 7.11: Log-residuals of displacements calculated by integration of estimated shear strain profile, conditional on CAV_{post}.

7.4 A Performance-Based Framework for Predicting Lateral Spreading Displacements

The semi-empirical lateral spreading framework presented in this chapter provides a probabilistic estimate of permanent displacement as a function of the relative density profile in the liquefiable zone, the slope inclination, and the overall PGA_M and CAV values at the base of the liquefiable zone. The standard deviation of the displacement estimates from this procedure reflect the uncertainties in each component of the model: the prediction of the reduction in demand of the input motion as it passes through liquefiable soils, the relationship between the pre- and post-triggering intensity measures, and the prediction of permanent shear strains as a function of the post-triggering shaking intensity, soil parameters and slope inclination. A more detailed formulation that separately accounts for the uncertaintiesin in the prediction of the pre- and post-triggering IMs, the estimation of the triggering limit-state PGA_M, the relationship between the normalized

evolutionary IMs α_1 and α_2, and the prediction of surface displacements from $IM_{2,L}$ given site and soil conditions, can be found in Appendix C.

In this section, these uncertainties are combined with the uncertainties inherent to estimating ground motion intensity measures (Section 2.4) to demonstrate how lateral spreading hazard curves can be calculated at an example site in San Francisco, CA. The incorporation of ground motion hazard curves into the displacement calculation framework converts the estimates of displacement probabilities into annualized rates of displacement, thereby contextualizing lateral spreading-related damage into risk-based assessments. It should be noted that the lateral spreading model presented in this chapter is conditional on a known PGA_M value at the time of triggering, and the uncertainty in $PGA_{M,trig}$ is not considered in this particular example application. The use of two intensity measures (PGA_M and CAV) in this framework requires the estimation of the conditional distribution of one IM given the second IM with a known hazard curve (also known as their joint hazard curve, or hazard surface), which can be calculated using the generalized conditional intensity measure approach (GCIM, Bradley 2010). Calculation of the displacement hazard curves is demonstrated for three simple soil profiles, each consisting of a 2 m-thick non-liquefiable crust, underlain by a 3 m-thick layer of liquefiable soil, with linearly increasing relative density, as summarized in Table 7.3; the profiles have a ground slope inclination of 2%. Ground motion intensity measures are estimated for a soft rock condition ($V_{s,30}$ = 760 m/s), corresponding to dense soils below the liquefiable zone, for a site in San Francisco, CA.

Table 7.3: Summary of parameters for demonstration soil profiles in lateral spreading hazard curve calculation

Profile ID	Average D_R (%)	D_R Range (%)	H_{Liq} (m)	z_{GWT} (m)	Ground Slope (%)
A	35	30-40	3	2	2
B	50	45-55			
C	65	60-70			

7.4.1 Calculation of PGA_M Hazard Curve

PGA_M is simply a measure of the peak ground acceleration weighted by the number of stress cycles in a particular time history. In simplified procedures this weighting factor is typically the magnitude scaling factor MSF (Equation 3.17). The hazard curve for PGA_M can therefore be calculated using an initial hazard curve for PGA and its deaggregated conditional magnitude distribution:

$$\lambda_{PGA_M}(pga_m) = \sum_{i=1}^{N_{PGA}} \sum_{j=1}^{N_{M_w}} \mathrm{P}[PGA_M > pga_m | pga_i, m_j] \cdot \mathrm{P}[m_j | pga_i] \cdot \Delta\lambda_{PGA}(pga_i) \tag{7.21}$$
$$= \sum_{i=1}^{N_{PGA}} \sum_{j=1}^{N_{M_w}} \mathrm{P}[pga_i / MSF(m_j) > pga_m | pga_i, m_j] \cdot \mathrm{P}[m_j | pga_i] \cdot \Delta\lambda_{PGA}(pga_i)$$

The hazard curve and deaggregation data for PGA were obtained using the `nshm-haz` computational platform (USGS). The probability of PGA_M exceeding some value pga_m, given a particular PGA-M_w combination, can be calculated from the standard normal distribution, assuming that $\mu_{\ln PGA_M} = pga_i / MSF(m_j)$ and $\sigma_{\ln PGA_M} = \sigma_{\ln PGA}$. In this case, $\sigma_{\ln PGA}$ was taken as the weighted average of the four NGAWest-2 GMM standard deviations for the given magnitude and distance (thus adding a third summation over source-site distance R in Equation C.12):

$$\lambda_{PGA_M}(pga_m) = \sum_{i=1}^{N_{PGA}} \sum_{j=1}^{N_{M_w}} \sum_{k=1}^{N_R} \mathrm{P}[PGA_M > pga_m | pga_i, m_j, r_k] \cdot \mathrm{P}[m_j | pga_i] \cdot \tag{7.22}$$
$$\cdot \mathrm{P}[r_k | pga_i] \Delta\lambda_{PGA}(pga_i)$$

The resulting hazard curve for PGA_M is shown in Figure C.1, along with the original PGA hazard curve upon which it was calculated. The higher rates of exceedance of PGA_M compared to PGA and the increased divergence between the two hazard curves reflect the increasing contribution of large-magnitude events to the PGA hazard at longer return periods and higher PGA levels. The increasing magnitude contribution results in longer-duration motions, and thus more stress cycles, leading to a larger magnitude-adjustment.

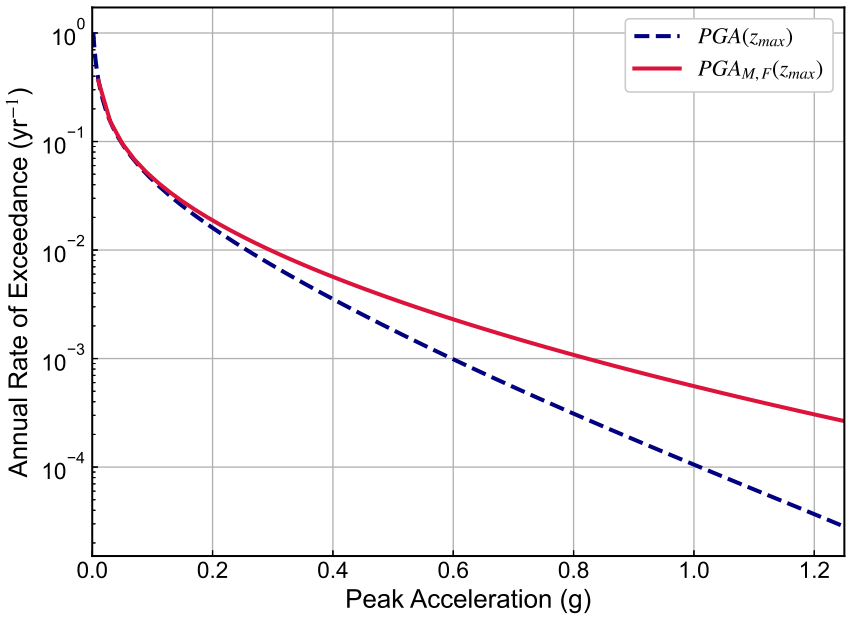

Figure 7.12: Hazard curves for PGA and PGA_M for input motions at the base of the liquefied zone for a site in San Francisco, CA.

In order to obtain the probability distribution of rupture scenarios contributing to the PGA_M hazard (for later use in the GCIM procedure to characterize CAV), the definition of a marginal rupture probability (Baker, 2008) can be utilized:

$$\mathrm{P}[Rup = rup | PGA_M > pga_m] = \frac{\lambda_{PGA_M,Rup}(pga_m, rup)}{\lambda_{PGA_M}(pga_m)} \tag{7.23}$$

where the numerator is calculated in a similar manner to Equation C.12, without the summation over M_w or R, and the MSF is calculated from the magnitude of the particular rupture scenario:

$$\lambda_{PGA_M,Rup}(pga_m, rup) = \sum_{i=1}^{N_{PGA}} \mathrm{P}[PGA_M > pga_m | pga_i, rup] \cdot \mathrm{P}[rup | pga_i] \cdot \Delta\lambda_{PGA}(pga_i) \tag{7.24}$$

The marginal probability of the rupture scenario given a particular pga_i (i.e. the second term inside the summation) can be obtained from the hazard deaggregation data for PGA.

7.4.2 Calculation of Joint Hazard Curves Using Generalized Conditional Intensity Measure Approach

Ideally, the joint hazard curve is most accurately obtained using some form of a vector-based PSHA. However, in many cases, current widely available PSHA computational platforms may not be particularly well-suited for vector-based PSHAs, particularly those involving less well-established earthquake intensity measures such as CAV or I_a. As a result, a specific application of the GCIM approach (Bradley, 2010) is proposed for developing a joint $PGA_M - CAV$ hazard curve, based on an initial hazard curve for PGA_M, along with its corresponding deaggregated hazard data.

For a given rupture scenario rup_i (i.e. a combination of M and R for a given source), the lognormal mean and standard deviation of CAV, conditional on the occurrence of some level of PGA_M can be approximated as:

$$\mu_{\ln CAV|Rup,\ln PGA_M}(rup_i, pga_m) = \mu_{\ln CAV|Rup}(rup_i) + \sigma_{\ln I_{a,T}|Rup}(rup_i)\rho_{\ln CAV,\ln PGA_M}\varepsilon_{\ln PGA_M} \tag{7.25a}$$

$$\sigma_{\ln CAV|Rup,\ln PGA_M}(rup_i, pga_m) = \sigma_{\ln CAV|Rup}(rup_i)\sqrt{1-\rho^2_{\ln CAV,\ln PGA_M}} \tag{7.25b}$$

where $\mu_{\ln CAV|Rup}(rup_i)$ and $\sigma_{\ln CAV|Rup}(rup_i)$ are the mean and standard deviation, respectively, of the predicted CAV for the given rupture scenario. These were calculated using the Campbell & Bozorgnia (2010) GMM for CAV. $\rho_{\ln CAV,\ln PGA_M}$ is the correlation coefficient between the two intensity measures, taken here to be 0.77 (Greenfield, 2017), based on comparisons of a suite of motions from crustal and subduction events. $\varepsilon_{\ln PGA_M}$ is the number of standard deviations the value of PGA_M is above the mean predicted value for the given rupture scenario, which is obtained for the hazard deaggregation. Knowing the probability distribution of all rupture scenarios for a given PGA_M, the overall conditional probability of CAV given PGA_M can be expressed as:

$$\mathrm{P}[CAV|PGA_M] = \sum_{j=1}^{N_{Rup}} \mathrm{P}[CAV|PGA_M, Rup = rup_k] \cdot \mathrm{P}[Rup = rup_k|PGA_M] \tag{7.26}$$

Conditional distributions of the overall base CAV, given several values of PGA_M, are shown in Figure 7.13. A resulting hazard curve for CAV can also be calculated by integrating over the PGA_M hazard curve (using the conditional probability of exceedance of CAV, rather than the probability density), and is shown in Figure 7.14.

$$\lambda_{CAV}(cav_j) = \sum_{i=1}^{N_{PGA_M}} \mathrm{P}[CAV > cav_j | pga_{m,i}] \Delta\lambda_{PGA_{M,F}}(pga_{M,i}) \tag{7.27}$$

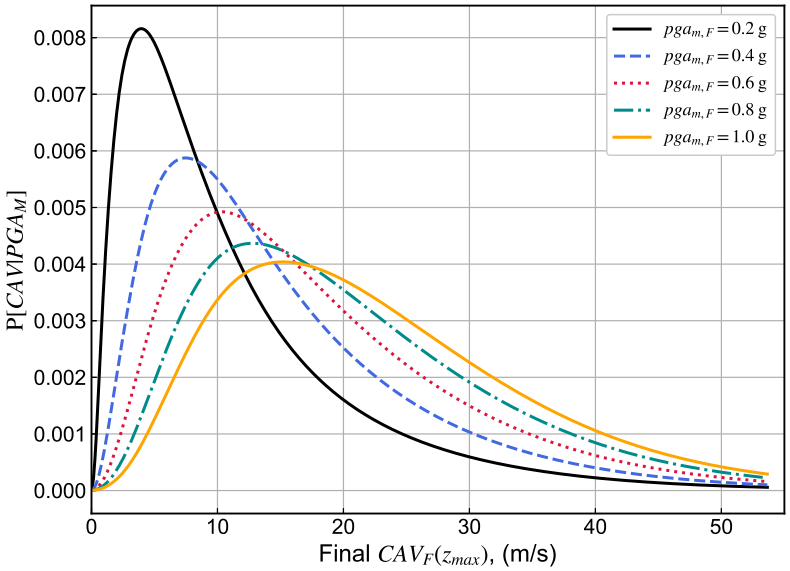

Figure 7.13: Conditional probability distribution of $CAV_F(z_{max})$ given $PGA_{M,F}(z_{max})$

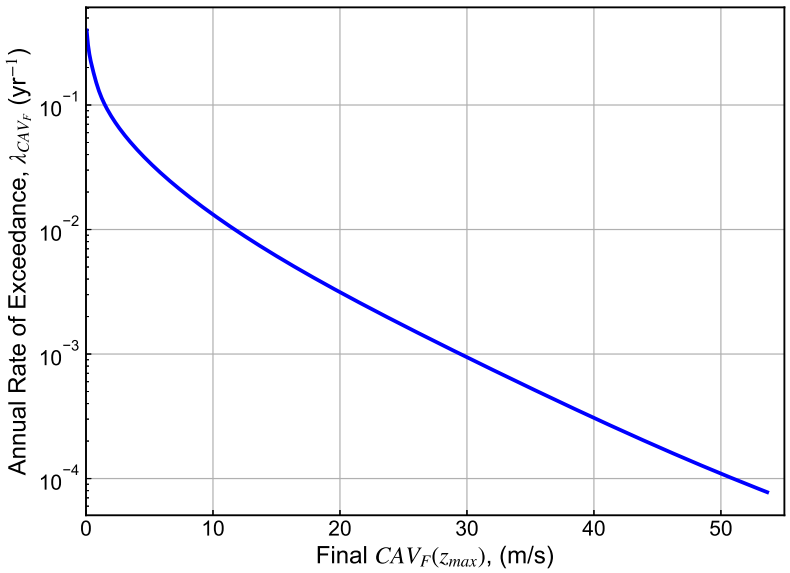

Figure 7.14: Hazard curve for $CAV_F(z_{max})$ based on GCIM calculation with respect to $PGA_{M,F}(z_{max})$

Discussion on the Consideration of "Rupture Scenarios" in the GCIM Approach

Ideally, the characterization of the conditional distribution of a $CAV|PGA_M$ relationship (or any generic $IM_2|IM_1$ relationship) would, at its highest level of sophistication, require calculating the conditional mean and standard deviation of CAV for every possible rupture scenario. In such a case, the term *Rup* (in $\mu_{\ln CAV|Rup,PGA_M}$ and $\sigma_{\ln CAV|Rup,PGA_M}$) would refer to the combination of magnitude (M_w), distance (R), and epsilon (ε) for every seismic source (e.g., all logic trees for the Seattle Fault Zone or Cascadia Subduction Zone characterization, every single coordinate of any gridded seismicity model) that causes significant levels of PGA_M. This would require knowledge of not only the percent contribution of every source to the hazard at a wide range of PGA_M levels, but also the marginal $M_w - R - \varepsilon$ distribution for each of these sources. This generally represents an immense amount of data that is typically not made available to users by widely available PSHA platforms.

As a result, some simplifications must be made as to what constitutes a "rupture scenario", based on the level of detail of the deaggregation data made available by the PSHA code being utilized. In the case of the USGS `nshmp-haz` code, the most detailed set of rupture scenarios can be defined in one of two ways:

1. The mean (or modal) M_w-R-ε combination from each earthquake source, along with the percent contribution to the PGA_M hazard for each source, which can be obtained from the summary of a given deaggregation calculation from `nshmp-haz`.

2. The full M_w-R-ε joint probability distribution for each source *type* (e.g. fault, interface, system, grid), as well as the percent contribution to the PGA_M hazard for each source type. In using an aggregation of individual sources, some generalization of the GMM calculation to generate $\mu_{\ln CAV|Rup,PGA_M}$ and $\sigma_{\ln CAV|Rup,PGA_M}$ would be necessary. For instance, to calculate the conditional distribution for the collection of fault sources, a single set of fault characteristics would need to be assumed, and differences in faulting style, dimensions, hanging-wall effects, etc. on the conditional CAV distribution would not be considered.

There are several other ways to represent rupture scenarios from deaggregation data that are considerably less detailed and easier to implement. The simplest method would be to generate $\mu_{\ln CAV|Rup}(rup_i)$ and $\sigma_{\ln CAV|Rup}(rup_i)$ using the mean rupture scenario ($\bar{M}_w$, $\bar{R}$, $\bar{\varepsilon}$) from the deaggregation at a given PGA_M level for all sources. While this might be reasonable in areas that are controlled by relatively tightly clustered source of seismicity, the mean rupture scenario in areas containing more diverse (and diffuse) sources of seismicity may not necessarily represent a realistic, physical rupture scenario. Alternatively, characterization of the conditional distribution

could potentially be refined by using the full range of $[M_w, R, \varepsilon]$ (and their corresponding joint distribution from the deaggregated hazard), rather than just the mean values. However, the problem remains that such a method does not differentiate between different types of seismic sources, and thus the GMM used to calculate $\mu_{\ln CAV|Rup}(rup_i)$ and $\sigma_{\ln CAV|Rup}(rup_i)$ may not be applicable to the rupture scenario it is purportedly considering.

7.4.3 Conditional Distribution of Permanent Displacements, Given PGA_M and CAV

For each combination of $PGA_{M,F}(z_{max})$ and $CAV_F(z_{max})$, a hypothetical timing-based strain integration procedure presented in this chapter is used to calculate the mean and standard deviation of the permanent lateral spreading displacements for each profile as follows:

1. The base PGA_M value is used to compute demand reduction factors (Equations 7.9 and 7.12) to estimate $PGA_{M,F}(z)$ and $CAV_F(z)$ profiles in the liquefiable zone.

2. The $\alpha_1(z)$ profiles at the time of triggering are computed as the ratio of the mean $PGA_{M,L}$ using the Boulanger and Idriss (2015) method and the estimated$PGA_{M,F}(z)$ values. In sublayers where $\alpha_1 \leq 1.0$, corresponding α_2 profiles are estimated using the Greenfield (2017) model (Equations 7.15 and 7.16).

3. $CAV_{post}(z)$ values are estimated from the overall $CAV_F(z)$ profiles and $\alpha_2(z)$ values, and multiplied by the estimated $\beta(z)$ to predict the permanent shear strain in each sublayer (Equations 7.18 and 7.19).

4. The mean surface displacement is estimated by multiplying the predicted strains by their sublayer thickness and summing the product over all sublayers (Equation 7.4). For the purposes of this example a constant standard deviation of 0.610 was calculated from the residuals of the strain-integrated fitted displacements Figure 7.11. An model standard deviation would need to be based on calibration to empirical data from field case histories.

The complimentary cumulative distribution functions, which describe the probability of exceedance of the estimated displacements are shown, conditional on three combinations of $PGA_{M,F}(z_{max})$ and CAV_F, in Figure 7.16, indicating an increase in median displacements with respect to both decreasing relative density and increasing ground motion amplitude in a manner consistent with the strain integration procedure presented in this chapter.

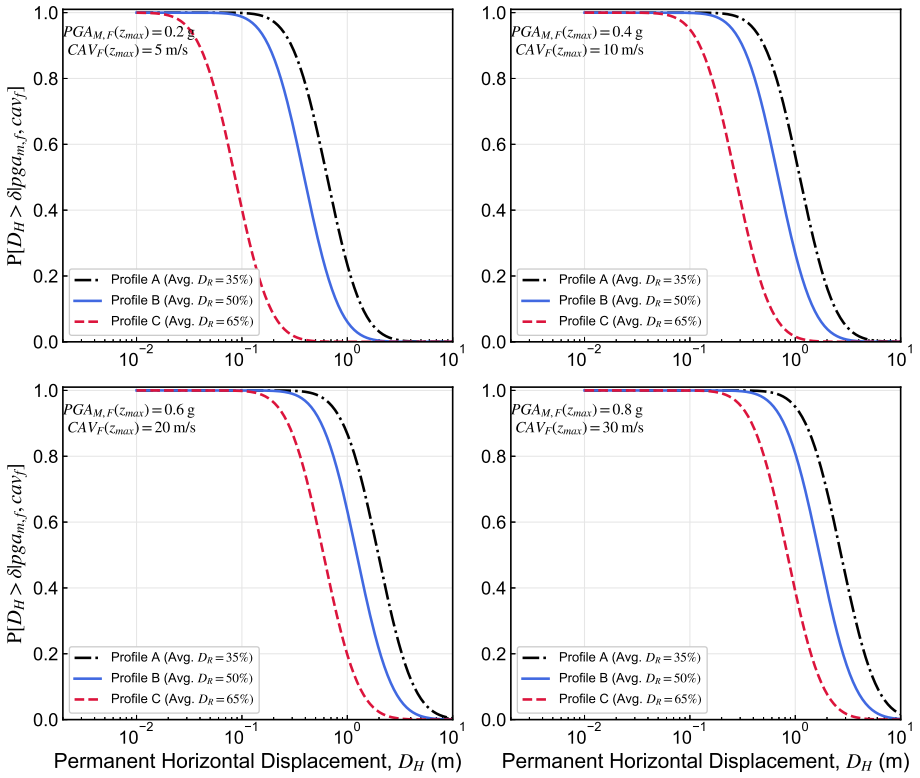

Figure 7.15: Cumulative distribution functions of predicted lateral spreading displacements using hypothetical strain integration model, for four combinations of base PGA_M and CAV, for three hypothetical profiles with varying relative densities.

7.4.4 Overall Hazard Curve for Lateral Spreading Displacement

The overall hazard curves for permanent displacements can be calculated by combining the three probabilistic components presented in this section, and summing over each of the variables:

$$\lambda_D(\delta) = \sum_{j=1}^{N_{CAV}} \sum_{i=1}^{N_{PGA_M}} \mathrm{P}[D > \delta | pga_{m,i}, cav_j] \mathrm{P}[cav_j | pga_{m,i}] \Delta\lambda_{PGA_{M,F}}(pga_{M,i}) \tag{7.28}$$

where $\mathrm{P}[D_H > \delta | pga_{m,i}, cav_j]$ is the probability the horizontal displacements exceeding a particular value δ, conditional on a given combination of pga_m and cav, the conditional probability $\mathrm{P}[cav_j | pga_{m,i}]$ is calculated using the GCIM framework (Equations 7.25 and 7.26), and $\Delta\lambda_{PGA_{M,F}}$ is the incremental exceedance rate of particular $(pga_{M,i})$, obtained by numerically differentiating the PGA_M hazard curve.

The final permanent displacement hazard curves for the three profiles are shown in Figure 7.16.

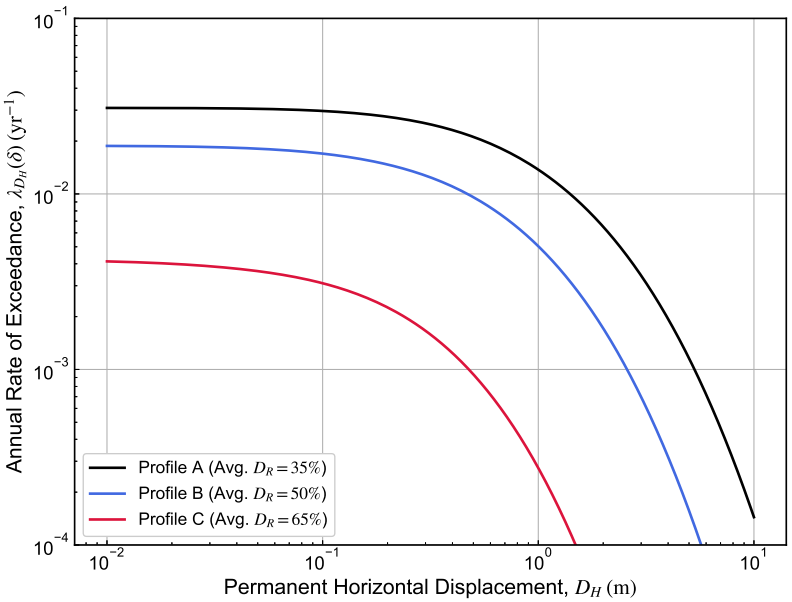

Figure 7.16: Annual rates of exceedance for predicted lateral spreading displacements using hypothetical strain integration model, for three hypothetical profiles with varying relative densities.

While these example analyses are purely hypothetical, displacement hazard curves can be utilized in a number of different ways to extract meaningful data to be used in decision-making about the site or asset in question. The level of displacement exceeded with respect to a particular return period may be of interest, for example. For the three profiles analyzed, Table 7.4 summarizes these values for the 475, 975, and 2475 years; in particular the results illustrate the sensitivity of lateral displacements to relative density, particularly in profiles underlain by thicker liquefiable deposits, with displacements ranging from tens of centimeters across most return periods in the denser cases to several meters in the looser profile cases.

Ideally, a truly probabilistic analysis of lateral spreading displacements would account for uncertainties in the estimated/measured relative density, either via multi-scenario analyses by the user, or by the model developer in calibrating a potential model to field case histories.

Table 7.4: Summary of estimated hazard-consistent displacements for three hypothetical soil profiles at a site in San Francisco, CA

T_{R,D_H} (yr)	Displacement (m)		
	Profile A	Profile B	Profile C
475	3.9	1.65	0.25
975	5.3	2.75	0.45
2475	7.5	3.7	0.83

7.5 Summary and Conclusions

The formulations and data presented in this chapter extend the basic concepts developed in the initial sensitivity study in Chapter 6 to more complex soil profiles. A method for efficiently randomizing and generating more soil profiles with between on and four liquefiable layers was presented and utilized to expand the suite of numerical effective stress analyses. The benefits of including more realistic soil profiles was to inject some further randomness into the characterization of the demand reduction and shear strain behavior, in order to ascertain if the formulations in Chapter 6 could be robustly applied to more complex systems.

By and large, the analyses showed that the general trends established could still be predicted in the randomized profiles, albeit with larger degrees of uncertainty. The demand reduction and shear strain prediction components were then integrated into a timing-based, strain-integration framework for predicting lateral spreading displacements. It was shown that the basic trends of the Greenfield (2017) relationship for pre- and post-triggering intensity measures could be applied to ground motions in potentially liquefiable elements (with some re-calibration needed), and that these relationships could be used to convert the overall estimated intensity measures to a post-triggering CAV in order to estimate shear strains.

While there are certainly components of the prediction methodology that require further development and refinement, its general framework can be used to demonstrate the fully-probabilistic characterization of lateral spreading displacements. An example performance-based analysis of lateral spreading was presented, in which the Generalized Conditional Intensity Measure approach (GCIM) was used to estimate the two IM hazard curves (PGA_M and CAV) needed for application to the lateral spreading framework, and probabilistic displacement estimates were made for each potential CAV-PGA_M scenario. The displacement probabilities were integrated with the joint IM hazard curves to produce annualized displacement exceedance curves for three hypothetical profiles at a site in San Francisco, CA.

Chapter 8

Summary of Research, Concluding Remarks, and Recommendations for Future Research

8.1 Introduction

Liquefaction and its related consequences have posed and continue to pose myriad hazards for the built and natural environments. These types of geotechnical problems have confounded researchers, practitioners, and public and private stakeholders for decades. While significant progress has been made in recent years, the current state of practice seems to suffer from biases and blindspots that are revealed with every new liquefaction event (or non-event). To be sure, this is in many ways a natural limitation of natural hazards research, and one can hardly claim that the earthquake geotechnics community, as a field of research and a profession, is not doing enough to advance the state of knowledge and the state of practice with the urgency that liquefaction problems require.

Current simplified empirical methods employed by nearly all practitioners are the baseline for liquefaction hazard analysis, and provide a strong mechanistic basis for evaluating triggering (based on laboratory data) that is calibrated to the available case histories of liquefaction that have been recorded in the field. However, this database is somewhat limited, particularly in terms of large-magnitude events with long-duration motions, and empirical procedures generally must be used with this knowledge in mind. Simplified methods are also inherently highly uncertain, and while probabilistic versions of these models are available that account for at least some of this uncertainty explicitly, their use in practice is limited. Most engineers pair deterministic triggering

analyses with probabilistic ground motions, typically obtained from a PSHA-based hazard curve at a targeted return period of ground shaking, in what is sometimes charitably referred to as a "hybrid probabilistic" procedure.

Simplified procedures also are limited by their utility in evaluating the effects of liquefaction, such as vertical ground settlements or lateral spreading deformations; several methods that tie ground deformations to FS_L are available, but all have relatively spotty track records in predicting actual ground damage in recent earthquakes. These types of methods have also been shown in recent years to have limited ability in capturing complex system effects.

The objectives of the research presented in this dissertation focused on addressing each of the aforementioned limitations to varying degrees. An improved and updated computational framework was developed and validated for performing probabilistic liquefaction hazard analyses for the triggering limit state. This platform was used in a large-scale parametric study to develop and validate a framework for mapping liquefaction-targeted ground motion parameters for use in current conventional analyses, in order to gain more uniformity in the levels of liquefaction risk that practitioners currently design to across the United States. Moving beyond current procedures and focusing on improving the characterization of liquefaction effects, a large-scale numerical parametric study was developed and deployed to investigate the sensitivity of liquefaction and lateral spreading to a wide range of source, site, and ground motion parameters, within a timing-based framework. From this study, several components of a prediction framework for lateral spreading were formulated. At the element level a relationship between post-triggering shaking intensity and permanent shear strain was presented; at the system level, a factor accounting for the reduction in seismic demands was developed. These components were incorporated into a potential fully-probabilistic, timing-based framework for predicting lateral spreading displacements.

8.2 Summary of Research

Chapter 2 presented the historical and scientific background of liquefaction, discussing some of the earliest and most damaging examples of earthquake-induced soil liquefaction, and providing the details on a mechanical level of how soils liquefy and what happens to them after they liquefy. The basics of the simplified cyclic stress-based method for assessing liquefaction triggering were presented, as well as the factor of safety-based extensions to assessing liquefaction-related effects. A brief primer on alternatives to the cyclic stress method was also presented, along with more recent research findings that have explored the use of more efficient evolutionary intensity measures to predict liquefaction triggering, and the motivations for considering the timing of liquefaction in hazard evaluations. Background on the phenomenon of lateral spreading was introduced, along

with its myriad complexities and the challenges in prediction of the deformations it causes. Finally, the performance-based earthquake engineering (PBEE) framework was presented in detail as a method for accounting for various uncertainties at every stage in earthquake engineering-related problems to produce rational and probabilistic estimates of losses.

In Chapter 3, an open-source, Python-based computational platform for performing fully-probabilistic liquefaction hazard analyses (PLHA) was developed, validated, and documented. The PLHA framework utilizes probabilistic liquefaction triggering models in conjunction with seismic hazard data to account for the contributions of all levels of ground shaking in the liquefaction hazard evaluation. The result is a hazard curve for FS_L, which can be used to ascertain the liquefaction potential associated with a specific return period of triggering. The Python library, known as `PyLHA`, utilizes the openly-available `nshmp-haz` platform, developed and maintained by USGS, to obtain the seismic hazard curves and magnitude deaggregation data needed to perform the fully-probabilistic analyses. `PyLHA` can be used for CPT- or SPT-based data, and utilizes three different liquefaction triggering models.

Chapter 4 introduced the concept of the liquefaction-targeted ground motion parameter. In the case of the simplified procedure for liquefaction triggering, this parameter is PGA_M, a magnitude-adjusted peak ground acceleration that can be mapped for a particular FS_L return period, and used in a deterministic LHA to obtain the same FS_L that would be obtained from a fully-probabilistic analysis. A framework for calculating this parameter from a PLHA calculation at a reference soil condition was presented; a large-scale parametric study on the sensitivity of PGA_M to varying depth, penetration resistance, and site V_{s30} was assessed at 100 geographic sites across the U.S., indicated that some modest factors would be needed for adjusting the mapped $PGA_{M,ref}$ from reference to site-specific conditions at a particular geographic location. The coefficients of these adjustment factors were found to vary systematically and predictably as a function of the underlying magnitude distribution at a particular geographic location, and sets of coefficients were regressed and presented for sites in the western and eastern United States. The framework for mapping and adjusting PGA_M was validated for 40 additional geographic locations distributed around the country, and was shown to produce FS_L values generally within 1-2% of the corresponding fully probabilistic values. Furthermore, the liquefaction-targeted values were shown to be considerably more consistent than the current mapped values used in conventional LHAs, which result in extremely inconsistent levels of liquefaction safety both within a given region and on a region-to-region scale. The PLHA-based mapping framework was shown to be quite feasible to scale up to high-resolution maps, and a roadmap for implementation into design codes was discussed.

Recognizing that there is more to liquefaction hazard evaluations than just the triggering limit state, Chapter 5 focused on the methodical development of a large-scale parametric study for

investigating the sensitivity of lateral spreading displacements to a wide range of source, site, and soil conditions. The numerical analyses consisted of one-dimensional, nonlinear, finite-element effective stress analyses of soil columns under infinitely sloping conditions, using the open-source computational platform OpenSees. A brief primer on constitutive modeling of liquefiable soils was presented, along with background on and element-level simulations of the PM4Sand and PM4Silt models for simulating the cyclic response of granular and silty soils, respectively. The details of model construction were presented, as well as the methodology used for selecting and scaling a suite of 188 ground motions from a wide range of geographic locations and seismotectonic regimes. A test analysis of a profile with multiple liquefiable layers was presented, the results of which illustrated the complexities inherent to characterizing liquefaction at both the element (layer) and system levels. This motivated a discussion on several aspects of the timing-based liquefaction framework, and specifically the need to account for system response effects in characterizing pre- and post-triggering demands at the element level.

In Chapter 6, the aforementioned finite-element model was deployed at scale. An initial set of about 15,000 effective stress analyses were generated, analyzed on the Stampede2 supercomputer (TACC), and post-processed to efficiently compile and view critical analysis data such as surface displacements, shear strains, various types of intensity measures, and maximum pore pressures and liquefaction times. These analyses, which were performed mainly on simple profiles with uniform layers of relative density, allowed for the systematic investigation of the sensitivity of lateral spreading-related mechanisms to ground shaking intensity, ground slope inclination, and soil properties such as relative density. The efficiency of PGA_M and CAV in predicting liquefaction triggering and post-triggering displacements, respectively, which had been proposed in earlier studies in a smaller range of conditions (Kramer et al. 2016) was confirmed in this larger study. The sensitivity study focused on the characterization of two key mechanisms: the reduction in seismic demands due to liquefaction in deeper layers, and the relationship between post-triggering shaking intensity and permanent shear strains. Functional forms for predicting both of these effects were established.

In Chapter 7, the demand reduction and shear strain formulations were evaluated against a larger set of about 40,000 randomized profiles, intended to represent a more realistic and broader range of soil and site conditions. With some modifications to account for the complex layering schemes encountered in these types of profiles, the basic trends observed and established in the preceding chapter were validated in the larger set of analyses (with larger uncertainties, as expected). A potential timing-based strain integration approach to lateral spreading was explored, and the use of a fully-probabilistic version of it was illustrated in a PBEE-type calculation to generate lateral spreading hazard curves for several example soil profiles in San Francisco, CA. The

use of the timing-based framework presented a unique opportunity to characterize the joint hazard curve of two intensity measures (PGA_M and CAV), using a potential novel application of the generalized conditional intensity measure approach (GCIM).

8.3 Conclusions

In the course of the research conducted in this dissertation, a number of broad themes emerged repeatedly, oftentimes in seemingly disparate investigation vectors; some of these themes are quite obvious, others may be more nuanced. The main conclusions drawn from the work presented here can be summarized as follows:

- Liquefaction triggering is an extremely complex, multi-layered, and multi-level phenomenon. Knowledge of its mechanical basis is necessary and useful, but there are both element- and system-level aspects of the problem that make it difficult to characterize, analyze and predict. It is a highly nonlinear phenomenon with large and sudden changes in material behavior. These complexities result in significant uncertainties in liquefaction-related problems; attempts to reduce those uncertainties are always worthwhile, but ignoring them entirely is poor science.

- Simplified procedures for liquefaction triggering are widely utilized in practice, but almost never in a manner that properly accounts for these uncertainties. This lack of treatment of uncertainty in practice leads to extremely inconsistent levels of liquefaction risk in design, with high variability in implied safety levels from one region to another, but also over the span of even a few kilometers in certain parts of the U.S.

- Fully-probabilistic analyses that account for uncertainties in liquefaction triggering over all levels of ground shaking are the most accurate and rational way to evaluate liquefaction hazards, but are computationally intensive. Nevertheless, more and more engineers are entering the profession with stronger coding backgrounds. Making computational tools for PLHA open-source can increase their visibility and use in practice, as well as improve them through valuable user feedback.

- At the same time, it would be unreasonable to require engineers to perform fully-probabilistic analyses for every liquefaction-related project. However, we should strive to be designing to consistent risk levels whenever possible, and large gains can be made in that sense by revising the mapped values that practitioners use in their conventional analyses to target a consistent, liquefaction-specific safety level.

- Ground motions can be "liquefaction-targeted" in a variety of ways, and not limited simply to the context of the simplified procedure and ground motion mapping. Different types of intensity measures, not just peak amplitude parameters, have been shown to be more efficient in liquefaction-related problems, and these IMs have and should continue to be targeted for use in liquefaction-related problems

- Efficient intensity measures should capture the ground motion characteristics that the system response of interest is sensitive to, i.e., amplitude, frequency content, and duration. Within the context of liquefaction, where the properties of the system vary drastically before and after liquefaction, it should not be surprising that different IMs can be more efficiently applied to the pre- and post-triggering portions of the problem. Understanding which IMs to use and when to use them is an important aspect to PBEE.

- In sites underlain by complex stratigraphies, the concept of a single time of liquefaction is not quite straightforward. Different layers may trigger at different times, and the triggering of one layer may alter the ground motions that propagate into shallower layers. In many cases, this reduction prevents the triggering of a layer that may otherwise have been expected to liquefy. It stands to reason, and has been borne out by the analyses performed in this dissertation, that demand reduction can be quantified, at least in a first-order sense, by considering the shaking intensity going into the liquefiable system, and the thickness and relative density of the liquefiable zone.

- Evaluating the timing of liquefaction and recognition of its effects on resulting shear strains at the element level has the potential to increase the accuracy of lateral spreading displacements pedictions. There is a strong mechanistic basis for predicting shear strains from the post-triggering IM, soil properties, and knowledge of the static shear stress conditions. At the same time, larger system-level effects must still be accounted for.

- The use of two IMs in a prediction framework does not mean that the uncertainty in ground shaking hazard characterization is doubling. Intensity measures are correlated to one another, some more than others, and these correlations can be utilized in a way that accommodates multiple IMs within a fully-probabilistic framework.

8.4 Recommendations for Future Research

As is the case with many research endeavors, and particularly so in natural hazards research, the work presented in this dissertation should is not a finished product. In order to be implemented and adopted into standard practice, the results of the liquefaction-targeted ground motion mapping framework must be published, disseminated, and submitted to the Provisions Update Committee

of the Building Seismic Safety Council (BSSC) for consideration in upcoming requirements for the International Building Code. This will likely require some additional verification and validation, as well as coordination with various agencies for creating the infrastructure needed to make these mapped parameters and adjustment factors available across the United States.

The PLHA computational platform presented in Chapter 3 is not intended to begin and end with the triggering of liquefaction as expressed by FS_L. In the near term, it should be extended to integrate with the various ground damage indices that utilize FS_L (e.g., LPI, LPI_{ISH}, LSN) and other liquefaction effects. Likewise, the feasibility of extending the liquefaction-targeted mapping concept to achieve greater consistency further down the PBEE integral towards more performance-relevant metrics should also be investigated. For extension outside of the FS_L-specific framework, `PyLHA` is maintained to be as modular as possible to accommodate newer triggering models, as well as other types of probabilistic models for the consequences of liquefaction, such as lateral spreading or ground settlement.

The numerical database developed for the lateral spreading study should have significant utility beyond the scope of the research presented in this dissertation. As discussed in Section 7.3.4, some revisions may be required in the initial parametric study; specifically, the time of liquefaction criteria should be calibrated to produce $PGA_{M,L}$ estimates that are consistent with those estimated using the simplified procedure, as well as to capture more elements that experienced significant permanent shear strains. There is also a clear static shear strain component to lateral spreading deformations; numerical models are not particularly well-calibrated to capture this aspect of post-triggering behavior, but future attempts to characterize this "slumping strain" component via laboratory methods (which present their own challenges) could yield significant benefits in the efficiency of a predictive framework. Another important extension of the numerical parametric study is in the context of two-dimensional problems with more complex slope topographies. The key elements of the numerical workflow can be used and adapted for 2D problems, but they require far more computing power and time, and data for post-processing. These types of conditions are more commonly encountered in the field, and any lateral spreading method will need to accommodate them.

Other potential areas of future research may exist in the form of alternatives to a strain integration-based procedure. Rather than attempt to estimate motions and shear strains at the element level, a potentially less complicated (but certainly less efficient) framework could be based on estimating the base motion, and characterizing susceptible soil layers using a density-weighted thickness parameter. Such a model could use either a timing-based or overall IM approach, and would be easier to deploy at scale for use in lateral spreading hazard mapping. Characterizing the soil conditions using a single parameter would allow for statistical interpolation to be used in

incorporating available subsurface data at in such large-scale mapping efforts.

Finally, it should be noted that, for all of the momentum building around using less traditional "liquefaction-targeted ground motions", current seismic hazard analysis infrastructure is still tilted heavily towards spectral amplitudes, and has largely not adapted much to accommodate these types of intensity measures. Most researchers (and practically all practitioners) cannot calculate hazard curves for CAV, cannot deaggregate the CAV hazard, and cannot select ground motions according to target CAV values. Advances can and should be made in making evolutionary IMs part of the seismic hazard framework, either through the development of multiple GMMs, or the expansion of the conditional IM method. In research pockets where hazard curves can be calculated, researchers should be investigating the impacts of their use in broader PBEE contexts, both to demonstrate their value and to refine the methodology for their application earthquake engineering.

Appendix A

Detailed Results of Liquefaction-Targeted Ground Motion Mapping Study

A.1 Liquefaction-Targeted Maps and Metadata for 475-year FS_L Return Period

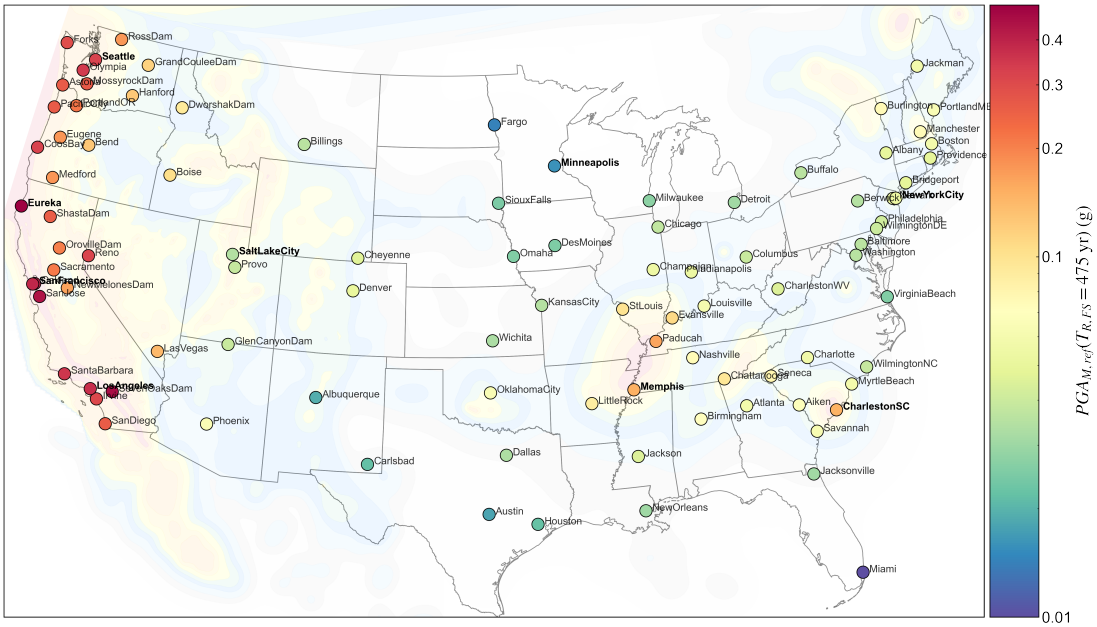

Figure A.1: Colormap scatterplot of mapped 475-year liquefaction-targeted PGA_M at reference site conditions ($z = 4$ m, $q_{c1Ncs} = 120$, $V_{s30} = 200$m/s) for 100 test locations.

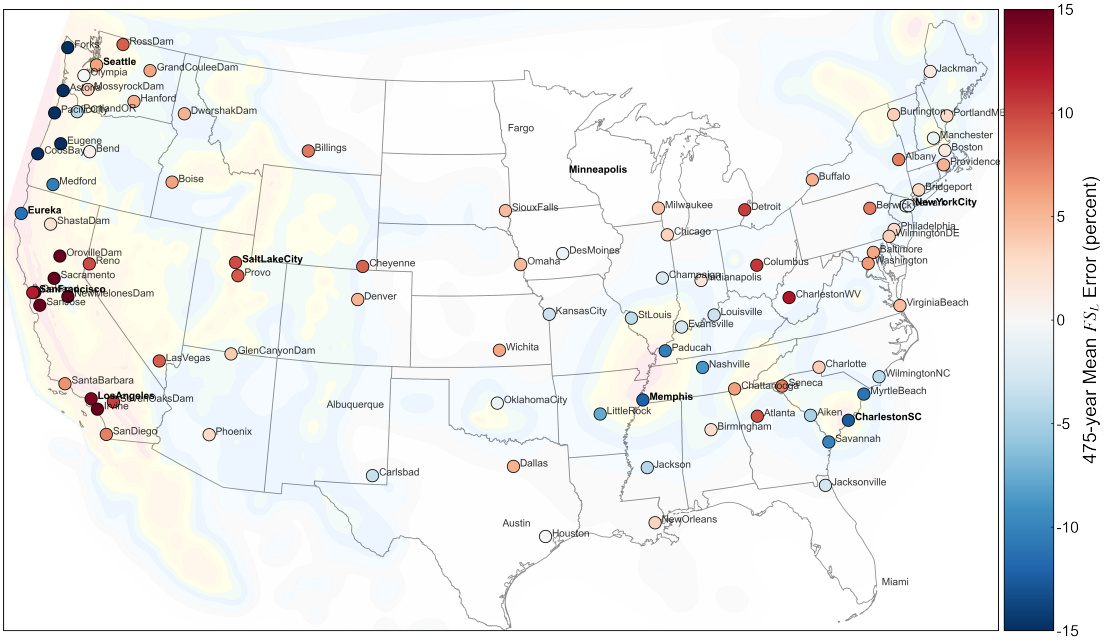

Figure A.2: Mean percent error in predicted 475-year factor of safety using conventional liquefaction hazard analysis procedures.

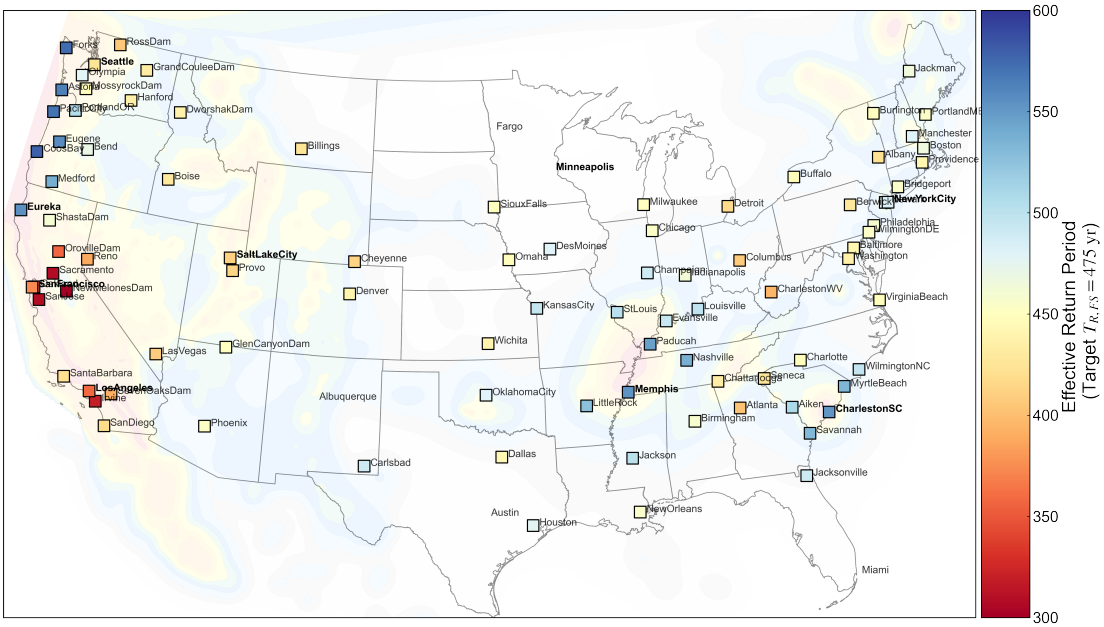

Figure A.3: Mean effective return period of predicted FS_L values using conventional liquefaction hazard analyses (target 475-year return period).

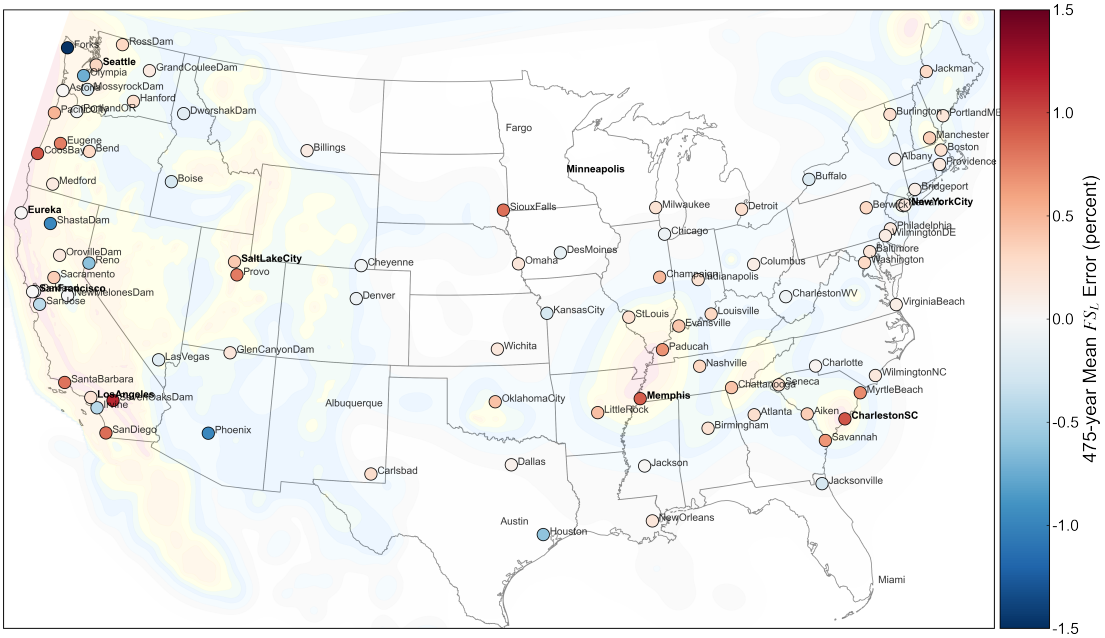

Figure A.4: Mean percent error in predicted 475-year factor of safety using mapped PGA_M procedure with estimated site adjustment factors.

Table A.1: PLHA metadata and comparison of estimated FS_L errors, effective return periods, and 50-year non-exceedance rates using mapped PGA_M (designated as "MAP") and conventional analyses (designated as "CON") for 475-year target FS_L, for Western U.S. sites.

Site	Lon.	Lat.	Reference PLHA Metadata					FS_L Error (%)				Effective T_R				50-year Non-exceedance (%)			
								MAP		CON		MAP		CON		MAP		CON	
			PGA_M	FS_L	$E[M_W]$	σ_{M_W}	γ_{M_W}	Mean	Std	Mean	Std	Mean	Std	Mean	Std	Mean	Std	Mean	Std
Astoria	-123.86	46.19	0.301	0.47	8.53	0.76	-1.7	0.02	1.32	-19.75	5.36	475	5	564	17	10	0.1	8.5	0.2
Bend	-121.32	44.06	0.11	1.31	7.47	1.28	-0.08	0.29	0.78	0.71	1.37	473	6	470	8	10	0.1	10.1	0.2
Boise	-116.21	43.62	0.085	1.74	6.46	0.8	0.55	-0.25	1.25	6.03	1.26	477	11	428	9	10	0.2	11	0.2
CoosBay	-124.22	43.37	0.401	0.35	8.57	0.7	-2.24	0.95	2.77	-22.34	3.25	473	8	580	9	10	0.2	8.3	0.1
DworshakDam	-116.3	46.52	0.071	2.08	6.45	0.93	0.9	-0.16	1.24	5.2	1.69	476	10	438	11	10	0.2	10.8	0.3
Eugene	-123.09	44.05	0.178	0.8	8.44	0.84	-1.54	0.77	1.58	-15.63	2.96	472	6	558	11	10.1	0.1	8.6	0.2
Eureka	-124.16	40.8	0.723	0.2	8.11	0.97	-0.76	0.01	2.55	-11.18	4.32	476	16	554	25	10	0.3	8.6	0.4
Forks	-124.39	47.95	0.353	0.4	8.35	0.92	-1.07	-1.48	3.07	-19.69	6.87	480	12	573	25	9.9	0.2	8.4	0.4
GrandCouleeDam	-118.98	47.96	0.097	1.51	6.67	1.13	0.82	0.13	0.75	5.94	2.72	474	6	432	17	10	0.1	10.9	0.4
Hanford	-119.49	46.55	0.109	1.34	6.79	1.13	0.69	0.24	0.75	5.43	2.42	473	6	435	15	10	0.1	10.9	0.4
Irvine	-117.83	33.68	0.377	0.39	6.85	0.86	-0.24	-0.42	0.88	19.24	5.82	480	10	319	30	9.9	0.2	14.6	1.4
LasVegas	-115.14	36.17	0.13	1.14	6.5	0.73	0.19	-0.18	0.62	9.07	2.78	476	5	408	19	10	0.1	11.6	0.5
LosAngeles	-118.24	34.05	0.482	0.3	6.91	0.8	-0.34	0.22	0.55	14.06	5.23	473	6	358	34	10	0.1	13.1	1.2
Medford	-122.88	42.33	0.176	0.81	8.29	0.95	-1.16	0.13	0.73	-10.43	3.74	474	4	539	19	10	0.1	8.9	0.3
MossyrockDam	-122.43	46.53	0.312	0.46	7.35	1.21	0.22	-0.23	0.95	3.48	2.32	477	8	449	13	10	0.2	10.6	0.3
NewMelonesDam	-120.54	37.99	0.16	0.91	7.02	0.91	0.1	-0.02	1.61	24.54	4.61	476	20	277	20	10	0.4	16.6	1.1
Oakland	-122.32	37.81	0.533	0.27	7.11	0.74	-0.69	0	0.73	15.57	4.15	475	8	342	26	10	0.2	13.7	1
Olympia	-122.9	47.04	0.429	0.34	7.55	1.12	0.21	-0.74	1.04	-0.27	1.73	481	8	477	14	9.9	0.2	10	0.3
OrovilleDam	-121.48	39.54	0.211	0.69	6.95	1.23	0.53	0.15	0.45	14.83	4.38	474	5	356	23	10	0.1	13.1	0.8
PacificCity	-123.96	45.2	0.306	0.46	8.56	0.74	-2.11	0.51	1.72	-20.69	3.66	474	5	570	11	10	0.1	8.4	0.2
Phoenix	-112.07	33.45	0.044	3.39	6.3	0.69	0.04	-0.98	4.04	3.02	0.61	484	30	453	4	9.9	0.6	10.4	0.1
PortlandOR	-122.68	45.52	0.233	0.62	7.69	1.3	-0.32	-0.04	1.2	-4.04	2.11	475	8	504	14	10	0.2	9.5	0.3
Provo	-111.66	40.23	0.022	6.87	5.78	0.63	0.34	0.78	2.07	9.22	0.6	470	16	413	4	10.1	0.3	11.4	0.1
Reno	-119.81	39.53	0.387	0.38	6.59	0.6	0.03	-0.62	2.25	9.75	3.01	483	25	389	25	9.9	0.5	12.1	0.8
RossDam	-121.07	48.73	0.171	0.85	6.91	1.13	0.62	0.32	1.07	8.98	3.25	473	10	406	18	10.1	0.2	11.6	0.5
Sacramento	-121.49	38.58	0.222	0.66	7.06	0.93	0.24	0.37	1.15	20.49	5.11	471	13	308	24	10.1	0.3	15.1	1.2
SaltLakeCity	-111.89	40.76	0.018	8.19	5.83	0.64	0.26	0.39	1.48	9.82	0.68	472	11	411	4	10.1	0.2	11.5	0.1
SanDiego	-117.16	32.72	0.296	0.5	6.7	0.72	0.15	0.84	2.59	7.53	4.87	470	23	417	34	10.1	0.5	11.4	0.9
SanFrancisco	-122.42	37.77	0.507	0.29	7.27	0.77	-0.99	0	0.57	11.82	3.7	475	6	373	27	10	0.1	12.6	0.9
SanJose	-121.89	37.34	0.606	0.24	6.97	0.74	-0.39	-0.41	1.33	19.59	4.2	480	16	309	24	9.9	0.3	15	1.1
SantaBarbara	-119.7	34.42	0.447	0.33	6.98	0.74	-0.43	0.81	2.45	6.76	4.26	470	23	420	32	10.1	0.5	11.3	0.9
Seattle	-122.33	47.61	0.399	0.36	7.23	1.03	0.63	0.32	0.73	6.08	2.44	473	7	426	13	10.1	0.1	11.1	0.3
SevenOaksDam	-117.1	34.12	0.641	0.23	7.15	0.86	-0.59	1.13	1.55	10.31	4.78	466	13	391	34	10.2	0.3	12.1	1
ShastaDam	-122.42	40.72	0.293	0.49	7.41	1.42	-0.09	-0.96	1.83	2.14	2.61	482	14	460	16	9.9	0.3	10.3	0.3

Table A.2: PLHA metadata and comparison of estimated FS_L errors, effective return periods, and 50-year non-exceedance rates using mapped PGA_M (designated as "MAP") and conventional analyses (designated as "CON") for 475-year target FS_L, for Central & Eastern U.S. sites.

Site	Lon.	Lat.	Reference PLHA Metadata					FS_L Error (%)				Effective T_R				50-year Non-exceedance (%)			
								MAP		CON		MAP		CON		MAP		CON	
			PGA_M	FS_L	$E[M_w]$	σ_{M_w}	γ_{M_w}	Mean	Std	Mean	Std	Mean	Std	Mean	Std	Mean	Std	Mean	Std
Aiken	-81.74	33.34	0.047	3.11	6.49	0.85	-0.57	0.37	0.52	-4.89	1.25	473	3	509	8	10	0.1	9.4	0.1
Albany	-73.76	42.65	0.031	4.82	5.86	0.73	0.38	0.09	0.46	7.73	0.17	474	3	422	2	10	0.1	11.2	0
Atlanta	-84.39	33.75	0.038	3.88	6.4	0.94	-0.03	0.25	0.48	9.57	0.42	473	4	402	2	10	0.1	11.7	0
Baltimore	-76.61	39.29	0.019	7.76	5.71	0.71	0.67	0.19	0.34	5.83	0.26	474	2	441	1	10	0	10.7	0
Berwick	-76.14	41.09	0.019	7.93	5.83	0.72	0.44	0.3	0.32	7.78	0.25	473	2	427	2	10	0	11.1	0
Billings	-108.5	45.78	0.02	7.68	5.73	0.63	0.41	0.13	0.44	7.87	0.49	474	3	424	3	10	0.1	11.1	0.1
Birmingham	-86.8	33.52	0.05	2.98	6.29	1.09	0.15	0.22	0.47	2.7	1.42	473	3	457	9	10	0.1	10.4	0.2
Boston	-71.06	42.36	0.038	3.93	5.67	0.69	0.7	0.23	0.47	1.47	0.24	473	3	465	2	10	0.1	10.2	0
Bridgeport	-73.2	41.19	0.029	5.1	5.66	0.68	0.68	0.1	0.39	3.2	0.14	474	3	455	1	10	0.1	10.4	0
Buffalo	-78.88	42.89	0.02	7.67	5.68	0.72	0.7	-0.22	0.56	5.45	0.73	476	3	446	4	10	0.1	10.6	0.1
Burlington	-73.21	44.48	0.055	2.72	5.79	0.74	0.53	0.25	0.7	3.67	0.43	473	5	449	3	10	0.1	10.6	0.1
Carlsbad	-103.79	32.37	0.01	15.33	5.53	0.64	0.94	0.27	0.17	-3.4	0.09	474	1	490	0	10	0	9.7	0
Champaign	-88.24	40.12	0.034	4.29	6.85	0.93	-0.72	0.48	0.56	-2.15	1.68	472	4	490	12	10.1	0.1	9.7	0.2
CharlestonSC	-79.93	32.78	0.137	1.08	6.35	0.93	-0.41	0.94	1.5	-12.64	1.85	470	8	553	9	10.1	0.2	8.7	0.1
CharlestonWV	-81.63	38.35	0.027	5.52	6.14	0.95	0.34	-0.07	0.43	12.25	1.6	476	3	395	8	10	0.1	11.9	0.2
Charlotte	-80.84	35.23	0.036	4.08	6.4	0.88	-0.31	0.04	0.52	3.71	0.4	475	4	448	3	10	0.1	10.6	0.1
Chattanooga	-85.31	35.05	0.074	2.01	5.94	0.95	0.7	0.42	0.79	6.17	2.4	472	6	433	15	10.1	0.1	10.9	0.4
Cheyenne	-104.82	41.14	0.028	5.39	5.8	0.66	0.31	-0.05	0.51	8.8	0.44	475	4	413	3	10	0.1	11.4	0.1
Chicago	-87.63	41.88	0.021	7.16	6.52	1.08	-0.21	-0.09	0.35	3.51	0.49	476	2	454	2	10	0	10.4	0.1
Columbus	-83	39.96	0.022	6.62	6.33	1.01	0.11	0.11	0.29	10.58	1.04	474	2	407	5	10	0	11.6	0.1
Dallas	-96.8	32.78	0.017	8.46	6.5	1.01	-0.13	0.07	0.21	5.34	0.24	475	1	443	1	10	0	10.7	0
Denver	-104.99	39.74	0.031	4.79	5.71	0.66	0.44	-0.07	0.51	5.16	0.21	476	4	441	2	10	0.1	10.7	0
DesMoines	-93.61	41.6	0.012	12.16	6.94	0.93	-0.93	-0.13	0.34	-0.93	0.69	476	2	480	4	10	0	9.9	0.1
Detroit	-83.05	42.33	0.016	9.34	6.08	0.99	0.49	0.24	0.29	10.39	1.83	474	2	417	9	10	0	11.3	0.2
Evansville	-87.57	37.97	0.091	1.62	6.57	1.07	-0.34	0.41	0.96	-2.66	0.66	472	6	494	5	10.1	0.1	9.6	0.1
GlenCanyonDam	-111.48	36.94	0.022	6.83	5.6	0.59	0.58	0.18	0.42	3.87	0.51	474	3	451	3	10	0.1	10.5	0.1
Houston	-95.37	29.76	0.01	14.93	6.4	1.1	0.01	-0.61	0.18	-0.17	0.16	478	1	476	1	9.9	0	10	0
Indianapolis	-86.16	39.77	0.034	4.36	6.61	1.03	-0.36	0.22	0.37	1.97	0.27	473	3	462	2	10	0.1	10.3	0
Jackman	-70.25	45.62	0.038	3.85	6.34	0.81	-0.34	0.29	0.54	1.42	1.29	473	4	464	10	10	0.1	10.2	0.2
Jackson	-90.18	32.3	0.027	5.44	7.03	0.89	-1.11	0.02	0.35	-4.25	1.65	475	2	501	10	10	0	9.5	0.2
Jacksonville	-81.66	30.33	0.016	9.21	6.7	0.81	-0.92	-0.25	0.77	-2.91	0.79	476	4	491	4	10	0.1	9.7	0.1
KansasCity	-94.58	39.1	0.019	7.72	6.92	0.96	-0.9	-0.25	0.48	-3.21	0.92	477	3	495	5	10	0.1	9.6	0.1
LittleRock	-92.29	34.75	0.067	2.2	6.76	1.05	-0.59	0.45	0.72	-7.68	0.84	472	4	527	4	10.1	0.1	9.1	0.1
Louisville	-85.76	38.25	0.039	3.71	6.82	0.95	-0.72	0.31	0.46	-3.21	1.35	473	3	498	9	10	0.1	9.6	0.2
Manchester	-71.45	43	0.054	2.8	5.59	0.67	0.85	0.35	0.58	-0.78	0.62	473	4	480	4	10	0.1	9.9	0.1
Memphis	-90.05	35.15	0.141	1.04	6.93	0.97	-0.97	0.91	1.42	-12.2	1.5	470	8	554	6	10.1	0.2	8.6	0.1
Milwaukee	-87.91	43.04	0.013	10.96	6.56	1.06	-0.25	0.22	0.19	4.43	0.42	474	1	450	2	10	0	10.5	0
MyrtleBeach	-78.89	33.69	0.038	3.85	6.7	0.73	-1.14	0.71	0.63	-11.02	2.58	472	3	534	13	10.1	0.1	8.9	0.2
Nashville	-86.78	36.16	0.054	2.7	7.13	0.77	-1.32	0.31	0.74	-8.83	2.44	473	5	537	16	10	0.1	8.9	0.3
Newark	-74.17	40.74	0.034	4.45	5.54	0.63	0.87	0.16	0.4	-1.3	0.22	474	2	482	1	10	0	9.9	0
NewOrleans	-90.07	29.95	0.015	9.54	6.6	1.08	-0.29	0.18	0.21	3.48	0.41	474	1	456	2	10	0	10.4	0
NewYorkCity	-74.01	40.71	0.034	4.46	5.54	0.63	0.87	0.15	0.4	-1.22	0.23	474	2	482	1	10	0	9.9	0
OklahomaCity	-97.52	35.47	0.042	3.55	5.84	0.86	0.72	0.44	0.42	-0.79	0.62	472	3	480	4	10.1	0.1	9.9	0.1
Omaha	-96	41.25	0.012	11.94	6.48	1.08	-0.11	0.18	0.2	4.82	0.53	474	1	448	3	10	0	10.6	0.1
Paducah	-88.6	37.08	0.154	0.95	6.82	1	-0.79	0.68	1.71	-10.38	1.43	471	10	546	7	10.1	0.2	8.8	0.1
Philadelphia	-75.17	39.95	0.024	6.35	5.62	0.66	0.76	0.16	0.33	3.04	0.09	474	2	457	1	10	0	10.4	0
PortlandME	-70.26	43.66	0.043	3.52	5.77	0.74	0.59	0.2	0.52	3.02	0.35	474	4	454	2	10	0.1	10.4	0
Providence	-71.41	41.82	0.03	5.09	5.74	0.71	0.58	0.15	0.4	5.18	0.16	474	3	441	1	10	0.1	10.7	0
Savannah	-81.1	32.08	0.042	3.52	6.68	0.76	-1.04	0.66	0.55	-10.02	2.33	472	3	531	12	10.1	0.1	9	0.2
Seneca	-82.89	34.79	0.058	2.56	5.89	0.87	0.57	0.24	0.99	7.51	2.16	473	7	426	13	10	0.1	11.1	0.3
SiouxFalls	-96.73	43.54	0.012	12.65	5.8	0.86	0.99	0.82	0.16	4.75	0.54	470	1	449	3	10.1	0	10.5	0.1
StLouis	-90.18	38.62	0.079	1.86	6.61	1.08	-0.37	0.24	0.81	-3.91	0.33	473	5	502	3	10	0.1	9.5	0.1
VirginiaBeach	-75.98	36.85	0.012	12.03	6.17	0.86	0	0.11	0.2	4.69	0.08	474	1	448	1	10	0	10.6	0
Washington	-77.04	38.91	0.019	7.76	5.76	0.73	0.65	0.29	0.28	6.4	0.21	473	2	437	1	10	0	10.8	0
Wichita	-97.33	37.69	0.017	8.51	6.56	1.02	-0.23	0.17	0.26	5.85	0.23	474	2	439	1	10	0	10.8	0
WilmingtonDE	-75.54	39.74	0.022	6.7	5.62	0.67	0.77	0.12	0.33	3.71	0.15	474	2	454	1	10	0	10.4	0
WilmingtonNC	-77.94	34.23	0.022	6.74	6.65	0.77	-1.02	0.18	0.3	-4.05	1.86	474	1	496	9	10	0	9.6	0.2

A.2 Liquefaction-Targeted Maps and Metadata for 975-year FS_L Return Period

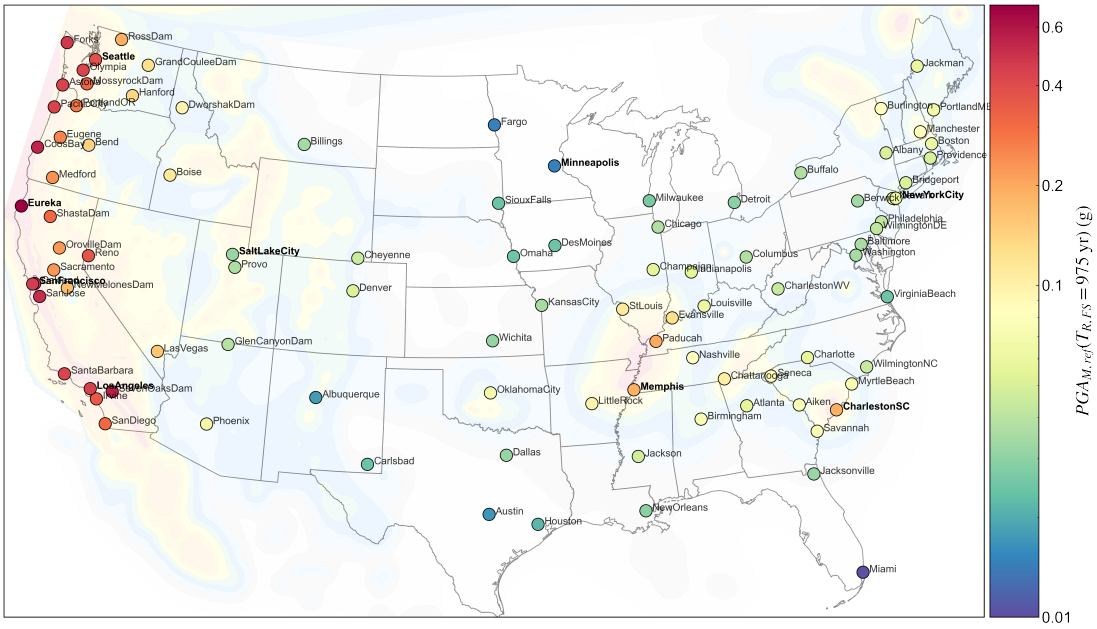

Figure A.5: Colormap scatterplot of mapped 975-year liquefaction-targeted PGA_M at reference site conditions ($z = 4$ m, $q_{c1Ncs} = 120$, $V_{s30} = 200$m/s) for 100 test locations.

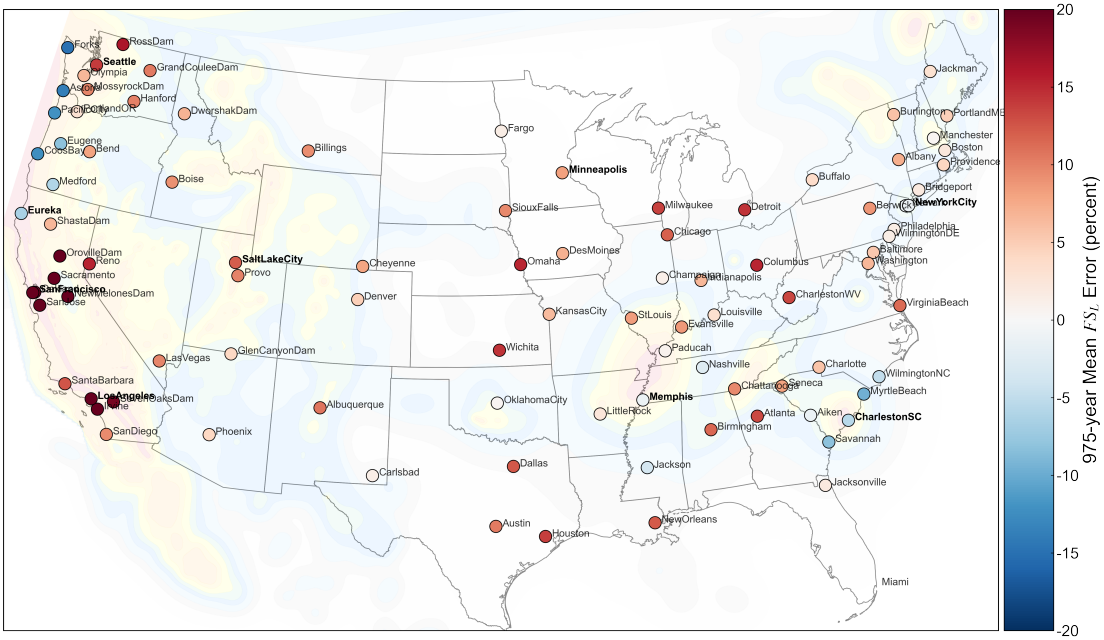

Figure A.6: Mean percent error in predicted 975-year factor of safety using conventional liquefaction hazard analysis procedures.

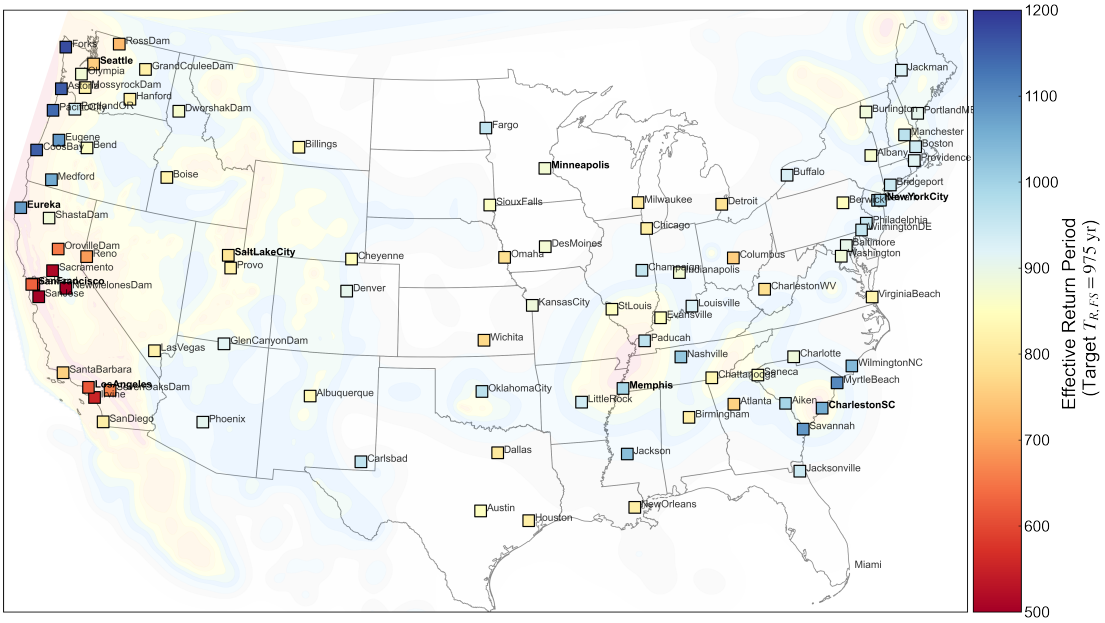

Figure A.7: Mean effective return period of predicted FS_L values using conventional liquefaction hazard analyses (target 975-year return period).

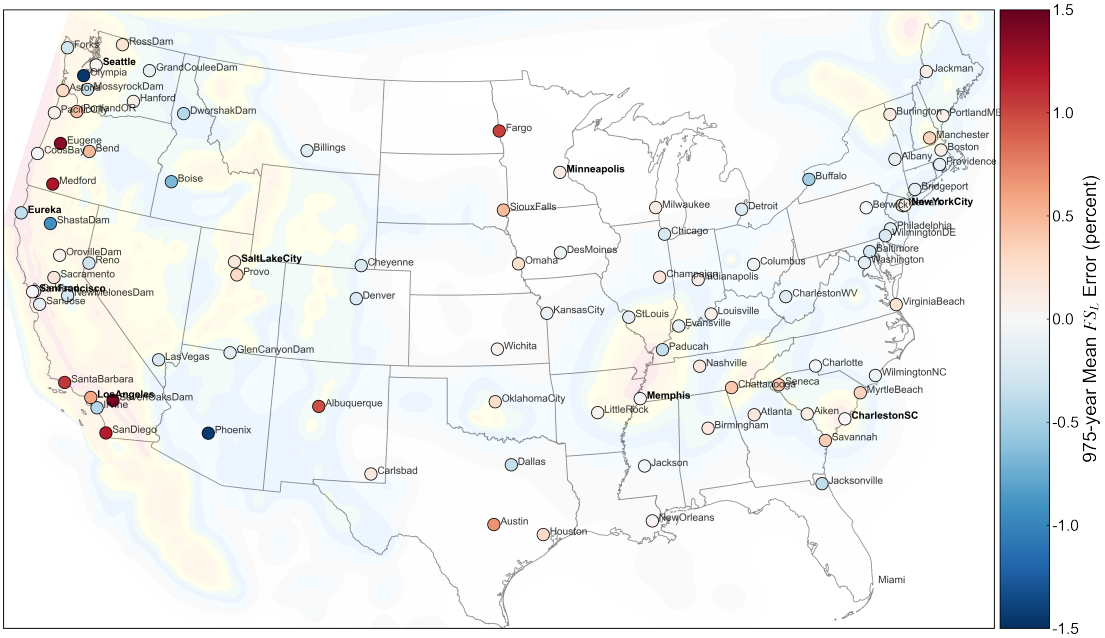

Figure A.8: Mean percent error in predicted 975-year factor of safety using mapped PGA_M procedure with estimated site adjustment factors.

Table A.3: PLHA metadata and comparison of estimated FS_L errors, effective return periods, and 50-year non-exceedance rates using mapped PGA_M (designated as "MAP") and conventional analyses (designated as "CON") for 975-year target FS_L, for Western U.S. sites.

Site	Lon.	Lat.	Reference PLHA Metadata					FS_L Error (%)				Effective T_R				50-year Non-exceedance (%)			
								MAP		CON		MAP		CON		MAP		CON	
			PGA_M	FS_L	$E[M_W]$	σ_{M_W}	γ_{M_W}	Mean	Std	Mean	Std	Mean	Std	Mean	Std	Mean	Std	Mean	Std
Astoria	-123.86	46.19	0.637	0.22	8.79	0.47	-2.7	0.3	2.28	-13.76	1.57	973	22	1157	15	5	0.1	4.2	0.1
Bend	-121.32	44.06	0.169	0.85	7.62	1.29	-0.23	0.49	1.07	8.01	4.44	968	18	859	47	5	0.1	5.7	0.3
Boise	-116.21	43.62	0.124	1.19	6.48	0.78	0.42	-0.67	2.28	9.08	2.04	988	44	824	30	4.9	0.2	5.9	0.2
CoosBay	-124.22	43.37	0.825	0.17	8.74	0.44	-2.45	-0.03	4.12	-12.39	1.59	981	48	1156	21	5	0.2	4.2	0.1
DworshakDam	-116.3	46.52	0.108	1.37	6.44	0.9	0.86	-0.43	1.75	6.97	2.57	982	31	867	36	5	0.2	5.6	0.2
Eugene	-123.09	44.05	0.337	0.42	8.65	0.67	-2.03	1.35	3.75	-8.16	1.02	961	44	1087	14	5.1	0.2	4.5	0.1
Eureka	-124.16	40.8	1.119	0.13	8.42	0.78	-1.35	-0.35	4.76	-6.54	5.22	990	66	1082	81	4.9	0.3	4.5	0.3
Forks	-124.39	47.95	0.702	0.2	8.71	0.61	-2.24	-0.28	2.11	-14.92	2.23	979	21	1173	22	5	0.1	4.2	0.1
GrandCouleeDam	-118.98	47.96	0.145	1.01	6.68	1.12	0.81	-0.11	1.36	10.46	5.38	977	25	818	63	5	0.1	6	0.5
Hanford	-119.49	46.55	0.162	0.9	6.83	1.12	0.67	0.1	0.88	10.13	5.16	973	16	820	61	5	0.1	5.9	0.5
Irvine	-117.83	33.68	0.496	0.29	6.91	0.85	-0.34	-0.44	1.49	25.84	7.54	986	39	552	71	5	0.2	8.8	1.2
LasVegas	-115.14	36.17	0.191	0.77	6.47	0.68	0.25	-0.26	0.87	9.73	3.68	979	16	820	53	5	0.1	5.9	0.4
LosAngeles	-118.24	34.05	0.642	0.23	6.97	0.76	-0.43	0.58	0.89	21.61	7.02	963	21	616	79	5.1	0.1	7.9	1.1
Medford	-122.88	42.33	0.304	0.46	8.57	0.77	-1.79	1.22	3.64	-6.02	1.49	961	47	1061	21	5.1	0.2	4.6	0.1
MossyrockDam	-122.43	46.53	0.446	0.32	7.58	1.22	0	-0.34	1.24	9.77	5.04	981	24	823	44	5	0.1	5.9	0.3
NewMelonesDam	-120.54	37.99	0.208	0.7	7.03	0.95	0.1	-0.28	1.94	31.43	7.62	984	52	478	57	5	0.3	10.1	1.3
Oakland	-122.32	37.81	0.699	0.21	7.17	0.71	-0.78	0.08	0.31	25.49	6.48	973	8	555	63	5	0	8.7	1
Olympia	-122.9	47.04	0.623	0.23	7.81	1.11	-0.05	-1.44	1.87	6.56	4.31	998	30	878	43	4.9	0.1	5.6	0.3
OrovilleDam	-121.48	39.54	0.288	0.51	7.06	1.29	0.44	0.07	1.58	21.19	10.36	975	32	655	81	5	0.2	7.5	1
PacificCity	-123.96	45.2	0.641	0.22	8.76	0.49	-2.78	0.08	2.69	-12.13	1.34	976	29	1141	15	5	0.1	4.3	0.1
Phoenix	-112.07	33.45	0.068	2.19	6.34	0.7	-0.03	-1.44	5.06	4.17	0.38	1004	86	910	6	4.9	0.4	5.3	0
PortlandOR	-122.68	45.52	0.363	0.39	7.97	1.24	-0.63	0.45	1.98	3.04	5.3	969	31	939	56	5	0.2	5.2	0.3
Provo	-111.66	40.23	0.033	4.52	5.86	0.65	0.22	0.3	1.65	9.9	0.58	970	29	822	10	5	0.1	5.9	0.1
Reno	-119.81	39.53	0.52	0.28	6.65	0.56	-0.06	-0.31	2.22	15.44	3.91	987	56	691	64	5	0.3	7	0.7
RossDam	-121.07	48.73	0.243	0.6	6.99	1.16	0.56	0.21	0.88	16.33	8.23	972	17	729	73	5	0.1	6.7	0.8
Sacramento	-121.49	38.58	0.291	0.5	7.09	0.96	0.24	0.19	0.8	29.65	9.62	971	20	513	70	5	0.1	9.5	1.4
SaltLakeCity	-111.89	40.76	0.028	5.38	5.92	0.66	0.15	0.17	1.72	12.16	0.64	973	31	790	10	5	0.2	6.1	0.1
SanDiego	-117.16	32.72	0.425	0.35	6.7	0.67	0.17	1.18	3.76	9.5	5.6	962	76	813	87	5.1	0.4	6	0.7
SanFrancisco	-122.42	37.77	0.675	0.21	7.37	0.74	-1.19	-0.03	0.81	20.65	5.48	977	20	626	61	5	0.1	7.7	0.8
SanJose	-121.89	37.34	0.781	0.19	7.03	0.72	-0.45	-0.16	0.51	29.13	6.45	980	14	499	56	5	0.1	9.6	1.1
SantaBarbara	-119.7	34.42	0.621	0.23	7.04	0.7	-0.58	1.08	3.22	12.53	5.24	961	70	758	78	5.1	0.4	6.5	0.7
Seattle	-122.33	47.61	0.557	0.26	7.38	1.04	0.54	0.03	1.94	13.99	6.33	975	40	756	53	5	0.2	6.4	0.5
SevenOaksDam	-117.1	34.12	0.862	0.17	7.27	0.8	-0.73	1.42	2.96	19.12	6.46	951	65	662	75	5.1	0.3	7.4	0.8
ShastaDam	-122.42	40.72	0.425	0.34	7.78	1.4	-0.52	-0.92	2	6.65	6	990	34	882	53	4.9	0.2	5.5	0.4

Table A.4: PLHA metadata and comparison of estimated FS_L errors, effective return periods, and 50-year non-exceedance rates using mapped PGA_M (designated as "MAP") and conventional analyses (designated as "CON") for 975-year target FS_L, for Central & Eastern U.S. sites.

Site	Lon.	Lat.	Reference PLHA Metadata					FS_L Error (%)				Effective T_R				50-year Non-exceedance (%)			
								MAP		CON		MAP		CON		MAP		CON	
			PGA_M	FS_L	$E[M_w]$	σ_{M_w}	γ_{M_w}	Mean	Std	Mean	Std	Mean	Std	Mean	Std	Mean	Std	Mean	Std
Aiken	-81.74	33.34	0.078	1.9	6.63	0.81	-0.89	0.11	0.5	-1.31	0.43	973	8	995	7	5	0	4.9	0
Albany	-73.76	42.65	0.048	3.11	5.9	0.76	0.32	-0.11	0.81	7.19	0.46	977	13	868	6	5	0.1	5.6	0
Atlanta	-84.39	33.75	0.014	10.81	5.98	0.69	0.08	0.97	0.32	10.7	0.23	961	5	839	4	5.1	0	5.8	0
Baltimore	-76.61	39.29	0.055	2.67	6.45	0.92	-0.1	0.16	0.56	13.14	1.5	972	11	762	17	5	0.1	6.4	0.1
Berwick	-76.14	41.09	0.013	11.34	6.28	1	0.18	0.67	0.14	10.39	1.22	966	2	851	13	5	0	5.7	0.1
Billings	-108.5	45.78	0.032	4.67	5.75	0.71	0.58	-0.27	0.83	5.33	0.22	979	12	902	3	5	0.1	5.4	0
Birmingham	-86.8	33.52	0.03	5.01	5.9	0.73	0.33	-0.01	0.8	8.77	0.24	975	13	848	4	5	0.1	5.7	0
Boston	-71.06	42.36	0.03	4.94	5.81	0.65	0.3	-0.18	0.88	9.37	0.51	978	15	835	8	5	0.1	5.8	0.1
Bridgeport	-73.2	41.19	0.078	1.9	6.26	1.09	0.23	0.16	0.76	11.54	4.08	972	13	816	47	5	0.1	6	0.3
Buffalo	-78.88	42.89	0.062	2.42	5.71	0.7	0.62	0.1	0.98	2.34	0.47	974	15	941	7	5	0.1	5.2	0
Burlington	-73.21	44.48	0.049	3.09	5.7	0.69	0.61	-0.11	0.91	1.97	0.27	977	13	947	4	5	0.1	5.1	0
Carlsbad	-103.79	32.37	0.034	4.42	5.65	0.7	0.74	-0.53	0.92	3.69	0.74	982	12	928	9	5	0.1	5.2	0.1
Champaign	-88.24	40.12	0.085	1.76	5.82	0.75	0.48	0.13	0.94	5.91	1.02	973	16	885	14	5	0.1	5.5	0.1
CharlestonSC	-79.93	32.78	0.02	7.53	5.53	0.62	0.91	0.16	0.98	1.31	0.15	973	11	961	2	5	0.1	5.1	0
CharlestonWV	-81.63	38.35	0.054	2.69	7.01	0.88	-1.05	0.18	0.39	1.11	0.53	972	6	957	9	5	0	5.1	0
Charlotte	-80.84	35.23	0.238	0.62	6.55	0.87	-0.82	0.01	1.22	-5.61	0.74	975	17	1060	10	5	0.1	4.6	0
Chattanooga	-85.31	35.05	0.041	3.65	6.09	0.92	0.38	-0.19	0.73	13.35	2.19	978	13	780	27	5	0.1	6.2	0.2
Cheyenne	-104.82	41.14	0.056	2.65	6.47	0.86	-0.48	-0.02	0.58	5.63	0.56	975	10	886	7	5	0	5.5	0
Chicago	-87.63	41.88	0.114	1.31	5.89	0.91	0.75	0.41	1.11	9.68	3.84	968	19	833	49	5	0.1	5.8	0.3
Columbus	-83	39.96	0.042	3.58	5.87	0.68	0.23	-0.24	0.83	7.93	0.26	979	15	849	5	5	0.1	5.7	0
Dallas	-96.8	32.78	0.033	4.41	6.51	1.08	-0.17	-0.24	0.49	11.88	2.39	979	8	814	26	5	0	6	0.2
Denver	-104.99	39.74	0.034	4.35	6.32	1	0.14	-0.08	0.53	15.23	2.2	977	10	755	24	5	0	6.4	0.2
DesMoines	-93.61	41.6	0.028	5.29	6.56	0.98	-0.21	-0.35	0.5	12.5	1.28	981	8	799	13	5	0	6.1	0.1
Detroit	-83.05	42.33	0.05	3.03	5.75	0.68	0.41	-0.23	0.91	4.74	0.34	979	14	905	4	5	0.1	5.4	0
Evansville	-87.57	37.97	0.021	7.04	7.03	0.93	-1.09	-0.08	0.34	7.13	0.27	976	5	877	2	5	0	5.5	0
GlenCanyonDam	-111.48	36.94	0.026	5.77	6.03	0.95	0.57	-0.2	0.77	14.4	2.43	978	12	788	26	5	0.1	6.2	0.2
Houston	-95.37	29.76	0.143	1.03	6.63	1.07	-0.42	-0.1	0.51	8.75	4.54	977	9	851	50	5	0	5.7	0.3
Indianapolis	-86.16	39.77	0.011	13.86	5.6	0.61	0.59	1.03	0.19	1.56	0.04	964	2	958	0	5.1	0	5.1	0
Jackman	-70.25	45.62	0.035	4.25	5.69	0.62	0.45	-0.17	0.94	4.09	0.55	978	15	914	8	5	0.1	5.3	0
Jackson	-90.18	32.3	0.017	8.51	6.35	1.09	0.11	0.29	0.57	13.8	2.84	971	8	817	27	5	0	5.9	0.2
Jacksonville	-81.66	30.33	0.054	2.74	6.66	1.04	-0.45	0.1	0.47	6.67	1.54	973	8	877	19	5	0	5.5	0.1
KansasCity	-94.58	39.1	0.059	2.49	6.47	0.81	-0.58	0.08	0.63	3.08	0.58	974	11	925	10	5	0.1	5.3	0.1
LittleRock	-92.29	34.75	0.045	3.21	7.18	0.85	-1.45	-0.04	0.31	-3.56	0.65	976	5	1032	9	5	0	4.7	0
Louisville	-85.76	38.25	0.028	5.16	6.79	0.77	-1.25	-0.37	0.43	2.01	0.27	980	6	948	4	5	0	5.1	0
Manchester	-71.45	43	0.031	4.64	7.01	0.96	-1.04	-0.08	0.29	6.29	0.52	976	5	884	5	5	0	5.5	0
Memphis	-90.05	35.15	0.109	1.34	6.87	1.03	-0.77	0.05	0.53	2.39	1.68	974	8	940	22	5	0	5.2	0.1
Milwaukee	-87.91	43.04	0.062	2.35	6.95	0.93	-0.95	0.09	0.38	3.13	0.51	974	6	925	6	5	0	5.3	0
MyrtleBeach	-78.89	33.69	0.09	1.67	5.6	0.67	0.81	0.34	1.18	0.37	0.86	970	17	970	12	5	0.1	5	0.1
Nashville	-86.78	36.16	0.236	0.62	7.09	0.91	-1.3	-0.03	0.5	-1.17	1.83	976	8	995	27	5	0	4.9	0.1
Newark	-74.17	40.74	0.022	6.58	6.58	1.06	-0.26	0.12	0.38	13.61	1.91	973	6	798	19	5	0	6.1	0.1
NewOrleans	-90.07	29.95	0.011	13.48	6.23	1.03	0.3	0.12	0.27	8.13	0.93	973	4	875	11	5	0	5.6	0.1
NewYorkCity	-74.01	40.71	0.074	1.97	6.94	0.58	-1.95	0.33	0.72	-9.68	1.36	971	8	1106	16	5	0	4.4	0.1
OklahomaCity	-97.52	35.47	0.088	1.64	7.29	0.7	-1.86	0.15	0.93	-2.64	1.12	973	14	1018	18	5	0.1	4.8	0.1
Omaha	-96	41.25	0.059	2.53	5.57	0.64	0.81	0.12	1.11	-1.22	0.4	974	15	991	5	5	0.1	4.9	0
Paducah	-88.6	37.08	0.026	5.73	6.62	1.09	-0.29	0.04	0.37	12.21	1.98	974	6	814	20	5	0	6	0.1
Philadelphia	-75.17	39.95	0.059	2.54	5.57	0.64	0.82	0.1	1.11	-1.15	0.41	974	14	990	5	5	0.1	4.9	0
PortlandME	-70.26	43.66	0.071	2.12	5.85	0.81	0.54	0.28	0.92	0.42	0.96	971	13	969	13	5	0.1	5	0.1
Providence	-71.41	41.82	0.021	7.16	6.49	1.08	-0.08	0.24	0.41	15.28	2.21	971	6	783	21	5	0	6.2	0.2
Savannah	-81.1	32.08	0.249	0.59	6.98	0.94	-1.11	-0.37	0.66	0.88	2.55	981	11	964	34	5	0.1	5.1	0.2
Seneca	-82.89	34.79	0.04	3.76	5.67	0.67	0.65	-0.17	0.9	1.43	0.19	978	13	955	3	5	0.1	5.1	0
SiouxFalls	-96.73	43.54	0.067	2.22	5.79	0.74	0.54	0.07	0.95	4.72	0.84	974	15	905	11	5	0.1	5.4	0.1
StLouis	-90.18	38.62	0.047	3.19	5.79	0.72	0.5	-0.12	0.85	4.22	0.25	977	13	913	3	5	0.1	5.3	0
VirginiaBeach	-75.98	36.85	0.078	1.86	6.9	0.63	-1.74	0.37	0.65	-8.15	1.33	971	8	1087	16	5	0	4.5	0.1
Washington	-77.04	38.91	0.092	1.63	5.82	0.83	0.64	0.4	1.48	8.05	3.24	969	23	862	42	5	0.1	5.7	0.3
Wichita	-97.33	37.69	0.02	7.37	5.79	0.8	0.96	0.48	0.8	9.6	0.79	968	11	855	9	5	0.1	5.7	0.1
WilmingtonDE	-75.54	39.74	0.125	1.17	6.67	1.08	-0.45	-0.16	0.49	8.31	3.76	978	8	855	43	5	0	5.7	0.3
WilmingtonNC	-77.94	34.23	0.021	7.19	6.22	0.87	-0.07	0.21	0.53	11.4	0.47	972	8	826	4	5	0	5.9	0

A.3 Liquefaction-Targeted Maps and Metadata for 2475-year FS_L Return Period

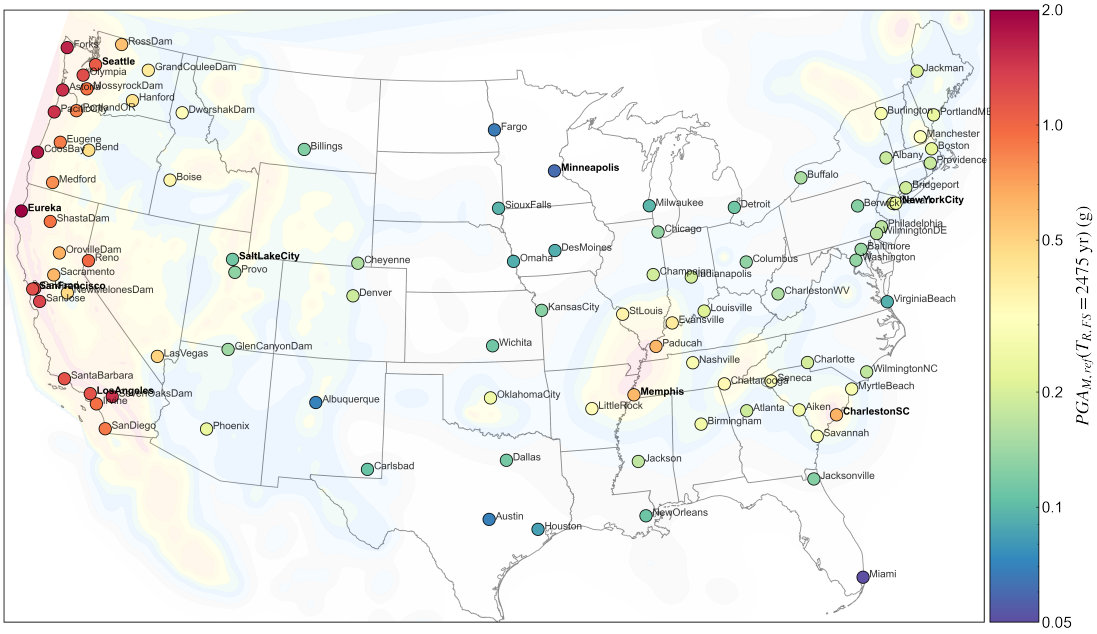

Figure A.9: Colormap scatterplot of mapped 2,475-year liquefaction-targeted PGA_M at reference site conditions ($z = 4$ m, $q_{c1Ncs} = 120$, $V_{s30} = 200$m/s) for 100 test locations.

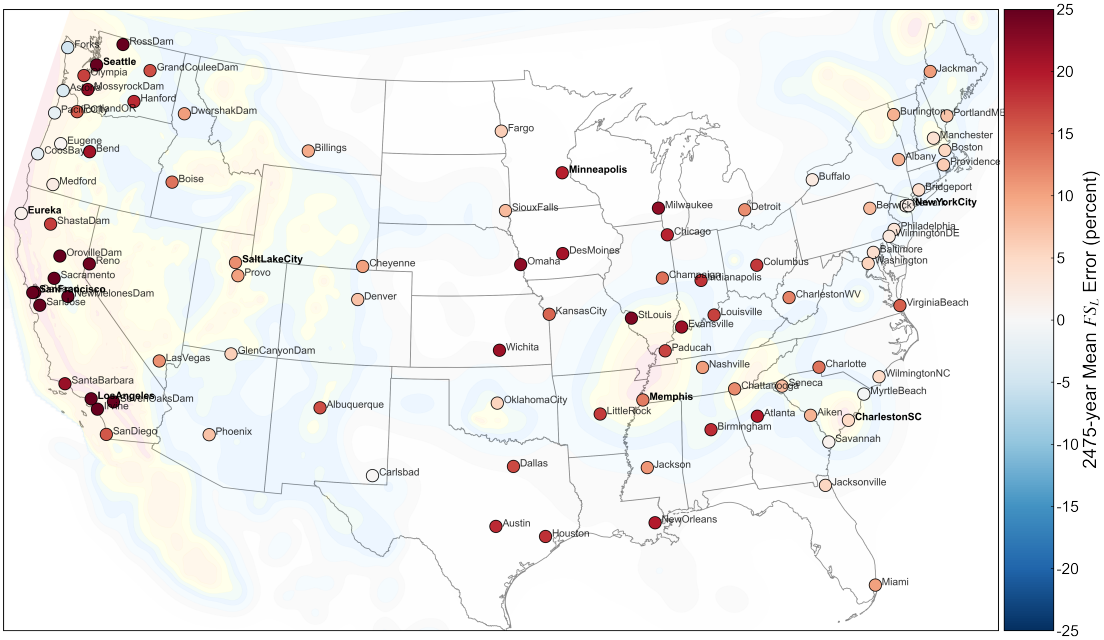

Figure A.10: Mean percent error in predicted 2,475-year factor of safety using conventional liquefaction hazard analysis procedures.

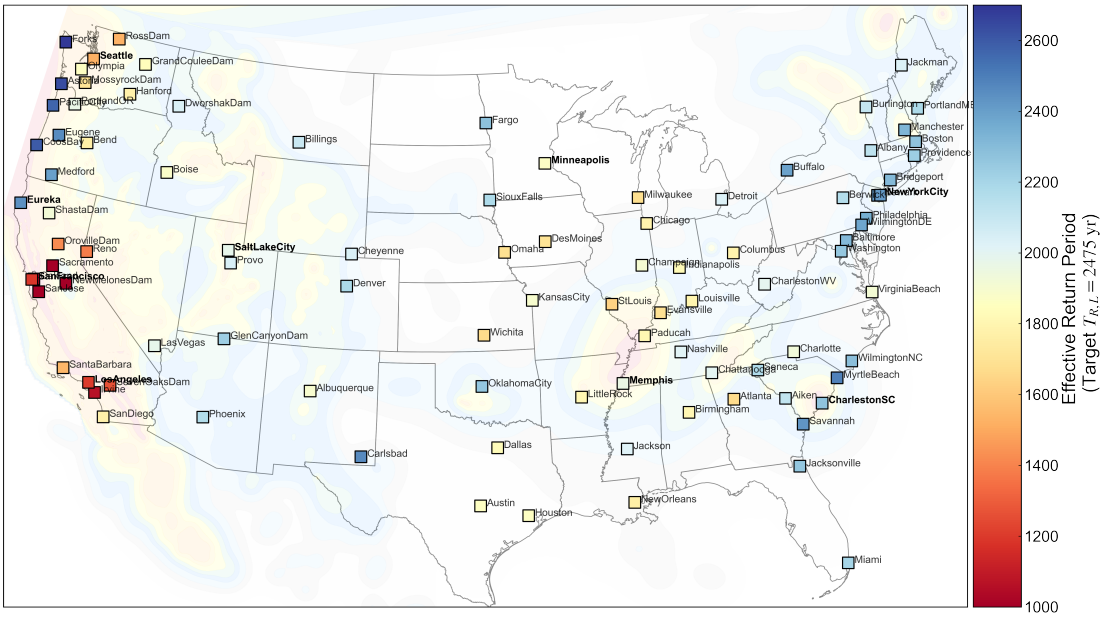

Figure A.11: Mean effective return period of predicted FS_L values using conventional liquefaction hazard analyses (target 2,475-year return period).

Figure A.12: Mean percent error in predicted 2,475-year factor of safety using mapped PGA_M procedure with estimated site adjustment factors.

Table A.5: PLHA metadata and comparison of estimated FS_L errors, effective return periods, and 50-year non-exceedance rates using mapped PGA_M (designated as "MAP") and conventional analyses (designated as "CON") for 2475-year target FS_L, for Western U.S. sites.

Site	Lon.	Lat.	Reference PLHA Metadata					FS_L Error (%)				Effective T_R				50-year Non-exceedance (%)			
								MAP		CON		MAP		CON		MAP		CON	
			PGA_M	FS_L	$E[M_W]$	σ_{M_W}	γ_{M_W}	Mean	Std	Mean	Std	Mean	Std	Mean	Std	Mean	Std	Mean	Std
Astoria	-123.86	46.19	1.225	0.11	8.88	0.33	-2.39	0.42	3.07	-3.61	1.58	2467	120	2639	73	2	0.1	1.9	0.1
Bend	-121.32	44.06	0.27	0.53	7.76	1.28	-0.36	1.08	2.06	20.97	13.51	2430	97	1761	252	2	0.1	2.9	0.5
Boise	-116.21	43.62	0.193	0.77	6.5	0.76	0.24	-1.39	3.77	13.55	3.37	2558	212	1883	119	1.9	0.2	2.6	0.2
CoosBay	-124.22	43.37	1.497	0.09	8.81	0.34	-1.59	0.08	2.89	-2.44	2.06	2480	126	2597	102	2	0.1	1.9	0.1
DworshakDam	-116.3	46.52	0.176	0.84	6.44	0.86	0.75	-0.76	2.34	10.48	4.14	2512	117	2040	144	2	0.1	2.4	0.2
Eugene	-123.09	44.05	0.621	0.23	8.79	0.55	-2.37	1.18	3.99	0.55	1.44	2436	162	2456	54	2	0.1	2	0
Eureka	-124.16	40.8	1.799	0.08	8.63	0.62	-1.85	0.28	7.16	1.37	7.21	2518	338	2445	329	2	0.3	2.1	0.3
Forks	-124.39	47.95	1.34	0.1	8.84	0.4	-2.86	0.24	6.2	-4.67	2.58	2500	255	2692	124	2	0.2	1.8	0.1
GrandCouleeDam	-118.98	47.96	0.229	0.64	6.7	1.1	0.82	-0.16	1.93	16.16	8.84	2485	98	1839	229	2	0.1	2.7	0.4
Hanford	-119.49	46.55	0.254	0.58	6.86	1.1	0.66	0.29	1.46	18.6	11.17	2462	72	1774	261	2	0.1	2.9	0.5
Irvine	-117.83	33.68	0.683	0.21	6.96	0.83	-0.48	-0.36	2.12	37.21	11.62	2502	153	1065	209	2	0.1	4.8	1
LasVegas	-115.14	36.17	0.303	0.49	6.42	0.6	0.34	-0.12	0.88	11.4	5.32	2481	46	1982	208	2	0	2.5	0.3
LosAngeles	-118.24	34.05	0.894	0.16	7.02	0.7	-0.53	0.62	1.39	31.54	8.91	2440	97	1201	208	2	0.1	4.2	0.8
Medford	-122.88	42.33	0.545	0.26	8.75	0.62	-2.27	1.07	4.18	2.02	2.07	2441	173	2397	72	2	0.1	2.1	0.1
MossyrockDam	-122.43	46.53	0.673	0.21	7.85	1.2	-0.28	-0.62	2.23	22.11	12.56	2506	116	1699	206	2	0.1	2.9	0.4
NewMelonesDam	-120.54	37.99	0.285	0.51	7.02	1	0.15	-0.62	3.14	43.36	16.09	2531	229	940	214	2	0.2	5.5	1.5
Oakland	-122.32	37.81	0.953	0.15	7.23	0.68	-0.87	-0.03	0.59	37.8	8.14	2480	45	1013	144	2	0	4.9	0.7
Olympia	-122.9	47.04	0.955	0.15	8.1	1.05	-0.4	-1.96	2.43	17.02	8.85	2573	120	1860	180	1.9	0.1	2.7	0.3
OrovilleDam	-121.48	39.54	0.418	0.35	7.21	1.34	0.3	-0.05	2.36	29.21	15.67	2486	124	1419	248	2	0.1	3.6	0.8
PacificCity	-123.96	45.2	1.203	0.12	8.85	0.37	-2.52	-0.01	3.44	-2.04	1.46	2488	142	2569	66	2	0.1	1.9	0
Phoenix	-112.07	33.45	0.113	1.31	6.39	0.7	-0.11	-2.09	6.16	7.28	1.16	2597	302	2168	47	1.9	0.2	2.3	0
PortlandOR	-122.68	45.52	0.59	0.24	8.25	1.13	-1	0.32	3.03	15.32	12	2464	140	1969	252	2	0.1	2.6	0.4
Provo	-111.66	40.23	0.054	2.77	5.95	0.68	0.12	0.53	1.47	10.26	0.29	2451	71	2043	15	2	0.1	2.4	0
Reno	-119.81	39.53	0.727	0.2	6.7	0.53	-0.15	0.07	2.09	24.26	5.12	2483	151	1382	171	2	0.1	3.6	0.5
RossDam	-121.07	48.73	0.362	0.4	7.07	1.18	0.49	0.21	1.32	25.49	12.89	2467	68	1529	237	2	0.1	3.3	0.6
Sacramento	-121.49	38.58	0.4	0.36	7.12	1.01	0.26	-0.14	1.21	41	14.34	2487	87	985	196	2	0.1	5.2	1.2
SaltLakeCity	-111.89	40.76	0.045	3.34	6.03	0.68	0.03	0.9	2.76	11.6	0.34	2436	138	1980	19	2	0.1	2.5	0
SanDiego	-117.16	32.72	0.638	0.23	6.7	0.62	0.16	1.52	4.7	15.52	5.94	2430	278	1775	228	2.1	0.2	2.8	0.4
SanFrancisco	-122.42	37.77	0.933	0.15	7.48	0.69	-1.44	-0.2	1.08	31.71	6.82	2493	78	1192	146	2	0.1	4.2	0.5
SanJose	-121.89	37.34	1.045	0.14	7.11	0.7	-0.5	-0.37	0.81	41.55	8.16	2507	66	899	129	2	0.1	5.5	0.8
SantaBarbara	-119.7	34.42	0.898	0.16	7.11	0.64	-0.77	0.85	3.87	21.51	6.87	2455	250	1538	224	2	0.2	3.3	0.5
Seattle	-122.33	47.61	0.814	0.18	7.54	1.05	0.42	-0.26	3.09	25.69	11.07	2495	183	1518	180	2	0.1	3.3	0.4
SevenOaksDam	-117.1	34.12	1.208	0.12	7.37	0.75	-0.86	1.37	4.67	30.53	7.72	2428	316	1263	175	2.1	0.3	4	0.6
ShastaDam	-122.42	40.72	0.665	0.21	8.21	1.26	-1.13	-0.82	2.77	17.29	13.52	2514	124	1922	246	2	0.1	2.6	0.4

Table A.6: PLHA metadata and comparison of estimated FS_L errors, effective return periods, and 50-year non-exceedance rates using mapped PGA_M (designated as "MAP") and conventional analyses (designated as "CON") for 2475-year target FS_L, for Central & Eastern U.S. sites.

Site	Lon.	Lat.	Reference PLHA Metadata					FS_L Error (%)				Effective T_R				50-year Non-exceedance (%)			
								MAP		CON		MAP		CON		MAP		CON	
			PGA_M	FS_L	$E[M_w]$	σ_{M_w}	γ_{M_w}	Mean	Std	Mean	Std	Mean	Std	Mean	Std	Mean	Std	Mean	Std
Aiken	-81.74	33.34	0.131	1.12	6.7	0.8	-1.08	-0.07	0.51	8.63	1.89	2478	25	2116	59	2	0	2.3	0.1
Albany	-73.76	42.65	0.082	1.82	5.91	0.79	0.32	0.07	0.79	8.78	1.56	2472	35	2135	52	2	0	2.3	0.1
Albuquerque	-106.61	35.09	0.024	6.16	6.05	0.71	0.01	0.23	0.74	16.12	0.14	2465	34	1890	6	2	0	2.6	0
Atlanta	-84.39	33.75	0.085	1.74	6.44	0.91	-0.12	0.23	0.48	19.76	3.84	2462	27	1670	106	2	0	3	0.2
Austin	-97.74	30.27	0.024	6.22	6.23	0.97	0.24	0.23	0.49	18.68	2.48	2466	21	1860	63	2	0	2.7	0.1
Baltimore	-76.61	39.29	0.058	2.58	5.79	0.73	0.49	0.03	0.87	4.29	0.46	2474	35	2314	16	2	0	2.1	0
Berwick	-76.14	41.09	0.051	2.94	5.97	0.75	0.22	0.05	0.81	7.9	0.3	2473	36	2158	9	2	0	2.3	0
Billings	-108.5	45.78	0.05	2.98	5.91	0.67	0.19	-0.11	0.89	9.19	0.34	2481	42	2092	17	2	0	2.4	0
Birmingham	-86.8	33.52	0.13	1.14	6.12	1.05	0.45	0.31	0.84	18.44	7.32	2460	40	1809	205	2	0	2.8	0.3
Boston	-71.06	42.36	0.11	1.37	5.75	0.72	0.55	0.24	0.89	5.16	1.08	2465	38	2272	38	2	0	2.2	0
Bridgeport	-73.2	41.19	0.088	1.71	5.75	0.72	0.55	0.16	0.89	4.33	0.81	2469	36	2309	28	2	0	2.1	0
Buffalo	-78.88	42.89	0.065	2.32	5.64	0.68	0.73	0.08	1.12	2.3	0.86	2473	41	2393	30	2	0	2.1	0
Burlington	-73.21	44.48	0.142	1.05	5.84	0.77	0.44	0.13	0.85	8.92	1.91	2470	40	2112	66	2	0	2.3	0.1
Carlsbad	-103.79	32.37	0.042	3.63	5.57	0.61	0.75	-0.24	0.97	0.33	0.23	2484	33	2464	8	2	0	2	0
Champaign	-88.24	40.12	0.089	1.64	7.07	0.87	-1.2	0.24	0.31	13.73	2.34	2463	16	1909	64	2	0	2.6	0.1
CharlestonSC	-79.93	32.78	0.412	0.36	6.72	0.8	-1.21	-0.28	1.16	4.89	2.15	2488	53	2272	72	2	0	2.2	0.1
CharlestonWV	-81.63	38.35	0.067	2.22	6.01	0.86	0.43	0.16	0.88	12.32	2.87	2468	41	1990	100	2	0	2.5	0.1
Charlotte	-80.84	35.23	0.091	1.63	6.48	0.87	-0.53	-0.05	0.48	13.52	2.78	2477	24	1928	83	2	0	2.6	0.1
Chattanooga	-85.31	35.05	0.187	0.8	5.83	0.85	0.77	0.6	1.19	11.78	4.88	2446	58	1997	164	2	0	2.5	0.2
Cheyenne	-104.82	41.14	0.068	2.19	5.93	0.7	0.17	-0.06	0.82	10.24	0.64	2478	40	2046	20	2	0	2.4	0
Chicago	-87.63	41.88	0.056	2.63	6.37	1.08	0.05	-0.04	0.6	19.18	5.17	2477	28	1789	145	2	0	2.8	0.2
Columbus	-83	39.96	0.055	2.72	6.24	0.96	0.24	0.13	0.6	17.67	3.42	2469	30	1784	106	2	0	2.8	0.2
Dallas	-96.8	32.78	0.046	3.21	6.56	0.96	-0.21	-0.92	0.65	16.42	2.7	2522	34	1832	79	2	0	2.7	0.1
Denver	-104.99	39.74	0.086	1.75	5.77	0.7	0.41	0.04	0.96	7.4	1.2	2474	42	2185	41	2	0	2.3	0
DesMoines	-93.61	41.6	0.035	4.21	7.02	0.97	-1.01	0.1	0.3	20.78	2.69	2470	15	1702	66	2	0	2.9	0.1
Detroit	-83.05	42.33	0.044	3.38	5.91	0.85	0.67	-0.15	0.85	11.72	2.2	2482	38	2033	76	2	0	2.4	0.1
Evansville	-87.57	37.97	0.23	0.64	6.6	1.07	-0.38	-0.22	0.61	21.34	8.51	2487	32	1688	206	2	0	3	0.4
Fargo	-96.79	46.88	0.023	6.54	5.64	0.62	0.53	-0.11	0.96	6.17	0.12	2479	33	2276	4	2	0	2.2	0
GlenCanyonDam	-111.48	36.94	0.061	2.46	5.79	0.65	0.32	0.05	0.92	5.98	0.33	2473	41	2231	15	2	0	2.2	0
Houston	-95.37	29.76	0.031	4.77	6.21	1.04	0.33	-0.1	0.59	18.32	3.91	2479	25	1861	106	2	0	2.7	0.2
Indianapolis	-86.16	39.77	0.09	1.64	6.61	1.05	-0.37	0.09	0.43	18.06	5.73	2471	21	1818	153	2	0	2.7	0.2
Jackman	-70.25	45.62	0.098	1.51	6.56	0.82	-0.73	0	0.55	10.53	1.38	2475	27	2034	39	2	0	2.4	0
Jackson	-90.18	32.3	0.077	1.89	7.22	0.87	-1.54	0.1	0.28	11.1	2.02	2470	14	2018	60	2	0	2.4	0.1
Jacksonville	-81.66	30.33	0.051	2.88	6.83	0.77	-1.37	-0.13	0.38	5.31	0.84	2481	17	2259	30	2	0	2.2	0
KansasCity	-94.58	39.1	0.052	2.79	7	1	-0.97	0.11	0.36	14.53	2.77	2469	18	1892	83	2	0	2.6	0.1
LittleRock	-92.29	34.75	0.179	0.82	6.91	1.04	-0.8	-0.17	0.78	17.44	6.38	2484	40	1808	162	2	0	2.8	0.3
Louisville	-85.76	38.25	0.1	1.45	6.97	0.95	-0.98	0.06	0.34	17.13	3.95	2472	18	1793	105	2	0	2.8	0.2
Manchester	-71.45	43	0.161	0.93	5.64	0.69	0.74	0.39	1.11	3.81	1.3	2460	47	2324	48	2	0	2.1	0
Memphis	-90.05	35.15	0.388	0.37	7.18	0.86	-1.53	0.01	0.5	12.89	5.2	2476	26	1958	143	2	0	2.5	0.2
Miami	-80.19	25.76	0.016	9.49	5.85	0.9	0.62	0.2	0.92	10.23	2.87	2469	27	2206	74	2	0	2.2	0.1
Milwaukee	-87.91	43.04	0.037	3.96	6.5	1.05	-0.11	0.02	0.43	22.11	4.25	2474	21	1682	109	2	0	2.9	0.2
Minneapolis	-93.27	44.98	0.02	7.3	6.12	0.98	0.47	0.31	0.65	19.37	2.88	2463	26	1869	74	2	0	2.6	0.1
MyrtleBeach	-78.89	33.69	0.141	1.03	7.06	0.49	-2.57	0.62	1.17	-0.43	0.34	2452	45	2492	14	2	0	2	0
Nashville	-86.78	36.16	0.144	1	7.36	0.7	-2.14	0.31	0.77	10.49	0.73	2460	40	2011	20	2	0	2.5	0
Newark	-74.17	40.74	0.112	1.35	5.63	0.67	0.73	0.4	1.07	1.65	0.8	2460	42	2412	29	2	0	2.1	0
NewOrleans	-90.07	29.95	0.043	3.42	6.52	1.08	-0.11	0.03	0.43	19.86	4.22	2474	20	1758	115	2	0	2.8	0.2
NewYorkCity	-74.01	40.71	0.112	1.34	5.63	0.67	0.74	0.39	1.09	1.68	0.82	2461	42	2411	30	2	0	2.1	0
OklahomaCity	-97.52	35.47	0.126	1.19	5.86	0.8	0.4	0.25	0.84	5.6	1.9	2465	36	2257	66	2	0	2.2	0.1
Omaha	-96	41.25	0.034	4.29	6.38	1.05	0.1	0.02	0.45	22.31	4.26	2474	22	1685	111	2	0	2.9	0.2
Paducah	-88.6	37.08	0.399	0.36	7.06	0.9	-1.3	-0.45	0.66	16.88	6.53	2501	37	1807	163	2	0	2.8	0.3
Philadelphia	-75.17	39.95	0.073	2.04	5.73	0.7	0.56	0.11	0.91	3.21	0.47	2471	36	2353	17	2	0	2.1	0
PortlandME	-70.26	43.66	0.116	1.29	5.81	0.75	0.49	0.19	0.86	7.2	1.58	2467	38	2188	55	2	0	2.3	0.1
Providence	-71.41	41.82	0.082	1.82	5.83	0.75	0.43	0.1	0.82	6.28	0.93	2471	35	2232	32	2	0	2.2	0
Savannah	-81.1	32.08	0.147	0.99	7	0.58	-2.22	0.48	0.82	1	0.33	2456	33	2434	14	2	0	2	0
Seneca	-82.89	34.79	0.159	0.94	5.73	0.78	0.72	0.59	1.32	7.76	3.59	2450	58	2172	130	2	0	2.3	0.1
SiouxFalls	-96.73	43.54	0.037	4.1	5.79	0.73	0.73	-0.11	0.82	7.98	0.55	2480	34	2179	19	2	0	2.3	0
StLouis	-90.18	38.62	0.2	0.73	6.62	1.1	-0.36	-0.29	0.58	23.29	9.35	2491	31	1633	213	2	0	3.1	0.4
VirginiaBeach	-75.98	36.85	0.035	4.21	6.23	0.86	-0.07	-0.09	0.59	14.95	1.39	2479	27	1915	39	2	0	2.6	0.1
Washington	-77.04	38.91	0.055	2.7	5.85	0.74	0.41	0.05	0.84	5.58	0.39	2473	35	2259	14	2	0	2.2	0
Wichita	-97.33	37.69	0.044	3.36	6.53	1.01	-0.16	0.07	0.42	21.34	3.68	2471	22	1668	99	2	0	3	0.2
WilmingtonDE	-75.54	39.74	0.072	2.08	5.7	0.7	0.63	0.13	0.95	2.63	0.64	2471	36	2379	22	2	0	2.1	0
WilmingtonNC	-77.94	34.23	0.078	1.89	6.86	0.74	-1.57	0.16	0.49	4.8	0.61	2469	20	2290	19	2	0	2.2	0

A.4 High-Resolution Liquefaction-Targeted $PGAM, ref$ Maps for Selected U.S. Regions

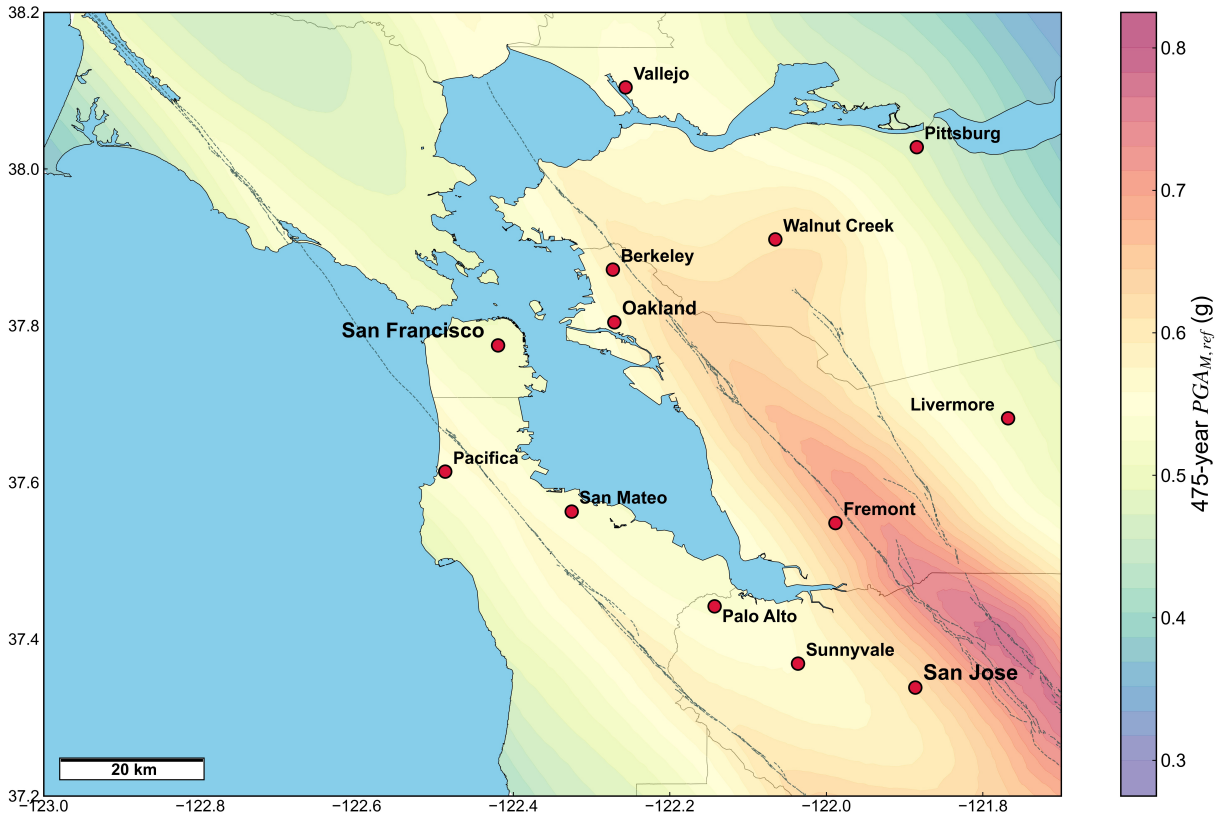

Figure A.13: Liquefaction-targeted $PGA_{M,ref}$ map of the San Francisco Bay Area, corresponding to the 475-year FS_L return period.

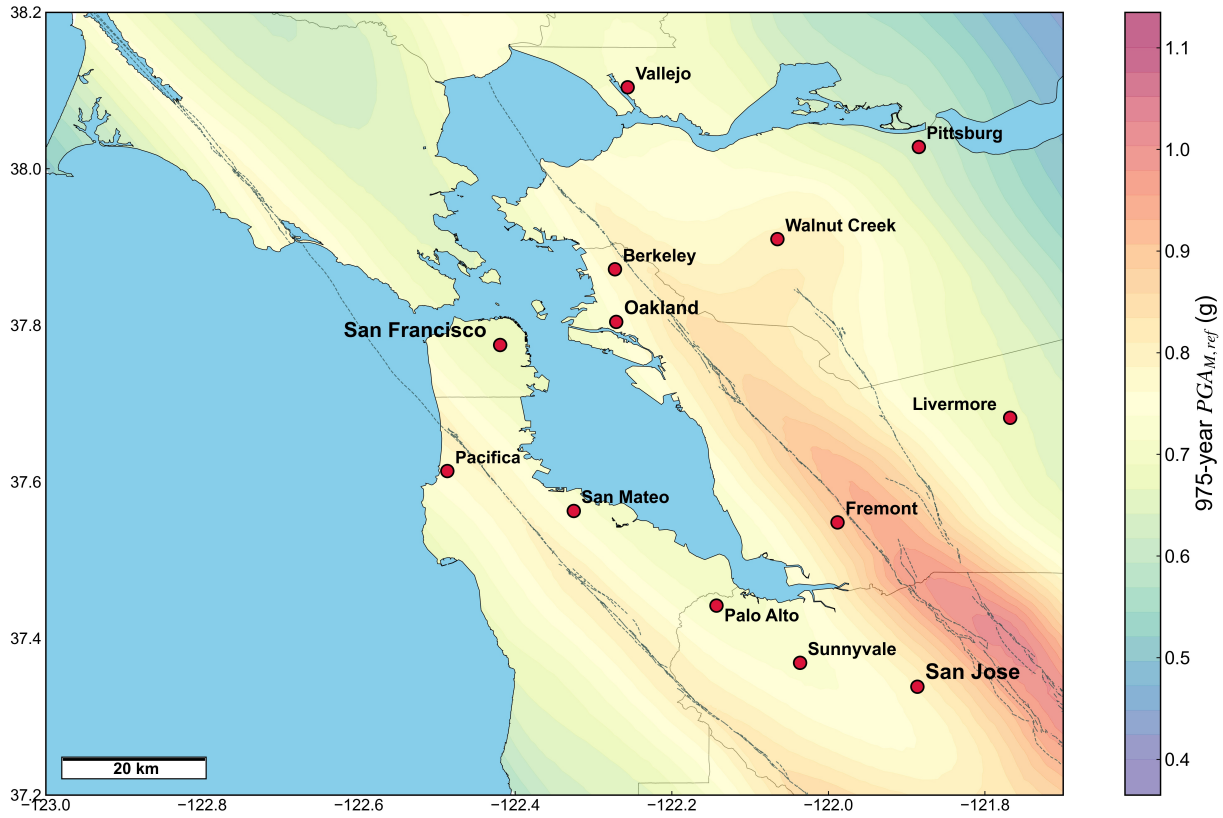

Figure A.14: Liquefaction-targeted $PGA_{M,ref}$ map of the San Francisco Bay Area, corresponding to the 975-year FS_L return period.

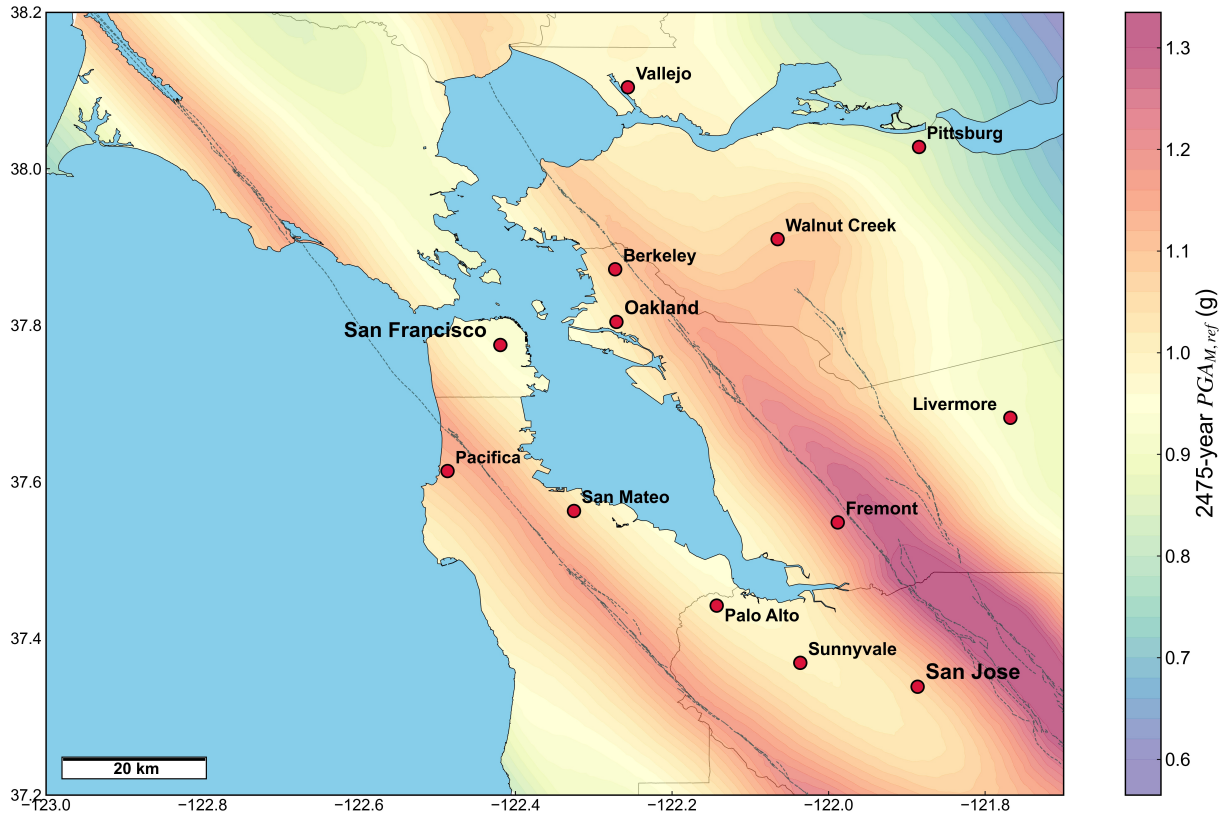

Figure A.15: Liquefaction-targeted $PGA_{M,ref}$ map of the San Francisco Bay Area, corresponding to the 2,475-year FS_L return period.

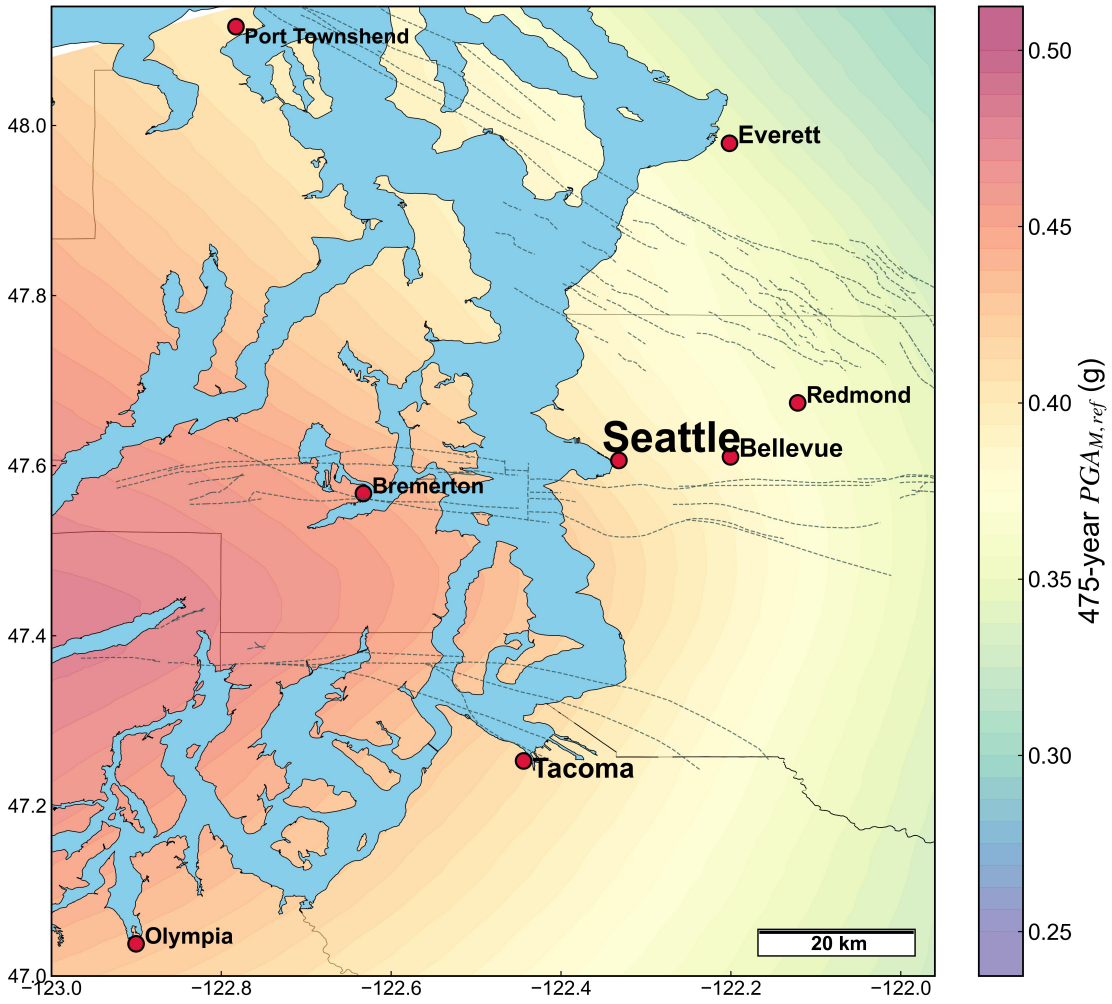

Figure A.16: Liquefaction-targeted $PGA_{M,ref}$ map of the Puget Sound Region, corresponding to the 475-year FS_L return period.

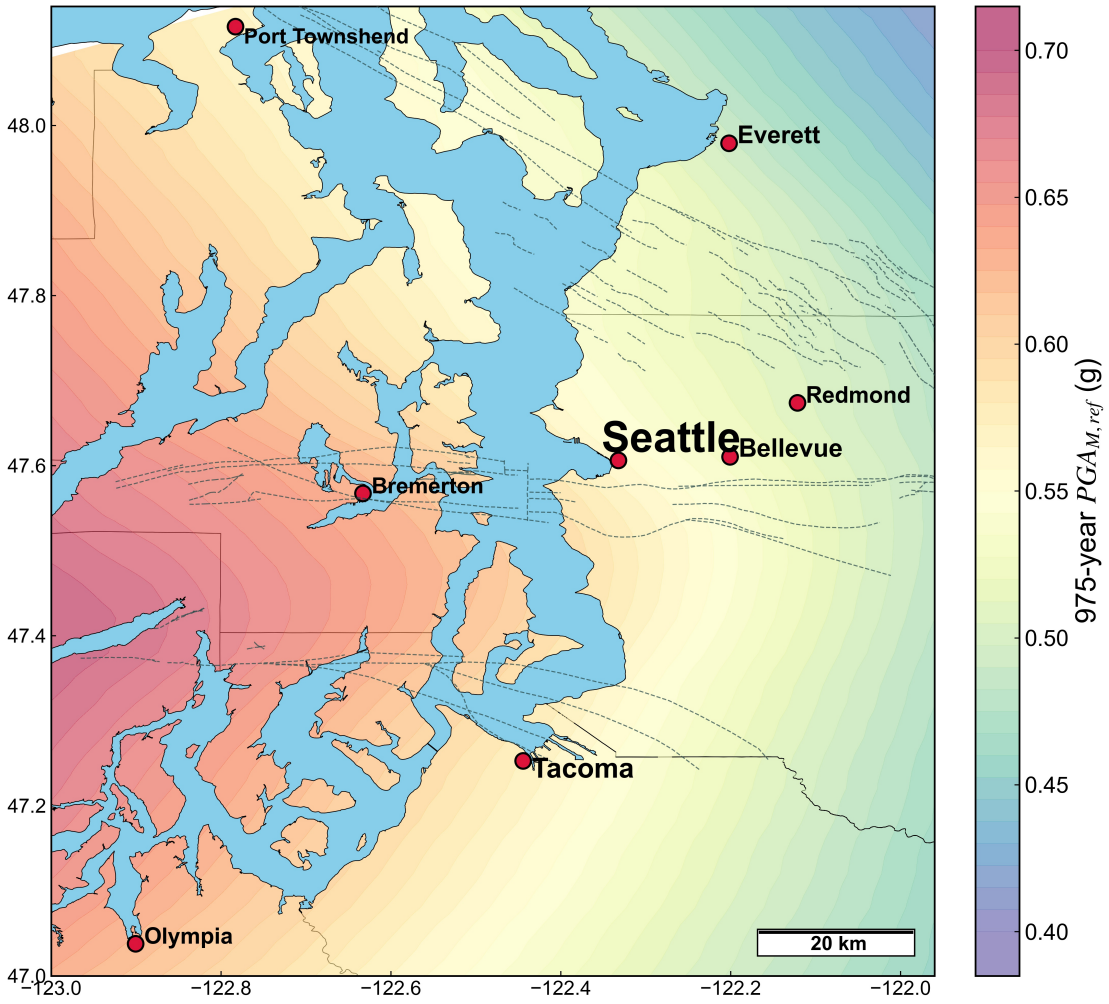

Figure A.17: Liquefaction-targeted $PGA_{M,ref}$ map of the Puget Sound Region, corresponding to the 975-year FS_L return period.

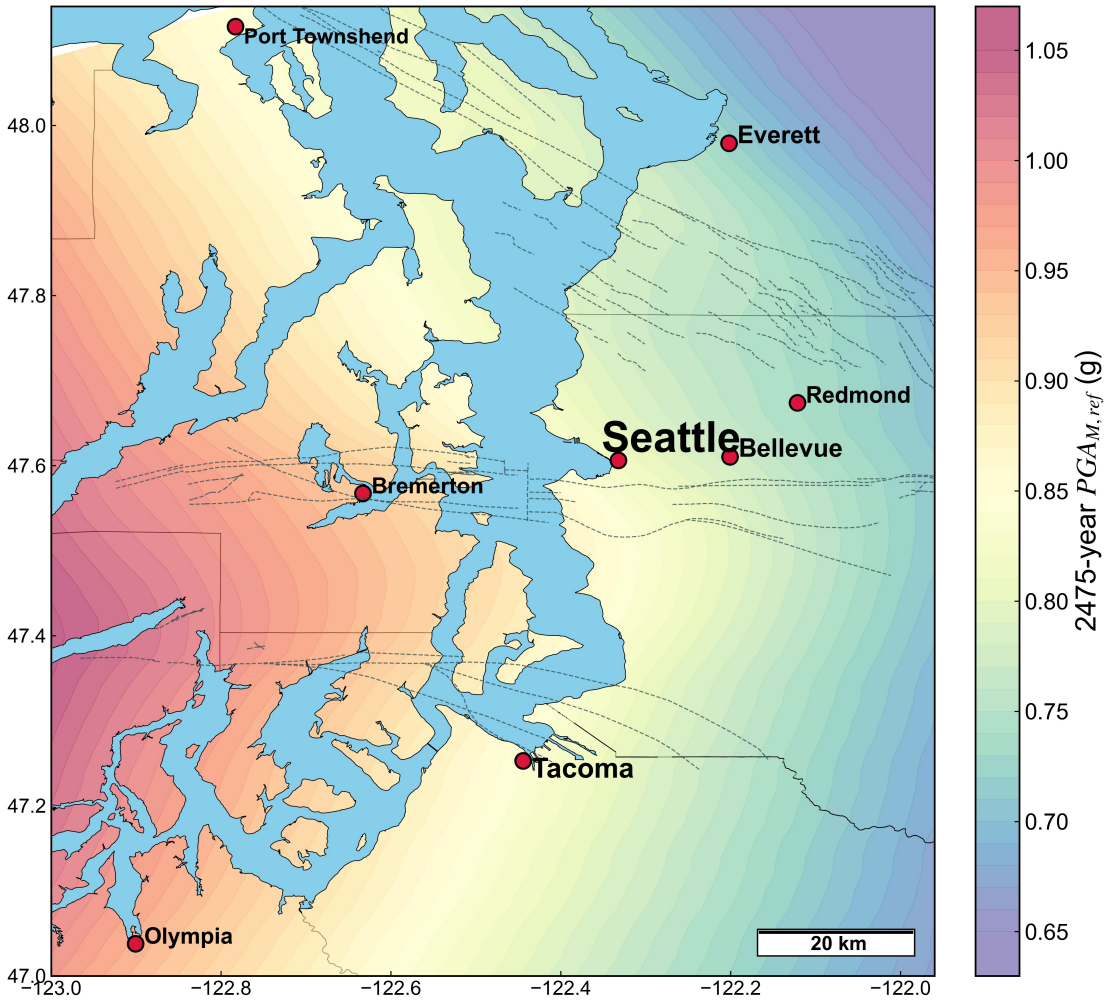

Figure A.18: Liquefaction-targeted $PGA_{M,ref}$ map of the Puget Sound Region, corresponding to the 2,475-year FS_L return period.

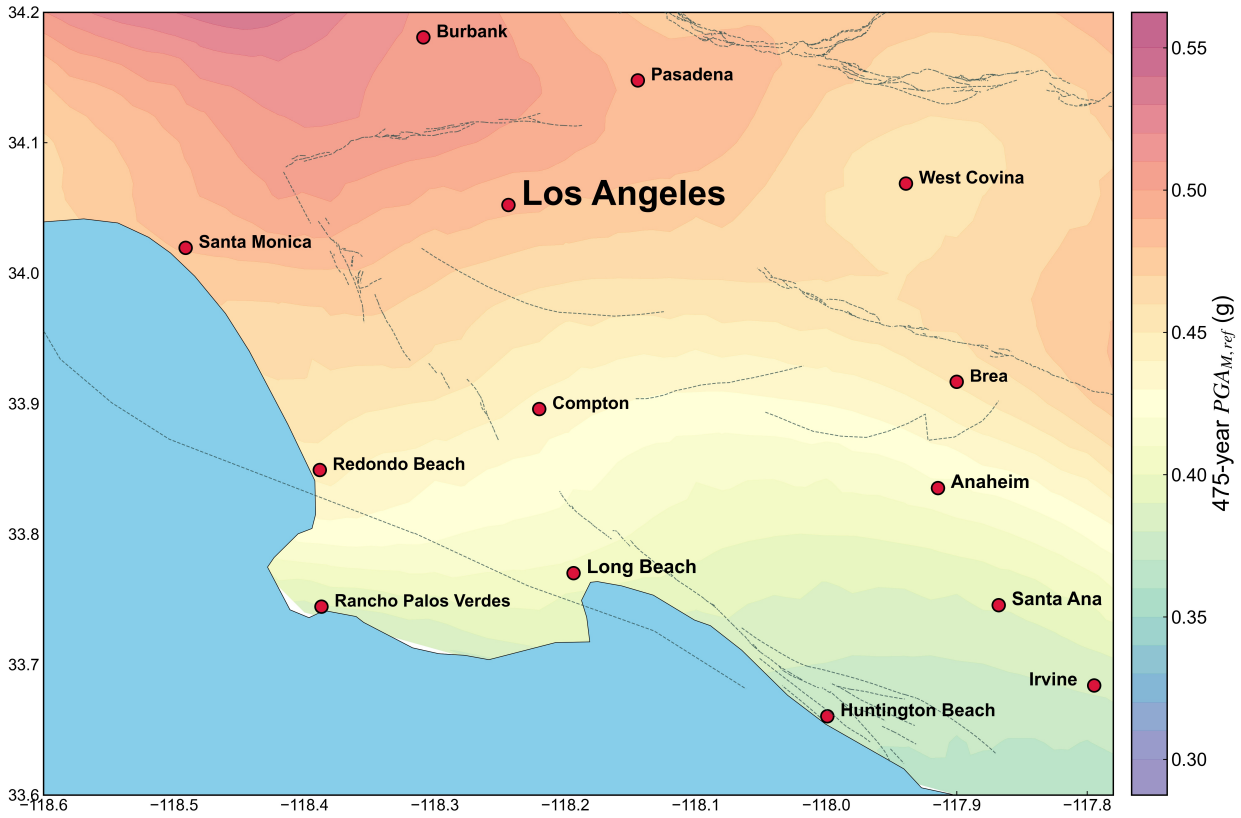

Figure A.19: Liquefaction-targeted $PGA_{M,ref}$ map of the Los Angeles Metropolitan Area, corresponding to the 475-year FS_L return period.

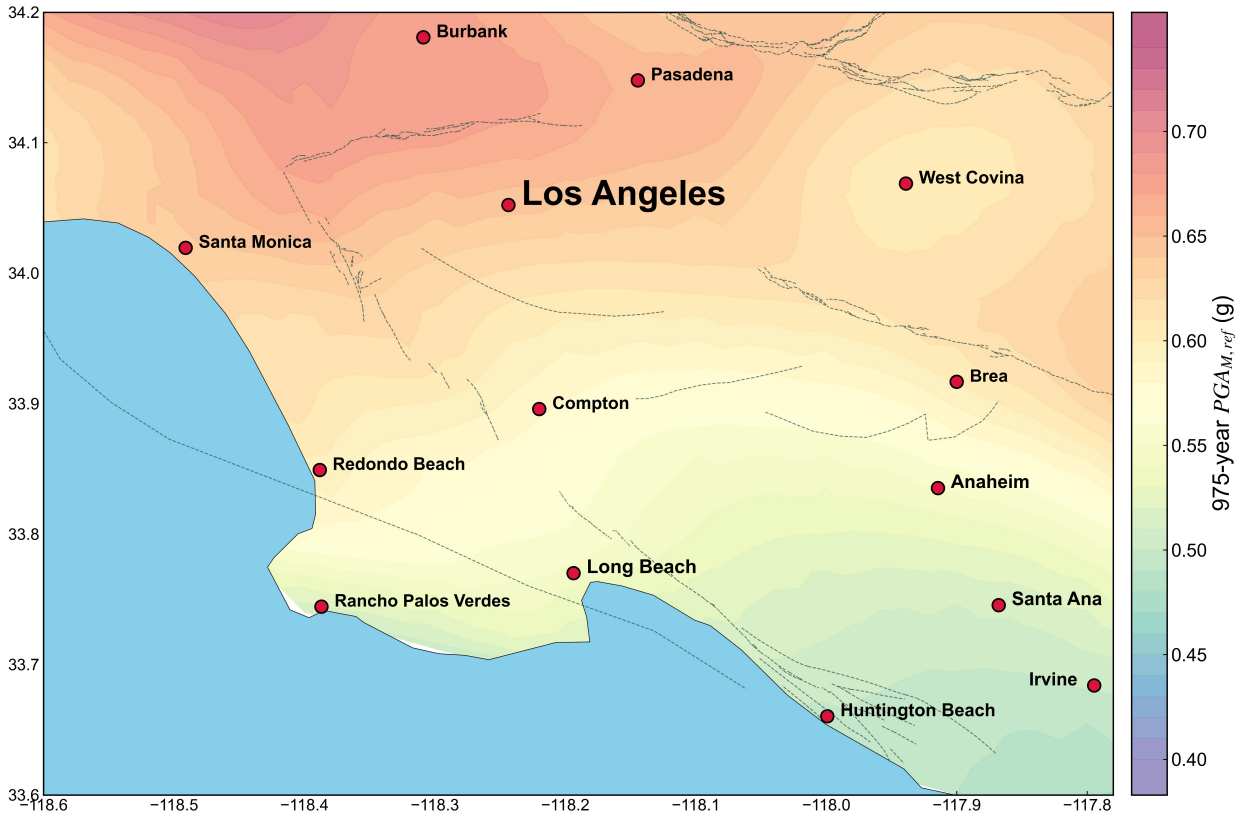

Figure A.20: Liquefaction-targeted $PGA_{M,ref}$ map of the Los Angeles Metropolitan Area, corresponding to the 975-year FS_L return period.

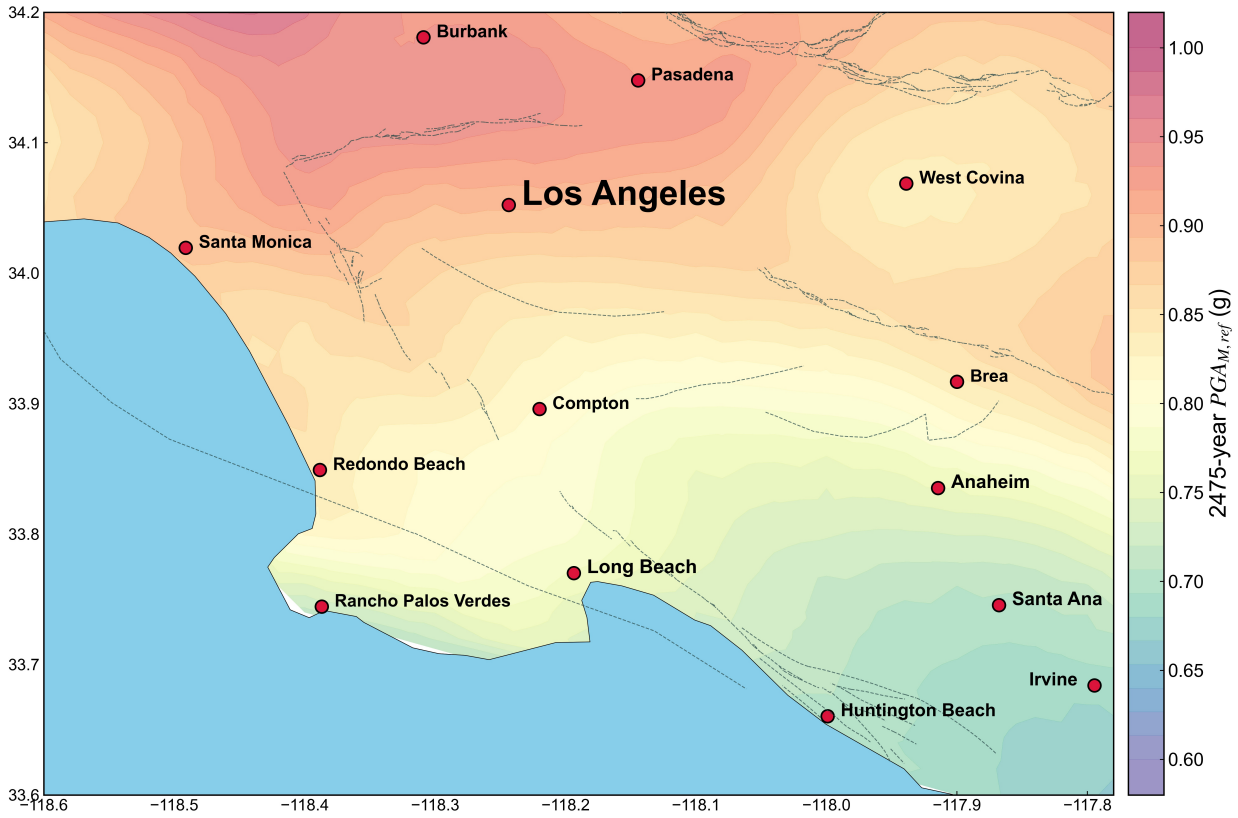

Figure A.21: Liquefaction-targeted $PGA_{M,ref}$ map of the Los Angeles Metropolitan Area, corresponding to the 2,475-year FS_L return period.

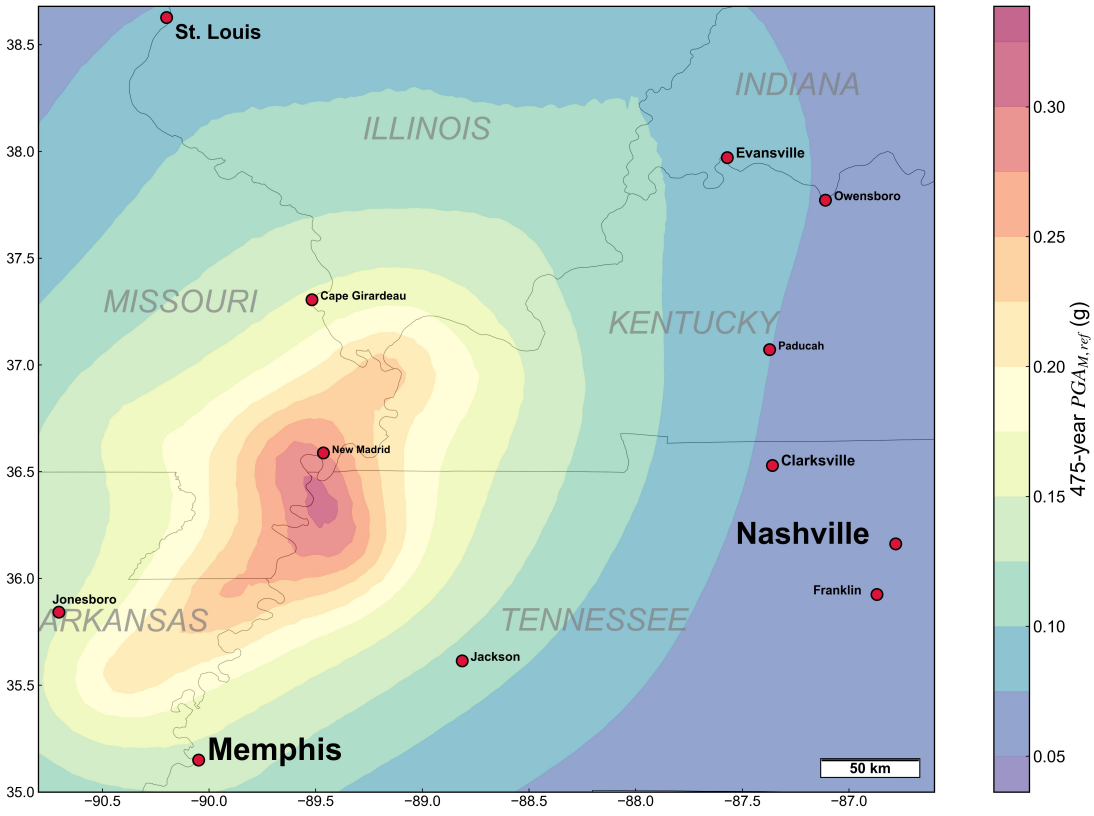

Figure A.22: Liquefaction-targeted $PGA_{M,ref}$ map of the region surrounding the New Madrid Fault Zone, corresponding to the 475-year FS_L return period.

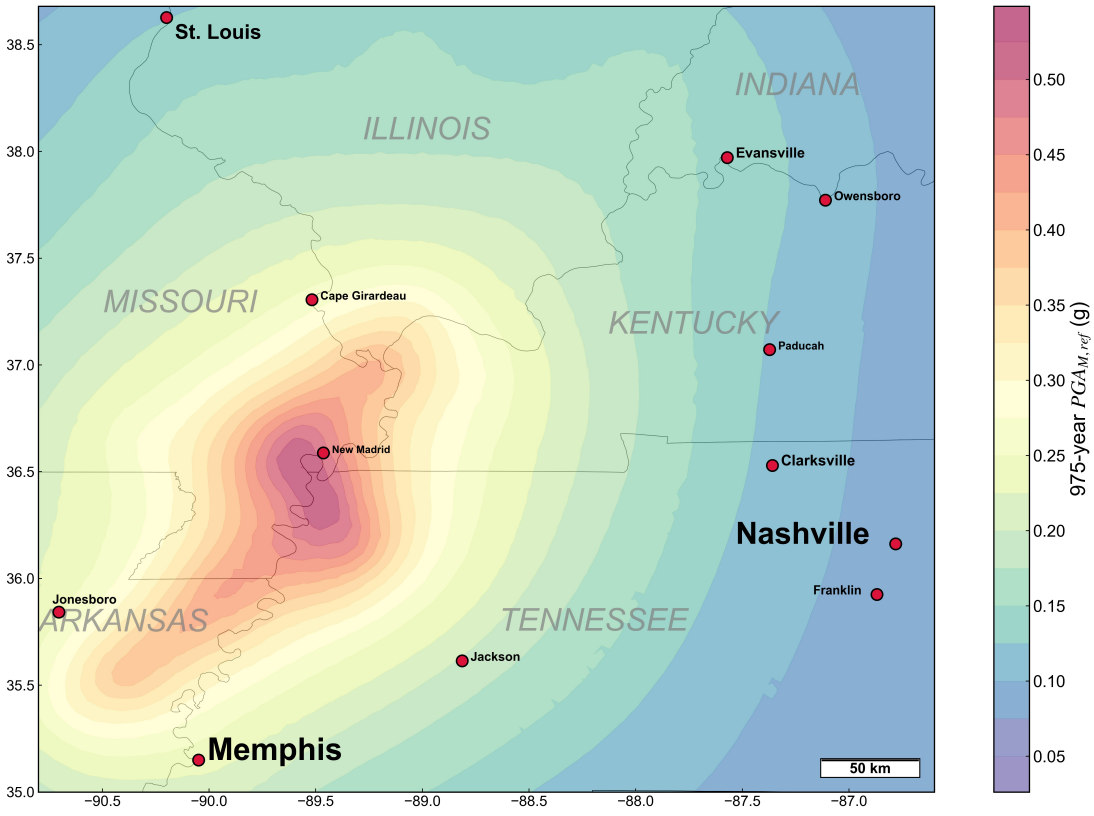

Figure A.23: Liquefaction-targeted $PGA_{M,ref}$ map of the region surrounding the New Madrid Fault Zone, corresponding to the 975-year FS_L return period.

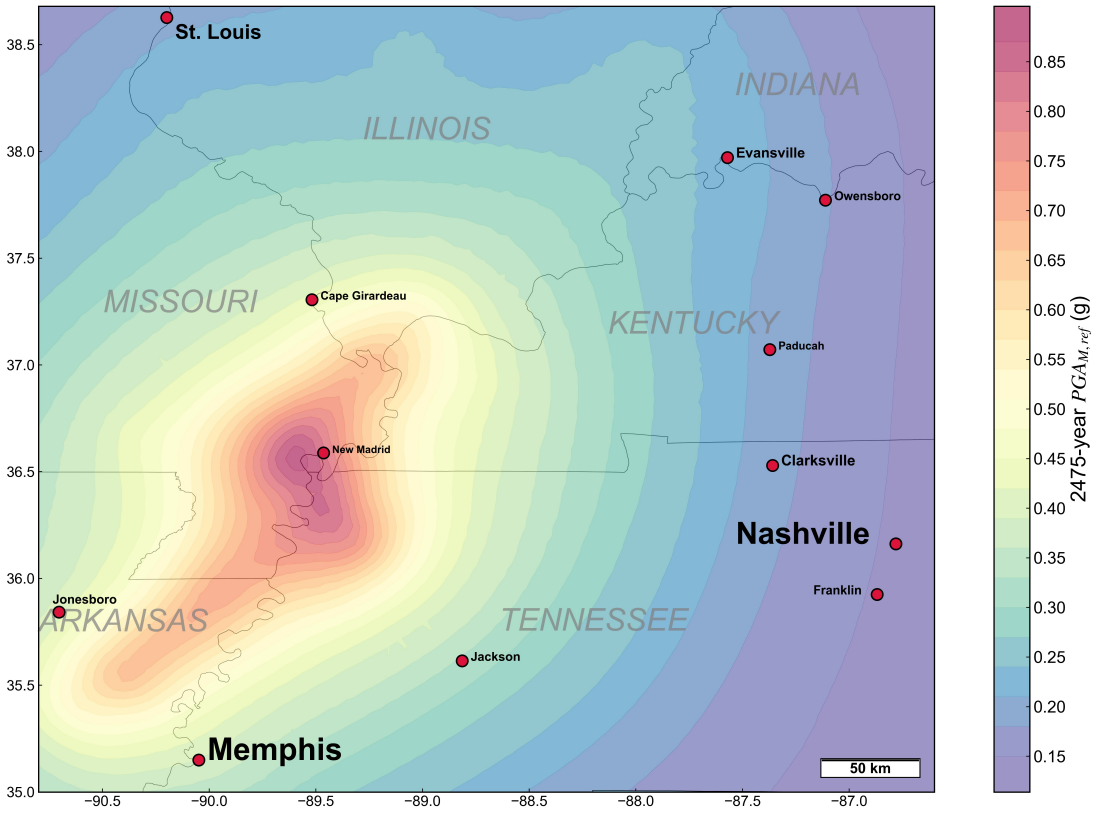

Figure A.24: Liquefaction-targeted $PGA_{M,ref}$ map of the region surrounding the New Madrid Fault Zone, corresponding to the 2475-year FS_L return period.

A.5 High-Resolution Maps of Effective Return Periods from Conventional Liquefaction Hazard Analyses for Selected U.S. Regions

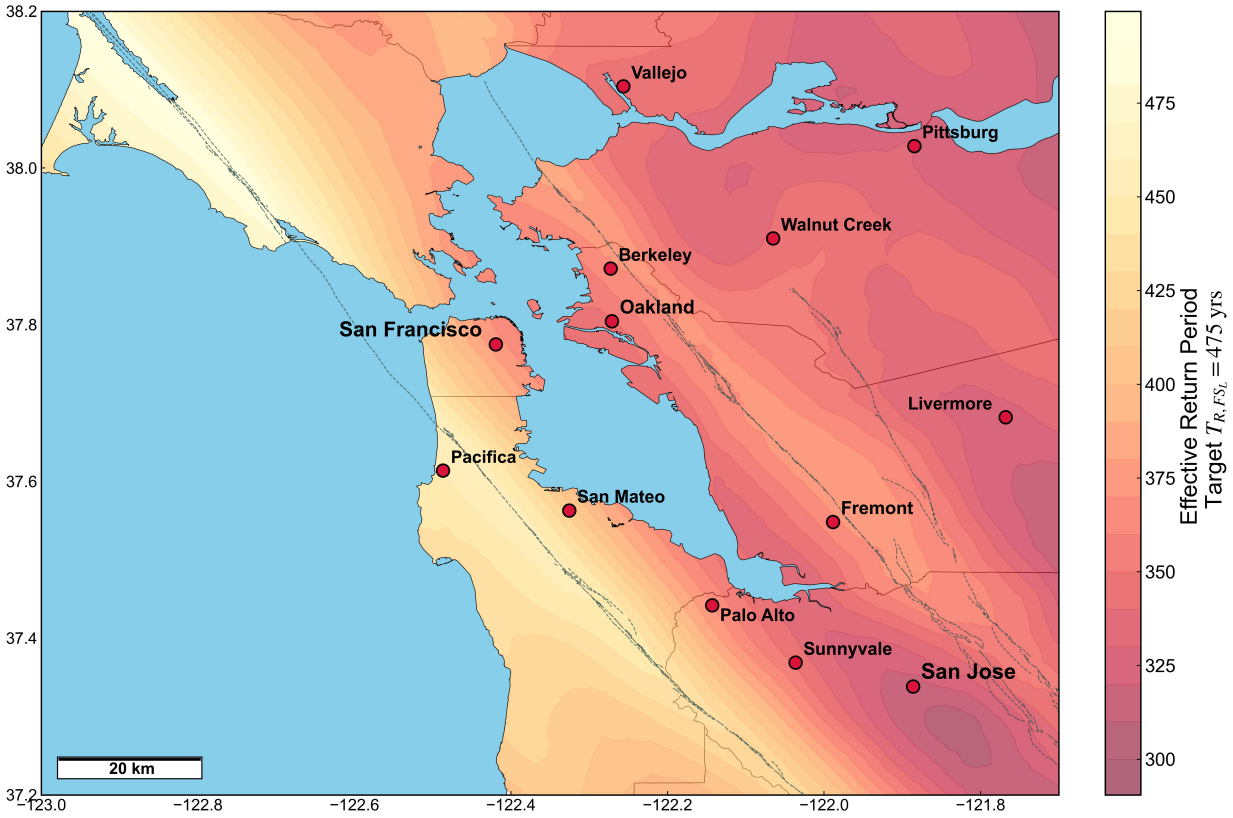

Figure A.25: Effective return period of predicted FS_L (target 475-year return period) for the San Francisco Bay Area at the reference soil condition.

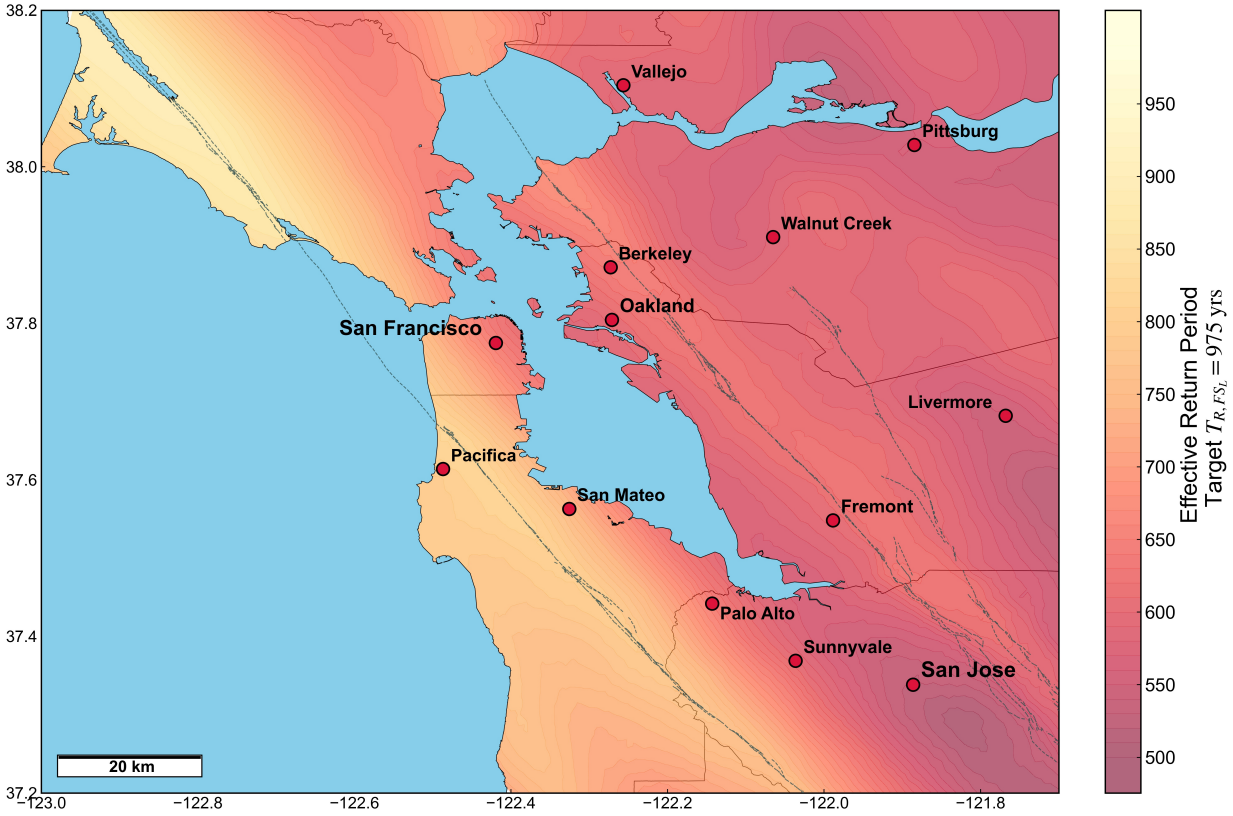

Figure A.26: Effective return period of predicted FS_L (target 975-year return period) for the San Francisco Bay Area at the reference soil condition.

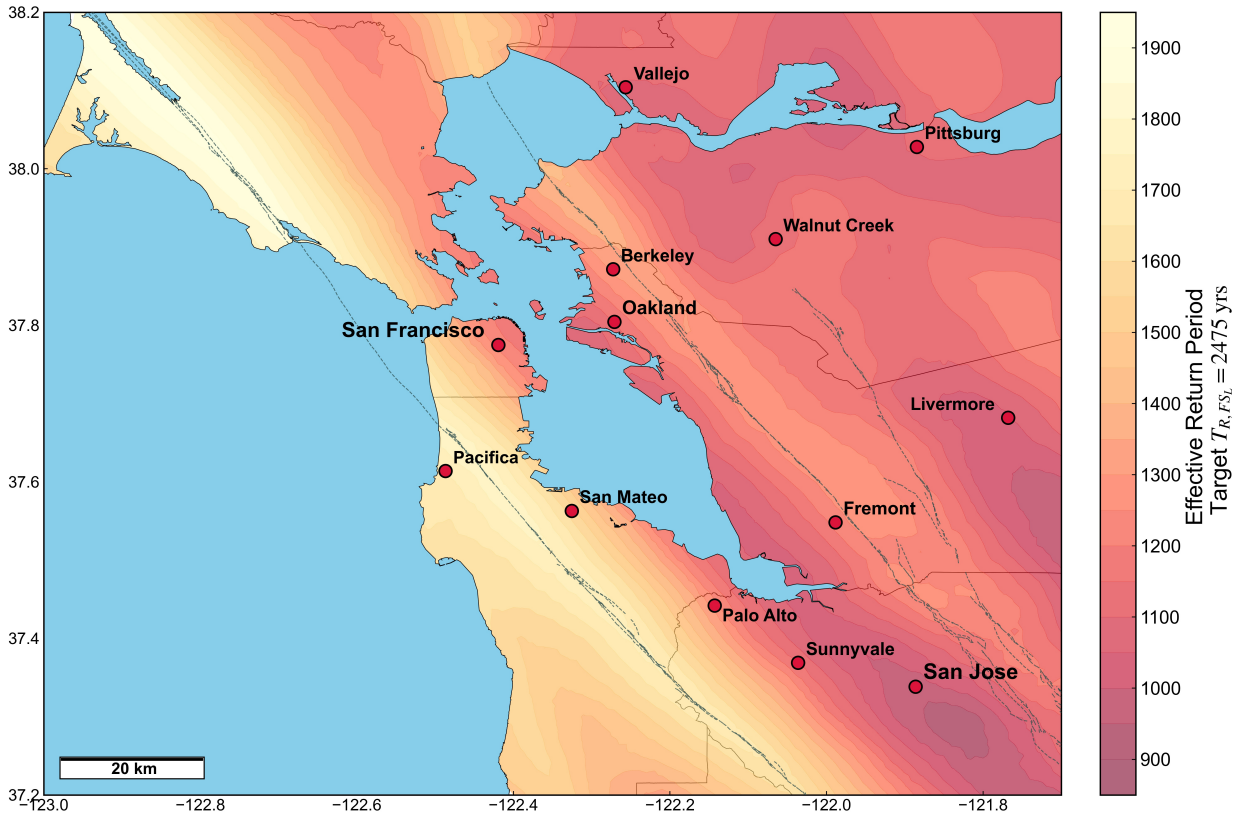

Figure A.27: Effective return period of predicted FS_L (target 2,475-year return period) for the San Francisco Bay Area at the reference soil condition.

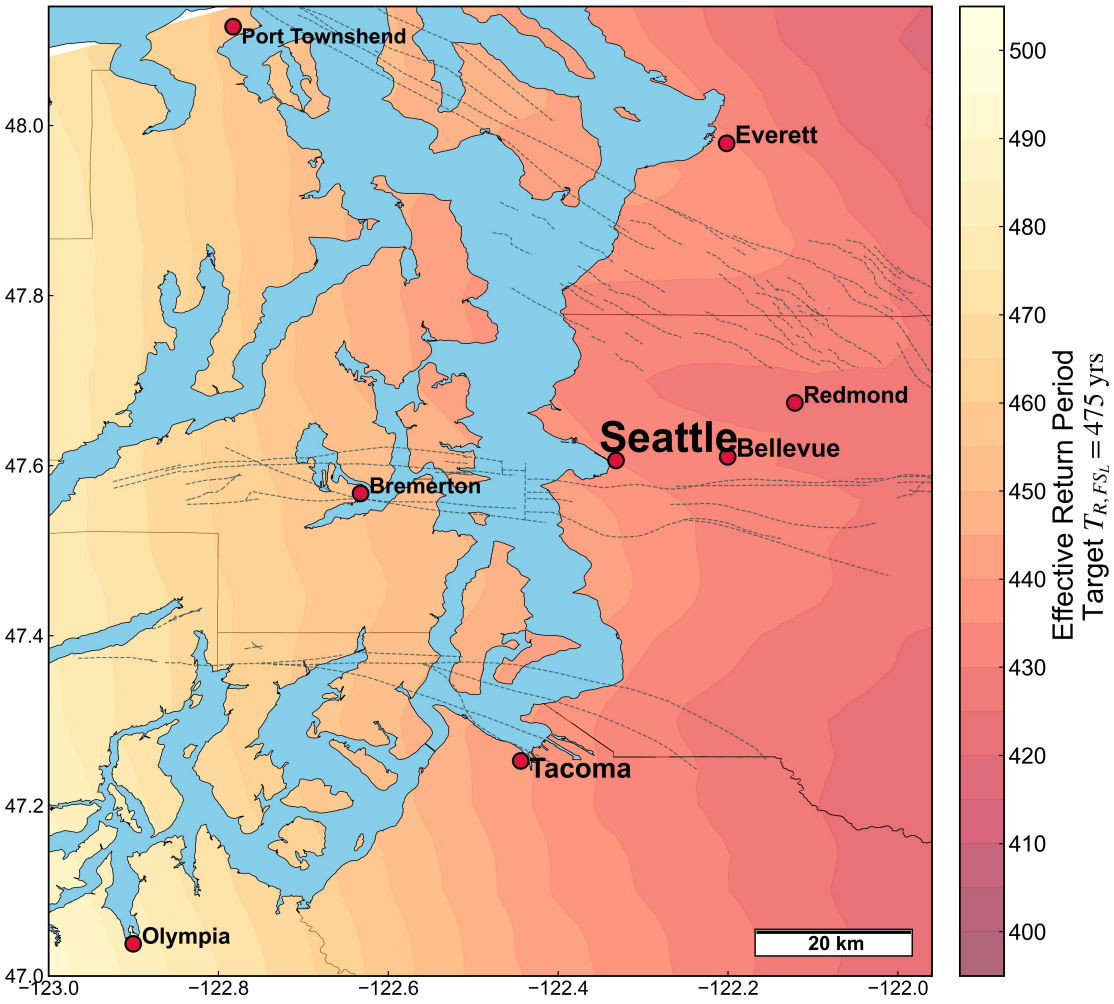

Figure A.28: Effective return period of predicted FS_L (target 475-year return period) for the Puget Sound Region at the reference soil condition.

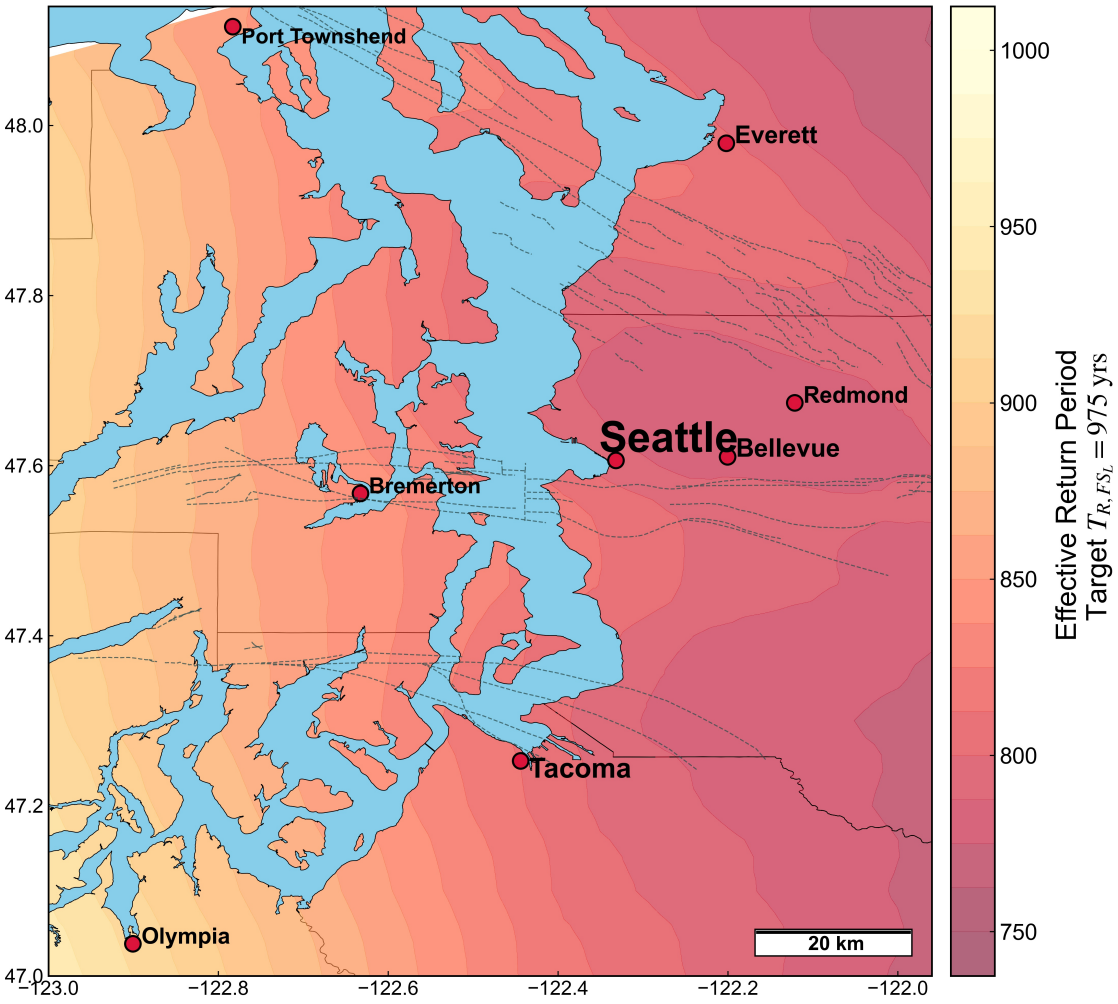

Figure A.29: Effective return period of predicted FS_L (target 975-year return period) for the Puget Sound Region at the reference soil condition.

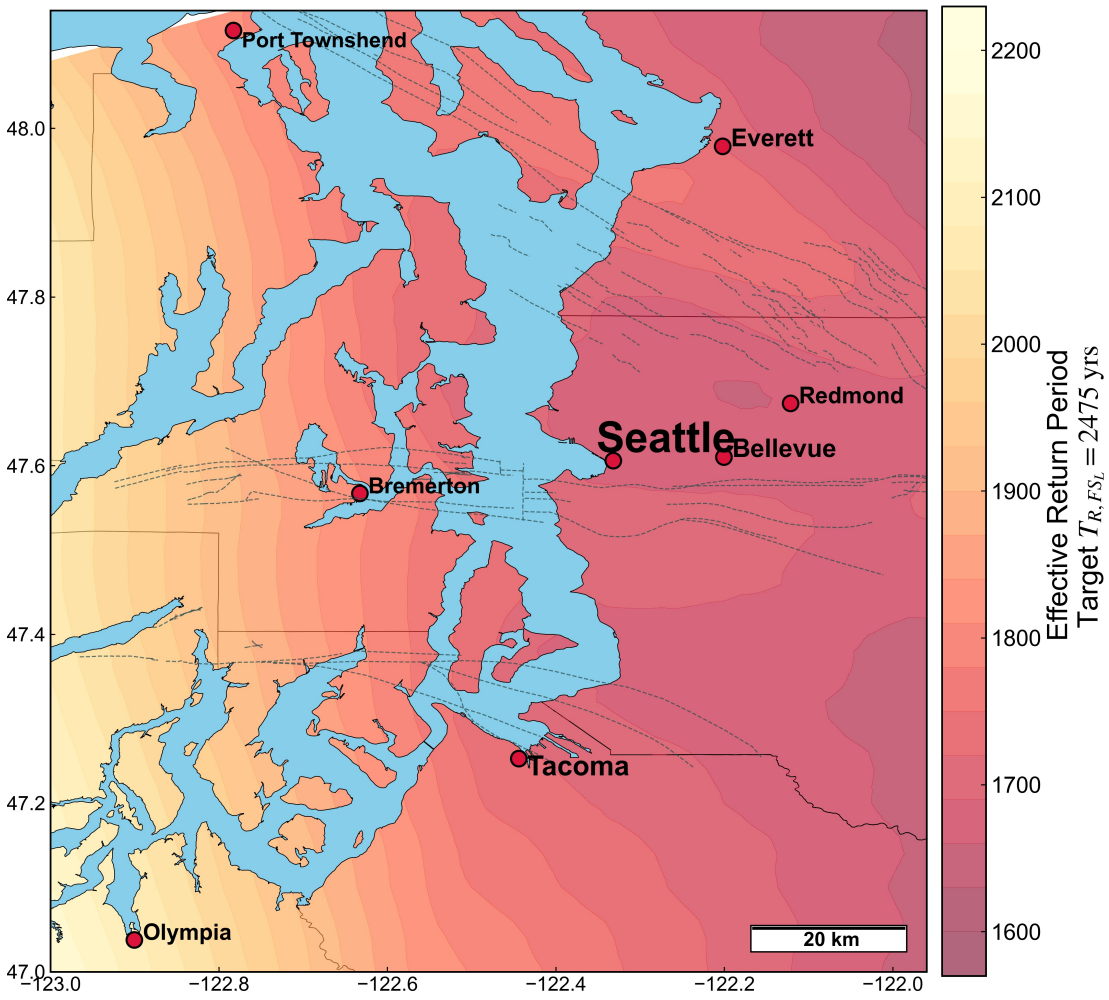

Figure A.30: Effective return period of predicted FS_L (target 2,475-year return period) for the Puget Sound Region at the reference soil condition.

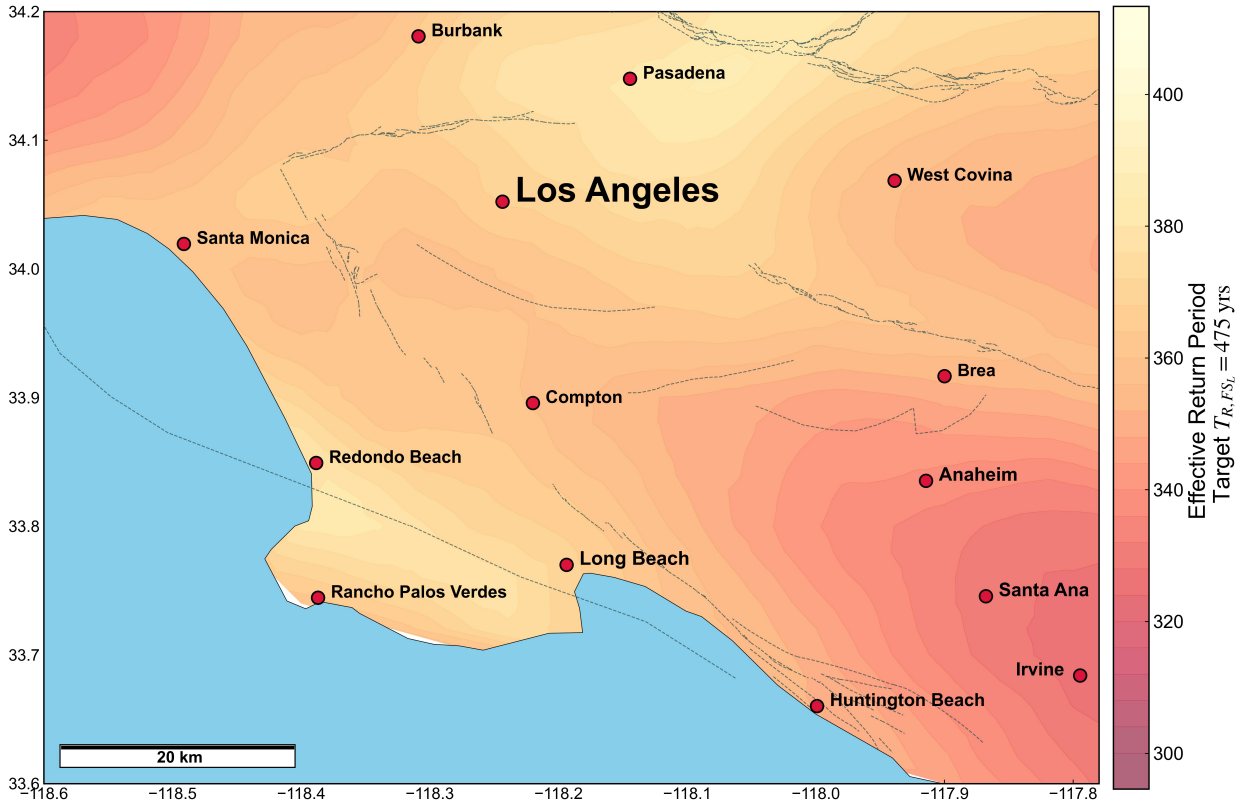

Figure A.31: Effective return period of predicted FS_L (target 475-year return period) for the Los Angeles Metropolitan Area at the reference soil condition.

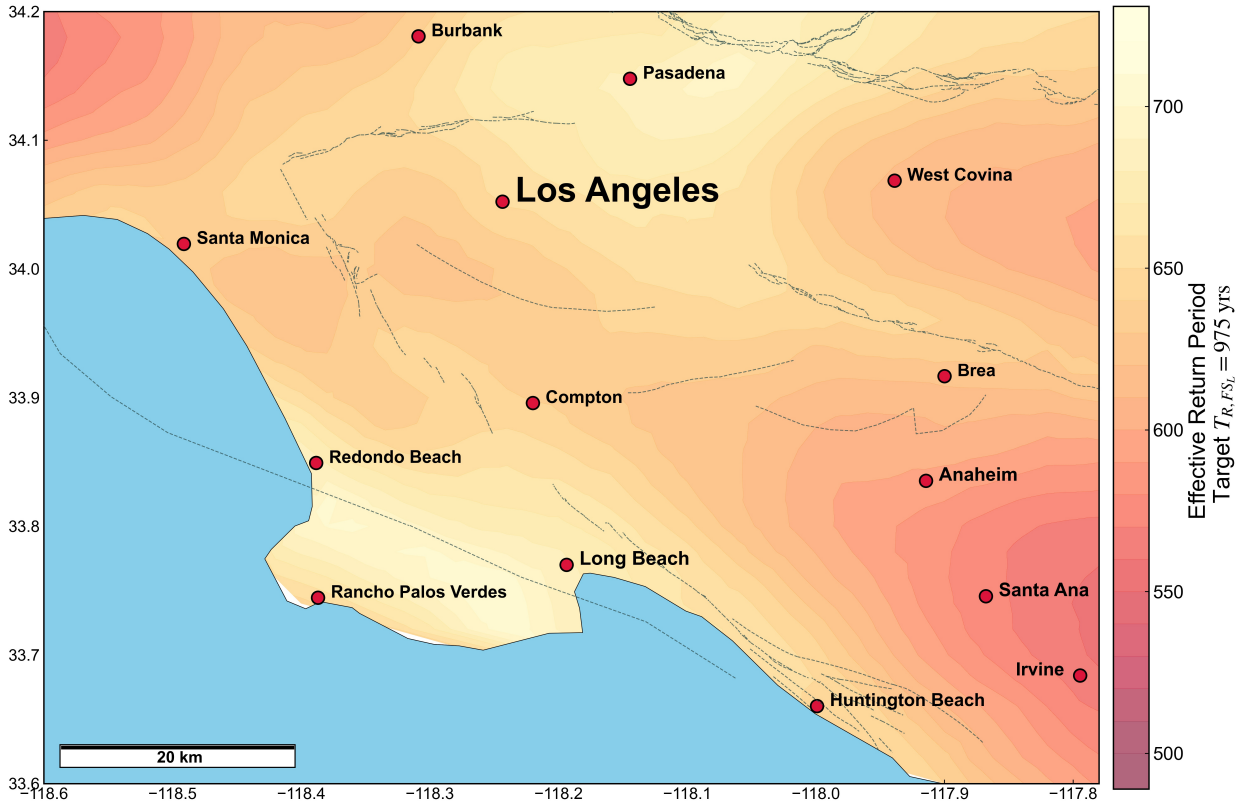

Figure A.32: Effective return period of predicted FS_L (target 975-year return period) for the Los Angeles Metropolitan Area at the reference soil condition.

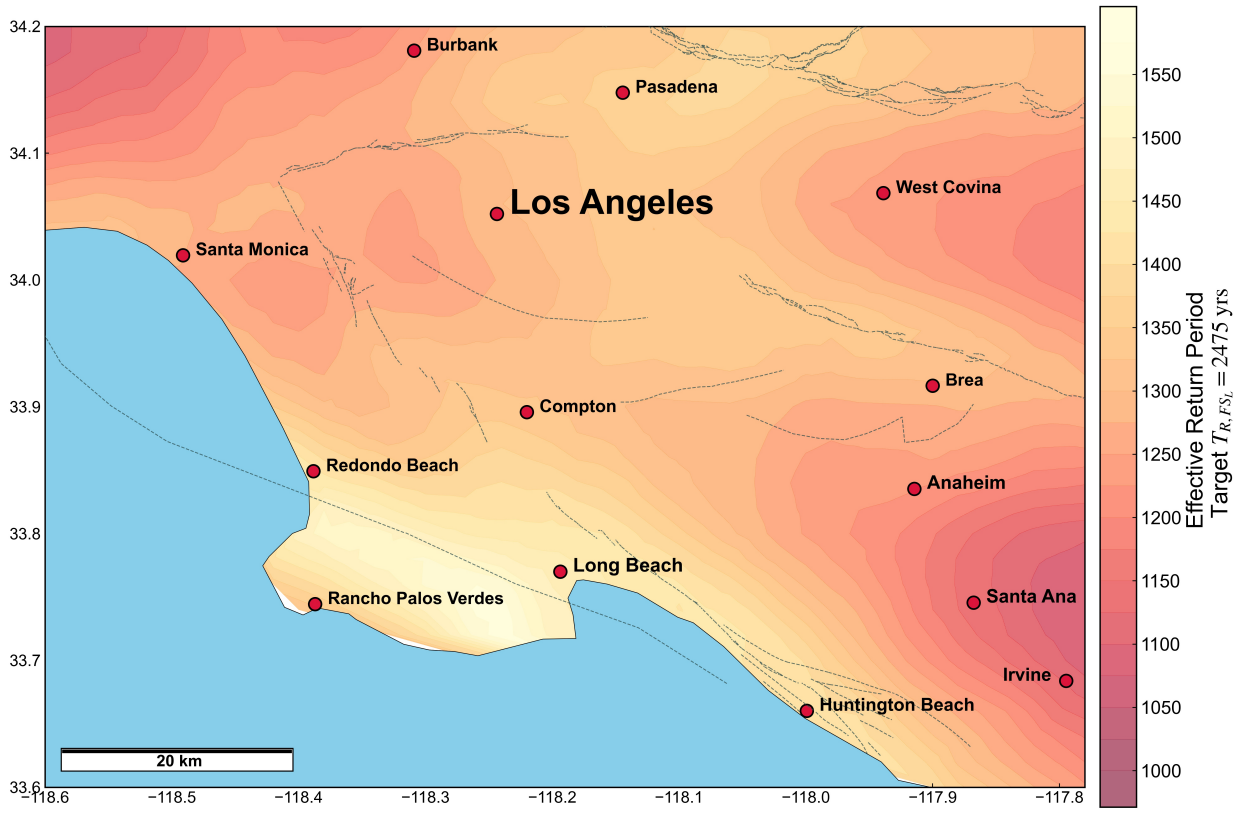

Figure A.33: Effective return period of predicted FS_L (target 2,475-year return period) for the Los Angeles Metropolitan Area at the reference soil condition.

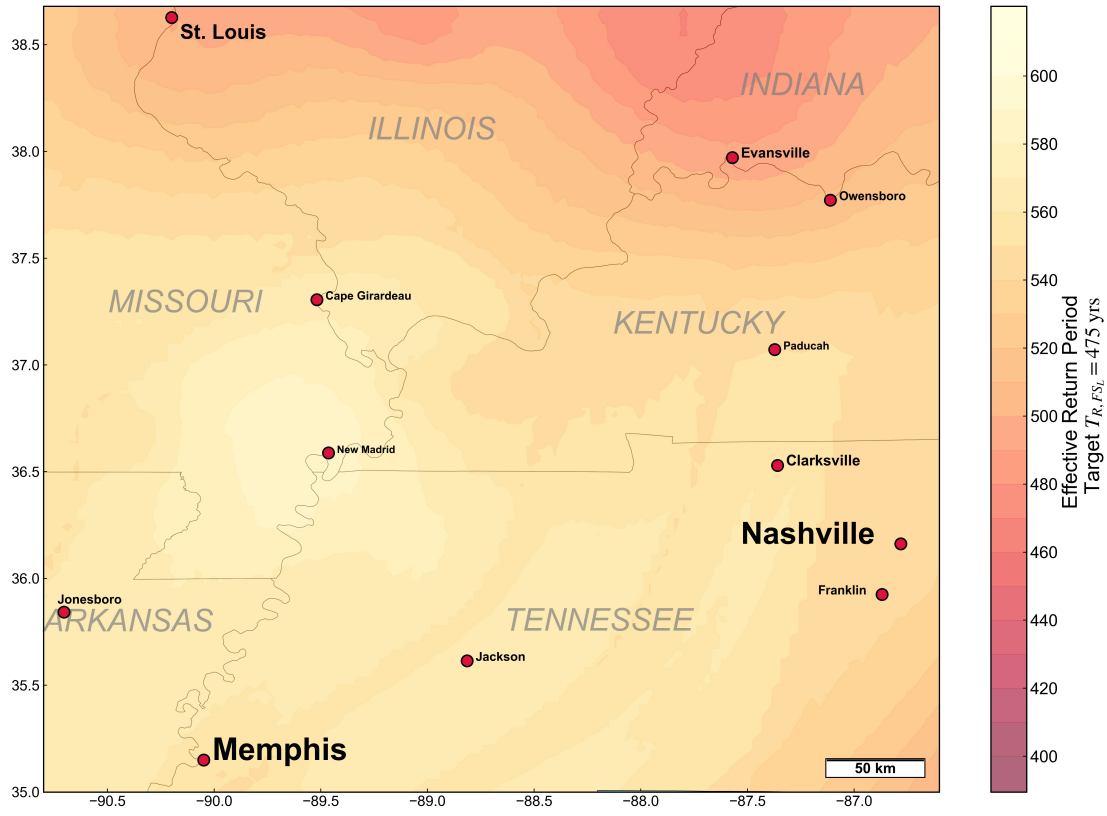

Figure A.34: Effective return period of predicted FS_L (target 475-year return period) for the region surrounding the New Madrid Fault Zone at the reference soil condition.

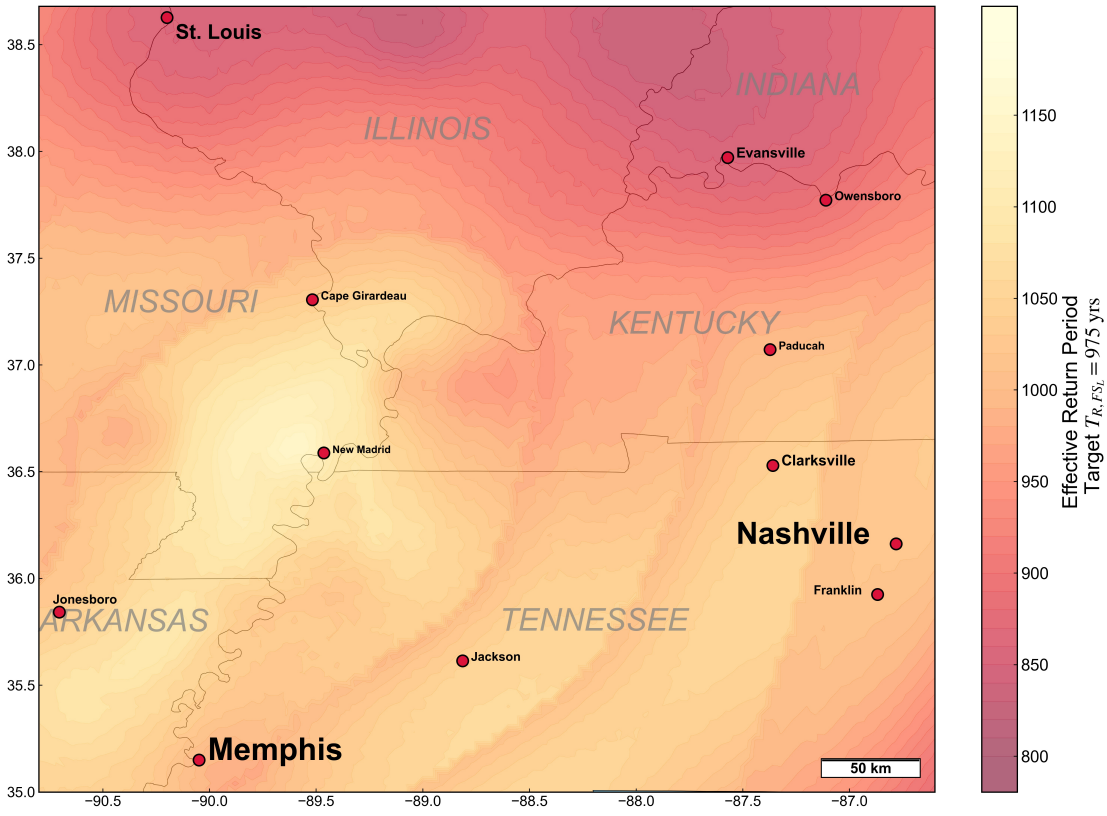

Figure A.35: Effective return period of predicted FS_L (target 975-year return period) for the region surrounding the New Madrid Fault Zone at the reference soil condition.

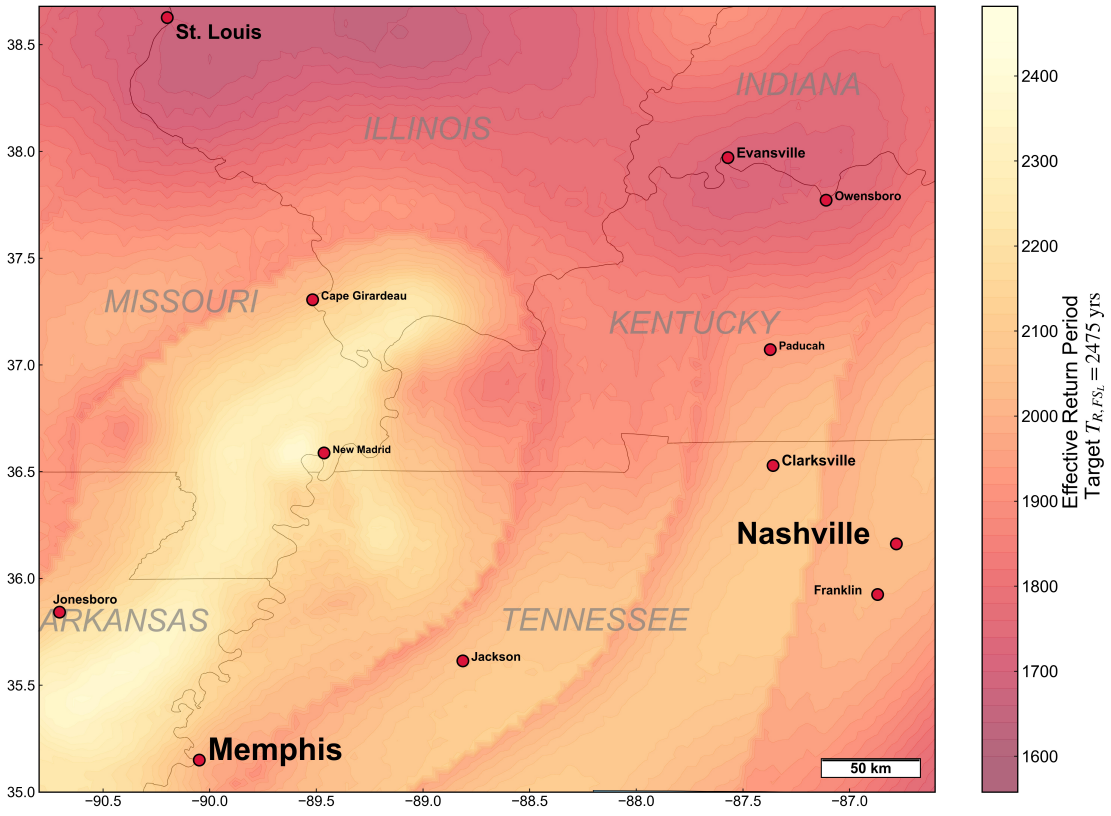

Figure A.36: Effective return period of predicted FS_L (target 2,475-year return period) for the region surrounding the New Madrid Fault Zone at the reference soil condition.

Appendix B

Summary of Selected Ground Motion Records for Numerical Parametric Study

B.1 Response Spectra for Selected Crustal Ground Motions

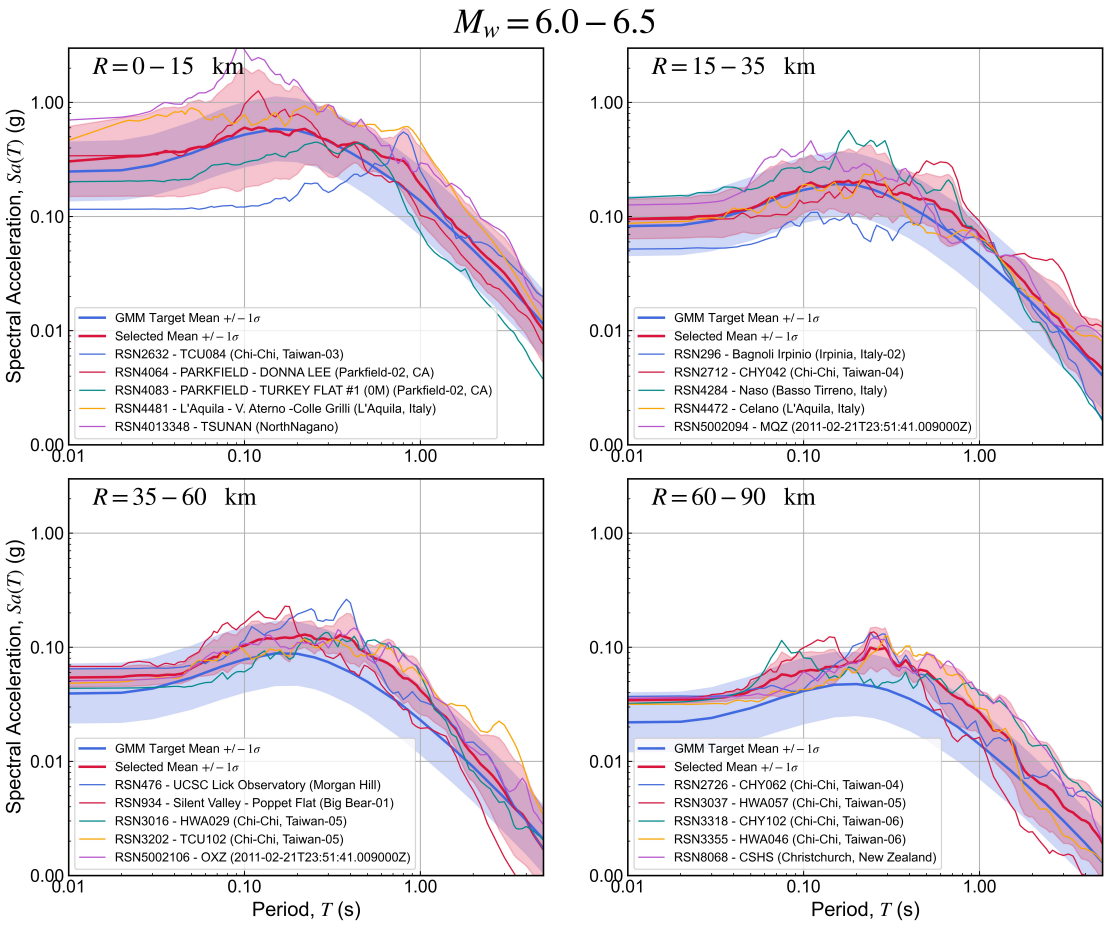

Figure B.1: Response spectra of selected crustal records for four distance bins corresponding to $M_W 6.0-6.5$. Shaded areas correspond to plus/minus one standard deviation of the target(blue) and selected (red) spectra.

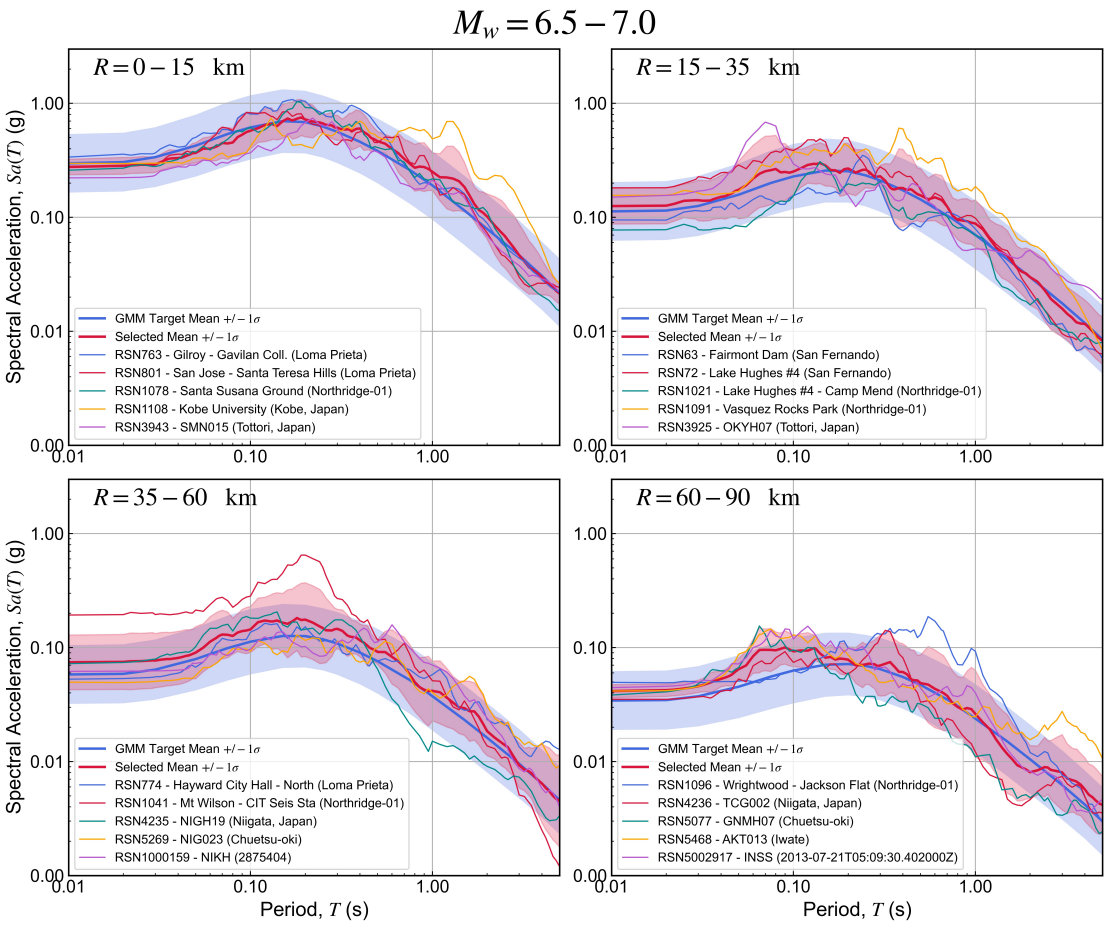

Figure B.2: Response spectra of selected crustal records for four distance bins corresponding to $M_W 6.5-7.0$. Shaded areas correspond to plus/minus one standard deviation of the target(blue) and selected (red) spectra.

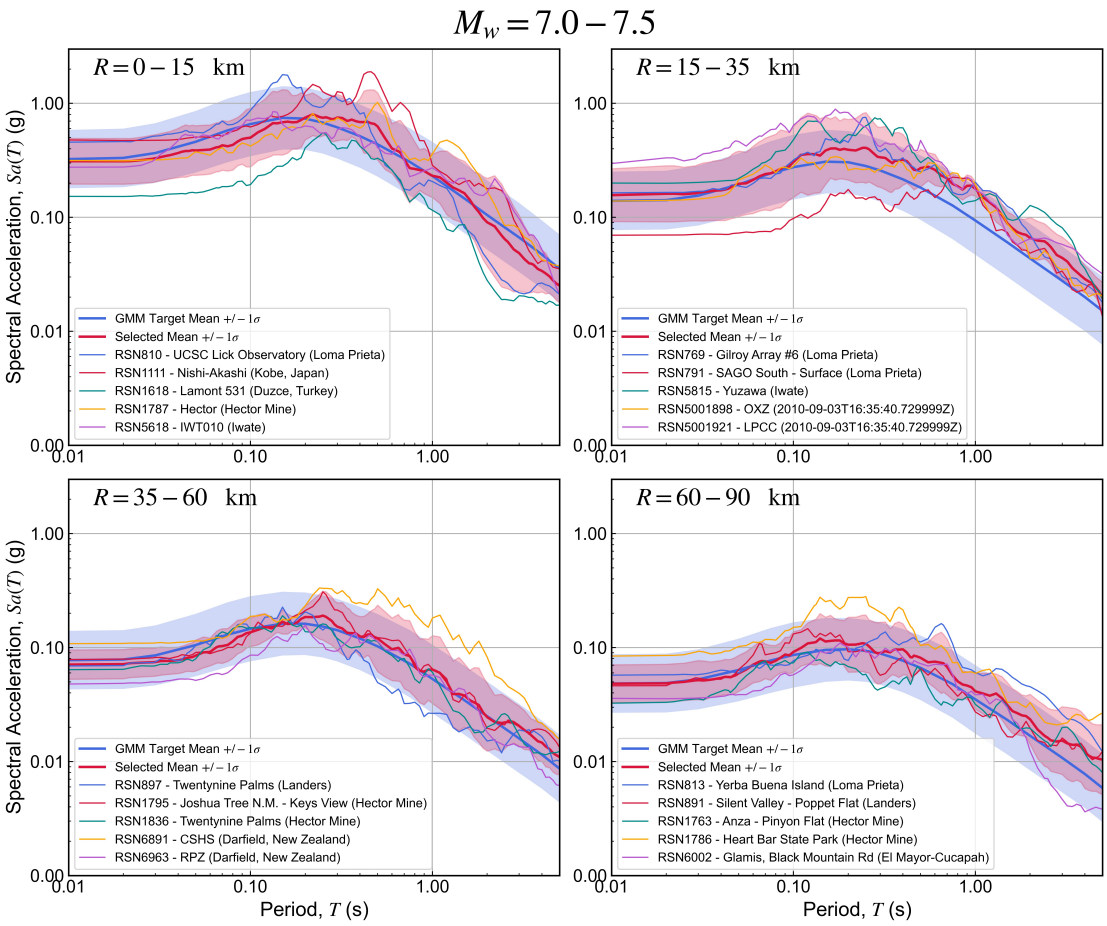

Figure B.3: Response spectra of selected crustal records for four distance bins corresponding to M_W7.0−7.5. Shaded areas correspond to plus/minus one standard deviation of the target(blue) and selected (red) spectra.

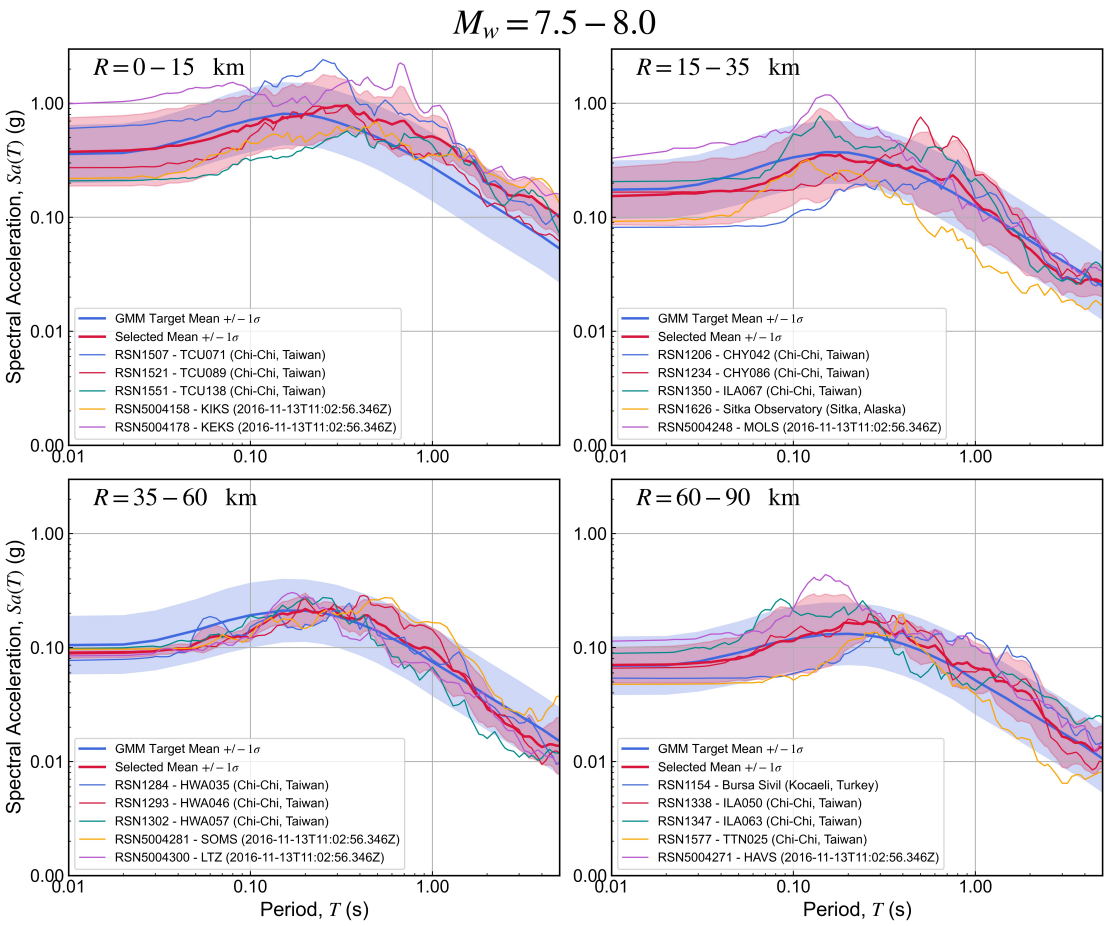

Figure B.4: Response spectra of selected crustal records for four distance bins corresponding to M_W7.5−8.0. Shaded areas correspond to plus/minus one standard deviation of the target(blue) and selected (red) spectra.

B.2 Response Spectra for Selected Subduction Ground Motions

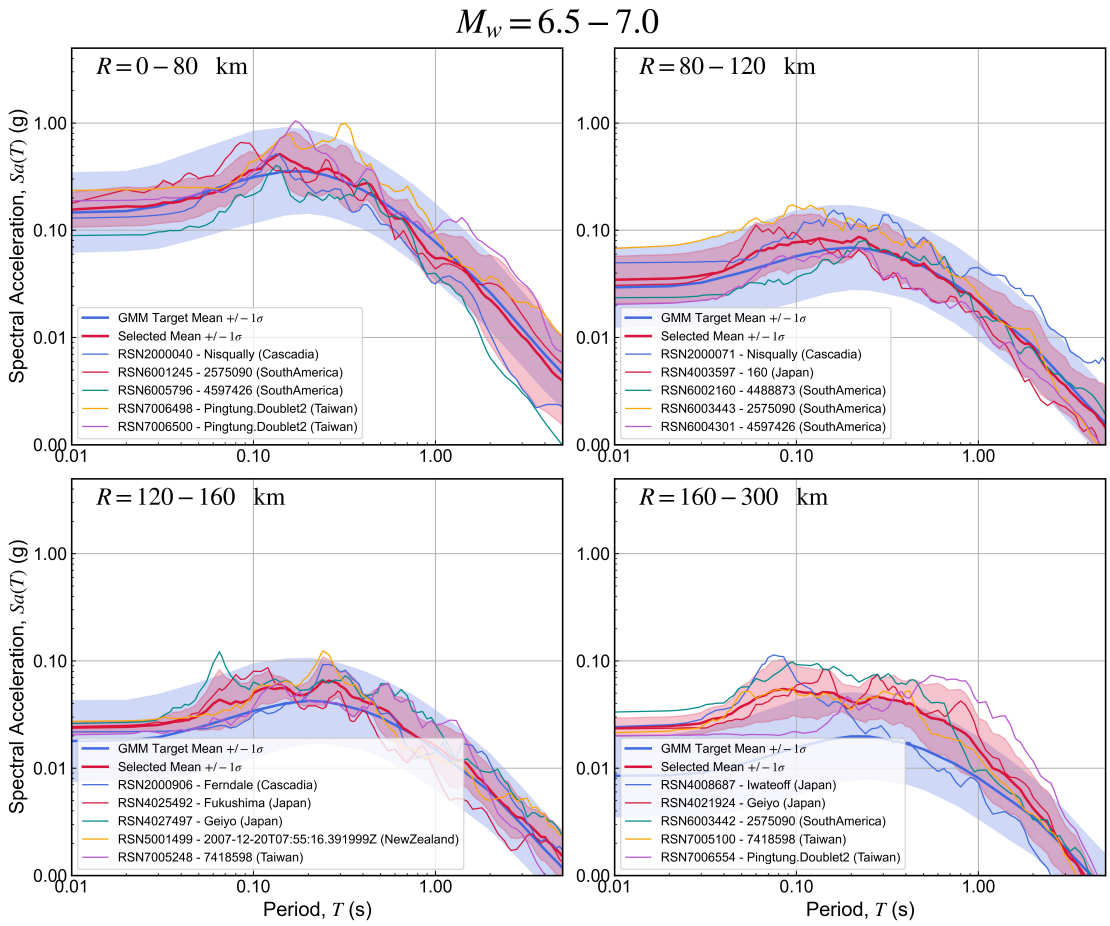

Figure B.5: Response spectra of selected subduction records for four distance bins corresponding to $M_W 6.5-7.0$. Shaded areas correspond to plus/minus one standard deviation of the target(blue) and selected (red) spectra.

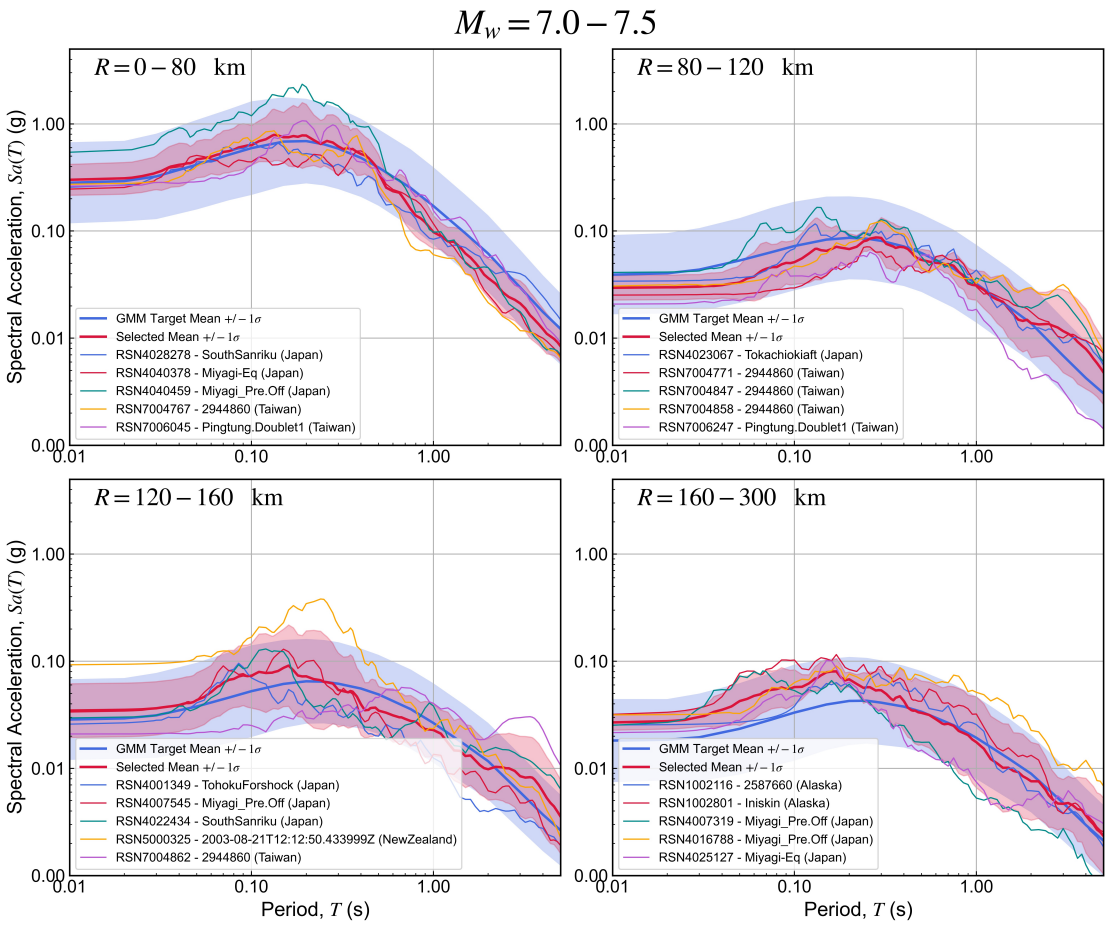

Figure B.6: Response spectra of selected subduction records for four distance bins corresponding to $M_W 7.0-7.5$. Shaded areas correspond to plus/minus one standard deviation of the target(blue) and selected (red) spectra.

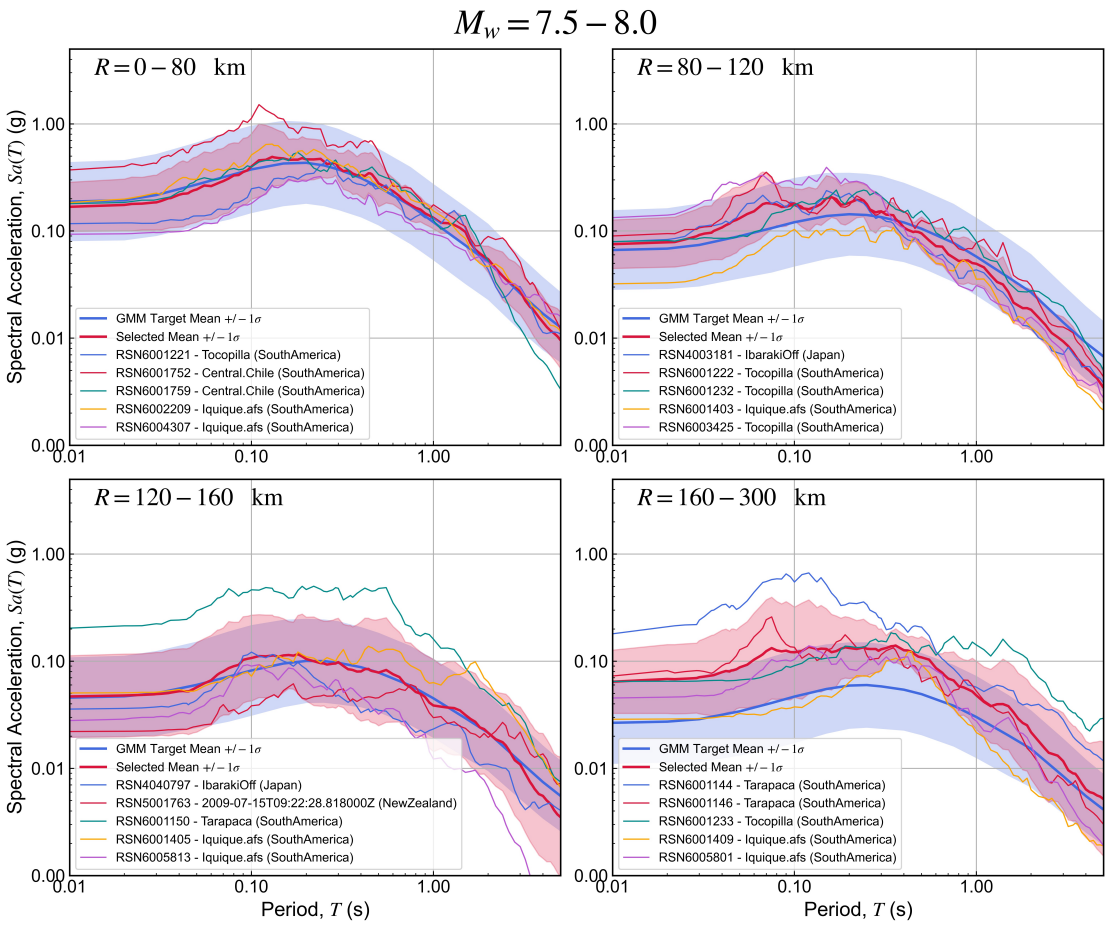

Figure B.7: Response spectra of selected subduction records for four distance bins corresponding to $M_W 7.5-8.0$. Shaded areas correspond to plus/minus one standard deviation of the target(blue) and selected (red) spectra.

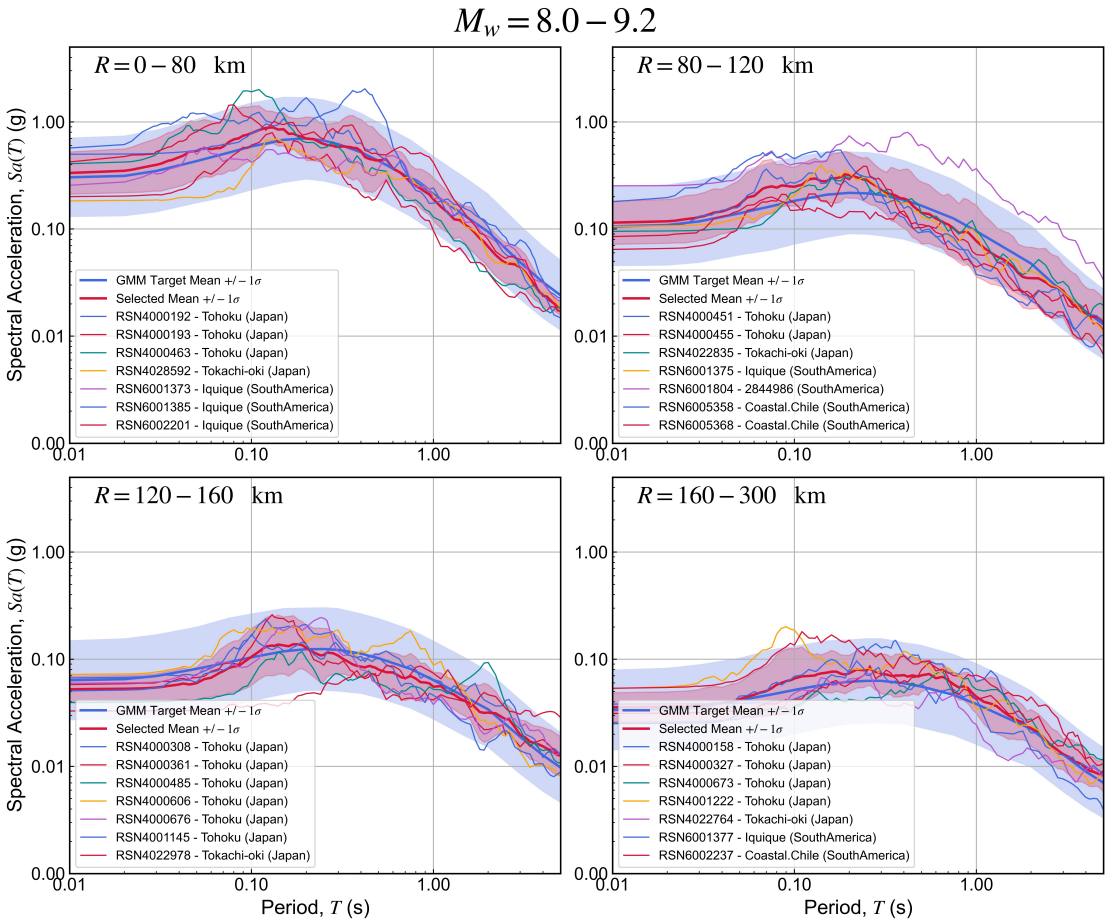

Figure B.8: Response spectra of selected subduction records for four distance bins corresponding to $M_W 8.0 - 9.0$. Shaded areas correspond to plus/minus one standard deviation of the target(blue) and selected (red) spectra.

B.3 Distribution of Selected Records by Geographic Region

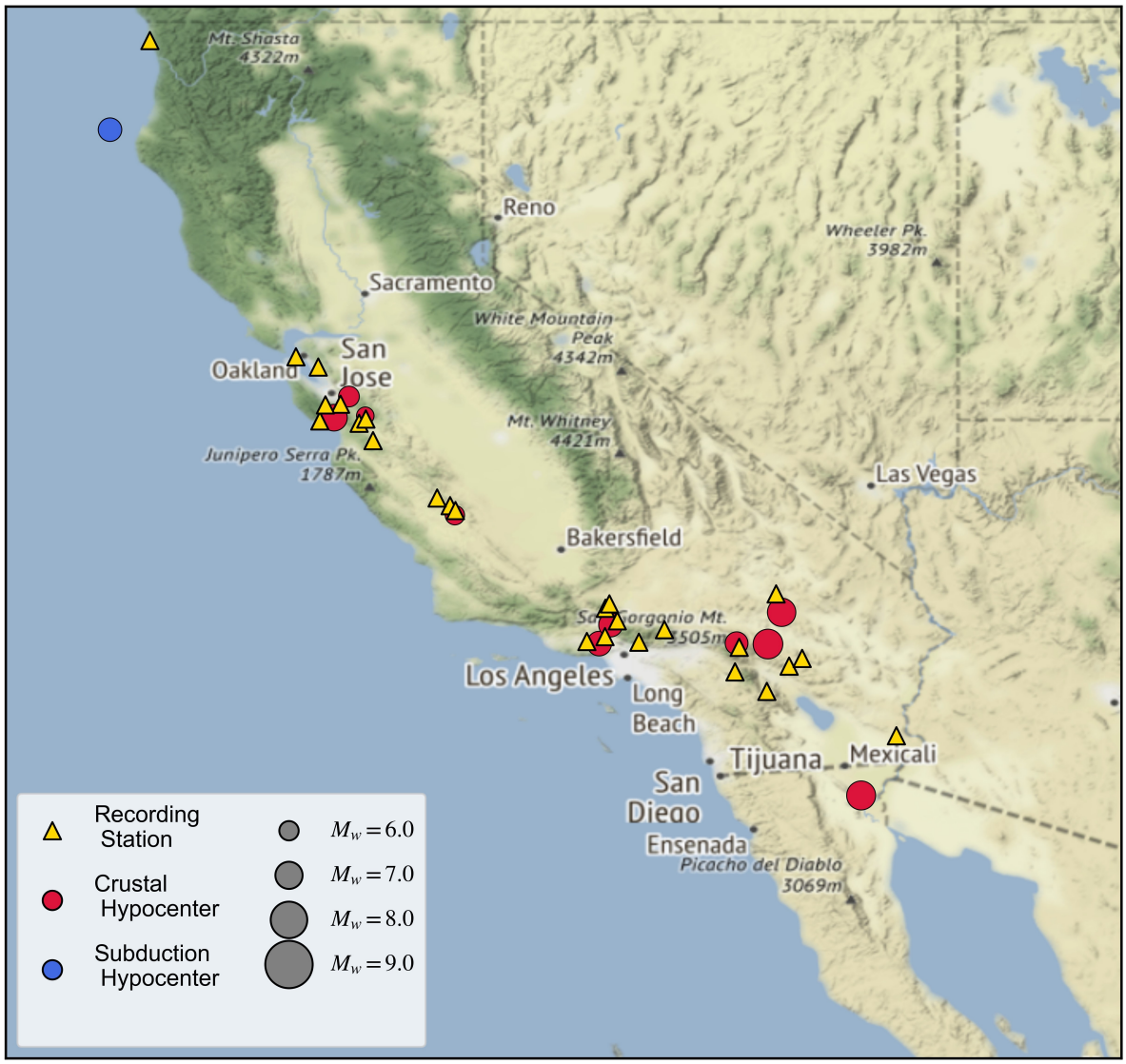

Figure B.9: Distribution of event hypocenters and recording stations from selected records in California.

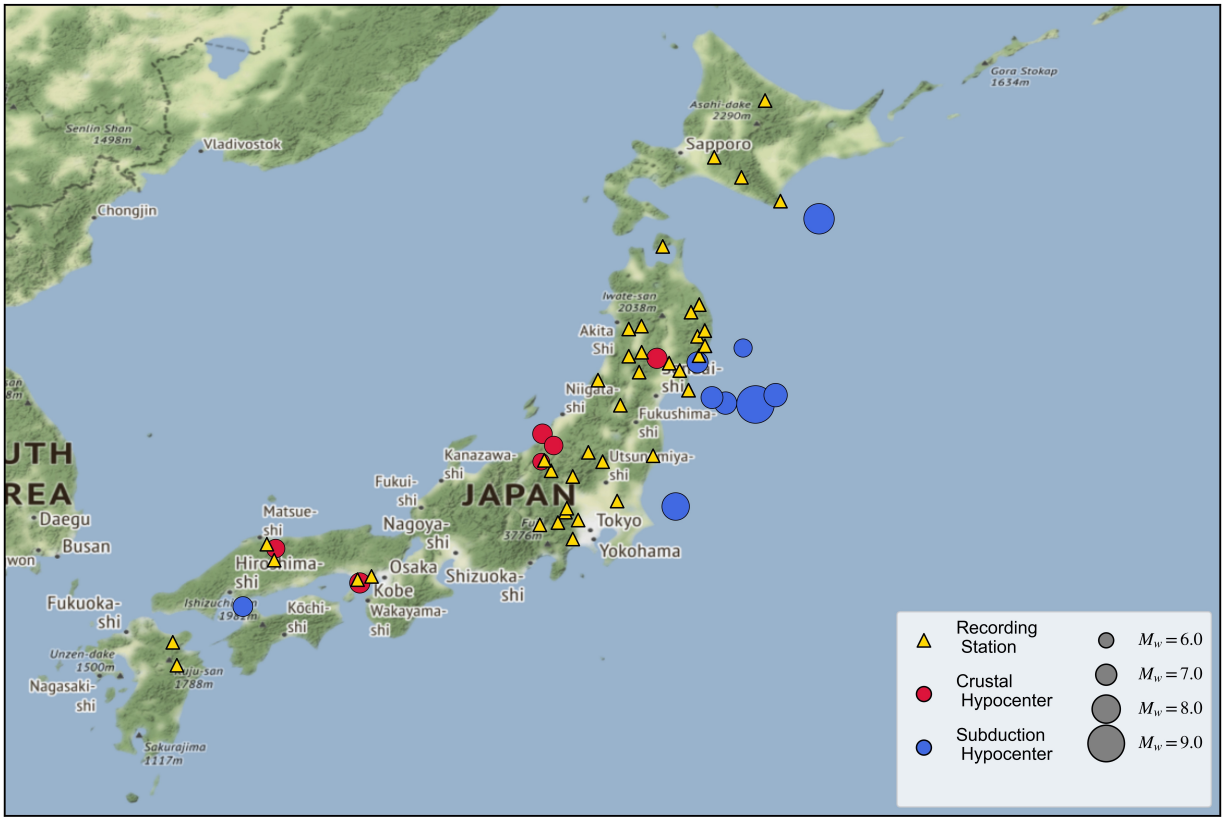

Figure B.10: Distribution of event hypocenters and recording stations from selected records in Japan.

Figure B.11: Distribution of event hypocenters and recording stations from selected records in New Zealand.

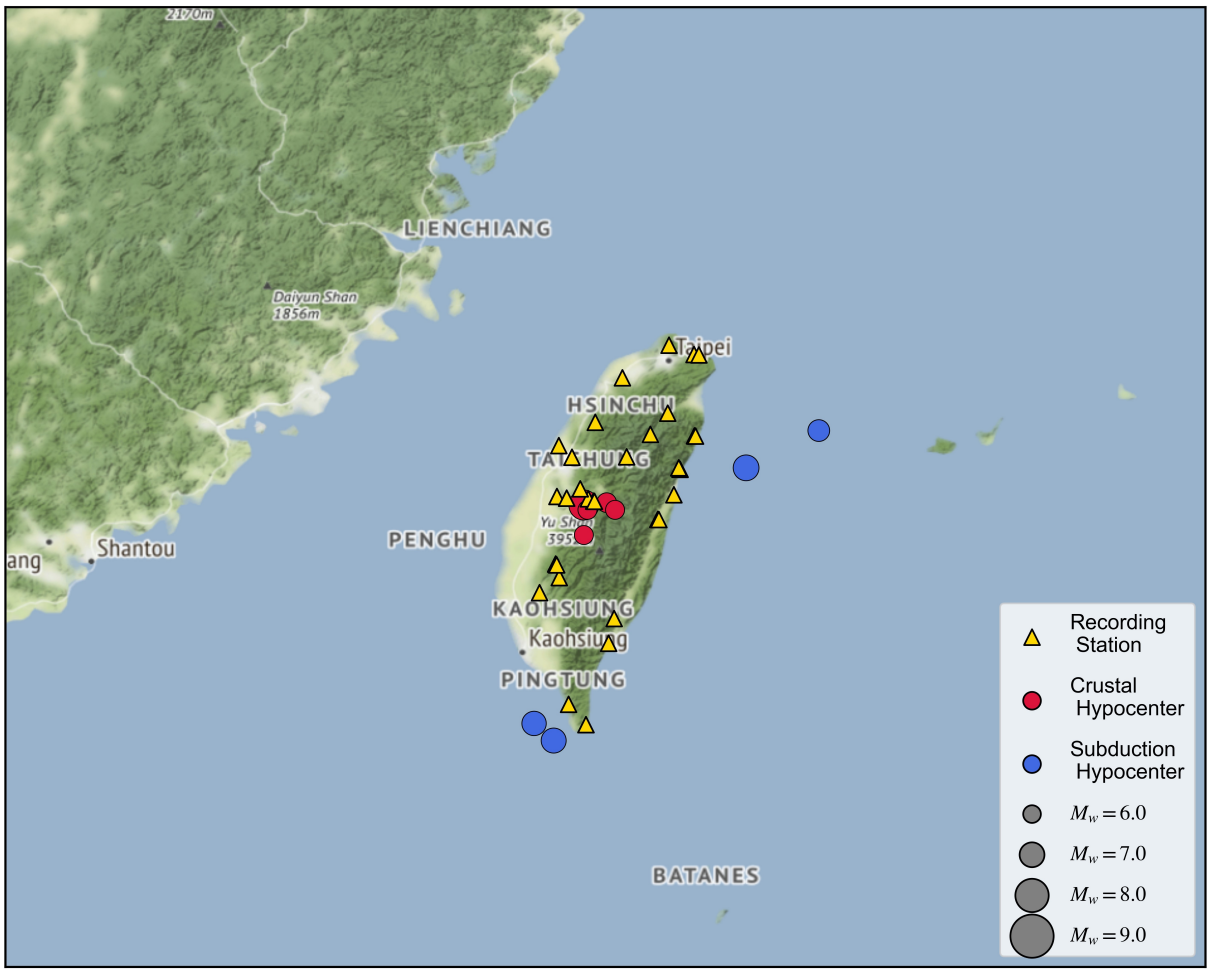

Figure B.12: Distribution of event hypocenters and recording stations from selected records in Taiwan.

Figure B.13: Distribution of event hypocenters and recording stations from selected records in South America.

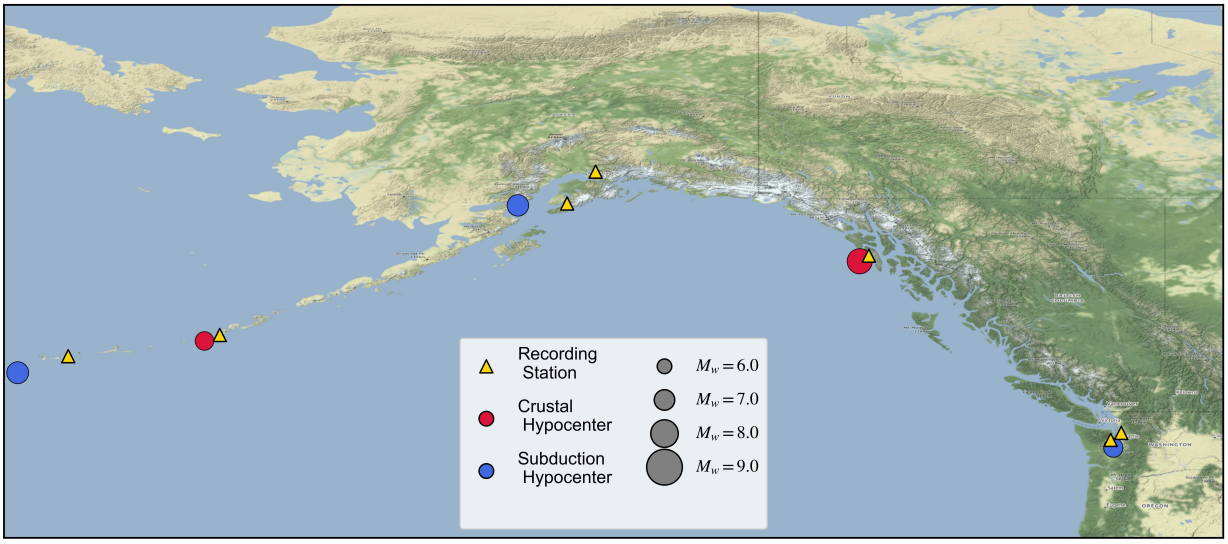

Figure B.14: Distribution of event hypocenters and recording stations from selected records in the Pacific Northwest United States and Alaska.

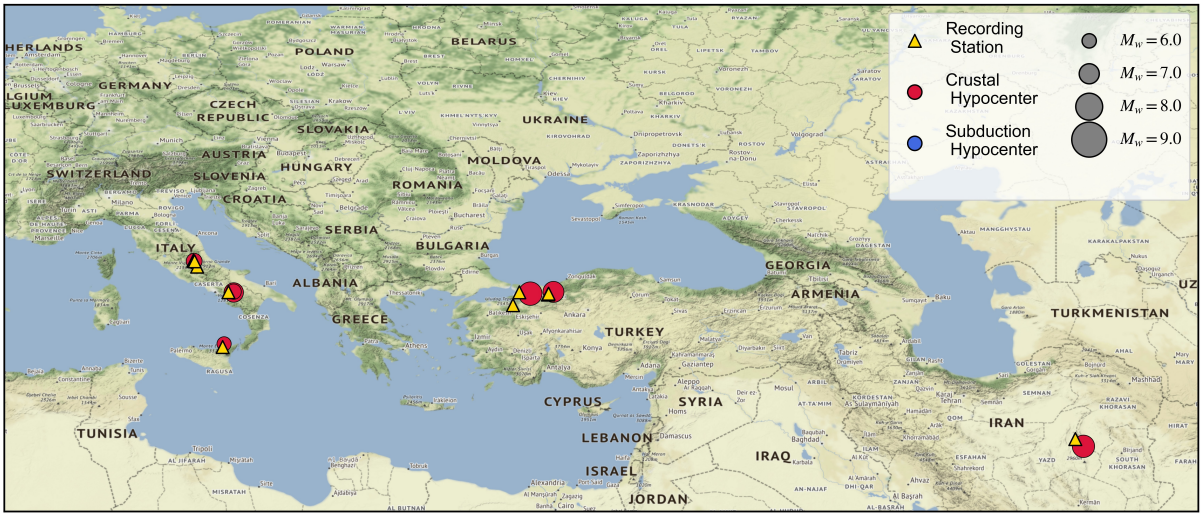

Figure B.15: Distribution of event hypocenters and recording stations from selected records in Europe and the Middle East.

Appendix C

Fully-Probabilistic Application of the Timing-Base Lateral Spreading Analysis

A fully-probabilistic application of the timing-based lateral spreading framework is presented herein. This framework is formulated from a "system-level" standpoint, in that the behavior of the geotechnical system is governed by a single time of liquefaction, and that a direct relationship exists (with some hypothetical uncertainty) between the post-triggering intensity at the base of the liquefiable zone and the surface displacements (rather than the strain integration-based approach outlined in Chapter 7). This formulation takes into account the uncertainties in (1) the prediction of the pre- and post-triggering IMs, (2) the estimation of the triggering limit-state PGA_M, (3) the relationship between the normalized evolutionary IMs α_1 and α_2, and (4) the prediction of surface displacements from $IM_{2,L}$ given site and soil conditions.

C.1 Probabilistic Formulation

The equations presented assume that two different ground motion intensity measures are used to predict the permanent lateral spreading displacements that occur after the triggering of liquefaction. The first intensity measure, IM_1, is used to predict the triggering of liquefaction, and the second, IM_2, is used to predict lateral spreading displacements; the two IMs are assumed to be correlated. The framework is presented assuming that probabilistic empirical models exist for predicting the likelihood of liquefaction triggering due to IM_1, as well as the magnitude of permanent displacement due to IM_2. The framework is presented initially, for the sake of simplicity, as a cal-

culation of the probability distribution of permanent displacements, conditional on the occurrence of some minimum magnitude event, with a joint probability distribution of the two IMs. The final expression for the annual rate of exceedance is presented by incorporating the joint annual rate of exceedance (also referred to herein as the joint hazard curve) of the two intensity measures of interest, rather than their joint probability distribution. It is also shown that the joint IM_1-IM_2 hazard curve can be readily obtained using the generalized conditional intensity measure approach (GCIM, Bradley 2010) from an initial hazard curve for IM_1, and the correlation between IM_1 and IM_2. The naming conventions for each of the variables are summarized in Table C.1.

Table C.1: Nomenclature for variables used in probabilistic lateral spreading calculation

Variable Name	Description
IM_1	Intensity measure used to predict liquefaction triggering limit state.
IM_{1T}	Total quantity of IM_1 over full duration.
IM_{1L}	Quantity of IM_1 at the time of liquefaction
α_1	Proportion of total IM_1 at time of liquefaction, IM_{1L}/IM_{1T}
IM_2	Intensity measure used to predict permanent deformations.
IM_{2T}	Total quantity of IM_2 over full duration.
IM_{2L}	Quantity of IM_2 after liquefaction
α_2	Proportion of total IM_2 remaining after liquefaction, IM_{2L}/IM_{2T}

C.1.1 Characterization of IM_1 for Triggering Limit State

We begin by considering the annual rate of exceedance of the total IM of interest for liquefaction triggering IM_{1T}, based on the results of a conventional scalar PSHA at the site of interest:

$$\lambda_{IM_{1T}}(im_{1T}) = \sum_{i=1}^{N_S} \nu_i \sum_{j=1}^{N_{Rup}} \mathrm{P}[IM_{1T} > im_{1T} | Rup = rup_j] P[Rup = rup_j] \tag{C.1}$$

where *Rup* represents a particular rupture scenario (e.g. magnitude and distance) for a particular source S_i, and ν_i is the annualized rate of exceeding some minimum magnitude threshold at S_i.

For a particular element of soil at the site having a particular resistance to liquefaction, a hypothetical probabilistic liquefaction triggering model can be used to determine the probability of liquefaction for a given triggering IM level (P[Liq|IM_1]). We are interested in estimating the level

of the triggering IM that would cause liquefaction for a given soil element, and thus assuming that liquefaction has indeed been triggered, the probability that it was triggered at a particular level of IM_1 can be simply expressed as:

$$\mathrm{P}[IM_{1L} = im_1] = \mathrm{P}[\mathrm{Liq}|IM_1 = im_1] \tag{C.2}$$

where the subscript L denotes the value of IM_1 at the instant liquefaction is triggered, in contrast to IM_{1T}, which refers to the total IM_1 level over the entire ground motion duration. Repeating this calculation for all values of IM_1 yields the probability distribution for IM_{1L}.

C.1.2 Characterization of $\mathrm{P}[\alpha_1]$ from IM_{1L} and IM_{1T}

We now have two probability distributions: one (IM_{1T}) describing the total level of IM_1 at the site (based on the scalar PSHA), and one (IM_{1L}) describing the level of IM_1 that would trigger liquefaction in a given soil element (based on the probabilistic triggering model). These two distributions can be compared to define a normalized IM at the time of triggering, represented by the parameter:

$$\alpha_1 = \frac{IM_{1L}}{IM_{1T}} \tag{C.3}$$

The quantity α_1 represents the fraction of the total triggering IM that is required to actually trigger liquefaction, and provides critical insight into the timing of liquefaction. Recognizing that α_1 is simply a function of two random, independent variables (IM_{1L}, which is a function of the soil's resistance to liquefaction, and IM_{1T}, which represents the expected levels of ground shaking), its probability density can simply be re-written in terms of the conditional probability density of one variable (IM_{1L}), integrated over all values of the other variable (IM_{1T}):

$$\mathrm{P}[\alpha_1 = a_1] = \sum_{i=1}^{N_{IM_{1T}}} \mathrm{P}[\alpha_1 = a_1|IM_{1T} = im_{1T,i}] \cdot \mathrm{P}[IM_{1T} = im_{1T}] \tag{C.4a}$$

$$= \sum_{i=1}^{N_{IM_{1T}}} \mathrm{P}[IM_{1L} = (a_1 \cdot im_{1T,i})|IM_{1T} = im_{1T,i}] \cdot \mathrm{P}[IM_{1T} = im_{1T,i}] \tag{C.4b}$$

At this point, the shorthand $\mathrm{P}[im_{1T,i}]$ is introduced to represent $\mathrm{P}[IM_{1T} = im_{1T,i}$, for brevity, and is used throughout the rest of this document for all variables.

C.1.3 Characterization of $\mathrm{P}[\alpha_2]$ from α_1

With the timing of liquefaction established, the subsequent relative quantity of the remaining effects intensity measure IM_{2L} must be characterized, given that liquefaction has been triggered at a particular time. This relative quantity, α_2, is expressed as:

$$\alpha_2 = \frac{IM_{2L}}{IM_{2T}} \tag{C.5}$$

where IM_{2L} is the effects IM that remains after liquefaction has been triggered, and IM_{2T} is the total effects intensity measure over the entire duration of shaking. Assuming there exists a probabilistic relationship between α_1 and α_2, the probability distribution of α_2 can be calculated by adding another layer to the total probability calculation, and integrating over all possible values of α_1:

$$\mathrm{P}[\alpha_2 = a_2] = \sum_{j=1}^{N_{\alpha_1}} \sum_{i=1}^{N_{IM_{1T}}} \mathrm{P}[\alpha_2 = a_2 | a_{1,j}] \cdot \mathrm{P}[\alpha_1 = a_1 | im_{1T,i}] \cdot \mathrm{P}[im_{1T,i}] \tag{C.6a}$$

$$= \sum_{j=1}^{N_{\alpha_1}} \sum_{i=1}^{N_{IM_{1T}}} \mathrm{P}[\alpha_2 = a_2 | a_{1,j}] \cdot \mathrm{P}[IM_{1L} = (a_1 \cdot im_{1T,i}) | im_{1T,i}] \cdot \mathrm{P}[im_{1T,i}] \tag{C.6b}$$

C.1.4 Characterization of Remaining Effects IM from α_2 and Total Effects IM

We now have a probability distribution for the relative amount of remaining IM_2 in our ground motion - however, the parameter of interest for lateral spreading is the actual value of the remaining ground motion intensity, not the relative amount. To get from α_2 to IM_{2L}, we again leverage the fact that IM_{2L} is a function of two random variables (IM_{2L} and IM_{2T}) to express the probability distribution of IM_{2L} as:

$$\mathrm{P}[IM_{2L} = im_{2L}] = \sum_{k=1}^{N_{IM_{2T}}} \mathrm{P}[IM_{2L} = im_{2L} | im_{2T,k}] \cdot P[im_{2T,k}] \tag{C.7a}$$

$$= \sum_{k=1}^{N_{IM_{2T}}} \mathrm{P}\left[\alpha_2 = \left(1 - \frac{im_{2L}}{im_{2T}}\right) | im_{2T,k}\right] \cdot P[im_{2T,k}] \tag{C.7b}$$

where the probabilistic characterization of IM_{2T} is obtained from either a PSHA, or a conditional

relationship to the triggering intensity measure, IM_{1T}. Substituting the expression for $\mathrm{P}[\alpha_2]$ from Equation C.6a, $\mathrm{P}[IM_{2L}]$ can be expressed as:

$$\mathrm{P}[IM_{2L} = im_{2L}] = \sum_{k=1}^{N_{IM_{2T}}} \sum_{j=1}^{N_{\alpha_1}} \sum_{i=1}^{N_{IM_{1T}}} \mathrm{P}\left[\alpha_2 = \left(\frac{im_{2L}}{im_{2T}}\right) | a_{1,j}, im_{2T,k}\right] \cdot \mathrm{P}[a_{1,j}|im_{1T,i}] \cdot \mathrm{P}[im_{2T,k}|im_{1T,i}] \cdot \mathrm{P}[im_{1T,i}] \tag{C.8}$$

where the final term in Equation C.8 is the probability of the total effects intensity measure, IM_2, conditional on the total triggering intensity measure, IM_1 .

C.1.5 Final Calculation of Exceedance Rate of Permanent Displacement

Finally, the probability distribution for IM_{2L} can be integrated with a hypothetical lateral spreading model describing the permanent displacement as a function of IM_{2L}. In order to express this an annualized rate of exceedance, the probability of exceeding a particular displacement δ conditional on IM_{2L}, $\mathrm{P}[D > \delta|IM_{2L}$ is calculated and integrated with Equation C.8, with the probability distribution $\mathrm{P}[im_{1T,i}]$ replaced by the annualized exceedance rate $\lambda_{IM_{1T}}(im_{1T,i})$.

$$\lambda_D(\delta) = \sum_{m=1}^{N_{IM_{2L}}} \sum_{k=1}^{N_{IM_{2T}}} \sum_{j=1}^{N_{\alpha_1}} \sum_{i=1}^{N_{IM_{1T}}} \mathrm{P}[D > \delta|im_{2L,m}] \cdot \mathrm{P}\left[\alpha_2 = \left(\frac{im_{2L}}{im_{2T}}\right) | a_{1,j}, im_{2T,k}\right] \cdot \mathrm{P}[IM_{1L} = (a_1 \cdot im_{1T,i})|im_{1T,i}] \cdot \mathrm{P}[im_{2T,k}|im_{1T,i}] \Delta\lambda_{IM_{1T}}(im_{1T,i}) \tag{C.9}$$

C.1.6 Calculating Joint IM Hazard Curves Using a Generalized Conditional Intensity Measure Approach

The final term ($\Delta\lambda_{IM_{1T}}$) in Equation C.9 is the joint hazard curve for the two IMs of interest, λ_{IM_1,IM_2}. Ideally, the joint hazard curve is most easily obtained using some form of a vector-based PSHA. However, in many cases, current widely available PSHA computational platforms may not be particularly well-suited for vector-based PSHAs, particularly those involving less well-established earthquake intensity measures such as CAV or I_a. As a result, a specific application of the GCIM approach (Bradley, 2010) is proposed for developing a joint $IM_1 - IM_2$ hazard curve, based on an initial hazard curve for IM_1, along with its corresponding deaggregated hazard data.

For a given rupture scenario rup_i (i.e. a combination of M and R for a given source), the

lognormal mean and standard deviation of some IM_2, conditional on the occurrence of some level of IM_1 can be approximated as:

$$\mu_{\ln(IM_2|Rup,IM_1)}(rup_i, im_1) = \mu_{\ln IM_2|Rup}(rup_i) + \sigma_{\ln IM_2|Rup}(rup_i)\rho_{\ln IM_2,\ln IM_1}\varepsilon_{\ln IM_1} \quad \text{(C.10a)}$$

$$\sigma_{\ln(IM_2|Rup,IM_1)}(rup_i, im_1) = \sigma_{\ln IM_2|Rup}(rup_i)\sqrt{1 - \rho^2_{\ln IM_2,\ln IM_1}} \quad \text{(C.10b)}$$

where $\mu_{\ln IM_2|Rup}(rup_i)$ and $\sigma_{\ln IM_2|Rup}(rup_i)$ are the mean and standard deviation, respectively, of the predicted IM_2 for the given rupture scenario. This requires at least one GMM for the given IM_2 of interest. $\rho_{\ln IM_2,\ln IM_1}$ is the correlation coefficient between the two intensity measures; numerous studies exist that explore the correlation structures for various combinations of intensity measures. $\varepsilon_{\ln IM_1}$ is the number of standard deviations the value of IM_1 is above the mean predicted IM_1 for the given rupture scenario. Knowing the probability distribution of all rupture scenarios for a given IM_1, the overall conditional probability of IM_2 given IM_1 can be expressed as:

$$\mathrm{P}[IM_2|IM_1 = im_1] = \sum_{i=1}^{N_{Rup}} \mathrm{P}[IM_2|IM_1 = im_1, Rup = rup_i] \cdot \mathrm{P}[Rup = rup_i|IM_1 = im_1] \quad \text{(C.11)}$$

Ideally, the characterization of the conditional distribution of $IM_2|IM_1$ would, at its highest level of sophistication, require calculating the conditional mean and standard deviation of IM_2 for every possible rupture scenario. In such a case, the term *Rup* (in $\mu_{\ln IM_2|Rup,IM_1}$ and $\sigma_{\ln IM_2|Rup,IM_1}$) would refer to the combination of magnitude (M_w), distance (R), and epsilon (ε) for every seismic source (e.g. all logic trees for the Seattle Fault Zone or Cascadia Subduction Zone characterization, every single coordinate of any gridded seismicity model) that causes significant levels of IM_1. This would require knowledge of not only the percent contribution of every source to the hazard at a wide range of IM_1 levels, but also the marginal $M_w - R - \varepsilon$ distribution for each of these sources. This generally represents an immense amount of data that is typically not made available to users by widely available PSHA platforms.

As a result, some simplifications must be made as to what constitutes a "rupture scenario", based on the level of detail of the deaggregation data made available by whatever PSHA code is being utilized. In the case of the USGS `nshmp-haz` code, the most detailed set of rupture scenarios can be defined in one of two ways:

1. The mean (or modal) M_w-R-ε combination from each earthquake source, along with the percent contribution to the IM_1 hazard for each source, which can be obtained from the summary of a given deaggregation calculation from `nshmp-haz`.

2. The full M_w-R-ε joint probability distribution for each source *type* (e.g. fault, interface, system, grid), as well as the percent contribution to the IM_1 hazard for each source type. In using an aggregation of individual sources, some generalization of the GMM calculation to generate $\mu_{\ln IM_2|Rup,IM_1}$ and $\sigma_{\ln IM_2|Rup,IM_1}$ would be necessary. For instance, to calculate the conditional distribution for the collection of fault sources, a single set of fault characteristics would need to be assumed, and differences in faulting style, dimensions, hanging-wall effects, etc. on the conditional IM_2 distribution would not be considered.

There are several other ways to represent rupture scenarios from deaggregation data that are considerably less detailed and easier to implement. The simplest method would be to generate $\mu_{\ln IM_2|Rup}(rup_i)$ and $\sigma_{\ln IM_2|Rup}(rup_i)$ using the mean rupture scenario ($\bar{M}_w$, $\bar{R}$, $\bar{\varepsilon}$) from the deaggregation at a given IM_1 level for all sources. While this might be reasonable in areas that are controlled by relatively tightly clustered source of seismicity, the mean rupture scenario in areas containing more diverse (and diffuse) sources of seismicity may not necessarily represent a realistic, physical rupture scenario. Alternatively, characterization of the conditional distribution could potentially be refined by using the full range of $[M_w, R, \varepsilon]$ (and their corresponding joint distribution from the deaggregated hazard), rather than just the mean values. However, the problem remains that such a method does not differentiate between different types of seismic sources, and thus the GMM used to calculate $\mu_{\ln IM_2|Rup}(rup_i)$ and $\sigma_{\ln IM_2|Rup}(rup_i)$ may not be applicable to the rupture scenario it is purportedly considering.

C.2 Demonstration of Probabilistic Timing-Based Lateral Spreading Analysis

A hypothetical application of the fully probabilistic timing-based framework is presented in the following section. It is assumed that the triggering IM is represented by the magnitude-adjusted peak ground acceleration, PGA_M, the effects intensity measure is taken as Arias intensity, I_a, and that relationships exist that allow for the probabilistic characterization of PGA_M at the time of liquefaction ($PGA_{M,L}$), the fractions of triggering and effects IMs α_2 and α_1, and a response model for predicting permanent displacements from the remaining Arias intensity, $I_{a,L}$. The analysis is performed for a site in San Francisco, with the seismic hazard contribution solely attributed to crustal seismicity, for a simple profile with a 5 m-thick layer of liquefiable soil with $q_{c1Ncs} = 110$.

C.2.1 GCIM Approach for Obtaining Total PGA_M Hazard Data from PGA

Given that PGA_M is a function of PGA and M_w, the annual rate of exceedance of PGA_M can be formulated conditionally on those two parameters:

$$\lambda_{PGA_M}(pga_m) = \sum_{i=1}^{N_{PGA}} \sum_{j=1}^{N_{M_w}} \mathrm{P}[PGA_M > pga_m | pga_i, m_j] \cdot \mathrm{P}[m_j | pga_i] \cdot \Delta\lambda_{PGA}(pga_i) \tag{C.12}$$
$$= \sum_{i=1}^{N_{PGA}} \sum_{j=1}^{N_{M_w}} \mathrm{P}[pga_i / MSF(m_j) > pga_m | pga_i, m_j] \cdot \mathrm{P}[m_j | pga_i] \cdot \Delta\lambda_{PGA}(pga_i)$$

The probability of PGA_M exceeding some value, pga_m, for a given PGA-M_w pair, can be calculated from the standard normal distribution, assuming that $\mu_{\ln PGA_M} = pga_i / MSF(m_j)$ and $\sigma_{\ln PGA_M} = \sigma_{\ln PGA}$. In this case, $\sigma_{\ln PGA}$ was taken as the weighted average of the four NGAWest-2 GMM standard deviations for the given magnitude and distance (thus adding a third summation over R in Equation C.12). The resulting hazard curve for PGA_M is shown in Figure C.1, along with the original PGA hazard curve upon which it was calculated.

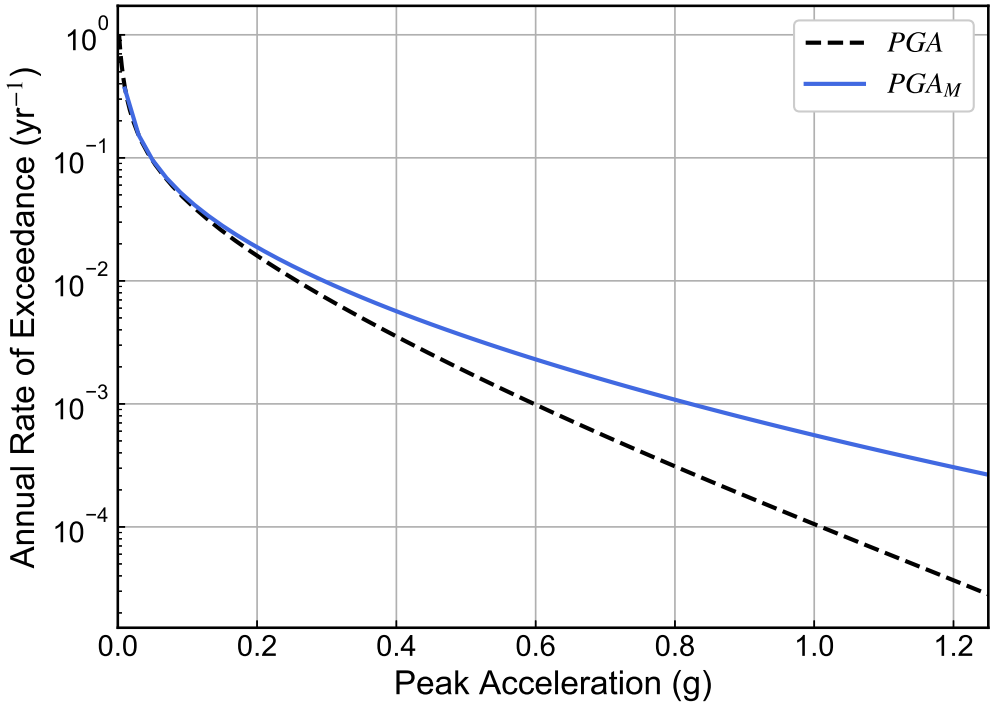

Figure C.1: Hazard curves for PGA and PGA_M, calculated conditionally on PGA, for a San Francisco site

In order to obtain the probability distribution of rupture scenarios contributing to the PGA_M hazard (for later use in the GCIM procedure to characterize I_a, the definition of the marginal rupture probability (Baker, 2008) can be utilized:

$$\mathrm{P}[Rup = rup | PGA_M > pga_m] = \frac{\lambda_{PGA_M, Rup}(pga_m, rup)}{\lambda_{PGA_M}(pga_m)} \tag{C.13}$$

where the numerator is calculated in a similar manner to Equation C.12, without the summation over M_w or R, and the MSF is calculated from the magnitude of the particular rupture scenario:

$$\lambda_{PGA_M, Rup}(pga_m, rup) = \sum_{i=1}^{N_{PGA}} \mathrm{P}[PGA_M > pga_m | pga_i, rup] \cdot \mathrm{P}[rup | pga_i] \cdot \Delta\lambda_{PGA}(pga_i) \tag{C.14}$$

The marginal probability of the rupture scenario given a particular pga_i (i.e. the second term inside

the summation) can be obtained from the hazard deaggregation data for PGA.

C.2.2 Conditional Distribution of Total I_a From Total PGA_M

Using the GCIM procedure, the conditional distribution of the effects intensity measure, I_a, given the triggering intensity measure, PGA_M, can be calculated from the statistical moments:

$$\mu_{\ln I_a|Rup,\ln PGA_M}(rup_i, pga_m) = \mu_{\ln I_a|Rup}(rup_i) + \sigma_{\ln I_{a,T}|Rup}(rup_i)\rho_{\ln I_a,\ln PGA_M}\varepsilon_{\ln PGA_M} \quad \text{(C.15a)}$$

$$\sigma_{\ln I_a|Rup,\ln PGA_M}(rup_i, pga_m) = \sigma_{\ln I_a|Rup}(rup_i)\sqrt{1-\rho^2_{\ln I_a,\ln PGA_M}} \quad \text{(C.15b)}$$

where $\mu_{\ln I_{a,T}|Rup}(rup_i)$ and $\sigma_{\ln I_{a,T}|Rup}(rup_i)$ were calculated using the Campbell and Bozorgnia (2010) GMM for Arias intensity. The correlation coefficient between PGA_M and I_a, $\rho_{\ln I_a,\ln PGA_M}$, was taken to be 0.95 (Greenfield, 2010). The standard normal distribution is used to obtain the conditional probability distribution, $\mathrm{P}[I_{a,T}|pga_{M,T}, rup_j]$. Assuming the probability of each rupture scenario for PGA_M is known (from Equations C.13 and C.14), the overall conditional probability of $I_{a,T}$ given PGA_M can then be expressed as:

$$\mathrm{P}[I_{a,T}|PGA_{M,T}] = \sum_{j=1}^{N_{Rup}} \mathrm{P}[I_{a,T}|PGA_M, Rup = rup_k] \cdot \mathrm{P}[Rup = rup_k|PGA_M] \quad \text{(C.16)}$$

Conditional distributions of $I_{a,T}$ given several values of PGA_M, are shown in Figure C.2. A resulting hazard curve for $I_{a,T}$ can also be calculated by integrating over the PGA_M hazard curve (using the conditional probability of exceedance of $I_{a,T}$, rather than the probability density), and is shown in Figure C.3.

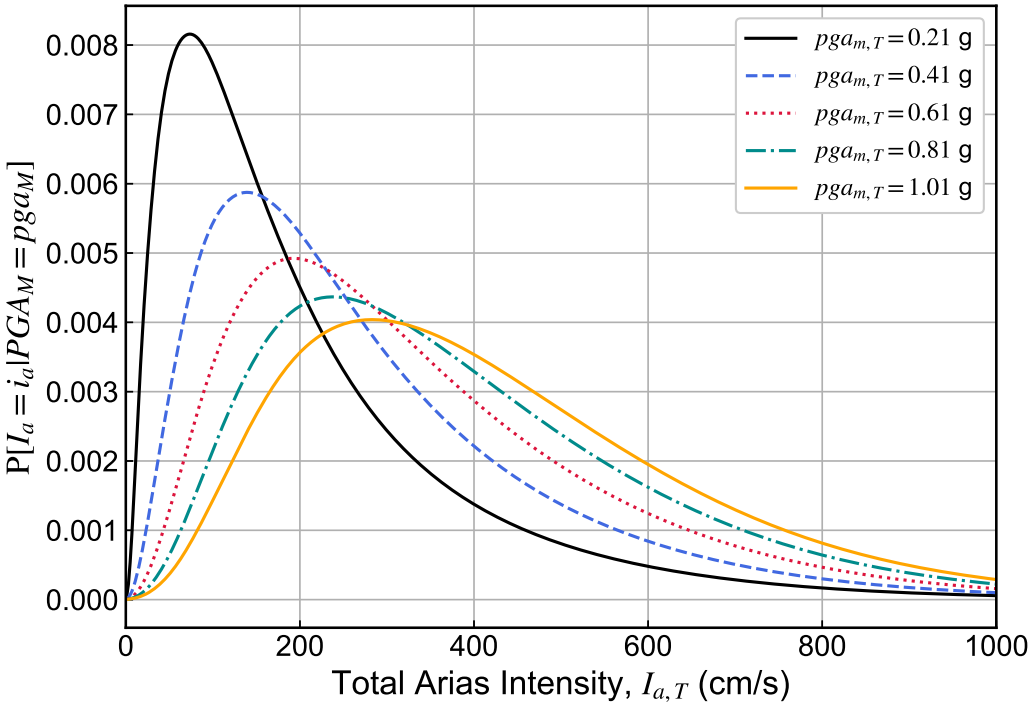

Figure C.2: Conditional probability distribution of $I_{a,T}$ given PGA_M

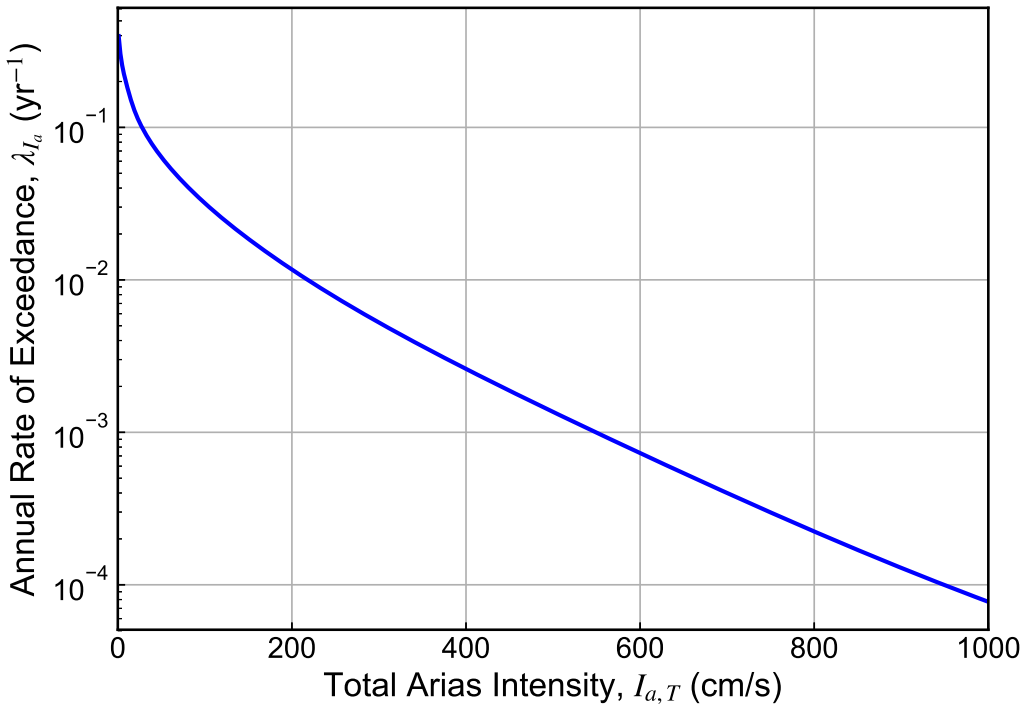

Figure C.3: Hazard curve for $I_{a,T}$ based on GCIM calculation with respect to PGA_M

C.2.3 Conditional Distribution of α_1, Given Total $\mathbf{PGA_M}$

Using Equations C.3 and C.4a, the probability density for α_1, conditional on the total triggering intensity measure $PGA_{M,T}$, i.e. the value of PGA_M computed for the entire ground motion, can be expressed as:

$$\mathrm{P}[\alpha_1 = a_1 | pga_{m,T}] = \mathrm{P}[PGA_{M,L} = a_1 \cdot pga_{M,T}] \tag{C.17}$$

where $PGA_{M,L}$ is the value of the triggering intensity measure at the time of liquefaction. Its probability distribution is estimated here, assuming lognormality and using statistical moments derived from the Boulanger and Idriss (2015) probabilistic, CPT-based triggering model:

$$\mu_{\ln PGA_M} = \ln CRR(q_{c1Ncs}) + \ln\left[0.65\frac{\sigma_v r_d}{\sigma'_v K_\sigma}\right] \tag{C.18}$$

$$\sigma_{\ln PGA_M} = \sqrt{\sigma^2_{\ln CRR} + \sigma^2_{\ln CSR}} \tag{C.19}$$

where $\sigma_{\ln PGA_M}$ was assumed to be 0.25 (based on the maximum likelihood estimates of $\sigma_{\ln S} = 0.20$ and $\sigma_{\ln R} = 0.15$ from Boulanger and Idriss, 2010) for this demonstration case. The resulting α_1 probability density is shown for multiple values of the total PGA_M in Figure C.4. It is clear from Figure C.4 that weak ground motions, which will tend to trigger liquefaction later in the motion, result in higher uncertainty in α_1.

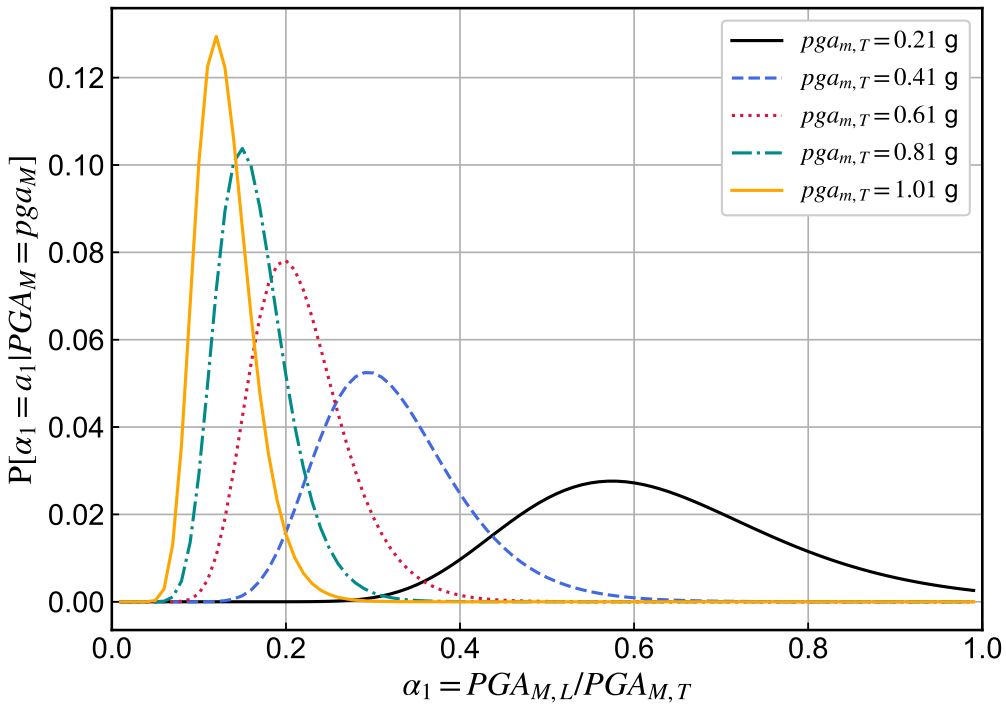

Figure C.4: Conditional probability distribution of α_1, given various values of $PGA_{M,T}$

C.2.4 Conditional Distribution of α_2, Given α_1

The probabilistic relationship between α_2 and α_1 was assumed to follow a beta distribution (Greenfield, 2016), with the conditional standard deviation of α_2 varying as a function of α_1. The $P[\alpha_2|\alpha_1]$ distribution is shown in Figure C.5. Note that when α_1 is very low (i.e. liquefaction has been triggered relatively early in the motion), the distribution of α_2 is centered at relatively high values, and with very little variance, indicating that a relatively large amount of the effects *IM* remains after triggering has occurred. As α_1 increases, a corresponding decrease in α_2 is observed, albeit with an increase in the conditional variance of α_2. Thus, not only do weak motions result in higher uncertainty in α_1, they also result in higher uncertainty in $\alpha_2|\alpha_1$.

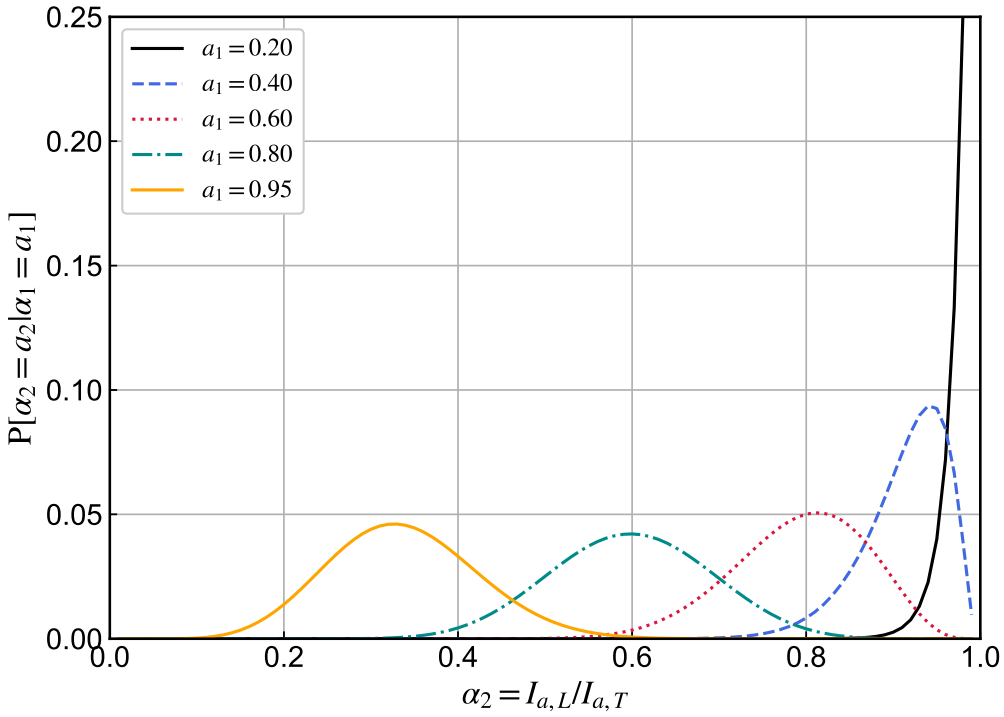

Figure C.5: Conditional probability distribution of α_2 given α_1

C.2.5 Conditional Distribution of $I_{a,L}$, Given $I_{a,T}$ and α_1

Recall that the remaining effects intensity measure, in this case represented by $I_{a,L}$ (with the subscript L now denoting the post-triggering portion of the intensity measure), can be characterized as a function of two random variables, α_2 and $I_{a,T}$. Its probability distribution is thus equivalent to the distribution of α_2, conditional on α_1 and $I_{a,T}$ as follows:

$$\mathrm{P}[I_{a,L} = i_{a,L} | \alpha_1 = a_1, I_{a,T} = i_{a,T}] = \mathrm{P}\left[\alpha_2 = \frac{i_{a,L}}{i_{a,T}} \middle| \alpha_1 = a_1\right] \tag{C.20}$$

The probability distributions of $I_{a,L}$, conditional on various combinations of $I_{a,T}$ and α_1, are shown in Figure C.6.

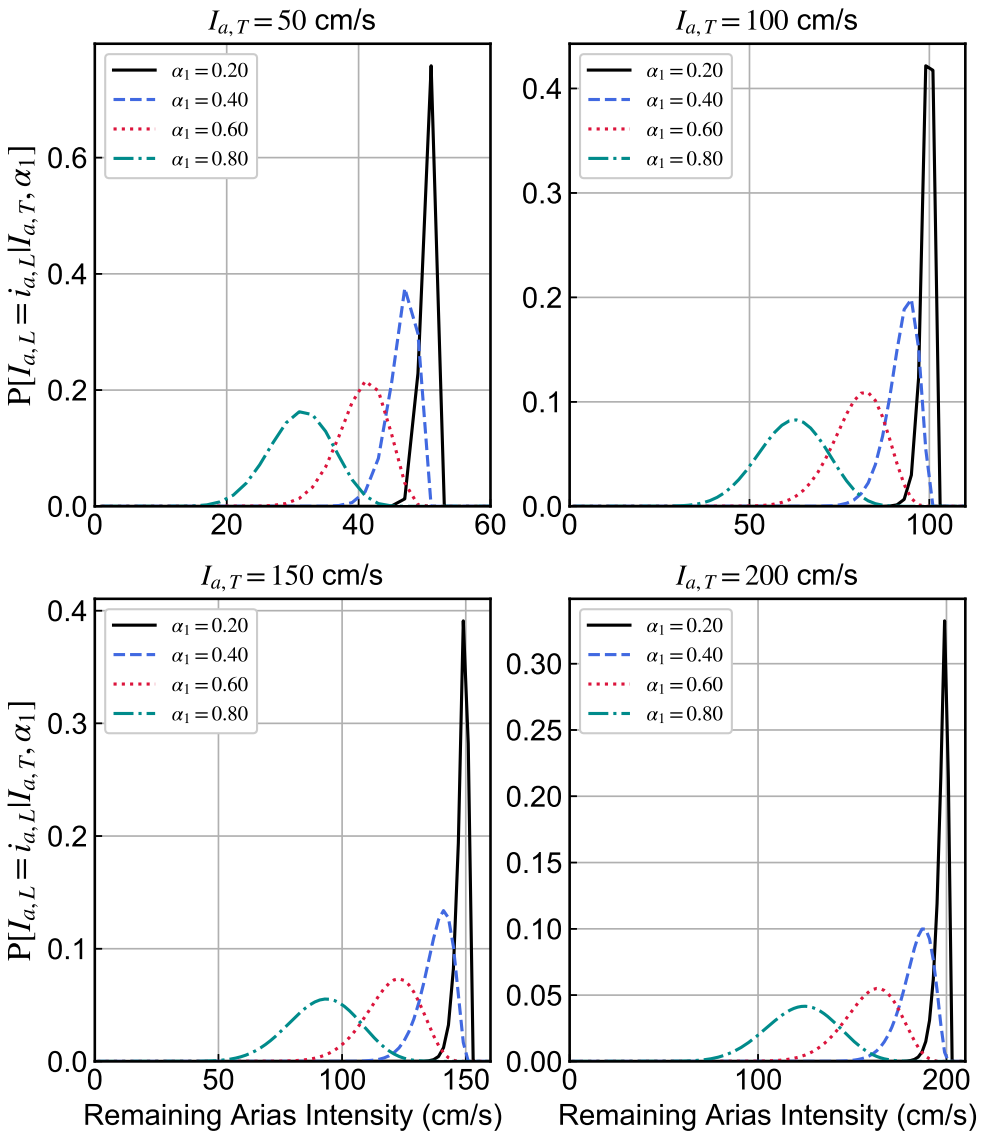

Figure C.6: Conditional probability distribution of remaining effects intensity measure, $I_{a,L}$, given total effects intensity measure, $I_{a,T}$ and α_1

C.2.6 Conditional Distribution of Permanent Displacement, Given $I_{a,L}$

Finally, a response model relating the remaining effects *IM*, $I_{a,L}$, to permanent lateral displacements was obtained from Greenfield (2016), based on numerical simulations of a simple profile with 5 m of loose to medium dense sand. Note that this model is not generalizable across a broad

range of actual sites, but will be sufficient here as an example of a potential response model. The lognormal mean and standard deviation of the permanent displacement are calculated via:

$$\mu_{\ln\delta} = -0.97 + -1.58 \ln\left[\frac{q_{c1Ncs}}{113}\right] + 0.40 \ln\left[\frac{I_{a,L}}{1\,\mathrm{m/s}}\right] \tag{C.21}$$

$$\sigma_{\ln\delta} = 0.45 \tag{C.22}$$

The conditional distribution of displacement, given several values of $I_{a,L}$, is shown in Figure C.7.

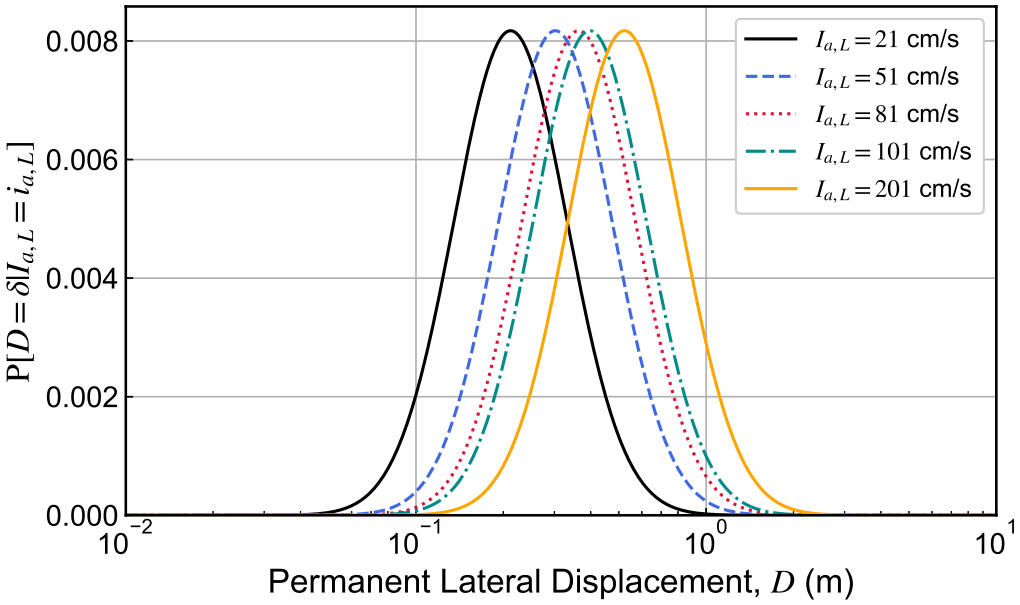

Figure C.7: Conditional probability distribution of permanent lateral displacement, given remaining effects intensity measure $I_{a,L}$

C.2.7 Final Hazard Curve for Permanent Lateral Displacement

The overall hazard curve for D can be calculated by combining each of the components that have been presented in this section, and summing over four variables: (1) The total triggering intensity measure, $PGA_{M,T}$; (2) the fraction of $PGA_{M,T}$ required for triggering liquefaction, α_1; (3) the total effects intensity measure, $I_{a,T}$; and (4) the remaining effects intensity measure, $I_{a,L}$:

$$\lambda_D(\delta) = \sum_{m=1}^{N_{I_{a,L}}} \sum_{k=1}^{N_{I_{a,T}}} \sum_{j=1}^{N_{\alpha_1}} \sum_{i=1}^{N_{PGA_{M,T}}} \mathrm{P}[D > \delta | i_{aL,m}] \cdot \mathrm{P}\left[\alpha_2 = \left(\frac{i_{aL,m}}{i_{aT,k}}\right) | a_{1,j}\right] \tag{C.23}$$
$$\cdot \mathrm{P}[PGA_{M,L} = (a_{1,j} \cdot pga_{MT,i}) | pga_{MT,i}] \cdot \mathrm{P}[i_{aT,k} | pga_{MT,i}] \Delta\lambda_{PGA_{M,T}}(pga_{MT,i})$$

The final hazard curve for permanent displacement, for this example case, is shown in Figure C.8.

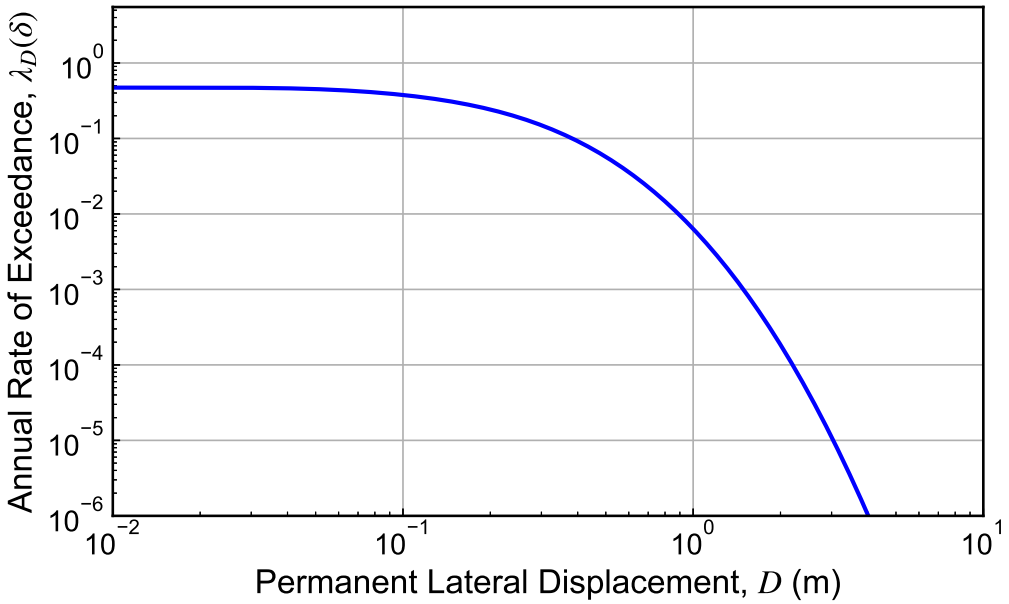

Figure C.8: Annual rate of exceedance of permanent lateral displacement, using timing-based procedure

Bibliography

Abrahamson, N. A., Silva, W. J., and Kamai, R. (2013). Update of the AS08 Ground-Motion Prediction equations based on the NGA-west2 data set. *Pacific Engineering Research Center Report, 4.*

ASCE. (2013). Minimum design loads for buildings and other structures. ASCE 7-10. Reston, VA: ASCE.

ASCE. (2014). Seismic evaluation and retrofit of existing buildings. ASCE/SEI 41-13. Reston, VA: ASCE.

ASCE. (2017). Minimum design loads and associated criteria for buildings and other structures. ASCE/SEI 7-16. Reston, VA: ASCE.

Baker, J. W. (2013). An introduction to probabilistic seismic hazard analysis. *White paper version*, 2(1), 79.

Bartlett, S. F., and Youd, T. L. (1992). Empirical prediction of lateral spread displacement. In *Proceedings from the fourth Japan-US workshop on earthquake resistant design of lifeline facilities and countermeasures for soil liquefaction* (pp. 351-65).

Been, K., and Jeffries, M. G. (1985). A state parameter for sands. *Geotechnique* 35(2), 99-112.

Bolton, M. D. (1986). The strength and dilatancy of sands. *Geotechnique* 36(1), 65-78.

Boore, D. M. (2010). Orientation-independent, nongeometric-mean measures of seismic intensity from two horizontal components of motion. *Bulletin of the Seismological Society of America* 100(4):1830-1835

Boore, D. M., Watson-Lamprey, J., and Abrahamson, N. A. (2006). Orientation-independent measures of ground motion. *Bulletin of the seismological Society of America*, 96(4A), 1502-1511.

Boore, D. M., Stewart, J. P., Seyhan, E., and Atkinson, G. M. (2014). NGA-West2 equations for predicting PGA, PGV, and 5% damped PSA for shallow crustal earthquakes. *Earthquake Spectra* August 2014, Vol. 30, No. 3, pp. 1057-1085.

Boulanger, R. W. (2003a). Relating K_α to relative state parameter index. *J. Geotech. Geoenviron. Eng.* 129(8), 770-773.

Boulanger, R. W., and Idriss, I. M. (2012). Probabilistic standard penetration test–based liquefaction–triggering procedure. *Journal of Geotechnical and Geoenvironmental Engineering*, 138(10), 1185-1195.

Boulanger, R. W., and Idriss, I. M. (2014). CPT and SPT Based Liquefaction Triggering Procedures. *Center for Geotechnical Modeling* Report No. UCD/CGM.-14, 1.

Boulanger, R. W., and Idriss, I. M. (2015). CPT-Based Liquefaction Triggering Procedure. *Journal of Geotechnical and Geoenvironmental Engineering*, 142(2), 04015065.

Boulanger, R. W., and Idriss, I. M. (2015). Magnitude scaling factors in liquefaction triggering procedures. *Soil Dynamics and Earthquake Engineering*, 79, 296–303.

Boulanger, R. W., and Truman, S. P. (1996). Void redistribution in sand under post-earthquake loading. *Canadian Geotechnical Journal*, 33(5), 829-834.

Boulanger, R. W., and Ziotopoulou, K. (2013). Formulation of a sand plasticity plane-strain model for earthquake engineering applications. *Soil Dynamics and Earthquake Engineering*, 53, 254-267.

Boulanger, R. W., and Ziotopoulou, K. (2019). A constitutive model for clays and plastic silts in plane-strain earthquake engineering applications. *Soil Dynamics and Earthquake Engineering*, 127, 105832.

Bozorgnia, Y., Abrahamson, N.A., Atik, L.A., Ancheta, T.D., Atkinson, G.M., Baker, J.W., Baltay, A., Boore, D.M., Campbell, K.W., Chiou, B.S.J. and Darragh, R. (2014). NGA-West2 research project. *Earthquake Spectra*, 30(3), 973-987.

Bozorgnia, Y., Stewart, J. P., and Abrahamson, N. A. (2020). Data Resources for NGA-Subduction Project. *Report PEER 2020/02*, Pacific Earthquake Engineering Research Center, UC Berkeley

Bullock, Z., Dashti, S., Liel, A., Porter, K., Karimi, Z., and Bradley, B. (2017). Ground-motion prediction equations for arias intensity, cumulative absolute velocity, and peak incremental ground velocity for rock sites in different tectonic environments. *Bulletin of the Seismological Society of America*, 107(5), 2293–2309.

Bradley, B. A. (2010). A generalized conditional intensity measure approach and holistic ground-motion selection. *Earthquake Engineering & Structural Dynamics*, 39(12), 1321-1342.

Campbell, K. W., and Bozorgnia, Y. (2010). A ground motion prediction equation for the horizontal component of cumulative absolute velocity (CAV) based on the PEER-NGA strong motion database. *Earthquake Spectra*, 26(3), 635–650.

Campbell, K. W., and Bozorgnia, Y. (2012). A comparison of ground motion prediction equations for arias intensity and cumulative absolute velocity developed using a consistent database and functional form. *Earthquake Spectra*, 28(3), 931–941.

Campbell, K. W., and Bozorgnia, Y. (2014). NGA-West2 ground motion model for the average horizontal components of PGA, PGV, and 5% damped linear acceleration response spectra. *Earthquake Spectra*, 30(3), 1087-1115.

Casagrande, A. (1936). The determination of the pre-consolidation load and its practical significance. In: *Proceedings of the International Conference on Soil Mech. and Found. Eng. (ICSMFE)*, Cambridge, MA, 22–26 June 1936, vol. 3. Harvard University, Cambridge, MA, USA, pp. 60–64.

Cetin, K. O., Seed, R. B., Der Kiureghian, A., Tokimatsu, K., Harder Jr, L. F., Kayen, R. E., and Moss, R. E. (2004). Standard penetration test-based probabilistic and deterministic assessment of seismic soil liquefaction potential. *J. Geotech. Geoenviron. Eng*, 130(12), 1314-1340.

Chen, L. (2020). *Implementation, Verification, Validation, and Application of Two Constitutive Models for Earthquake Engineering Applications*. Doctoral dissertation, University of Washington.

Chen, L., and Arduino, P. (In Review) Implementation, Verification, and Validation of the PM4Sand Model in OpenSees. *PEER Report No. XXXX/XX* Pacific Earthquake Engineering Research Center, University of California, Berkeley, CA

Chiou, B. S. J., and Youngs, R. R. (2014). Update of the Chiou and Youngs NGA model for the average horizontal component of peak ground motion and response spectra. *Earthquake Spectra*, 30(3), 1117-1153.

Cornell, C. A., and Krawinkler, H. (2000). Progress and challenges in seismic performance assessment. *PEER Center News 3*. University of California, Berkeley.

Cubrinovski, M., Rhodes, A., Ntritsos, N., and Van Ballegooy, S. (2019). System response of liquefiable deposits. *Soil Dynamics and Earthquake Engineering*, 124, 212-229.

Dafalias, Y. F., and Manzari, M. T. (2004). Simple plasticity sand model accounting for fabric change effects. *Journal of Engineering mechanics*, 130(6), 622-634.

Dashti, S., and Karimi, Z. (2017). Ground Motion Intensity Measures to Evaluate I: The Liquefaction Hazard in the Vicinity of Shallow-Founded Structures. *Earthquake Spectra*, 33(1), 241-276

Golesorkhi, R. (1989). *Factors influencing the computational determination of earthquake-induced shear stresses in sandy soils*. Ph.D. thesis, University of California, Berkeley.

Greenfield, M. W. (2017). *Effects of long-duration ground motions on liquefaction hazards*. Doctoral dissertation, University of Washington.

Hanks, T. C., Abrahamson, N. A., Board, M., Boore, D. M., Brune, J. N., and Cornell, C. A. (2005). Observed ground motions, extreme ground motions, and physical limits to ground motions. In *Directions in Strong Motion Instrumentation* (pp. 55-59). Springer, Dordrecht.

Hueste, M. B. D., Kang, T. H. K., and Robertson, I. N. (2009). Lateral drift limits for structural concrete slab-column connections including shear reinforcement effects. In *Structures Congress 2009: Don't Mess with Structural Engineers: Expanding Our Role* (pp. 1-10).

Idriss, I. M. (1999). An update to the Seed-Idriss simplified procedure for evaluating liquefaction potential. *Proc., TRB Worshop on New Approaches to Liquefaction*, Publication No. FHWA-RD-99-165, Federal Highway Administation.

Idriss, I. M., and Boulanger, R. W. (2008). *Soil Liquefaction During Earthquakes*, Earthquake Engineering Research Institute, Berkeley, California.

International Code Council. (2018). International building code. Falls Church, Va.: International Code Council

Ishihara K. (1985). Stability of natural deposits during earthquakes. *Proceedings of the 11th international conference on soil mechanics and foundation engineering, vol. 1. San Francisco.* pp. 321–76.

Ishihara, K., and Yoshimine, M. (1992). Evaluation of settlements in sand deposits following liquefaction during earthquakes. *Soils and Foundations*, 32(1), 173-188.

Iwasaki, T., Arakawa, T., and Tokida, K. (1982) Simplified procedures for assessing soil liquefaction during earthquakes. *Proceedings of the conference on soil dynamics and earthquake engineering. Southampton.* pp. 925–39.

Jalayer, F. (2003). Direct probabilistic seismic anaysis: implementing non-linear dynamic assessments. *Doctoral dissertation, Stanford University.*

Juang, C. H., Ching, J., and Luo, Z. (2013). Assessing SPT-based probabilistic models for liquefaction potential evaluation: a 10-year update. *Georisk*, 7(3), 137–150.

Karimi, Z., and Dashti, S. (2017). Ground Motion Intensity Measures to Evaluate II: the Performance of Shallow-Founded Structures on Liquefiable Ground. *Earthquake Spectra*, 33(1), 277–298.

Konrad, J.-M. (1988). Interpretation of flat plate dilatometer tests in sands in terms of the state parameter. *Geotechnique* 38(2), 263-277.

Kramer, S. L. (1996) *Geotechnical Earthquake Engineering*, Prentice Hall, Upper Saddle River, New Jersey.

Kramer, S.L. (2009). "Evaluation of Liquefaction Hazards in Washington State," Washington State Transportation Center, Final Report.

Kramer, S. L., and Mayfield, R. T. (2007). Return period of soil liquefaction. *Journal of Geotechnical and Geoenvironmental Engineering*, 133(7), 802–813.

Kramer, S. L., and Mitchell, R. A. (2006). Ground motion intensity measures for liquefaction hazard evaluation. *Earthquake Spectra*, 22(2), 413–438.

Kramer, S. L., Sideras, S. S., and Greenfield, M. W. (2016). The timing of liquefaction and its utility in liquefaction hazard evaluation. *Soil Dynamics and Earthquake Engineering*, 91, 133–146.

Kramer, S., L., and Makdisi, A., J., (2017). Applicability of sliding block analyses to lateral spreading problems, *3rd International Conference on Performance-based Design in Earthquake Geotechnical Engineering (PBDIII)*, Vancouver

Krawinkler, H. (2002). A general approach to seismic performance assessment. In *Proceedings, International Conference on Advances and New Challenges in Earthquake Engineering Research* (pp. 19-20).

Kuehn N., Bozorgnia Y., Campbell K.W., and Gregor N. (2020). Partially nonergodic ground-motion model for subduction regions using NGA-Subduction database, *PEER Report No. 2020/04*, Pacific Earthquake Engineering Research Center, University of California, Berkeley, CA.

Lee, K. L., and Seed, H.B. (1967). Drained strength characteristics of sands. *J. Soil Mech. Found. Engrg. Div.*, 93(SM6), 117-141.

Luco, N., Ellingwood, B. R., Hamburger, R. O., Hooper, J. D., Kimball, J. K., and Kircher, C. A. (2007). Risk-targeted versus current seismic design maps for the conterminous United States. *SEAOC 2007 Convention Proc.*, Structural Engineers Association of California, Sacramento, CA.

Lysmer, J., and Kuhlemeyer, R. L. (1969). Finite dynamic model for infinite media. *Journal of the engineering mechanics division*, 95(4), 859-877.

Macedo, J., Abrahamson, N., and Bray, J. D. (2019). Arias Intensity Conditional Scaling Ground-Motion Models for Subduction Zones. *Bulletin of the Seismological Society of America*,109(4), 1343-1357.

Makdisi, A. J., and Kramer, S. L. (2019). Applicability of sliding block analyses for lateral spreading problems. *Soil Dynamics and Earthquake Engineering*, 124, 374-388.

Malvick, E. J., Kutter, B. L., and Boulanger, R. W. (2008). Postshaking shear strain localization in a centrifuge model of a saturated sand slope. *J. Geotech. Geoenviron. Eng.*, 134(2), 164-174.

Manzari, M. T., and Dafalias, Y. F. (1997). A critical state two-surface plasticity model for sands. *Geotechnique*, 47(2), 255-272.

Marafi, N. A., Makdisi, A. J., Berman, J. W., and Eberhard, M. O. (2020). Design strategies to achieve target collapse risks for reinforced concrete wall buildings in sedimentary basins. *Earthquake Spectra*, 36(3), 1038-1073.

Mason, H.B., Gallant, A.P., Hutabarat, D., Montgomery, J., Reed, A.N., Wartman, J., Irsyam, M., Simatupang, P.T., Alatas, I.M., Prakoso, W.A. and Djarwadi, D (2019). The 28 September 2018 M7. 5 Palu-Donggala, Indonesia Earthquake: Version 1.0. *Geotechnical Extreme Events Reconnaissance Association Report GEER-061*

Maurer, B.W., R.A. Green, M. Cubrinovski, and B.A. Bradley. (2014). Evaluation of the liquefaction potential index for assessing liquefaction hazard in Christchurch, New Zealand. *J Geotech Geoenviron Eng* 140(7), 04014032

Maurer, B.W., R.A. Green, and O.-D.S. Taylor. (2015). Moving towards an improved index for assessing liquefaction hazard: lessons from historical data. *Soils and Foundations*, 55(4), 778-787.

Mayfield. R.T. (2007) *The return period of soil liquefaction.* Ph.D. dissertation, Department of Civil and Environmental Engineering, University of Washington.

McGann, C. R., Arduino, P., and Mackenzie-Helnwein, P. (2012). Stabilized single-point 4-node quadrilateral element for dynamic analysis of fluid saturated porous media. *Acta Geotechnica*, 7(4), 297–311.

McKenna, F., Scott, M. H., and Fenves, G. L. (2010). Nonlinear Finite-Element Analysis Software Architecture Using Object Composition. *Journal of Computing in Civil Engineering*, 24(1), 95–107.

Moehle, J., and Deierlein, G. G. (2004). A framework methodology for performance-based earthquake engineering. In *13th world conference on earthquake engineering*(Vol. 679).

Mogami, T., and Kubo, K., (1953). The Behaviour Of Soil During Vibration *Proceedings of the Third International Conference on Soil Mechanics and FoundationEngineering*, (1), 152-153.

Moss, R. E., and Hollenback, J. C. (2009). Discussion of "Analyzing Liquefaction-Induced Lateral Spreads Using Strength Ratios" by SM Olson and CI Johnson. *J. Geotech. Geoenviron. Eng.*, 135(12). 2006-2008.

Olson, S. M., and Johnson, C. I. (2008). Analyzing liquefaction-induced lateral spreads using strength ratios. *J. Geotech. Geoenviron. Eng.*, 134(8), 1035-1049.

Park, D., and Kutter, B. L. (2009). Discussion of "Analyzing Liquefaction-Induced Lateral Spreads Using Strength Ratios" by SM Olson and CI Johnson. *J. Geotech. Geoenviron. Eng.*, 135(12), 2008-2010.

Parker G.A., Stewart J.P., Boore D.M., Atkinson G.M., and Hassani B. (2020). NGA-subduction global ground motion model with regional adjustment factors, *PEER Report No. 2020/03*, Pacific Earthquake Engineering Research Center, University of California, Berkeley, CA.

Petersen M. D. Moschetti M. P. Powers P. M. Mueller C. S. Haller K. M. Frankel A. D. Zeng Y. Rezaeian S. Harmsen S. C., and Boyd O. S., et al. (2014). Documentation for the 2014 update of the United States national seismic hazard maps, *U.S. Geol. Surv. Open-File Rept.* 2014-1091 , 243

Potts, D. M., and Zdravković, L. (1999). Finite Element Analysis in Geotechnical Engineering: Theory, 34 Thomas Telford.

Rauch, A. F. (1997). *EPOLLS: an empirical method for prediciting surface displacements due to liquefaction-induced lateral spreading in earthquakes* (Doctoral dissertation, Virginia Tech).

Rauch, A. F., and Martin III, J. R. (2000). EPOLLS model for predicting average displacements on lateral spreads. *Journal of Geotechnical and Geoenvironmental Engineering*, 126(4), 360-371.

Seed, H.B., and Idriss, I. M. (1971). Simplified procedure for evaluating soil liquefaction potential. *J. Soil Mech. Found. Engrg. Div.*, 107 (SM9) 1249-1274

Shahi, S. K., and Baker, J. W. (2014). An efficient algorithm to identify strong-velocity pulses in multicomponent ground motions. *Bulletin of the Seismological Society of America*, 104(5), 2456-2466.

Shome, N., and Cornell, C. A. (1999). Probabilistic seismic demand analysis of nonlinear structures. *Report no. RMS-35. Research Management System (RMS) Program*, Department of Civil Engineering, Stanford University, Stanford, CA.

Strasser, F. O., Bommer, J. J., and Abrahamson, N. A. (2008). Estimating ground-motion variability: Issues, insights and challenges. In *Proceedings of the 14th World Conference on Earthquake Engineering.*

Texas Advanced Computing Center (TACC). The University of Texas at Austin

Van Ballegooy, S., P. Malan, V. Lacrosse, M. E. Jacka, M. Cubrinovski, J. D. Bray, T. D. O'Rourke, S. A. Crawford, and H. Cowan. (2014). Assessment of liquefaction-induced land damage for residential Christchurch. *Earthquake Spectra*, 30(1), 31-55.

Yoshida, N., Tazoh, T., Wakamatsu, K., Towhata, I., Nakazawa, H., and Kiku, H. (2007). Causes of Showa Bridge collapse in the 1964 Niigata earthquake based on eyewitness testimony. *Soil and Foundations* 47(6), 1075-1087

Yoshimine, M., and Ishihara, K. (1998). Flow potential of sand during liquefaction. *Soils and Foundations*, 38(3), 189-198.

Youd, T. L. (1972). Compaction of sands by repeated shear straining. *J. Soil Mech. Found. Engrg. Div.*, 98(7), 709-725.

Youd, T. L., Hansen, C. M., and Bartlett, S. F. (2002). Revised multilinear regression equations for prediction of lateral spread displacement. *J. Geotech. Geoenviron. Eng.*, 128(12), 1007-1017.

Youd, T. L., Steidl, J. H., and Nigbor, R. L. (2004). Lessons learned and need for instrumented liquefaction sites. *Soil Dynamics and Earthquake Engineering*, 24(9-10), 639-646.

Zhang, G., Robertson, P. K., and Brachman, R. W. I. (2004). Estimating liquefaction-induced lateral displacements using the standard penetration test or cone penetration test. *J. Geotech. Geoenviron. Eng.*, 130(8), 861-871.

Zhu, M., McKenna, F., and Scott, M. H. (2018). OpenSeesPy: Python library for the OpenSees finite element framework. *SoftwareX*, 7, 6–11.